The Dissertation Committee for Thomas William Jarvis
certifies that this is the approved version of the following dissertation:

Novel Tools for Ultrafast Spectroscopy

Committee:

Xiaoqin Li, Supervisor

Manfred Fink

John Keto

Sang-Hyun Lim

Chih-Kang Shih

Greg Sitz

Novel Tools for Ultrafast Spectroscopy

by

Thomas William Jarvis, B.S.

DISSERTATION

Presented to the Faculty of the Graduate School of

The University of Texas at Austin

in Partial Fulfillment

of the Requirements

for the Degree of

DOCTOR OF PHILOSOPHY

THE UNIVERSITY OF TEXAS AT AUSTIN

December 2011

Dedicated to my late friend Edward J. O'Leary, Jr.

Acknowledgments

This project would be impossible without the guidance and expertise of my advisor, Dr. Xiaoqin 'Elaine' Li. She is an excellent scientist and role model, and a patient advisor. I would also like to thank my coworkers in Elaine's group, my fellow graduate students in the Department of Physics at the University of Texas, and the outstanding professors under whom I studied there. I particularly wish to thank Professors Gleeson and Fink for demonstrating so consistently why becoming a physicist is a good idea.

An experimentalist at Texas succeeds only due to the exceptional support of the Machine and Cryo Shop staff; it is impossible for me to overstate their efforts, or those of all the staff in the Department of Physics.

To my colleagues, friends, and family I simply extend the invitation 'Veni ad litus, conveniemus, paulum ridebimus.'

Novel Tools for Ultrafast Spectroscopy

Publication No. _____

Thomas William Jarvis, Ph.D.
The University of Texas at Austin, 2011

Supervisor: Xiaoqin Li

Exciton dynamics in semiconductor nanostructures are dominated by the effects of many-body physics. The application of coherent spectroscopic tools, such as two-dimensional Fourier transform spectroscopy (2dFTS), to the study of these systems can reveal signatures of these effects, and in combination with sophisticated theoretical modeling, can lead to more complete understanding of the behaviour of these systems.

2dFTS has previously been applied to the study of GaAs quantum well samples. In this thesis, we outline a precis of the technique before describing our own experiments using 2dFTS in a partially collinear geometry. This geometry has previously been used to study chemical systems, but we believe these experiments to be the first such performed on semiconductor samples. We extend this technique to a reflection mode 2dFTS experiment, which we believe to be the first such measurement.

In order to extend the techniques of coherent spectroscopy to structured systems, we construct an experimental apparatus that permits us to control

the beam geometry used to perform four-wave mixing reflection measurements. To isolate extremely weak signals from intense background fields, we extend a conventional lock-in detection scheme to one that treats the optical fields exciting the sample on an unequal footing. To the best of our knowledge, these measurements represent a novel spectroscopic tool that has not previously been described.

Table of Contents

List of Figures

Chapter 1

Introduction

We develop nonlinear optical spectroscopic tools to study semiconductor nanostructures. This thesis is divided into several sections, which we note here.

In the first chapter, a basic history of condensed matter physics is presented, with emphasis on those points relevant to the nonlinear optical spectroscopy of semiconductors. A review of energy bandstructure is presented first. The conduction and valence bands of states are then approximated as discrete levels near the band edge, developing a model of optical excitation. Linear absorption is considered, first neglecting the interaction of the constituent carriers. Including the residual Coulomb interaction between holes and electrons, the hydrogenic exciton picture is used. Phonons are briefly considered, due to the significance of scattering by the acoustic phonon population at low temperatures. The modified behaviour of the electronic states is then considered in the context of discrete nanostructures, viz. quantum wells.

A review of the basics of light-matter coupling is provided in the second chapter of this thesis. A classical analysis is used to study the Lorentz model of atomic absorption. While this simply model has some surprising predictrive

value, it is considered first in order to develop an intuitive understanding of light absorption, emission, and the relaxation of excited states. A corresponding quantum mechanical model is described, then used to consider a system's nonlinear optical response. The utility and validity of the desntiy operator as a tool to study nonlinear optical processes is considered, and the geometric Feynman-Bloch vizualisation model is described due to its frequent use in the study of photon echoes and other nonlinear optical effects.

The third chapter contains a selected history of exciton optics, first considering the analogous spectroscopic tools developed in nuclear resonance. Spin echoes, four-wave mixing, and transient gratings are described. Four-wave mixing optical experiments are then described. The use of self-diffracted four-wave mixing measurements to extract dephasing times is explained. Reflection geometry measurements are noted, and the results of some simple three-pulse four-wave mixing measurements are provided. Time-resolved four-wave mixing results are presented. An analysis of these prevoius results recounts the failure of a simple, non-interacting density matrix model to describe these systems.

The fourth chapter provides some background on three-pulse four-wave mixing measurements and the previous studies of coupling and interaciton among excitons optically created in semiconductor quantum wells. We then outline the basic principles of two-dimensional Fourier transform spectroscopy, a powerful experimental method that provides more conclusive results than prior, simpler four-wave mixing measurements. Various experimental and technical details are considered. We present some results obtained in our group

using two-dimensional Fourier transform spectroscopy to study the coupling of excitons, before turning our attention to another implementation of this technique, using a different phase-matching geometry. We consider the various issues relevant to performing two-dimensional Fourier transform spectroscopy in this geometry, before presenting data collected in both a conventional transmission and novel reflection geometry. We consider the benefits of performing this measurement in the partially collinear geometry.

The fifth chapter describes a novel, three-pulse, four-wave mixing spectroscopic method we developed. We hope to eventually apply this method to the study of complicated, structured samples not conducive to study with simpler four-wave mixing techniques. This technique makes use of a three-frequency modulation scheme that permits the phase-sensitive detection of the signal of interest necessary to implement two-dimensional Fourier transform spectroscopy or other sophisticated coherent techniques.

Chapter 2

Elementary condensed matter physics

2.1 Bloch theory and the band structure of solid state matter

The motion of electrons in a solid, even a periodic material, is extremely complicated in its full analysis. From this point, we assume that the Born-Oppenheimer approximation has been made to allow us to separate nuclear and electronic dynamics, due to the vastly differing time scales in which those effects occur. This reduces the complexity of the problem, which can be expressed with a simplified Hamiltonian

$$H = \sum \frac{p_i^2}{2m} + \frac{1}{2} \sum_{i \neq j} \frac{e^2}{|r_i - r_j|} + \sum_{n,i} V_n(r_i - R_n)$$

containing kinetic energy, electron-electron Coulomb interaction, and a periodic crystal potential [77]. Even with this simplification, the behaviour of this system as presented is still an intractable many-body problem.

If we also assume the validity of the Hartree approximation we may then approximate the many-body electron-electron interaction problem with an effective mean field theory description that simplifies the physics to a single electron's interaction with a fictitious potential approximating the actual

interaction (see, for example, [17]. The specific form of this interaction is considered elsewhere; for now we consider the effect of the interaction of that single electron with the ionic crystal lattice.

The interaction between that electron and those ionic cores is embedded in the crystal potential, here simply $V(\mathbf{r})$, which necessarily exhibits the same periodicity as the crystal lattice it describes. The problem of understanding that interaction can be expressed with the simplest Schrodinger equation

$$\left[-\frac{\hbar^2}{2m}\nabla^2 + V(\mathbf{r})\right]\psi(\mathbf{r}) = E\psi(\mathbf{r})$$

where strictly speaking, the potential is an operator and should take a carat to denote that fact. We have omitted this particular proper notation as it is familiar to all students of quantum mechanics. The only assumption made thus far is that the potential is periodic.

If the crystal potential arises due to a periodic lattice of ions that exhibits all the symmetry of the ideal crystal structure, it is a relatively straightforward matter to decompose that potential using a Fourier series, making use of the reciprocal lattice vectors $\{\mathbf{G}\}$

$$V(\mathbf{r}) = V(\mathbf{r}+\mathbf{R}) = \sum_{\mathbf{G}} c_{\mathbf{G}} e^{i\mathbf{G}\cdot\mathbf{r}}$$

where the first equality obtains trivially due to the symmetry of the crystal under translation by any real space lattice vector $\mathbf{R}$, and the $c_{\mathbf{G}}$ are

simply the coefficients of the Fourier decomposition of the crystal potential. Without specifying the exact form of the eigenfunction $\psi(\mathbf{r})$, we may decompose it in a similar fashion,

$$\psi(\mathbf{r}) = \sum_{\mathbf{q}} a_{\mathbf{q}} e^{i\mathbf{q}\cdot\mathbf{r}}$$

The exact form of the coefficients $a_{\mathbf{q}}$ will depend on how precisely we define the boundary conditions and Fourier transform from the real to the reciprocal space. These details are not important to our current goal, which is to develop an intuitive understanding of how electrons propagate in crystals (or indeed, how any single particle Schrodinger equation may be solved for a periodic, non-pathological potential).

If that Fourier series is re-written so that every wave vector $\mathbf{q}$ is expressed instead as the sum of some reciprocal lattice vector $\mathbf{G}$ added to a wavevector restricted to take on values only in the first Brillouin zone, $\mathbf{q} = \mathbf{k} + \mathbf{G}$, the resulting ansatz may be substituted into the Schrodinger equation along with the decomposition of the crystal potential to yield, after some algebra, the secular equation

$$\left(\frac{\hbar^2 |\mathbf{k}+\mathbf{G}|}{2m} - E\right) a_{\mathbf{k}+\mathbf{G}} + \sum_{\mathbf{G}'} a_{\mathbf{k}+\mathbf{G}'} c_{\mathbf{G}-\mathbf{G}'} = 0$$

which, for any given wave vector $\mathbf{k}$ defines a set of equations, with the sets members enumerated by the Fourier component $\mathbf{G}$ in the Fourier decomposition of the wavefunction $\psi(\mathbf{r})$. Thus,

$$\psi_k(\mathbf{r}) = \sum_{\mathbf{G}} a_{\mathbf{k}+\mathbf{G}} e^{i(\mathbf{k}+\mathbf{G})\cdot\mathbf{r}} = e^{i\mathbf{k}\cdot\mathbf{r}} \sum_{\mathbf{G}} a_{\mathbf{k}+\mathbf{G}} e^{i\mathbf{G}\cdot\mathbf{r}} = e^{i\mathbf{k}\cdot\mathbf{r}} u_{\mathbf{k}}(\mathbf{r})$$

This shows that the wavefunction that provides a solution to this Schrodinger's equation is a plane wave with momentum $\mathbf{k}$, modulated by a function $u_{\mathbf{k}}$ that inherits the periodicity of the crystal. In developing this solution, note, we restricted the allowed values of the wave vector $\mathbf{k}$ to the first Brillouin zone, i.e. the Wigner-Seitz cell of the reciprocal lattice (e.g., for a simple cubic lattice with lattice constant a, that amounts to restricting the wave vector to $\{-\pi/a,\ \pi/a\}$ (we note in passing that another equivalent formulation of the Bloch problem would result in a Brillouin zone of identical size, but which would run from m 0 to π/a)).

It is relatively straightforward conceptually to calculate a solution to the Schrodinger equation for an arbitrary periodic crystal potential at this point. Nontrivial solutions may be found by setting the determinant of the matrix of coefficients of $a_{\mathbf{k}+\mathbf{G}}$ to zero,

$$\left\| \left(\frac{\hbar^2 |\mathbf{k}+\mathbf{G}|^2}{2m} - E \right) \delta_{\mathbf{G},\mathbf{G}'} + c_{\mathbf{G},\mathbf{G}'} \right\| = 0$$

Though in actual practice, band structures will most often be calculated using other algorithms. The true importance of this result is that it provides us with useful information regarding the form that the eigenfunctions will take subject to a periodic crystal potential. We also learn that restricting our

analysis to the first Brillouin zone does not neglect any physically significant solutions, since those within our scope already are a complete basis set. Any wavefunction – not necessarily an eigenfunction of the Hamiltonian – may be decomposed using this basis.

We note that by finding momentum eigenstates in the Bloch analysis, we have, as a result, developed a set of eigenfunctions that are completely delocalized in real space, due to the Heisenberg uncertainty principle. Any localization that may occur in a physically realizable system – due to breaking of the infinitely spatially extending, perfect crystal symmetry, for example – will require the formation of wave-packets out of these Bloch basis functions. Depending on the degree of localization that occurs, then – or, stated another way, depending on how many momentum eigenstates must be summed in order to approximate the behaviour of a particle exhibiting a certain degree of localization in real space – the Bloch solutions permit a particle to effectively sample a certain extended volume in real space. For perfect crystal systems where particle lifetimes are infinite, the Bloch eigenfunctions are themselves accurate descriptions of the particle's behaviour, and that particle will sample all of the space. If a particle is localized to only a single atomic site, a very large number of these eigenfunctions will necessarily be coherently added in order to approximate its distribution in real space. The delocalized Bloch functions would propagate perfectly through an ideal crystal; it is only deviation from the periodicity of this mathematical construct that results in scattering and particle localization.

Solution of the Bloch problem yields a single electron dispersion relationship, relating the energy of an electron to its momenta in the reciprocal lattice space defined by the Fourier transform of the real space crystal lattice. Often, this relationship, $E_n(\mathbf{k})$, where the label n denotes any other pertinent quantum numbers needed to distinguish the electron state, is referred to itself as the band structure of the material. A substantial fraction of the information necessary to understand the behaviour of carriers in a material is encoded in the band structure.

Typically, we do not need to consider the full band structure of a semiconductor material in order to understand the optical response of the system. When using laser excitation near or below the band gap energy of a direct gap semiconductor, it is usually possible to simply consider the bottom of the conduction band and the maxima of the valence bands. In Gallium Arsenide, we only concentrate on the nearly parabolic band extrema centered on the $|\mathbf{k}| \sim 0$ region of the dispersion relation.

2.2 Optical electronic and excitonic excitation

The discussion presented here depends heavily upon[17], [270], and [307], and [5].

There is of course significant general interest in studying the optical properties of a semiconductor for their potential application or development. In our own experimental program, however, instead exploit use those properties of these bulk or structured materials (in the case of semiconductor quan-

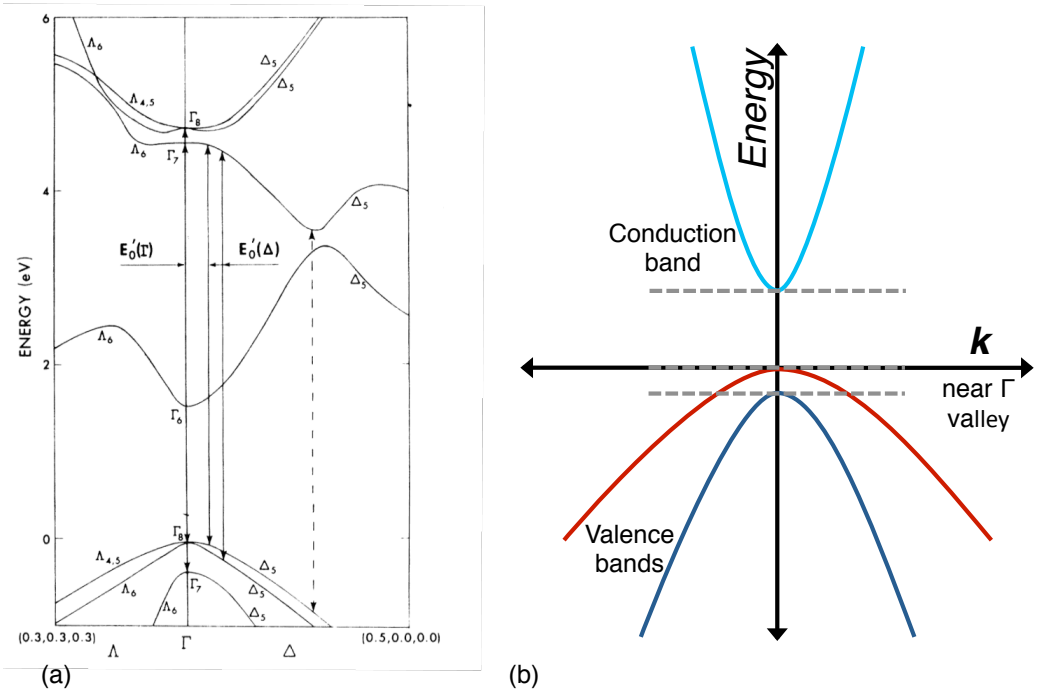

Calculated band structure for GaAs (a), reproduced from Chelikowsky and Cohen, Phys. Rev. Lett. 32:674 (1974), and a cartoon sketch of the band extrema near the bad gap (b). The third conduction band in the calculation is not reproduced in the cartoon because it is sufficiently separated in energy and is thus neglected.

Figure 2.1: GaAs band structure

tum nanostructures) to determine how the constituent particles and excitations that comprise the sample interact with light, themselves, and the bulk material.

We know that the colour and transparency of a material is related to its electronic properties. Light absorption and emission is related to the imaginary part of the susceptibility. The most significant parameter necessary to describe the opto-electronic properties of a semiconductor is its bandgap, but this alone cannot explain the complexity of the spectral features that such materials exhibit in the neighbourhood of that energy. The electron dynamics of carriers are closely connected to these optical properties, and a discussion of the interaction of light with electrons, holes, and electron-hole pairs is necessary to understand the means by which these processes give rise to observable, macroscopic effects.

The linear absorption spectrum of a semiconductor near its bandgap is dominated by two features: a set of discrete, sharp lines at lower energies, and an essentially smooth continuum at higher photon energies. One of the most significant absorption processes to occur is the destruction of a photon, the quantum of light, the destruction of an electron in a valence band state, the creation of a hole in the corresponding state, and the creation of an electron in the conduction band. The sharp, well-defined feature (or features, as in some semiconductor materials only one such peak can be differentiated from the nearby continuum feature) is due to the presence of an exciton.

An exciton is a hydrogenic, bound electron-hole pair. Given that one

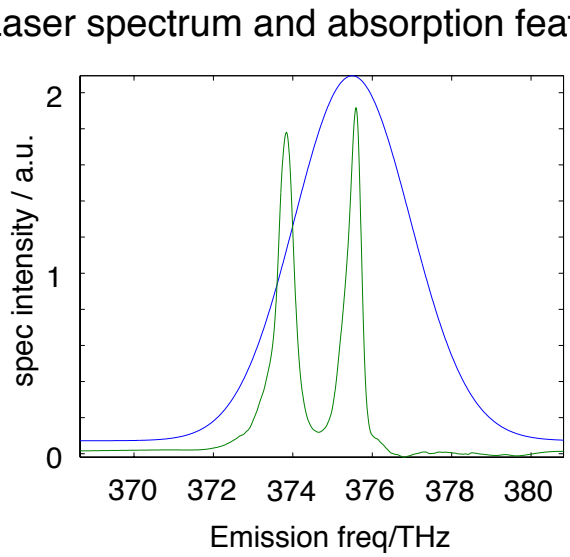

Laser spectrum (blue) used to study the optical response of a GaAs semiconductor quantum well and the corresponding absorption spectrum (green) showing heavy-hole and light-hole exciton resonances (in order of increasing energy). The two curves are not drawn to the same scale.

Figure 2.2: GaAs quantum well linear absorption spectrum

of its constituent particles is, in fact, a quasi-particle, the exciton itself is ipso facto a quasi-particle. Also, since the hole itself is used to simplify the many-body physics of an electron promoted into an excited state interacting with all those other electrons in a solid that remain in the ground state, the exciton itself is actually a scheme used to simplify many-body physics in a material.

A description of the infrared spectra of semiconductors, which may be related to phonon processes in IR optically active materials, is reasonably well approximated by models that assume a more or less instantaneous response of the system to an optical field. Since light at that frequency couples effectively to the lattice vibration modes, and since nuclear motion often tends to so be sufficiently slow that a classical description of such processes does not introduce enormous errors, a simple treatment of IR processes using classical equations of motion is an excellent starting point. As the frequency of electromagnetic oscillation approaches the visible portion of the spectrum, however, one may no longer assume an instantaneous system response to the electromagnetic field. Significant dispersion and absorption are exhibited by the electronic polarizability of materials under such conditions. The effect of the light on a semiconductor crystal is mediated by the interatomic interactions that will occur in the solid – the result is an electric polarization field that may propagate through the material. Exciton may be viewed as quasi-particles used to model such a system [271].

2.2.1 Linear absorption

We will consider first the case of photons with sufficient energy to create free carriers in a semiconductor. The absorption of a photon with energy greater the bandgap of a semiconductor results in the annihilation of an electron in the filled valence band, the creation of an electron in the empty conduction band, and the creation of a hole in one of the hole bands. We are being careful here in our exact nomenclature: it would not be correct to say that the hole is created in the vacancy left in the electron valence band – the hole is a free carrier in the material, and thus it would only be logical to label the relevant band a conduction band. The confusion over the labeling seems to this author to arise from a casual use of two different paradigms for discussing phenomena in condensed matter systems. The language we have used here is that of the second quantization formalism, where we describe these physical processes at creation and annihilation events. We chose to do so because, as a matter of fact, all the particles discussed are in fact quasi-particles, and not truly physically substantial in the same way that an isolated particle would be – even the electron, in any band in any material, is not really an electron, but an unfortunately named quasi-particle. The distinction lies in the fact that we frequently treat its behaviour as an isolated particle with a different mass than the bare electron have; therefore, even in our single electron wavefunctions (for example) we are implicitly using a quasi-particle description of the

processes that are occurring in a many-body system[1]. The second possible way to describe these processes is to refer to an electron being excited from one state to another, as we would in a simple atomic system with far fewer degrees of freedom – but strictly speaking, in that case there is no reason to refer to the creation of a hole. It is the casual mixing of these two different descriptions that leads to confusion. But we digress.

The electron and hole in their respective bands are attracted to each other via the Coulomb interaction. These Coulomb effects affect the resulting band-edge absorption and result in the formation of excitons, to be treated somewhat later. Although the simplification of the many-body dynamics that is gained in going to an electron-hole picture of the system are designed to obviate the further consideration of interaction among the constituent particles of an excited solid, the residual Coulomb interactions (and indeed, other effects that give rise to excitonic nonlinearities) are found to be of great significance in predicting the system's physical behaviour.

To understand these effects, we first consider the treatment of linear optical properties, specifically band-edge absorption, related to the creation of free electron-hole pair but neglecting the Coulomb interaction. We do not

[1]For further see, for example, [159], or [372] with its now endearing insistence on adhering to the 1947 Congress of the International Union of Physicists proclamation that electrons and positrons were henceforth to be known as 'negatons' and 'positons,' respectively, and that the two were both taxonomically 'electrons.' Our current difficulties with hole band names is in essence no different; though not physically significant, it is a problem of some confusion in scientific correspondence. More troubling is the consistent mis-plotting of hole energy bands – these should be the additive inverse of the electron energy bands that are usually mislabelled as hole bands [307].

expect these results to closely mimic the real spectrum, which we already know exhibits the effects of Coulomb interaction in the fingerprint of excitonic absorption lines – and, though we may not be aware of it so immediately, in the changed shape of the continuum absorption feature – but this analysis does serve as a starting point for understanding these physical processes.

2.2.2 Linear absorption without Coulomb interaction

Optical effects of semiconductors depend greatly upon the band structure of the material in question. The division into direct band gap semiconductors, such as GaAs, GaSb, GaN, InP, for example, and indirect gap semiconductors, such as diamond, Si, Germanium, or AlGaP, for example, is significant for optical interactions. Photon emission and absorption processes require the simultaneous conservation of momentum and energy. In a transition in a direct gap material, then,

$$\begin{aligned} E_i + \hbar\omega_i &= E_f \\ \hbar\mathbf{k}_i + \hbar\mathbf{q} &= \hbar\mathbf{k}_f \end{aligned}$$

where the wave vector $\mathbf{q}$ of the photon will typically be small compared to the wave vectors of the electron. It is generally sufficiently small that it can be neglected in the analysis of momentum conserving transitions [270]. As a result, in a direct gap material it is necessary only to ensure that energy is conserved and that the initial and final momenta of the electron are equal.

In the absence of Coulomb interaction, a semiconductor should be transparent to light that does not have sufficient energy to promote an electron to the conduction band. Optical transitions in direct band gap semiconductors should connect states that are vertically aligned in the plot of the dispersion relation. The absorption coefficient for photons with more than the bandgap energy can be very high in direct gap materials, from 10^4 to 10^5 cm^{-1} – thus only a few microns of material typically suffices for a sample to be opaque [270].

Transitions that occur in indirect gap materials will typically satisfy the momentum and energy conservation requirements with the involvement of another quasi-particle, most frequently a phonon. It is possible to have a direct transition occur in a semiconductor if the photon involved is sufficiently energetic to lift a photon from its initial state to one with equal momentum at a higher energy than the conduction band minimum.

We use a semiclassical approach to describe the absorption process, where the optical field will be represented without quantization, but a quantum mechanical analysis will be used to describe the behaviour of matter. This suffices to describe many optical processes, but cannot reproduce the effects that depend upon the quantum mechanical nature of the electric field, such as the spontaneous emission rate. We are interested in the behaviour of the system in the linear regime, where the material response to the optical field is independent of the intensity of the incident field.

Starting with a prototypical Hamiltonian for the interaction of a charged

particle with an electromagnetic field

$$\hat{H} = \frac{1}{2m_0}\left(\mathbf{p} - \frac{e}{c}\mathbf{A}\right)^2 + + e\phi + V_{crystal}\left(\mathbf{r}\right)$$

[206] , [270], [195], [142]) where the electron momentum is $\mathbf{p} = m_{effective}\mathbf{v}$ (i.e. not the crystal momentum but the actual momentum of the electron), $\mathbf{A}$ is the vector potential of the electromagnetic field and ϕ is the electric potential. The quantity $V_{crystal}$ is simply referred to as a periodic potential energy function, but if we consider our previous discussions it is apparent that in this single electron Hamiltonian this potential necessarily contains the interaction between the electron and the crystal lattice as well as an effective mean field potential to account for the interaction with all the other electrons in the material. In the appropriate gauge, this Hamiltonian simplifies to

$$\hat{H} = \frac{p^2}{2m_0} + V_{crystal}\left(\mathbf{r}\right) - \frac{e}{m_0 c}\mathbf{A}\cdot\mathbf{p} + \frac{e^2}{2m_0 c}\mathbf{A}^2 \sim \frac{p^2}{2m_0} + V_{crystal}\left(\mathbf{r}\right) - \frac{e}{m_0 c}\mathbf{A}\cdot\mathbf{p}$$

where the last term may typically be neglected in the linear regime (typically for intensities less than $10^6\,\mathrm{Wcm}^{-2}$ [270]. This leaves only one term describing the coupling between the light and matter, the last term on the righthand side of the equation. It is generally more amenable to calculate in the coordinate space rather than the momentum space; it may be shown that the interaction Hamiltonian is written in that space as

$$\hat{H_{int}} = -\mu\cdot\mathbf{E}$$

(see, for example, [406], [40], [95]). From this interaction Hamiltonian it is a relatively straightforward process to calculate a transition rate via Fermi's golden rule. The absorption coefficient that is derived from this transition rate is

$$\alpha(\omega) = \frac{\hbar\omega}{\pi nc} \left|\langle\varphi_c| e\mathbf{r}\cdot\mathbf{E}|\varphi_v\rangle\right|^2 \int_0^\infty d\omega_{cv} g(\omega_{cv}) \delta(\hbar\omega_{cv} - \hbar\omega)$$

where the integrand contains the density of states $g(\omega_{cv})$ and the Dirac delta function ensures conservation of energy. The index of refraction n enters from the time-averaged Poynting vector, which is used in this calculation to relate incident power of the beam to the strength of its electric field while propagating through a dielectric medium.

In the case of a direct transition, such as we are most interested in for our studies of GaAs semiconductor materials, we have assumed that the conservation of momentum is essentially automatically satisfied and ignore the momentum of the photon. Near the Γ point in the Brillouin zone, the absorption coefficient may be shown to be

$$\alpha = \frac{2}{nc} \left|\langle\varphi_c| e\mathbf{r}\cdot\mathbf{E}|\varphi_v\rangle\right|^2 \left(\frac{2m_{reduced}}{\hbar^2}\right)^{3/2} \left\{\theta(\hbar\omega - E_g)(\hbar\omega - E_g)^{1/2}\right\}$$

where the reduced mass term refers to the reduced mass of the electron-hole pair. Of significance to spectral analysis are the terms in the curly braces.

Note that there is hard 'turn-on' of absorption occurring, as expected, when the photon energy exceed the band gap of the semiconductor. From that point, the absorption should increase smoothly in intensity as the square root of the photon energy increase. The interband transition matrix element will depend on the specifics of the material under consideration and the electric field.

We are less concerned with indirect transitions, since our studies have concentrated on a direct band gap semiconductor. Nonetheless, due to the manner in which phonons contribute to the excitonic transition properties of direct gap semiconductors under certain conditions, it behooves us to briefly mention an analogous result for indirect gap semiconductors.

In such a material, the momenta of the highest occupied states, at the top of the valence band, is substantially different from the momenta of the lowest unoccupied states in the conduction band. This difference cannot be discounted, as in direct gap materials, and transitions cannot occur unless mediated by another quasi-particle with well-defined momentum that permits satisfaction of momentum-energy conservation requirements. Generally, transitions between the two bands at the lowest possible photon energy will require the emission or absorption of a phonon. This process is by definition a second order quantum mechanical process, involving two quanta of different fields. As a result, such a process is typically several orders of magnitude weaker than the transition rates exhibited by direct bandgap semiconductors. This difference essentially lies at the heart of the preference for direct gap materials in optoelectronic applications.

Since the photon absorption process may be mediated by either the absorption or emission of a phonon, it is necessary to calculate an absorption coefficient for each of those two possible mechanisms. The result is

$$\alpha = A' \left\{ \frac{\left(\hbar\omega - E_g + \hbar\Omega\right)^2}{e^{\hbar\Omega/k_B T} - 1} + \frac{\left(\hbar\omega - E_g - \hbar\Omega\right)^2}{1 - e^{-\hbar\Omega/k_B T}} \right\} \theta\left(\hbar\omega - E_g \pm \hbar\Omega\right)$$

[270]. Again, we see a hard 'turn-on' of the phonon-mediated absorption process, although here there are two different effects that contribute and which occur at two different photon energy – if phonon absorption occurs, the energy of the phonon contributes to the optical transition and lowers the energy from the band gap. If phonon emission occurs, the extra energy must come from the optical field, and so only photons with that excess in addition to the band gap can cause transitions to occur. The coefficient A' contains the quantum mechanical parameters related to the transition matrix elements for photon and phonon processes. Note that the predicted functional form for phonon-mediated indirect gap absorption is quadratic in photon energy – a significant difference from the square-root energy dependence of direct gap absorption.

As noted above, however, both of these models for absorption neglect the Coulomb interaction between the created hole and electron pair. This interaction actually leads to the most dominant band edge absorption features, and significantly alters the functional form of the continuum absorption feature. An interesting historical note is that the residual Coulomb attraction

between the hole and electron, once accounted for with the excitonic description of optical transitions in semiconductors, still fails to capture the full detail of the system's dynamics – further attention must be paid to the residual Coulomb interaction among excitons. Other physical processes will also affect the nonlinear spectrum, certainly, but the residual Coulomb coupling between excitons is one of the most significant effects.

2.2.3 The exciton quasi-particle and optical absorption

The Coulomb interactions among electrons and holes significantly affects the optical response of a crystal at photon energies near the bandgap. It lowers the energy at which stops being transparent and begins to absorb photons. A full analysis of optical transitions at energies near the bandgap requires consideration of the Coulomb interaction between the electron and hole quasiparticles.

The most significant result of the Coulomb interaction is the formation of an exciton, another quasiparticle. The exciton is a hydrogenic system, with a positively charged particle (hole) and a negatively charged particle (electron) bound by an attractive potential. Many of the results from the analysis of the hydrogen atom are almost directly applicable to the study and understanding of the exciton, with only certain specific changes in the constants used (to the mass, to the dielectric constant, etc). The exciton is an electrically neutral particle, and can move easily through the crystal, as an atom would move through free space. We note that this is consistent with

the language we have used thus far, in which a quasi-particle in a solid has a well-defined wave vector associated with its propagation. The departures from that quasi-particle propagation behaviour occur due to physical defects (crystal defects such as impurities, vacancies, or dislocations [399], and even the finite size of a crystal) in the materials that can actually be realized in a laboratory environment. In addition to the by now many-body complexity of the real crystals, even the zero point motion of the sample's constituent particles would complicate the nature of the system, even in the ideal limit of a perfect crystal sample of infinite size [92].

As we recall from our high school chemistry, bonding processes result in the liberation of energy, while the dissolution of a bond requires the addition of extra energy from outside the system. In the context of the exciton, the 'final' product (the bound, hydrogenic electron-hole system) is a lower energy state than the 'initial' product, the unbound electron and hole. We feel compelled to use the scare quotes to indicate that we need not think of exciton formation as a process that takes time – it is not necessary to create a free electron-hole pair and wait for those two quasi-particles to dissipate some energy, relaxing into a bound state. Instead, it is possible for the exciton to be formed directly by absorption of a photon. This allows absorption of photons with less energy than the material's bandgap to when the conservation of energy permits the formation of an exciton.

The concept of the exciton was first proposed Yakov (sometimes transliterated as from the Russian as Jacov) Frenkel in 1931. His work was aimed at

showing that the absorption of light by an isolated atom was not an accurate picture of the actual process as it occurred in a solid, but rather that the absorption would be possible via excitation waves that he viewed as similar to those acoustic used to describe thermal motion in the crystal. He describes this excitation as a superposition of degenerate states wherein only one member of a set of atoms (or molecules) would move from its ground to excited state, and notes that a number of such N-fold degenerate states [92] could be summed together to produces an excitation packet – what we might call a wave packet – that, which is in essence, an exciton. While in an isolated atom a resonant external field would result in the mixing of two different quantum states – for example, the coupling of an s- and p-orbital. The extent of that coupling is determined by the detuning of the driving radiation field from resonance with the energy difference between the two states, as well as by the strength of the interaction of the light with the electron of interest (in a single-electron picture) and the interplay of interaction with those other charged particles in the atom; after the external perturbation is removed, the atom would oscillate, with the frequency of the polarization oscillation determined by the energy difference of the two states. If instead of an isolated atom, however, an atom in a crystal lattice were similarly perturbed, the degeneracy of its atomic energy levels with those of the other constituent atoms would allow the excitation to propagate from one atom to another through the material [271].

Perhaps because of his interest in thermal processes, which Frenkel seems to see as intimately tied to the absorption process (in his time the

ultrafast experiments that permit the study of any but the very long-time behaviours of a population of excitons would be, of course, quite impossible) he notes that the coupling of excitons to phonons would allow the dissipation of absorbed light by heating of the material, via a radiationless transition. Discounting in his model the possibility of strong coupling among adjacent atoms, Frenkel restricts his treatment to non-metals, and calculates some transition probabilities for the radiationless decay of excitations [127]. The characteristic energy needed to create such an exciton can be shown to roughly scale with the energy needed to excite a free atom of the species present in the crystal, which is somewhat intuitive in the conception of the Frenkel exciton as a 'zero-radius' limit for excitation, which does not substantially sample the crystal as a whole and is instead a phenomenon largely contained within a single crystal unit cell at a time [92], though it is not permanently localized to that point in the lattice.

This original exciton idea is indeed a fairly accurate description of the fundamental aspects of an exciton – but only in systems with small dielectric constants. In such a material, the Bohr radius of the resulting exciton (q.v. sub) will be small, and the exciton will tend to be well-localized to a single site in the crystal at any instant, though it can propagate relatively freely from site to site. In the limit of molecular excitations this species of exciton is, of course, bound to a single molecule. Frenkel excitons possess much greater binding energies than those which arise in materials with large dielectric constants. Those are known as Wannier excitons, or sometimes Wannier-Mott

excitons. These are a more accurate model for the excitons we see in the materials we study. In such materials, the atoms that comprise the crystal are no longer sufficiently dilute that one may neglect the extension of the atomic wavefunctions into neighbouring sites, and, as a result, an effective dielectric medium exists that will mediate the interaction between an electron and the hole it vacates (or indeed, any other charged particle Coulomb interaction) [92].

In 1937 Gregory Wannier describes the other end of the exciton spectrum, considering the excitation of a crystal with a large dielectric constant. In his analysis, the band gap energy acts as the ionization potential for a series of bound states that occur when an electron is excited out of its band but cannot escape the Coulomb interaction of its hole. These states form a discrete spectrum analogous to an atomic or molecular system [381].

In 1937 Gregory Wannier developed another theory of the exciton; along with the formulation developed by Frenkel, this new analysis effectively forms the range of possible exciton quasi-particles. Wannier proceeds in a surprisingly simple but modern analysis to develop three consistent basis sets for the electron wave functions in a crystal and shows how to transform among the three in order to use the most convenient set for a particular calculation. With the preferred basis set he calculates the energy for the degenerate first excited state and shows that the only novel aspect of the system's behaviour is caused by those matrix elements that arise from the Coulomb interaction between the electron and the hole created by its promotion, and which (the

matrix elements) depend only upon the relative motion of the two particles but not upon their absolute position in space. This allows him to separate the center-of-mass motion from the relative, quantized motion of the electron and hole. Since the center-of-mass motion is completely uncoupled from the Coulomb interaction Hamiltonian, the electron-hole pair can be treated as a neutral particle that propagates as a free particle through the crystal. This agrees well with our repeated insistence that quasi-particles be characterized by a well defined wave vector [381].

Noting that the Coulomb interaction, as it is attractive, can only result in the lowering of any electron state's energy, and therefore will not result in the presence of any discrete states formed above the Bloch conduction band, Wannier then shows that the equation for relative motion between the electron and hole is of the exact form as the simple Schrodinger equation for the Hydrogen atom. He notes the existence of a discrete, hydrogenic spectrum for the exciton, as well as the presence of an unbound continuum of states, which simply form the conduction band from the Bloch analysis of the crystal. The discrete states cannot carry a current, though it would be possible for the continuum states to do so [381] under application of a potential.

Wannier also reiterates Frenkel's observation that momentum conservation must hold for the excitation induced by absorption of a photon, and the resulting creation or annihilation of a phonon necessary to allow the process. He notes that the essentially 'electronic' part of the spectrum (that part where the phonon interaction will be minimized and thus not blur the discrete state

into a band broadened by the energy of the phonon) will occur when considering transitions occurring with an exciton wave vector of zero. The result is a set of hydrogenic discrete states occurring below the continuum [381].

The assumption that only a single electron is excited in the crystal greatly simplifies the analysis, but it can be relaxed somewhat. So long as the number of photo-excited electrons is small compared to the number of crystal unit cells, the optical response of the material should be qualitatively similar to that predicted by the Wannier exciton, but when the exciton gas is no longer dilute substantial changes are to be expected. Wannier's analysis also notes the possibility of other weak transitions that violate the Franck-Condon[2] principle [381].

Perhaps the most significant difference in these two results is that the Wannier model of the exciton concentrates on its hydrogenic features. In fact, the model of the more tightly localized excitation described by Frenkel occurs in materials with lower dielectric constants, where the Coulomb attraction is not so substantially diminished and the resulting Bohr radius of the exciton is greatly reduced. In contrast, the Wannier exciton accurately describes the behaviour of excitons in high dielectric materials, where the Bohr radius becomes large compared to the lattice unit cell, and the electron-hole pair now simultaneously sample the potentials of a relatively large number of lattice sites. This is characteristic of many III-V semiconductor materials. Frenkel

[2]The original paper mispells the name 'Frank.'

excitons, on the other hand, have a Bohr radius that is typically small or comparable to the lattice unit cell, and the exciton tends to experience only one local cell's potential at a given instant [92]. These excitons are found often in wide gap semiconductors, or in organic molecules.

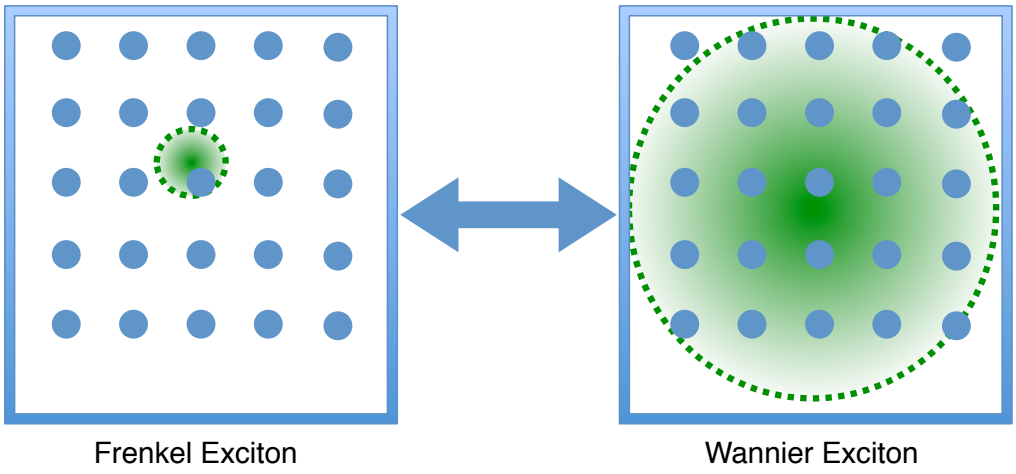

Figure 2.3: Sketch of Wannier-Frankel excitons

Experimental observation of tightly bound Frenkel excitons was suggested by [14], [16], [15], [168] where studies of the migration of energy through excited ionic crystals indicated the presence of an intermediate step whereby some of the collected photoelectrons were not immediately emitted, but instead that the energy propagated with a wavelike nature through the crystal medium. Other contemporaneous studies [150], [13] suggest experimental ob-

servation of weakly bound Wannier excitons [186].

At zero temperature, no excitons will be thermally excited, and the Fermi level of an idealized semiconductor should sit in the middle of its bandgap. As we approximate that limit experimentally with cryogenic cooling techniques, we may use those conditions as a starting point to understand the behaviour of the systems we investigate.

The treatment presented here is a relatively simple quantum mechanical description that relies on the underlying electronic band structure of a crystal to develop many of its results. The actual excitation of a crystal with light may result in a coupled photon-exciton mode, known as a polariton. We discuss this hybridization in passing in our survey of nonlinear optical studies of excitons in semiconductor crystals, and at greater length in the chapter on novel spectroscopic techniques developed to study the coupling of various different excitation modes.

2.2.3.1 The Wannier Equation

Wannier's approach to studying excitons approaches the lowest possible excitation the system can support, analyzing a single electron-hole pair in order to understand the effect the Coulomb interaction will have on the optical properties of the material. The effects of the crystal lattice are treated by using an effective mass approximation to describe the motion of the electron and hole; this approximation is most useful in the vicinity of the extrema, such as at the Γ point in a direct gap semiconductor like GaAs.

Consider the exciton wave function. In our direct gap material, the exciton wave function may be expressed as a wave packet, using a linear combination of the electron and hole Bloch wavefunctions

$$\begin{aligned}\psi\left(\mathbf{r}_e,\mathbf{r}_h\right) &= \sum_{\mathbf{k_e},\mathbf{k_h}} \Phi\left(\mathbf{k}_e,\mathbf{k}_h\right)\varphi_{c\mathbf{k}_e}\left(\mathbf{r}_e\right)\varphi_{v\mathbf{k}_h}\left(\mathbf{r}_h\right) \\ &= \sum_{\mathbf{k}_e,\mathbf{k}_h} \Phi\left(\mathbf{k}_e,\mathbf{k}_h\right) u_{c\mathbf{k_e}}\left(\mathbf{r}_e\right) e^{i\mathbf{k}_e\cdot\mathbf{r}_e} u_{v\mathbf{k}_h}\left(\mathbf{r}_h\right) e^{i\mathbf{k}_h\cdot\mathbf{r}_h}\end{aligned}$$

where function Φ is a coefficient for the expansion of the exciton wave function onto the bilinear form of the product of the electron conduction band Bloch functions and the hole valence band Bloch functions. Typically the atomic part of the Bloch functions (the u terms) vary slowly as functions of $\mathbf{k}_e$ and $\mathbf{k}_h$, and as a result for states near the band extrema at the center of the Brillouin zone the atomic part (the u functions) of the Bloch wave functions can be approximated as the atomic part for $\mathbf{k}_e = \mathbf{k}_h = 0$. Then

$$\Psi(\mathbf{r}_e,\mathbf{r}_h) \backsimeq u_{c_0}u_{v_0}\sum_{\mathbf{k}_e,\mathbf{k}_h}\Phi(\mathbf{k}_e,\mathbf{k}_h)e^{i\mathbf{k}_e\cdot\mathbf{r}_e}e^{i\mathbf{k}_h\cdot\mathbf{r_h}} \simeq u_{c_0}u_{v_0}\Phi(\mathbf{r}_e,\mathbf{r}_h)$$

since $e^{i(0)} = 1$, the exponential functions describing the plane wave portion of the Bloch functions are, in this approximation, set equal to unity. In this approximation, then, the coefficient in the expansion of the wave packet is now treated as the exciton envelope wave function,

$$\Phi(\mathbf{r}_e, \mathbf{r}_h) = \sum_{\mathbf{k}_e, \mathbf{k_h}} \Phi(\mathbf{k}_e, \mathbf{k}_h) e^{i\mathbf{k}_e \cdot \mathbf{r}_e} e^{i\mathbf{k}_h \cdot \mathbf{r}_h}$$

The total exciton wave function Ψ, therefore, can be understood as an envelope function $\Phi(\mathbf{r}_e, \mathbf{r}_h)$ modulated with the periodicity of the atomic lattice by the atomic part of the Bloch functions for the electron and hole [270]. The envelope function, as Wannier conceived it, describes the spatially extended, relative motion of the electron and hole [381], while the periodic modulation of that probability distribution arises due to the periodic crystal potential. Note that this expression for Ψ does not explicitly contain here a dependence on the center of mass motion of the electron-hole pair; that dependence will be introduced by a subsequent change of variables in later analysis.

The envelope function obeys a two-particle Schrodinger equation

$$\left(-\frac{\hbar^2}{2m_e}\nabla_e^2 - \frac{\hbar^2}{2m_h}\nabla_h^2 - \frac{e^2}{\epsilon_{bkgnd}\left|\mathbf{r}_e - \mathbf{r}_h\right|} \right) \Phi = \varepsilon \Phi$$

where the energy ε is now defined relative the the bandgap energy E_g. Here is is clear that this equation for the relative motion involves only the Coulomb coupling described by Wannier: the third term on the left hand side is the attractive coulomb potential (the electron has charge -e, the hole has charge +e), we the denominator is proportional to the background dielectric constant for the bulk semiconductor material, as this affects the strength of the interaction and thus determines how tightly bound the hydrogenic wave

function will be. This equation is mathematically identical to the Schrodinger equation for the Hydrogen atom (discounting those higher order corrections leading to the fine and hyperfine structure, etc), and the solutions to that well-known problem directly apply to this system.

By separation of variables one may split the Hamiltonian into two separate operators acting upon independent wave functions that depend explicitly either on the relative displacements of the electron and hole – effectively the internal energy of the exciton, or upon the center of mass displacement, which may be understood as the kinetic energy of the quasi-particle [92]. The center of mass equation $-\frac{\hbar^2}{2m_{\mathbf{R}}}\nabla^2_{\mathbf{R}} = \varepsilon_{\mathbf{R}} g(\mathbf{R})$ leads to an expression for the center-of-mass wave function $g(\mathbf{R}) = e^{i\mathbf{K}_C \cdot \mathbf{R}}$ with the parabolic, free particle dispersion relation between momentum and energy $K^2 = \frac{2M\varepsilon_{\mathbf{R}}}{\hbar^2}$.

The hydrogenic part of the problem, meanwhile

$$\left(-\frac{\hbar^2}{2m_{reduced}}\nabla^2_{\mathbf{r}} - \frac{e^2}{\epsilon_{bkgnd} r}\right)\phi(\mathbf{r}) = \varepsilon_{\mathbf{r}}\varphi(\mathbf{r})$$

takes its straightforward solution using the example of the hydrogen atom, with the only changes made being the use of the effective mass used to calculate the reduced electron-hole mass, instead of the electron-proton effective mass, as well as the previously noted change in the dielectric constant [270], [92]. This is known as the Wannier equation, and describes only the relative motion of the electron and the hole. These exciton energy levels will occur inside the electronic bandgap of a semiconductor, as the Coulomb inter-

action permits states to occur that the previous analysis found to be forbidden. Studying the hydrogen Schrodinger equation solutions, one may note that exciton binding energy is inversely proportional to the exciton Bohr radius – the more tightly bound the electron and hole are, the more energy is liberated in the formation of the exciton, and thus the lower the total energy of the system. Also, exciton binding energy is inversely proportional to the square of the background dielectric constant of the semiconductor. Since larger gap semiconductors tend to have smaller background dielectric constants, excitons created in these materials will possess a higher binding energy. In our own work we have considered the appeal of working with semiconductors near the telecom wavelengths, but frequently discount such ideas due to the difficulties that would arise in these smaller gapped materials.

The free-particle dispersion relation for the center of mass motion shows the exciton moves through the material as a free particle through a vacuum. This is true for either Frenkel or Wannier excitons, as it is not necessary for there to be significant wavefunction overlap for effective exciton propagation to occur. An exciton, with a well-defined wavevector, may propagate by virtual dipole interaction if the atomic wavefunctions do not significantly extend among neighbouring lattice cells [179]. Both Wannier and Frenkel excitons are analytically developed by assuming the lowest-lying excitations of a non-metallic crystalline solid will be described accurately with a well-defined wave vector $\mathbf{K}$. In the limit that this momentum is precisely known, application of the uncertainty principle results in completely de-localized excitations – the

excitons that would be created by optical absorption (or by any other process, really) would be completely spatially extended over the entire solid. Indeed, since the initial analysis assumes that the solid extends infinitely in space, the exciton wave function would also extend infinitely. Therefore, the exciton wavefunction at $\mathbf{R}$would be the exact same as at $\mathbf{R}+\mathbf{G}$, where $\mathbf{G}$ is any lattice vector. In this limit, there are no scattering or interaction processes that affects the exciton in any way. The excitation can be characterized by its wave vector and momentum, $\mathbf{K}$ and $\hbar\mathbf{K}$, with a velocity $\mathbf{v}=\hbar\mathbf{K}/M^{*}=\frac{1}{\hbar}\nabla_{\mathbf{K}}E\left(\mathbf{K}\right)$, and effective mass tensor $\frac{1}{M^{*}}=\frac{1}{\hbar}\nabla_{\mathbf{K}}\nabla_{\mathbf{K}}E\left(\mathbf{K}\right)$ [92]. We don't have to worry too much about the seemingly unphysical implications of infinitely extending wavefunctions, since the assumptions of perfect, infinite crystals is clearly unphysical. More to the point, treating the excitation as a particle with a single, well-defined wave vector would actually, under the strictest application of conservation of momentum selection rules, result in a very small number of allowed transitions. The presence of crystal imperfections is in fact responsible for the formation of absorption bands, rather than isolated, single transitions. Theoretical work prior to [91] neglect these effects of real systems, ignoring surface effects, deviations from the ideal periodicity, and the attenuation of light propagating through the material.

The total wavefunction for the exciton can be expressed in the center of mass/relative motion coordinate system used here as

$$\Psi(\mathbf{r},\mathbf{R})=u_{c_0}u_{v_0}\phi(\mathbf{r})e^{i\mathbf{K}_c\cdot\mathbf{R}}$$

The first two terms are related to the atomic orbitals that are used to calculate the band structure, and, as note above, are approximated with the $\mathbf{k} \sim 0$ orbitals. The symmetry of those functions in coordinate space will determine the strength of the interband optical transition [270], as they can be used to calculate the matrix elements of interest in an expression for the transition rates – by applying Fermi's Golden Rule, for example. $\phi(\mathbf{r})$ is an envelope function that describes the relative motion of the hole and the electron that comprise the exciton, and is found by solution of the Wannier equation, *sup*. The center of mass term clearly has a plane-wave like character in this expression for Ψ.

Direct observation of the Rydberg-like series of energy states is difficult as it is not trivial to experimentally measure the exciton binding energy, as it is often difficult to observe the more than two spectral lines of the hydrogenic series. Broadening mechanisms, arising from many-body interactions, for example, can blur these spectral features and make it impossible to fit this simple model to an experimental result.

The angular momentum states that arise in the Wannier equation are described similarly to those in the hydrogen atom, so that an exciton can be described as having an s-like or p-like angular momentum and so on.

Excitons behave as approximate composite bosonic particles [186]. That approximation may break down for high density n, though it should hold so long as $na^3 \ll 1$ for lattice spacing a.

2.2.3.2 Optical absorption with excitons

We now turn our attention to the specifics of optical processes involving the creation or destruction of excitons.

In addition to its own various dynamics, the the exciton quasi-particle has a second role as the quantum of an electric polarization wave that is coupled to an optical field. As a result of this coupling, the occupation of various energy states by the exciton can be resolved from absorption or emission spectra. Applying a weak probe to a population of excitons permits the observation of such a spectrum [271].

The Coulomb interaction results in a tendency for the motion of an electron and hole to correlate. If the excitation that annihilates a valence band electron, creates a conduction band electron, and creates a hole in the state vacated by the original electron occurs with a definite, well-defined momentum, it will result in momentum eigenstates for the electron and hole, which will therefore be delocalized. As a result they can interact locally since they overlap in space

The effects of exciton formation on absorption spectra were observed in the early 1950's, and could be qualitatively explained using the predictions of Wannier's exciton theory. A relatively complete treatment of this problem was developed by Elliott [109]. We examine these results now and note the improvement they offer compared to those models that neglect Coulomb interaction, as described previously.

In excitonic absorption, as elsewhere, the conservation of momentum and energy must be satisfied. Since the momentum of an absorbed photon will (again) be small compared to the scale set by the Brillouin zone for crystals such as those we are interested in, the resulting center of mass motion of the created exciton will be closely centered on $\mathbf{K}_c \sim 0$. We typically assume that the excitons created by optical absorption are essentially at rest, and that the parabolic, free particle dispersion relation for excitons – which, if taken into account, would result in the formation of a band of possible exciton states – may be neglected. This agrees with the experimental observations of a fairly sharp spectral line associated with the exciton transition.

Photons carry angular momentum; the hydrogenic, relative motion exciton wavefunction permits the familiar manifold of angular momentum eigenstates well known from analysis of the hydrogen atom. Conservation of angular momentum must hold for an optical absorption process to occur.

We noted previously that there are different paradigms for understanding the absorption process. In one picture, we consider an initial state with no holes, one electron in the valence band with a certain angular momentum, and one photon with its angular momentum; the corresponding final state after the transition has one hole in either the heavy or light hole band with a well defined angular momentum, an annihilation of of the valence band electron, an annihilation of one photon, and one electron in the conduction band with its well defined angular momentum. In another picture for understanding the absorption process, we consider an initial state of no excitons

and one photon, and after the transition an exciton but no photon. We use this quasi-particle exciton picture now to understand the excitonic absorption process. In this picture, annihilation of the photon leads immediately to the momentum conservation rule that $\triangle l = \pm 1$. The change in angular momentum that occurs in an excitonic transition can be split into two separate components: angular momentum related to the envelope, and that related to the internal motion of the electron-hole system. We express this conservation rule as $\triangle l = \triangle l_{int} + \triangle l_{env} = \pm 1$. For an exciton wave function $\Psi(\mathbf{r}, \mathbf{R}) = u_{c_0} u_{v_0} \phi(\mathbf{r}) e^{i\mathbf{K}_c \cdot \mathbf{R}} \sim u_{c_0} u_{v_0} \phi(\mathbf{r})$ the internal motion of the electron-hole system is described by the product of the two periodic portions of the Bloch functions used to construct the wavefunction, $u_{c0} u_{v0}$, while the envelope function is the $\phi(\mathbf{r})$ term.

We note that changes in angular momentum can not be split into halves. This follows from the argument that hydrogenic envelope wave function has integer differences in its angular momenta states, and that even if internal $u_{c0} u_{v0}$ part could change by half-integer values of angular momenta, there is no possibility for the 'left-over' half to be absorbed or emitted anywhere. Therefore, the entire $\triangle l = \pm 1$ change must be absorbed by one or the other parts of the wave function,

$$\triangle l_{int} = \pm 1, \ \triangle l_{env} = 0$$

or

$$\triangle l_{int} = 0,\ \pm 2,\ \triangle l_{env} = \pm 1$$

for the first possible way to apportion the angular momentum (i.e., the change occurring on the internal wave function), photon absorption corresponds to a dipole transition between energy bands that are derived from atomic orbitals with angular momenta that differ by +/-1, i.e. between a p-like state and s-like state, or any other possible combination of energy bands with principal contributions from atomic orbitals that have a difference of one between their angular momenta. If this is the case, the envelope function of the exciton must be s-like to satisfy angular momentum conservation – before the photon absorption, the exciton does not exist, and therefore cannot possess $l = 1$ angular momentum, so when it is created, it is created in an s-like, spherically symmetric state.

For the second set of transitions, the interband transition is dipole-forbidden due to angular momentum conservation, but the transition will still occur if the angular momentum quantum is absorbed by the envelope function, which will take a +/- 1 angular momentum change. This transition is generally significantly weaker than the allowed first order dipole transitions. The exciton created is (at the lowest) a 2p or higher exciton function, as the 1p solution does not exist (can only have 1s) [270].

If the crystal has inversion symmetry, exciton states with $\mathbf{K}_c \sim 0$ can be described as having a definite, well-defined parity. If that is the case, group

theory can be used to determine which exciton transition states are allowed according to the conservation of parity.

2.2.3.3 Photon absorption by excitons in direct-gap semiconductors

As always, we are principally concerned with processes in direct gap semiconductors. Consider the dipole-allowed transitions occurring at the center of the first Brillouin zone, where the exciton exhibits essentially no center of mass motion. This requires computing the matrix element for an interband transition connecting all possible pairs of electron and hole states that comprise the exciton wave packet. We seek the transition probability $w \propto \left| \sum_{\mathbf{k}_e, \mathbf{k}_h} \Phi(\mathbf{k}_e, \mathbf{k}_h) \left\langle c, \mathbf{k}_e \left| \mathbf{e_q} \cdot \mathbf{d} \right| v, \mathbf{k}_h \right\rangle \right|^2$ subject to the ever present requirement that we conserve momentum. This approach results in an expression known as the Elliott formula, which is used to describe exciton creation by absorption near the band edge. If we continue using the notation already develop to describe exciton wave functions, the absorption coefficient that results is given by

$$\alpha(\omega) = \frac{8\pi^2 \omega \left| d_{cv} \right|^2}{n_b c} \sum_n \left| \phi(\mathbf{r} = 0) \right|^2 \delta \left(\hbar\omega - E_g + \frac{E_B}{n^2} \right)$$

[270]. Here we see that absorption depends on the electron and hole occupying the same lattice site (the $\phi(\mathbf{r} = 0)$ term requires that $\mathbf{r} = \mathbf{r}_e = \mathbf{r}_h = 0$) and forces conservation of energy, where the photon energy must now equal the bandgap less the binding energy of the exciton – as mentioned in our

description of exciton formation, the binding of the electron hole pair results in a lowered energy necessary for photon absorption. In a hydrogenic system, orthogonality of the eigenfunctions results in only the s orbitals exhibiting a non-zero probability density at $\mathbf{r} = 0$ (see, for example, [46]), therefore only the creation of s-state excitons will contribute to the optical absorption.

It is possible to further develop this expression for the absorption coefficient in order to describe both absorption into the discrete excitonic energy levels as well as into the electron conduction continuum, frequently referred to as free-carrier states. The resulting expression is

$$\begin{aligned} \alpha_{Elliott}(\omega) &= \frac{e^2\omega\left|d_{cv}\right|^2}{n_b c\epsilon_0}\left(\frac{2m_r}{\hbar^2}\right)^2 \times \\ &\left[E_B\sum_{n=1}^{\infty}\frac{4\pi}{n^3}\delta\left(\hbar\omega - E_g + E_B/n^2\right) + \theta\left(\hbar\omega - E_g\right)\frac{\pi e^Z}{\sinh\left(Z\right)}\right] \end{aligned}$$

where the first term describes absorption into the discrete states and the second term describes absorption into the continuum states. The constant Z is related to the square root of the exciton binding energy, normalized by the energy difference between the photon and the bandgap

$$Z = \pi\sqrt{E_B/\left(\hbar\omega - E_g\right)}$$

[270]. This expression is usefully compared to that obtained for free carrier absorption in the previous analysis, which neglects the Coulomb inter-

action between the electron and hole, and only treats absorption by continuum states:

$$\alpha_{free} = \frac{2}{nc} \left| \langle \varphi_c | \, e\mathbf{r} \cdot \mathbf{E} \, | \varphi_v \rangle \right|^2 \left(\frac{2m_{reduced}}{\hbar^2} \right)^{3/2} \left\{ \theta \left(\hbar\omega - E_g \right) \left(\hbar\omega - E_g \right)^{1/2} \right\}$$

Note that not only does the inclusion of Coulomb interaction result in the formation of the discrete excitonic Rydberg series below the conduction band, but the absorption into continuum states is also substantially altered. This Coulomb enhancement is present even in the limit that the photon energy decreases to the bandgap – the shape of the continuum absorption feature is fundamentally different once Coulomb interactions are considered.

There should be a hydrogenic series of exciton states formed below the bandgap, where the oscillator strength of each exciton state decreases with $1/n^3$ where n is the principal quantum number for the exciton envelope function. Experimentally, however, broadening mechanisms result in only a few – or even only one – observable exciton states. These broadening effects cannot be completely eliminated, even at low temperatures, where interaction with acoustic phonons will still broaden the exciton spectral features.

In addition to these features, much weaker transitions involving p orbital exciton wavefunctions are also possible. These will be difficult to resolve.

2.2.3.4 Absorption by excitons in indirect gap semiconductors

As in the free electron-hole absorption process, the absorption of a photon by an exciton in an indirect gap semiconductor requires the presence of an additional quasi-particle or particle, and is thus by definition a higher order process than the corresponding absorption in a direct gap semiconductor.

The conservation of momentum requires that the creation of an exciton by photon absorption requires the emission or absorption of another momentum carrying particle at the same time. Exciton mediated absorption of a photon will typically occur by creating or destroying a phonon carrying momentum $\hbar\mathbf{K}$.

The likelihood of absorption of a phonon is proportional to $n_{\mathbf{K}}$, the occupation number for phonons in the $\mathbf{K}$ mode, while the likelihood for emission of a phonon is proportional to $n_{\mathbf{K}} + 1$ – that probability must logically be greater than that for absorption, since otherwise no phonon emission could occur in a crystal that started with no phonon population. Since phonons are (like excitons) approximate composite bosons, they obey the Bose-Einstein distribution function, $n_{\mathbf{K}} = \frac{1}{e^{\hbar\Omega_{\mathbf{K}}/k_B T}-1}$, and therefor the relative likelihood of emission to absorption, which must be proportional to $n_{\mathbf{K}+1}/n_{\mathbf{K}}$, is give

$$\frac{n_{\mathbf{K}}+1}{n_{\mathbf{K}}} = e^{\hbar\Omega_{\mathbf{K}}/k_B T}$$

from which we see that at low temperatures (ie those when $k_B T$ becomes small compared to the phonon energy $\Omega_{\mathbf{K}}$, when such an exponential

starts to diverge significantly from unity), the phonon emission process will come to dominate [270]. That is to say that at low temperatures, indirect bad gap materials will exhibit exciton formation by optical absorption preferentially relying on the creation of phonons to conserve angular momentum.

The phonons have an essentially continuous spectrum – their energy spacing is extremely small in a macroscopic crystal – with wave vectors running over the first Brillouin zone. This allows any exciton state with a momentum in that Brillouin zone to be accessed with the emission or absorption of the appropriate phonon. The rate of optical absorption will tend to increase with increasing photon energy, though this effect is due to the increased density of states. The end result is a rounded stair-step of absorption spectrum, with each new step up occurring as the next energetically higher exciton becomes accessible to a transition.

2.2.3.5 Exciton relaxation

Having considered the absorption of photons in the context of Coulomb interactions between electrons and holes, we now consider the inverse process by which photons are emitted.

Excitons exhibit a finite lifetime; this may appear counter-intuitive given the stability of the hydrogen atom. In fact, a one-body treatment of an exciton would appear to result in an infinite lifetime, but a three-body calculation or a more sophisticated field theoretical treatment of exciton creation and annihilation can be used to show that the exciton lifetime should

be finite [186]. Excitons may decay by dissociating into a free electron-hole pair by absorbing a necessary quantum of energy, or by the recombination of the electron-hole pair. If that decay occurs via the emission of a photon the process is known as luminescence.

The decay of an exciton may occur via relaxation involving some defect in the system or via the intrinsic, free exciton luminescence. An example of the former process is the emission of a photon mediated by crystal defects. Impurities in a crystal, in the form of substitutional atoms, will result in strong exciton luminescence lines with characteristic wavelengths that depend upon the type of substitutional atom and the concentration of such defects. The process is somewhat analogous to emission by trace atoms in an excited buffer gas. The latter process, free exciton luminescence, entails the recombination of the electron and hole. The 'free' nomenclature here refers to the exciton's nature as a neutral, unbound particle that moves freely through the crystal medium.

In a sufficiently low exciton density gas, which we may refer to as the weak excitation limit, the exciton many body physics may be ignored, assuming the characteristic time scale for exciton-exciton interactions are long compared to the relaxation rate, or that the interactions are sufficiently weak to be completely neglected. In this approximation, the exciton population ca be treated as a gas of independent quantum emitters.

In a direct band gap material, excitons that are essentially motionless ($\mathbf{K}_c \sim 0$) can decay without any other particle interactions. The emitted

photons, however, will have a high likelihood of re-absorption by the material by another exciton process, which may then subsequently decay and be re-absorbed. The result is a propagating mode of excitation: this is a reasonably intuitive picture of the excitonic polariton – a couple excitation comprising a propagating electromagnetic mode mixed with a quasi-particle material excitation mode. This polariton will only result in the creation of a free (not mixed with other mode) photon when it leaks through a boundary of the material. This is not a certainty in most real solids, however, as the excitons have a high probability to be trapped by crystal defects. As a result, the direct free exciton luminescence is typically a very weak emission, as only a small subset of the exciton population will undergo decay in this manner.

For this reason we turn our attention to indirect free exciton luminescence, the process by which a phonon is absorbed or emitted to allow the exciton decay process to satisfy the simultaneous requirements of conservation of energy and momentum. Due to the similarity to indirect, phonon-mediated photon absorption processes we have included descriptions of those effects *sup.*

Typically, indirect free exciton luminescence will involve the optical phonon. Since the optical phonon is essentially dispersionless (it exhibits a relatively flat curve as a function of momentum $\mathbf{k}$), conservation of momentum may be satisfied for any essentially exciton since there is an optical phonon available for any given momentum in the Brillouin zone. Instead of the small subset of excitons that can participate via direct free luminescence, the entire population can decay via this indirect process.

At low temperatures such as those we consider, the equilibrium thermal population of optical phonons is negligible, so the indirect free exciton decay will typically proceed via emission of optical phonons.

We return out attention to the trapping of excitons at crystal defects. The imperfections in a real crystal will act as localization sites, with excitons becoming relatively closely bound to the imperfection site. That binding energy will typically be on the scale of only a few meV, and thus will only tend to occur at low temperatures. We might naively assume that bound excitons would exhibit limited effect on exciton luminescence, since the number of crystal defect site is typically orders of magnitude smaller than the number of perfect sites. Most free excitons, however, cannot directly decay without interacting with another particle or quasi-particle. These excitons will thus propagate through the crystal until such time as they undergo an indirect decay process. During this time there is some chance that they will be trapped at an imperfection site; the likelihood of exciton capture at a defect can be estimated with the same kind of back-of-the-envelope calculation that leads to estimates of mean free path and mean time to scatter in any dilute gas – the cross section for the capture process is approximately given by the exciton's Bohr radius. The capture lifetime is smaller than the exciton lifetime in some semiconductors.

Localization at an imperfection permits the exciton to then decay directly – before the capture, the exciton could not decay without the mediation of a phonon due to momentum conservation requirements. After the cap-

ture, however, the exciton is localized at one specific point. Application of the uncertainty principle results in an exciton with a broadened extension in momentum or k-space, which can now proceed to directly luminesce without the creation or annihilation of a phonon. This effect induces direct exciton decays even in an indirect gap semiconductor. The bound exciton transition will result in a very sharp spectral line, since there are fewer broadening perturbations for the exciton bound at an impurity site, which no longer is subject to the same thermal broadening\wider energy distribution associated with free excitons [270].

2.2.3.6 Formation of excitation from free carriers

Absorption of a photon with greater than the band gap energy results in the formation of an unbound e-h pair that possess an energy excess compared to those formed in excitons below the band gap. That excess will be dumped into the thermal in a rapid scattering process, typically via the emission of successive optical phonons. This process is fast compared to the lifetime of the exciton as long as the excess energy is greater than the energy of the longitudinal optical phonon, allowing the creation of those quanta while satisfying the conservation of energy requirements. The net result of this scattering process is to transform a population of free electrons and holes created in a low temperature crystal into a population of excitons in the $n = 1$ kinetic energy band.

Further relaxation of the excess exciton kinetic energy occurs via the

emission of acoustic phonons, which have available energy eigenstates all the way down to zero energy, permitting them to 'carry' any amount of excess energy away from a scattering process [270]. Unlike the optical phonon, the acoustic phonon branches are clearly not dispersionless, and thus there will not always be a 'good' phonon state available to carry off the right amount of kinetic energy while satisfying the conservation of momentum requirement; as a result this relaxation process is slower than the preceding step. It typically takes something on the order of a nanosecond for the exciton population to reach thermal equilibrium with the crystal lattice, which may exceed the exciton lifetime in some materials. As a result, it is possible that the entire population will have decayed via indirect free exciton decay before this thermalization process fully occurs.

If the exciton system were sufficiently long-lived that it had time to thermalize completely via acoustic phonon scattering, the expected state could be described with Bose-Einstein statistics,

$$g(\varepsilon)f(\varepsilon) = g(\varepsilon) \times \frac{1}{e^{(\varepsilon-\mu)/k_BT} - 1}$$

where the density of states used is that for free particles, $g(\varepsilon)d\varepsilon = \frac{1}{2\pi^2}\left(\frac{2m_0}{\hbar^2}\right)^{3/2}\varepsilon^{1/2}d\varepsilon$. The population distribution will deviate from this functional form if that thermal equilibration has not gone to completion.

If transition probability is approximately independent of energy, then the spectral intensity of luminescence is proportional to the energy density of

the excitons,

$$I(\hbar\omega) \propto \int n(\varepsilon)\delta_\Gamma(\hbar\omega - \varepsilon)d\varepsilon \sim \int g(\varepsilon)f(\varepsilon)\delta_\Gamma(\hbar\omega - \varepsilon)d\varepsilon$$

where the function $\delta_\Gamma(\hbar\omega - \varepsilon)$ is a broadened lineshape that relates the emitted photon energy $\hbar\omega$ to the energy of the exciton.

But, if that is the case, examining the lineshape of the exciton luminescence would suggest the underlying $n(\varepsilon)$ thermal distribution of exciton energies – in that case, the lineshape for phonon-assisted free exciton decay should be a reasonably good model for the thermal distribution of the exciton energies. This approximation will break down at higher exciton densities, which will require a quantum mechanical treatment for their energy distribution function [194], [153], [268], [267].

2.2.4 Phonons

2.2.4.1 Basic phonon physics

The discussion presented here depends heavily upon[17], [270], and [307].

Due to their much greater mass, the movement of the positively charged ions that constitute the crystal lattice are, for a roughly equivalent electrical force (depending on their ionization number) smaller in amplitude than the oscillations exhibited by electrons. If this is a valid assumption, it is possible to approximate the restoring force with a Hooke's law model, and assume

simple harmonic motion for the resulting motion. The oscillation of these ions can be treated with the phonon quasi-particle, which is a quantum mechanical treatment of the normal modes of oscillation exhibited by the lattice. An intuitive understanding of this system can be gained by evaluating the response of a system of classical oscillators subject to coupling between neighbours (or neighbours and next-nearest neighbours), then determining the quantum mechanical analog of this behavior by applying the correspondence principal (viz., by asserting the position-momentum commutation relations, etc, and thus 'quantum-izing' the normal mode vibrations).

We find that in the dispersion relationship for phonons the same limitation is present on allowed momenta as we found in the analysis of the electron wavefunctions in a periodic medium – the momenta are in both cases restricted to the range $\{-\pi/a,\, \pi/a\}$. We note the important result that, after a quantum mechanical analysis of phonons shows that the energy eigenstates for the normal modes of the lattice are found by solution of a simple harmonic oscillator Hamiltonian, it is common to refer to a phonon of energy level $n_{\mathbf{q}}$ (where q labels the phonons crystal momentum) with energy $E_{n_{\mathbf{q}}} = \hbar\omega_{\mathbf{q}}\left(n_{\mathbf{q}} + \frac{1}{2}\right)$as actually a population of n phonons of 'type' $\omega_{\mathbf{q}}$. In this language, the term phonon emission is used to refer to raising the harmonic oscillator to the next highest state, which in the language of a population of phonons is equivalent to creating another phonon of a certain specific type. Similarly, phonon absorption is the process of lowering the harmonic oscillator by one state, and corresponds to the annihilation of one phonon quasi-particle. The expectation

value of the harmonic oscillator principal quantum number $\omega_{\mathbf{q}}$ is the phonon occupation number, and refers to the number of quasi-particle phonons that are present in some volume[17]. Starting from a normalized Boltzmann distribution in order to determine the likely occupation number,

$$\langle n_{\mathbf{q}} \rangle = \sum_{n_{\mathbf{q}}} n_{\mathbf{q}} e^{-E_{n_{\mathbf{q}}}/k_B T} \left(\frac{1}{\sum e^{-E_{n_{\mathbf{q}}}/k_B T}} \right)$$

(see, e.g. [217], [308] or [190]), it is possible to show that the phonons behave as approximate Bosons and obey statistical predictions made with Bose-Einstein statistics,

$$\langle n_{\mathbf{q}} \rangle = \frac{1}{e^{-E_{n_{\mathbf{q}}}/k_B T} - 1}$$

The paradigm we have outlined here for understanding the behaviour of phonons in a crystal starts with the assumption of small amplitude excursions from ionic position equilibria leading to harmonic motion, finding the classical solution for a network of couple oscillators thereby determining the set of classical normal modes for oscillations of the crystal lattice, and only then applying the correspondence principle and developing a quantum mechanical treatment of the problem. We then find that the energy eigenstates for the vibrational motion are those of a harmonic oscillator, and re-interpret that quantum model as a population of enumerable quasi-particles – this is the point where we properly begin to say that we have developed a cohesive phonon picture. We then note the statistical properties that these quasi-particles will

obey. The one additional feature that is necessary to stipulate for the quasi-particle picture to obtain properly is that there are solutions – at least in three-dimensions – for the propagation of these modes as plane waves through the crystal medium. More formally, it is possible to use the second quantization formalism (see e.g. [330]) that uses creation and annihilation operators to treat the phonon field [270].

The great passion of condensed matter theory in recent years is to reduce any quantum mechanical model to a set of enumerable "-ons" that can be treated as quasi-particles; this trend certainly holds true for a great number of effects in the solid state systems we are interested in.

Phonons are almost solely responsible for the thermal properties of certain crystals – the thermal conductivity, heat capacity, and thermal expansivity of insulators are largely determined by phonon interactions. This is physically intuitive, since in such materials the electrons will be tightly bound to specific sites in the crystal, and cannot serve to communicate changes between different parts of the solid. In materials with more free electrons, the phonon contribution to these effects may still be significant.

Some phonon modes in semiconductors can couple directly with light – typically, these will be IR-active modes in semiconductors – and are correspondingly responsible for significant absorption or reflection effects in these materials. Other phonons do not directly couple to the optical field but may indirectly result in significant scattering. We may naively expect that by reducing the phonon population we can neglect these effects and thereby inves-

tigate the electronic system response, but in fact it is necessary to consider the effect of these quasi-particles in order to properly understand the electronic absorption processes that they mediate.

Consider a one-dimensional model in order to develop some intuitive understanding of phonons. In a linear chain of atoms, a diatomic unit cell will result in a crystal that typically exhibits a phonon dispersion relationship with two branches. The higher energy phonon band is called the optical phonon branch, and is typically flatter than the acoustic phonon branch, which is lower in energy but exhibits more dispersion. The flat dispersion relation of the optical phonons indicate that the energy of these quasi-particles does not depend strongly on the crystal momentum that they carry, while the acoustic phonon energy is strongly dependent upon its crystal momentum. As a result, the population of optical phonons that is created by thermal processes in a solid will tend to contain many different momentum states, since the Boltzmann factor for any given optical phonon is roughly equal (GaAs longitudinal optical phonons, for example, are about 36meV [180]; a back-of-the-envelope calculation to approximate the binding energy between two atoms in a molecular bond will typically scale to about 30meV [92]). Contrarily, acoustic phonons will tend to populate the lowest energy modes first at low temperatures, with the higher energy phonons only appearing as the temperature of the system is increased. Consequently, it is impossible to ever completely freeze out the acoustic phonons from a material, since there are available states extending downward to zero energy.

In a diatomic material, at zero momentum, the acoustic phonon mode corresponds to motion in-phase of neighbouring atoms of different species, whereas the optical phonon mode corresponds to out-of phase motion of those neighbouring atoms. Thus, center of mass motion is largely mediated by acoustic phonons, while relative motion of the unit cell atoms is treated with the optical phonon mode. If the material is polar, such as ionic crystal like NaCl, the two different atoms in the unit cell will have different electronegativities and thus will possess opposite charge. The oscillation corresponding to an optical phonon mode, then, will correspond to an array of oscillating dipoles, thus intimately connecting this phonon mode with the optical field – thus the name optical phonon. Optical phonons can be excited by a wave of light, as the propagating electric field will tend to accelerate the oppositely charged atoms away from one another.

The array of optical phonon dipoles does not necessarily arise in all materials, however. If the unit cell of the crystal has two identical atoms that are covalently bonded only, there will be no difference in charge between the two ions. The term optical phonon is still used to describe the out-of-phase motion of these atoms, but there is no dipole associated with these oscillations, and therefore this mode will not couple strongly to incident light. These phonons are said to exhibit low optical activity.

In three dimensions a similar analysis can be performed to study the phonon dispersion relationship. The motion is now decomposed into what are termed longitudinal and transverse phonons; longitudinal phonons refers

to motion of the ions parallel to the wave vector that describes the phonon's propagation through the crystal, while in a transverse phonon the ions move perpendicularly to that wave vector. One longitudinal mode and two transverse modes are necessary to span the three-dimensional space of the crystal. For a given momentum, longitudinal phonons tend to be higher energy than transverse modes, since the restoring force is typically greater in the direction parallel to the phonon propagation [270].

If the Wigner-Seitz unit cell contains only a single atom, there will be three acoustic modes, corresponding to vibrational motion along the x, y, and z directions. There will be no optical phonon modes present – we cannot logically speak of out-of-phase motion of atoms in the same unit cell if there is only one atom per cell. A diatomic unit cell material will have six phonon branches, three acoustic and three optical. In general, a three dimensional crystal with a unit cell containing p atoms will have 3p phonon bands, three of which correspond to acoustic phonon branches, and 3p-3 of which will be optical phonons. The dispersion relations for these phonon modes is not necessarily isotropic in k-space, but will depend on the geometry of the crystal.

2.2.4.2 Optical excitation of phonons

Note that the momentum carried by a photon is typically very small compared to the scale set by the dispersion relations in a solid. Processes involving those characteristic momenta will occur in the vicinity of $|\mathbf{k}| \sim 0$ in the Brillouin zone of a semiconductor.

The acoustic phonon dispersion curve does not intersect the photon's linear dispersion curve in the vicinity of this point; therefore, it is not possible to annihilate a single photon and create a single acoustic phonon while conserving momentum. This process is a first-class forbidden transition. The dispersion relationship for the optical phonons does intersect the photon dispersion line, however, which means that these phonons can be excited by a photon while satisfying the conservation of momentum and energy [270].

Optical phonons will typically lie in the IR region of the spectrum [92] and, as a result, ionic solids that are optically active will typically exhibit substantial reflection and absorption related to optical phonon processes in this wavelength range. If the incident optical field's frequency becomes approximate to the phonon frequency, resonant excitation of that phonon mode may occur, resulting in a significant increase in absorption.

Coupling between a photon and a phonon results in a polariton quasiparticle. This is a mixture of the phonon field, which is related to a mechanical oscillation of the ions, and the light, which is related to a transverse oscillation of the electromagnetic field. A polariton is always formed where the photon dispersion relation intersects with and couples to the dispersion relation of a transverse excitation, such as the transverse optical phonon. Near the vicinity of the intersection the effect of coupling is strong, and it is necessary to consider the hybrid photon-phonon polariton mode, but further away from that point the strength of coupling decreases and the lower polariton mode essentially resembles a pure phonon mode, while the upper polariton mode

essentially resembles a free photon mode [270]. We are interested in exciton-photon polaritons in our own studies, but do not investigate photon-phonon polaritons in this work; we mention them here for completeness.

2.2.4.3 Optical scattering by phonons

We note here that we have not given a proper or rigorous treatment of what is meant by a scattering process. The intuitive understanding that is developed in an elementary physics education – classical two-body scattering problems, as well as Rayleigh or Thomson scattering, or other similar processes – lends to most physicists a general fluency with the idea of scattering processes that would be exhausting to try to cover here. Nonetheless, we mention in passing another perspective that may be illuminating. In many analyses we do not have available the actual stationary eigenfunctions and energy spectrum of a quantum mechanical system; instead we use an idealized version of the system and use its complete basis to attempt to calculate its approximate behaviour. Naturally, the initial values of the physical system will result in a different condition at some later time than that which we calculate – the usefulness of our approximate model is how closely the two sets of outcomes, real and calculated, resemble one another. The end result of the real physical evolution will be a state with contributions from (likely many) multiple states of the ideal system. It is possible to describe, and indeed calculate, the transformation from the idealized final state to the physically realized final state using the language of scattering. This scientific philosophy stems from [307].

Light can scatter either elastically ($(\hbar\mathbf{q}_i, \hbar\omega_i) \rightarrow (|\hbar\mathbf{q}_f| = |\hbar\mathbf{q}_i|, \hbar\omega_f = \hbar\omega_i)$) or inelastically ($(\hbar\mathbf{q}_i, \hbar\omega_i) \rightarrow (|\hbar\mathbf{q}_f| \neq |\hbar\mathbf{q}_i|, \hbar\omega_f \neq \hbar\omega_i)$) off phonons, whether acoustic or optical. In an inelastic scattering process the difference in energy and momentum is exchanged with the medium: if the scattered photon energy is lower than the initial energy, this is called a Stokes process and involves phonon emission; if greater, an anti-Stokes process, causing phonon absorption. Either process involving an acoustic phonon is known as a Brillouin scattering process; similarly, either of those scattering processes involving optical phonons is known as a Raman process. Even though acoustic phonons are not optically active and do not result in the strong IR absorption and reflection associated with optical phonons, they are active Raman modes. The symmetry exhibited by the crystal, as well as the normal requirements for conservation of energy and momentum, result in a set of complicated selection rules specific to a given crystal structure; this can in principle be mapped out in the vicinity of $|\mathbf{k}| \sim 0$ by performing an angle-resolved Raman or Brillouin scattering measurement.

Rayleigh, or elastic scattering, does not involve a shift of the optical frequency, as it involves coupling to a non-propagating mode (which, thus, does not mesh well with our taxonomy of quasi-particles, which we stipulate possess a well-defined wave vector), such as a thermal diffusion or heat wave. This does not shift but does broaden the optical frequency distribution somewhat, as scattered photons fluctuate in a small band (typically 10ˆ4 to 10ˆ-9 inverse cm) around the central wavelength [270].

The phonon scattering processes as described here are spontaneous in origin, and result in a very weak signal even if the phonon population is relatively large, as in room temperature measurements. It is possible to conduct a resonant Raman experiment, however, involving two incident laser beams – optical fields with well-defined momenta and energies are necessary for such experiments. The momentum difference between the two beams is selected by their relative angle. As the frequency difference between the two beams is tuned into resonance with a particular phonon mode, the lattice oscillation driven by the two lasers will result in a macroscopic population of that specific phonon, resulting in a much larger signal. This two beam experiment, and three beam experiments like CARS (technically a four-wave mixing technique, where the output signal is the fourth 'wave') are used to coherently probe vibrations in various materials.

2.3 Quantum well physics

2.3.1 Quasi-2D semiconductors – quantum wells and superlattices

Many interesting optical effects arise when light is trapped in high-finesse cavities that permit or forbid certain frequencies of oscillation. The allowed modes for such systems are determined by boundary conditions that require only certain numbers of half-wavelengths of light to propagate inside the cavity. Similarly, the confinement of particles in small material structures results in the emergence of quantum mechanical effects, where the wavelike properties of those particles become significant.

The development of modern growth techniques such as molecular beam epitaxy have made it possible to fabricate layered materials with a great deal of control. It is possible to produce materials that exhibit high quality interfaces, with sophisticated control of the doping concentrations introduced into the raw materials.

If a semiconducting material is grown under sufficiently controlled conditions, the width of the deposited layer may be sufficiently thin that excitons produced in that sample will exhibit novel (?) quantum mechanical effects. For such behaviour to emerge, the structure must be grown so that the thickness of the layer of interest is comparable to the Bohr radius of an exciton.

A quantum well is an ultra-thin layer of one kind of semiconductor sandwiched between two layers of a larger gap semiconductor. In order to reduce the occurrence of disorder and defects at the interface, the materials should be chosen to be approximately lattice matched – the lattice constants of the two materials should be comparable. If the one material is epitaxially deposited on top of another with a substantially different crystal structure it is possible that the new material will deform and produce a crystal material under strain, where the lattice constant and the bond angles may be substantially altered due to the interaction with the lower layer. The growth of lattice mismatched materials, however, is limited to a certain critical thickness – if a layer thicker than t_c is deposited, it will be more energetically favourable for dislocations and faults to occur in the material than for the crystal to continue growing under strain. The resulting crystal defects tend to ruin devices whose per-

formance is based upon the electron behaviour adhering to that expected for a perfect crystal. Careful control over epitaxial growth conditions may allow the fabrication of a metastable layer thicker than t_c but subsequent thermal cycling may result in a sudden phase change to the energetically favoured, high defect state [307]. From our remarks here on strain, it might appear that such a situation should be carefully avoided, but in fact the reduction of crystal symmetry that can occur when growing epitaxial semiconductors under strain may have interesting and useful applications, particularly in determining which states carriers will tend to occupy preferentially.

For optical applications, the absence of defects in the crystal and at the interfaces is of high importance. Additionally, the physics of excitation and emission tend to favour direct band gap materials. As such, the choice of AlGaAs-GaAs-AlGaAs sandwiches have become highly favoured for use in optoelectronic structures. GaAs, which has a bandgap of approximately 1.5eV, is the second most commonly used semiconductor after Silicon. Pure AlGaAs itself is not actually used, but rather $Al_xGa_{1-x}As$ where the molar fraction of Aluminum substituted into the GaAs material is x, and ranges between $0 < x < 1$. If the molar fraction of Aluminum is less than 0.4, the AlGaAs material is a direct bandgap semiconductor with a bandgap of around 2eV, where the precise gap depends upon the aluminum concentration.

One commonly fabricated heterostructure is a multiple quantum well stack. This sample has multiple layers of GaAs separated by layers of the AlGaAs alloy, with the AlGaAs layer typically thicker. In an ideal structure,

the MQW would behave like a single quantum well but with the optical density along the growth axis multiplied by the number of quantum well periods. Obviously, not all optical properties will simply scale the number of layers in an MQW – the effect upon coherent emission, for example, will depend upon geometrical effects, where the path length between wells will determine how modes with well-defined phase relationships will add.

If a sufficient number of layers are grown in an MQW sample, the structure is referred to as a superlattice – the AlGaAs layers in such samples are typically thinner, resulting in greater overlap of the wavefunctions of excitons or free carriers formed in the GaAs layers. The term superlattice is used to denote that in addition to the underlying periodicity of the crystalline materials used, the deposition of alternating materials has created a second, larger dimension periodicity of the quantum well layers.

The interest in quantum confined structures arises from the ability they offer to control the optical properties of a material – the inherent properties of bulk materials are determined by the quantum mechanical interaction of their constituent particles, and cannot be adjusted. An engineered material allows some control over the optical (and other) properties it exhibits, as its quantum mechanical behaviour by potentials arising at interfaces – quantum confinement effects – in such ways that it exhibits different macroscopic behaviour than the bulk material would. GaAs quantum wells, for example, allow the adjustment of the band edge absorption from 820nm to 650nm by varying the quantum well width [270].

2.3.2 Models of quantum wells – the infinite potential barrier square well

In a great many situations it is possible to model the behaviour of a particle semi-classically, where the particle motion is described as a free quasi-particle with an effective mass tensor, derived from the curvature of the particle's bandstructure [307]. We are most familiar with this technique when calculating the properties of electrons and holes near the band extrema, where a parabolic dispersion relationship is a natural approximation, but there is no formal reason this method cannot be extended to other quasi-particles in analogous circumstances, such as for neutral atoms in a periodic optical potential. As shown *sup*, excitons in a bulk material will also exhibit an essentially classical center-of-mass motion.

When a particle's bandstructure changes rapidly in real space, however, such as it may at a material interface or under application of external potentials, it is necessary to use a more overtly quantum mechanical treatment of the particle's motion [307]. Without this treatment certain physical phenomena, such as tunneling or the formation of energy subbands in nanostructures, cannot be explained.

It is possible to still incorporate the effects of the underlying bandstructure by use of an effective mass Schrodinger equation

$$\left(\sum_i -\frac{\hbar^2}{2m_i} \partial_{r_i}^2 + V_{app}\left(\mathbf{r}\right) \right) \varphi\left(\mathbf{r}\right) = E\varphi\left(\mathbf{r}\right)$$

which can be solved for an envelope function $\varphi(\mathbf{r}) \cong \sum_{\mathbf{k}\cong\mathbf{k}_0} a_{\mathbf{k}} e^{i(\mathbf{k}-\mathbf{k}_0)\cdot\mathbf{r}}$ where it has been assumed that the wavefunction can be approximated as one depending only upon Bloch functions near some extrema $\mathbf{k}_0$ present in the bulk material dispersion relation [307]. The full wavefunction is not often needed, but will consist of the envelope function multiplied by the spatially extended Bloch function at the momentum $\mathbf{k}_0$; this will simply introduce lattice-scale oscillations to the longer ranged features described by the envelope function. Further accuracy may be provided by allowing the effective mass to assume position dependence. There may be some issues that require care to be taken with the exact nature of boundary conditions (this will be important when we consider finite potential barriers) in order to ensure particle conservation [307]. Since we are interested only in the approximate behaviour of our systems we do not explore those issues further here. Greater rigor is required for transport matrix numerical solutions for effective mass Schrodinger equations.

The simplest model of a quantum confined nanostructure relies upon one of the elementary undergraduate problems – the particle in a box. In this application, however, it is necessary to consider the motion of both the electron and hole:

$$\left[\frac{-\hbar^2}{2m_{e,h}}\nabla^2_{e,h} + V(z_{e,h})\right]\psi_{e,h}(x_{e,h}, y_{e,h}, z_{e,h}) = \varepsilon_{e,h}\psi_{e,h}(x_{e,h}, y_{e,h}, z_{e,h})$$

where the two possible subscripts indicate that there are actually two separate equations, one single-particle Schrodinger equation describing the

behaviour of an electron, and one for a hole. The coordinate axis is chosen such that direction of the layered structure growth is along the z direction, and the potential is then given as

$$V(z) = \begin{cases} 0 & -L/2 < z < L/2, \\ \infty & |z| > L/2 \end{cases}$$

For simplicity, we drop the e, h subscript notation subsequently unless needed for clarity. Prompted by the quasi-two dimensional nature of the system, we seek solutions in the form $\psi(x, y, z) = \varphi(x, y)\zeta(z)$ where the phi function descries the electron's or hole's wavefunction related to its probability distribution in the plane of the layered structure, and the zeta function is related to its probability distribution normal to that plane. Alternatively, it is also possible to dimensionally simplify this problem by noting that in non-confined directions, motion can still be treated semi-classically.

Separating the derivative operator into a longitudinal and transverse operator, $\nabla^2 = \nabla_\perp^2 + \partial_z^2$, allows us to write two separate differential equations

$$\frac{-\hbar^2}{2m}\nabla_\perp^2\varphi(x, y) = \varepsilon_\perp\varphi(x, y)$$

and

$$\left[\frac{-\hbar^2}{2m}\partial_z^2 + V(z)\right]\zeta(z) = \varepsilon_z\zeta(z)$$

The differential equation for transverse motion clearly leads to the common plane-wave eigenfunctions and their energy eigenvalues. Without specifying the nature of $V(z)$, it is impossible to generally formulate a solution for the second equation. Using the hard-walled particle-in-a-box potential described above, we can obtain the well known sinusoidal solutions for that problem. The resulting energy for the particle in this well is

$$\varepsilon = \frac{\hbar^2}{2m_{e,h}} \left(\frac{j^2\pi^2}{L^2} + k_x^2 + k_y^2 \right)$$

where the integer j labels the sub-band that the particle resides in due to quantum confinement, while the other two coordinates (x, y) exhibit the parabolic dispersion of a free particle. Note that, as mentioned in passing, the unconfined motion recovers its semiclassical dispersion relation here.

Note also from our previous examination of the exciton behaviour, we already know that this cannot be a completely accurate description of the behaviour of carriers in this system – neither an electron nor a hole are neutral, and cannot move completely freely through the crystal without considering Coulomb interactions. This single particle expression for energy is for *either* an electron or a hole created by absorption of a photon and does not describe the correlated motion of the pair.

This analysis only considered parabolic, non-degenerate energy bands – in fact, this is not an unreasonable restriction on the behaviour of carriers, given that strain will typically lift the degeneracy of the electron valence bands

in a real crystal system. The more unphysical aspect of this model is that there are an infinite number of possible energy levels, as there is no bound on j. There is neither an explicit bound on the momentum in the plane of the well, but we know a priori that the parabolic nature of the relevant bands is only applicable over a limited range of momenta – therefore there is a failing of this model in its explicit dispersion relationship, which does not place limits on the allowed wavevectors for which it is an accurate description of free electron or hole behaviour, but that weakness was implicit (and known) in its starting assumptions. The failing added by this model as regards the infinite number of j-dependent energy levels it allows is the new deviation from physical reality. There are also issues that may be raised due to the failure to consider spin degeneracy.

2.3.3 Electronic states with finite potential barriers

The change in potential at the edge of a quantum well is, of course, never infinite. The approximation of the system as a square potential well fails to consider the bending of the bands that must occur at the boundaries, but with this model we will obtain a somewhat more realistic description of electron and hole behaviour than is possible with an infinite square well model.

{The AlGaAs-GaAs-AlGaAs quantum well sandwich has a bandgap structure that looks like ˜2eV - 1.5eV - 2eV (where all values approximate and dependent on doping\alloy concentrations). {material about the three types of hetero-interfaces here}}

The half eV difference in bandgaps – which we label V_0 in this analysis – between AlGaAs andGaAs results in a potential well that will trap electron-hole pairs created in an optical transition from the ground state. We assume that the states involved are non-degenerate and found in parabolic bands (the assumption of non-degeneracy fails for AlGaAs-GaAs as the highest energy valence band in GaAs is four-fold degenerate. Nonetheless, this treatment serves as a conceptual model that illustrates the physical origin of some of the behaviours of this system). The potential, as before, is divided into two regions

$$V(z) = \begin{cases} 0 & -L/2 < z < L/2, \\ V_0 & |z| > L/2 \end{cases}$$

The treatment of motion of the electrons (or holes) in the plane of the quantum well is also unchanged from the analysis used to analyze the infinitely deep square well. And, in fact, the differential equations describing the system in the well region is actually unchanged, although different boundary conditions must now be enforced. Rather than requiring the probability distribution for the wavefunction to be zero outside of the quantum well (as in the case of the infinite potential well) we now simply require that the wave function amplitude decay exponentially as the particle penetrates into the barrier.

The analysis of this problem is well understood (see, for example [149], and leads to a transcendental equation for energy eigenvalues. An algebraic solution is not available. As long as the potential of the barrier, V_0, is greater

than the potential inside the quantum well (chosen to be zero, here), there will be at least one even parity bound state solution. As the depth increases a bound odd state is available, and then higher bound states of either parity. The solution does not require the existence of a bound odd eigenstate.

For even states, the energy can be found by approximating the solutions (e.g. by a graphical solution that plots both sides of the following as a function of the energy eigenvalue and seeks points where the two functions intercept) to

$$\sqrt{\varepsilon_z^+}\tan\left(\sqrt{\frac{m\varepsilon_z^+}{2\hbar^2}}L_z\right)=\sqrt{V_0-\varepsilon_z^+}$$

where the + sign denotes even states, and the subscript z refers to the fact that this energy eigenvalue is the solution to the separated variable Schrodinger equation that describes only motion in the direction perpendicular to the quantum well plane.

For odd states, similarly, the solutions may be found by solving the transcendental equation

$$-\sqrt{\varepsilon_z^-}\cot\left(\sqrt{\frac{m\varepsilon_z^-}{2\hbar^2}}L_z\right)=\sqrt{V_0-\varepsilon_z^-}$$

where a similar notation is employed.

Note that as the width of the well is reduced, the energies of the bound states increase: the smaller the well width, the greater the resulting blue shift from this quantum size effect.

The total single particle wave functions for free electrons or holes in a semiconductor quantum well with a non-degenerate, parabolic dispersion relation are plane waves that describe motion in the plane of the well, with particle-in-a-box motion in the direction perpendicular to the quantum well plane. That perpendicular motion exhibits the sinusoidal characteristic wavefunctions that decay exponentially as the particles penetrate into the barrier, and results in energy sub-bands that depend on the perpendicular motion quantum number j. The energy for these states varies as j^2/L_z^2.

2.3.4 Density of states in 2-d

We note the density of states in passing. Quantum confinement leaves the electron-hole motion in the plane of a semiconductor quantum well largely unaffected, as the differential equation for the fully three-dimensional Schodinger equation is separable in Cartesian coordinates. In the direction perpendicular to the plane of the quantum well, motion is quantized, and only wave vectors allowed that are multiples of π/L, where L is the quantum well layer thickness.

The single particle density of states may be represented as a function of energy as

$$g^{2d}(\varepsilon)d\varepsilon = g^{2d}(k_\perp)d^2k_\perp$$

where the wavevector $k_\perp$describes motion only in the plane of the quantum well. The density of states in k-space is explicitly

$$g^{2d}(k_\perp)d^2k_\perp = \left(\frac{1}{2\pi}\right)^2 2\pi k_\perp dk_\perp$$

which is valid if the density of states only need be used in quantities where the directionality of the wavevector $k_\perp$ is unimportant – i.e. those quantities that depend only on the magnitude of $k_\perp$.

2.3.5 Excitons in two-dimensions

As we noted in our description of optical absorption, it is necessary to consider the electron-hole Coulomb attraction in order to recreate the observed spectral features of a semiconductor. We now turn our attention to a description of the effects of Coulomb interaction on the behaviour of electrons and holes in a quantum well. The total Hamiltonian for carrier pairs in a quantum well may be written

$$H = -\frac{\hbar^2}{2m_e}\nabla_e^2 - \frac{\hbar^2}{2m_h}\nabla_h^2 + V_{confinement} + V_{Coulomb}$$

We change to a center-of-mass and relative position coordinate system; in those variables, the Hamiltonian may be rewritten

$$H = -\frac{\hbar^2}{2m_e}\partial_{z_e}^2 - \frac{\hbar^2}{2m_h}\partial_{z_h}^2 - \frac{\hbar^2}{2M_{xy}}\left(\partial_X^2 + \partial_Y^2\right) - \frac{\hbar^2}{2m_{XY}}\left(\partial_x^2 + \partial_y^2\right) + V_0(z_{e,h}) - \frac{e^2}{\epsilon_0 r}$$

Here, capital letters, as in the partial derivative operators, represent some quantity related to the center of mass, while lower case letters denote

quantities related to relative electron-hole motion. For example, M_{XY} is the in-plane total mass of the electron and hole, and m_{xy} is the reduced in-plane mass of the electron-hole pair, where

$$M_{XY} = (m_e + m_h)_{xy} \text{ and } \frac{1}{m_{xy}} = \left(\frac{1}{m_e} + \frac{1}{m_h}\right)_{xy} \text{and } \mathbf{r} = \mathbf{r_e} - \mathbf{r_h}$$

The total wave function $\psi(\mathbf{r})$ can then be separated into z and (x, y) dependent sub-functions,

$$\psi(\mathbf{r}) = \Phi_n^{xy}(\mathbf{r}_{xy})\,\zeta_{ei}(z_e)\zeta_{hj}(z_h)$$

where the function

$$\Phi_n^{xy}(r_{xy}) = u_{c0}u_{v0}\varphi_n^{xy}(r_{xy})e^{i\mathbf{K}_c^{xy}\cdot\mathbf{R}_{xy}}$$

defined with the periodic parts u_{c0} and u_{v0} of the conduction and valence band Bloch functions, and φ_n^{xy}, an exciton envelope function that describes the extent of the exciton in the x, y plane, and an exponential term that describes a plane wave solution for the center-of-mass motion of the exciton system in the x, y plane. On the ζ functions, the labels i and j denote the sub-band quantum numbers that describe the quantized motion in the direction perpendicular to the plane of the quantum well – these quantum numbers label the appropriate energy eigenstate and sinusoidal eigenfunction for perpendicular quantized electron or hole motion.

An analytical solution exists for the two-dimensional exciton; however

it's general case, for arbitrary quantum numbers, is not immediately enlightening, just as in the three dimensional case. The full expression in three dimensions is

$$\psi_{nlm}(\mathbf{r}) = -\sqrt{\left(\frac{2}{na_0}\right)^3 \frac{(n-l-1)!}{2n\left[(n+l)!\right]^3}} \left(\frac{2r}{na_0}\right)^l e^{-\left(\frac{2r}{na_0}\right)/2} L_{n+l}^{2l+1}\left(\frac{2r}{na_0}\right) Y_{lm}(\theta,\phi)$$

and in two dimensions

$$\begin{aligned}\psi_{nm}(\mathbf{r}) &= \sqrt{\frac{1}{\pi a_0^2\left(n+\frac{1}{2}\right)^3}\frac{(n-|m|)!}{\left[(n+|m|)!\right]^3}}\left(\frac{2r}{\left[(n+1/2)\,a_0\right]}\right)^{|m|} \times \\ &\quad e^{-\frac{1}{2}\left(\frac{2r}{\left[(n+1/2)a_0\right]}\right)} L_{n+|m|}^{2|m|}\left(\frac{2r}{\left[(n+1/2)\,a_0\right]}\right) e^{im\phi}\end{aligned}$$

[165]. More useful, perhaps, is a comparison of the ground state radial wave function in three dimensions

$$f_{1,0}(|\mathbf{r}|) = \frac{1}{a_0^{3/2}} 2e^{-r/a_0}$$

and in two dimensions

$$f_{0,0}(|r|) = \frac{1}{a_0} 4e^{-2r/a_0}$$

Where we can see, clearly, that the Bohr radius for the exciton in the quantum well is half that for the three dimensional bulk material [165].

The spectrum for the two dimensional, quantum confined system is

$$\varepsilon_n^{2d} = E_g + \frac{h^2\pi^2 j^2}{2m_r L_z^2} - \frac{E_B}{\left(n_j - \frac{1}{2}\right)^2}, n_j = 1, 2, 3, \ldots$$

with E_B the exciton Rydberg energy found for the Schrodinger equation for an exciton in in three dimensions, $E_B = \frac{\hbar^2}{2m_r a_B^2}$ where a_B is of course the exciton Bohr radius and m_r the reduced mass of the exciton system, calculated using the effective electron and hole masses [270].

The second energy term, explicitly proportional to j^2/L_z^2 , is the energy resulting from quantum confinement of the electron-hole pair. The last term, proportional to the exciton Rydberg, is due to the hydrogenic exciton system's binding energy. Note that compared with the three-dimensional exciton, the n term has changed to $n - 1/2$.

As a result, for $n = 1$, $E_{2d} = 4 \times E_{3d}$; the result of quantum confinement is that the exciton ground state is shifted further away from the bandgap than it would be in three dimensions. Experimentally, this makes it easier to excite excitonic states without also causing the excitation of a large number of free carriers. Additionally, the Bohr radius for the exciton confined in two dimensions is half that of the Bohr radius for the free, three-dimensional exciton. The increase in binding energy that occurs with the restriction to a two-dimensional system may be attributed to the exciton decreasing its Bohr radius isotropically, and as a result, raising its binding energy, in order to conserve spherical symmetry. While this does raise the binding energy of the exciton, it is energetically favourable compared to the admixture of states

that would be necessary to distort the exciton into an asymmetric probability distribution [165].

In AlGaAs-GaAs-AlGaAs quantum wells, the background dielectric is roughly equal in both the well and barrier. If the well dielectric is significantly larger than the barrier dielectric, there will be further enhancement of the exciton binding energy – this should only be a minor effect in the samples we investigate, as the GaAs has a slightly higher dielectric constant. This is called the local field effect, and results from the electron-hole Coulomb interaction being mediated differently by the different materials of either the barrier or the well [270].

Using the two-dimensional wavefunctions to evaluate the Elliott formula for optical absorption, we find a new selection rule that obtains for a strictly 2d system (i.e., one where the thickness of the well is small). In that limit, ζ functions, which describe the quantized motion of electron and hole perpendicular to the well, exhibit smaller and smaller overlap integrals until they effectively become orthonormal. As a result, when evaluating the Elliott formula for optical transitions, first class dipole transitions will only occur for $i = j$, i.e., only between quantized electron and hole states with the same quantum number.

The net result is that the Coulomb interaction, which is responsible for exciton transitions, modifies the stair-step absorption spectrum produced by free carrier absorption to include additional excitonic spectral line series that occur at each step.

2.3.6 AlGaAs-GaAs-AlGaAs multiple quantum wells

A multiple quantum well sample contains a number of quantum wells grown in the direction perpendicular to the plane of the well, with a barrier thickness sufficient to prevent the overlap of exciton wave functions from one well to another. We study a prototypical MQW material, fabricated with lattice matched, zincblende structured AlGaAs-GaAs-AlGaAs quantum wells. Both of these materials are direct band gap semiconductors with band extrema around $|\mathbf{k}|$ 0. The difference in the bandgaps of the two materials, which is termed the confinement energy, is split into an offset of the conduction bands and an offset of the valence bands.

As noted in our discussion of single quantum wells, these quasi-two dimensional systems permit some (quantized) motion in the direction normal to the plane of the well. The simple picture for this motion that we note above neglects degeneracy and assumes band parabolicity. As a result of those assumptions it is better suited to the description of the conduction band electrons rather than the valence band holes, as the conduction band does not exhibit the degeneracy present in the valence band states near the $|\mathbf{k}| \sim \mathbf{0}$ extrema. The dispersion relations for the two hole bands that interact significantly at energies near the band energy, the light- and heavy-hole bands (the split-off band is shifted in energy by the spin-orbit interaction and is sufficiently far from the band edge to neglect in a model of optical absorption) are the sum of two parabolic dispersion relations, one that describes the perpendicular motion and one that describes motion in the plane of the quantum

well:

$$\varepsilon_{hh} = -\frac{\hbar^2 k_z^2}{2\left(\frac{m_0}{\gamma_1 - 2\gamma_2}\right)} - \frac{\hbar^2 k_\perp^2}{2\left(\frac{m_0}{\gamma_1 + \gamma_2}\right)},\ J_z = \pm 3/2$$

and

$$\varepsilon_{lh} = -\frac{\hbar^2 k_z^2}{2\left(\frac{m_0}{\gamma_1 + 2\gamma_2}\right)} - \frac{\hbar^2 k_\perp^2}{2\left(\frac{m_0}{\gamma_1 - \gamma_2}\right)},\ J_z = \pm 1/2$$

where the Luttinger parameters γ_n are simply a system used to relate the effective masses of the holes to the rest mass m_0 of a free electron. They were derived [225] as terms in an approximate Hamiltonian to describe the motion of holes near the Γ point. In bulk GaAs, the two different masses of the light and heavy holes are actually equal at $|\mathbf{k}| \sim 0$, but the quantum confinement lifts this degeneracy. As a result of the different masses of the two hole bands, the quantum confined motion of excitons will be different depending on which band the holes come from. The effect is understood intuitively by considering the dependence of the energy of a particle in a box on the particle's mass. This lifts the degeneracy of the two different species of excitons, and, as a result, allows them to be spectrally resolved.

For GaAs, the heavy hole mass is greater than the light hole mass for motion quantized along the normal to the quantum well – $m_{hh,z} \sim 0.5 m_0 > 0.086 m_0 \sim m_{lh,z}$, but for motion in the plane, the light hole effective mass is actually greater, $m_{hh,\perp} \sim 0.11 m_0 < 0.23 m_0 \sim m_{lh,\perp}$.

If the quantum well layer is thin enough, the splitting between the light and heavy hole will be sufficient to observe a doublet exciton line for the $j = 1$ set of transitions (where here the quantum number j refers to transitions involving the lowest order quantized motion in the direction normal to the plane of the well). This is clearly the case in our single and MQW samples.

Fluctuations in the well layer growth will result in a broadening of the exciton lines, as compared to that seen in bulk GaAs. Well thickness will fluctuate during growth, with the distribution of variations in the layers typically obeying some sort of $L_z \pm \triangle L_z$ spread. The energy levels of the excitons in quantum wells vary as $1/L_z^2$, analogously to the energy levels of particles in a box, so that linear fluctuations in well width will lead to a quadratic spread in the transition energies of the exciton lines. This is an inhomogeneous broadening effect. A high-quality quantum well grown without any extrinsic doping to a thickness of 10nm should typically exhibit approximately 2meV of broadening at low temperatures; this compares to approximately 0.1meV linewidth in bulk samples for high quality GaAs at similar temperatures. Due to the inverse square nature of the dependence on well thickness, broadening will become progressively worse for thinner wells.

Since the quantum confinement related effects lead to a substantial increase in the exciton binding energy, a room temperature spectrum of an AlGaAs-GaAs-AlGaAs quantum well system may exhibit some exciton features even at room temperatures where the bulk material would fail to do so due to thermal interactions. This effect is not necessarily observable in

room temperature measurements of wide gap semiconductors, as may naively be expected – a simple analysis might suggest that since those materials also had higher exciton binding energies, an exciton absorption feature would also be visible in their spectra. But in these wide gap materials the scattering of excitons by longitudinal optical phonons increases correspondingly with the increase in bandgap, and, as a result, the exciton features cannot be observed in the spectrum.

2.3.7 Absorption anisotropy in GaAs MQW's

The most important selection rule obtained for the absorption of light by quantum wells is that allowed transitions will occur between valence electron states and conduction electron states that have the same quantized motion perpendicular to the plane of the quantum well – that is to say, to states that have the same j quantum number, where j describes which sinusoidal solution to the quantum well potential describes the motion of the electron (or hole, since those obey a similar solution). That selection rule is derived on the basis of the behaviour of the solutions to the infinitely deep quantum well; since the actual quantum well is not infinitely deep, there is some departure from this behaviour, and indeed, transitions that connect states that have different j quantum numbers do occur. These are forbidden transitions, which and are weak in comparison to the first-class, allowed transitions.

Transitions coupling to either the light-hole exciton or heavy-hole exciton depend strongly on the polarization of the photon that is absorbed.

Chapter 3

Light-matter interaction

3.1 Introduction

It appears that for any thesis dealing with the interaction of light and matter, the consensus opinion of Ph.D. candidates asserts the necessity of an elementary description of the quantum mechanical nature of these processes. Often, a description of the resonant interaction of light with a two-level system is provided; in this document, we consider several different schemes, beginning with the classical Lorentz model for the interaction of light with matter, then present the two-level model with a description of the Feynman-geometric model for that interaction, a derivation of the optical Bloch equations, a description of the semiconductor optical Bloch equations, and a digression on more sophisticated methods for describing the interaction of light and matter. This chapter is a digression itself, in a sense, but it provides context for our subsequent history of certain particular experimental and theoretical work on exciton optics, and is useful in understanding the density matrix toy model we develop for partially collinear 2d Fourier transform spectroscopy.

The ubiquitous *Optical Resonance and Two-Level Atoms* [6] is a reference recommended to the reader as an introduction to the classical light-mater

coupling material presented here, as is Haug and Koch's text [166] for classical and quantum material. The 1953 paper by Feynman et al. developing a geometric scheme to visualize the evolution of non-interacting two-level systems subject to external perturbation [121] is – again by apparent consensus of thesis authors – not optional. Diels and Rudolph's text [96] raises interesting questions about the underlying quantum theory we typically apply blithely to the study of problems such as ours .The search for a truly intuitive treatment of the semiconductor optical Bloch equations that does not depend upon a thorough understanding of quantum field theory is left as an exercise for the reader.

3.2 Resonant light and two-level systems

In the linear regime the response of a material system to an incident optical field may be described using the conventions of linear response theory. In that picture, if we assume a primarily electric response (an assumption that will not hold for magnetic materials or substances excited under extreme conditions), an effective transfer function may be defined in terms of the complex dielectric constant function $\epsilon(\omega)$, and the problem of understanding the linear interaction of light and matter reduces to finding this function [96]. The imaginary part of this function describes loss or gain processes by which the intensity of the optical field will change, while the real part describes dispersive phenomena – resulting, for example, in changes to the phase or group velocity of the optical field passing through the medium.

Subsequently, we will also consider the nonlinear interaction of light and matter. In that case, the polarization that is induced in the material cannot be so simply described, and is instead separated into first-order linear effects and a nonlinear response, $P = P^L + P^{NL}$. It is possible in some systems that the linear and nonlinear response of a material system arise due to different constituent parts of the medium interacting differently with incident optical fields. This is to be expected in the semiconductor systems we study, where the exciton features dominate the optical spectrum near the band edge, but the host or matrix dielectric material will interact with the same optical fields in a linear fashion.

3.2.1 A classical precursor – the Lorentz model

To a remarkable degree, the behaviour of the light-matter interaction can be developed using a classical oscillator model as derived by Lorentz, then extended by Planck and Einstein. Typically, this model is applicable – or at least, useful as an approximation – in the regime where the frequency of the light is insufficient to ionize any electrons [166]. The classical scattering formulae developed by Raleigh and Thomson are typically fairly good approximations until light in the deep x-ray regime is considered, and the first quantum mechanical models developed by Kramers and Heisenberg were found by application of the correspondence principle to the classical model of Lorentz [6]. We outline that theory here; perhaps its greatest utility is simply that it provides us with a standard, common language to use in discussions of optical

radiation processes.

Most optical phenomena derive from the interaction of electric charge with the electromagnetic field [253]. We are particularly interested in phenomena related to polarization. When matter is excited with a periodic oscillatory transverse electric field – light – a polarization oscillation is induced in the substance. Since most charge in conventional matter is bound to positive ionic cores, and exhibits only small amplitude oscillations about its equilibrium positions, the optical response can be assumed to depend largely on the motion of the most loosely bound electrons relative to the ionic crystal. The motion of an electron-ion pair is essentially a simple harmonic oscillator, which couples to the electromagnetic field via a dipole interaction.

Starting with the simplest equation of motion,

$$m_0 d_t^2 x_a(t) + m_0 \omega_a^2 x_a(t) = eE(t, \mathbf{r}_a)$$

where the subscript a simply labels a particular dipole oscillator in the crystal, we recognize that the classical description of the resulting motion leads directly to the conclusion that the accelerating charges involved will radiate, and that the classical amplitude of their oscillation will decay to zero in some finite period. By radiating, the oscillator loses energy to the electromagnetic field. Typically, atomic systems are expected to radiate on a characteristic time scale of tens of nanoseconds [6] due to this radiation reaction. Including such damping in the equation of motion in order to model this dissipation, one

obtains the equation of motion

$$m_0 d_t^2 x_a(t) = -2m_0\gamma d_t x_a(t) - m_0\omega_a^2 x_a + eE$$

where the decay time $\frac{1}{\tau_0} = \gamma = \frac{3m_0c^3}{e^2\omega_a^2}$ [93], [6] is expected to depend only upon the reduced mass and the resonant frequency of the oscillator (and certain fundamental constants).

The derivation of the classical analog to the Rabi problem demonstrates that damping of the oscillator results in an inherent linewidth to these transitions. Assuming that the perturbation is due to a harmonic driving field near the oscillator's resonant frequency,

$$E = \tilde{E}e^{-i\omega t} + c.c.$$

then the motion of each dipole oscillator may be decomposed into in- and out-of-phase terms,

$$x_a = x_0\left[u_a \cos\omega t - v_a \sin\omega t\right]$$

where the amplitude x_0 may be taken as a contant, but where the coefficients u_a and v_a are time-dependent. With some simpler calculation, an expression for the dipole amplitude may be obtained for long times

$$x_a(t) = \frac{e}{m_0}\widetilde{E}\left(\frac{e^{i\omega t}}{\omega_a^2 - \omega^2 + \frac{2i\omega}{T}} + c.c.\right)$$

where the decay term τ_0 used previously is replaced by a faster relaxation time T, based on the assumption that the dipole amplitude will decay more rapidly in a real, physical environment due to perturbative interactions or scattering events than it would in an otherwise empty universe. Indeed, in a quantum electrodynamic treatment, even if the oscillator were completely isolated from any other matter, the vacuum fluctuation of the electromagnetic field would still result in a decrease of the decay time.

Analyzing this expression for $x_a(t)$, it is apparent that the dipole is effectively driven into oscillation at the frequency of the incident field, but it exhibits a non-zero phase relation with that field. The full solutions for the in- and out-of-phase components may also be found in a straightforward fashion [6] – though we see little practical utility in doing so to interpret actual experimental results, as the early time classical solutions will deviate from the real, coherent, quantum mechanical response of the material system.

From the equation of motion, a polarization may be calculated

$$\mathcal{P}(\omega) = -\frac{n_0 e^2}{m_0} \frac{1}{\omega^2 + 2i\gamma\omega - \omega_0^2} \mathbf{E}(\omega)$$

where the subscripts used previously have been dropped for simplicity. Here, $\mathcal{P}(\omega)$ is the polarization per unit volume. We may define the optical susceptibility in a straightforward fashion as

$$\chi(\omega) = -\frac{n_0 e^2}{m_0} \frac{1}{\omega^2 + 2i\gamma\omega - \omega_0^2}$$

The renormalized resonance frequency for the transition – the actual energy at which the dipole oscillates – is shifted as a result of the damping term, and is given by $\omega_0^{'} = \sqrt{\omega_0^2 - \gamma^2}$. This permits the expression for the dielectric function,

$$\epsilon(\omega) = 1 + 4\pi\chi(\omega) = 1 - \frac{\omega_{plasma}^2}{2\omega_0^{'}}\left(\frac{1}{\omega - \omega_0^{'} + i\gamma} - \frac{1}{\omega + \omega_0^{'} + i\gamma}\right)$$

where the plasma frequency $\omega_{plasma} = \sqrt{\frac{4\pi n_0 e^2}{m_0}}$ is defined for a mean oscillator density n_0 [166]. The plasma frequency is the eigenfrequency for small oscillations of an electron plasma about its equilibrium density when perturbed. To be more physically concrete, we may sat that the plasma frequency is defined for an electron density n_0, and represents driven oscillations of the electron density distribution in the material. Discounting the non-resonant second term in the expression for the dielectric function, which we do under the assumption that the denominator $\omega + \omega_0^{'} + i\gamma$ will be large compared to 1 since the decay term γ is small compared to the resonance frequency ω_0, there is a straightforward expression available for the real and imaginary parts of the dielectric function

$$\epsilon'(\omega) = 1 - \frac{\omega_{plasma}^2}{2\omega_0}\frac{\omega - \omega_0}{(\omega - \omega_0)^2 + \gamma^2}$$

$$\epsilon''(\omega) = \frac{\omega_{plasma}^2}{4\omega_0}\frac{2\gamma}{(\omega - \omega_0)^2 + \gamma^2}$$

which describe, respectively, the diffractive and absorptive aspects of the optical response. The imaginary portion is related to absorption and emission events, and therefore is directly related to the lineshape of absorption spectral features. The lineshape that results from this kind of oscillation – recall that this expression for the dielectric is derived from a classical, damped, driven oscillator – is a Lorentzian function,

$$\frac{2\gamma}{(\omega - \omega_0)^2 + \gamma^2}$$

where the absorption resonance falls off as $1/(\omega - \omega_0)^2$ as the frequency of radiation diverges from the resonance. By way of contrast, the real part of the dielectric function, related to dispersive effects, falls off more slowly – as $1/(\omega - \omega_0)$ away from the resonant line.

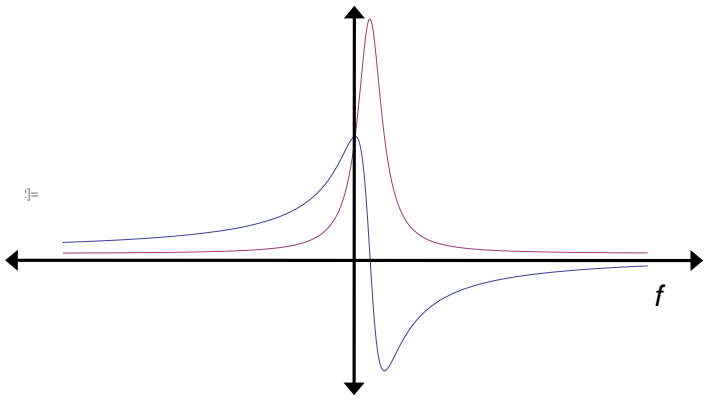

Dispersive (blue) and absorptive (red) lineshapes derived using a Lorentzian model.

Figure 3.1: Characteristic Lorentzian lineshapes

Though this classical model of absorption, emission, and dispersion seems far removed from a modern experiment designed to probe transient, coherent features in the response of semiconductor nanostructures subjected to precisely controlled ultra-fast laser pulses, it is worth noting that the separation of these different aspects of the optical response is of great significance in the analysis of those results as well. It is therefore illustrative to show that even the simplest model of light-matter interaction can illustrate the different aspects of the material behaviour under optical excitation. Obtaining a dispersive and absorptive two-dimensional lineshape is of no little interest in the semiconductor spectroscopy community and the ability to separately resolve these lineshapes in a multi-pulse experiment without relying upon post-experimental analysis is a non-trivial challenge.

The interaction of light and matter that we consider depends upon solution of the Maxwell equations using a (for now) macroscopic model of the polarization that acts as a source term in these equations. Having outlined a classical, Lorentzian model for the microscopic origin of that polarization, we now look past the particulars of its physical origin, since we will shortly replace that part of our model with a semi-classical, quantum mechanical model for the microscopic origin of the polarization.

Assuming a solution to Maxwell's equations that propagates in the z direction with wave vector k and extinction coefficient κ, both of which are frequency dependent,

$$E = E_0 \left(e^{i(k+i\kappa)z} + e^{-i(k+i\kappa)z} \right)$$

We find the following elementary dispersion relations

$$\begin{aligned} k^2(\omega) - \kappa^2(\omega) &= \frac{\omega^2}{c^2}\epsilon'(\omega) \\ 2\kappa(\omega)\, k(\omega) &= \frac{\omega^2}{c^2}\epsilon''(\omega) \end{aligned}$$

defining the index of refraction by $n(\omega) = ck(\omega)/\omega$ and the absorption coefficient as $\alpha(\omega) = 2\kappa(\omega)$ we can relate these constants, derived in the context of macroscopic, classical optics, to the microscopic, classical, damped oscillator model that we have used to approximate the real light-matter interaction

$$\begin{aligned} n(\omega) &= \sqrt{\frac{1}{2}\left[\epsilon'(\omega) + \sqrt{\epsilon'^2(\omega) + \epsilon''^2(\omega)}\right]} \\ \alpha(\omega) &= \frac{\omega}{n(\omega)\, c}\epsilon''(\omega) \end{aligned}$$

These results are the simplest useful model for the interaction of light with a material system.

The polarization derived in the context of the classical Rabi problem illustrates that even if each oscillator in the ensemble exhibited the exact same resonant frequency, the relaxation terms in the equation of motion result in an inherent linewidth rather than a Dirac delta function in frequency space.

This homogeneous broadening is given by the inverse of the lifetime, denoted T above.

Of course, a real array of dipole oscillators such as we study in the laboratory will always exhibit some distribution of natural resonant frequencies – the system response is that of an ensemble of individual oscillators, each with a certain probabilistic likelihood to possess a particular transition frequency. Perturbative effects will influence each quantum emitter in an ensemble slightly differently, resulting in a spread in their resonance frequencies. In gaseous systems, atoms or molecules at finite temperatures exhibit Doppler broadening, due to the spread in the velocities of the constituent particles; in a solid, similar broadening may arise due to variations in the local environment from strain or defects in the sample. Essentially, the indistinguishability of the members of the ensemble is reduced. As a result, a large, macroscopic number of natural emission lines will occur in the light radiated by this dipole array as the material dumps energy into the electromagnetic field. If the lines are well-separated spectrally, it is possible to treat separately the dipoles that are oscillating within a given frequency range, barring the occurrence of some other coupling mechanism between oscillators – for example, in a quantum mechanical treatment, lines that are spectrally close will be inherently quantum mechanically coupled via level repulsion, etc.

If each member of an ensemble exhibits different transition frequencies, there will be a resulting spread in the polarization (and subsequent radiation) in the material. The spread in these frequencies will result in a line that is by

definition greater than the homogeneous width of the isolated quantum emitter's transition. This width is termed the inhomogeneous linewidth, because it occurs due to the inhomogeneity experienced by the members of the ensemble in their local environments. This width can generally be treated with a normalized distribution function, $G(\omega_0)\, d\omega_0$, determined by the fraction of oscillators that exhibit a characteristic frequency that falls within $\pm d\omega_0/2$ of the center frequency ω_0. For many calculations, this normalized distribution is actually expressed instead with the detuning as the independent variable that describes members of the ensemble, $\int_{-\infty}^{\infty} d\Delta' g(\Delta') = 1$ where $\Delta = \omega_0 = \omega$ and the lower limit of integration can almost always be extended to negative infinity.

3.2.2 A discrete level quantum mechanical system coupled to a classical light field

By the equivalence principle, the quantum mechanical picture of light-matter interaction may be derived from the results obtained in a classical analysis. The analysis here follows that found in [166].

We consider an optical field coupled to the dipole moment of an isolated quantum mechancial system – the prototype is a hydrogenic atomic system – resulting in a time-dependent mixing of its eigenfunctions. The time evolution of the state $|\psi\rangle$ is given by

$$i\hbar\partial_t |\psi\rangle = \left[\hat{H}_0 + \hat{H}_{int}\right] |\psi\rangle$$

with

$$\hat{H}_{int}(t) = -e\,x\,E(t) = -d\,E(t)$$

where we assume the electric field is polarized along the $\hat{x}$ direction for specificity. The wavefunction $|\psi\rangle$ is decomposed onto the basis states of the unperturbed Hammiltonian, which allows calculation of the set of expansion coefficients $\{a_m(t)\}$. To first order, the coefficients are found by

$$a_n^{(1)}(t) = \frac{-d_{nl}}{\hbar}\int d\omega\,\frac{E(\omega)}{2\pi}\frac{e^{-i(\omega+E_{nl}/\hbar)t}}{\omega+E_{nl}+i\gamma}$$

where the energy differences E_{nl} separate the two states coupled by the matrix elements d_{nl}, which will be zero for diagonal elements $n = l$. This is a linear response analysis, as it does not consider higher order terms in the applied field.

The calculation of those coefficients allows us to calculate $\mathcal{P}(\omega)$ and, thereby, the optical susceptibility

$$\chi(\omega) = -\frac{n_0}{\hbar}\sum_m |d_{lm}|^2\left(\frac{1}{\omega+E_{lm}/\hbar+i\gamma} - \frac{1}{\omega-E_{lm}/\hbar+i\gamma}\right)$$

where the summation over the various m states permits the possibility of more than two eigenstates coupling to the ground state l due to the interaction with the electric field. This is a semiclassical result, which may be compared to the classical, Lorentz model result

$$\chi(\omega) = -\frac{n_0 e^2}{m_0} \frac{1}{\omega^2 + 2i\gamma\omega - \omega_0^2}$$

and which clearly exhibits a similar resonance structure. The classical result obtained above is remarkably effective at approximating the semi-classical, weak field result.

For simplicity, we now consider only two levels coupled by the optical interaction, with (without any loss in generality) state 2 higher in energy than state 1. Assuming that the driving field is a simple, monochromatic electrical field, we obtain the following equations describing the populations of those states

$$\begin{aligned} i\hbar d_t a_1 &= -d_{12} \frac{E(\omega)}{2} \left[e^{-i(\omega + E_{21}/\hbar)t} + e^{i(\omega - E_{21}/\hbar)t} \right] a_2 \\ i\hbar d_t a_2 &= -d_{21} \frac{E(\omega)}{2} \left[e^{-i(\omega - E_{21}/\hbar)t} + e^{i(\omega + E_{21}/\hbar)t} \right] a_1 \end{aligned}$$

If the optical field is nearly resonant with the transition, the exponential function that depends on $(\omega - E_{21}/\hbar)$ will be a slow function of time, while the other exponential function will oscillate at approximately twice the optical frequency. The effect of this fast term will typically be discounted, as it is not expected to produce a resonant effect in the resulting susceptibility. Thus, the simplified expressions for the coefficients $\{a_1,\ a_2\}$ are found to be

$$
\begin{aligned}
i\hbar d_t a_1 &\simeq -d_{12}\frac{E(\omega)}{2}e^{i(\omega-E_{21}/\hbar)t}a_2 \\
i\hbar d_t a_2 &\simeq -d_{21}\frac{E(\omega)}{2}e^{-i(\omega-E_{21}/\hbar)t}a_1
\end{aligned}
$$

This simplification is known as the rotating wave approximation, after the analysis of spin states undertaken by Bloch, where the time-dependence of the coefficients in the two approximate equations above will be described as a rotation of the Bloch vector in a (non-physical) space, and these equations are known as the optical Bloch equations (in an eigenstate coefficient representation).

In the case of an exact resonance, the exponential terms go to zero in both of these time-evolution equations, and the resulting solution is

$$
a_2(t) = a_2(0)\, e^{\pm i\omega_R t/2}
$$

where the Rabi frequency, a measure of the coupling strength between the two levels, is given by $\omega_R = \frac{|d_{21}\, E|}{\hbar}$. As a result, the wavefunction for the state can be given

$$
|\psi(t)\rangle = a_1(0)\, e^{-i(E_1/\hbar\pm\omega_R/2)t}\,|\psi_1\rangle + a_2(0)\, e^{-i(E_2/\hbar\pm\omega_R/2)t}\,|\psi_2\rangle
$$

Clearly, we can see from this expression that the original eigenenergies for the unperturbed system are shifted into the new eigenenergies of the perturbed, interacting system. The effect of the light field has been to split the

initial states $|\psi_j\rangle$ into two doublets. As a result, there are now three possible transitions, one at the original, resonant condition, and two transitions arising from the splitting of the original levels, with energy differences $E_{21} \pm \hbar\omega_R$. The new levels that arise result in transitions that are labelled the Rabi sidebands. In order to observe these splittings it is necessary to use a sufficiently strong field that the Rabi frequency exceed any line broadening that occurs on the transition.

If the applied electric field is not exactly resonant, but has some finite detuning $\varpi = E_{21}/\hbar - \omega$, the solution is somewhat altered, resulting in

$$\begin{aligned} a_1(t) &= a_1(0)\, e^{\pm i\Omega t} \\ a_2(t) &= a_2(0)\, e^{\mp i\Omega t} \end{aligned}$$

where we have a generalized Rabi frequency defined by $\Omega = -\frac{\varpi}{2} \pm \frac{1}{2}\sqrt{\varpi^2 + \omega_R^2}$. The coupling again results in a splitting of the original energy levels; here, the two manifold of frequencies occur as

$$\begin{aligned} E_2 \;&\Rightarrow\; \hbar\Omega_2 = E_2 + \hbar\Omega = E_2 - \hbar\left(\frac{\varpi}{2} \pm \frac{1}{2}\sqrt{\varpi^2 + \omega_R^2}\right) \\ E_1 \;&\Rightarrow\; \hbar\Omega_1 = E_1 - \hbar\Omega = E_1 + \hbar\left(\frac{\varpi}{2} \pm \frac{1}{2}\sqrt{\varpi^2 + \omega_R^2}\right) \end{aligned}$$

The renormalized energies and corresponding states of the atom perturbed by the interaction Hamiltonian are called the dressed atomic states.

The splitting and shift of the energy levels is called the optical Stark effect, due to its similarity to the modification of the atomic spectrum in a DC electric field.

3.2.3 Nonlinear optical processes

There are a number of texts that describe at length the study of nonlinear optics. Boyd's often appears the favourite of many and is certainly recommended [41].

The optical response of a material system may be characterized by the polarization induced in the material as a function of the strength of the incident fields applied to it. For sufficiently strong excitation fields, the effect of the light upon a material may no longer be described within the framework of a linear response theory. Instead, we describe that nonlinearity with a susceptibility that is a function of the applied field

$$\begin{aligned} \mathbf{P} &= \epsilon_0 \overleftrightarrow{\chi}(E)\mathbf{E} \\ &= \epsilon_0 \left(\chi^{(1)}E + \chi^{(2)}E^2 + \chi^{(3)}E^3 + \ldots\right) \\ &= P^{(1)} + P^{(2)} + P^{(3)} + \ldots \end{aligned}$$

In general, the strength of two successive terms in the nonlinear expansion of the polarization can be estimated from

$$\left|\frac{P^{(m+1)}}{P^{(m)}}\right| = \left|\frac{\chi^{(m+1)}E}{\chi^{(m)}}\right| \approx \left|\frac{E}{E_{matt}}\right|$$

where the final ratio is the relative amplitude of the incident field compared to a characteristic electric field inherent to the material under consideration. Higher order nonlinear terms are expected to be weaker than lower order effects, though of course, that trend is not strictly followed – see, for example, the absence of a second order nonlinear response in most materials that nonetheless exhibit third order nonlinearities under sufficiently intense fields.

In general, $\chi^{(m)}$ is a tensor, and the vector quantity $\mathbf{P}^{(m)}$ is a product of that tensor with up to m optical fields, which may or may not be the same incident field – the nonlinear polarization may depend on field mixing effects. The m-th nonlinear polarization uses the $m+1$-th order tensor susceptibility $\chi^{(m)}$ to couple the applied field or fields. Nonetheless, for simplicity the tensor and vector notation may often be omitted.

The nonlinear polarization cannot be accurately represented by approximating the optical response as an instantaneous process. More properly, we reflect this by defining the response as a product in the frequency space $\mathbf{P}(\omega) = \epsilon_0 \left(\chi(\omega)^{(1)} E(\omega) + \chi(\omega)^{(2)} E(\omega)^2 + \chi(\omega)^{(3)} E(\omega)^3 + \ldots \right)$. In some cases it may be possible to approximate the system response as occurring infinitely quickly, but for the time scales of interest relevant to our experiments, it is necessary to consider the non-instantaneous nature of the nonlinear response of the system to electromagnetic radiation. A memory effect, as it were, of the past electric fields, persists until phase decoherence and energy relaxation processes erase their effects. To analyze the nonlinear response in

the time domain we use

$$\begin{aligned} P^{(n)}(t) &= \epsilon_0 \int\int \ldots \int \chi^{(n)}(t_1, t_2, \ldots, t_n) E(t - t_1) E(t - t_1 - t_2) \ldots \\ &\quad \times E(t - t_1 - t_2 - \ldots - t_n) dt_1 dt_2 \ldots dt_n \end{aligned}$$

in other words, we have to keep track of a time convolution function in order to understand the nonlinear polarization at any given time. This intuitively corresponds to the simple product noted above when working in the Fourier frequency space.

In particular, our experimental program is concerned with the third-order nonlinear optical response of a semiconductor system. In some cases, nonlinear processes may be exploited as light sources for wavelength ranges that are not otherwise readily available; for our purposes, however, the nonlinear response is of interest as a tool to observe the microscopic processes that occur on ultrafast time scales in the samples we study. The microscopic phenomena may be built into the macroscopic susceptibility, and measuring the behaviour of a nonlinear emission allows us to infer the parameters that correspond to our microscopic theory. The details of calculating a nonlinear susceptibility based on microscopic behaviour informs the greater part of the theory discussed in this thesis.

3.3 A density operator theory for nonlinear optics

3.3.1 Basic density matrix theory

It is a relatively straightforward matter to use either the Schrodinger or Heisenberg picture in order to determine the time-evolution of a quantum mechanical system if the initial conditions of that system can be adequately expressed. For example, if the measurement of an observable represented by the operator $\hat{O}$ is performed on a system that results in its wavefunction collapsing into an eigenstate that is a simultaneous eigenstate of the Hamiltonian (the necessary and sufficient condition is that the commutator of the operator commutes with the Hamiltonian, viz. $\left[\hat{H}, \hat{O}\right] = 0$), it is trivial to determine the subsequent behaviour of that system: the Hamiltonian or energy eigenstates are the stationary states of the system. Thus, this system would exhibit only a trivial evolution in time.

An apparently more complicated initial condition is also easily studied. If the system is prepared in a quantum mechanical state that is not a simultaneous eigenstate of the Hamiltonian, it is still proves to be a trivial matter to determine its behaviour at future times. The solution proceeds, as always, by first decomposing the initial state upon some convenient basis. If we make use of the energy eigenstates, their evolution is trivial, and simply by keeping track of the time-dependent coefficients of the component eigenstates we may readily understand the time evolution of the non-stationary state. Again, either the Heisenberg or Schrodinger picture can be used to determine the subsequent state of the system.

In the Schrodinger picture, we keep track of the evolution of a state ket,

$$|\psi_\alpha(t)\rangle = e^{-i\hat{H}t/\hbar}\,|\psi_\alpha(t=0)\rangle$$

where we have assumed that the relevant Hamiltonian is time-independent for the sake of simplifying this explanation. We may take the expectation value of an operator of interest at a later time, $\left\langle \hat{A} \right\rangle_t$, calculated using the appropriate bra dual to the ket for the state of interest. Note the choice of notation here, with the subscript indicating that the operator $\hat{A}$ is not a function of time. Time t appears here only as a parameter.

Compared to the Schrodinger picture, working in the Heisenberg picture is somewhat simpler if we are only interested in the evolution of a particular expectation value. We find

$$d_t A(t) = d_t\left[e^{i\hat{H}t/\hbar} A_{Schro.} e^{-i\hat{H}t/\hbar}\right] = \frac{i}{\hbar}\left[\hat{H}, A(t)\right] + \partial_t A(t)$$

In most problems we consider, there is no explicit time dependence for the Heisenberg observable A, and the last term on the right hand side is dropped.

The equivalence of these two different methods for studying time evolution was shown by Neumann Jnos. Thus, we seem to have a relatively straightforward scheme for predicting the evolution of a system if its initial

states is known. There is another type of uncertainty that often arises in consideration of quantum mechanical systems, however, and which is not due to non-commutability of operators. We now turn out attention to this difficulty: it is very likely that one will not possess sufficient initial condition information to completely describe a quantum mechanical system and thereby calculate its time evolution, i.e. that one does not have sufficient information to completely determine the wavefunction. In that case, it is still possible to describe substantially the behaviour of the system in time using the density matrix formalism.

In classical statistical mechanics, a measure of the likelihood of finding a system in a particular configuration is given by a phase space probability distribution (see, for example [190]. The quantum mechanical analog is the density matrix ρ.

The density matrix is not simply another way to calculate the time evolution of a quantum mechanical system. Instead, it allows us to consider mixed states,{this is the part we need} such as those that arise when phenomenologically treating dephasing and relaxation processes.

The density operator may be defined as $\hat{\rho} = |\psi\rangle \langle\psi|$ for a single quantum system. In matrix form, the density matrix elements ρ_{ii} determine the population of the i-th state in the system, while the off-diagonal elements ρ_{ij}, $i \neq j$, are referred to as the coherences between the i-th and j-th states. The equation of motion for the density operator may be defined using the Schrodinger picture equation of motion for $|\psi\rangle$ noted above. Straightfowardly

one may find (see, for instance, [315], [81], or many other texts on quantum mechanics)

$$\begin{aligned}
\partial_t \hat{\rho} &= \partial_t \left[|\psi\rangle \langle\psi| \right] \\
&= \left(\partial_t |\psi\rangle \right) \langle\psi| + |\psi\rangle \left(\partial_t \langle\psi| \right) \\
&= -\frac{i}{\hbar} \hat{H} |\psi\rangle \langle\psi| + \frac{i}{\hbar} |\psi\rangle \langle\psi| \hat{H} \\
&= -\frac{i}{\hbar} \left[\hat{H}, \hat{\rho} \right]
\end{aligned}$$

where we made use of the relation $\partial_t |\psi(t)\rangle = -\frac{i}{\hbar} \hat{H} |\psi(t)\rangle$. In the case that the Hamiltonian is not time-dependent this relationship can be obtained directly from the expression noted above for the time evolution of a ket in the Schrodinger picture. We note in passing that the time evolution of the density operator obeys a 'wrong-signed' Heisenberg equation of motion. This result is somewhat similar in its use to the classical Liousville equation, which describes the evolution of a probability distribution in phase space. It is not strictly correct to call this result a quantum Liouville equation, however, as that name is used for an equation that describes the time evolution of the Wigner probability distribution. Nonetheless, this name is often used.

To this point, however, the use of a density operator does not seem to provide any particular advantage as compared to considering the evolution of the wavefunction. For an ensemble, however, the density matrix operator can be defined as

$$\rho = \sum_{\alpha} p_{\alpha} \left|\psi_{\alpha}\right\rangle \left\langle\psi_{\alpha}\right|$$

allowing us to treat mixed states that cannot be modelled simply using a single state.

The density operator formalism also allows us to phenomenologically treat dephasing and decay processes. A generalized master equation that contains these population decay\transition rates and, additionally, terms describing the change in coherences between the levels of the system is known as the Lindblad equation. The details of mathematical physics that underlies this formalism is outside the scope of the current work; we will makes use of the practical results of this type of analysis to treat spontaneous emission from excited to lower levels, and to describe dephasing processes that occur in the systems under study. The use of this formalism in this limited application is intuitive and straightforward.

We may use the density operator to determine ensemble averaged expectation values in a straightforward fashion. For a given observable represented by the operator $\hat{O}$ we may find that observable's expectation value by tracing out the product of the density operator and that operator, viz. $\left\langle \hat{O} \right\rangle = Tr\left\{\hat{\rho}\hat{O}\right\}$.

3.3.2 Applicability of a density matrix model to ultrafast dynamics

Even an approximate description of the various ultrafast process in a solid is prima facie a complicated project. After excitation of a condensed system with a sufficiently fast laser pulse or pulses, the behaviour of an ensemble of dipole oscillators can be broken down into several different time scales. At very early times after the pulse interacts with the material, the light-matter interaction drives a coherent, oscillating polarization that arises due to a coherent coupling between optically coupled band states. This is a collision-free, coherent regime, where rapid transition – Rabi flopping – occurs among the coupled states, which are not dissimilar from a two (or few) level atomic system.

During the second period, phase relaxation occurs due to fast processes – such as carrier-carrier and carrier-phonon scattering in solid materials, which dominate and cause real (as opposed to virtual) excitation [270]. The carriers in such a system now occupy a non-thermal distribution among the relevant energy bands. During this time period, the coherence oscillation among band states ceases, and the ensemble of oscillators are no longer coherently coupled to the optical field. Phase relaxation has eliminated the well-defined phase relationship between the optical cycle of the exciting pulse and the oscillation of the quantum emitters.

Further collisions and scattering continue, and the system evolves in this third period from a non-thermal distribution back to a quasi-thermal equilibrium state. This is not a true equilibrium, which would require the

relaxation of the population to its original, unperturbed occupation of the various available states. This time period is sometimes called the hydrodynamic regime, and optical nonlinearities during this period arise principally due to many-body effects – Coulomb screening, state-filling, and so on.

Despite this complexity, a remarkable amount of headway in attacking the problems of describing these dynamics may be made using simple models in a density matrix theoretical treatment. Typically, such a method will treat the system as an ensemble of two-level systems that are resonant with an incident optical field – in the case of broadband excitation such as we use in our experiments, resonant simply means that the spectrum of the excitation pulses is sufficiently broad in the vicinity of the transition to result in gain or loss. We consider here the applicability of such a treatment to the physical systems we are most interested in – typically, it is simply assumed that such a treatment is valid. Given the interest in exploring non-Markovian dynamics with multi-dimensional spectroscopy, however, we would be remiss to fail to describe the criterion for using a density matrix model. Our discussion here follows [96].

The complexity of the system dynamics arise due to the interaction of particles with one another or with a non-resonant background. The resonant system – the ensemble of two-level systems – is assumed to be coupled to a dissipative bath with a large number of particles, with a large number of degrees of freedom. Since a large number of interacting particles involved, it is computationally intractable to calculate an approximate quantum mechanical

response for each member of the ensemble and to combine those responses to determine the macroscopic ensemble response. Very often, however, it is not necessary to treat each member's individual response, since the perturbations on each given member of the ensemble will often by stochastic in nature, when considered on a time scale greater than a certain correlation time. If the system under consideration is polled only at a frequency slower than the correlation time τ_C there will be no net effective force on an individual particle, as the particular stochastic processes during the period between measurements will have averaged to zero. For a homogeneous system the perturbations on all members of the ensemble should be similar. If the macroscopic measurement performed by an experimenter takes some finite amount of time to proceed its value will be a sampled property, averaged over the stochastic evolution of the ensemble during some measurement period T_M:

$$\overline{X}(t) = \frac{1}{T_M} \int_{t-T_M/2}^{t+T_M/2} X(t')dt'$$

[96]. So long as the measurement time is greater in duration than the correlation time characteristic of the stochastic perturbations, the behaviour of every ensemble member should appear identical. If the measurement time is less in duration than the correlation time, the perturbative forces acting on an ensemble member cannot be considered stochastic and will not average to zero during this interval; in this case, the members of the ensemble will appear distinguishable.

In room temperature condensed matter systems, the relevant correlation time is typically on the order of $10^{-14}s$, but this value may change substantially at lower temperatures. Since our experiments make use of a pulse duration on the order of $10^{-13}s$ this may be of significance to our measurements, and we expect that some effect may be observed as an unavoidable increase in noise, since the repeated measurement of an individual member of the ensemble may not be assumed to provide perfectly repeatable results even absent any noise of purely experimental origin. In practice we find good repeatability in most of our measurements, suggesting that the experiment is not limited by this possibly non-stochastic perturbative behaviour. As such, we assume the bath can be regarded as only a weakly perturbing influence on the behaviour of the resonant systems, and we may proceed using the density matrix formalism. While we have not shown conclusively that this is the case, our results do not suggest otherwise.

In this density matrix formalism, the effects of the dissipative bath are characterized by only two constants. The validity of this model only holds on time scales where the measurement occurs more slowly than the characteristic correlation time describing stochastic perturbations by the bath, limiting the useful temporal density of measurements that can be performed on such a system.

3.3.3 Coherent phenomena

One of the two phenomenological constants that quantifies the relaxation of an ensemble of quantum systems in the density matrix formalism is the dephasing time T_2, which may be probed with coherent spectroscopy techniques. This parameter describes how a coherent optical field creates a coherent excitation that then loses its well-defined phase relationship with that field over time [80]. We briefly describe the general nature of this relationship, to provide a better understanding of what we mean by coherent phenomena.

A high quality example of a coherent source is a continuous wave laser, which may be considered a nearly monochromatic source of radiation. The spectral power density for such a source is nearly a Dirac delta function at some specific frequency. If this light were emitted from a point source, it would have a nearly infinite coherence length and infinite coherence time. While actual laser sources used in experimental physics are by no means perfectly operating coherent devices, the electromagnetic radiation they emit nonetheless exhibits a remarkably well-defined phase relationship. The temporal coherence may be quantified with the correlation function

$$\left\langle \tilde{E}(t)\tilde{E}^{\star}(t+\tau)\right\rangle / \sqrt{I(t)I(t+\tau)}$$

and may be measured with, for example, a Michelson interferometer. Note that a bandwidth limited pulse would have unity temporal coherence using this definition.

Coherent phenomena in materials, however, are typically studied using pulsed sources with broad spectral bandwidth. As a general rule, the smaller the pulse width used in a given experiment, the greater temporal resolution that method can provide. It is frequently repeated that some coherent spectroscopic techniques provide temporal resolution determined by the precision with which pulses may be delayed rather than the temporal width of the pulse itself. Since those arguments frequently rely upon a theoretical model that depends upon an analytically straightforward perturbation solution for the system dynamics, the validity of that statement must be tested[96]. Caveat ad sapiens.

A similar correlation function can be used to quantify spatial coherence. If the source of some radiation field has a characteristic length scale much smaller than the wavelength of the emitted light, i.e. $d \ll \lambda$, the emitted radiation will have perfect spatial coherence. As an example, consider a single atom radiating perfect spherical wavefronts: any fluctuations in the transition frequency at the time of emission should propagate outwards from this isolated emitter at the same velocity. Therefore, any point on a given spherical surface centered on the atom will have perfect spatial coherence with anywhere else on that sphere. The degree of spatial coherence as a function of position in the radiation field may be probed in an analogous fashion to the measurements of temporal coherence; for example, using a Young's double slit experiment [96].

Most macroscopic sources studied in nonlinear optical spectroscopy are arrays, possibly ordered, of oscillating electric dipole sources. The coherent

four-wave mixing emissions we discuss at length in this thesis are emitted from arrays of dipoles – generally, analytical results will be developed to describe the radiated signal in terms of a macroscopic array of dipoles [402]. The antenna-like properties of these arrays may be exploited to study microscopic phenomena by collecting the highly directional radiation resulting from the polarization induced in these materials [183].

The spatial coherence of emitted radiation must be considered, at least in passing. Point source emission is not a realistic model for most of the light sources one will study in a typical experiment, and certainly not for four-wave mixing experiments on quantum wells where the laser spot on a sample may be tens of microns in diameter. Since $d \gg \lambda$ here, any sufficiently advanced model for the nonlinear optical response should consider the effects of the spatial array on the emission – including the consideration of the effect of disorder in the material [357]. Although little attention is generally paid to these effects in practice, in principle the angle between non-collinear beams, and indeed, the numerical aperture of those optics that focus all the beams used in an optical experiment, should be considered in order to ensure that the coherence length scale is appropriate for studying the material of interest. Generally, the relevant length scale is determined by the absorption length, and an angle between beams for which the coherence length (inversely proportional to the square of the angle) is approximately equal to the absorption length is appropriate. This assumes that the interaction length scale is essentially limited to a few times the absorption length [96].

3.4 The optical Bloch equations and geometric model

3.4.1 Vector model for quantum states on the Bloch sphere

Shortly after the war Felix Bloch outlined a basic theory of nuclear magnetic resonance using phenomenological relaxation parameters – the longitudinal and transverse relaxation times – to describe the decay of an inductively detected RF signal emitted from a precessing macroscopic magnetic moment [34]. In normal materials the application of a strong DC magnetic field results in nuclear paramagnetic polarization, as the individual magnetic moments of the constituent nuclei align parallel to the bias field lines. Subsequent application of an RF pulse (or series of pulses) at right angles to the bias field will result in a precession of the net magnetic polarization around that bias field. In a vectorial description, where the bias field forms the z-axis and the direction of the pulsed RF drive field forms one of the other two axes (for specificity let us choose the x-axis direction), the polarization may be represented by a vector that will sweep out paths of decreasing latitude as the frequency of the applied field approaches the Larmor frequency for the material sample – quantum mechanically, we may think of this as the applied field approaching resonance with the nuclear spin-flip transition. The result of the precessing magnetic field vector is an oscillating component of the nuclear polarization that lies at right angles to both the bias field and the applied RF field. Using material parameters for various prototypical substances of interest (for example, the proton spins on H_2O at room temperature and pressure, with a bias field of 1T) estimates suggest the feasibility of detecting the rapidly oscillating

field component arising due to spin precession using inductive pickup coils.

For completeness we note that this was not the first nuclear magnetic resonance experiment, as magnetic resonance techniques had previously been used by Rabi, Alvarez, Bloch, and others [297], [298], [299], [7] to measure the spin magnetic moments of nuclei. These previous experiments were in essence an extension of the Stern-Gerlach space quantization experiments that use an inhomogeneous magnetic field to separate a beam of atomic nuclei with different spins. Prior spin measurement experiments based on magnetic resonance relied on the application of an RF field in a region of space between different analyzer magnets. Tuning the applied field to resonance with a specific nuclear spin state transition effects a modulation of the intensity of the spin analyzed beam. Bloch et al.'s work was motivated by a scientific interest in developing a more direct probe of these transitions, which would not rely on spatially separating various constituent populations of a beam. As a footnote of some curiosity to the scientific historian we note that the Stern-Gerlach space quantization technique is still an experimentally useful tool, finding application today in the field of cold atom physics (for example), where it is employed to separate stretched spin states in quantum gases (see, for example [55].

We return to the Bloch nuclear paramagnetism studies. Quantum mechanically, the application of the bias magnetic field provides a quantization axis and splits the otherwise energetically degenerate magnetic sub-level states. The spin dipole interaction Hamiltonian may be written

$$H = -\mu \cdot \mathbf{B}$$

for a magnetic dipole μ in a static magnetic field $\mathbf{B}$. The energy levels of such a Hamiltonian are clearly determined by the spin quantum number of the particle of interest; in the case of a spin 1/2 particle there will be two magnetic energy levels.

Once these two levels have been spectrally resolved by the Zeeman effect (see, for example [340]), they can be coupled via an RF transition. A relatively straightforward problem in quantum mechanics follows, where the transition rates may be calculated if the wavefunctions for the two states are known, and a description of the dynamics may be found without too much difficulty. The RF pulse sequence prepares an ensemble of two-level systems in a coherent superposition, which possesses a macroscopic dipole moment. The excited material volume is a phased array of dipoles, and is capable of acting as a source term in the Maxwell equations

The elementary two-level quantum mechanical system is, however, unable to properly describe this system. As noted previously, the introduction of phenomenological relaxation rates, T_1, describing spontaneous emission from the excited state, and T_2, a dephasing rate describing the loss of phase coherence among the oscillators in the ensemble, is the two simplest parameter scheme that extends the usefulness of this model. In the field of magnetic resonance experiments, this was found to provide a useful model for interpreting

many of the physical phenomena observed. Indeed, the experimental result [35] published in the same issue of Physical Review demonstrated the success of the principle of nuclear induction.

The T_1 and T_2 parameters parameters exhibit a complex dependence on the specific details of a given system, and are generally impossible to calculate from first principles. Even in the absence of a conventional dissipative bath, if the ensemble of two-level systems were to reside in a perfect vacuum, the vacuum field itself would act as a perturbation. In this limiting case the vacuum fluctuations result in the inherent, natural line broadening of the transition. Of course, in most realistic systems, there are an enormous number of perturbations that perturbatively affect the individual oscillators in a macroscopic ensemble. We discuss elsewhere in this thesis the limits that stochasticity places on the time scales that may be probed using such a simple model for relaxation. For now, we turn our attention to visualization tools that are commonly used to develop an intuitive understanding of Bloch-like systems.

Feynman et alia describe a geometric method for visualizing the Schrodinger evolution of non-interacting, two-level quantum mechanical systems under the influence of some generalized perturbation [121]. They demonstrate that by performing a transformation of variables, the Schrodiinger equation may be written in the form

$$d_t \mathbf{r} = \omega \times \mathbf{r}$$

where the components of the vector $\mathbf{r}$ are defined such that they completely determine the state $|\psi\rangle$ of the system, and the components of ω are chosen such that it describes the perturbation that couples the two states. In developing this formalism they frequently refer to their prototype system, a magnetically coupled spin 1/2 system. In that case, the space in which the vector r is embedded is the real, three-dimensional physical space, though this is not generally true for an arbitrary two-level problem.

Nonetheless, if the Hamiltonian of an arbitrary two-level system may be written in an isomorphic functional form, then the evolution of that system is equivalent to the prototype spin 1/2 system, and may therefore be understood in a similar fashion. The authors suggest using this formalism to study and analyze various MASER problems, making the explicit connection between the relatively low frequency regime of NMR and the highest frequency regime accessible at the time (this 1957 paper predates the invention of the laser).

From this point, the connection between the underlying concepts of spin and electronic physics provides a robust foundation for a broad range of optical experiments. The advent of the colliding pulse mode-locked laser was still decades away and the time scales of interest could not yet be probed in semiconductor, but there was now a program to use the Bloch theory formalism to model the dynamics of optical excitations in solid state systems.

The geometrical representation developed in this paper doesn't actually provide any problem-solving capability not already present in a more conventional analysis of the Schrodinger equation, and no results can be obtained

that aren't already accessible to straightforward calculation, but it does provide a rapid pictorial representation of these problems that provides a more immediate sense of physical intuition.

Reaching back conceptually to Bloch's papers on spin dynamics [34], [35], the authors note that a complete, rigorous geometrical model of the Schrodinger equation evolution for a two level system is equivalent to the well-studied classical mechanics problem of the procession of a gyromagnet in a magnetic field (a gyromagnet is any object whose magnetic dipole moment is coupled to the magnitude and direction of its angular momentum, whether intrinsic spin or classical angular momentum). Restricting their attention to the dipole transition coupling of quantum two-level systems, they develop explicit analyses of MASER oscillators and radiation damping effects.

The wave function for a particular individual member of an ensemble of spatially distinct quantum emitters may be written

$$\psi(t) = a(t)\,\psi_a + b(t)\,\psi_b$$

where the state ψ is decomposed onto the two eigenstates of the Hamiltonian, which have eigenenergies $W + \hbar\omega_0/2$ and $W - \hbar\omega_0/2$. For the rest of the analysis, one may without loss of generality take the mean energy of this single system to be $W = 0$. In practice, it will be determined by the kinetic energy of the individual system, and possibly by any internal degrees of freedom that are not affected during the time period of interest. The resonant

frequency for the transition, ω_0 is taken to be positive semidefinite.

Frequently one will solve Schrodinger's equation for some quantum mechanical system subject to a perturbation V, obtaining the coefficients $a(t)$ and $b(t)$, and then use that knowledge of the complete wavefunction to calculate expectation values for any observables of interest for any subsequent time. But the complex coefficients do not immediately yield the values of the physical properties of the system, viz. the expectation values of operators corresponding to observables.

Nor is it sufficient for our purposes to solve for the magnitudes of these coefficients – which would only determine the population of the levels and the likelihood (probability) of a transition. In order to study any processes that depend upon coherence between the states it is required to solve for the phases of a and b – however, since the overall phase of the wavefunction is not significant, and can be set arbitrarily, the wavefunction $\psi(t) = a(t)\,\psi_a + b(t)\,\psi_b$ actually requires only three real numbers to be completely determined – the magnitudes of a and b and their relative phase.

The Bloch vector $(r_1,\ r_2,\ r_3)$ is formed from three real-valued functions of the coefficients $a(t)$ and $b(t)$ that may be shown to have a straightforward physical interpretation (unlike the coefficients themselves)

$$
\begin{aligned}
r_1 &= ab^* + ba^* \\
r_2 &= i\left(ab^* - ba^*\right) \\
r_3 &= aa^* - bb^*
\end{aligned}
$$

If an individual two-level system is perturbed in such a way as to move it into the ψ_a state, with no projection along ψ_b, r_3 takes on the value of unity. Of course, this would destroy any coherence between the two levels, which is reflected by $r_2 = r_3 = 0$. If the population is moved entirely to the other state, i.e. the projection of ψ onto ψ_b is 1, this will result in the Bloch vector $\hat{x}_3$-coordinate projection taking the value of -1, and again, the other two components will be zero. The Bloch vector will describe motion on a spherical surface; the first and second components describe the coherence between the two states while the third is determined by the population inversion.

It is also possible to express these quantities in terms of the density operator matrix elements – see, for example, [166] for a treatment of the Bloch vector description using density matrices. In some cases an alternate definition is preferred for the Bloch vector that eliminates fast, optical frequency oscillation from the geometric picture by defining the coherence components r_1 and r_2 to be proportional to the optical cycle by including a factor of $e^{i\omega t}$.

If a density matrix treat; the exponential term cancels out the fast oscillation by effectively moving into a coordinate system that co-moves with resonance Rabi oscillation in the x-y plane.

The time evolution of the vector $\mathbf{r}$ is found from Schrodinger's equation, which yields

$$i\hbar d_t a = a\left(\frac{\hbar\omega_0}{2} + V_{aa}\right) + bV_{ab}$$

Similar expressions may be obtained for $d_t b$, $d_t a^*$, and $d_t b^*$. These time derivatives of the coefficients may be used to construct the vectorial differential equation noted earlier,

$$d_t \mathbf{r} = \omega \times \mathbf{r}$$

where the vector ω is defined in the same space in which $\mathbf{r}$ is embedded, by

$$\begin{aligned}
\omega_1 &= \frac{1}{\hbar}\left(V_{ab} + V_{ba}\right) \\
\omega_2 &= \frac{i}{\hbar}\left(V_{ab} - V_{ba}\right) \\
\omega_3 &= \omega_0
\end{aligned}$$

All of these components are also all real valued functions. The only remaining real bilinear combination of the a and b coefficients is, by design, equal to the length of the vector $\mathbf{r}$:

$$|\mathbf{r}| = \sqrt{r_1^2 + r_2^2 + r_3^2} = aa^* + bb^*$$

and is constant in time.

The equation of motion described by

$$d_t \mathbf{r} = \omega \times \mathbf{r}$$

is isomorphic to that of the precession of a classical gyromagnet in a magnetic field. Logically, then, in the case that the two-level system of interest is in fact a spin 1/2 particle that can transition between two magnetic levels, the geometrical space in which $\mathbf{r}$ embedded is also the real physical space. In this case the components of $\mathbf{r}$, r_1, $r_{2,}\, r_3$ will be equal to (within some constants of proportionality) the expectation values of the dipole operator, μ_1, μ_2, μ_3, and the components ω_1, ω_2, ω_3 will be propotional to the components of the magnetic field H_x, H_y, H_z

In general, however, this formalism does not describe an $\mathbf{r}$-space that is necessarily equivalent to the real physical space. Nonetheless, the behaviour in the $\mathbf{r}$-space of some two-level system may be understood by analogously considering the equivalent dynamics of the well understood physical system of spin precession using a classical vector model (e.g. using something akin to a single site of a classical Heisenberg lattice model).

Significantly, this analysis permits the study of the effects of the material system acting back upon the electromagnetic field, – the effects of spin dynamics are typically observed by the emission or absorption of RF fields. It is easily shown that the energy for a single system in the ensemble is given

$$\left\langle \hat{H} \right\rangle = \int \psi^* \hat{H} \psi dV = \frac{\hbar\omega}{2} \left(aa^* - bb^* \right) = r_3 \frac{\hbar\omega}{2}$$

If energy is measured in units of $\hbar\omega/2$ then the total energy for the ensemble is the sum of all the r_3 values for each individual system, or, alternatively, is found from the projection onto the $\hat{x_3}$ axis of the vector sum

$$\mathbf{R} = \sum_i \mathbf{r}^i$$

integrated over the volume of interest in the material system. A superscript is used here to index the Bloch vectors of individual quantum emitters in the ensemble so as to avoid confusion with the components of those vectors.

More generally, any one particle operator $\hat{\varsigma}$ can be written as the sum of several bilinear terms in the coefficients $a\left(t\right)$ and $b\left(t\right)$,

$$\hat{\varsigma} = \varsigma_{ab} \sum_i \left(a^i \right)^* b^i + \varsigma_{ba} \sum_i \left(b^i \right)^* a^i + \varsigma_{aa} \sum_i \left(a^i \right)^* a^i + \varsigma_{bb} \sum_i \left(b^i \right)^* b^i$$

where the sum over i refers to the summation over each individual system in the ensemble. As a result, the operator $\hat{\varsigma}$ is a linear combination of the r_j or R_j components, and its value may be found as the projection of the vector $\mathbf{R}$ along some direction in the $\mathbf{r}$ space.

Transitions between the states can be modeled directly in this space as well. For an electric dipole, $\triangle m = 0$ transition, the perturbing potential that couples the two states may be written (as usual) as

$$V_{ab} = -\mu_{ab} E$$

For simplicity the matrix element μ_{ab} is taken to be real. Then the components of ω may be found

$$\begin{aligned} \omega_1 &= \frac{1}{\hbar}\left(V_{ab} + V_{ba}\right) = -\frac{2\mu_{ab}}{\hbar} E \\ \omega_2 &= \frac{i}{\hbar}\left(V_{ab} - V_{ba}\right) = 0 \\ \omega_3 &= \omega_0 \end{aligned}$$

then in this case, the expectation value for the dipole operator may be found using the appropriate bilinear combination of the a and b coefficients,

$$\langle \mu \rangle = a^* b \mu_{ab} + b^* a \mu_{ba} = r_1 \mu_{ab}$$

or, stated in the language of the macroscopic effects that occur due to the ensemble behaviour, the polarization of the system, $\mathbf{P}$, along the electric field, is equal to the projection of $\mathbf{r}$ on the $\hat{x_1}$ axis in the volume of interest.

For electric dipole $\triangle m = \pm 1$ transitions, assuming E_x and E_y to be the fields coupling to the dipole, then

$$V = -\frac{1}{2}\left(\mu^+ E^- + \mu^- E^+\right)$$

with $E^{\pm} = E_x \pm iE_y$, $\mu^{\pm} = \mu_x \pm i\mu_y$, which by some manipulation of the dipole $\mu^{\pm}$ operators yields the matrix elements coupling the two states

$$\begin{aligned} V_{ab} &= -\frac{1}{2}\mu_{ab}^{+}\left(E_x - iE_y\right) \\ V_{ba} &= -\frac{1}{2}\mu_{ba}^{-}\left(E_x + iE_y\right) \end{aligned}$$

again, taking μ_{ab}^{+} as real, $\mu_{ab}^{+} = \mu_{ab}^{-} = \gamma$, and

$$\begin{aligned} \omega_1 &= -\frac{\gamma}{\hbar}E_z \\ \omega_2 &= -\frac{\gamma}{\hbar}E_y \\ \omega_3 &= \omega_0 \end{aligned}$$

In both cases, the interaction can be envisioned by considering the behaviour of a corresponding gyromagnet precessing in a classical magnetic field.

The geometric formalism outlined here explicitly only treats the explicit quantum mechanical coupling that we obtain from the Schrodinger equation; nonetheless, an extension of this method that relies on the density matrix formalism permits the addition of the phenomenological relaxation effects that appear in the Bloch equations. In particular, such an analysis lends itself to the analysis of the photon echo effect (for which see elsewhere in this thesis).

That approach (after [166]) is useful for considering the coherent regime that occurs after ultrafast excitation couples two states in a semiconductor

system (or more accurately, two bands of states) coupled by an harmonic electric field $E(t) = \frac{E_0}{2}(e^{i\omega t} + e^{-i\omega t})$. If the the rotating wave approximation is applied, a single particle density matrix may be written

$$\rho(\mathbf{k}, t) = \sum_{\alpha,\alpha'} \rho_{\alpha'\alpha}(\mathbf{k}, t) |\alpha'\mathbf{k}\rangle \langle\alpha\mathbf{k}|$$

where α refers to the particular band of states (in our cases of interest, the conduction and two valence bands) and $\mathbf{k}$ refers to the crystal momentum of that state. Note that this analysis does not contain any interaction between different momentum states, i.e. this is still a non-interacting ensemble model.

The density matrix time evolution will satisfy the normal equation of motion for a density operator

$$d_t\rho(\mathbf{k}, t) = -\frac{i}{\hbar}[H_\mathbf{k}, \rho(\mathbf{k}, t)]$$

Working in the interaction picture (see, for example [315]) allows a simple calculation of the density operator matrix elements, which we will then use to determine the density operator matrix elements in the standard Schrodiner picture. In the interaction picture, the elements are found from the equation of motion

$$d_t\rho^{int}(\mathbf{k}, t) = -\frac{i}{\hbar}\left[H^{int}_\mathbf{k}, \rho^{int}(\mathbf{k}, t)\right]$$

where the interaction Hamiltonian will be diagonal – again, this analysis relies upon the assumption that one may ignore Coulomb interaction between states with different momenta $\mathbf{k}$. Working with the interaction density operator, defined by

$$\rho^{int}(\mathbf{k},t) = e^{i\hat{H}_0 t/\hbar}\rho(\mathbf{k},t)\, e^{-i\hat{H}_0 t/\hbar}$$

is equivalent to working in a rotating frame. A density operator matrix element in this picture will be associated with a particular transition between a valence and conduction band state for some particular momentum,

$$\rho^{int}_{cv}(\mathbf{k},\ t) = \left\langle c,\ \mathbf{k}\left|\rho^{int}(\mathbf{k},\ t)\right|\ v,\ \mathbf{k}\right\rangle$$

One may transform back to the Schrodinger picture to obtain the density operator matrix elements

$$\rho_{cv}(\mathbf{k},\ t) = \rho^{int}_{cv}(\mathbf{k},\ t)\, e^{-i(E_{c\mathbf{k}}-E_{v\mathbf{k}})t/\hbar}$$

The interband equations may be expressed as a simplified Liouville equation

$$(d_t + i\varpi_{\mathbf{k}})\,\rho_{cv}(\mathbf{k},t)\, e^{i\omega t} = -\frac{i\omega_R}{2}\left[\rho_{cc}(\mathbf{k},t) - \rho_{vv}(\mathbf{k},t)\right]$$

where the detuning is defined as $\varpi = (E_{c\mathbf{k}} - E_{v\mathbf{k}})/\hbar - \omega$ and the Rabi frequency as $\omega_R = \frac{d_{cv}E_0}{\hbar}$. This quantity is real as long as the dipole off-diagonal

matrix element is real. Again, for simplicity, this analysis uses the normal convention of assuming no diagonal matrix element for the dipole operator, and that $d_{cv} = d_{vc}$,

It is now possible to define a Bloch vector using these density matrix elements. In this treatment, the Bloch vector comprises three components,

$$\begin{aligned} U_1(\mathbf{k},t) &= 2Re\left\{\rho_{cv}(\mathbf{k},t)\, e^{i\omega t}\right\} \\ U_2(\mathbf{k},t) &= 2Im\left\{\rho_{cv}(\mathbf{k},t)\, e^{i\omega t}\right\} \\ U_3(\mathbf{k},t) &= \rho_{cc}(\mathbf{k},t) - \rho_{vv}(\mathbf{k},t) \end{aligned}$$

from which we immediately see that the $\hat{x}_3$-component again describes the population difference, while the first and second components describe the coherence between the coupled states. The exponential term in the coherence dependent terms removes the fast oscillation by moving into a coordinate system that co-moves with a resonant Rabi oscillation in the $\hat{x}_1$-$\hat{x}_2$ plane.

The time evolution of the density operator Bloch vector can be written in a compact form similar to that which we used previously, although due to the slightly different definitions used here, the equation

$$d_t\mathbf{U}(\mathbf{k},\, t) = \mathbf{\Omega} \times \mathbf{U}(\mathbf{k},\, t)$$

now depends on the vector $\mathbf{\Omega} = \omega_R\mathbf{e}_1 - \varpi_{\mathbf{k}}\mathbf{e}_3$, which determines the frequency of precession of the Bloch vector. As before, we understand this

equation in the context of the motion of a vector $\mathbf{g}$ that satisfies

$$d_t \mathbf{g} = \eta \times \mathbf{g}$$

which describes the rotation of $\mathbf{g}$ around the axis defined by the vector η at an angular frequency $|\eta|$. In the coherent regime, the optical Bloch equations represent the light-matter interaction as a rotation of the Bloch vector at a frequency determined by the inherent energy spacing of the different levels and the detuning of the optical field coupling them. If the field is turned off at some time, the time rate change of the Bloch vector goes to zero, and the Bloch vector remains frozen in that position.

If the system is excited on resonance (the detuning parameter $\varpi \to 0$), then the vector describing the perturbation, $\mathbf{\Omega_{res}} = \omega_R \mathbf{e}_1 - 0 \cdot \mathbf{e}_2$, lies along the $\mathbf{e}_1$ axis. The resulting evolution of the Bloch vector then simplifies to rotation around $\mathbf{e}_1$. Assuming that the population is initially distributed only in the lower level (note that we no longer refer to projection of a single quantum state onto a specific ψ_a or ψ_b as we are now working in an inherently many-body picture, albeit one without any interaction among its constituent members), on-resonant excitation will begin transferring population to the higher state; after a time $\omega_R t = \pi/2$, the $\hat{x}_3$-component of the Bloch vector, U_3, will equal zero. As noted, this component depends upon the population inversion, and at this point there is an equal population distribution in both states. At the same instant, the polarization, represented by the U_2 component, will

be maximal since the Bloch vector will lie in the $\hat{x}_1$-$\hat{x}_2$ plane. Continued excitation will decrease the value of U_2 and, by extension, of the polarization, as more population is moved into the higher energy level. After a time $\omega_R t = \pi$ the population is completely inverted, with $U_3 = 1$; at this point there is no polarization. Continued excitation from this point results in the system returning to its initial condition after time $\omega_R t = 2\pi$, at which point one whole cycle has been completed. This process is commonly known as Rabi flopping, and may be directly observed in optical nutation; for example, see the observation of transient spin nutation in nuclear magnetic resonance [364] or transient optical nutation [181].

A pulse of given duration will always result in rotation of the Bloch vector by a certain angle in this geometrical picture. For any non-zero detuning, the Ω_3 component of the perturbation vector is also non-zero value, and as a result the Bloch vector now rotates around an axis with a non-zero $\hat{x}_3$-component. The path that the Bloch vector traces on the Bloch sphere no longer passes through the inversion extrema (i.e. those points where $U_3 = \pm 1$). Thus for a finite detuning there is always some distribution of the population in both energy states.

As we have noted in this thesis, one of the significant advantages of using any density operator formalism is the flexibility it permits to add phenomenological dissipative terms 'by hand' to account for relaxation processes. Transverse relaxation time T_2 here results in the decay of the transverse components U_1 and U_2 (for the sake of clarity we note that this is not the origin

of this piece of jargon, as the nomenclature of "'longitudinal' relaxation time" and "'transversal' relaxation time" may be found in Bloch's theoretical paper outlining his formalism for nuclear magnetic resonance [34]). The population inversion U_3 decays by spontaneous emission or other non-radiative mechanisms, which are together described by the longitudinal relaxation time T_1. Deriving these quantities from theory is extremely challenging and most often an empirical value or semi-empirical value must be used. Including these effects, we re-write the optical Bloch equations

$$\begin{aligned} d_t U_1(\mathbf{k},t) &= -\frac{U_1(\mathbf{k},t)}{T_2} + \varpi_{\mathbf{k}} U_2(\mathbf{k},t) \\ d_t U_2(\mathbf{k},t) &= -\frac{U_2(\mathbf{k},t)}{T_2} - \varpi_{\mathbf{k}} U_1(\mathbf{k},t) - \omega_R U_3(\mathbf{k},t) \\ d_t U_3(\mathbf{k},t) &= -\frac{U_3(\mathbf{k},t)+1}{T_1} + \omega_R U_2(\mathbf{k},t) \end{aligned}$$

The simplest way to study the effect that these dissipative terms have is to assume the creation of an initial state for the Bloch vector, and then apply these time derivative equations in order to understand the subsequent rotation and decay of the polarization induced by the initial preparation. We do not consider specific examples here. We note again that this density theoretical, geometrical Bloch picture lends itself to an analysis of the photon echo type of experiment, which we shall turn to in depth later.

More important to us than the particular details of either of these two methods for visualizing the Bloch equations is the fact that the paper

outlining the original idea for a geometric scheme to aid in interpreting Bloch dynamics makes clear a concrete connection between the dynamics of a broad range of two-level systems. As long as the dynamics of an ensemble may be assumed to be dominated by the unperturbed energy structure of an isolated single oscillator and the coupling perturbation, the Bloch equations (for spin physics) or optical Bloch equations (for optically coupled electronic states) are expected to provide a reasonably accurate model for their temporal evolution. To some extent this is true, but the inclusion of many-body physics effects that are wholly inconsistent with the Bloch equation picture has proven necessary. Indeed, it is in the failure of the Bloch equations to adequately describe exciton dynamics in semiconductor nanostructures that has driven a great part of the scientific interest in this field, as new and more sophisticated theoretical frameworks have been developed to understand these many-body systems.

3.4.2 Semiconductor optical Bloch equations

The relatively tractable models based on the Bloch equations used to describe nuclear resonance are useful tools to develop an intuitive understanding of the dynamics of an ensemble of dipole oscillators, such as excitons created in a semiconductor quantum well. Nonetheless, these models are largely based upon the assumption that for a sufficiently low excitation density the system will behave as a non-interacting ensemble of two-level systems. A number of experiments test the validity of such theories, and indeed, prove that they cannot accurately describe the nonlinear optical response of Wannier excitons

in semiconductors. A more sophisticated model is necessary to understand the effects that exciton-exciton interaction have on the coherent emission. An immediate extension of the optical Bloch equation/Taira model is a number of results collectively referred to as the semiconductor optical Bloch equations. In particular, these models are well-suited to the study of higher excitation densities and the related nonlinear phenomena. A useful introduction to the semiconductor optical Bloch equations can be found in reference [166], which we largely follow here – the quality of this source should perhaps not be surprising given the authors' close involvement with the development of these theories (see, for example [251]).

In brief, the semiconductor optical Bloch equations are a set of differential equations derived in the second quantization formalism that describe the dynamics of coupled electron and hole populations and the resulting optical polarizations in the spectral region close to the band gap. The coupling between bands is described with a generalized Rabi frequency, resulting from the additive effects of the externally applied optical fields and the internal dipole field due to induced electron-hole excitations. Analysis of the semiconductor optical Bloch equations leads to the distinction of several distinct regimes, considered in terms of excitation density and characteristic timescale :

1. Low excitation regime – here, exciton resonances, and in some circumstances the formation of bi-excitons, dominate most optical properties. Phonon scattering is the most important relaxation and dephasing process. With greater density the scattering between multiple electron-hole

excitations becomes more significant. We note that most experimental work is typically performed in a low excitation regime in order to minimize the complexity that can arise in a denser system. At the low temperatures used to study exciton dynamics in semiconductor quantum wells, scattering is typically dominated by acoustic phonons.

2. High excitation regime – here, the process of optical excitation may create an electron-hole plasma. Coulomb screening of the carriers by other optically excited carriers and the collective plasma oscillations (plasmons, if they can be well characterized by a quasi-particle description) alter the optical properties of the material. The principal dissipative effects are carrier-carrier Coulomb scattering.

3. Quasi-equilibrium regime – here, the relevant system dynamics occur on relatively long timescales, or put differently, the relaxation processes tend to exhibit fairly long durations compared to the individual events that move the system back toward equilibrium. The populations of the excited states may be approximated with thermal distribution functions using an effective temperature. The relaxation toward an actual thermal equilibrium state is relatively slow and can be treated with semi-classical relaxation and dephasing kinetics.

4. Ultrafast regime – here, coherent quantum effects and the initial dissipative processes significantly determine the material's optical response. Decoherence processes, initial relaxation, and the development of cor-

relations (which require time to build up) are determined by quantum kinetics that may be non-Markovian, and generally depend on carrier-carrier and carrier-phonon scattering.

The semiconductor optical Bloch equations provide a relatively straightforward treatment of multi-pulse experiments and allow the study of both relaxation processes and the build-up of correlation among excited quasi-particles. Significant effort concentrates on explaining the results of four-wave mixing spectroscopy and time-resolved differential transmission spectroscopy that were not amenable to analysis using the optical Bloch equations.

The semiconductor optical Bloch equations, not surprisingly, bear a functional resemblance to the optical Bloch equations for an ensemble of non-interacting two-level systems:

$$\begin{aligned}
\partial_t P_k &= -i\left(e_{e,k}+e_{h,k}\right)P_k - i\left(n_{e,k}+n_{h,k}-1\right)\omega_{Rk} + \partial_t P_k\mid_{scattering} \\
\partial_t n_{e,k} &= -2Im\left\{\omega_{Rk}P_k^*\right\} + \partial_t n_{e,k}\mid_{scattering} \\
\partial_t n_{h,k} &= -2Im\left\{\omega_{Rk}P_k^*\right\} + \partial_t n_{h,k}\mid_{scattering}
\end{aligned}$$

where the polarizations P_k would correspond to the off-diagonal terms in a density operator calculation, while the populations $n_{e/h,\,k}$ would correspond to the diagonal terms. The index e/h labels an electron or hole states here, while k is the normal crystal momentum. The terms $e_{e/k,\,k}$ are single particle energies for an electron or hole state at a given momentum. The

terms proportional to $2Im\{\omega_{Rk}P_k^*\}$ describe the light-matter coupling that generate electron and hole pairs via absorption. If the scattering terms are discounted, the rate change of the hole and electron terms are equal. The term in the first of the SOBE's proportional to $(n_{e,k} + n_{h,k} - 1)$ may be re-written $-(-n_{e,k} - n_{h,k} + 1) = n_{v,k} - n_{c,k}$ and is clearly just the population inversion for states with momentum $\mathbf{k}$. The effects of this term on the polarization are known variously as Pauli blocking, state filling, or phase space filling, and contribute significantly to the many-body dynamics of an exciton system. These effects were among the first studied in the development of the semiconductor optical Bloch equation [322]. The saturation of an exciton absorption resonance due to free carrier plasmas or exciton gases was studied in a relatively low density regime, where the interactions were mediated by long-range phase-space filling and exchange forces. The screening of Coulomb forces was found to be relatively weak in a two-dimensional exciton gas, permitting the effect of these perturbations to extend across the relatively large inter-particle spacing.

Superficially, it may appear that these equations are decoupled in terms of momentum $\mathbf{k}$, and that this is not actually a many-body theory at all. The interaction effects are present, nonetheless, and appear implicitly in the generalized Rabi frequency. This generalized frequency ω_{Rk} actually couples states of different momenta to the state k; physically, that coupling is due to the effective field's dependence on Coulomb mediated interactions with the induced polarization as well as usual, external optical fields. The exciton-exciton in-

teractions also appear in the form of the Coulomb interaction terms in the exchange energy, which in part determines the renormalized single particle energies $e_{h/e,\,k}$.

Mean field theories – those that assume that a single particle wave function interacting with an average field that approximates the effect of many-body interactions along with any external perturbations – may be considered without introducing the scattering terms in the semiconductor Bloch equations. All the interactions beyond the mean field are contained in the scattering terms, which describe dissipative behaviour like dephasing for the inter-band polarization and population distribution relaxation induced by collision. Those relaxation mechanisms cause system to return to thermal equilibrium before a purely radiative decay would occur if the system comprised only a single isolated oscillator subject to no external perturbations; this is analogous to the substitution $\tau_0 \rightarrow T$ in our description of the relaxation of a classical Lorentz oscillator.

Again, it is analytically and numerically intractable to model the perturbative forces that enhance relaxation processes from first principles, and again, a phenomenological description of relaxation is used. This requires at least two relaxation time constants, $T_1^{'}$and T_1:

$$d_t n_{e,k} \mid_{scattering} = \frac{f_{e,k} - n_{e,k}\,(t)}{T_1^{'}} - \frac{n_{e,k}\,(t)}{T_1}$$

where the first term models intra-band relaxation, as a non-equilirium

distribution in a given band evolves toward its thermal distribution without changing the number of carriers, while the second term describes the inter-band recombination of carriers. The simplest description of dephasing kinetics for the interband polarization once again uses a constant transverse relaxation time T_2. Nonlinear and non-Markovian effects establish the limits of applicability of this approximation, but when it is valid is tends to work well even if the underlying dynamics that result in dephasing are quite complex. Conceptually, we might suggest that if the perturbations may be viewed as stochastic on those time scales that are probed with macroscopic optical measurements, these relatively simple models for dephasing and population relaxation are satisfactory.

In certain regimes, the use of ultra-short pulses may require abandoning the Markov approximation that allows the scattering terms described here to be dealt with using a Boltzmann-like scattering form. In the ultra-short regime it may be necessary to use quantum kinetics that keep track of the scattering processes with a memory structure that describes processes that are not completed during the duration of the pulse – quantum coherence among electron states influences the scattering dynamics, giving rise to a combination of coherent and dissipative effects.

In the limiting case of no interaction the semiconductor optical Bloch equation can be used to reproduce the results of the Wannier equation for electron-hole pairs or the optical Bloch equations for free carrier transitions.

Typically, a self-consistent treatment using the semiconductor optical

Bloch equations to describe the source polarizations in the Maxwell equations is necessary to describe the complete physics of a system exited by a pulsed source if the material system has sufficient spatial extension that propagation effects cannot be ignored – such as the polariton effects that arise when a photon and exciton mode mix into a propagating hybrid mode. These propagation effects are generally neglected in optically thin samples, though the validity of that assumption as applied to even the thinnest direct band gap materials may be questionable for resonant or near-resonant excitation. If it is reasonable to consider the material as an optically thin sample, the transmitted optical field is simply proportional to the calculated polarization field induced in the material, and an integro-differential equation describing propagation effects can be avoided.

We note for the sake of completeness that a significant portion of the work on semiconductor optical Bloch equation theory was developed in the context of the excitonic optical stark effect, where sub-resonant excitation was observed to result in the splitting of the exciton peak near resonance in differential transmission, pump-probe measurements. We do not discuss this problem at length here.

Chapter 4

A history of exciton optics

4.1 Nonlinear optical spectroscopy and its relation to nuclear resonance

Early spectroscopic measurements of excitation in semiconductors concentrated on the dynamics of free photo-excited carriers. After Elliott's description of optical absorption by exciton emission, a significant effort was made to understand the dynamics of these bound electron-hole pairs. Most studies interpreted the results of time-resolved spectroscopy of excitons following the models previously developed with great success in NMR. Coherent optical spectroscopic tools were developed to study the process of optical decoherence, that is, to understand how a population of excitons coherently created by ultrafast laser pulses would lose their well-defined phase relationship.

The Bloch equations [34] were found to be successful in describing the dynamics of an ensemble of magnetic spins aligned by a bias field and subsequently excited and studied with pulsed RF electromagnetic fields [35]. The particular utility of this theory for understanding the behaviour of so broad a range of phenomena was due to its description of the relaxation toward thermal equilibrium using only two physical parameters, the population decay time T_1 and the dephasing time T_2, frequently called the longitudinal and transverse

relaxation times for historical reasons. It is assumed that there is some set of perturbative processes that induce relaxation that are generally too complicated to describe from first principles, but which may be approximated on a sufficiently long time scale by a straightforward decay of coherence and population among the members of the excited ensemble. See elsewhere in this thesis for a brief description of the applicability of this density operator theoretical model as regards to the assumption of stochasticity of the perturbing forces acting upon the ensemble.

An enormous body of scientific progress has been performed using nuclear magnetic resonance techniques to study a wide variety of systems for which spin flip transition energies and relaxation times – in part, the broad applicability of such techniques is only possible by a happy accident of the value of material parameters that results in the emission of RF signals that can be readily detected in a normal laboratory environment.

4.1.1 Spin echoes and the development of photon echoes

Significant advancements in nuclear resonance relevant to our own include the development of multiple-pulse experiments, which frequently serve as a model for developing corresponding optical spectroscopic techniques. Notable among these are the spin echo technique [156]. In a spin echo experiment, a series of RF pulses with temporal widths sufficiently short compared to the relevant relaxation times are used to resonantly excite spin-flip transitions in a liquid. After the pulse sequence has finished, the macroscopic magnetiza-

tion induced in the material continues to evolve, as the individual magnetic moment vectors precess freely around the quantization axis.

For an inhomogeneously broadened transition, the statistical distribution of the Larmor frequencies for each of the members of the ensemble also determines these magnitude of those individual moments. The individual magnetic moment vectors will fan out due to their different precession rates, resulting in a rapid decay of the macroscopic magnetization due to this dephasing, and therefore in the intensity of the inductively detected radiation. Nonetheless, the series of applied pulses determines specific times in the future when there will be a constructive interference among the individual magnetic moment vectors, resulting in the observation of a revival – the spin echo – in the spontaneous nuclear induction signal.

This effect is described using the Bloch theory, and allows direct measurement o f the relaxation times by observation of the amplitude of the spin echo signal as a function of the delay times used for the pulse sequence. An early extension of the spin echo technique was used to measure both transverse and longitudinal relaxation times [59], studying the effect of artificially induced inhomogeneous broadening on the temporal line shape of a spin echo signal. This allowed the study of the effects that diffusion has on a coherently prepared ensemble of oscillators – illustrating a clear direction for a large volume of later work using photon echoes or similar multiple pulse optical spectroscopic methods.

The conceptual connection between the Bloch model for nuclear res-

onance and excitation of optical frequency transitions was made explicit in the mid-1950's, shortly after these early papers on spin echo methods demonstrated the capabilities of sophisticated spectroscopic techniques for characterizing and describing a broad range of material systems [121]. Feynman et alia describe a geometric method for visualizing the Schrodinger evolution of non-interacting, two-level quantum mechanical systems under the influence of some generalized perturbation. While useful as a tool for developing physical intuition for the evolution of two-level systems, this paper is more important for our purposes for its role as a link between the well-developed field of nuclear resonance physics and the optical science that was possible after the development of coherent radiation sources at the appropriate wavelength – i.e., the invention of the laser [259].

After light sources in the infrared and optical range became available, a number of experimental programs were conducted to demonstrate optical analogs of phenomena observed in nuclear spin transitions. While these results were scientifically important in so much as they characterized the optical response of a number of materials, they are more significant for developing nonlinear optical techniques that would be used to study a broad range of systems.

Early results from the Columbia Radiation Lab included the observation of a photon echo – analog to spin echo – in a solid state sample. Ruby crystals had been used to develop the first visible wavelength lasers, and were studied in a number of early nonlinear optical experiments [229]. Two pump

pulses are used to induce the emission of a photon echo, observed after a delay almost exactly equal to the delay between the two incident pulses, in a result analogous to spin echo observations [156].

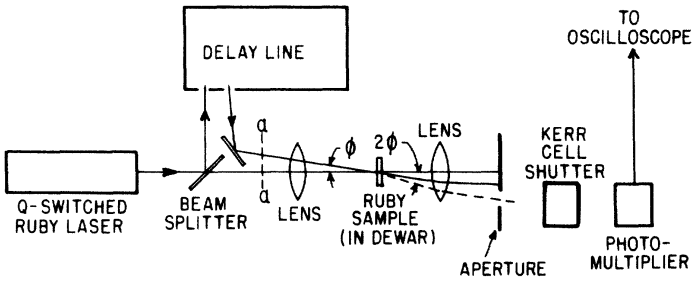

Schematic for first photon echo experiment. Reproduced from Kurnit et al. Physical Review Letters 13:567 (1964).

Figure 4.1: First photon echo schematic

Here, the photon echo measurement was used to study the dephasing of electron spins on chromium ions in the ruby matrix, due to spin flips with adjacent aluminum nuclei and electrons.

The first excitation pulse induces a Lamb-Dicke superradiant state [94] in the material, which has a large macroscopic dipole moment due to correlations among the individual emitters in the ensemble. This macroscopic ensemble will oscillate at the optical frequency, emitting radiation, until it decays via population relaxation and/or dephasing. In some materials, the time scales of those two processes are comparable, although in these samples

dephasing processes will dominate due to the relatively long population lifetime, while dephasing occurs due to inhomogeneity principally arising from crystal strain. After significant dephasing has occurred but the population is predominantly still present in the excited state (at this point, the population relaxation continues by normal spontaneous emission), a second pulse arrives and induces a reverse time evolution for the ensemble. After a waiting time equal to the delay between the two incident pump pulses, this rephasing process (as it is called) will have caused a revival of the macroscopic dipole state, emitting a correspondingly intense coherent pulse of radiation. This is the photon echo.

The first experimental observation of the photon echo [229] used a q-switched pulsed laser source to produce 10 ns pulses. The limits of laser technology at the time restricted the materials tractable to this type of time-resolved spectroscopy. Non-collinear pump pulses excite a ruby crystal sample at liquid Helium temperatures, producing a photon echo signal in the phase-matched direction. A significant fraction of the experimental effort in these early results was focused on demonstrating that the photon echo was not a spurious signal.

The photon echo is explained using an ensemble of two-level systems [2], explicitly noting the similarity between its behaviour and spin echo systems by referencing the Feynman paper on two-level systems [121]. There is a distinction made between the nature of the emission, which in a nuclear resonance experiment depends on the vector sum of individual magnetic moments

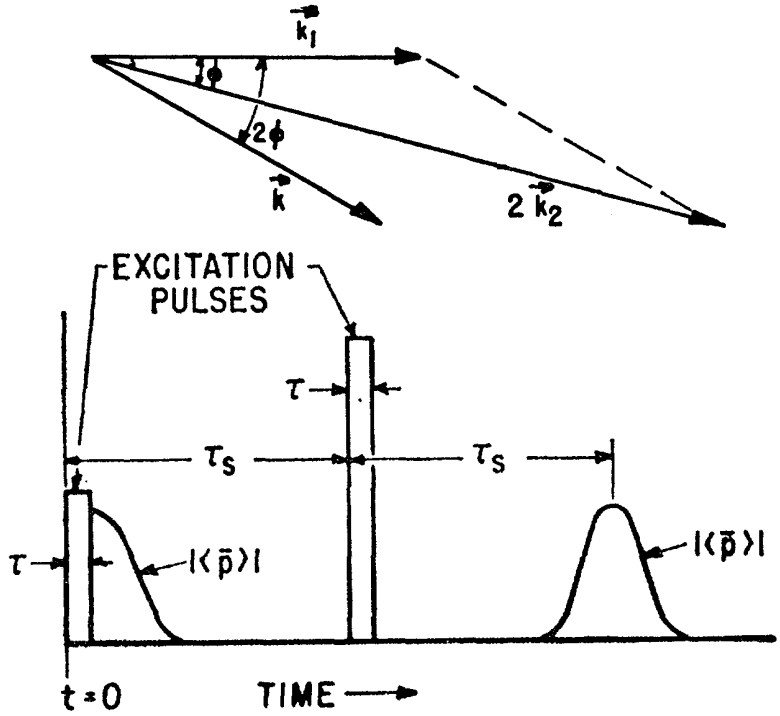

Phase-matching geometry (a) and timing sequence (b) for the first photon echo experiments. The nonlinear signal is emitted along ***k***, in a background free direction. The timing diagram indicates the relative timing of the photon echo signal (and the initial free-induction decay) relative to the two intense excitation pulses. The photon echo is indicated here by the revival of the dipole expectation value. Adapted from Abella et al., Physical Review 141:391 (1966).

Figure 4.2: Phase-matching and timing for photon echo

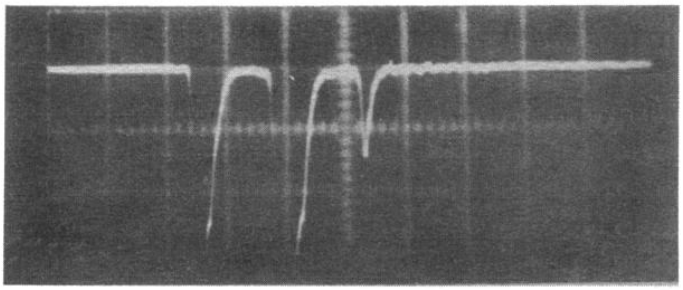

First photon echo signal. Time increases from left to right in the oscilloscope traces. The right-most feature is the photon echo signal observed in a ruby crystal. Reproduced from Kurnit et al. Physical Review Letters 13:567 (1964).

Figure 4.3: First observed photon echo signal

– both the ground and excited states have a permanent magnetic dipole – whereas in an optical photon echo experiment, the electric dipole moment depends on a coherence induced between two states, since no permanent electric dipole moment generally exists for either states. Nonetheless, the dependence of the ensemble's temporal evolution on a dipole matrix element is similar in both cases.

An optical Bloch equation can be used to describe the evolution of a pseudo-electric dipole moment vector that represents the transverse components of the electric dipole moment and the degree of excitation of the system, similar to the Bloch equations used for magnetic dipole evolution under an applied field. Similarly, phenomenological relaxation terms may be used to

describe decoherence and population relaxation.

In order to predict a photon echo, it is necessary to develop a theoretical treatment that can describe the inhomogeneity present in the material system. After the first pump pulse excites a coherence in the sample, the individual Bloch vectors (using a geometrical model where an individual vector describes the evolution of each emitter in the ensemble – see our previous description of geometric\Bloch sphere models) fan out in the space in which the Bloch vectors $\mathbf{r}^i$ are embedded, as each evolves with a different resonant frequency. That fanning out reduces the magnitude of the vector sum of the individual dipole moments that comprise the net, macroscopic polarization, a function of $\mathbf{R} = \sum_i \mathbf{r}^i$ in the Bloch vector space. As the polarization is reduced, the power radiated by the system decreases.

The second pump pulse induces evolution that reverses the motion of the Bloch vectors. More specifically, in the geometric picture, the second pump pulse actually rotates all the Bloch vectors through π radians, so that the staggered order of the individual vectors has been effectively reversed, with the fastest evolving oscillators now lagging the slowest. During the subsequent evolution, those fastest precessing vectors will now 'catch up' with the slower Bloch vectors. After a waiting period equal to the delay between the two pump pulses the individual Bloch vectors have rephased and are now closely bundled in the Bloch vector space. After rephasing, the macroscopic electric dipole is a linear combination of superradiant states that emits strongly due to coherence among the individual emitters; the intensity of this, given by Dicke [94], is

$$I = \frac{1}{2}N\left(\frac{1}{2}N + \frac{1}{2}\right)I_0$$

where I_0 is the intensity emitted from a single, isolated quantum emitter, and N is the number of emitters in the volume of interest in the material (the volume is assumed sufficiently small that the electric dipole approximation is valid, i.e. that the variation of the electric field across the volume is small). This superradiant emission is strongly enhanced compared to incoherent radiation from N emitters without correlation,

$$I_{incoherent} = \frac{1}{2}NI_0$$

arising from an ensemble with random phases. If the spatial extension of the sample is considered the electric dipole approximation will typically need to be dropped, but the emission from a phased array of dipoles will likely give rise to a strongly directional, intense photon echo emission that may be detected in the phase-matched direction, while the emission will average to zero over most other directions. For pump pulses along $\mathbf{k}_1$ and $\mathbf{k}_2$, phase-matched emission occurs along $2\mathbf{k}_2 - \mathbf{k}_1$ – a background-free direction that permits the use of a sensitive detector to pick out the photon echo signal and reject the pump beams. Collinear photon echo geometries were also explored [2], but were only feasible because a fast shutter could effectively block the pump power from saturating the detector.

Subsequent experiments in the gas phase studied the decay of photon

echo signals to extract dephasing times for transitions of ro-vibrational states [285]. The absence of tunable lasers limited the frequency range of transitions that were amenable to photon echo experiments, but early projects recognized the future development possibilities with the advent of new light sources. Controlling the polarization states used to excite the sample allowed isolation (by angular momentum selection) of the particular transition giving rise to the photon echo [145].

Semiconductor materials can also give rise to photon echoes, even if the system does not exhibit inhomogeneous broadening; this effect, due to the properties of the interband continuum of excitation states, is not simply analogous to the photon echo observed in atomic systems. See, for example [250] for a numerical solution of the semiconductor optical Bloch equations for a two pump non-collinear photon echo experiment, and an analysis of the transition between free-induction decay and photon echo.

Three pulse photon echo experiments have also been performed, and can provide information on complex dynamics in a system. See, for example. [284].

4.1.2 Early four-wave mixing, photon echo, pump-probe and related coherent experiments

Frequency degenerate four-wave mixing was observed in a non-collinear geometry using a q-switched pulsed (14ns pulse duration) laser to excite a liquid sample [56], with two 'input' and two 'output' beams. The $\chi^{(3)}$ nonlinear

effect observed in this demonstration resulted in no time-averaged addition of energy to the medium, as it is a passive effect that depends on virtual excitation. Again, for these early results, significant experimental effort was necessary to ensure that the detected signal was a real four-wave mixing emission rather than a spurious reflection. Spectral analysis demonstrated that light emitted in the phase-matched direction was not due to inelastic Brillouin, Raman, or similar scattering processes.

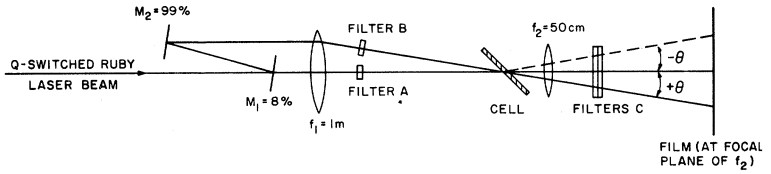

Experimental schematic for first observation of self-diffracted four-wave mixing. Reproduced from Carman, Phys. Rev. Lett. 17:1281 (1966).

Figure 4.4: Schematic for four-wave mixing experiment

The four-wave mixing process was noted to rely upon kinematics (i.e. the momentum and energy conservation of a parametric process) identical to those described in the contemporaneous photon-echo experiments in ruby [2] – the distinction made was that the four-wave mixing observed here in nitrobenzene did not use a time delay between excitation beams and the detected signal was therefore not dependent on the rephasing process. This result is significant as it reflects an increasing scope in the different aspects of the nonlinear optical response that may be induced and observed with pulsed light sources. We outline some of those effects here; not all are strictly four-wave mixing

phenomena, but all depend on nonlinear optical processes studied with visible light. An extensive four-wave mixing optical spectroscopic toolkit was developed as these experiments proceeded.

The first coherent transient phenomena studied in the radio frequency regime ([364], [156]) were observed after the development of necessary tools to emit and detect coherent radiation of the appropriate energy, an outgrowth of technological advancement that occurred during the war. The development of multiple pulse methods allowed the separate examination of different spin dephasing mechanisms; spectrally resolving a spin transition provided further information on the dynamics of these systems.

A similar advancement of the study of transient phenomena occurred in the visible wavelength range after the development of new laser technologies made it possible to probe the relevant excitations. While optical coherence experiments had been performed previously – after all, the Young's double slit experiment depends upon spatial coherence of light, the Michelson interferometer measures temporal coherence, and the Brown-Twiss experiment studied intensity correlation; all of these (and other experiments) pre-date the invention of the laser – new coherent visible light sources permitted the study of optical analogs of previously observed spin transients. The similarity of the electric dipole transitions and spin flip transitions was not certain prior to laser measurements of light-matter interaction, but work by Dicke demonstrated their equivalence and suggested that these analogous processes could exist [94].

Although photon echo experiments occurred first, optical nutation was demonstrated soon after (reversing the order in which the corresponding nuclear resonance effects were seen). A q-switched, pulsed CO_2 laser was used to drive an oscillation between the upper and lower levels in a infrared rovibrational transition in a molecular gas. Repeated cycling occurs via stimulated emission and absorption, repeating until the end of the laser pulse; that oscillation results in a cyclical reduction and increase of the transmitted beam intensity [181].

After the pulse has passed through the sample, the dipoles formed by the coupling of the upper and lower states have a well-defined phase relationship, and emit an intense, coherent beam of radiation; this is analogous to the free induction decay observed in nuclear resonance experiments [51], although the nomenclature is awkward since the detection does not occur via the eponymous inductive pickups used in NMR. The well-defined phase relationship among the N quantum emitters results in an emission intensity that scales as N^2, far exceeding the spontaneous emission intensity (N). For completeness, we note that these optical nutation experiments did not rely upon pulsed laser systems at the appropriate wavelength – which would limit the systems that could be studied to those for which suitably fast pulsed lasers were available. Instead, a Stark switching scheme was used that brought transitions into and out of resonance with a continuous wave laser [50]. An early two-dimensional spectrally resolved technique that recorded only amplitude information was developed using Stark switching that measured the ampli-

tude of photon echo signals as a function of the pump delay [151]. A related technique to study transients in the UV and visible regions were developed using frequency switching of a continuous laser; this is conceptually similar to the Stark switching method but does not require Stark tunable molecules and is therefore applicable to a broader range of materials [48]. We note that this technique is not suitable for the study of semiconductor systems, even if fast enough switching time were achievable (an electro-optic crystal inside the laser cavity shifts the laser frequency in and out of resonance with a molecular transition by changing the effective cavity length; they attained switching times of ˜50ps), due to the problems that would occur with off-resonant excitation of free carriers. While these methods were extended to a number of optical transients, their utility is less significant today due to the development of tunable, ultrafast lasers.

Another significant development in the study of optical transients was the observation of a two-photon photon echo [123], using two lasers to produce a sum-frequency two-photon analog of the normal photon echo response in an alkali vapour. This experiment observed quantum beating and studied relaxation of the superposition of two optical states. Echo effects had been predicted for multiple photon transitions earlier (see, for example [163]) but never previously observed in the optical regime (two quantum transitions had been observed in, of course, nuclear resonance experiments [164] shortly prior to this result). The two photon photon echo was used to study the dephasing effects caused by the introduction of buffer gases into the sodium vapour.

Photon echo experiments were conducted to study heavy hole excitons confined to a Gallium Arsenide quantum well [324], [329]. Previously, excitation of carriers above the bandgap had been observed, with rapid relaxation into bound electron-hole pairs that exhibited dephasing times of a few hundred femtoseconds, while photon echoes were observed from excitons bound to impurity ions on the order of up to a hundred picoseconds. When the pulse duration is comparable to the dephasing rate, significant deviation from the theoretical behaviour of the system is to be expected (q.v. *sub* for a description of the Taira model used to describe exciton dynamics). Temporal line shape analysis provides a measurement of the coherence time (i.e., the dephasing rate) as a function of wavelength across the strongly broadened exciton resonance. This can be used to fit for T_2 even as the pulse duration approaches the dephasing time, using a model that considers the possibility of phase relaxation occurring even during the excitation pulses. This modification is still possible within the basic framework of a third-order density matrix calculation. The experimental measurement of the photon echo temporal line is provided by performing cross-correlation with an additional pulse derived from a reference beam. Spectrally resolving the emission across the exciton resonance – fluctuations in the well width in these early experiments resulted in strong inhomogeneous broadening – demonstrates a strong dependence of population relaxation time T_1 and dephasing time T_2, reflected in qualitative changes in the photon echo lineshape (photon echo emission becomes symmetric if the decoherence time is shorter than the pulse duration).

Near the center of the exciton resonance, the decay of the polarization responsible for four-wave mixing emission is primarily driven by a fast dephasing, suggestive of spectral diffusion processes. Below the line center the dephasing appears much slower. This result suggests that the higher energy excitons in the inhomogeneously broadened line are more de-localized and therefore undergo significant dephasing interactions throughout the fluctuating quantum well, while the more localized excitons below the line center are less likely to dephase so rapidly. We note in passing that some effort would be necessary to understand this result in the context of motional narrowing [36], and indeed, it is probably not possible to do so without much more sophisticated measurements. Two-dimensional Fourier transform spectroscopic studies of spectral diffusion here would be an interesting project, were it not for the fact that higher quality samples are now available that exhibit homogeneous broadening.

These early photon echo measurements of decoherence in semiconductor quantum well samples [329] already suggest that the optical Bloch/Taira model would be unable to accurately describe the behaviour of these systems, where exciton-exciton interactions could be probed due to the higher excitation powers possible compared to previous frequency-domain measurements. A model considering intensity dependent relaxation processes is suggested in [90]. At higher energies, the fit increasingly failed to adequately describe the correlation curve for the time-integrated photon echo signal. Closer fits were obtained with a decay depending on $e^{-2\tau_{12}/T_2}$, where the τ_{12} is the delay be-

tween the two pump pulses used, with an extracted value of dephasing time T_2 estimated to be 13 picoseconds. Using the normal photon echo fit suggests a dephasing time and a population decay time of 4 ps (for both values), which is not a physically meaningful result. All two-level system photon echo results should in principle consider the effects of the relative optical phase of the excitation pulses used, but most experiments do not provide the necessary path length stability [382]. It is a common assumption in experimental optical science that acoustic noise will typically blur out the phase-dependent features of most measurements, but the validity of this assumption must always be tested.

The first saturated absorption experiments performed in the visible range with appropriate temporal resolution to study fast electronic dynamics essentially invented pump-probe optical spectroscopy [19], [333], [211]. These experiments provided picosecond studies of the behaviour of carriers excited by a strong pulse. The results of Kennedy et al. fit a value for the intraband relaxation time (estimated at less than 5ps, the observed width of the saturated absorption feature and the instrument resolution) for carriers optically excited in high quality Germanium crystals. Subsequent re-analysis, however, indicated that the feature observed was actually a coherence spike that occurs in pump-probe spectroscopy as power from the intense pump beam is parametrically coupled into the much weaker probe [335]. Performing a saturated absorption measurement scanning over a longer delay indicated a slowly pump-probe feature that builds relatively slowly before decaying due to free

carrier recombination. Similar pump-probe measurements were used to study dye molecules in solution [336], studying relaxation as a function of solvent density. That experiment demonstrated the significance of polarization analysis as a method to separate isotropic and anisotropic dichroism, permitting the separation of orientational relaxation processes from population decay. Other related experiments included sub-picosecond spectroscopy of hemoglobin complexes [338].

In addition to their scientific merit and the usefulness of the pump-probe techniques they pioneered, these experiments were significant for the discovery of the parametric coupling effects at early times, when coherent effects dominate the nonlinear optical response of these materials. We present further discussion on this subject elsewhere in this thesis in the context of our own differential transmission experiments, but note here that this result leads conceptually to the self-diffracted four-wave mixing experiments (and subsequent four-wave mixing based techniques) that were used in extensive studies of semiconductor (and other) materials.

A great deal of that work depends upon a model that uses a non-interacting ensemble of two-level systems to model the excitation, following the early work of Yajima and Taira [402]. That paper is perhaps as significant to the scientific understanding of exciton nonlinear optics as Bloch's original papers were for the interpretation of nuclear induction results. We will describe their theory and experiment at length due to its significance; not simply due to the substantial body of experiments whose results were interpreted using that

model, but because breaking that model and pursuing new replacement models proved such a significant achievement in the field of ultrafast spectroscopy of semiconductors.

Nonetheless, we first turn out attention to another line of experimental research – the foundational work on transient gratings – which are useful to understand the underlying principles of the non-interacting two-level system ensemble model.

4.1.3 Transient gratings

The process of scattering light off a transient grating induced in a sample (typically) by interfering optical fields has seen application in a number of different spectroscopic techniques used to study microscopic phenomena in various materials. A grating induced by some light-matter coupling mechanism that does not depend upon optical damage will inherently be transient in nature, and will persist (after the driving fields are removed) only until the relaxation processes in the system have dispersed the excitation (via mechanisms such as diffusion or orientational relaxation) or the coherence or population have decayed to thermal equilibria. The time resolved diffraction of light from such a grating may be used to characterize those various relaxation processes. We consider some results here.

Perhaps the first transient grating experiment also appears in a report of the first observation of degenerate optical four-wave mixing [56], where light was parametrically scattered out of two incident beams used to excite a liquid

sample – although we note that this paper never uses the word 'grating' to describe this process. A grating phenomenon induced by spatial spectral hole burning in a saturable absorber (a liquid used as a q-switch in laser cavities) was shown to exhibit Bragg scattering [162] Shortly thereafter, an interference pattern of carriers produced from two laser beams was shown to act as a diffraction grating [398]. Experiments performed with pulsed ruby lasers used to induce a grating that scatters an Argon ion laser permitted the study of the relaxation time of thermal gratings [213], demonstrating the usefulness of these techniques for studying time domain behaviours. This experiment was limited by the relatively long pulse duration that only permitted the study of slow, thermal effects. Similar experiments were performed with other light sources [106]. The use of picosecond lasers permitted the first study of fast grating relaxation [317]. Previous experiments had observed stimulated Brillouin scattering from an intense MASER beam into a weaker beam via the coupling through an acoustic wave in a crystal, but were subject to specific constraints on the geometry of the interacting beams, determined by momentum conservation requirements that depended upon the geometry of the crystal. Only certain geometries led to a buildup of sufficiently intense acoustic waves to make the coupling possible [72]; analogous effects were also observed in liquids [49]. The advantage presented by the transient grating techniques was the flexibility it offered – the geometry of the interfering pulses that form the grating may be altered according to the problem interest, permitting the study of various orientational effects.

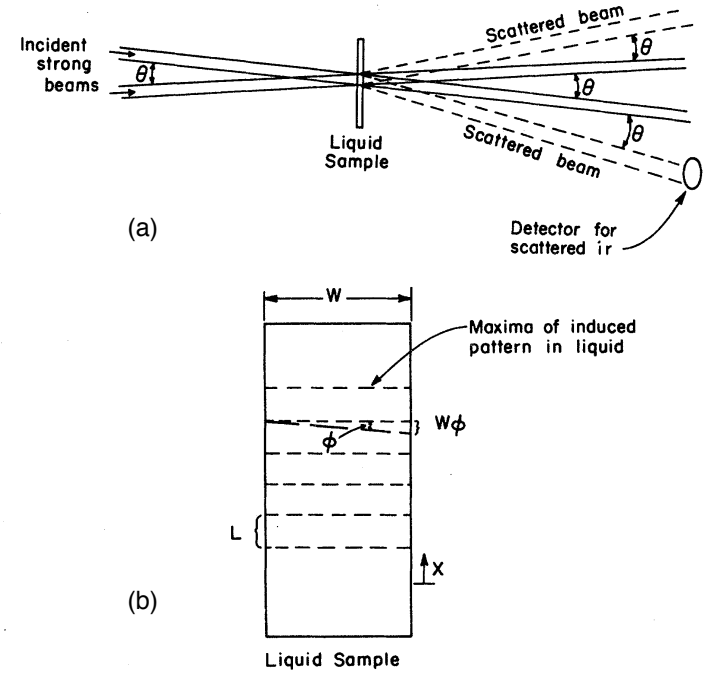

Transient grating experimental geometry (a) used to study fast stimulated Rayleigh and Brillouin scattering processes in a liquid (b). Reproduced from Scarlet, Physical Review A, 6:2281 (1972).

Figure 4.5: Schematic for transient grating experiment

Motivated by the contemporaneous pump-probe spectroscopy measurements of relaxation processes in semiconductors [211], diffraction from a transient grating in a reflection geometry was demonstrated and suggested as a diagnostic technique for characterizing relaxation processes in similar materials [396]. Transient phase gratings in the semiconductor zinc oxide had already been previously used to study free carrier and thermal dynamics [85], where a weak probe was scattered from the induced grating, in addition to the observation of self-diffraction of the pump beams used to create the grating via two-photon absorption. Thermal grating effects could be resolved from the phase grating by monitoring the time required for the diffracted intensity to decay. Siegman and coworkers demonstrated transient grating spectroscopy of a dye molecule in a liquid solution using mode-locked pulsed lasers operating in the sub-ns/ps pulse range [290]. The interference of two pulses induced a spatial pattern of excited state population in the material, creating a transient hologram in the liquid sample. A delayed pulse was again diffracted by this periodic structure, and again, by scanning the delay between the pulses the lifetime of the photoexcited phenomena could be estimated to within the precision of the pulse temporal width. The construction of this experiment allowed easy substitution of the lenses used to focus the interfering beams; this additional degree of geometrical control permits the measurement of spatial domain effects separate from the lifetime decay. Rotating the fringe direction permits the study of anisotropic diffusion effects. Other experiments demonstrated the scattering of a laser pulse by a transient grating as a measurement

of optical coherence times below the pulse width limit [104].

The self-diffracted processes observed in transient grating techniques are the most significant for the development of the first transient tools used to characterize excitation and relaxation processes in semiconductor samples. These results are readily understood in the context of Raman-Nath scattering theory [85] for diffraction of coherent light from a thin volume grating, although thick gratings may also be studied [197]. The use of two-photon nonlinear absorption processes extends the range of materials that can be studied since a resonant excitation source is no longer required. The particular details of self-diffracted four-wave mixing spectroscopy (and, additionally, three pulse transient grating four-wave mixing techniques) will be explained at length later in this chapter.

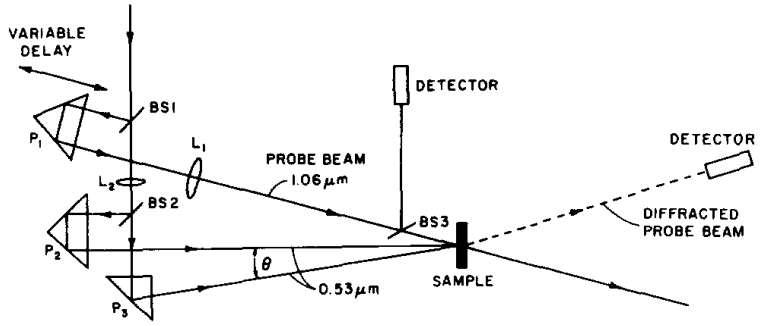

Experimental schematic for a three-pulse experiment used to study relaxation processes in a transient grating induced by the first two pulses. Reproduced from Hoffman, Appl. Phys. Lett. 33:536 (1978).

Figure 4.6: Schematic for three-pulse photon echo

Three pulse picosecond transient grating processes have also been used to study relaxation processes [182]. A carrier plasma grating is induced at

a semiconductor surface or interface due to the interferometric absorption of picosecond laser pulses; another pulse, at a longer wavelength so as to avoid exciting above the band gap, scatters from the transient grating. The intensity of that diffracted light is a measure of the grating modulation depth and can be used to study its temporal evolution. Various population processes – diffusion, recombination in the bulk, and recombination at the surface – can be studied with this technique, though we note that it was *not* used to study dephasing dynamics. Three pulse transient grating methods were subsequently developed to do precisely that [347]; we describe them at length elsewhere in this thesis, as the three pulse method is largely similar to the optical physics of two-dimensional Fourier transform spectroscopy.

4.1.4 Taira model and four-wave mixing spectroscopy of semiconductors

After the realization that fast processes [335] in the early time evolution of pump-probe spectroscopy were determined by coherent parametric coupling, a self-diffracted four-wave mixing spectroscopic technique was described and demonstrated by Yajima and Taira [402] to exploit conceptually related coherent transient phenomena to study the dephasing processes on either homogeneously or inhomogeneously broadened transitions. Previously, information about dephasing rates had been obtained by frequency domain measurements with a precision approaching 100 fs, but these were indirect methods requiring more careful analysis to extract the relaxation time (for example spectral hole burning measurements of dye molecules [263], measurements of absorp-

tion saturation in Germanium [210], a preliminary study of spectrally resolved four-wave mixing using two optical frequencies that both lie inside an inhomogeneously broadened line [400], [401], and two-frequency technique that makes use of polarization analysis to estimate dephasing times [353]). These indirect techniques are deprecated if a direct time-domain measurement of dephasing can be obtained that does not depend upon any substantial modeling of the system under consideration – ideally, a method should be found for which dephasing and population decay may be studied without any prior knowledge of the time scales in question. Self-diffracted four-wave mixing techniques such as those described in [402] do not perfectly meet that description, but do serve reasonably well for many cases of interest, and moreover serve as an intermediate step necessary to understand more sophisticated three pulse transient grating and other four-wave mixing techniques. We describe the basic self-diffracted four-wave mixing method and theory here, before considering a range of experimental results significant to the materials we study in our own experimental program.

Two non-collinear beams are used to excite a resonant medium, resulting in a self-diffracted four-wave mixing emission that is detected in a phase-matched direction. Conceptually, the experiment may be understood as the scattering of some fraction of light from one pulse by a transient diffraction grating formed by the interference of that same pulse with another that preceded it by less than the dephasing time of the material. The energy of the diffracted pulse as a function of the delay between the pump pulses may be

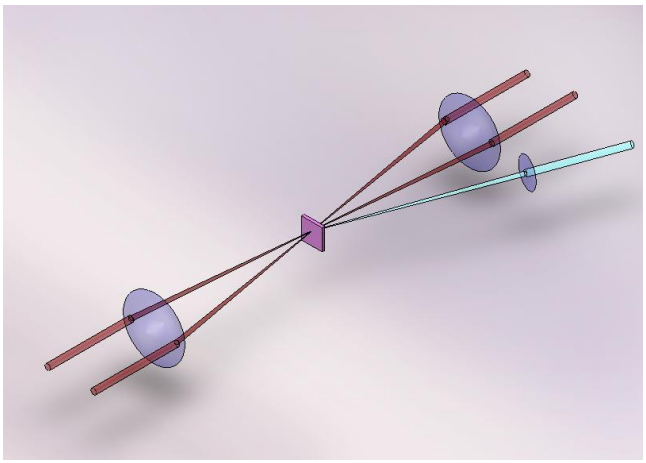

Typical geometry used for the self-diffracted four-wave mixing experiments frequently analyzed using a Taira-type model. The laser pulses propagate from left to right in this diagram. One beam path is shaded blue to indicate that it is the signal field, emitted in the phase-matched direction, but all of the pulses are frequency degenerate.

Figure 4.7: Geometry for self-diffracted FWM experiment

analyzed to obtain information about the decay of a macroscopic polarization on a time scale principally determined by the dephasing time. This method builds directly upon the transient grating effect used to study relaxation processes [290], but with the use of sufficiently short pulses (temporal width less than dephasing time T_2) fast decay processes may be observed that can be analyzed to back out a measurement of the dephasing time. Strictly, the decay of the measured correlation trace is a function of the dephasing and population relaxation rates, but if the two are substantially different it is possible to neglect the relatively slow population decay. In some materials that is not the case, as the dephasing and population decay rates approach each other, but for semiconductor materials similar to those in which we are interested there is something like a two order of magnitude difference between dephasing and decay times.

To derive the underlying theory for their experiment, Yajima and Taira use an elementary perturbation calculation to obtain n-th order corrections to the density matrix elements describing the population of and coherence between two energy bands. This calculation (outlined here) is performed in the interaction picture (see our discussion of the second Bloch geometrical formalism) and makes use of the rotating wave approximation to simplify the result by discounting weak non-resonant effects.

To obtain the macroscopic polarization (which, modulo a phase shift of i, is proportional to the diffracted signal, since the polarization serves as a source term in Maxwell's equations) it's necessary to integrate the dipole-

coherence product over the broadened line,

$$\hat{P}^{(n)} = N \int_0^\infty d\omega_0 \mu_{ab} \hat{\rho}_{ba} \left(\mathbf{r},\, t,\, \omega_0\right) g\left(\omega_0\right)$$

where N is the number density for emitters in a volume of the sample sufficiently small to be treated with the electric dipole approximation (see our previous discussion of thin samples in the chapter on light-matter interaction). It is necessary to apply a normalization condition on the distribution of the inhomogeneous broadening function $g\left(\omega_0\right)$,

$$\int_0^\infty g\left(\omega_0\right) d\omega_0 = 1$$

Results for homogeneously broadened materials may be found by taking the limit that the inhomogeneous width (the width of the distribution function $g\left(\omega_0\right)$ tends to zero). In our own calculations we will favour this conditions, partially because of the high quality molecular-beam epitaxy samples we study, but principally because it simplifies the calculations.

Calculated to the third-order in the perturbing electric fields, the off-diagonal terms of the density matrix contain components at four different wave vectors, $\mathbf{k}_1$, $\mathbf{k}_2$, $\mathbf{k}_3 = 2\mathbf{k}_2 - \mathbf{k}_1$, $\mathbf{k}_4 = 2\mathbf{k}_1 - \mathbf{k}_2$; this analysis only considers the transmitted beams and we neglect (for now) the backward directed emission. Both cases are possible, since the ensemble of dipole oscillators induced in the material act as a phased array antenna, giving rise to strongly directional

emissions. Detection in a specific geometry picks out a certain component of the coherence induced by the two pump pulses.

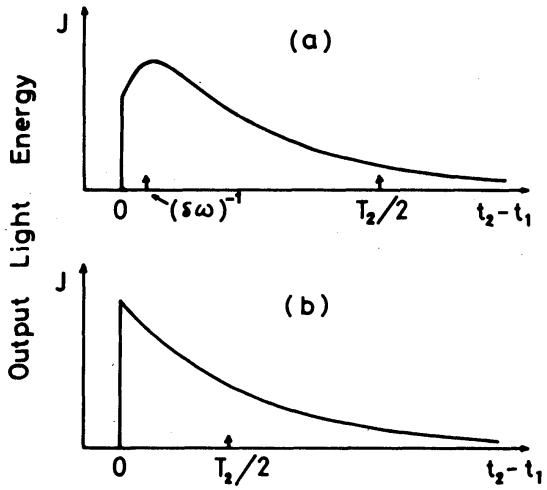

A non-interacting ensemble of two-level systems predicts different temporal lineshapes for the time-integrated transient self-diffracted four-wave mixing emission. In the inhomogeneous case (a), where the line is an order of magnitude broader than the homogeneous line, four-wave mixing intensity peaks later due to the photo echo emission that occurs at a revival time equal to the pulse delay. In the homogeneous limit (b), four-wave mixing emission decays exponentially to the background level. Reproduced from Yajima and Taira, Journal of the Physical Society of Japan 47:1620 (1979)

Figure 4.8: Taira model for FWM temporal lineshape

Analysis of the third-order nonlinear optical response detected in a phase-matched direction reveals different behaviour for inhomogeneously vs homogeneously broadened ensembles, and for short vs long pulse separation. The by now familiar photon echo is found to be one specific case of this response; specifically, it is the observed response for a system with inhomogeneous broadening and long waiting time between pulses. The spatial parametric effect described by this density operator theoretical treatment is a broader

class of phenomena, and the photon echo is in this model seen as a specific aspect of that more general effect.

It is not necessary to resolve the temporal lineshape of the transient self-diffracted four-wave mixing emission in the time-domain emission in order to extract information regarding the relevant dynamical parameters. Instead, it suffices to examine the slow, time-integrated response measured along the $\mathbf{k}_3$ direction as a function of the delay between the two pump pulses, $t_2 - t_1$.

From Maxwell's equations, the integrated energy of the optical emission is found to be proportional to the integrated square of the polarization,

$$J = \int_{-\infty}^{\infty} dt \left| \hat{P}_3^{(3)} (\mathbf{r}, t) \right|^2$$

which may be considered for either case of homogeneously or inhomogeneously broadened samples. For inhomogeneously broadened transitions, i.e. those with a spectral line width greater than the dephasing rate, $\delta\omega \gg \frac{1}{T_2}$,

$$J = \begin{cases} A \left\{ 1 + \Phi \left[\frac{\delta\omega}{\sqrt{\pi}} (t_2 - t_1) \right] \right\} e^{[-4(t_2 - t_1)/T_2]}, & t_2 - t_1 > 0, \\ 0, & t_2 - t_1 < 0 \end{cases}$$

where the photon echo shape function Φ is defined by

$$\Phi (x) = \frac{2}{\sqrt{\pi}} \int_0^x e^{-t^2} dt$$

Whereas for the homogeneously broadened case, the integrated energy detected along the phase-matched direction may be shown to be

$$J = \begin{cases} Be^{-\frac{2}{T_2}(t_2 - t_1)}, & t_2 > t_1 \\ 0, & t_2 < t_1 \end{cases}$$

In either case, the signal strength A or B is independent of the delay between the pulses. In the limit of short pulse duration, the decay of the correlation trace for output energy as a function of pulse delay is determined by the dephasing time T_2 for either type of broadening. Analysis of the time-integrated energy as a function of that delay will directly yield this decay constant – $2/T_2$ for homogeneous and $4/T_2$ for inhomogeneously broadened systems. The decay of the second case is slower because the emission of a photon echo occurs after a delay equal to $t_2 - t_1$ has passed following the interaction with the second pulse. For inhomogeneously broadened samples, peak emission occurs at $t_2 + (t_2 - t_1)$, while the homogeneously broadened sample emission peaks at t_2. Again, it is not necessary to actually resolve the temporal structure of this emission. Instead, measurement of the decay of the diffracted energy, combined with spectral information obtained via simple absorption spectroscopy (for example), allows one to determine whether a particular transition in some sample is inhomogeneously or homogeneously broadened, and to extract a value for the dephasing time.

If the pulse width for the laser used to perform a self-diffracted four-wave mixing experiment is comparable to dephasing time, the trace of the integrated emission energy as a function of delay between the pulses is a more complicated function of both the pulse parameters and the relaxation parameters. If that pulse is well-characterized, it is still possible to back out the

dephasing time.

If the dephasing time is much shorter than the pulse duration, four-wave mixing emission occurs only during the interval when the pulses overlap temporally. In this case, the trace of emission as a function of delay only contains information regarding the pulse parameters, and it is not possible to extract a value for the dephasing time T_2. At best, the experiment places an upper bound on T_2 – the width of the laser pulse.

For discussion of a similar model that considers more sophisticated relaxation channels, distinguishes among gratings formed by several different photo-excitation processes, and considers four-wave mixing emission in both the probe and conjugate [175], [351] directions (the particular analysis used in this paper is concerned primarily with transient phenomena observed by pump-probe measurements that reveal transient grating coherent effects, but uses a similar density operator formalism) we refer the reader to [395].

The Taira model can be understood as an extension of the optical Bloch equations to the analysis of four-wave mixing. It once again asserts that that relaxation process for a macroscopic ensemble may be understood simply in terms of population decay and dephasing of coherence. Critically, this theory assumes a non-interacting ensemble of two-level oscillators. A great deal of subsequent experimental work uses this basic concept to explain a broad range of results, studying changes to dephasing rates seen under different conditions. While somewhat successful, ultimately this theory needs to be increasingly patched to account for various observations. Ultimately, in the case of

semiconductor samples such as those we are interested in, it can be shown to completely fail to predict significant aspects of the nonlinear optical response. In order to understand those effects, more sophisticated theories were introduced – semiconductor optical Bloch equations and other microscopic theories – and many-body physics came to be seen as the dominant force determining the behaviour of these systems. In turn, the advancement of the theoretical modeling of these materials interaction with light drove the development of new, more complicated optical spectroscopic tools to resolve those details of the nonlinear response unavailable to simpler techniques. In that context we find ourselves using two-dimensional Fourier transform spectroscopy to study outstanding problems in exciton optics, and developing new tools to resolve effects previously unseen in semiconductor and semiconductor hybrid nanostructures. A description of the development of those methods forms the last portion of this thesis.

4.2 Ultrafast four-wave mixing experiments on semiconductor nanostructures

4.2.1 Self-diffracted four-wave mixing measurements to extract dephasing time

The development of ultrafast pulsed laser sources with pulse widths on the order of less than a tenth of a picosecond (for example, colliding-pulse mode-locked lasers [124]) made it possible to perform transient nonlinear optical experiments on semiconductor systems; as a result, significant advances were made in studying the behaviour of excitons in both quantum confined

structures and bulk materials. Further developments in laser technology – particularly the development of tunable, ultrafast Titanium-Sapphire lasers – greatly simplified the experimental difficulties of working with these samples.

A large number of experiments concentrated on studying the dephasing processes of excitons in single quantum wells. We note a few significant results here, which made use of the Taira model of an ensemble of non-interacting two-level systems to interpret their results.

Early experiments studied the dephasing processes for the inhomogeneously broadened heavy hole exciton resonance in GaAs multiple quantum well samples [329], [324]. We noted these result previously, in the context of photon echo experiments, but the experimental technique used is no different from the self-diffracted four-wave mixing techniques described in this section. In both cases, four-wave mixing processes in the material result in the emission of a coherent signal along a phase-matched direction, and measurements of the decay of the scattered energy. The distinction arises due to the difference in material samples studied; in the photon echo case, poor interface quality in the quantum well structure results in inhomogeneous broadening of the transition, while later results were obtained with higher quality quantum wells that exhibited homogeneously broadened exciton resonances.

Picosecond pulses were used to perform transient four-wave mixing measurements on thin Gallium Arsenide layers to study the decoherence and orientational relaxation of excitons [326]. Coupling between different excitation modes – in this case, between an exciton and a photon – may be under-

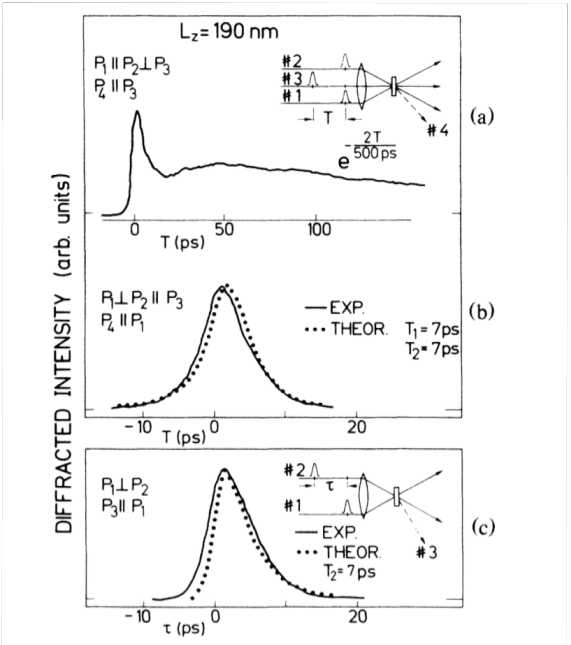

Experimental results from four-wave mixing measurements on thin GaAs slivers. Transient grating measurements (a) measure the intensity scattered from a grating induced by the first two pulses, which are separated by a fixed delay. A three-pulse four-wave mixing measurement (b) plots the diffracted as a function of delay between the first two pulses for fixed *T* delay. The third plot (c) shows self-diffracted four-wave mixing emission that can be analyzed using a Taira-like model. Reproduced from Schultheis et al., Phys. Rev. Lett. 57:1797 (1986).

Figure 4.9: Four-wave mixing data from Schultheis et al.

stood conceptually as a new quasi-particle, a polariton, which is an eigenstate of the interacting exciton-photon system and exhibits its own dispersion relationship. The polariton is a useful interpretation of the excited light-matter system if strength of the coupling between the exciton and photon states is sufficiently strong compared to the coupling between an exciton and the combined bath of the crystal and other excitons. A measure of the coupling strength between the exciton and photon is the oscillator strength for the transition that is excited in exciton emission, whereas the coupling between an exciton and the crystal-many exciton system may be characterized with the T_2 time (a slower dephasing process indicates a stronger coupling among excitons, an intuitive result). A test of the validity of the polariton picture may be performed by comparing the longitudinal-transverse splitting for the polariton mode (i.e., measure the oscillator strength) to the inverse of the dephasing time, but prior to the development of four-wave mixing techniques an accurate value for T_2 was not available. Prior work had assumed a sufficiently long coherence time without actually demonstrating it.

To measure the dephasing time accurately, extremely low excitation densities were used to reduce the exciton-exciton interaction. Thus, the relaxation time measurement reflects the residual interaction of an exciton with phonons and crystal defects (interface roughness is not a significant factor in this experiment, since 100nm to 200nm GaAs slices were used). The dephasing rate (7 ps) was found to be independent of excitation density below a certain threshold, and suggests that the coupling of an exciton to the photon

is insufficiently strong by comparison to validate the polariton picture. The small value of T_2 indicates that the coherent coupling between an exciton and photon is substantially disturbed; in a bulk sample, a propagating polariton excited near resonance would be attenuated before traveling a single wavelength. The imaginary part of the dispersion relation for polariton modes must be considered in these materials.

This experiment relied on the Taira model, assuming a homogeneously broadened ensemble of non-interacting two-level systems, to extract the decoherence time T_2. The authors do note a slight discrepancy in the temporal lineshape, which they suggest may be due to an asymmetric pulse (using an asymmetric pulse envelope provides a better fit of the experimental data, but do not have any independent measurements to suggest that the pulses used are not symmetrical Gaussians).

Optical dephasing measurements were also performed on exciton transitions in GaAs quantum with a similar technique in order to determine the nature of the broadening as homogeneous or inhomogeneous and, if possible, to identify the processes that dominate the broadening of the exciton resonance [325].

Inhomogeneity in these systems is believed to arise primarily due to the well width fluctuation. The effect of inhomogeneity is to broaden the resonance (naturally) and to result in a shift of the emission maximum to lower photon energies compared to the maximum of the absorption line. This Stokes shift is due to the energy loss exhibited by an exciton in the quantum well prior to

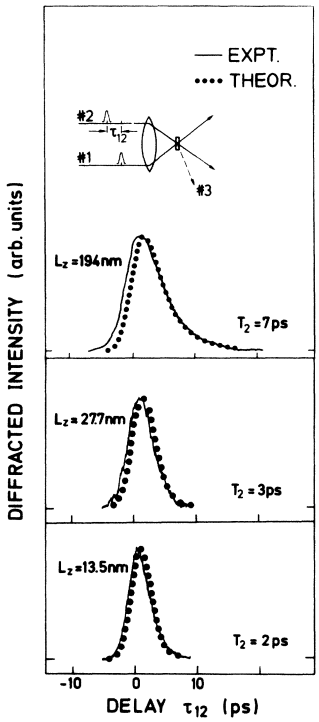

Self-diffracted four-wave mixing intensity from three different GaAs quantum wells. Analysis of the temporal lineshape allows extraction of the dephasing time, but requires an additional measurement to prove the sample is homogeneously broadened. Reproduced from Schultheis et al., Physical Review B 34:9027 (1986)

Figure 4.10: PS Four-wave mixing data from various QW's

recombination and emission of a detectable photon. In an inhomogeneous line those excitons excited above the maximum of the absorption feature – i.e. the higher energy excitons within the line – are less localized in the quantum well and exhibit more translational kinetic energy. That population of excitons undergoes fast momentum and energy relaxation due to scattering with acoustic phonons, crystal defects (impurities), and interface fluctuation. By contrast, excitons found below the center of the absorption line appear more localized, and relaxation processes were found to be less efficient. On this slower time scale, spectral diffusion may be found to occur

For these samples, however, spectral measurements of absorption features provided linewidths that corresponded to the excitonic phase coherence time (7 ps in bulk; 2-3 ps in quantum well samples measured here, with shorter times observed for lesser well width), indicating that the exciton resonances in these materials are homogeneously broadened. For a completely homogeneous line, the linewidth is expected to vary as $\Gamma = 2/T_2$.

Again, these results were obtained by fitting self-diffracted four-wave mixing energy to the small signal optical Bloch equations as described by the Taira model. A linear dependence of the homogeneous linewidth on temperature was found, indicating that one phonon scattering by acoustic phonons is primarily responsible for the line broadening observed at low temperatures, where the optical phonon mode is frozen out. It was not possible, of course, to vary the interface fluctuation that is expected to contribute significantly to the exciton dynamics, but exciton resonances in the sample studied exhibited no

Stokes shift between emission and absorption maxima. This suggests an ideal 2d exciton, with a single energy level on a global spatial scale, rather than a local spatial scale. The emission linewidth was found to correspond exactly to absorption linewidth, consistent with homogeneous line broadening.

Coherent polarization interactions were introduced into the description of exciton dynamics in an attempt to accurately reproduce experimental results [242]. Time integrated self-diffracted four-wave mixing emission had been observed to rise and decay asymmetrically for homogeneously broadened heavy hole exciton resonances in GaAs multiple quantum well samples, already indicating that the Taira/optical Bloch model does not accurately describe the physics of this system. Significantly, this paper studied time-integrated four-wave mixing that was emitted at the 'wrong' time – straightforward density operator calculation, such as the Taira/optical Bloch equation model, indicates that no four-wave mixing emission should be detected along the phase matched direction $2\mathbf{k}_2 - \mathbf{k}_1$, unless the $\mathbf{k}_2$ pulse arrives after the $\mathbf{k}_1$ pulse; obviously, this result is symmetric under interchange of the indices, and no emission should be detected along $2\mathbf{k}_1 - \mathbf{k}_2$ unless the $\mathbf{k}_1$ pulse arrives after the $\mathbf{k}_2$ pulse. Previous work had concentrated on studying the decay of the emission, and had not accounted much significance to this wrong time signal.

The dephasing time appears to be approximately twice the rise time. At higher temperatures or increased exciton density that relationship between rise and decay times changes, albeit at the limit of the experiment's detection ability, presumably due to enhanced dephasing. For InGaAs multiple quantum

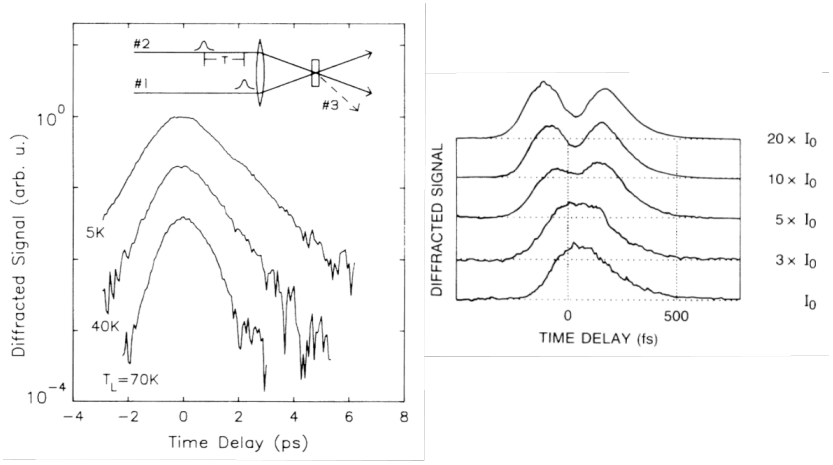

Time-integrated self-diffracted four-wave mixing emission occurs at negative pulse delays (a) and develops distortion in its temporal peak at higher excitation densities (b). Neither effect can be accounted for in a Taira-like model. Adapted from Leo et al., Phys. Rev. Lett. 65:1340 (1990).

Figure 4.11: Four-wave mixing with unexplained temporal lineshape

wells, the time integrated self-diffracted four-wave mixing signal exhibited the same asymmetry as seen in GaAs samples. The faster relaxation rates found for this material is likely due to scattering from local variations in the band gap due to ternary alloy fraction fluctuations [346] not present in the binary GaAs material. As the excitation power used increased, the shape of the diffracted energy curve evolves, with the peak flattening and subsequently splitting into two temporally resolved maxima. The minimum between the two peaks occurs at zero delay between the two pump pulses.

These behaviours cannot be explained using the ensemble of non-interacting two-level systems. Instead, a microscopic theory that treats the interaction of the excitons (and other excitations) created in the nonlinear polarization

present in the quantum well [320], [321], [319], [354]. These theoretical treatments consider the applied optical field and the Coulomb interaction among excitons on an equal footing. Without the Coulomb interaction, the Rabi oscillation of the exciton amplitudes $\psi_{\mathbf{k}}$, created by vertical transitions at wave vectors $\mathbf{k}$, do not undergo a simple Rabi oscillation at the frequency determined by the electric field strength and the interband dipole matrix element – $\mu_k E$ – but instead experience the potential of all the other excitations created at some other wavevectors Thus, the total coupling may be represented by

$$\triangle_{\mathbf{k}} = \mu_{\mathbf{k}} E + \sum_{\mathbf{k}'} V_{\mathbf{k},\mathbf{k}'} \psi_{\mathbf{k}'}$$

If the pulse temporal envelope is approximated with a Dirac delta function, the first term in $\triangle_{\mathbf{k}}$ results in a diffracted four-wave mixing emission that exhibits the same time dependence as that predicted by the Taira/optical Bloch theory.

Including the effects of the induced exciton amplitude $\psi_{\mathbf{k}}$ gives rise to the second term in $\triangle_{\mathbf{k}}$ which exhibits a steplike rise and a subsequent e^{-t/T_2} decay for the four-wave mixing emission.

The wrong time emission is the result of coherent polarization interactions. The simplest picture for four-wave mixing emission considers a parametric process that describes the scattering of some fraction of the power in the second pulse by a phase grating caused by a coherently induced population grating. Emisssion can also be described by considering the scattering of light

from a *polarization* grating, $P = \sum_k \mu_k^* \psi_k$, resulting in emission at both positive and negative time delays T. Two polarization waves propagating in the $\mathbf{k}_2$ direction, and one in the $\mathbf{k}_1$ direction, result in the characteristic e^{4T/T_2} rise in intensity of four-wave mixing emission during the negative T delay period. This effect can be described in the context of a fourth-order perturbation calculation, which is a simple extension of the third-order calculation describing the scattering of an electric field from the population grating. Due to the finite pulse duration and high excitation density only numerical simulations can be found, which exhibit qualitative agreement with the observed experimental results, but which seem to depend strongly on the exact excitation conditions used.

These effects were further studied with faster pulses, using self-diffracted four-wave mixing to study the many-body effects on the nonlinear optical response of GaAs quantum wells [241]. Wrong-time signals were again explained as a result of the coherent interaction among excitons that substantially alters the temporal lineshape of four-wave mixing emission. The faster pulses used in these experiments also had sufficient bandwidth to simultaneously excite light hole and heavy hole exciton resonances, resulting in the observation of an oscillatory four-wave mixing signal due to either polarization or quantum interference (the specific mechanism was not able to be resolved in these experiments). Again, for either homogeneously or inhomogeneously broadened resonances, the correlation trace of the emission is expected to exhibit a step-like turn on and exponential decay, given by

$$I_{homogeneous}\left(T\right) \sim \begin{cases} 0, & T < 0 \\ e^{-2T/T_2}, & T > 0 \end{cases}$$

and

$$I_{inhomogeneous}\left(T\right) \sim \begin{cases} 0, & T < 0 \\ e^{-4T/T_2}, & T > 0 \end{cases}$$

As we noted, polarization interactions have been used to explain the wrong time signal in these systems. While the positive time decay of the emission is dominated by the coupling due to the applied optical field, the wrong time behaviour exhibits a slower rise due to the interaction of the polarization term\exciton correlation effects. Including these effects, the line shape for homogeneously broadened transitions may be described with

$$I\left(T\right) \propto \begin{cases} e^{4T/T_2}. & T < 0 \\ e^{-2T/T_2}, & T > 0 \end{cases}$$

If there is an inhomogeneous distribution of resonant frequencies in the ensemble of oscillators, the macroscopic polarization $P = \sum_k \mu_k^* \psi_k$ appearing in the coupling $\triangle_{\mathbf{k}} = \mu_{\mathbf{k}} E + \sum_{\mathbf{k}'} V_{\mathbf{k},\mathbf{k}'} \psi_{\mathbf{k}'}$ will decay more rapidly, compared to the case of a homogeneous polarization, which would decay as e^{-t/T_2}. As a result the wrong time signal can be expected to vanish within the temporal resolution of the experiment if the transitions exhibit very strong inhomogeneous broadening. Therefore, four-wave mixing emission observed at negative times is an indicator of high quality samples with largely homogeneous broadening.

High quality samples may be studied using photoluminescence to demonstrate the homogeneity of the exciton transitions. Exciting one resonance at a time permits a study of the rise and decay times of the emission, which follow the predicted 2:1 ratio at low temperatures. At higher temperatures, the ratio increases, suggesting that decoherence effects due to phonon scattering affect the decoherence but not the many-body correlations that result in wrong time signals. Introducing additional dephasing processes – via temperature control, the injection of free carriers or incoherent excitons, or via increasing the exciton density, can provide some ability to study the underlying physics of the rise and decay times of the emission, but self-diffracted four-wave mixing measurements cannot directly distinguish between the particular contributions to four-wave mixing signals. We note that this is a particular strength of 2dFTS [113]. Excitation density effects are easily studied by increasing the strength of the pulses used, with the temporal lineshape largely similar to that seen at lower power, albeit with faster rise and decay. Off resonance, the lineshape becomes more complicated due to interference effects between higher order nonlinear processes. $\chi^{(5)}$ effects with an opposite sign to the emission due to $\chi^{(3)}$ processes affect the lineshape near the temporal overlap of the two pulses, but fall off more rapidly and do not contribute to the behaviour of the emission at greater magnitude pulse delays. The dependence on detuning cannot be understood directly in the context of this theory and experiment, which do not distinguish the particular microscopic processes leading to four-wave mixing emission.

4.2.2 Reflection geometry four-wave mixing experiments

Self-diffracted four-wave mixing was also demonstrated in a reflection geometry on single quantum well systems [183]. For transmission measurements it can be shown that the strength of the four-wave mixing signal field increases quadratically with the thickness of the sample (until saturation occurs, due, e.g. to the depletion of the incident fields, phase mismatching that eventually becomes significant over greater penetration lengths, etc.), whereas in a reflection geometry the polarization that acts as a source term in Maxwell's equations does not exhibit the same favourable phase matching with the propagating incident beams. As a result, the intensity of the backwards-directed emission oscillates sinusoidally as a function of the sample depth – for very thin samples, however, the forward and backward emissions are of theoretically comparable intensities. Thus, reflection geometry experiments can be used to study exciton dynamics in quantum wells.

More completely, the polarization induced in a material is determined by the incident beams, and therefore in either detection geometry is given by

$$\mathbf{P}\left(\mathbf{r},\, t,\, T\right) \propto C\left(t,\, T\right) e^{i(\omega t - (2\mathbf{k_2} - \mathbf{k_1})\cdot \mathbf{r})}$$

where the integral function $C\left(t,\, T\right)$ describes the interaction of the electric fields of the exciting pulses and the material response. This nonlinear polarization results in the emission of an electric field $\mathbf{E_n}$ directed into a new, different direction $\mathbf{n}$ that has a phase mismatch, compared to the nonlinear

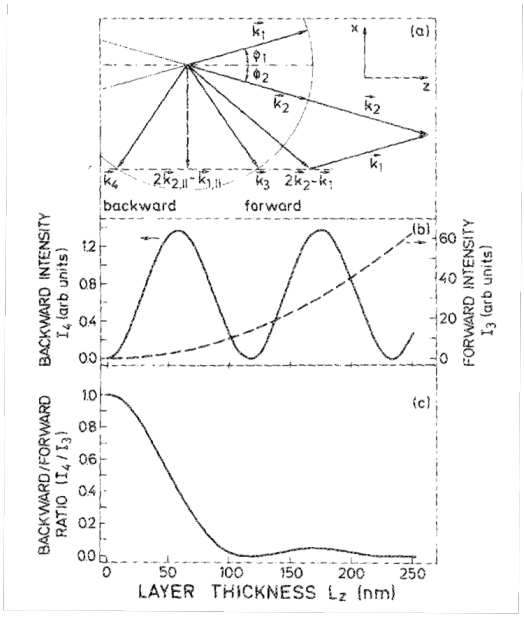

Phase matching for four-wave mixing experiments in reflection (k4) and transmission (k3) detection geometries (a). The greater mismatch in reflection mode results in a sinusoidal dependence on sample thickness for the four-wave mixing intensity (dashed curve), while the transmission mode increases monotonically (solid curve) (b). The ratio of the two intensities is nonetheless large if the sample thickness is relatively small (c). Reproduced from Honold et al., Appl. Phys. Lett. 52:2105 (1988).

Figure 4.12: Phase matching for reflection geometry four-wave mixing

polarization's wave vector, of $\triangle \mathbf{k_n} = \mathbf{k_n} - 2\mathbf{k_2} + \mathbf{k_1}$. For small angles of incidence, the signal intensity – given in either reflection or transmission geometry by

$$I_n(T) \propto L_z^2 \frac{\sin^2(\triangle k_n L_z/2)}{(\triangle k_n L_z/2)^2}$$

where L_z is the depth travelled into the material – grows monotonically for the transmission phase-matched direction but oscillates sinusoidally for measurements detected along the reflection phase-matched direction. In both cases, the signal intensity will be given by the square of a sinc function, but the relevant length scale determined by the phase mismatch will be much shorter for reflection measurements. Thus, the intensity of transmitted four-wave mixing signals should always be greater than the intensity of reflected signals, but for very thin samples the ratio of the two fields should be small.

Two pulse self-diffracted four-wave mixing experiments were performed on single GaAs quantum well samples, exciting only the heavy hole exciton resonances. Using the reflection geometry self-diffracted four-wave mixing technique it was possible to accurately fit a dephasing rate for this transition (6 ± 0.5 ps).

Additionally, three pulse measurements are performed, where the scattered energy from additional pulse is used to determine population relaxation time constants (rather than dephasing rates). By controlling the polarization states of the two pulses used to form the transient grating in the quantum well

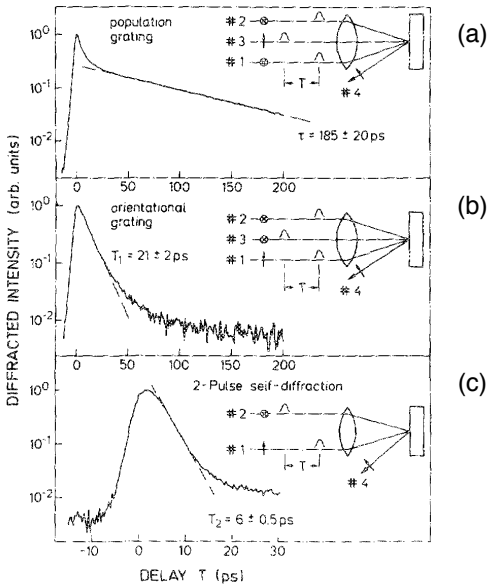

Data from transient grating measurements are used to study population relaxation (a) and orientational relaxation (b) in a reflection geometry experiment. Self-diffracted four-wave mixing is also demonstrated in a reflection mode experiment (c). Reflection measurements possess numerous advantages we outline in the main text. Reproduced from Honold et al., Appl. Phys. Lett. 52:2105 (1988).

Figure 4.13: Reflection geometry experiment schematic and data

it is possible to isolate the population decay rate and the orientational relaxation rate. These experiments provide an independent measurement of prior results obtained in a transmission geometry [326]. The underlying theory for three pulse transient grating measurements is discussed at length elsewhere in this thesis.

The dephasing rate of an exciton coherence induced in such a sample can, of course, be readily measured in transmission geometry. Indeed, even under the optimum reflection-to-transmission intensity conditions (ie in the limit that the single quantum well thickness tends to zero – which, consider that when that limit is reached the four-wave mixing signal itself necessarily goes to zero intensity) the transmitted signal is more intense. Nonetheless, the reflection geometry has a number of advantages that transmission experiments cannot provide. We detail those elsewhere in this thesis, in consideration of our development of a three pulse reflection geometry phase-sensitive spectroscopic technique designed to detect weak four-wave mixing signals superimposed on a strong pump-probe and transmitted probe background. The particular results of the reflection geometry measurements described here are not as important here for our own experimental program as is the analysis explaining the fundamentally weaker signals that must be studied using reflection mode four-wave mixing.

Other reflection mode, self-diffracted four-wave mixing measurements of the dephasing of homogeneously broadened heavy hole exciton resonances have been performed on single quantum wells in order to investigate the

exciton-exciton and exciton-free carrier scattering processes [184]. In a two-dimensional system, exciton-exciton scattering is predicted to blue-shift the exciton resonances and to reduce the oscillator strength. Exciton-free carrier scattering, on the other hand, should only cause the transition bleaching, but not the shift. The dephasing effects of these scatterers may be separately probed by introducing a population of free carriers or incoherent excitons, i.e. excitons without a well-defined phase relationship to the coherence and population induced by the two pump pulses in a self-diffracted four-wave mixing experiment. The introduction of free carriers or incoherent excitons is accomplished by the use of a second laser, which is time-synchronized but is not phase locked to the laser source used to perform the four-wave mixing experiment. Incoherent excitons are produced by applying the extra laser pulse 20ps prior to the arrival of the four-wave mixing pump pulses, while free carrier scattering is studied by synchronizing the additional laser with first four-wave mixing pump pulse, so that there is insufficient time for the photoexcited carriers to relaxed into bound excitons. In both cases, the homogeneous exciton resonance linewidth is observed to broaden, but for excitation of free carriers the effect is eight times as large as that seen for incoherent excitons, presumably due to Pauli pressure between the free carriers and the constituent electrons and holes the excitons comprise. To study these effects, reflection mode measurements are preferred, since the result will not be altered by excitation of the substrate material. A solution for the Taira model\optical Bloch equations is used to analyze the relaxation processes of this system. The homogeneous

linewidth function is shown to depend linearly on the density of scatterers, with a density-independent contribution due to the residual interaction of the excitons with acoustic phonons and impurity ions (leading to homogeneous broadening) and interface fluctuations and alloy concentration fluctuations at those interfaces (contributing to some degree of inhomogeneous broadening).

4.2.3 Some simple three pulse four-wave mixing results for semiconductor quantum wells

We have noted that three pulse four-wave mixing measurements have been performed to measure population relaxation and diffusion processes (see, for example [182], [183]), where control of the polarization state used permits the separation of population decay from orientational relaxation times. Of greater interest are measurements where the use of an additional pulse permits the experimental separation of the dephasing time T_2 from the population relaxation time T_1. Two pulse, self-diffracted four-wave mixing measurements provide data that can be used to extract the dephasing rate if the population relaxation rate is known from an independent measurement (e.g. from a pump-probe measurement), but the three pulse technique does not require an additional experiment.

Three pulse four-wave mixing experiments have been used to study the dependence of decoherence and orientational relaxation on excitation density and the validity of the polariton picture [326]. The polariton description of excitation assumes that the interacting light-matter system is not well

described using separate exciton and photon modes, but rather the coupled exciton-phonon eigenmodes, or polaritons. The coupling between photons and excitons, characterized by the oscillator strength, must be sufficiently strong, compared to the exciton-exciton and exciton-bath interactions, characterized by the dephasing time T_2, for this picture to be valid. By performing experiments at very low excitation densities, the exciton-exciton interaction can be neglected. In this case the decoherence is determined by scattering by residual acoustic phonons and impurities. Two pulse self-diffracted experiments are performed to determine the dephasing time, but three pulse measurements are also performed to study the orientational grating induced by two preceding parallel pump pulses. The short dephasing time T_2 indicates that the coupling between the exciton and the bath is stronger than the exciton-photon coupling; this indicates that the polariton picture is not valid for these samples. The coherent interaction between light and the exciton population is insufficiently strong to result in a coherently propagating coupled excitation mode – the exciton polariton – which would be expected to decay within a single wavelength in these systems. We note here that we do not consider this result further in our own experiments on polaritons that describe coupled plasmon-photon modes.

Further self-diffracted four-wave mixing measurements were able to refine the model for exciton-exciton and exciton-free carrier scattering [328]. Again, an additional laser was used to inject free electron-hole pairs or incoherent excitons. A detailed examination of the dependence of the decoherence

time on the density of the scatterers provides a measure of the dephasing efficiency of each collision process. Efficient scattering occurs even at low excitation densities of $5 \times 10^{14}\text{cm}^{-3}$, where the inter-exciton distance of approximately 100nm is nearly ten times the exciton Bohr radius of 13nm in GaAs. These experiments also iteratively solved a Taira\optical Bloch model to find theoretical fits to the temporally resolved time-integrated four-wave mixing signal. We note that while the decay of this correlation trace appears well fit in their results, the rising portion of the diffracted signal is not well fit in this model. Moreover, proper comparison between theoretical and experimental collision efficiencies is impossible in this model. Only an approximate comparison is offered, since the validity of the theoretical approaches used to describe three- and four-particle scattering has not been demonstrated for semiconductor systems.

These experiments also provide a more complete description of the frequently unspecified interactions among excitons and carriers, and relate those microscopic processes to macroscopic spectroscopic observations. The exciton-exciton interaction should resemble an attractive van der Waals force and a repulsive hard-core force that results from Pauli pressure. The observed blue shift of the exciton resonances due to injection of incoherent excitons suggests that the repulsive forces dominate under the conditions probed in these (and, by extension, most all) GaAs quantum well exciton experiments. The exciton-carrier interaction, however, should resemble the polarization of a neutral particle (the hydrogenic exciton) by a charged particle (the free carrier); this is

an attractive interaction. There is also a repulsive force for exciton-carrier interactions, due to an exchange interaction for parallel electron spins. The lack of any spectral shift observed for exciton-carrier scattering experiments suggest these interactions are balanced in these systems.

Furthermore, the observed exciton-exciton scattering rates suggest that this process cannot drive the system from a non-thermal to a thermal, quasi-equilibrium distribution of excitons on a time scale comparable to the time scale. Instead, this relaxation must be driven principally by interaction with phonons and impurities.

4.2.4 Time-resolved four-wave mixing experiments

We have described some three pulse four-wave mixing measurements. Perhaps more enlightening in dissecting the problems of many-body effects in semiconductor quantum wells are the results of time-resolved four-wave mixing experiments. Certainly, we note that the time-integrated self-diffracted four-wave mixing experiments already show some deviation from the simple Taira model of a non-interacting ensemble of two-level systems governed by the optical Bloch equations.

The optical Bloch equations were first been rigorously tested as a description of optical interactions in solids in studies of Praseodymium impurity atoms in Lanthanum Fluoride ($Pr^{3+} : LaF_3$), chosen due to its substantially different time scales for decoherence and population decay [90] (Other measurements based on optical analogs of several NMR techniques had previously

been used to validate the optical Bloch equation description of light-matter interaction in atomic and molecular systems [28]. A small spectral band of Praseodymium ions in the inhomogeneously broadened line are excited using an ultra-stable cw dye laser. The excitation is then removed very rapidly switching the laser frequency [48], [89]. The resulting optical free induction decay measurements (q.v. *sup*) are then fit using a free-induction decay solution to the Bloch equations at low Rabi frequencies, or using a modified model that considers NMR saturation in solid samples [306] for high Rabi frequencies. It is assumed that the dephasing rate is not (or is only weakly) dependent on the excitation density used. The simple theory provides a close fit for this system, but notes that using a single-valued dephasing time T_2 will fail at sufficiently high intensities.

The applicability of the Taira\optical Bloch model is susceptible to even more substantial issues in semiconductor exciton systems. While self-diffracted four-wave mixing experiments suggested problems with the temporal lineshape of the time-integrated emission, time-resolved four-wave mixing measurements demonstrated that the ensemble of non-interacting two-level systems with relaxation processes described by T_1 and T_2 times was unable to describe the dominant effects in the third-order nonlinear optical response.

Time-resolved four-wave mixing is a straightforward extension of the two-pulse, self-diffracted four-wave mixing experiment used to study dephasing in semiconductors. The phase-matched coherent emission is collected and temporally resolved, typically by performing a nonlinear upconversion process

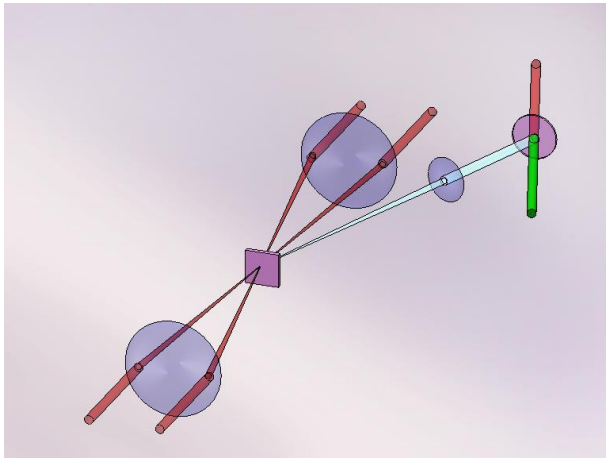

Sketch of experimental geometry for time-resolved transient four-wave mixing measurement. The signal field, indicated in blue, is mixed with a local oscillator field. Adjusting the delay of the local oscillator pulse maps out the intensity of four-wave mixing emission. In this diagram, the heterodyne field (green) suggests collinear coupling, but non-collinear geometry up-conversion in a nonlinear crystal is frequently used.

Figure 4.14: Sketch of transient four-wave mixing experiment

using an independently delayed reference pulse, detecting light at the upconverted, higher frequency, and using its intensity to determine the intensity of four-wave mixing emission as a function of the reference pulse delay. Essentially, it is a standard self-diffracted four-wave mixing technique, but with a more sophisticated detection scheme that maps out the temporal lineshape of the nonlinear response.

The wrong time exponential rise of four-wave mixing emission at low excitation density and temporal splitting of four-wave mixing emission at high intensity [242] have been noted elsewhere in our discussion of self-diffracted four-wave mixing experiments. These effects may be explained in theories that consider exciton-exciton coherent interactions; these appear to be general many-body effects that are not expected to be limited to the specific materials studied.

We have discussed the nature of relaxation processes elsewhere in this thesis [329], [328], [326], [183], [184], considering the effect of incoherent scattering of excitons by acoustic phonons, impurities, other exciton populations, and free carriers in four-wave mixing experiments. Quantum beating effects have also been studied with four-wave mixing [141]. The analyses of these two pulse measurements indicate that Coulomb forces among excitons result in nonlinearities in the optical response of these systems, arising due to coherent exciton-exciton interactions. These correlations among members of the interacting ensemble of excitons have previously been studied in the context of the excitonic AC Stark shift, the results of which led to the development of the

semiconductor optical Bloch equations [320], [321], [323]. Theory developed in the context of the exciton Stark shift is based on unrestricted Hartree-Fock or BCS approximations, and can be successfully used to describe the coherent exciton-exciton correlations [319], [354], [108], [414], [107], [318].

In addition to the dephasing processes previously studied, coherent spectroscopic techniques have been shown to also probe exciton-exciton interactions in a population of Wannier excitons under resonant excitation [3].

To study the failures of the simple models, time resolved four-wave mixing was performed on an inhomogeneously broadened exciton resonance [387]. Excitation below resonances permits resolution of the dephasing time T_2 within the precision of the laser temporal width. As the excitation intensity is increased, the wrong time four-wave mixing signal increases correspondingly, but develops a more complicated, two peak temporal lineshape.

The optical response of this system is governed by exciton effects. Nonlinearity is affected by the exciton-exciton correlation and anharmonicity in the exciton-photon coupling. These effects can be considered in a BCS semiconductor model with a potential that couples the various exciton states via a Coulomb force. The density matrix describing the system may be written

$$\hat{n}_k(t) = \begin{pmatrix} n_{ck}(t) & \psi_k(t) \\ \psi_k^*(t) & n_{vk}(t) \end{pmatrix}$$

where $\hat{n}_k$ is a 2x2 block in the density matrix that describes those members of the inhomogeneously broadened ensemble of two-level systems

labeled by wave vector $\mathbf{k}$, where the subscript c represents a conduction band state and v the valence band states. The n terms in the matrix block are populations, whereas the ψ terms are pair amplitudes. This density matrix evolves according to a Liouville equation,

$$\partial_t \hat{n}_k(t) = -i\left[\hat{\varepsilon}_k,\ \hat{n_k}\right] + \partial_t \hat{n}_k|_{relaxation}$$

where the energy matrix contains not only self-energy terms and the optical coupling, but also the Coulomb interaction,

$$\hat{\varepsilon}_k(t) = \begin{pmatrix} \varepsilon^0_{ck} & -\mu E(t) \\ -\mu^* E^*(t) & \varepsilon^0_{vk} \end{pmatrix} - \sum V_{\mathbf{k},\mathbf{k}'} \hat{n}_{\mathbf{k}'}(t)$$

The inclusion of the Coulomb term will renormalize the valence and conduction band energies, and the coupling to the light field is modified

$$\mu E(t) \rightarrow \Delta_k(t) = \mu E(t) + \sum_{\mathbf{k}'} V_{\mathbf{k},\mathbf{k}'} \psi_{k'}(t)$$

Physically, the interpretation of this interaction potential is that the optically coupled conduction and valence states at a particular momentum $\mathbf{k}$ are subject not only to the incident optical fields, but rather experience a self-consistent local field Δ_k, due to the sum of those applied external fields and the so-called molecular field that arises due to the other optically coupled states at different wave vectors. Phenomenological relaxation terms are still

used in the Liouville equation to approximate stochastic perturbations leading to decoherence and spontaneous emission in the ensemble.

Using the renormalized energies and modified interaction, it is possible to obtain a time-dependent Wannier equation that describes the induced change in coherence. If the Coulomb interaction among the excitons is set to zero in this equation, and a perturbation solution is found to the third order in applied fields, the normal Bloch equations for an inhomogeneously broadened ensemble of non-interacting two level systems is recovered. This shows that the BCS theory of band-edge excitations can recreate the simpler non-interacting exciton theory. In the BCS expressions for the time-evolution of coherences or populations, the exciton-exciton Coulomb coupling terms will appear nearly step-like in their onset, then exhibit a subsequent decay governed by dephasing and population relaxation times. This BCS theory can accurately reproduce the temporal lineshape of the observed four-wave mixing emission, including the wrong time emission, rising with half the time constant that describes the emission decay, as well as predicting the formation of the double peak at higher excitation density. These results suggest that the temporal lineshape of four-wave mixing emission from excitonic systems is largely due to the Coulomb interactions that nonlinearly couple the population and coherence. Nonetheless, since the numerical simulations used to evaluate the predictions of this model are computationally intensive. This theory is therefore of limited predictive utility in understanding the nature of the processes involved, as it is difficult to understand which particular mechanisms directly

affect the calculated or experimentally resolved four-wave mixing signal.

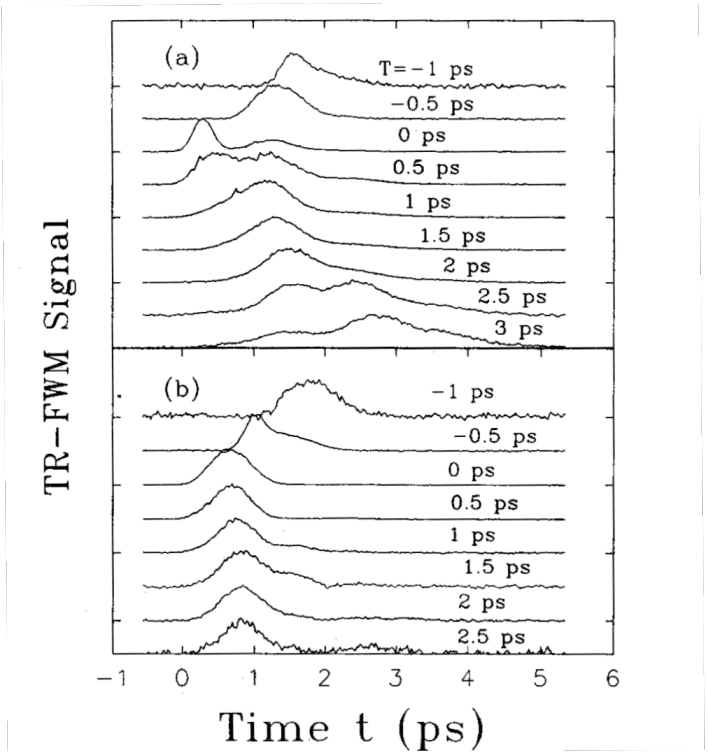

Time-resolved self-diffracted four-wave mixing from GaAs quantum wells, shown as a function of the local oscillator delay time for a number of different delays between the two pump pulses. A non-interacting model cannot explain emission in the phase-matched direction for negative pump delay times. The traces are normalized to the same peak value, and show co-linear (a) and cross-linear (b) polarizations. Reproduced from Kim, Phys. Rev. Lett. 69:2725 (1992).

Figure 4.15: Time-resolved transient four-wave mixing temporal lineshapes

Femtosecond time-resolved four-wave mixing spectroscopy on high quality GaAs wells can provide definitive proof that the Taira/optical Bloch model is unsuitable to describe the nonlinear processes in this system [216]. The simpler models predict a temporal lineshape for time-resolved four-wave mixing

emission (not to be confused with the temporal lineshape of time-integrated emission as a function of the pump pulse delay) that peaks at or shortly after the coincidence of the two pump pulses. Experimentally, it can be shown that the temporally resolved diffracted power exhibits a slow turn on (1.5ps in the samples studied, some ten to fifteen times the laser pulse duration), with the peak occurring at a delay approximately equal to the dephasing time T_2. The effect is suspected to be due to the Coulomb interactions that have been used to explain the time-integrated temporal lineshape. Unlike time-integrated four-wave mixing, time-resolved spectroscopy permits the separation of the relative strengths of the Taira/optical Bloch contribution to the four-wave mixing signal from the interaction-induced contributions. Time-resolved emission suggests that the interaction-induced emission is as much as two order of magnitude stronger than the response that can be explained in the context of a non-interacting ensemble of emitters. Negative delay emission can also be resolved temporally in these measurements. Assuming that a local field effect can be used to explain the interaction induced emission allows an estimate of the strength of that perturbation, obtaining a value of a few meV – on the order of the exciton binding energy.

Chapter 5

Two-dimensional Fourier Transform Spectroscopy – background and experiments

5.1 Background and context: three pulse four-wave mixing measurements and the coupling of exciton resonances

5.1.1 Three pulse four-wave mixing experiments: underlying theory

We have mentioned some three pulse experiments already, but did not yet spend significant time outlining the underlying theory for those techniques. Rather, we consider the optical physics of three pulse measurements here, due to their significance for two dimensional Fourier Transform spectroscopy.

An implicit theme throughout this thesis is that the dephasing processes that govern the relaxation of a macroscopic polarization can reveal fundamental static and dynamic properties of material systems. In many media and in structured samples, significant dephasing of coherence among quantum emitters can occur on a sub-picosecond time scale. Inhomogeneous broadening of a transition may complicate the analysis of the particular details of phase relaxation processes. Frequency domain spectral hole burning measurements can provide information on homogeneous widths concealed by

inhomogeneous broadening [128], [155], [119], [60], but are deprecated if dephasing times may be measured directly in the time-domain. Photon echo and self-diffracted four-wave mixing measurements are available to study dephasing times, and have been described elsewhere in this thesis, but suffer from some disadvantages when studying certain media. Given the substantial interest in understanding the behaviour of material's optical response using a Bloch formalism, wherein relaxation processes are characterized using only two parameters, an experiment that can accurately measure dephasing and population decay simultaneously is of significant scientific merit.

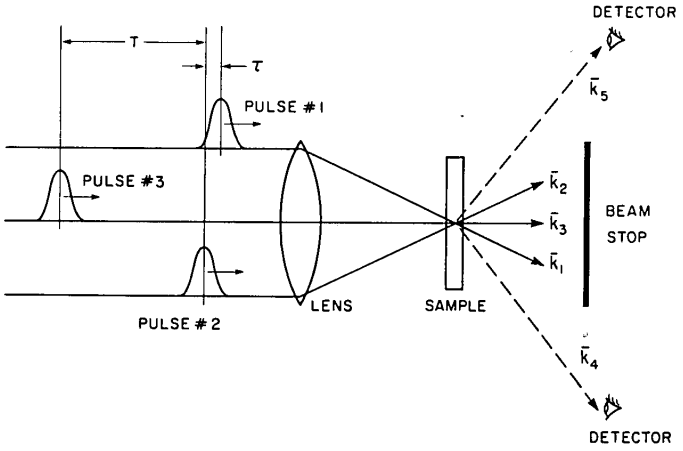

Typical three-pulse four-wave mixing experimental schematic. Background-free emission occurs along either of two separate phase-matched directions, determined by the pulse time ordering. Scanning the delay between the first two pulses allows direct extraction of the dephasing time. Scanning the delay between the last two pulses provides the population relaxation rate. Reproduced from Weiner, J. Opt. Soc. Am. B 2:654 (1985).

Figure 5.1: Three pulse four-wave mixing schematic

Three pulse four-wave mixing experiments provide several advantages

compared to self-diffracted four-wave mixing spectroscopic techniques, with accuracy better than the laser temporal pulse width, and can discriminate between homogeneous and inhomogeneous broadening without the need for additional spectral measurements [392], [391]. Three-pulse transient grating experiments were previously used to study population and orientational relaxation in condensed matter systems, as noted elsewhere in this thesis [106], [290], [347], but had not been applied to studying dephasing processes. We describe the three pulse experiment in some detail here, as it relates directly to the optical processes upon which two-dimensional Fourier transform spectroscopy depend.

The three pulse experiments require more complicated experimental infrastructure to implement, but offer two significant advantages for which these methods are preferred to the two pulse, self-diffracted four-wave mixing techniques. First, three pulse transient grating techniques can separately measure dephasing and population relaxation rates. The delays between the pulses used in the three pulse scattering measurement may be scanned in such a way as to probe only T_2 time, whereas the two-pulse self-diffracted techniques produce results that depend on a combination of the dephasing and population relaxation times. As a result, self-diffracted measurements experimental access T_2^*, where $\frac{1}{T_2^*} = \frac{1}{T_2} + \frac{1}{T_1}$. It is certainly possible to use a two-pulse measurement to extract the dephasing time only if the population relaxation time is also known, but this requires a second measurement. Moreover, if the population relaxation is comparable to the dephasing rate, the analysis of the observed

polarization decay curve becomes more prone to error, as it is more difficult to distinguish the effects of dephasing from the longitudinal relaxation. The three pulse measurement also permits a direct measurement of $T_2 = 0$ curve, which the two-pulse scattering method cannot provide due to the inherent mixing of the two parameters in the observed correlation traces. The three pulse measurement therefore can directly access both dephasing and population decay times.

Second, the three pulse measurement may also distinguish between homogeneous and inhomogeneous broadening. Two pulse experiments may do so only if the dephasing rate is sufficiently clearly resolved from the population relaxation, which then permits a comparison with spectral data to determine the broadening mechanism. Weiner et alia assert that the temporal line shape observed in three pulse transient grating spectroscopy is indicative of the nature of the broadening mechanisms for the transition of interest; this certainly is the case within the framework of a density matrix theoretical model that treats the system as an ensemble of non-interacting two-level oscillators, but we note here that the failure of the Taira model to accurately capture those many-body effects that depend upon correlation among excitons may call into question the validity of this statement. If that model is valid, however, it can be shown that the temporal envelope of the energy diffracted in a three pulse experiment is a symmetric function of the τ delay for a homogeneous line, whereas an inhomogeneous line exhibits a unit step behaviour at $\tau = 0$, with no wrong-time emission predicted by a Taira-like model. The stimulated pho-

ton echo effect [262] is viewed here as a strong-field limit for the three pulse transient grating experiment.

In either broadening case, this assumes that the probe delay T has been chosen to be less than the spectral diffusion time; typically, the delay T is chosen to be longer than the pulse length t_p so as to ensure that the grating formation process has gone to completion, and in some systems slower than any extremely fast relaxation times (for a molecular dye, for instance, choosing T to be fast enough for fast vibrational state relaxation process to occur; in the semiconductor materials of interest to us, a comparable time scale would be the exciton formation time. This is expected to occur extremely rapidly – on the femtosecond timescale – and is thus not a significant factor in the design of an experiment for GaAs nanostructures).

In a three pulse measurement, the second pump pulse to interact with the sample induces a transient grating if it arrives prior to significant dephasing of the coherence induced in the material by the first pulse. Interference results in a spatially periodic pattern of excitation. The grating modulation depth is then measured by scattering a third pulse from the grating. As long as the pulse width t_p is not long compared to the dephasing rate, T_2 can be extracted directly by scanning the delay τ between pump pulses. If, on the other hand, $t_p \gg T_2$, then the scattered energy measured from either a homogeneous or inhomogeneous transition is simply related to the square of the electric field autocorrelation,

$$U_{k_3 \pm (k_1 - k_2)} \propto \left| \int dt E(t) E*(t+\tau) \right|^2$$

This may be moderately useful as a diagnostic tool [105], but essentially it restricts the usefulness of three-pulse grating experiments as a simple diagnostic for samples with dephasing rates slower than the available laser pulse. We note here that this is no different from the restriction on self-diffracted four-wave mixing experiments performed with only two pulses, which exhibit the same limitation. Technically, it is possible to extract dephasing information even in the case of long pulses ($t_p \gg T_2$) in a three pulse experiment, since the laser autocorrelation is readily available from an independent measurement. Comparison to the data obtained in a three pulse transient grating experiment should permit an estimate of the dephasing time, but this indirect technique requires an additional measurement, which obviates one of the principal advantages of the three pulse methods.

If the pulse duration is not greater than the dephasing time, the temporal evolution of the four-wave mixing signal may be analyzed to determine the nature of the broadening, as noted above. For a homogeneously broadened transition, a single grating is induced in the sample, with the complex grating amplitude determined by an integral function of the envelopes of the incident electric fields. The total diffracted energy is then proportional to the simple decay function

$$U_{k_4} \propto e^{-2|\tau|/T_2}$$

In the case of inhomogeneous broadening, the four-wave mixing emission is no longer a symmetric function of the pump pulse delay τ. In this case, the first two pulses induce a set of population gratings, each with different spatial periodicity determined by a particular frequency on the inhomogeneous line. For very large inhomogeneity, the spatial distribution of the photo-excitation may approach a uniform mean density – but will still result in diffraction into the phase-matched direction. The probe pulse, arriving after the waiting period T, induces a third-order nonlinear polarization for each grating, with the initial phase of that polarizations evolution determined by the spatial phase of that grating. Each individual polarization in the set oscillates at a particular resonant frequency and together constitute the inhomogeneously broadened emission line. The resulting scattered intensity is given by

$$\begin{aligned} \tau &\geq 0: \qquad U_{k_4} = 0; \qquad U_{k_5} \propto e^{-4\tau/T_2}, \\ \tau &\leq 0: \qquad U_{k_4} \propto e^{4\tau/T_2}; \qquad U_{k_5} = 0 \end{aligned}$$

i.e. there are two possible phase-matched directions, due to the symmetry of the interaction under interchange of the pump pulses. In both cases, there is only emission along a phase matched direction in the 'right' time window – there should be no 'wrong' time emission if the Taira model is valid.

As noted, and similar to other four-wave mixing techniques, the signal of interest here is emitted along a phase-matched direction. The results cited

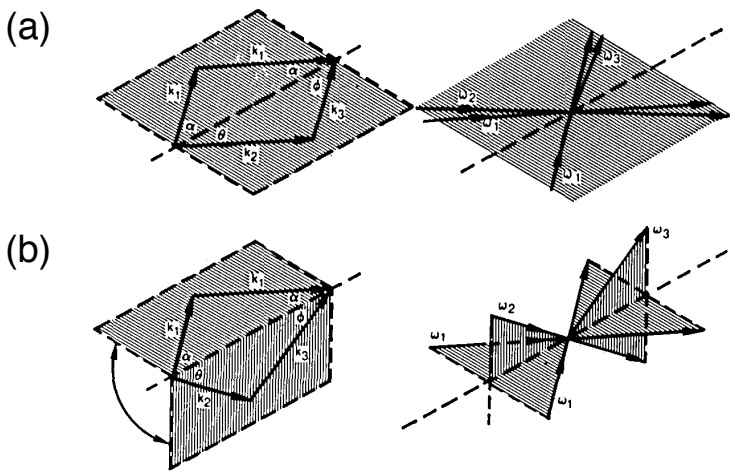

The planar phase-matching and beam geometries used for CARS four-wave mixing experiments (a) can be folded into the BOXCARS phase-matching and beam geometries (b), which take advantage of an additional spatial dimension to better separate the signal field from the excitation lasers. Reproduced from Eckbreth et al., Appl. Phys. Lett. 32:421 (1978)

Figure 5.2: BOXCARS phase-matching geometry

here [392] make use of a folded BOXCARS geometry [343], which is of significance to our experimental efforts as this configuration remains the principal geometry favoured by 2dFT spectroscopists. CARS, or Coherent anti-Stokes Raman Spectroscopy, is a sophisticated nonlinear spectroscopic tool based on a parametric process, used to study a broad range of materials [27]. Typically, a four-wave mixing effect results in emission at $2\omega_1 - \omega_2$ when the difference frequency $\omega_1 - \omega_2$ matches a Raman transition in the system under excitation. This process is known as an anti-Stokes spectroscopy because the phase-matched emission occurs resonantly at at $2\omega_1 - \omega_2 = \omega_1 + (\omega_1 - \omega_2)$, corresponding to the fundamental (ω_1) frequency plus the anti-Stokes shift due to coupling with a Raman mode at $\omega_1 - \omega_2$. Early CARS experiments were

often performed in a collinear excitation geometry, resulting in emission of the signal of interest along the same beam path; for sufficiently large frequency shifts, the CARS signal is readily separable using any common spectrally dispersive element. To measure small shift CARS signals, however, such as those arising due to rotational states, requires the use of a non-collinear geometry to spatially separate the signal of interest from the background of the intense beams used to drive the non-degenerate frequency mixing process [103]. The folded BOXCARS geometry [343] uses a non-collinear, non-coplanar beam arrangement to induce four-wave mixing along a direction that is well separated from the excitation beams. The BOXCARS geometry allows the observation of CARS signals even in the case of a completely degenerate energy structure (i.e. for zero Raman shift). A third-order nonlinear signal detected in this direction may be interpreted as the convolution of the susceptibility $\left|\chi^{(3)}\right|^2$ with the spectrum of the excitation pulses.

The underlying optical physics is the same in the transient grating three pulse experiments, and indeed, in non-collinear 2dFTS. In transient grating three pulse spectroscopy, the folded boxcars configuration results in exact phase matching for one of the scattered beams.

Excitation may be performed with co-parallel and cross-parallel beams. When using all co-parallel beams, a slow thermal grating may be induced in the material sample in addition to the population grating expected from the light-matter interaction; this thermal effect may exhibit a lifetime greater than the pulse repetition period, and can affect the interpretation of signals collected

in this or similar techniques. The emergence of a thermal grating may be investigated by selecting negative probe delays T; if there is a slow, persistent thermal grating, diffraction should be observed even at large negative times. We note here that in our three pulse experiments (partially collinear 2dFTS and a modified partially collinear three pulse experiment with heterodyne signal selection) no such effects were observed. If problematic thermal gratings are demonstrated for a given medium, the effect may be decreased by using orthogonal polarizations for the pump pulses, though this necessarily restricts the range of polarization configurations that may be considered.

No issues with slow, persistent thermal grating diffraction are expected in our experiments, as 2dFTS measurements return a null spectrum for negative probe delay times T. There is an unresolved question to consider for other similar experiments on these materials, as it may be possible that the null spectrum is obtained only because the thermal grating does not exhibit the appropriate frequency dependence to be found in the signal spectral region of interest. We do not consider this problem at length here.

Three pulse transient grating spectroscopic techniques also provide sensitivity to spectral cross-relaxation, an effect that occurs when the resonant frequency of an absorber is not fixed, but instead migrates within the inhomogeneous line. This is not the dominant behaviour in the systems we study in this thesis, since excitons emitted near the band edge in a direct gap semiconductor have nearly zero momenta, but we note that it is possible for non-localized exciton states to be formed by above-bandgap excitation, and

that similar spectral shift behaviour may occur in such scenaria. Indeed, a significant fraction of four-wave mixing experiments noted in this thesis consider the question of exciton de-localization. There is an interplay between disorder and delocalization for these exciton states: counter-intuitively, the exciton linewidth may be reduced by motional narrowing, as mobile excitons experience only an average perturbation during their evolution, whereas localized excitons may experience significantly different potentials due to their local environment (typically, due to interface fluctuation that changes the confinement energy, although in less finely grown samples, impurity atoms may also affect the exciton energy; that effect is, of course, not independent of the exciton localization that impurity ions may cause).

Spectral cross-relaxation may be characterized by some time scale (say, T_3). If the delay of the probe pulse is greater than this time, i.e. $T \gg T_3$, then the various gratings induced by the first two pulses are no longer distinct entities (n.b. that without spectral cross-relaxation the population of excitons excited into a given grating would differ (due to their place in the inhomogeneous line) from the excitons comprising a second grating) , and the rephasing that results in the emission of a photon echo for inhomogeneous systems will not occur. Rather, there is only a total population grating, with an amplitude that may be obtained by summing the individual complex grating amplitudes, weighted by the inhomogeneous distribution function. in this case, where $T \gg T_3$, the scattered energy is once again a symmetric function of the delay between the first two pulses, even though the resonance has been

assumed a priori to be inhomogeneously broadened. This of course is not a contradiction, as the introduction of any kind of spectral diffusion process is not included in the Taira-esque models used thus far to describe these systems. If the probe time is greater than the spectral cross-relaxation time, the temporal width of the symmetric diffracted energy curve reflects the inverse of the absorption width, rather than the actual dephasing time T_2. By the time the probe waiting period is approximately ten times the spectral cross-relaxation time, the diffracted four-wave mixing signal's temporal profile appears more or less indistinguishably symmetric [391].

The effect upon the temporal line may be considered an asset rather than a weakness of the three pulse experiment if it is possible to resolve T delays less than the spectral cross-relaxation time. If it is, data may be obtained with a range of probe waiting times, and changes in the behaviour of the temporal lineshape may be used to investigate spectral diffusion processes. We suggest that this may not be reliable if the spectral relaxation times are less than the pulse duration. In our own experiments we do not consider this effect, as the evolution of an exciton population during the waiting period T is not not yet well understood in the context of the many-body theory used to analyze our results.

Three pulse measurements are sensitive to a conceptually related effect, the transition from Markovian to non-Markovian dynamics. The correlation function for frequency fluctuations on an optical transition may be extracted in a three pulse measurement [205], [83]. If the geometry of the beams used

to excite the sample can be varied, diffusion process may be studied additionally. This diagnostic method is essentially a straightforward extension of transient grating spectroscopy. We mention the sensitivity of these effects only in passing, as we do not explore those topics in our own research.

We also note certain aspects of the application of three pulse experiments to multi-level systems, which are of some interest to us in the context of the three-band model frequently used to study exciton physics in a semiconductor quantum well. With a broadband laser pulse it is possible to excite several transitions simultaneously, resulting in interference between the various individual coherences created among the ground and excited state manifolds. That interference typically results in faster dephasing than would occur with excitation of a single resonance; dephasing due to multiline excitation is a non-reversible process, by way of contrast to the inhomogeneous broadening dephasing, where a revival (the photon echo) may occur. For time-domain three-pulse transient grating measurements, if the individual transitions unresolved, the decay of the four-wave mixing signal will provide an effective dephasing time that is the inverse of the total absorption width. By way of contrast, a technique like 2dFTS that spectrally resolves this emission can provide dephasing times for each resonance.

Analysis of the three-pulse, four-wave mixing experiment has been performed using a non-perturbational theoretical treatment, demonstrating the interplay between the population decay time T_1 and the dephasing time T_2 as the principal cause of decoherence in the quantum mechanical ensemble,

and illustrating the conceptual connection between the irreversibility of the relaxation processes and the symmetry breaking for phase-matched emission. The general usefulness of grating models is explored in reference [102].

In summary, three pulse transient grating spectroscopy offers significant advantages compared to the two pulse self-diffracted four-wave mixing measurements: improved temporal resolution, a clear distinction between homogeneously and inhomogeneously broadened lines (assuming the validity of the Taira model, which we obviously call into question), and an insensitivity to fast longitudinal relaxation (a fast population decay) that makes interpretation of self-diffracted four-wave mixing experiments difficult or impossible. The dependence of the diffracted energy on the two pulse delays can be found, in a Taira/optical Bloch type of density operator treatment, to be given by

$$I_s(\tau,\, T) \propto \theta(\tau)\,\theta(T)\, e^{-2\gamma_{ph}\tau} e^{-\gamma_{gr}T}$$

for a homogeneously broadened system of two-level non-interacting oscillators, and

$$I_s(\tau,\, T) \propto \theta(\tau)\,\theta(T)\, e^{-4\gamma_{ph}\tau} e^{-\gamma_{gr}T}$$

for an inhomogeneously broadened system of two-level non-interacting oscillators. Straightforward extensions of optical Bloch/Taira type models for exciton dynamics with few but greater than two levels are quite tractable, but tend not to provide such simple analytical results. Two-level model analysis is

useful for developing an intuitive understanding of the relevant physical processes – specifically, how relaxation affects the nonlinear polarization induced in the material.

5.1.2 Coupling of excitons in semiconductor quantum wells

The failure of the simple, non-interacting ensemble model for exciton dynamics described in the previous chapters led to a renewed interest in studying the many-body physics that was shown to dominate the nonlinear optical response of this system. One particular question of interest, the nature of coupling between excitons, was studied extensively.

Two-dimensional Fourier transform spectroscopy (2dFTS) is a particularly suitable tool for studying these effects, since it directly reveals the presence of coupling between spectrally resolved states in any system with a third-order nonlinear response. While only certain materials possess a second order response (within the assumption of electric dipole processes dominating the optical response of the material, any substance with a centrosymmetric structure will not possess a second order response in the bulk, although even those materials may exhibit some second order nonlinearity at boundaries or due to cascaded higher-order optical effects [177]), any material will exhibit some third-order nonlinearity under sufficiently strong excitation. As such, nonlinear optical methods that depend upon $\chi^{(3)}$ processes are popularly developed to study a broad range of systems. 2dFTS is such a tool, and is well-suited to revealing directly the nature and strength of the coupling between spectrally

resolved excitons in quantum confined condensed matter systems.

The body of literature considering the existence and particular nature of this coupling – which is speculative, and a matter of some dispute – is too broad and sophisticated to cover completely in this thesis. Instead we simply present some significant results and consider the conflicts among them. Exciton states in quantum well structures were studied using the techniques we have described in detail previously [243], [141], [241], [244]. Oscillations in the decay of the nonlinear polarization, determined by self-diffracted transient four-wave mixing measurements, or in pump-probe measurements of population, are argued by some to indicate a quantum beating effect.

Using ultrafast pulses with sufficient bandwidth to overlap a number of energy eigenstates of the exciton system results in the creation of a linear superposition of those states; the time evolution was studied with a delayed pulse. A two pulse experiment on an asymmetric double quantum well system can be used to study the dephasing processes by examining the diffracted energy, while population dynamics are revealed by resolving the change in transmitted probe intensity [244]. The application of a bias electrical field can control the coupling of exciton states in the two wells, resulting in localization of the state in one side of the structure, or achieving roughly equal probability distributions in both wells. The splitting between the exciton states in the two wells is sufficient to allow selective optical excitation, or both well excitons can be simultaneously excited with appropriate tuning of the laser. The oscillatory diffracted four-wave mixing and transmitted pump-probe signals can be

modulated by tuning the electronic levels of the two quantum wells into or out of resonance; the observed decay will exhibit oscillation when the two states are coupled by the electrostatic potential.

Similar wavepacket dynamics had been observed in atomic systems [408], [362], and molecular systems [313], [25], [125] previously, but this study [244] was the first observation of extended electronic wave packets in a solid state system (while it may be expected that quantum beating of extended electronic states could not be observed due to the extremely fast polarization decay expected for the distribution of transition energies described by the bandstructure [26], exciton emission provides sharper energy eigenstates that can exhibit little inhomogeneity and support coherent oscillation [241], [141]. We note here that quantum beating had been previously observed in solid state systems but was attributed to interference of quantum mechanical states associated with colour centers in atomic [69] or molecular crystals [374] rather than the interference of extended electronic states. Oscillatory decay of the emission observed in molecular systems was also interpreted as quantum beating in a number of these experiments (see, for example, [313], [25]).

These double quantum well results are interpreted in a relatively straightforward three-level theory that correctly describes the splitting of the exciton states and the resulting oscillations in the four-wave mixing and pump-probe measurements, but we note that it does not accurately predict the temporal lineshape of these signals. The failure to correctly model the early time behaviour is dismissed as unimportant due to the increased importance of the

pulse temporal lineshape during these periods, but it is likely that a many-body theory is necessary to properly model the behaviour of this system. This result is significant to the investigation of coupling because it demonstrates an experimental control of the coupling of excitonic states via an applied field that tunes the otherwise localized excitons into resonance across the double quantum well structure. The demonstration of coupling in a system that is mismatched by design suggests that coupling of spectrally resolved excitons may be possible in a system where the resonances are not so substantially separated.

We note that the analysis of a lineshape that is not completely understood or modeled to assert the existence or absence of coupling cannot provide ironclad proof of the presence or absence of such an effect.

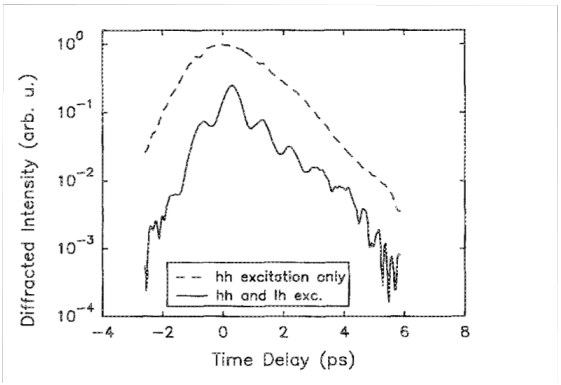

Selective excitation of only one exciton resonance in a quantum well causes smooth decay of self-diffracted four-wave mixing, while simultaneous excitation of both resonances results in an oscillatory signal. Reproduced from Leo et al., Appl. Phys. Lett. 57:19 (1990).

Figure 5.3: Oscillatory beating in four-wave mixing

Similar self-diffracted four-wave mixing experiments were performed using faster pulses to study the dynamics of simultaneously excited exciton resonances in a single quantum well [243], [141], [241]. The first measurements indicated coupling of heavy and light hole excitons occurring when the excitation laser was tuned to span both resonances, while a simpler temporal lineshape without oscillation was observed when only the heavy hole exciton was excited [243]. We note (a frequent refrain in discussion of time-resolved four-wave mixing experiments studying exciton coupling) that the temporal lineshape itself is not well understood in either case, as we have discussed extensively elsewhere in this thesis.

In these measurements, the oscillation in the four-wave mixing signal was attributed to an interference occurring in the macroscopic polarization due to interaction of these exciton states [241], which was judged to be a quantum beating effect similar to those observed in a broad range of atomic, molecular, and atomic nuclear [139] systems. These measurements considered the distinction between quantum beating arising when two excited states share a common ground state [78], [345], [146], [344] and the quantum beating that may occur if two or more two-level systems with slightly different transition energies are excited simultaneously [237]. The oscillation appearing in the emission due to a nonlinear polarization comprising contributions from both heavy hole and light hole excitons is essentially a three-level system, since both species of exciton depend upon the creation of an electron in the conduction band, and is therefore more analogous to the former interference effects, while the coupling

of spectrally resolved excitons would be more analogous to the latter. We will discuss relevant measurements of spectrally resolved exciton states shortly. In the case of these light hole and heavy hole beating effects, the energy states are resolved due to the quantum confinement; in bulk materials, the conduction bands coincide, but in quantum wells there is a finite heavy hole-light hole splitting. Again, excitation of just the heavy hole resonance results in a simple exponential decay of the four-wave mixing emission, while excitation of both resonances results in an oscillatory decay. The period of this oscillation is equal to the energy splitting of the two states obtained by independent spectral measurements. The same caveats to the poorly modeled temporal lineshape apply here as elsewhere, but with the additional observation that including the finite pulse widths does not effectively model the slow rise of the diffracted four-wave mixing at negative times [244]. Spectrally resolved time-integrated transient four-wave mixing was used to investigate the distinction between polarization interference and quantum beating (on the distinction of which, q.v. *sub*) of light and heavy hole excitons in GaAs quantum wells and impurity localized excitations in CdSe [257].

Beating effects may also arise in the coupling of free and bound exciton states [240], [241], where the presence of beats in the decay but not in the rise of the diffracted four-wave mixing was assumed to demonstrate a weaker coupling of bound and free exciton states compared to the interaction observed in experiments claiming to show coupling between light and heavy hole excitons [243].

Of significant interest to our own group is the coupling of excitons that are spectrally resolved by interface fluctuations. In this case, two (or more) two-level systems are relatively independent, in that they do not share a common ground state is in the case of the light hole - heavy hole exciton coupling. Instead, a particular resonance (generally, the heavy hole exciton is studied because of its greater oscillator strength and lower transition energy, allowing excitation of just the heavy hole without the light hole and free carrier states by careful adjustment of the laser center wavelength) is split by extrinsic defects in the fabrication of the quantum well structure.

Spectral structure to the exciton resonances suggests fluctuations of the quantum well width on the order of atomic monolayers, which would shift the resonance energy due to the particle-in-a-box effect of quantum confinement [143]. In particular, photoluminescence measurements of exciton resonances exhibited energy splittings in agreement with the values expected for monolayer fluctuations for samples that were shown to exhibit precisely such well width fluctuations using x-ray diffraction [88]. Energy splittings corresponding to half-monolayer fluctuations were also observed with photoluminescence [310]. The presence of well width fluctuation was shown to be somewhat controllable, with disorder introduced by interruption of the molecular beam epitaxy growth process resulting in an increase of intrinsic dopants and the formation of islands of monolayer-flat regions [365]. Scanning microscopy techniques (scanning cathode luminescence and chemical mapping via scanning transmission electron microscopy) permitted imaging of the island structures

formed during interrupted growth processes [30], [282] though we note that the surface structure cannot be assumed to remain unchanged after subsequent growth steps deposit the AlGaAs boundary layer and GaAs capping layer on quantum well samples. A more complete description of the interface disorder is suggested to account for inconsistencies with various optical and microscopy measurements of the surface [383].

These variations in well width result in spectral resolution of the exciton resonances. While coupling of light and heavy hole excitons in one region is expected from the behaviour of these quasiparticles observed in lines broadened by more substantial fluctuation, the existence of coupling of excitons in different width regions is not known.

Self-diffracted four-wave mixing experiments were used to study these effects, and attempt to resolve the question of coupling of these spectrally resolved excitons by analysis of the temporal lineshape [241], [141]. Comparison of quantum wells grown with and without interruption permit study of exciton dynamics in wells with semi-controllable interface disorder. Photoluminescence reveals splitting of heavy hole exciton resonances, but does not indicate localization of excitons to individual defect sites in the lattice. In those materials fabricated with growth interruption, only a weak oscillation is observed in the decay of the four-wave mixing signal, while a strong beating effect can be seen in the samples fabricated with growth interruption. Variation of the temperature and excitation density does not affect the oscillation period, suggesting that this effect is due to the quantum mechanical

coupling of the spectrally resolved exciton states rather than to some particular detail of the experimental parameters. It is suggested that the beating effect is analogous to the quantum beating observed in isotopically labelled molecules [237]. If similar measurements are performed but with much narrower wells, the splitting between spectrally resolved heavy hole excitons is now greater compared to the heavy hole energy, due to the increased ratio of the width fluctuation compared to the width. In this case, no oscillation is observed, since the split heavy hole exciton states are sufficiently energetically spaced as to be decoupled. Once again, these results are interpreted using the Taira/optical Bloch model, despite its inability to completely account for many of the features of the temporal lineshape of four-wave mixing emission from exciton systems. This simple model suggests that strong inhomogeneous broadening will suppress the oscillation. Even in homogeneously broadened resonances the modulation depth is not expected to reach 100%, the result found for a simple three level system with completely discrete energy levels.

We note again the vulnerability of any conclusions drawn from the study of temporal lineshapes given the inability to model properly the lineshape for any interacting exciton system. These assertions of coupling between spectrally resolved excitons all depend on the observation of oscillations in the nonlinear polarization, with a period equal to that expected from the energy splitting of the resolved exciton states. If there is quantum mechanical coupling of the two (or more) two-level systems, such a beating would be expected – but it could also be polarization beating. The name is somewhat misleading

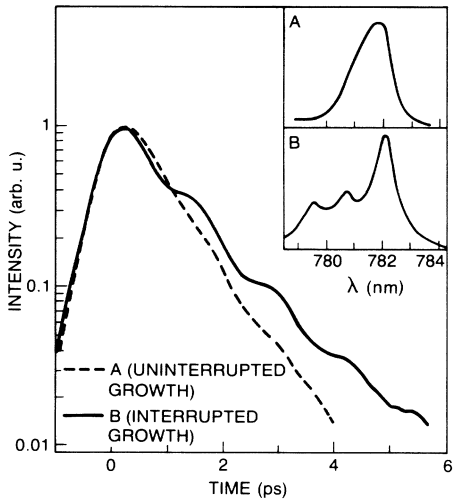

The amplitude of oscillations in four-wave mixing emission can be greatly increased by altering the growth method to increase structural disorder. The fluctuation in well width results in splitting of the photoluminescence peak (b) compared to the smooth feature observed in normally grown samples (a). Reproduced from Göbel et al., Phys. Rev. Lett. 64:1801 (1990).

Figure 5.4: Oscillatory beating and interface disorder

here, in that we are not considering an oscillation in the polarization, which we have modeled in this thesis as a macroscopic observable related to the coherence among quantum states, but rather to the classical interference between electromagnetic fields emitted from two sources that are not coupled in their dynamics, but which are observed with the same detector. The self-diffracted four-wave mixing measurements (e.g. [141]) cannot be definitively shown to be due to one or the other interference effects. In a system that comprises two independent two-level systems without broadening, the Taira/optical Bloch model predicts a fairly straightforward result for the nonlinear polarization, the oscillatory lineshape of which which may be distinguished from a polarization interference [191]. In homogeneously broadened systems, the distinction between polarization and quantum beating is not so clear, and indeed, all these models are questionable given their failure to properly predict the overall temporal envelope of four-wave mixing for an interacting system of excitons. It is argued that performing time-resolved transient four-wave mixing instead of the simpler time-integrated transient four-wave mixing measurements can provide proof of the nature of the interference [223]. We note several objections to this result: the distinction depends upon the observation of a periodic oscillation that occurs only a few times before the nonlinear polarization has decayed, the result depends upon a Taira/optical Bloch model for the polarization induced by the ultrafast pulses, and the result depends upon the assumption that the system is purely homogeneously broadened. Moreover, the experimental results obtained used multiple quantum well samples where the ability

to produce identical wells cannot be independently verified. The theoretical model also neglects the effects of dephasing and Coulomb correlation among the excitons, both of which have been shown to have significant effect on the dynamics of these systems. The argument offered in reply is that those effects not considered in the simple model only affect the overall envelope of the four-wave mixing signal; it is hard to agree with the statement that some as yet unknown but correct theory could not result in a different envelope and alter the oscillatory behaviour of the four-wave mixing emission. This result, then, should be considered suggestive but not irrefutable proof of quantum beating occurring in GaAs quantum wells. Indeed, the inclusion of the effects of dephasing and inhomogeneous broadening into this model can be shown to produce a quantum beating that is indistinguishable from polarization interference [413]. Some caveats apply to the model of broadening used to obtain those results [222]. The effects of inhomogeneously broadening of the exciton resonances were considered at further length, demonstrating that correlation among these states can strongly affect the modulated temporal lineshape [79], giving us further reason to be suspicious of assertions of coupling dependent on the observation of oscillations in the nonlinear polarization. Subsequent work using spectrally resolved transient four-wave mixing asserted that quantum beating could be observed in the four-wave mixing emission from GaAs quantum wells, and could be shown to occur for spectrally resolved excitons that shared no common ground state, and that both quantum beating and polarization interference in these systems arose from the interference of macroscopic

optical polarizations [291], however these results were interpreted using a modified Taira\optical Bloch model that includes corrections for exciton-exciton interaction but which can only provide a qualitative description of the system dynamics.

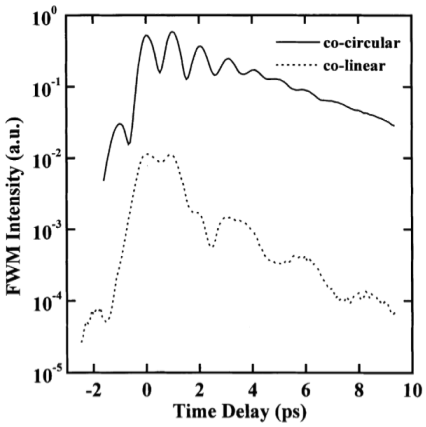

The dependence of the oscillations in a spectrally resolved four-wave mixing signal is argued to indicate evidence of coupling between excitons spectrally resolved by interface fluctuations. Reproduced from Phillips et al., Solid State Communications 111:317 (1999).

Figure 5.5: Spectrally resolved oscillatory FWM

The general trend of these results would suggest that there is very likely coupling occurring in these systems. Problematically, the model for the temporal lineshape is not complete and cannot describe the dominant envelope features for the four-wave mixing emission. More significant, perhaps, are results from highly sensitive spectrally resolved two colour experiments that indicate that there is no coherent coupling for spectrally resolved excitons [117]. Partially non-degenerate four-wave mixing was used to study the

third-order nonlinear optical response of this system, with an initial, narrow bandwidth pulse (temporal width ˜2 to 3 ps) used to excite a coherence, while a broadband, 100 fs pulse then transforms that coherence into a population grating before some fraction of its energy is scattered into the phase-matched direction. Scanning the wavelength of the narrowband pulse across the exciton absorption features and spectrally resolving the emission permits the creation of a two-dimensional map that reveals diagonal features corresponding to energy eigenstates and off-diagonal features that demonstrate coherent coupling between those states. An asymmetric quantum well with two different regions was fabricated and shown not to exhibit coupling by design, but high quality samples with three spectrally resolved heavy hole exciton states also failed to indicate any coherent coupling.

The question of coupling between spectrally resolved excitons in quantum wells is thus an open one, and one which seems highly suited to the technique of two-dimensional Fourier transform spectroscopy. Our own experimental program begins with the application of a standard non-collinear 2dFTS experiment to prototypical GaAs quantum wells to study the problems of exciton coupling, and leads us to the development of new spectroscopic tools for studying a broad range of systems. First, we turn out attention to a brief discussion of two-dimensional Fourier transform spectroscopy.

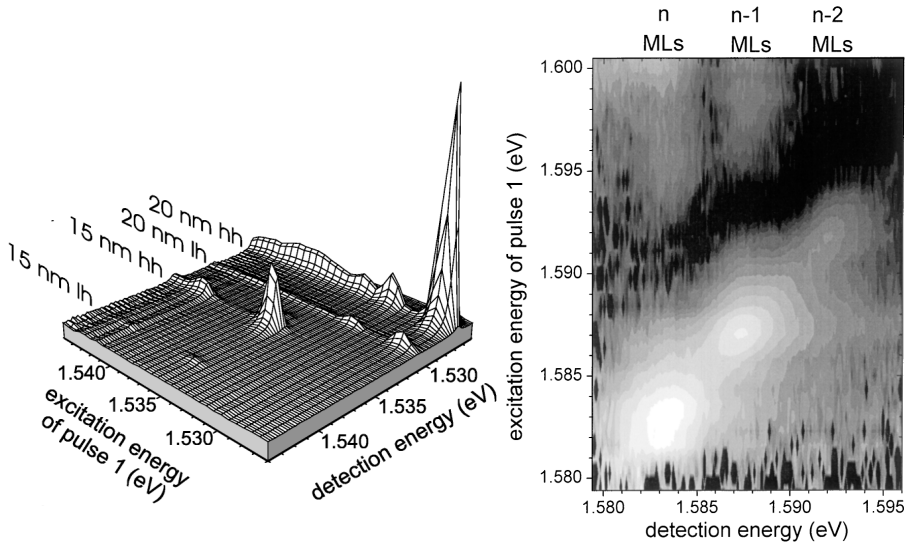

Coherent excitation spectroscopy performed on a sample designed to exhibit no coupling between spectrally resolved excitons (a) due to intentional large mismatch between and on a sample where monolayer fluctuations suggest coupling could occur (b). In the mismatched sample, off-diagonal peaks indicating light hole-heavy hole exciton coupling occurs within each of the two regions, but no diagonal is observed coupling resonances in different regions. The monolayer sample shows three heavy hole excitons, along the diagonal, with no coupling features present off the diagonal. The second plot (b) uses a logarithmic grey scale running over 3 orders of magnitude. Reproduced from Euteneuer et al., Physical Review Letters 83:2073 (1999).

Figure 5.6: Coherent excitation spectroscopy

5.2 Two-dimensional Fourier Transform Spectroscopy

5.2.1 What is 2dFT spectroscopy?

Optical 2dFT spectroscopy is a powerful, ultrafast spectroscopic technique that may be used, among other applications, to resolve the question of coupling between spectrally resolved excitons. 2dFTS is particularly suited to the study of coupling processes due to its ability to reveal correlations between the dynamics of an ensemble of oscillators occurring in two different time periods. 2dFTS can show correlations between an initial absorption and a subsequent absorption, emission, or change in refractive index; making use of these capabilities, it is employed to study electronic coupling, energy transfer, electron transfer, and relaxation processes [192].

2dFTS data are plotted in a two dimensional spectrum, typically as a function of two frequencies. Spectral features in such a plot are interpreted as a probability map connecting events that occurring during the first period at frequency $\omega_\tau/2\pi$ to events that occur in a second period at a frequency $\omega_t/2\pi$ [238]. Those features appearing along the diagonal, where $\omega_\tau = \omega_t$, contain similar information to that found in a normal, one-dimensional experiment, although the shape of these features provides additional details regarding the inhomogeneous and homogeneous widths of the resonances. Specifically, a feature will be present for every absorption or emission that occurs at any energy level present within the laser bandwidth [132]. The off-diagonal events, where $\omega_\tau \neq \omega_t$, reflect coupling processes between different energy states. Optical 2dFT experiments analogous to COSY and NOESY nuclear resonance tech-

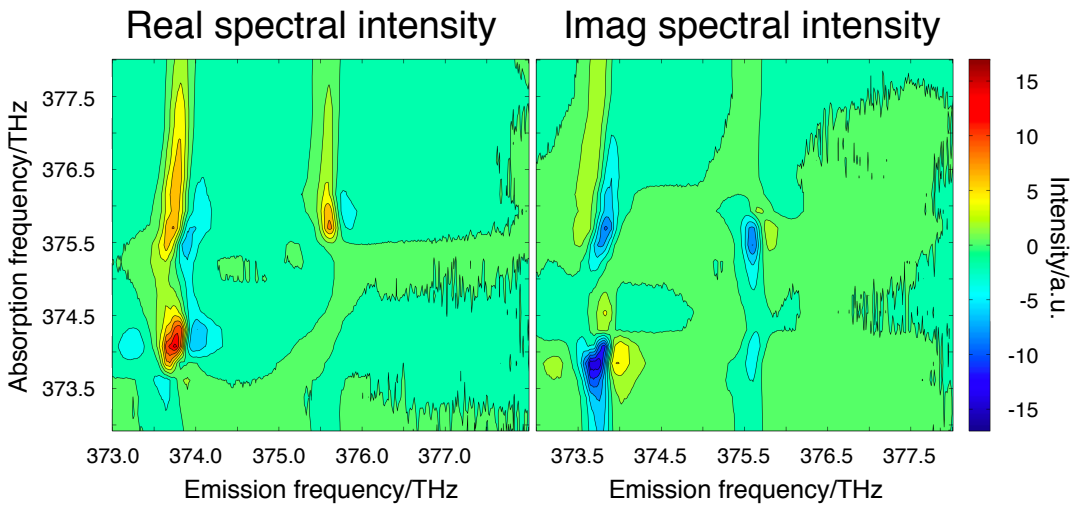

2dFTS spectrum collected in a partially collinear geometry from a GaAs multiple quantum well sample, using 1.00mW pump pulses and 0.10mW probe pulse, with a probe delay of T=-0.01ps and a τ scan slightly greater than 3ps. Features along the diagonal indicate energy levels, while off-diagonal terms indicate coupling.

Figure 5.7: Sample 2dFTS spectra

niques may readily be performed with the sample apparatus to distinguish between coupling processes that occur coherently and those that occur as a result of relaxation processes. Experimentally, the distinction between the two techniques is trivially made by choosing either a zero or finite duration population time. Since relaxation is (in a reasonable treatment) a probabilistic process, no relaxation cross-features should appear at zero waiting time, while coherent coupling processes may occur, resulting in characteristic cross-peaks. A two-dimensional plot characterizing the nonlinear polarization of the material also spreads complicated spectral features out over a larger space, permitting easier analysis of those features – especially the identification of coupling between energy states [132].

In general, 2dFTS experimental and theoretical programs tend to pursue three different approaches – analyzing the couplings between transitions in order to determine the nature of the microscopic Hamiltonian, characterizing the lineshape in a 2dFTS spectrum in order to permit comparison to some more generally sophisticated model, or performing non-equilibrium 2dFTS measurements to study the effects of some additional excitation or perturbation of the system [20] – not unlike the self-diffracted four-wave mixing measurements of exciton dynamics performed after non-coherent excitation or carrier injection noted previously.

Those more sophisticated 2dFTS experimental projects generally proceed by developing a model thought to accurately represent the microscopic physics of some system of interest. That model is used to calculate parameters

that can be compared to the macroscopic quantities studied using a 2dFTS measurement in the lab. The data obtained in experiment is used to adjust the model to obtain more accurate results. The whole process may be iterated to satisfaction. It is also possible, however, to extract some immediate results from a single 2dFTS experiment that are of significant interest to theorists – such as estimates of the spectral correlation functions for oscillators, found by measuring spectral shifts in 2dFTS plots [238].

Before considering the optical 2dFTS experiments used to study electronic states in condensed matter systems, we turn our attention to a brief discussion of multi-dimensional spectroscopy in other contexts. Later we will discuss results obtained in our group using non-collinear 2dFTS to study the coupling of spectrally resolved exciton states in semiconductor quantum wells [358], [359], [116]. This project and its preceding results demonstrating the suitability of 2dFTS as a tool to study exciton systems in semiconductors [410], [39], [248] led to the development of a new, partially collinear 2dFT experiment [198] that has been used to demonstrate polarization selection rules for exciton systems and perform reflection geometry 2dFTS for (we believe) the first time [115]. These experiments prompted us to develop new spectroscopic tools, which we describe in the next chapter.

5.2.2 2dFTS advantages compared to other ultrafast techniques

Fourier transformation of the detected four-wave mixing signal with respect to two time intervals – the coherence time τ and the detection time t

– yields a frequency-frequency spectrum that separates dense1-d spectral features into a two-dimensional space and permits easy correlation among events that occur at two different times. In particular, that permits the experimental study of systems with overlapping bands of states with fast dynamics time scales, where the interpretation of frequency selective pump-probe spectroscopic measurements is difficult.

Significant effort was applied previously to performing spectrally resolved pump-probe spectroscopic measurements. For molecular systems, a non-interacting ensemble of two-level systems(Taira/optical Bloch-type) model of femtosecond pump-probe differential transmission spectroscopy supported experimental observations of spectral hole burning that can be analyzed to determine the population decay time time; a free-induction type effect with a rise time determined by the dephasing rate and a parametric pump-probe coupling that occurs when the two pulses temporally overlap (a coherence spike) were also seen in the spectra [334]. These hole-burning measurements require pump pulses with less spectral width than the transitions under consideration, while the probe pulse can have an arbitrarily large bandwidth, and thus, be arbitrarily short. Density matrix theoretical calculations for this system use a first-order perturbation to consider the effect of the probe beam and a second-order perturbation to consider the effect of the pump beam; hence, it is conceptually similar to other differential transmission, pump-probe spectroscopic methods, and is distinguished from those methods rather by the use of different pulses and spectral resolution of the probe beam. The time dependent

linear optical susceptibilities due to the electronic coupling of two manifolds of vibrational energy states was explored with a similar technique, showing that the the coupling of a weak probe field to the population induced by a pump would result in the time-dependent, oscillatory emission rapidly decaying due to frequency-dependent phase factors in the product $\chi_0(\omega,\ t)\, E_{pr}(t)\, e^{i\omega t}$ [294], or to study the coupling of nuclear motion to the electronic states by observing changes in a probe absorption spectrum due to a strong pump field [126]. All of these techniques depend upon the spectral resolution of the probe beam in a two-pulse experiment, in order to detect the coherent emission along this particular phase-matched direction. These measurements are all fundamentally limited in the temporal resolution that they can provide, however, since they cannot resolve any frequency-dependent temporal process that evolves on a timescale faster than the probe pulsewidth [132]. The common tradeoff in ultrafast experiments certainly obtains here, as a narrower pulse allows more selective excitation of a particular set of lines or subset of inhomogeneously broadened features, which may facilitate the analysis of coupling (e.g. by exciting at one wavelength and detecting emission at another), but the reduced bandwidth pulse is necessarily longer in duration and cannot be used to study the fast dynamics of the system. These problems are further complicated if there are overlapping spectral features in the region of interest.

2dFT is not subject to these restrictions, as its resolution is not limited by the pulse duration but is instead a function of the number of data points collected. It is possible, perhaps surprisingly, to increase the signal res-

olution using zero-padding of a data set collected with relatively short time scan [296]. We discuss that subsequently in our description of 2dFT data analysis. In principal, the linewidth of the spectral features in a 2dFT plot are limited only by the homogeneous linewidth of the ensemble studied – the limiting factor in a 2d measurement is in fact the resolution of the quantum emitter itself [132]. The time and frequency resolution are limited only by the sample itself if the time scans are taken arbitrarily large – of course, the scan of τ and the spectrometer resolution for ω_t set a practical limit [202]. A more sophisticated treatment of the experimental resolution limits occurring in Fourier transform spectral interferometry suggests significant attention be paid to spectrometer calibration and characterization. A significant improvement in data quality may be obtained by performing an FFT transformation from the spectrometer's wavelength space into a conjugate time domain, correction for the spectrometer response function and filtering for artifacts, then transforming back into the wavelength space to extract the spectral phase of the signal field, although this is likely not an issue for the electric field reconstruction utilized in 2dFTS [100].

While other nonlinear optical spectroscopic methods are well developed tools for studying inhomogeneously broadened systems or evaluating coupling in the spectra of a complicated interacting system, 2dFTS also can perform experiments that are problematic for other, simpler techniques. Photon echo measurements, as described elsewhere in this thesis, are a frequently used tool for studying dephasing processes, but are limited in their ability to resolve

ultrafast processes. The temporal resolution of a photon echo experiment is not simply limited to the pulse temporal width, but is instead complicated by a free induction decay signal that occurs at early times. Due to inhomogeneity in the system (or, in the case of semiconductor materials, even in homogeneously broadened systems [250]), the optical free-induction decay falls off very rapidly due to the dephasing of oscillators with different resonant frequencies. In most photon echo experiments, this early time behaviour is typically ignored, while the coherence revival peak that occurs at later times is analyzed to understand the dynamics of the system. If, however, a rapid dephasing process is to be studied, the delay between the pump pulses must be made correspondingly short, and temporal overlap between the photon echo peak and the otherwise neglected free induction decay complicates the interpretation of small time photon echo signals [284], [83].

5.2.3 Multidimensional techniques from NMR and other spectroscopic fields

Prior to the demonstration of optical, electronic 2dFT [192] previous multi-dimensional experiments had been performed on a number of material systems. Ernst and coworkers demonstrated a nuclear magnetic resonance experimental method that could be used to extract a more complete characterization of a system under study [18]; the relative simplicity of controlling and detecting RF signals with a high degree of phase stability permitted the rapid expansion of this field. Although the application of these methods to the study of visible and IR electronic and vibrational transitions was suggested im-

mediately, the experimental implementation of multi-dimensional methods in optical physics took some time. While a multi-dimensional Fourier transform spectrometer is something of a general purpose spectroscopic tool, somewhat more restricted optical techniques had been demonstrated previously.

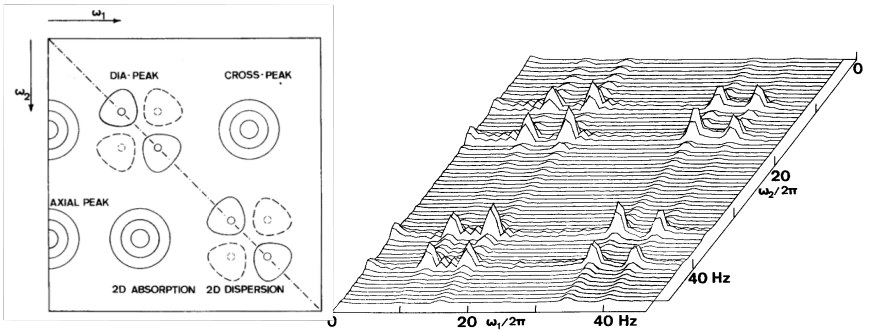

Cartoon of 2dFTS features found in NMR experiments (a) and experimental data from a nuclear measurement on an organic molecule (b). N.b. the extremely low frequencies of the transitions involved. Reproduced from Aue et al., J. Chem. Phys. 64:2229 (1976).

Figure 5.8: NMR 2dFTS spectra

Phase cycling techniques were used to isolate signals in a three pulse measurement analogous to NOESY techniques from NMR using RF signals to probe the coupling between levels in the hyperfine manifold of chlorine atoms in a relatively simple halogenated alkene [375] (specifically, ethylene with two hydrogens substituted for a a chlorine and fluorine on one of the two carbon atoms); the use of phase cycling to isolate a particular coherent signal from the background of the excitation pulses and scattered radiation is a direct extension of nuclear resonance detection schemes (q.v. *sub*). Two pulse

COSY analogue experiments were also performed, which can be used to reveal coherent coupling that occurs with no relaxation time. Two-dimensional microwave Fourier transform spectroscopy [376] can provide more information than simpler double resonance experiments where the introduction of a tuned RF pulse decouples some sub-ensemble of nuclei from the rest of the molecule, simplifying the normally split lines of other nuclei coupled to that subset. While double resonance can provide structural information from the indirectly determined coupling, microwave 2dFT measurements [12] provide a direct spectral measurement of these effects with narrower spectral resolution. There are the additional, often repeated benefits of spreading one-dimensional spectral information into a two-dimensional space to facilitate interpretation of complicated spectral features, as well as the ability to observe dynamics such as relaxation in the system that double resonance cannot probe. These techniques were direct extensions of NMR methods, and the relevant energy scale for the transitions involved did not pose experimental difficulties for the generation of pulse sequences with well-defined phase and timing control.

Optical two dimensional spectroscopy had been used to study the transfer of coherence among Zeeman sub-levels in sodium vapor [360] he energy structure of the ground state of an alkali gas was studied using two pulses derived from a single laser source. The first pulse prepares a coherence between two hyperfine sub-levels of the ground state, which then evolves during a subsequent waiting period. A second laser pulse initiates a mixing period, wherein the coherence created between two sub-levels to a different pair of

sub-levels. During the subsequent detection period the emission is observed on that second transition. While this experiment does use visible radiation (the D1 resonance occurs at 590 nm, coupling the $3^2S_{1/2}$ ground state manifold and the $3^2P_{1/2}$ manifold), the actual coherences between the hyperfine levels of the ground state are on the order of a GHz. As a result, experimental control of the the pulse sequence is substantially simpler than the later experiments that perform 2dFT on an optical transition; moreover, no phase data was derived from the correlation plots obtained with this technique. Similar experiments were performed using a periodic optical perturbation with repetition rate chosen to match the Larmor frequency of a specific Zeeman sub-level of an alkali atom in a tunable magnetic field; 2d spectra taken in this manner were recorded as a function of the optical field detuning and the magnetic field strength. The lineshape along the optical axis reveals the dispersive lineshape of the Zeeman resonances [378]. Two dimensional correlation plots were also obtained for molecular compounds in the near-IR, using a fifth-order phase-matched experiment that detected a signal dominated by a cascaded third-order nonlinear process [32]. This technique apparently does not depend upon any active phase stabilization. The Fourier transform spectral interferometry techniques subsequently used for the detection of four-wave mixing signals in 2dFTS were previously applied to measure the transient,t second-order, nonlinear, non-resonant response of a KDP crystal, essentially providing a measurement of the frequency map where phase-matched emission occurred in a two-pulse experiment [246].

5.2.4 Optical 2dFTS contrasted with 2dNMR

Multidimensional spectroscopy as described by Ernst and coworkers in the late 1970's comprised a set of nuclear magnetic resonance experimental methods that could be used to extract a more complete characterization of a system under study, but even in the first two-dimensional NMR papers the possibility of extending these techniques to the optical regime was considered [18]. This early work on outlines a number of possible different two-dimensional techniques, considering frequency-frequency measurements, a mixed frequency-time space measurement, a time-time measurement, and a stochastic noise technique that correlates a spectrally broad noise input to a noise output. In each of these techniques, the signal of interest is mapped onto a pair of independent variables. Frequency-frequency measurements performed using double resonance were already commonly practiced, using a strong, perturbing field to modify the system of interest in a nonlinear fashion, and a second, weakly interacting field to study that system – in some senses, one may argue that this is still a simple, single dimensional spectroscopic technique that measures only the changes in the probing field, but if that change is correlated with the parameters of the strong exciting field, a multidimensional spectroscopic domain is obtained. The primary interest of these research programs was the development of time-time methods, where a pair (or more complicated train) of RF pulses was used to excite a system, with the relative delays between pulses and between the last pulse and the detected emission forming the pair of independent variables in a two-dimensional experiment.

The adaptation of spectroscopy tools developed in the radio frequency region of the electromagnetic spectrum to the higher frequency regime of optical spectroscopy is complicated by a number of substantial experimental hurdles – although conceptually similar and relying upon the same fundamental quantum mechanical physics as NMR methods, the substantially greater optical frequencies and correspondingly shorter wavelengths make it difficult to perform experiments that rely upon well-defined phase and time relationships among the optical pulses.

Multi-dimensional spectroscopic techniques may be regarded as conceptually similar, whether the experiments are performed with radio frequency, in the microwave region, or even with visible or UV light. The similarity between these nonlinear spectroscopic methods is due to the invariance of the quantum mechanical equations of motion that govern the electric dipole coupling and stochastic relaxation of multiple level systems across this broad range of frequencies. Nonetheless, while optical 2dFTS does resemble nuclear resonance multi-dimensional spectroscopy, there are some significant differences between these experiments.

In particular, the optical pulses used have a far smaller number of cycles per pulse compared to the corresponding RF excitation pulses used in NMR experiments, which may have millions of pulses. In our experiments, performed in the vicinity of 800 nm, typically we expect something on the order of a few tens of optical cycles per pulse.

In NMR experiments, a spin flip does not result in considerable change

of the local environment. Essentially, the weak nuclear magnetic dipole results in only a small perturbation of the potential experienced by other spins in the sample. Due to the presence of a strong bias field, spin flip transitions can be viewed as perturbations localized along the quantization axis. In contrast, the electronic and vibrational excitations created in optical 2dFTS have a strong perturbative effect on the local environment. Without the presence of an externally applied quantization axis, a spatially three-dimensional set of excitations is possible in optical experiments. As a result, control of the polarizations of the excitation fields may now significantly affect the observed system response. Perhaps counterintuitively given that the effect of the nonlinear polarization induced in a multi-dimensional experiment may be more pronounced at optical wavelengths than for nuclear resonance measurements, optical 2dFTS experiments must be performed in the so-called weak pulse limit, since there is not an easily defined pulse area theorem (e.g. there is not a straightforward way to generate an optical analog of a π or $\pi/2$ pulse) in a system with multiple optical transitions [202].

5.2.5 Optical 2dFTS measurements

The 2dFTS experiment itself can be understood as a three pulse transient grating method, as described in a previous section. It is only in the particular details of the detection scheme, the dense set of spectrally resolved emission data collected, and the relatively simple post-experiment analysis that 2dFTS is distinguished from other three pulse experiments. Indeed,

because 2dFTS is something of a universal femtosecond spectrometer [132], Fourier projection may be used to reduce the 2dFTS results to simpler representations mimicking these other three or two pulse measurements [202]. In practice, obtaining the necessary phase stability between the two coherent pulses and between the four-wave mixing signal of interest and the reference field [235] used for optical heterodyne detection [131] in 2dFTS are the most significant technical difficulties that complicate the experimental implementations of an otherwise conceptually straightforward measurement. In the mid to near-IR, such problems are generally not insurmountable, but as experiments move into the visible spectrum it becomes necessary to go to substantial length to perform phase-stable optical multidimensional measurements.

In both 2dFTS and the other three-pulse experiments, however, the light-matter interaction may be intuitively understood by considering a stepwise process where a two-level system is dipole coupled via a resonant optical field at three different moments in time. We explicitly consider a simple density operator theoretical treatment of the relevant exciton dynamics for our partially collinear experiment elsewhere in an appendix to this thesis; now, we only briefly describe the basic concepts of the optical interaction and relaxation processes. We neglect the interaction among members of the ensemble to simplify the discussion of the optical physics.

To first order in a perturbation calculation, the first pulse excites a dipole oscillation, creating a coherence that can be described by an off-diagonal term ρ_{ab} in a density matrix. The second pulse that arrives will either enhance

or suppress that oscillation, depending on timing and relative phases of the second pulse and the oscillation induced by the first pulse. If the second pulse arrives prior to the occurrence of significant dephasing, the dipole oscillation still possesses a well-defined phase relationship with the first pulse. Although the phase of the oscillation and the second pulse cannot be directly observed or controlled at this point, interferometrically precise control of the arrival time of the second pulse relative to the first will thus provide an indirect control of the second light-matter interaction. To the second order in a perturbation calculation, this interaction creates a population ρ_{bb} in the excited states. The phase of the second pulse relative to the coherence created by the first determines the extent to which the excited state is populated. As long as the delay τ between the two initial pulses is comparable to the dephasing time, the interference of these optical fields results in a transient grating of the electronic state population in the sample, which exhibits both dispersive and absorptive properties [273]. After an additional waiting time T during which population relaxation processes may occur, a third pulse interacts with the population grating. In the third-order perturbation calculation, this field again induces a coherence ρ_{ab} between the optically coupled states; the dipole moment of a given oscillator is given by the product $\mu_{ab}\rho_{ba} + \mu_{ba}\rho_{ab}$, and a macroscopic dipole due to the ensemble of phased oscillators emits light along certain phase-matched directions. Alternatively, the coherent emission can be interpreted as light from the last pulse scattered by the grating created by the coherent interaction of the first two pulses. The diffracted four-wave

mixing signal is then detected as a function of its emission time t after the final pulse. In yet another interpretation, the emission after the third pulse may be viewed as a free induction decay that occurs from a coherent superposition of wavefunctions created by the three preceding pulses [202]. Fourier transform of the measured four-wave mixing electric field over the two time periods τ and t provides a 2dFT spectrum.

As the coherence time τ is increased the finesse of the grating increases while perturbations from the environment have more time to destroy phase coherence or induce spontaneous emission [238]. This effect of increasing the grating finesse may be understood by considering the interference between two co-propagating pulses with some variable delay – when the two pulses are temporally overlapped, the spectrum is a smooth function (e.g. a Gaussian or the square of a hyperbolic secant or similar, depending on the light source), but as the delay between two pulses is increased the spectrum develops fringes, with the number and finesse of the fringes increasing as the delay is increased. Intuitively, then, higher frequency components are introduced into the electrical field spectrum by scanning larger values of τ, and as a result the spectral resolution along the Fourier transformed axis ω_τ is increased. The maximum frequency signal that can be resolved in the experiment is still limited by the step size used to scan τ, as we discuss elsewhere (q.v. our extended discussion of undersampling). The modulation of the spectral fringes may be alternatively understood as the switching-on and -off of various frequency components by control of the pulse delay, with the system response analyzed as a result

of some particular combination of those frequency components. Traditional one-dimensional Fourier transform interferometry experiments are sometimes described in this manner, as some material containing an ensemble of oscillators, each subset of which possesses a slightly different resonant frequency, is excited by the various combinations of frequency components and its response measured interferometrically [202]. Interferometric control of a delayed pump pulse pair has been previously demonstrated as a tool for coherent control of exciton populations in quantum wells [256], [169]. In the 2dFTS experiment, the phase modulation is stored by the population grating resulting from the second pulse. After that pulse, dephasing no longer plays a role in the dynamics, and the slow population decay time allows a long-time storage of that phase modulation information in the excited state population grating.

Subsequently, during the mixing period T, perturbation from the environment will again affect the grating structure. Subsequently, a third pulse is scattered from this grating and the diffracted four-wave mixing field is characterized. In 2dIR experiments where the light-matter interaction is not a strong perturbation, it is possible to transmit both the third pulse and an additional, phase-stabilized pulse that acts as a local oscillator; in that case, the scattering of these two pulses may be interpreted as a measurement of the correlation of the gratings induced by the two pulse pairs. In semiconductor systems such as those we study, it is not possible ot transmit the local oscillator/heterodyne pulse through the material, since the many-body dynamics of interest are highly sensitive to the excitation density. The additional interac-

tion of the fourth pulse would significantly affect the response of the system; as such, a substantial effort is placed on re-routing the heterodyne field along a separate optical path while maintaining the interferometric stability with the third pulse [410].

Phase sensitive measurements of the electric field of the four-wave mixing signal emitted the final excitation pulse completely characterizes the system response, as both the amplitude and overall (rather than relative [70]) phase of the signal field are measured. In practice, the second time period t is not scanned, and the electric field is not recorded in the time domain. Rather, the four-wave mixing is spectrally resolved and the amplitude and phase of the signal are characterized [131]; the first demonstration of optical 2dFT and most other optical implementations still use spectral interferometry to extract the signal field from the detected heterodyne measurement [245].

5.2.6 Optical analogues to COSY and NOESY distinguish coherent and incoherent coupling

For a given optical 2dFTS experiment, the mixing period T is kept fixed, while the evolution time τ is scanned. Changing this time period allows the observation of different coupling processes in the system, as coherent processes can be observed at $T = 0$, in an optical analogue of the NMR COSY experiment. COSY, or Correlation Spectroscopy, first proposed by Jeener [199], [260] in an unpublished lecture, relies on a two-pulse RF sequence that prepares a coherent superposition, allows it to evolve during the period between

the pulses, then detects a time-resolved free-induction decay signal emitted after the arrival of the second pulse. Transfer of magnetization among nuclei via indirect dipole coupling had been observed previously in spin echo experiments [157], [305]; in COSY experiments this coupling was observed as off-diagonal peaks in a 2d spectrum obtained by varying the pulse delay time and recording the induction signal as a function of the time after the final pulse [18].

If the population time T is non-zero, the 2dFT experiment can probe non-coherent relaxation processes, which require finite time to occur due to their probabilistic nature. This is analogous to the NOESY (Nuclear Overhauser Effect Spectroscopy) experiment in NMR. In practice, the NMR NOESY experiment is distinguished from the COSY experiment by the addition of a third pulse; the experiment is not conceptually too dissimilar from a three pulse photon or spin echo measurement but with the second pulse now chosen to have a $\pi/2$ pulse area instead of π. In the NMR experiment, a first $\pi/2$ pulse rotates the spins' magnetic moments into the transverse plane, where they precess at different rates around the quantization axis. A subsequent, equal area pulse moves all the spin vectors back parallel to the bias field. During the subsequent mixing time, the nuclear Overhauser effect incoherently transfers the magnetization from some set of nuclear spins to another set, after which a third pulse rotates the spins back into the x-y plane. Detection of the free-induction decay occurs during this last period; if the Overhauser effect resulted in the transfer of spin polarization from one set of spins to another with a different chemical shift, cross-peaks will appear in the resulting

2dFT spectrum [76]. This relaxation process takes time, and in spin systems, only couples adjacent nuclei – unlike the coherent coupling observed in COSY measurements that detect interaction mediated by the electronic bonds in a molecule.

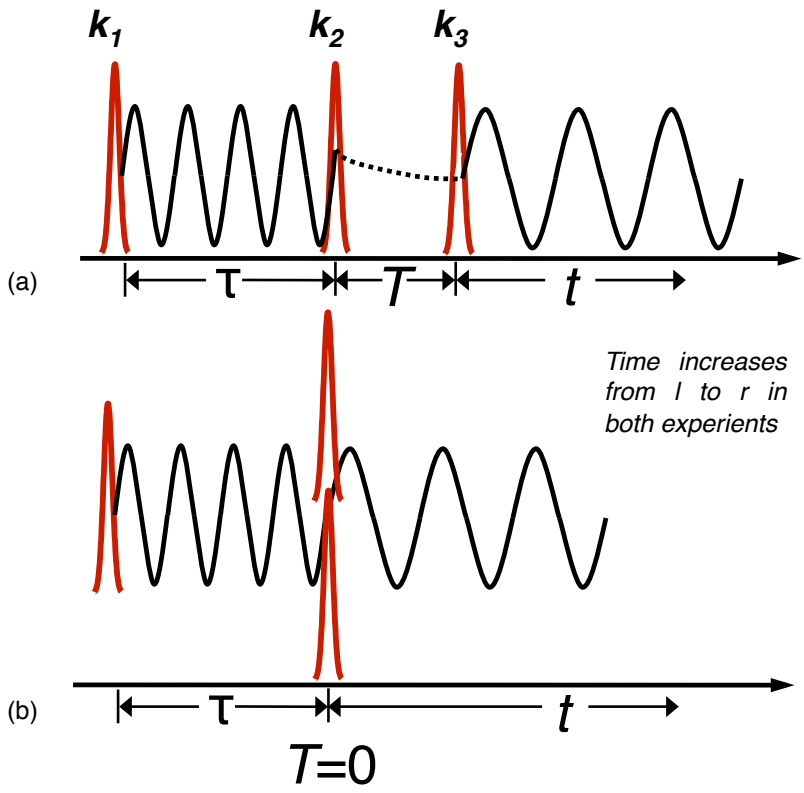

Excitation pulse sequences for the optical 2dFTS analogues of NOESY (a) and COSY (b) experiments.

Figure 5.9: Optical analogues of COSY and NOESY

The popular electronic 2dFTS technique pioneered by Jonas and co-workers [192] and replicated by a number of other groups permits easy optical

analogues of both COSY and NOESY experiments. The original demonstration and the majority of subsequent experiments were performed in a BOXCARS geometry (described elsewhere in this thesis) which allows 2dFTS measurements with zero or non-zero T, since the arrival time of the final pulse in the experiment is controlled using a delay stage or other mechanism.

5.3 Experimental and technical considerations for 2dFTS

5.3.1 Phase matched coherent emission of temporally ordered four-wave mixing

Some techniques for calculating the nonlinear optical response of the system require subsequent multiplication by a spatial filtering function to permit straightforward comparison to the experimentally measured four-wave mixing signal, as only certain terms in the optical response will result in coherent, beamed radiation. Since we use density operator-perturbation theory methods to compute simple models for the nonlinear optical polarization, allowing us to develop an intuitive understanding of the optical physics involved, we do not need to consider this additional complication. The coherence terms calculated in such an approach (and the related macroscopic polarizations) have a well-defined wave vector, which permits us to keep track of those terms that contribute to the macroscopic phase-matched polarization that emits along the detection direction. Other terms in the perturbation calculation, which do not correspond to propagating modes with the appropriate wavevector, can be discarded. This simplifies the interpretation and analysis

of experimental results, connecting the changes in a measured signal directly to quantities of interest that appear in simple model calculations [132].

Temporal ordering of the pulses also simplifies the analysis of the observed four-wave mixing field, as only certain quantum mechanical pathways (a precise definition of this term, pathway, is not obvious, but inspection of our simple calculation elsewhere in this thesis for the partially collinear geometry experiment makes clear what we mean by pathway) have the right time ordering of the electric fields. Therefore, only those terms contribute to the radiated signa, although 'wrong time' sequence pathways will contribute during those times when there is pulse temporal overlap.

In a density operator theoretical treatment, the coherence, off-diagonal elements of the density matrix will depend upon a sum of different combinations of the normal,

$$\widetilde{E}_i = E_i(t)\, e^{i(\mathbf{k}_i \cdot \mathbf{r} - \Omega_i t)}$$

and conjugate

$$\widetilde{E}_i^* = E_i^*(t)\, e^{-i(\mathbf{k}_i \cdot \mathbf{r} - \Omega_i t)}$$

complex fields, which are summed to give the real electrical field $E(t) = \widetilde{E}_i(t) + \widetilde{E}_i^*(t)$. Choosing the direction of observation and the temporal ordering of the pulses determines the signs of the exponents in the product of complex fields that interact with the sample during the time periods τ and t. This, in essence, is what is meant by phase-matching in this context: only certain

quantum mechanical pathways in the density matrix calculation, depending on the appropriate combination of electric fields, results in a coherent, beamed emission along a specific direction. This is readily understood as the optical expression of conservation of momentum for these parametric processes.

Of particular interest are the relative signs of the exponents of the complex fields of the first two pulses to interact with the material sample. If those signs are opposite in a given quantum mechanical pathway, that pathway is known as a rephasing pathway, and is understood by analogy to the rephasing of an inhomogeneous ensemble of oscillators that occurs during photon echo experiments, as described previously in this thesis. If the signs of those exponents are identical, it is termed a non-rephasing pathway, and no macroscopic revival and photon echo is expected; the third complex field to interact with the sample will then have an opposite signed exponent in order to result in a frequency degenerate four-wave mixing emission. Obviously, in the case of rephasing quantum mechanical pathways, no significant statements can be made on the sign of the exponent of the third complex field. The emission for the non-rephasing pathways, where the signs of the exponents are the same for the first two pulses, may be called a virtual photon echo or anti-echo [102].

The optical 2dFTS technique developed by Jonas et al. [192] used the non-collinear (BOXCARS) geometry described previously to produce phase-matched four-wave mixing emission, which was widely emulated for other optical multi-dimensional experiments, but their early analysis of this technique also outlined an alternative method using a partially collinear beam geometry

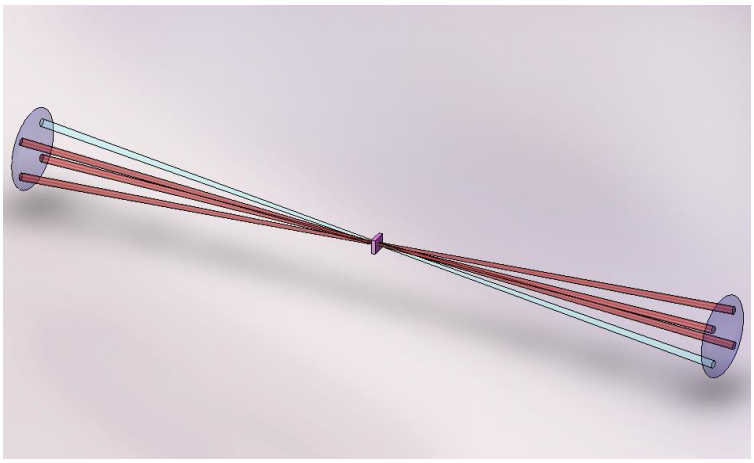

BOXCARS geometry for 2dFTS experiments. One beampath, marked in blue, indicates the beam that is missing from the square box on one side of the sample and the signal emission direction on the other.

Figure 5.10: BOXCARS geometry phase-match for 2dFTS

[132], which was subsequently demonstrated experimentally [87], [152]. We discuss 2dFTS in this geometry at some length subsequently.

5.3.2 Detection

While measurements of a small number of photons are technologically feasible, 2dFTS, like most other nonlinear experiments, relies upon the detection of a macroscopic observable, viz. the detection of an optical field whose classical properties (e.g. intensity, electric field strength, polarization, etc., where all these quantities are measured in the limit of large photon number where quantum optics effects may be discounted – the study of these effects via detected photons is sometimes described as quadrature-in-field, to distinguish the observation from a direct measurement of the oscillating field itself [371])

can be correlated with microscopic, quantum mechanical processes occurring within the system of interest. As described elsewhere in this thesis, in wave-mixing experiments of this ilk the selection of a particular set of wavevectors for the excitation pulses results, via the conservation of momentum, in a specific phase-matched direction along which a macroscopic array of dipoles will emit coherent radiation. The timing sequence of the pulses used will, in some geometries, allow the selection of a particular subset of quantum mechanical pathways that will radiate along this path. There is a specific density operator coherence pathway that connects the various energy levels and exhibits the appropriate phase-matching for signal radiation in this direction. While emission will occur in all directions, except along those where a phase-matching condition obtains there will be no coherent, intense, directed radiation.

This is an experimental distinction from the phase cycling methods used to detect the signals of interest in a multi-dimensional NMR technique. In those experiment, the pulsed RF fields used to excite the material are described by a cw carrier multiplied by an envelope function, whereas in nonlinear optical experiments using pulses created by changes in path length the electric field is better described by an envelope function and a carrier wave that both change their time argument. In other words, the optical phase is also affected by the pulse delay in optical 2dFTS, and needs to be accounted for to properly explain the optical response. The absolute phase of the polarization (and hence, the four-wave mixing signal field) in the optical case depends on the absolute phase of the three excitation pulses, $\varphi_{signal} = f(\varphi_1, \varphi_2, \varphi_3)$, where the function f

will be a simple linear combination of the absolute phases of the excitation pulses. In the case of the popular non-collinear 2dFTS experiments, it will look something like $\varphi_{signal} = \varphi_3 + \varphi_2 - \varphi_1$ for a rephasing pathway. A constant shift of ϕ added to each of the excitation pulses will result in a phase shift of $\sum_{i=1} s_i\phi$ where $s_i = \pm 1$ is the sign of the i^{th} excitation pulse's wavevector in the direction of the phase-matched emission – in this case, again, for the non-collinear technique, that will result in a shift of $-\phi + \phi + \phi = 2\phi$. Scattered, incoherent signals detected along the same direction will not exhibit the same dependence on the phase of these pulses. In an NMR experiment, the signal of interest is detected by adjusting the phase of the excitation pulses and keeping those contributions that exhibit the correct dependence on that phase. This technique allows the isolation of a signal of interest from other that do not depend upon the quantum mechanical pathway of interest and do not exhibit the correct dependence on phase of the excitation pulses – and which therefore may be averaged out to zero or subtracted [202].

This is the general principle of phase-cycling, which in optical experiments may be replaced with the detection of the macroscopic optical field propagating along the phase-matched direction, although there are many extensions of this technique that can be applied to optical experiments to reduce the contribution of incoherent scattered light to the detected signal. We do not implement phase-cycling in the experiments in this thesis, but our use of AOM's to frequency shift the excitation beams in our 2dFTS experiment and to control the relative phases and modulate the intensities of the beams in

our new experiments certainly make such methods possible. For the partially collinear geometry we are particularly interested in, phase-cycling schemes have been described [403] and demonstrated using pulse shapers [342], [266].

The chemistry 2dFTS community tends to describe all of the phase-matched signals collected and analyzed in coherent spectroscopy experiments as free-induction decays occurring subsequent to some complicated wave-packet preparation [202]; on the other hand, in the semiconductor physics community the trend is to view the four-wave mixing signal of interest detected in a 2dFTS experiment as taxonomically distinct from the pump-probe artifact signals and incoherent emissions that may accompany it. It is true that in all of these cases, an oscillating electric dipole emits radiation observable in a far field, but the beam-like properties and dependence on material relaxation processes of coherent four-wave mixing emissions make them far more suitable as a macroscopic probe of microscopic physics of interest. It is in studying the relationship of the emission to the independent variables, rather than in any particular property of the radiated field itself, that the physics of interest may be revealed.

2dFTS depends upon correlating optical events occurring in the first coherence period τ with those that occur in a second, phase-sensitive detection period t. In practice, the second time period t is not scanned, and the electric field is not recorded in the time domain. Rather, the four-wave mixing is spectrally resolved and the amplitude and phase of the signal are characterized [131]. The first demonstration of optical 2dFT and most subsequent optical

implementations still use spectral interferometry to extract the signal field from the detected heterodyne measurement [245].

2dFTS depends upon a phase-sensitive optical detection technique. In the nuclear resonance experiments upon which optical 2dFTS is largely based, direct resolution of the electromagnetic field radiated from an ensemble of dipoles is possible, but for the corresponding optical frequencies immediate, direct measurement of the rapidly oscillating electric field is not available. As noted in our previous discussion of time resolved four-wave mixing measurements, it is possible to determine the temporal lineshape of emission via simple nonlinear optical processes, such as frequency upconversion in a nonlinear crystal. This cross-correlation method will only provide a measurement of the intensity profile, however, and not the amplitude and phase of the emission that we are interested in. More sophisticated heterodyne measurements may be performed in the time domain, but typically require scanning a delay for one reference pulse mixed with an unknown signal pulse. Performing phase sensitive heterodyne measurements in the time domain may extend the laboratory time needed to perform a 2dFTS experiment too far for such methods to be practical. Fortunately, heterodyne interferometry in the frequency domain provides a more rapid method to retrieve the amplitude and phase of transient nonlinear optical fields [112]. Frequency domain interferometry measurements are single shot techniques if the spatially dispersed spectral components of the interfering fields can be simultaneously measured. This kind of multiplex technique is common to spectrally resolved measurements using array detectors,

such as the CCD's commonly used for 2dFTS experiments. In the context of signal-to-noise analysis, where multiplexed measurements benefit from simultaneously recording all the channels of interest for the entire period the measurement is performed, this is known as Felgett's advantage [316].

Since the electric field $E(t)$ emitted in a four-wave mixing process is, of course, a real-valued quantity, its frequency power spectrum is also real. This is directly measurable, and completely independent of spectral phase. Once this spectrum is known, measurement of the corresponding spectral phase $\phi(\omega)$ uniquely determines the electrical field $E(\omega)$ and its Fourier conjugate $E(t)$.

The fringe pattern produced by the interference of two pulses that are identical other than a delay of one relative to the other is well understood. Nonetheless, quantitative measurements based on this interference effect were not used to characterize the amplitude and phase of an unknown field combined with a reference pulse prior to the development of spectral interferometry and the corresponding algorithms for reconstruction of the unknown pulse [245]. These methods provide the envelope of the signal field and its spectral phase relative to the reference field. Careful characterization of the reference pulse is not even strictly necessary if the delay between the signal field and the local oscillator is made sufficiently long [4], [202].

The only problematic aspect of these spectral heterodyne methods is that they are insensitive to an overall relative spectral phase for the retrieved signal field. As such, the phase between the signal field and the reference field must be fixed by some other method. In the case of homotime detected

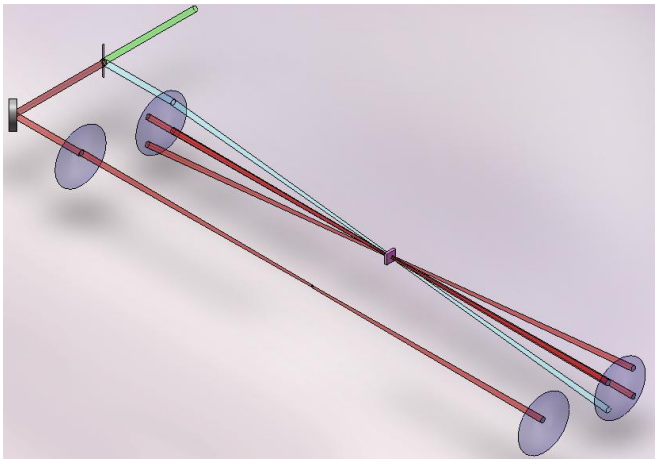

2dFTS in the BOXCARS geometry, where a phase-stabilized reference pulse (lower left) is mixed with the four-wave mixing emission (following the beam path marked in blue) to perform spectral interferometry on the heterodyned signal (in green).

Figure 5.11: Spectral interferometry detection schematic

partially collinear 2dFTS, the two fields co-propagate, and that phase relationship is trivially zero. Fixing the global phase ambiguity for non-collinear, BOXCARS geometry experiments is more difficult, and requires an additional, independent measurement – commonly, a two pulse, pump-probe, spectrally resolved transient absorption measurement is compared to the $\tau = 0$ portion of the raw 2dFTS data to correctly fix this ambiguity, although there are known drawbacks to this technique. Correctly determining the absolute phase of the nonlinear response is essential for the correct separation of the real and imaginary portions of any 2dFTS spectrum.

5.3.3 Spectral issues, spectral resolution, effects of laser spectrum

A familiar result from more conventional one-dimensional Fourier transform spectroscopy – a frequently employed tool for material characterization – is that the frequency resolution of such an experiment is limited only by the maximum delay τ set between the pulses, and not by the pulse spectral bandwidth. This result is particularly approachable in light of our description of a pulse pair's spectral fringes being switched on or off as the delay is scanned. A similar result obtains in 2dFTS, where the frequency variable ω_τ conjugate to the time domain variable τ is limited in resolution only by the maximum scan length. Since raw 2dFTS data are collected as dense spectra samples indexed by the variable τ, increasing this resolution requires longer duration experiments, but in principle 2dFTS data could be captured as long as the apparatus could be kept interferometrically stable. A similar result would also obtain for the other frequency variable, ω_t, if the raw data in a 2dFTS experiment were collected in an analogous time domain scan. The shortcut of single-shot direct spectral resolution by spectral interferometry precludes this, however, but in principle a time-time domain experiment can be performed, with the experimental resolution on either axis limited only by the homogeneous linewidth of the transition studied. [132]

We consider the effects of finite duration pulses elsewhere in this thesis, where we discuss the connection between phase twisting and temporal pulse overlap.

Other than those effects, the simulated spectra calculated with finite

duration pulses show no substantial differences from those computed using Dirac delta function pulse envelopes; limiting the bandwidth of the excitation pulses effectively acts as a spectral filter [203]. If the pulse used in an experiment has sufficient bandwidth to cover all the spectral features of interest, its duration does not affect the experimental results [132]. We note that infrared 2dIR has also been demonstrated using a pulse spectrum that does *not* span all the features of interest, where data are collected by tuning the laser across a set of vibrational modes in an aromatic compound. The off-diagonal peaks, representing coupling between different modes, were used to fit a Hamiltonian model to determine the three-dimensional structure of the molecule [158]. There should be no further complications due to reduced optical bandwidth, since the nonlinear optical response of the material is, in the frequency domain, given by a product of the nonlinear optical susceptibility $\chi^{(3)}(\omega)$ and the various excitation fields. Since that expression for the polarization is linear in the frequency domain system response function and all of the fields, reduced bandwidth excitation will have no effect on the nonlinear polarization for frequency components where the system impulse response function has already gone to zero [202].

Eliminating the tradeoff between spectral and temporal resolution common to other nonlinear spectroscopic tools permits multi-dimensional spectroscopic methods to be treated as nearly universal spectrometers [132].

Some consideration of the interplay between causality and a Kramers-Kronig relationship for nonlinear spectroscopy is also warranted. The nonlin-

ear susceptibility $\chi^{(3)}$ may be defined to span all frequency components running from negative to positive infinity. The use of excitation pulses with finite spectral bandwidth in these experiments applies a frequency domain window to the possible effects that can be observed. To ensure detection of as broad as possible of a frequency range of phase-matched nonlinear products, using the broadest pulse available is desirable – though again, not necessary to capture rapid dynamics, since the bandwidth and resolution of the experiment are now determined by the conditions of the phase-controlled time domain scans. In many cases, such as the study of semiconductor optics, it may be desirable to use slower pulses to avoid excitation of strongly resonant modes – such as the common practice of frequency domain pulse-shaping to avoid the excitation of free carriers in semiconductors.

If delta function pulses *were* available, the real and imaginary portions of a 2dFTS spectrum would exhibit a Kramers-Kronig relationship due to causality – but the requirement of infinite bandwidth, extending from negative to positive infinity along the frequency axis clearly cannot be met. If it could be, the ability of 2dFTS to simultaneously record absorptive and dispersive spectra would not be so scientifically significant, since either could be obtained once the other was measured. This is, incidentally, in contrast to the situation that obtains in NMR measurements, where the available pulse bandwidth can be made so large as compared to the relevant transition frequencies, including extending to DC (certain phenomena related to the behaviour of the imaginary part of the dielectric constant must be considered to ensure that the Kramers-

Kronig relationship is properly obtained without considering the divergence of n' – these effects are not problematic if the material is not conductive [277]), that the difference between infinite and nearly infinite isn't significant, and a Kramers-Kronig relationship is available [296].

5.4 Data processing and analysis for 2dFTS

There are optimum conditions for the collection of 2dFTS spectra to study some particular system of interest, but in practice it may be difficult to perform an experiment that satisfies these requirements. Nonetheless, certain steps may be taken to improve the usefulness of collected 2dFTS data by performing linear filtering processes. Linear filtering will neither create nor destroy frequency components, or result in the nonlinear mixing of frequency components. As such, linear filtering techniques described here permit more effective study of 2dFTS data.

The principles of linear filter analysis for multi-dimensional spectroscopy are well known from nuclear resonance experiments [296]. For our purposes, we are interested in resolution enhancement by zero-padding and apodization to reduce ripple in the 2d spectra. A linear transformation to perform either of these steps can be represented by the convolution integral of the measured signal and the impulse response of the filter process. For a spectrum $S(\omega)$ and frequency-domain filter $H(\omega)$ we have

$$S_f(\omega) = H(\omega) \star S(\omega)$$

where one may evaluate convolution in frequency space, or alternatively take the product of a time domain signal $s(t)$ with the corresponding time domain filter function

$$s_f(\omega) = h(t) \cdot s(t).$$

Thus, in a Fourier transform spectroscopy analysis, linear filtering is performed by multiplication of the signal of interest (what chemists would call a free induction signal) by some appropriately chosen weighting function $h(t)$ prior to the transformation. Fourier transform spectroscopy thus has a simple method of filtering, though it requires computation of a transformation (relatively computationally slow) in order to see the effects of a choice of a new filter.

5.4.1 Undersampling raw 2dFTS data

An astute reader may note issues related to the precision movement of the delay stages used in the 2d experiment. With the current experimental apparatus as described, it is impossible to move the τ delay stage in steps less than half of the HeNe wavelength – approximately 316.41 nanometers – which results in a delay step equal to the time it takes for light to travel twice that distance, approximately 632.82nm. This corresponds to a sampling frequency of 473.61338 THz. From the foundational papers of Nyquist and Shannon we know that this sampling frequency limits the highest frequency component of the signal that may faithfully be recreated (see, for example,

[24] for an introductory explanation of the sampling criterion and the lesser known conditions for high fidelity (see, for an explicit formulation of a fidelity criterion as concerns the sampling of continuous, analog signals [341]) signal reproduction from sampled data originally described in [278] from the discrete set of data points to $f_{Nyquist} = f_{sampling}/2 \simeq 236.81$ THz. This frequency falls below the range of frequencies in which we are interested, unfortunately – the heavy hole and light hole exciton resonant absorption features are observed to occur in the 370 to 380 THz frequency range for Gallium Arsenide – Aluminum Arsenide quantum well system such as those we study. This would appear to be a serious dilemma for our experimental program, as a straightforward application of the Nyquist criterion would appear to prevent the observation of any oscillatory behaviour in the four-wave mixing emission as a function of the τ delay; thus, Fourier transformation of the data collected in this experiment might be expected to fail to reveal spectral features related to the excitons.

This is not an irreconcilable dilemma, however. We may make use here of a sampling process that is normally considered undesirable – aliasing. Simply put, if there is an oscillatory component present in an analog sample that is recorded using a discrete sampling method but which occurs at a frequency greater than the Nyquist frequency, "aliases" of this signal will still appear at a lower frequency in the spectrum after Fourier transform. This effect is normally considered the source of deleterious artifacts, as the high frequency signal's aliased features may be confused for oscillations that actually occur in the desired frequency range. This aliasing is already described in Nyquist's

early work [278], where the redundancy of information contained within the higher frequency bands and their aliases in the DC-to-Nyquist frequency band is explicitly illustrated. Nyquist notes that the contents of adjacent frequency bands of width $N/2$, where N is the number of sampled points collected, are symmetric about their boundaries.

In a pedagogical article motivated by the development of the Fast Fourier Transform algorithm, Brault and White describe the utility of signal processing techniques well known in the field of telecommunications as a tool for processing and analyzing scientific data, concentrating on the analysis of long, continuous signals, albeit ones typically recorded directly in a frequency space [47]. Nonetheless, these signals are band-limited by the nature of the measurement apparatus used to record them, and the Fourier analysis described is not dissimilar. Here, they show explicitly the effects of introducing an anti-aliasing filter to remove replica fast spectral features that appear within the Nyquist band due to a sampling rate insufficient to properly resolve the appropriate spectral components. In the case that these aliased spectral features overlap with features of interest that appear at the correct frequency in the transformed spectrum, the transform is considered unreliable as it is not possible to discriminate between the genuine and artifact features. Here the Nyquist frequency is explicitly referenced as the folding frequency around which spectral features are reflected down into lower bands; the value of the spectrum at any frequency point f in the transformed domain is not equal to only the amplitude of the recorded signal at f, but rather the sum of the am-

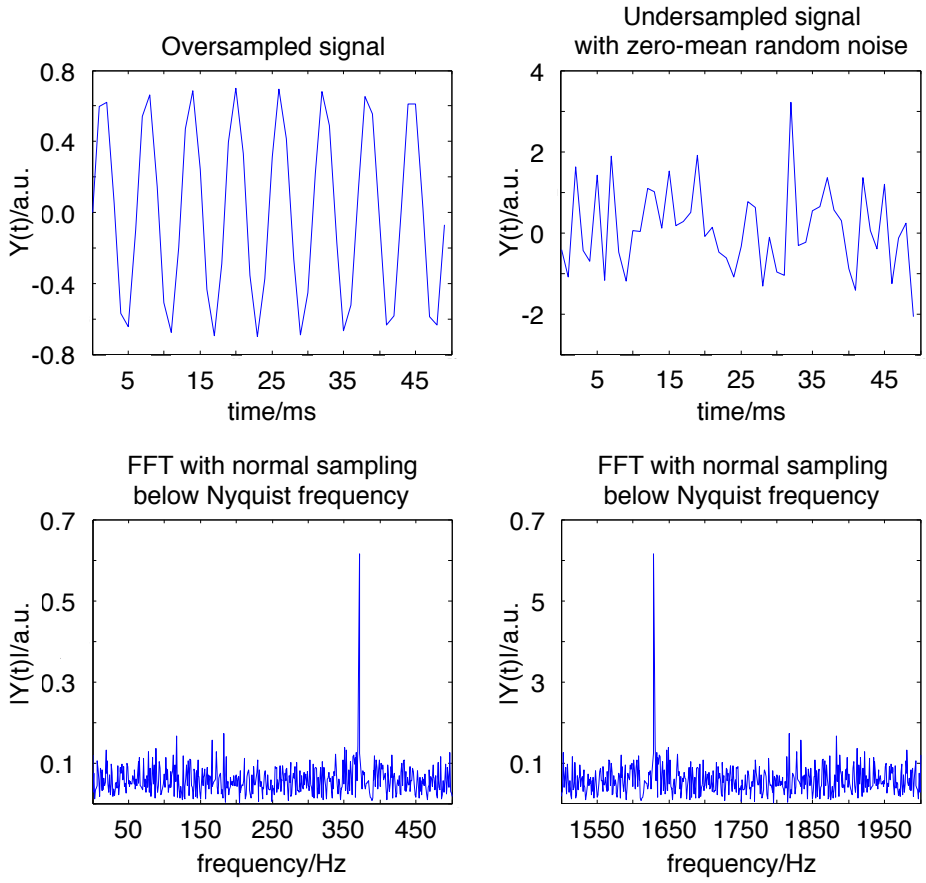

A sinusoidal signal is simulated at 1629.3Hz, then sampled at 10kHz (a). After adding simulated noise fluctuations, the signal is re-sampled at 1kHz (b), which is below the Nyquist frequency for the signal of interest. Normal interpretation of the Fourier transform data assigns the signal power to an incorrect frequency component due to aliasing (c). A correct undersampling interpretation can correctly find the actual frequency of this oscillation (d). Note in particular that the ordering of frequency components is not always identical when assigning the appropriate frequency band.

Figure 5.12: Principles of undersampling

plitudes of that component and certain components at frequencies greater than $f_{Nyquist}$ which satisfy the appropriate reflection symmetries. A more rigorous explanation may be found in [43].

Typically, as we noted, the presence of these higher frequency aliases appearing inside the Nyquist pass band are unwanted artifacts that complicate the interpretation of a Fourier transformed spectrum.

It has been demonstrated that Fourier transform spectroscopy can unambiguously recover spectra from interferograms that were collected at less than the Nyquist frequency [272], motivated by a desire to reduce the time required for data collection in order to avoid slow noise processes that would only significantly affect measurements taken over long time intervals. The mechanics of this measurement are not dissimilar from our own, in that an optical path length difference is introduced between two different signals derived from the same source (here, an external astronomical measurement). The delay is varied in discrete steps, a data point is collected, and the process is repeated. During the detection period the translation mirror is fixed and the modulated signal is detected via lock-in amplification – as a result, collecting a complete data set is a slow process, as in our own experimental work. In that work, the long duration of a data collection period would introduce noise from long period variations that do not affect quicker measurements; as such, significant interest was directed to the problem of reducing the time necessary to unambiguously collect FTIR spectra. It was shown that with a significantly undersampled data set a high-quality spectrum could be reconstructed,

provided that there are no other features present at either the fundamental frequencies within the Nyquist band or at even higher frequencies that satisfy the appropriate folding conditions to be rendered by aliasing within the spectral region of interest. In an astronomical observation such as this, we expect that appropriate choice of optical filters could prevent any ambiguity in spectra; in our own experiment, we do not expect any emissions in either the true frequency region in the DC-to-Nyquist frequency band or at higher, folded frequencies. This may be deduced from the band nature of the semiconductor system, which does not (to a first approximation) exhibit lower energy emission than the exciton resonances, and from the fact that any higher energy, unintentionally aliased emission would likely be weak due to its origin in some multi-photon or multi-excitation process.

In signal processing applications, an anti-aliasing filter is often applied to the analog signal *prior* to the sampling. This step removes the high frequency components from the raw signal, and prevents aliasing of those signal components into the DC-to-Nyquist band. In this application we expect it is not necessary, as no other emissions are expected to appear other than those we are intentionally aliasing into the frequency region of interest.

We are not specifically concerned with reducing the experimental time, although that is beneficial in that a reduced experiment length would somewhat reduce the chances of the interferometer slipping due to external noise in the laboratory. Rather, we are simply unable to satisfy the Nyquist sampling criterion using the step size determined by the HeNe wavelength, and make

use of the aliasing effect to pull our signal of interest down into an accessible region of the Fourier transform spectrum.

We note that a common weakness to this data collection scheme is that it is performed sequentially, and is thus more susceptible to systematic effects than if the data were collected in a randomized τ order. We take data sequentially do the accuracy requirements on τ, which can be easily satisfied by the step-integrate-repeat scheme, wherein the interferometer is only briefly unlocked and (if desired) the fringe can be observed during the movement of the translation stage to ensure that no 'slips' occur (when the stage moves by more or fewer than the number of fringes expected). Since the total throw of the piezo-mounted crystal is several microns, such an error may be introduced if the experiment is not operating properly, and is partiuclarly likely if the interferometer is not well aligned. Evidence of such a slip may be present if the servo controlling the pzt re-locks at a different voltage; this is likely, but in pathological cases it is possible to imagine gross error in stage positioning could occur without a corresponding jump in the voltage used to position the pzt. We monitor the pzt drive voltage at each step during data acquisition, and if there is no evidence that the interferometer is not behaving properly we assume that the absence of any pzt voltage jumps indicates a good data set was collected.

In the data presented here we have only made use of a two-fold understampling, since the inherent Nyquist frequency (˜237 THz) doubled (˜474 THz) is sufficient to properly reveal all of the spectral features of interest asso-

ciated with the exciton resonances in GaAs quantum wells. In practice, the undersampling process merely consists of deriving the appropriate frequency axes with which to label the spectral region of interest in the Fourier transformed plots. This is performed in Matlab. A normal sampling discrete frequency axis may be derived by creating a vector of frequency values equally spaced from 0 to the Nyquist frequency in increments determined by $f_{Nyquist}/(N/2)$ for N data points. Typically, we collect 1500 different spectra in a single experiment, but then pad the raw data set to bring it to an even power of two; in that case, it is the power of two ($2^{11} = 2048$) that would be used for N when determining the frequency spacing (q.v. *sub* for further description of zero-padding). The undersampling axis is derived by creating a vector of frequency values equally spaced from $(U-1) \times f_{Nyquist}$ to $U \times f_{Nyquist}$, where U is the undersampling ratio used, in increments of $f_{Nyquist}/\left(N/2\right)$.

5.4.2 Zero-padding raw 2dFTS data

An elementary result from Fourier analysis is that the frequency resolution available from a data set is proportional to the length of the time-domain data set. In the limit that the temporal data extend to positive and negative infinity and the sample spacing T of time-domain data points $x_n = x\left(nT\right)$, for some continuous function $x\left(t\right)$, the finite Fourier transform $X\left(\omega\right) = \sum_{n=-\infty}^{n=\infty} x_n e^{-i\omega n}$ can be taken to be equal to the continuous transform $X\left(\omega\right) = \int_{-\infty}^{\infty} dt x\left(t\right) e^{-i\omega t}$. In this limit, the frequency resolution is infinite, since both the time-domain and frequency-domain representations of the

signal are continuous functions.

Increasing the resolution of a fixed, sampled set of data is possible, however, by simply adding null data to the end of an existing data set . This process, known as apodization, provides some ability to artificially increase the resolution of spectral features, thereby narrowing resonance lines. The consequences of this technique, which clearly cannot provide us with a free Fourier lunch, are increased noise; in particular, some apodization schemes that increase frequency resolution by performing a weighted discrete Fourier transform place more weight upon later data points, which can significantly increase the high-frequency noise present in the spectra. Some utility can certainly be gained by using such a technique if the increased noise occurs outside the spectral region of interest. Doubling the resolution can, as a general rule, reduce the sensitivity by an order of magnitude [296].

In our own experiments, we perform a small amount of zero-padding, but this is not done in an attempt to improve signal resolution; rather, we wish to bring the length of our data sets to the nearest power of 2, so as to make use of the FFT algorithm more efficiently.

5.4.3 Windowing of raw 2d data

Apodization, the use of a window function to pre-process multi-dimensional data, is a well-established technique in the field of NMR spectroscopy. Typically, the acquisition time t_{max} used to record a free induction decay is limited for practical reasons, and the radiated signal is only recorded from $t = 0$ to

$t = t_{max}$.

In the partially collinear geometry, the phase-matching condition as derived from a third-order density matrix treatment indicates that the four wave mixing signal of interest co-propagates with the probe beam. The pump-probe signal also is emitted in this direction; therefore, any detection scheme that measures the difference between the probe beam recorded with the pump beams on and the probe beam recorded when they are off will resolve the sum of the desired four-wave mixing signal and two pump-probe signals – one arising due to the interaction of the static pump and probe with the material sample and one arising due to the interaction of the dynamic pump and probe with the material sample. Fourier transformation along the τ axis will shift these pump-probe artifacts out of the spectral region of interest, but they still complicate the interpretation of 2d data due to their much slower decay.

While the desired four-wave mixing signal analyzed with 2dFTS is expected to decay exponentially with a time constant determined by the dephasing time T_2 – see, for example [391], [393] for a description of the temporal lineshape observed with three pulse transient grating experiments (or see for example [228] for an introduction to spectral diffusion processes that result in a more complicated, arbitrary transverse relaxation function in place of the simple exponential dephasing) – the pump-probe signal will decay according to the population relaxation time T_1. It is not necessarily the case that $T_2 \ll T_1$, and in fact in many systems the two relaxation time scales are comparable; for excitons in semiconductor quantum wells, however, the dephasing time is

much shorter (typically a few picoseconds) than the population relaxation time (on the order of a few hundred picoseconds). As as result of the significantly different time scales for the four-wave mixing and pump-probe signals, we expect that the coherent processes will have damped out to their background level in a few picoseconds, but that the pump-probe artifacts will persist and prevent the detected signal from decaying to the background noise level. The pump-probe artifact originating due to the interaction of the static pump and probe pulses with the sample remains constant and will contribute to the experiment's background level. Upon Fourier transform this DC component is shifted outside the spectral region of interest. The pump-probe artifact that occurs due to the interaction of the dynamic pump and probe pulses with the sample will decay as the τ delay is incremented; we expect that the exponential decay of the dynamic pump-probe signal will not readily be apparent if data are collected over an interval only long enough to probe the coherent behavior motivating these experiments. Upon Fourier transform the slowly decaying portion of the dynamic pump-probe artifact will be shifted out of the spectral region of interest; the oscillatory behaviour that is observed at short times may at first appear problematic as it shares the same frequencies as the four-wave mixing signal, but upon a more careful consideration we note that the separation of the detected signal into pump-probe and four-wave mixing is somewhat artificial at these short times. Indeed, the oscillatory behaviour at early pump-probe delay times reflects the coherent response of the material sample and is part of the focus of these measurements.

Regardless, it is not possible to collect densely spaced spectra over a delay sufficiently long to allow the emission to completely decay to the background level, as the experiment time necessary to collect a sufficiently large data set would be impractical. We perform transient absorption spectroscopy (differential transmission and differential reflectivity measurements) as part of the daily warm-up procedure for the experiment. These data indicate the exciton population created in this sample exhibits a lifetime of hundreds of picoseconds. Since the greater fraction of the population decay trace occurs after dephasing processes have destroyed the coherence in the exciton population, the dynamics reflected in that slow decay are of little interest to our studies of exciton-exciton correlation.

We typically collect only a few ps worth of data (represented here by 1500 separate spectra) in order to study the early time evolution of the nonlinear optical response. This is insufficiently long to allow the pump-probe artifacts to decay to a constant background level. Fourier transformation along τ of the abruptly cut-off of polarization will introduce ringing artifacts into the 2dFT spectra, as this is equivalent to the measurement of the actual, complete physical decay convoluted with a square pulse window function applied in the τ time domain [341]. The application of a square pulse window in the time domain is equivalent to the convolution of the undistorted spectrum $S(f)$ with the Fourier transform of the weighting function, which may be directly shown to be a sinc function. In the frequency space, the convolution of the undistorted spectrum with the sinc function introduces oscillatory tails to

the spectral features, which adversely affects the signal resolution. Intuitively, the ripple effects may be associated with the high frequency components introduced into a time-domain signal by the sharp cut-off – the point in the data space where the signal abruptly drops from some finite value to zero is an infinitely fast process, and will exhibit significant high frequency components. To reduce this effect, a window function is applied to force the signal to tend to zero at $t = t_{max}$ [296]. There is an extensive body of applied mathematical research to determine the optimum window function to prevent distortion of the particular spectral features of interest, but in practice little effort is typically applied when developing a new experimental technique, and a simple time-domain filter such as a cosine window function will be used (see, e.g. [152]).

This effect is reduced by applying a Hanning window function

$$\frac{1}{2} + \frac{1}{2}\cos\left(\frac{2\pi\tau}{N}\right)$$

to the raw time domain data before transformation into the frequency space. Here N is the number of spectra obtained (1500 spectra, for example – we do not round up to the nearest power of two for window function).

Since coherent effects are expected only during the first few picoseconds, this manipulation of the raw data should not deleteriously affect our results, but it will result in a degree of spectral broadening along the ω_τ axis, where features will exhibit a linewidth equal to their natural width convoluted with

the inverse of the greatest τ delay. As an illustrative example, we note that the scan time used here (¿3ps) would result in the broadening of a frequency domain delta function to a 0.316THz line.

We observe a not insignificant elongation of spectral features along the ω_τ axis; part of this effect is due to the truncation of the τ scan before the emission has completely decayed to background levels. Obviously some of the distortion along the vertical axis is due to this effect, but other processes are thought to contribute to this selective absorption frequency broadening. Certain features are also elongated due to the physical phenomenon of absorption from free carrier states; the light hole exciton diagonal feature and the light hole exciton absorption – heavy hole exciton emission off-diagonal feature are both asymmetrically broadened on the high-frequency side of the line. We refer the reader to our preceding description of optical excitation of excitons in semiconductor quantum confined nanostructures, which rephrases the taxonomy of excitons and free carriers in terms of bound and unbound (continuum) exciton states – by analogy to an atomic system, it is easy to understand the disassociated, free electron-hole pair in a picture analogous to the continuum states of an electron-proton system. It is clear that absorption occurring above the light hole exciton resonance depends significantly on excitation of these continuum states, with subsequent relaxation to the exciton resonance for emission. Note the absence of an extended diagonal feature at higher frequencies, suggesting that any emission at those energies relaxes rapidly to the exciton state prior to emission – the continuum diagonal is absent even as

$T \rightarrow 0$ (or indeed for $T < 0$), indicating the rapid nature of this process. Our current investigation of the sophisticated numerical model developed to consider the effects of phase space filling and residual Coulomb coupling may further explain these spectral lineshapes.

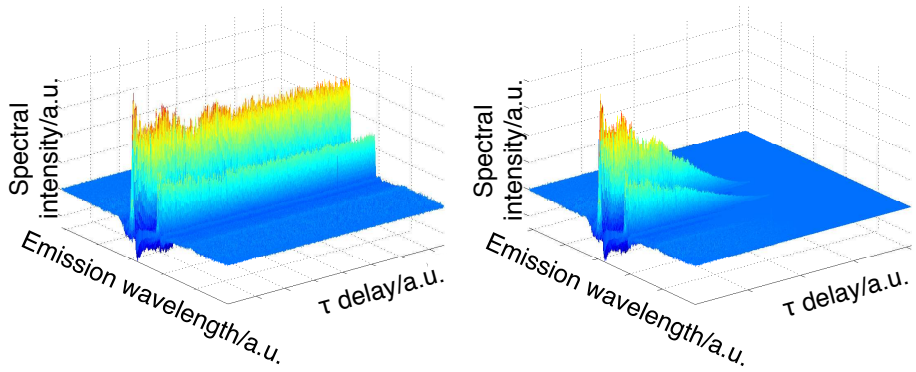

Minimally pre-processed data (divided by probe transmission spectrum) (a) and a windowed, apodized set of data (b). The Hanning window forces the pump-probe artifact to decay to background level within a reasonable time. Zero-padding does increase frequency resolution as a side effect, but we make use of it simply to use an optimized FFT algorithm.

Figure 5.13: Zero padded and windowed raw 2dFTS data

It can be easily demonstrated that using shorter window functions begins to obscure the detailed structure of the observed 2d spectra.

5.4.4 Analysis of 2dFTS spectra contents

In contrast to simpler four-wave mixing techniques, electronic 2dFT recovers both the absorptive and dispersive lineshapes of the third-order nonlinear polarization for a material system. By simultaneously measuring the phase and amplitude of the radiated four-wave mixing signal [131] it is possi-

ble to correctly determine the amplitude and phase of the system's response function, whereas simpler techniques are largely limited to studying the square modulus of the amplitude of the signal of interest. The ability to separate absorptive and dispersive features, with correct recovery of the overall, global phase of the system's response, is advantageous in comparison to microscopic theories predicting the nonlinear polarization, but it also has a more immediate utility in that it permits better spectral resolution of coupling and energy level features. Dispersive lineshape features decay relatively slowly, as $1/(\omega - \omega_0)$ away from the resonant line, whereas absorptive features decay as $1/(\omega - \omega_0)^2$ [6], [166]. Thus, the ability to separate these two components permits more precise analysis of complicated spectral features where multiple transitions overlap. Furthermore, a measurement resulting in a multidimensional plot of the absolute value of either the dispersive or absorptive spectrum is not as useful as a plot that properly assigns the sign of the response to the observed spectral features. The sign of features in a 2dFT spectrum provides information about the nature of the quantum mechanical pathways that involved in the optical transition [132]. To perform a complete, signed measurement of a 2dFT spectrum it is necessary to measure the electric field of the emitted four-wave mixing signal, rather than simply record the intensity as is more common in three pulse four-wave mixing experiments.

The signal electric field spectrally resolved at ω_t is directly proportional to the third order nonlinear polarization, the frequency ω_t, and the length of the sample l. It is inversely proportional to the $n(\omega_t)$ and to the speed of

light c. There is also a phase shift of i between the nonlinear polarization and the emitted signal field. The detection scheme used in 2dFT preserves phase information that is lost in simpler 2d correlation spectra. The phase sensitive detection of the scattered field permits the separation into real and imaginary components of the 2d spectrum [192]. The phase of a spectral feature in a 2dFTS plot is determined by the relationship between the phase of the final dipole oscillation relative to the initial dipole oscillation.

As in spectrally resolved pump-probe spectroscopy, a positive peak in a 2dFTS spectrum (assuming for the moment that the spectrum is collected in transmission mode, as is common) is a bleach; in a two-level model for the nonlinear optical response, those features correspond to a reduction in ground state absorption or increase in excited state emission. A negative peak, meanwhile, corresponds to an increase in the amount of light absorbed at those frequencies [132], [203].

2dFTS spectra are essentially a Fourier separation of the the various frequency components present in the observed four-wave mixing signal. Fourier analysis separates the electric field contributions according to the initial electronic dipole oscillation frequency ω_τ that they possess during the coherence time τ between the first two pulses, and according to the final electronic dipole oscillation frequency ω_t that they possess after the final pulse interacts with the system (if measured in the time domain, the electric field would be resolved at some time t after the third pulse) for a fixed mixing time T [202]. The correlation between these initial and subsequent events provides the capability

of 2dFTS to reveal couplings between different energy states in the system of interest.

More sophisticated analysis of the lineshape of spectral features can provide the necessary information to apply sophisticated models that relate microscopic processes to the macroscopic optical response (see, for example, [404], which studies a Brownian oscillator model suitable for studying solvation dynamics) – in our own case, we are particularly interested in lineshape analysis based upon theoretical work modeling the many-body interactions of excitons in semiconductors [113].

Nonetheless, certain straightforward, qualitative results are immediately available from inspection of 2dFTS spectra – the most immediately obvious are these coupling peaks, but there is also significant information available from the general lineshape of the measured spectral features. The spread of a feature along the diagonal $\omega_\tau = \omega_t$ is a well-known measure of the inhomogeneous, Gaussian width of the ensemble, while the broadening perpendicular to this diagonal is determined by the homogeneous, Lorentzian width. Consequently, the ellipticity of the features on this diagonal is related to the ratio of the homogeneous to inhomogeneous broadening in the system [281]. This simultaneous, clear measurement of both homogeneous and inhomogeneous dephasing times is one of the most significant strengths of 2dFTS compared to simpler one-dimensional experiments. The ellipticity of 2dFTS spectra may be related quantitatively to a correlation function describing the spectral diffusion processes exhibited by the material during its evolution [238].

Although the mixing time T is fixed for a given 2dFTS experiment, it can be varied from one experiment to another to study the various dynamics that result in spectral relaxation (q.v. *sup* our discussion in the extended description of three pulse four-wave mixing experiments). Perhaps most simply, the distinction between the correlation spectra that occur for zero or finite T permit the study of coupling that is coherent (the former) or due to relaxation. In some systems, particular quantum mechanical pathways may give rise to a coherence $\rho_{ab}^{(3)}$ that is the sum of two contributions with opposite signs. At some values of the mixing time T those may cancel each other out, resulting in the absence of any corresponding feature in the 2d spectrum; varying the mixing time permits the study of the temporal evolution of those pathways. Alternatively, changing the pulse sequence and Fourier transforming with respect to different time variables permits different types of two-dimensional experiments that provide different information regarding the system's evolution [71], albeit frequently at the cost of complicated changes to the apparatus to ensure the requisite phase stability between the relevant pulses. The logical conclusion of such steps is to perform a fully three-dimensional Fourier transform experiment (assuming only three excitation pulses are available) where the delays between each pulse are varied interferometrically. These experiments have been performed (see, for example, three-dimensional experiments on GaAs quantum well exciton systems [367] that reveal spectral features with greater clarity than is possible in the two-dimensional space) but are generally difficult and may require inconveniently long experiment times that would make

active interferometric stabilization difficult to implement. Dedicated, actively stabilized, multi-dimensional spectrometers suitable for such experiments have been constructed [54]. We do not attempt to explain fully those dynamics that may be studied by varying the delay T because the Taira/optical Bloch models we develop for intuitive understanding of the nonlinear optical response are not well suited to model the fluctuating environment of the different quantum emitters in the ensemble, principally because these dynamics cannot be well separated into infinitely fast relaxation processes, which would determine the homogeneous broadening of the transition, and infinitely slow processes, which would be associated with local environments and the related inhomogeneous broadening of the ensemble [132]. The characterization of the relaxation dynamics using simple exponential decays of populations and coherences depend upon the stochasticity of perturbative effects on the appropriate time scale (see our description of the applicability of density operator theoretical models elsewhere in this thesis for further discussion).

We do not explore the concept in detail, but phase-twisting may occur in certain two-dimensional spectra, and must be treated with care if properly phased spectra are desired. The complex nature of the nonlinear susceptibility leads to both absorptive and dispersive components in a 2d spectrum; as such, any 2dFTS generated spectrum should contain both real and imaginary parts . Generally, this effect arises when there is an unintended mixing of the absorptive and dispersive portions of a 2dFTS spectrum. If a purely absorptive spectrum (it is frequently desirable to separate these contributions not only in

order to narrow the spectral features and provide increased resolution as noted, but also to provide more direct comparison to theoretical or simulated results) is found by summing the results of two independently measured spectra that separately describe the rephasing and non-rephasing response of the system [214], any imbalance in the signals that may be artificially introduced by the typical complications of laboratory science will result in unintended phase-twisting of the spectral features. This will, of course, reduce the resolution of the experiment due to the mixing of the narrower absorptive resonances with the slower decaying dispersive features. Moreover, it results in changes to the lineshape of spectral features – any more sophisticated theoretical treatment of the results of 2dFTS than what we present here will rely upon the shape of these features to model the system dynamics; for example, analysis of a dispersive spectrum's node line separating positive from negative features will tilt away from the vertical if the dynamics of the system result in a temporal peak shift for the four-wave mixing emission [132]. One significant reason to work in a partially collinear geometry instead of the more conventional non-collinear BOXCARS geometry is that the absorptive and dispersive features are both simultaneously detected (albeit in the time domain), and as such, separation of these components is not as prone to the introduction of error as the corresponding technique for non-collinear experiments [132], [152], [342], [266], [403].

In the non-collinear experiment, the pulse-ordering sequence determines whether the recorded spectra reflect rephasing or non-rephasing dynamics. As-

suming that no significant drift occurs during this longer experiment, correctly interchanging the first two excitation pulses' temporal ordering and applying the appropriate double-sided Fourier transform to the detected four-wave mixing signal may eliminate the artificial lineshape distortion [132], although some phase-twist may inevitably occur if there are unequal strength quantum mechanical pathways. This imbalance is inherent to some transitions and cannot be eliminated under these phase matching conditions.

While phase-twisting is more problematic in non-collinear experiments, even in partially collinear 2dFTS measurements some mixing of the lineshape will occur. In both cases, the proper phasing of spectra is complicated at early times – if the mixing time T is less than the pulse duration, the stronger re-phasing and weaker non-rephasing pathways do not contribute with equal strength, resulting in phase-twists for these early times [132].

After this initial phase-twisting dies off, any remaining twist detected in a partially collinear geometry experiment is due to an inherent imbalance in the pathways strengths. 2dFTS measurements taken at sufficiently large T (i.e., longer than the pulse temporal width) correspond to the relaxation spectra measured in NOESY spectroscopy. The connection between COSY and 2dFTS spectra taken with zero mixing time is not so simple, however, because of the unavoidable phase-twisting that occurs at early times. These plots are qualitatively similar, and interpretation of the off-diagonal peaks as markers of coherent coupling is still useful, but the bandstructure of the excited and ground state manifolds may result in changes in the lineshape of

spectral features that are not easily accounted for [132]. It can be shown that the order of coherence, determined by the sum of the signs of the individual excitation pulses (e.g. $-k_1 + k_2 + k_3$ for a non-collinear 2dFTS experiment), describing the light-matter coupling in the optical analogue of the COSY and NOESY experiments corresponds to the appropriate NMR experiments.

We note in passing that in a completely collinear geometry the rephasing and non-rephasing pathways are always matched in the strength of their contributions to the detected nonlinear polarization, and that the artifact phase-twisting will be eliminated for all mixing times T. Thus, it would be possible to determine an intrinsic twisting (i.e. due to the different actual strengths of those pathways) at any given T, even for those short compared to pulse duration [132]. This experiment is extremely difficult to implement, except in materials where fluorescence detection is possible [87].

5.5 Non-collinear (BOXCARS geometry) 2dFTS and results from our group on the coupling of spectrally resolved excitons

The first demonstration of electronic 2dFTS was performed using a non-collinear BOXCARS geometry (we describe this beam configuration in our general discussion of three pulse four-wave mixing experiments) [192]. This non-collinear geometry permits easy detection of a phase-matched four-wave mixing signal emitted in a background free direction, similar to the simpler four-wave mixing experiments described in the previous chapter. Moreover, in

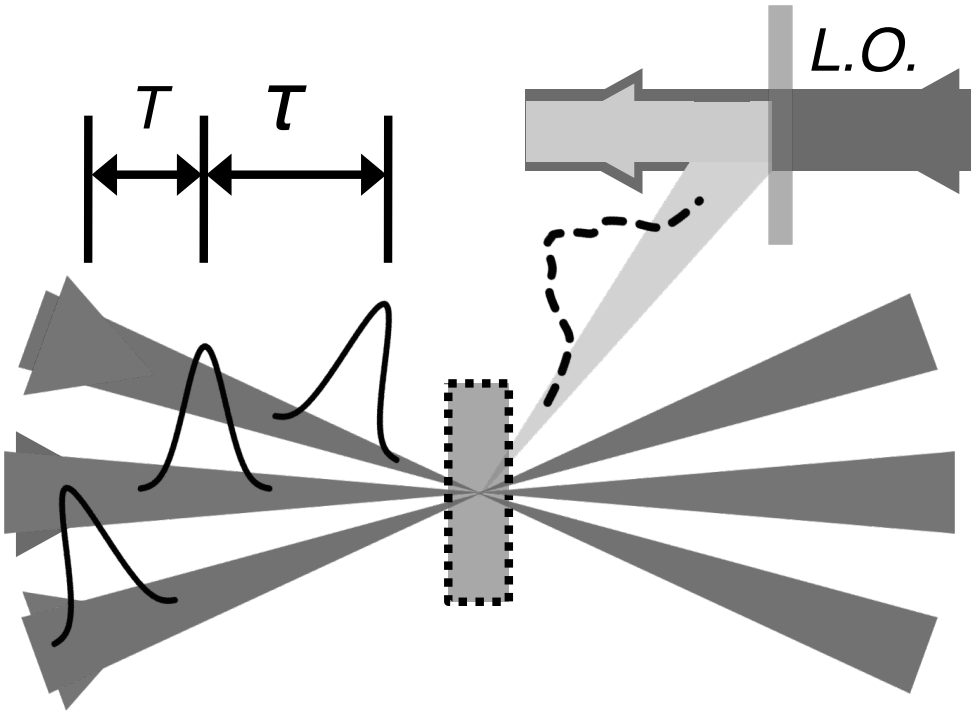

Two-dimensional Fourier transform spectroscopy is most frequently performed in a non-collinear, BOXCARS geometry, using an additional phase-stabilized local oscillator pulse to perform heterodyne spectral interferometry to characterize the four-wave mixing emission.

Figure 5.14: Sketch of non-collinear 2dFTS experiment

this phase-matching geometry, the pulse sequence order allows the selection of a subset of the electronic nonlinear processes.

The non-collinear experiment may be understood in a very direct fashion as an induced transient grating method – the first two pulses induce an excitation grating that diffracts energy from the third pulse into the 'empty' beam path at the fourth corner of the box [202]. The signal field will not exhibit the same temporal behaviour as the excitation pulses, and may express either normal [132] or virtual photon echo behaviour. Rather than measure the four-wave mixing emission directly in the time domain, the signal of interest is detected by frequency domain interferometry using an additional pulse derived from one of the excitation pulses. Since the power, delay, and phase of this local oscillator pulse is independently controlled, the detection method is a true heterodyne technique and permits direct adjustment of the signal to noise and optimization of the excitation pulse power for four-wave mixing [247].

In this geometry, a tracer pulse may be sent down the missing beam path in the BOXCARS arrangement, exiting the sample and co-propagating with the four-wave mixing signal. This beam thus traverses the same optical path as the signal, so that it has a well-defined phase relationship with the emission and undergoes the same dispersion due to optics after the sample. The delay of this tracer pulse is set in the interferometer so that it is synchronized with the third pulse that scatters the four-wave mixing emission from the transient grating.

During actual experiments the tracer pulse is blocked in order to avoid excitation of the material sample. A tracer-reference interferometric measurement is made to determine the phase difference between the tracer and the separate reference pulse used for heterodyne spectral interferometry. Then, during actual experiments, a signal-reference phase-sensitive measurement measurement is performed,from which the phase of the signal relative to the tracer can be determined. The delay of the tracer has been previously adjusted to possess the phase as third pulse; it is vital to match the arms of the interferometer precisely to minimize the differences in the dispersion of these pulses. A difference of even a fraction of a wavelength is enough to introduce errors in phase measurements [202].

2dFTS has been performed on semiconductors previously using a non-collinear geometry [410], [39], [248], [356], [366], [232], [231], [207]. In our own group we perform measurements on GaAs semiconductor quantum wells to determine the coupling between excitons spectrally resolved by interface fluctuations. The disorder in these systems affect the wavefunctions of the exciton states, which, in turn affects the coupling among the excitons.Thus, disorder in the crystal strongly albeit indirectly affects the nature of the coupling between these states. These 2dFTS studies provide the first quantitative measurement of the strength of coupling in these systems; previous spectroscopic tools could only suggest the presence or absence of this coupling from the changes it made to the four-wave mixing lineshape.

Shown here is a rephasing spectrum, where the complex electric fields

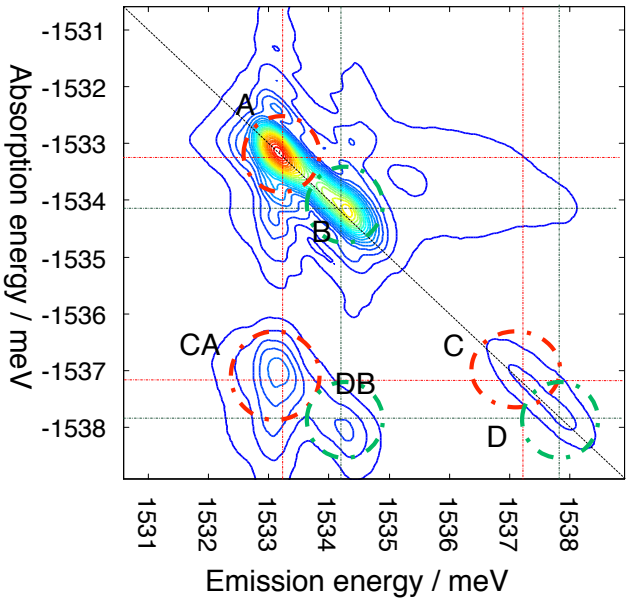

Real portion of a rephasing 2dFTS spectrum collected using the non-collinear, BOXCARS geometry to study a GaAs multiple quantum well sample using co-circular excitation. The splitting of the heavy hole exciton resonance into the doublet A, B is clearly seen. The light hole exciton resonance is also split, into the C, D resonance. Coupling between the two species of excitons is seen within each region, viz. the CA, DB cross-peaks. No coupling can be clearly resolved for the spectrally heavy hole excitons, however, as there is no clear peak at AB; similarly for the light hole excitons.

Figure 5.15: 2dFTS measurement of spectrally resolved excitons

of the first and second pulses interact with opposite signs inducing the nonlinear third order polarization. Clear splitting of both the light and heavy hole excitons is observed in the spectrum of an 8 period 13nm GaAs quantum well separated by AlGaAs barriers held at approximately 6K. While cross-peaks indicating the coupling of light and heavy hole excitons are present for both of the two regions, there is no clear evidence of cross-peaks indicating a coupling of the spectrally split heavy hole excitons or the split light hole excitons. It is possible, using 2dFTS, to establish quantitative limits on the strength of the coupling here; for the heavy hole resonances, the ratio of a cross peak to the diagonal features is less than 0.1. Spectral features suggesting coupling can be eliminated using other polarization configurations, suggesting these features actually arise due to biexciton formation, and are shifted in energy by the biexciton binding energy. No cross peaks are clearly present for the light hole excitons; quantitatively, the strength of the coupling to diagonal features can be estimated as less than 0.3. Previous studies of exciton coupling concentrated on the heavy hole exciton features, since the absorption from free carrier states tends to obscure the features expected for light hole exciton coupling. In 2dFTS, these spectral features are better separated, spaced out into two dimensions, and are more easily distinguished. The absence of coupling observed using 2dFTS on this sample has been reported [358], [359], [116], but further experimental work is under way to study the possibility of coupling in similar systems grown under different conditions, with the intention of affecting the characteristics of interface disorder in the sample.

The effect of that disorder on the spectral lineshape of excitons in semiconductors is studied using a three band model, considering light hole, heavy hole, and conduction band states [114]. This theory considers the effects of phase-space filling, an approximate mean field arising due to exciton-exciton interaction, and a force-force correlation effect arising due to two exciton correlation effects. The temporal evolution of the nonlinear polarization is approximated (here, the Planck constant is taken to be unity) as

$$\begin{aligned} i\partial_t P_\sigma^{(3)}(\mathbf{R},\, t) &= \left(\hat{H}_\sigma(\mathbf{R}) - i\Gamma_\sigma\right) P_\sigma^{(3)}(\mathbf{R},\, t) - \\ &\frac{1}{2}\sum_{\sigma_i}\int d\mathbf{R}_1 d\mathbf{R}_2 d\mathbf{R}_3 \widetilde{\beta}_{\sigma_1,\sigma}^{\sigma_2,\sigma_3}(\mathbf{R}_1,\, \mathbf{R};\, \mathbf{R}_2\, \mathbf{R}_3) \\ &\times P_{\sigma_1}^{(1)*}(\mathbf{R}_1,\, t)\, P_{\sigma_2}^{(1)}(\mathbf{R}_2,\, t)\, P_{\sigma_3}^{(1)}(\mathbf{R}_3,\, t) \end{aligned}$$

where $\sigma = \{\sigma,\, s\}$ indexes the spin state σ of the holes and s of the electrons, $\mathbf{R}$ is the centerl of mass spatial coordinate, Γ_σ describes relaxation processes, and $P_\sigma^{(1)}$ is a linear polarization. Of particular interest to us are the many body parameters $\widetilde{\beta}$, a four-point effective potential function that is used to include the effects of Coulomb interactions that occur among the holes and electrons. This effective potential function determines the approximate spatial area from which a coherent four-wave mixing emission will occur; its functional form is complicated and not well understood, but it is expected to fall off at least as rapidly as the van der Waals r^{-6} potential once the distance between an electron (or hole) and hole (or electron or another hole) is greater than some critical range on the order of the exciton Bohr radius. This fast

decay of the correlation function $\widetilde{\beta}$ limits the area of the sample from which coherent emission can arise. The dependence of the many body parameter is due to its dependence on the approximate single particle Hamiltonian for an exciton, $\hat{H}_\sigma = -\frac{1}{2M_\sigma}\nabla^2_{\mathbf{R}} + W_\sigma(\mathbf{R})$, where the potential W contains the effect of the fluctuation disorder.

If the interface disorder is modeled with a binary system, i.e., assuming that there are only monolayer fluctuations in the well thickness, that there are sharp transitions in the quantum confinement between the regions of greater and lesser thickness and that there are no edge effects, the fluctuation potential is well modeled by a binary value, either 0 or $-V_\sigma$. The formation of islands of greater or lower well width (and hence, lower or greater exciton transition frequencies) may be considered using a correlation function that describes the likelihood of the interface fluctuation being the same or different at some distance r,

$$K(r) = \langle W_\sigma(\mathbf{R})\, W_\sigma(\mathbf{R}+\mathbf{r})\rangle - \langle W_\sigma(\mathbf{R})\rangle^2$$

For islands of typical size r_c, $K(r)$ will decay exponentially with characteristic length scale r_c. The optical response of the sample is then found to depend largely on the ratio of this length scale to the confinement length, $r_c/\xi_0 = r_c/\left(\pi\hbar/\sqrt{2M_\sigma V_\sigma}\right)$. The confinement energy is a typical length scale for the quantum confined system, and is equal to the island size for which an exciton confined to that island would possess a kinetic energy less than its potential energy [61]. As the characteristic disorder length scale r_c increases, the

exciton resonance splits from a single inhomogeneous transition into a doublet. The spectra taken for the sample studied in our lab shows two clearly separated features, indicating that the disorder length scale (i.e., the island size) is indeed greater than this confinement size; in this case, the excitons' kinetic energy may be neglected, simplifying the calculations for the nonlinear optical response. The transition between a single broad feature and a split doublet is not specific to this system, but should be a feature of other microscopic, disordered materials.

Some coupling should always be expected at the edge of island features, where the wavepackets of spectrally resolved excitons should overlap and directly couple, but the emissions from these edge excitons are not expected to result in a coherent, beamed emission that would dominate the phase-matched four-wave mixing signal from excitons located in the islands themselves. The disorder in the quantum well system does break the simple conservation of momentum phase-matching geometry, but the statistical homogeneity of the system results in a strong emission along that direction as the small scale fluctuations 'average out.'

Further study is needed of prototypical GaAs quantum well systems to completely characterize the possible coupling features that may or may not appear in these structures.

5.6 Partially collinear 2dFTS experiments on GaAs quantum wells

5.6.1 Motivation for performing 2dFTS in a partially collinear geometry

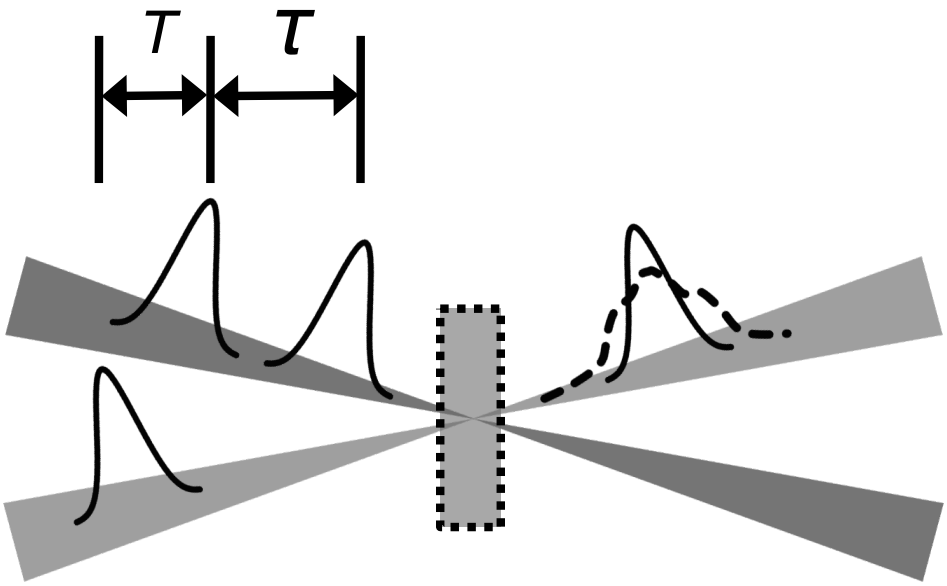

Two-dimensional Fourier transform spectroscopy can be performed in a partially collinear geometry experiment, where the two pump pulses are collapsed onto a single beampath. The four-wave mixing emission co-propagates with the probe beam, which acts as a local oscillator field. The combined signal and probe field is spectrally resolved, providing one frequency axis. The τ delay is scanned through some interval, and the resulting data are Fourier transformed along that time axis to obtain the second frequency dimension.

Figure 5.16: Partially collinear 2dFTS measurement

The results of the non-collinear 2dFTS experiments performed in our group [358], [359], [116] have been studied using a modified mean field theory that treats exciton-exciton correlations exactly, while viewing the optical cou-

pling as a perturbation [114]. This approach is somewhat counter-intuitive, given the previous theoretical studies of exciton dynamics in semiconductors, which, perhaps due to the early successes of the Taira/optical Bloch models, frequently consider the optical excitation of the exciton states first, and then typically try to 'add in' many-body effects. This non-conventional modified mean field theory has successfully reproduced the qualitative features of our 2dFTS measurements, but it does depend upon phenomenological quantities extracted from 2dFTS data – or results from some other spectroscopic technique – that can separate the contributions of the light and heavy hole excitons to the transient grating induced in the sample. Most 2dFTS experiments are typically understood in terms of a nonlinear susceptibility that obscures the microscopic physics occurring in the material, whereas the modified mean field theory calculates the equation of motion for the polarization and the emitted electric field directly.

Nonetheless, the ability to precisely model the exciton dynamics in these systems is still greatly limited. The Coulomb correlations present in this system are described with many body parameters $\widetilde{\beta}$ that can be understood as effective four-point potentials in the equation of motion for the nonlinear polarization. Each $\widetilde{\beta}$ parameter corresponds to a specific optical helicity; in general, that nonlinear polarization is found by summing over these different optical polarization states. Thus, a polarization due to excitation by linearly polarized light will contain contributions from both right-handed and left-handed many body parameters. Experimentally, 2dFTS measurements using

linearly polarized light are simpler to implement, but will be more difficult to analyze within this framework. While more complicated to perform, experiments using only a single optical helicity to excite the semiconductor system would provide more accurate fits of the $\widetilde{\beta}$ parameters.

The majority of semiconductor 2dFTS has been performed using linearly polarized light, although some experiments have been performed with co-circularly polarized. It is now possible to perform a non-collinear experiment with arbitrary polarization control [53], but these methods require an additional optical experiment to eliminate the global phase ambiguity inherent to the non-collinear 2dFTS technique.

To study arbitrary polarization configurations, we constructed a partially collinear geometry 2dFTS apparatus. 2dFTS based on a simpler, partially collinear geometry was described in [132] and experimentally demonstrated in [87], [152], but has not previously been used to study semiconductor materials. We present the first such demonstration, and the first demonstration (so far as we know) of reflection mode 2dFTS experiments [115].

5.6.2 Other possible geometries and approaches to 2dFT

For completeness, we note that 2dFTS has also been performed in a completely collinear geometry [363], [379], but those measurements relied on phase cycling to study the nonlinear polarization [212] rather than directly resolving the coherent four-wave mixing signal. While the phase cycling [212] modulation scheme employed is largely analogous to the nuclear resonance

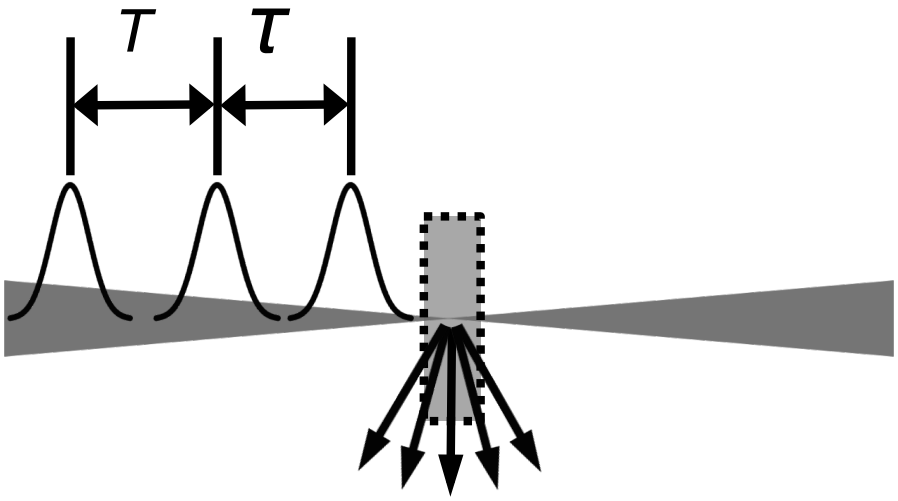

Two-dimensional Fourier transform spectroscopy has been performed in a fully collinear geometry on samples where phase-cycled fluorescence detection is possible.

Figure 5.17: Fully collinear 2dFTS measurement

antecedents of 2dFTS, the observation of an incoherent signal has some disadvantages. In particular, that method can only measure the absorptive part of the third order nonlinear polarization, unlike 2dFTS measurements that collect a phase matched emission. Moreover, this technique depends upon measurement of fluorescence, and cannot be used to study materials that do not strongly emit.

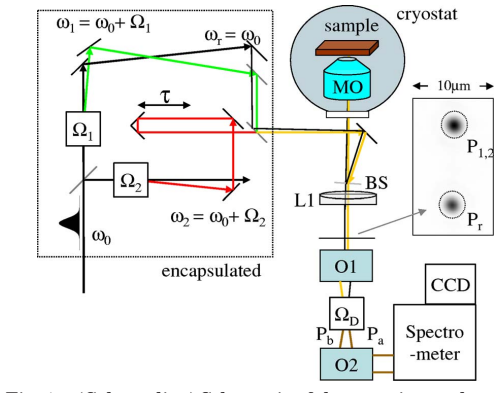

A nearly collinear nonlinear optical measurement performed on single quantum dots. This technique does not actively stabilize the two pump pulses, but instead relies on a high degree of passive stability for the experimental apparatus. Reproduced from Langbein and Patton, Optics Letters 31:1151 (2006).

Figure 5.18: Nearly collinear multi-dimensional heterodyne spectral interferometry

An approximately collinear two-dimensional spectroscopic method has been demonstrated [234], [287], but used nearly collinear rather than fully collinear beams – albeit with wavevectors sufficiently close to degenerate to permit resolution of individual quantum emitters. More significantly, that approach did not actively stabilize the visible wavelength ultrafast pulses used,

and therefore cannot provide separation of the two dimensional spectrum into its real and imaginary parts.

Completely collinear measurements are generally thought to be too difficult to implement and instead rely on transverse measurements of incoherent emission [382] to avoid saturating the detector attempting to observe a phase matched emission co-propagating with the excitation pulses. Our recent results suggest otherwise, as it may be possible to isolate weak four-wave mixing signals from intense background fields, but further experiments are necessary (q.v. our discussion in the next chapter).

An alternative non-collinear approach, substantially different from those presented perviously in our discussions of 2dFTS, has also been demonstrated [84]. This technique uses four pulses, created interferometrically in two phase-locked pairs, to record phase and amplitude data for stimulated photon echo signals.

As a compromise between background-free non-collinear 2dFTS experiments and the indirect measurement of fully collinear, fluorescence detected 2dFTS, the partially collinear geometry allows us to spectrally resolve the interference between the signal field and one of the three excitation pulses [132], [152].

5.6.3 Properly phasing 2dFTS spectra in the partially collinear geometry

Partially collinear 2dFTS possesses two particular advantages compared to other techniques, both of which are related to the particular phase matching geometry used. We first consider the automatic phasing of the 2dFTS spectra.

Non-collinear 2dFTS experiments exhibit a global phase ambiguity, as noted in our description of the frequency domain spectral interferometry detection scheme used to characterize the four-wave mixing emission. To properly separate the magnitude of the nonlinear response into its real and imaginary parts, a separate, independent phase measurement must be used to correctly fix the overall phase of spectra detected in this fashion.

In non-collinear experiments, the four-wave mixing signal is emitted in a background-free direction, but is then mixed with a well-characterized (at least, in the ideal world), phase-locked reference pulse before it is spectrally resolved [245], [4]. Frequency domain spectral interferometry provides direct experimental control of the heterodyne signal level by adjustment of the intensity of the local oscillator pulse, but the phase-sensitive measurement requires the construction of a second interferometer to stabilize the reference beam. Since the reference pulse and the four-wave mixing signal propagate along different beam paths there is an inherent phase ambiguity between the two optical fields. In order to properly separate the recorded 2dFTS signal of interest into its real and imaginary parts this additional degree of freedom must

be fixed by characterizing the absolute phase of the system response. This requires an additional experiment as the global phase cannot be extracted from the existing data.

A two-pulse, spectrally resolved pump-probe measurement is approximately equivalent to the integral over the ω_τ frequency axis from $\omega_\tau = -\infty$ to $\omega_\tau = \infty$. The ambiguous 2dFTS data is integrated, compared to the independent spectral measurement, then re-adjusted and compared again until the phases match [132], [202]. Alternatively, a spectrally resolved transient absorption measurement may simply be compared to the $\tau = 0$ spectrum acquired during the 2d experiment. While not formally equivalent, this approximation generally provides a fairly accurate fit and is less susceptible to the integrated noise present in the ω_τ-integrated 2dFTS spectrum .

The use of either additional measurement is not ideal, since it limits the possible set of polarization-dependent measurements that can be performed, as the set of possible two pulse polarization configurations cannot reproduce the response of the set of possible three pule polarization configurations. As a result the global phase cannot be set for experiments with cross-polarized pump pulses. The different geometries of the spectrally resolved two-pulse measurements and the non-collinear 2dFTS experiment itself are another weakness of this technique; this would make it impossible to study samples where the optical physics depend on momentum transfer. Properly phasing the non-collinear 2dFTS measurements is partially a technical difficulty, but it also represents a fundamental experimental limit for experiments performed in this geometry.

Recently, an all-optical method for fixing the ambiguous global phase degree of freedom in non-collinear 2dFTS measurements has been demonstrated. This all optical phase retrieval method permits 2dFTS experiments with arbitrary polarization configurations, including the use of cross-polarized pump beams, or two quanta coherence experiments, that could not previously be performed in a non-collinear geometry. This method relies on a precise measurement of pulse temporal overlap and the extraction of relative pulse phases via an interferometric measurement based on the comparison of pairwise fringe patterns [53]. In the case of semiconductor samples, which are highly sensitive to the excitation power used, these phase measurements are performed at a replica focus rather than the prime focus of the excitation beams at the point probed on the sample. This technique has been used to produce high quality 2dFTS measurements with arbitrary control of linearly polarized excitation pulses, but makes use of more complicated infrastructure [54] than the partially collinear 2dFTS technique, or the popular non-collinear measurements.

We perform our 2dFTS measurements using a partially collinear geometry, which provides automatic phasing of 2dFTS spectra [132], and does not require an additional measurement. The correct overall phase of the spectrum obtains due to the identical optical paths traversed by the probe pulse and the emitted FWM signal. The phase ambiguity in non-collinear experiments results from heterodyning the four-wave mixing field with a reference pulse that propagates through a similar but not identical beam path; in the partially

collinear geometry, the four-wave mixing signal co-propagates with the probe beam that induces its emission. The four-wave mixing emission is no longer background free, but it gains the advantage of a trivial phase relationship with its heterodyne field. Measuring the interference between an excitation pulse and the signal of interest is known as homotime detection [4], and sacrifices the flexibility of a heterodyne scheme in order to eliminate the phase ambiguity between signal and local oscillator fields. in heterodyne detection methods. The loss of the heterodyne knob is unfortunate, and in partially collinear experiments this degree of freedom is no longer available to maximize the signal to noise. Moreover, since the signal is emitted along a phase matched direction identical to the wavevector of the probe field, the measurement is no longer background free. Scattering is expected to play a more deleterious role in these measurements compared to the non-collinear geometry. The relative length scales of sample imperfections and visible wavelengths are comparable in these materials, and incoherent scattering may be substantial, but 2dFTS is less susceptible to these problems than other coherent spectroscopic techniques since the integrated noise power is now distributed throughout the 2d spectrum. This results in reduced noise power spectral density within the spectral region of interest. Additionally, the 2dFTS signal of interest is now superimposed (in the time-domain) on the optical free-induction decay of the probe (non-coherent, non-phase matched but some power still emitted into the transmitted probe direction), the depleted probe pulse itself, and two pump-probe artifacts. Nonetheless, the greatest drawback of this geometry is not the

presence of these backgrounds, which should not result in significant spectral features in the region of interest after Fourier transform [132]), but is rather the loss of the phase degree of freedom. If for any reason the experimenter should wish to adjust the relative phase of the signal field, she is not able to do so in a post-experiment process.

The automatic phasing of *transmission mode* partially collinear 2dFTS works even in a structured sample, such as the multiple quantum well sample we studied. While the probe pulse will have travelled a different path length and thus possess a different phase when it interacts with different layers of a structured material, the emitted four-wave mixing signal from each well will reflect that phase, and will still overlap temporally with the local oscillator, *viz.* the probe beam itself.

5.6.4 Measurement of rephasing & non-rephasing pathways to produce absorptive spectra

The second significant advantage of the partially non-collinear geometry is related to set of quantum mechanical pathways that are sampled in this phase matched geometry. In non-collinear 2dFTS, temporal ordering of the excitation pulses selects emission of either the rephasing or non-rephasing set of quantum mechanical pathways in the phase-matched direction [265]. Collapsing the non-collinear pump beam paths into a collinear pump pair permits simultaneous measurements of the rephasing and non-rephasing sets of quantum mechanical pathways [132] in the time domain (although in the

frequency-frequency space the results are not quite so simple to separate – nevertheless, simple techniques have been demonstrated to extract the separate pathways or properly combine the two sets to render purely absorptive features from a single pc2dFTS experiment [342], [403], [266]).

Since different components of the $\chi^{(3)}$ response are measured in the two geometries, the lineshape for partially collinear experiments is expected to be substantially different from that observed in other geometries, due to the different sets of quantum mechanical pathways that are sampled. 2dFT data recorded in the completely non-collinear geometry separately sample either the rephasing or non-rephasing pathway, depending on the pulse ordering. To produce an absorptive spectrum requires two separate non-collinear measurements, two independent measurements to fix their global phases, and the summation of the resulting spectra to render absorptive\dispersive spectral features [214]. This technique presents a number of possible points where errors may be introduced that would result in phase-twisting of the spectral features.

These absorptive plots are advantageous for several reasons. First, purely absorptive spectral features are narrower than those comprising an absorptive resonance mixed with a more slowly decaying dispersive spectral feature. Separating the nonlinear polarization into absorptive and dispersive features thus increases the frequency resolution of the experiment and the amount of information conveyed by the collected data. This can be particularly useful for studying coupling between closely spaced features (we note that this geom-

etry may be useful to study the coupling of spectrally resolved excitons that we have previously examined using non-collinear 2dFTS for this reason). Absorptive features also have a more immediate, physically intuitive interpretation than spectra related to certain sets of quantum mechanical processes. This permits relatively straightforward connection between the 2dFTS results and measurements from other kinds of experiments. Non-collinear 2dFTS is also susceptible to worse phase-twisting problems due to imbalances between the rephasing and non-rephasing pathways during those periods when the pulses overlap, and are thus not quite as effective as a universal spectroscopic tool. The proper separation of these pathways that is possible in partially collinear experiments improves the time resolution of the technique at short mixing times T. We discuss this at length elsewhere in this chapter.

We note here that if a strongly coupled system is studied in 2dFTS with simultaneous, coherent excitation of multiple levels, it is impossible to say which frequency component was absorbed in the excitation of a coherent superposition of several states. 2dFTS permits the correlation of an initial dipole oscillation at a particular frequency with the amplitude and phase of each final oscillation frequency present in the emission, but the exact nature of the connection – what precise processes result in spectral features in a complicated system – is not necessarily known from this plot. In such cases, spectra should be labelled only as real or imaginary, without necessarily associating either of those parts of the complex spectra with strictly absorptive or dispersive parts of the susceptibility [132].

5.6.5 Delay stages vs pulse shapers

Although pulse shaping presents an attractive means to construct a partially collinear 2dFTS experiment, we constructed our apparatus using precision translation stages that delayed pulses by interferometrically controled changes of optical path length. In part, this choice was prescribed by our familiarity with these techniques, but there are significant advantages to performing 2dFTS spectroscopy with path length delayed pulses rather than using pulse shaping. We consider the distinction between the two here.

We first note that a significant difference exists between optical pulse trains generated by path length variation [4], [132] and those RF pulse trains used in nuclear resonance experiments – and, interestingly, optical pulse trains derived by some pulse shaping techniques.

Other than some in models of some 2d THz spectroscopic measurements, early theoretical treatments of 2dFTS resembled their antecedents in nuclear resonance, and used a pulse description that considered only the delays of pulse envelopes without changing the phase of the optical frequency carrier wave. Theoretical work by Mukamel and co-workers (for example) used solutions to the nonlinear exciton equations derived with Green's functions, incorporating exciton interactions using a scattering matrix. Calculated model spectra were demonstrated for various proposed techniques that made use of a number of different phase-matching directions and pulse ordering schemes to probe coupling between molecular states, and it was suggested that inverting 2d spectra thus obtained could provide sufficient structural information to

model the molecular system, analogously to 2d NMR experiments [71].

This model for phase sensitive measurements depends upon what might be thought of as an unaltered carrier multiplied by some time domain shape function. This type of pulse train is essentially a cw carrier that is turned on and off by a pulse envelope that has a controllable delay. Such a pulse sequence is not dissimilar to the results of certain kinds of pulse-shaping [209], [101]. Those methods, often using acousto-optical pulse shaping, may be used to perform multiple pulse, phase coherent spectroscopy [382]. But in the first electronic optical 2DFTS experiments [192], the excitation pulses were created by changing a delay arm of an interferometer. Keeping track of the carrier phase is necessary to properly understand the microscopic response; without correct treatment of the pulse delays, 2dFTS spectra will not accurately reflect the real and imaginary parts of the nonlinear optical response. The phase of a four-wave mixing signal detected in a 2dFTS experiment can be shown to depend upon the phases of the pulses used to excite the third-order nonlinear polarization, the particular details of the relaxation processes determining the decay of the nonlinear polarization, the product of the four relevant transition dipole matrix elements involved in the excitation of the nonlinear polarization and the subsequent emission, and the optical phase arising due to the delay of the pulses produced by varying the optical path lengths of the experiment [133]. The method used for creating the delayed pulse sequence must be considered when modeling the nonlinear optical response in order to correctly recover the electronic frequency information encoded in an electronic 2dFTS

experiment. The analysis we use in our own calculations (see elsewhere in this thesis for extensive description of and calculation of density operator matrix perturbation models) uses envelope delayed form of pulses generated by a path length difference in an interferometer; as such, the envelope functions are changed $\varepsilon(t) \rightarrow \varepsilon(t + \Delta t)$, with the carrier function for the electric field also affected, $\cos(\phi(t)) \rightarrow \cos(\phi(t + \Delta t))$ [4].

Tokmakoff and coworkers first demonstrated partially collinear 2dFTS using optical wedges mounted on translation stages to generate the phase locked pump pulses [87]; however, after [152] it has become increasingly popular to use a pulse shaper to generate the phase-locked pump pulse pair (see, for example, [266]). While well-suited to multidimensional spectroscopy of atomic vapours and molecular solutions ([342], [361], and others), the use of pulse shaping to generate the pump pulse pair is contraindicated for experiments on semiconductors. In those materials, relevant time scales may require the generation of pump pulse pairs separated by relatively long delays. Pulse shapers typically introduce artifacts or distort the pulses when used to create delays greater than some critical time – see, for example [152] for comment on the limits of pulse shaping in pc2dFT. For high repetition rate laser systems, the use of liquid crystal based pulse shapers is prevalent in ultrafast laser spectroscopy, since AOM based shapers are better suited to amplified\low-rep lasers where the acoustic wave grating pattern does not substantially differ from shot to shot [390], [389]. The pixellation of LC devices results in the formation of periodic replica pulses [283], [394] – although present at much

lower intensity, these pulses are problematic for the study of semiconductor materials (see below). These difficulties are further compounded by the presence of finite pixel gaps in the LC spatial light modulator. Even for an ideal modulator, there are still fundamental limits to the time aperture that arise due solely to optical effects for any typical pulse shaper [388].

The introduction of artifacts and the variations in pulse power are not pathological to many systems of interest to 2d spectroscopists, but in the materials we study they present a serious complication. Many-body dynamics in semiconductor nanostructures are sensitive to excitation density (see for example [31], [380], [254]), due in part to the dependence on exciton-exciton Coulomb correlation interactions. Even in cases when optical selection rules prevent the formation of bound biexciton states, correlation in the biexciton continuum – or among a higher number of excitons – can significantly alter the nonlinear optical response of a semiconductor. Even at reduced numbers, the inadvertent emission of excitons by artifact pulses may significantly alter the observed nonlinear polarization. Pulse shaping is not ideally suited to the generation of exact replica pulses separated by a variable delay, whereas moving a delay stage in an interferometer is precisely equivalent to shifting the vector origin of a ray.

Compared to the pulse-shaping based method described in [152], our technique is somewhat more cumbersome, but it provides high phase stability and allows the generation of pulse pairs separated by longer delays. The advent of polarization control in pulse shaping means that this feature of our

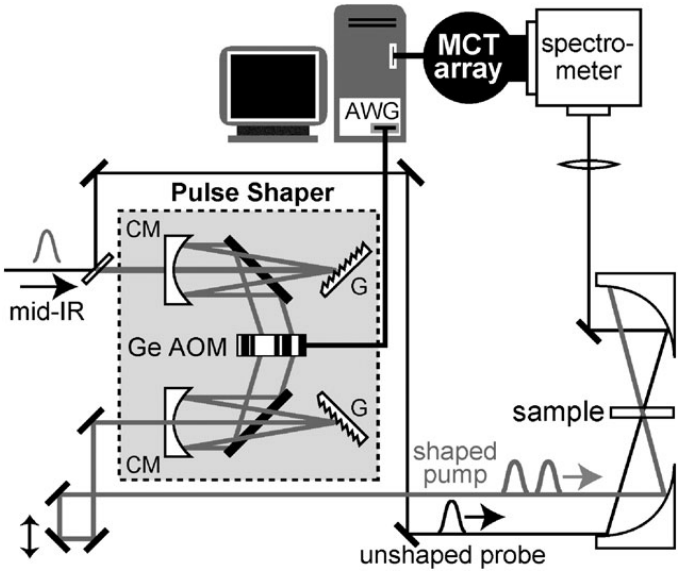

A partially collinear geometry 2dFTS experiment, using a Germanium acousto-optic modulator as a phase mask in a 4-*f* beam shaper to generate the phase-locked pump pulse pair. The transmitted probe beam is spectrally analyzed and recorded, then the pump pulse pair sequence is incremented. Reproduced from Shim and Zanni, Physical Chemistry Chemical Physics 11:737 (2009).

Figure 5.19: Partially collinear 2dFTS with pulse shaping

experiment is no longer a true advantage compared to such techniques, but the interferometric experiment does allow individually addressable control of the separate pulses – this allows the introduction of detection techniques relying on amplitude or frequency modulation of the excitation pulses, which would not be easy to implement using a pulse-shaper. So long as the interferometer can still be locked and stabilized with the HeNe beam, any property of the Ti:Sapph pulses may be manipulated as desired.

As an aside, we note that signal distortion effects occurring due to propagation through dispersive media – the sample as well as the glass optics used in the visible regime – are expected to be minor for pulse trains that are generated using conventional interferometers, where the pulse amplitude fronts are kept parallel to the wavevector in non-absorbing media [409].

5.6.6 Experiments with partially collinear 2dFTS

We perform 2dFTS experiments analogous to COSY and NOESY measurements in a transmission geometry using linearly and circularly polarized light. We collect data at a number of different values of mixing time T; the modified mean field model developed to study 2dFTS lineshapes as yet does not properly treat the relaxation that occurs during this second time period (n.b. in the equation of motion for the nonlinear polarization, no distinction is made between the dephasing and population decay processes affecting the polarization – relaxation is instead lumped generally into the Γ_σ terms. Nonetheless, collecting this data may be useful for subsequent study of these

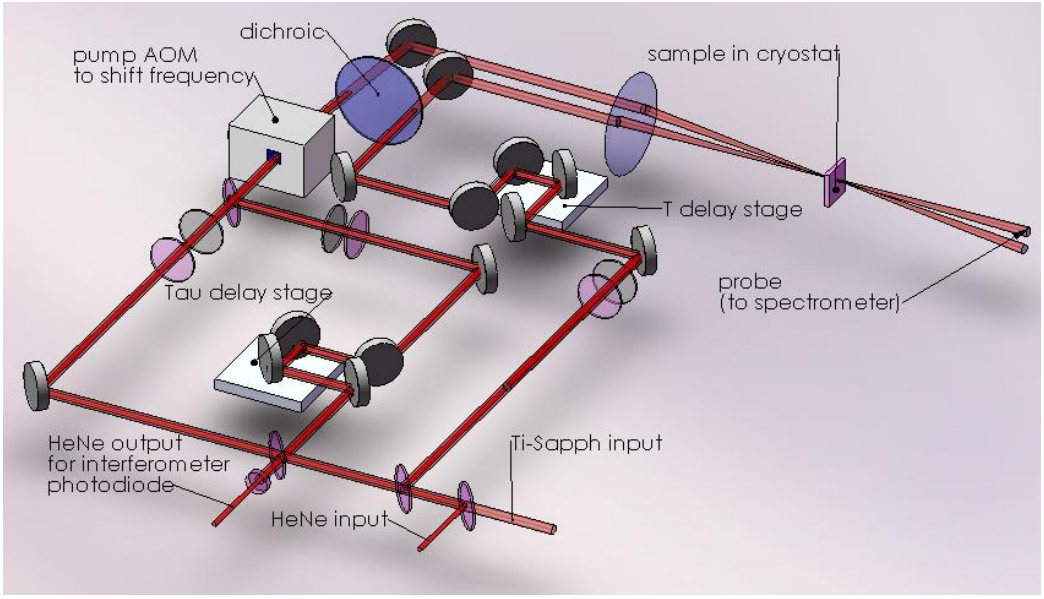

Experimental apparatus we constructed for performing 2dFTS in a partially collinear geometry. The Ti-Sapph beam is split into two portions. The probe portion is sent to a precision delay stage used to set the T delay, passing through a half-wave plate and linear polarizer that can be used to set its power and polarization. The probe is then focused onto a sample mounted in the cryostat. The other portion of the Ti-Sapph beam is sent to a Mach-Zehnder interferometer. Each arm has its own half-wave plate and linear polarizer to control power and polarization; one arm has a precision delay stage used to set the τ delay. After they are recombined on a beamsplitter, the collinear pump pulse pair are focused onto the same spot on the sample. If circularly polarized light is desired, a quarter-wave plate is placed in one or both beam paths after the dichroic mirror (q.v. *sub*).

A second laser, a HeNe is also coupled into the experimental apparatus. The HeNe traces out the same beam path through the Mach-Zehnder interferometer as the Ti-Sapph, but is retroreflected by the dichroic mirror. The HeNe back-propagates through the experiment and is collected on the beam splitter used to divide the beams entering the interferometer.

The HeNe beam exiting the interferometer is used to derive an error signal that permits active stabilization of the interferometer path length via a mirror mounted on a PZT.

After the probe beam transits the sample, it is collected and collimated, then sent to a spectrometer where its spectrum is recorded using a CCD.

For the 2dFTS experiments here, an acousto-optic modulator is used to apply an 80 MHz shift to the pump pulses. In order to maintain an equal path length and manage dispersion, another modulator is placed in the probe beam path (not shown), but is not powered.

Figure 5.20: Our partially collinear experimental apparatus

effects. It might be interesting to consider a denser set of data collected at very early times T, in order to observe the relaxation of free carrier pairs into exciton states (for instance, permitting experimental determination of the branching ratio for light hole and heavy hole excitons). It is possible to take data at arbitrarily small or negative mixing times because the temporal resolution of the 2dFTS technique is determined by the scan of the coherence and detection times, but the early time results of such experiments must be analyzed carefully since phase-twisting will occur even in this partially collinear geometry due to the inherent mismatch in magnitudes of the rephasing and non-rephasing pathways during the temporal overlap of the pulses.

Subsequently, we perform 2dFTS measurements on quantum well samples in a reflection geometry. To the best of our knowledge, this is the first such reflection geometry experiment. The lineshape is complicated in comparison to that observed for the transmission measurements; we suspect this is due to coherent emissions from a number of different wells in the sample. The detection scheme measures (effectively) the interference between those emissions and the strong reflection of the probe beam from the front surface; each emission from different depths has a different phase relationship with that probe reflection, resulting in a spectrum that is difficult to interpret intuitively.

These reflection geometry measurements lead directly to our interest in performing coherent, homotime reflection spectroscopy of more complicated nanostructures. To do so, we develop a new spectroscopic technique, described in the next chapter of this thesis.

5.6.7 Laser source, samples, general experimental methods and data processing

These experiments are all performed using light produced by a commercial Titanium:Saphire laser (Coherent, Mira 900D, operated in femtosecond mode, pumped by a 10W Coherent Verdi cw DPSS laser), producing mode locked pulses of approximately 130-150fs duration at a 76MHz repetition rate, centered at 797nm with a spectral bandwidth of approximately 10nm. We do not pay substantial attention to the pulse characteristics, although an autocorrelation measurement is made every day; the particular temporal characteristics are not important in understanding the response measured with the 2dFTS experiment. The laser is tuned so that the light hole exciton resonance is more strongly excited than the heavy hole exciton resonance; this choice is made since the oscillator strength for the heavy hole exciton is much greater than the light hole exciton. Nonetheless, tuning the laser to far to the blue is not desirable since it will increase the number of free carrier states created in the GaAs material.

All beamsplitters used in this experiment are custom optics designed and fabricated by CVI-Melles Griot for ultrafast laser pulses. These beamsplitters were designed for use at 671nm in the interest of exploring samples at these wavelengths, but performed satisfactorily at the longer wavelengths used here. The mirrors used for this experiment were uncoated silver mirrors fabricated by JML Optical for use with pulse laser sources. Polarcor thin film polarizers are used due to their ability to withstand high intensity

pulses. Waveplates were purchased from Custom Optics for the use in this wavelength range. The lenses used were conventional BK-7 glass with a near-IR anti-reflection coating, purchased from Thorlabs. A dichroic mirror was custom designed and fabricated by CVI-Melles Griot to transmit 800nm and reflect 633nm light at zero angle of incidence. A small short-wave pass filter from Thorlabs was used prior to the interferometer photodiode to block the Ti:Sapph laser while allowing the HeNe to pass through to this detector. The cw HeNe laser used to measure path length variation in the interferometer is a temperature stabilized device purchased from Melles Griot, but successful stabilization was also demonstrated with an un-stabilized surplus HeNe head previously used as an alignment tool for alignment of medical instruments.

The data presented in this chapter were all taken using a 10 period GaAs/AlGaAs multiple quantum well sample cooled to approximately 10K. This is sufficiently low to freeze out the longitudinal optical phonon mode, but acoustic phonons will still be present in the material since their dispersion relationship permits states of essentially arbitrarily small energy. The samples are prepared by using a chemical-mechanical etching process to remove the majority of the substrate and capping layer, leaving a thin wafer that can be studied in transmission geometry. That processes sample is then attached to a sapphire disk using a thermal adhesive (Crystalbond). The mounted sample is then placed in a sample holder that clamps it between two copper elements; a small piece of niobium wire is placed between the upper clamp and the sapphire disk to provide a soft cushion and prevent fracture of the rigid sapphire. We

have also performed experiments where the sapphire disk is adhered to a copper slug directly using the same thermal adhesive, but find this technique prone to occasional failure as the sapphire, adhesive, and copper possess different coefficients of thermal expansion; frequently, the sapphire disk will pop off the copper sample holder if direct adhesion is used. We use a copper sample holder with a through hole machined in it to permit transmission experiments. The sample and holder are placed in the coldfinger of a commercial cryostat (Cryo Industries of America), and liquid Helium is used to cool the system to its desired temperature. The temperature is monitored constantly during the experiments; it is possible to use active temperature stabilization with a built-in heater element, but this was not deemed necessary for this project.

The entire experiment is enclosed inside a 3/8" aluminum box to isolate the the apparatus from the laboratory environment. This provides the high degree of passive stability necessary to perform phase-sensitive measurements, but active phase stabilization is still required to produce high quality 2dFTS spectra. Without the enclosure caps in place, the interferometer cannot be stepped through a large number of positions without a phase slip.

Careful optical alignment of the 2dFTS experiment is crucial to achieve high precision stepped control of the pulse timing using delay stages. In particular, the motion of travel for the translation stages must be made as parallel as possible to the direction of beam propagation; this ensures that a move Δx in the stage position along its travel results in a change in the pulse delay of precisely $2\Delta x$. In order to achieve this, a portion of the laser power is split

off at two separate points prior to the actual experiment and then sent to two quadrant photodiode detector arrays that are used to precisely, repeatably align the experiment using two steering mirrors prior to the experiment. The quadrant photodiode is a circular detector divided into four $\pi/2$ slices. Adding the photocurrents from the top two and the bottom two segments, then taking the difference using analog op amp circuits provides a vertical alignment measurement. Adding the photocurrents from the left two and bottom two segments and taking the differences provides horizontal alignment. Zeroing the differences of both simultaneously implies that the laser spot is centered. Zeroing the differences of both degrees of freedom for both detectors simultaneously implies that the laser is centered on both detectors; since two points uniquely define a line, the position and pointing of the laser is now reliably known. Once the experiment has been constructed and carefully aligned, the optics that occur downstream of the beam splitters that send the laser to the quadrant detectors are not moved, in order to maintain the beam path from day to day.

The Ti:Sapph pulse is split into two portions upon entering the experiment, with one half used as the probe and the other used to interferometrically generate a pump pulse pair. The probe portion is sent to a precision translation stage, used to set the T mixing time delay, passes through a half-wave plate and polarizer to control the power and polarization, and is then focused onto the sample with a 20cm lens. The other portion of the Ti:Sapph beam is split with a MachZehnder interferometer, one arm of which contains a high-

precision, high-accuracy translation stage, used to set the evolution time τ. This beam path is referred to as the dynamic pump path, while the one without the translation stage is referred to as the static pump path, referring to the ability to change the path length and hence delay of either arm. Both arms of the MZI contain half-waveplates and polarizers, allowing independent control of power and beam polarization. Upon exiting the interferometer, the collinear pump pulse pair are focused onto the sample, using the same lens as the probe beam, and onto the same spot illuminated by the probe beam. The pump pulse pair beam and the probe beam form a small angle in the horizontal plane. Irises are used to restrict the size of the pump beams prior to the focusing lens to ensure that the spot they form on the sample is larger in size than that of the probe.

For 2dFTS experiments both active and passive stabilization techniques are used to ensure the phase control between the pump pulses that interact coherently to produce the transient grating in the material. A high degree of passive stability is a prerequisite for active stabilization techniques to work properly. To this end, the entire experiment is encapsulated to reduce the effects of acoustic noise or fluctuations in the air currents or temperature of the room. An active stabilization system is used to provide a well-defined, controlled phase relationship between the pump pulses. One of the arms of the MZI used to generate the pump pulses contains a mirror mounted on a piezo that can scan the beampath over a few microns with a bandwidth of several kHz. This mirror is used to actively stabilize the phase between the

pump pulses with interferometric precision, using a servo mechanism based on an error signal derived from a second laser that co-propagates with the Ti:Sapph.

A cw Helium Neon laser beam is introduced into the experiment along with the Ti:Sapph. The two are spatially mode-matched, and co-propagate throughout the entire experiment until the HeNe beam is retroreflected by a dichroic mirror that passes the longer wavelength Ti:Sapph but reflects the shorter wavelength HeNe back along its own beam path, retracing the beam path through the interferometer. A fraction of the reflected HeNe power is then collected at the input beamsplitter for the MZI and sent to a homebuilt silicon PIN photodiode.

A sinusoidal voltage can be sent to the piezo mount in the interferometer, resulting in a corresponding dither motion of that mirror. Dithering that mirror produces a typical interferometer fringe; the magnitude of the displacement is approximately linear to the applied voltage for small excursions. During the experiment, a loop filter is used to derive an error signal from the photodiode voltage as the optical components of the MZI drift, resulting in a change in path length. This signal can be amplified and fed back to the piezo, counteracting that drift and achieving a typical stability of $\lambda/150$. The servo mechanism is controlled by a TTL pulse switch that permits the experiment computer to temporarily unlock the interferometer while the delay stage is moved and to re-establish the lock at a zero-crossing of the HeNe fringe after the motion has ceased. In this manner, phase stable data may be collected

during a locked period, the interferometer is unlocked, the τ translation stage is moved, and the interferometer is re-locked prior to collecting another data point. Measurements of the interferometer error signal, the output of the servo circuit, and the piezo drive voltage (divided by a factor of approximately 10 to avoid overloading the analog data collection circuit) are made after each interferometer lock. If those signals are seen to be nearly constant over the course of the interferometer, it is assumed that the experiment has been performed properly without an unintended 'phase slip' – the name given to the experimental error when the analog electronics result in the piezo-mounted mirror moving too far in one direction or another to lock to the incorrect fringe zero-crossing. If a sufficient number of data points are captured prior to a phase slip, it is possible to cut the data taken subsequently from the raw 2dFTS set and still obtain a high quality spectrum.

It was found impractical to use the same quadrant detectors to align the HeNe laser as were used for the Ti:Sapph laser due to the drastically different power levels of the different light sources. A homebuilt amplifier system was built to compensate for this using switched gain, but was found to be impractical due to (we suspect) different zero positions at different gain levels due to analog input current errors in the circuit. As such, the alignment of the HeNe was made by checking that the two lasers co-propagated over a long distance; in order to facilitate this, a flip mirror was placed prior to the dichroic mirror. A series of parallel mirrors were used to extend the path length of the two beams to something like 10 to 15 meters, allowing the experimentalist to

check that the spatial modes were well overlapped over long distances. The alignment of the HeNe could be optimized by examining the fringe patterns appearing in its spot, and tweaking the HeNe input steering mirrors to obtain a more homogeneous interference pattern.

Data are collected by detecting the transmitted probe beam. After the sample, the probe is collimated using another 20cm lens, then coupled into a single mode fiber used to bring the signal beam to a different part of the optical table while providing some degree of noise rejection for scattered light. For differential transmission measurements, the probe intensity is measured using a home-built amplified Silicon PIN photodiode and an SRS830 lock-in amplifier, using a chopper beam on the pump pulses after they exit the stabilized interferometer to modulate the signal of interest, typically at 1-2kHz. For spectrally resolved data, such as that used for a 2dFTS experiment, a flip mirror is removed from the beam path, allowing the probe beam to be focused using an f-number matched optic onto the slit of a 750 mm spectrometer with a 1200 groovers/mm grating. Prior to the spectrometer, a number of neutral density filters are used to reduce the probe power in order to avoid saturating the CCD used to detect the signal. Spectra are typically collected with the CCD cooled to approximately -20C, using an Andor CCD and home-written Labview control software that coordinates control with the rest of the experiment. For the 2dFTS experiment, spectra were recorded with the pump pulses on and with them blocked, the difference is saved and Fourier transformed to obtain the spectrum of interest. The pump pulses are blocked

or transmitted using a mechanical chopper, with the CCD triggered by a TTL pulse derived from the chopper driver. The maximum rate at which data could be captured without running into timing issues that could result in spectra with incorrectly gated pump pulses was 25Hz; since the duty cycle of this experiment ('on' minus 'off') is 50%, that means that 12.5 data points can be collected per second. The neutral density filters mentioned above were chosen each day to ensure that as much of the CCD dynamic range was used as possible without saturating the device given the exposure time determined by the chopper synchronization (only a small fraction of the on-off cycle, typically on the order of 4-8ms).

After subsequent study of the literature on 2dFTS experiments, we believe that no such modulation of the pump pulses is necessary. The component of each on-spectrum that is due only to the probe beam will be shifted out of the region of interest by Fourier transformation; as such, higher quality data may be collected by optimizing the spectral measurements without the constraints of synchronizing the CCD capture and readout with the mechanical chopper. Nonetheless, measuring data in the fashion described here is still useful for early experiments proving the capabilities of this experiment because it permits more direct comparison to differential transmission measurements, conventionally reported as dT/T.

After an experiment is completed, raw data are analyzed by a home-written Matlab program. This software package analyzed spectrally resolved differential transmission measurements to provide plots of two-pulse experi-

ments that can be compared to the $\tau = 0$ spectrum in the raw 2dFTS experiment to understand the phase relationship among the three pulses used to excite and detect the nonlinear signal of interest. The 2dFTS data is collected as a function of wavelength, but the analysis program transforms it into a frequency space, then divides the raw data by the spectrum of the probe beam obtained with the pump beams blocked. A temporal window is then applied to the data; we discuss the use of Hanning windows to eliminate ringing effects elsewhere in this thesis. The software uses a fast Fourier transform algorithm to transform the windowed data from the (ω_t, τ) domain to the (ω_t, ω_τ) domain, then maps the data into the undersampled frequency space; we discuss the frequency domain sub-Nyquist sampling issues elsewhere in this thesis. The Matlab code then outputs a number of different graphical representations of the data, including pseudo three-dimensional and contour plots of the real and imaginary parts of the 2dFTS spectrum.

Initially, no acousto-optic modulators were used to frequency shift the beams used in the experiment, although these devices were found to be necessary to avoid interference effects (q.v. *sub*). We describe the introduction of acousto-optic devices at some length.

The pulse delay zeroes are calibrated by taking cross-correlation measurements of the probe beam with the static pump beam to find the $T = 0$ position for the probe, and cross-correlation measurements of the dynamic pump with static pump beam to find the $\tau = 0$ position for the dynamic pump. These measurements are taken using a two-photon detector – a photo-

diode with a bandgap greater than the photon energy of the Ti:Sapph laser, which will therefore respond to the intensity squared of the combined optical field (the electric field to the fourth power). We discuss the correlation measurements at length in a subsequent chapter, as they were found to behave in a more complicated fashion when more complicated modulation schemes were used. Here, to pick out the nonlinear signal, a mechanical chopper is used in combination with an SRS-830 lock-in amplifier. To detect the probe-static pump correlation trace, the static pump is chopped at 1-2 kHz, while the probe is unmodulated. The correlation observed by stepping the probe delay stage is related to the square of the envelope function for the laser pulse, and can in principle be de-convoluted to make a more accurate estimate of the pulse shape (we do not trouble ourselves with that for these experiments for the reasons noted above). To detect the static pump-dynamic pump correlation trace, both beams are passed through the same chopper and modulated at the same rate. The resulting signal contains information about the pulse envelope, but for these co-propagating pulses there is also an interference term that oscillates rapidly. In both cases, a slow envelope function is fit to the data to obtain an approximate value of the zero delay positions.

Having spent further effort studying multi-dimensional spectroscopy after performing these experiments, we have determined that greater care should be taken with these measurements to provide a more precise and accurate measurement of the zero delay positions. Moreover, the use of independent acousto-optic modulators to actively control the individual phases of the beams

is desirable to ensure that this phase relationship is completely characterized.

We emphasize that 2dFTS experiments performed in a partially collinear geometry requires only one interferometer to stabilize the pump pulses, since the 'heterodyne' field for the four-wave mixing emission is simply the depleted, co-propagating pump beam. This greatly simplifies the construction of the apparatus in comparison to the non-collinear 2dFTS experiments.

5.6.8 Differential transmission measurements of GaAs quantum wells

We began the partially collinear 2dFTS experimental program by performing two-pulse experiments. We performed differential pump-probe measurements on the multiple quantum well sample in transmission mode as an initial step to test our experimental apparatus.

Pump-probe spectroscopy is an elementary ultrafast technique [211], albeit one that still provides surprisingly useful results – particularly when some additional property of the two pulses used is introduced as an independent variable. In its simplest form, pump-probe spectroscopy uses a strong pulse to induce excitation in a sample. Subsequently, after a controllable delay, a weaker probe pulse interacts with the material. To be experimentally useful, some property of the probe beam (intensity, polarization, etc) must be modified by its interaction with the material, and that effect must be sufficiently large to be measured. Plotting the effective change in the probe as a function of its delay relative to the pump pulse permits time-resolution of dynamic processes in the material under study. In the limit of an optically thin sample,

the time resolution of the experiment is limited only by the temporal pulse width – or, if two separate lasers have been used to produce the two different pulses, by the time jitter between the two pulses [331], [211].

We use the simplest form of pump-probe spectroscopy, where the two pulses are essentially degenerate. Both pulses were derived from a commercial Titanium Sapphire laser, producing pulses of approximately 130 fs duration (FWHM), with a repetition rate of 76MHz. The laser repetition frequency places a hard limit (approximately 13 ns) on the slowest phenomena that may be observed in an experiment before arrival of the next pulse from the laser disturbs the evolution of the system.

For these experiments, the time-integrated change in probe power was measured. An unbiased Si PIN photodiode (Hamamatsu) and home-built amplifier (based on the Analog Devices OP27G op amp) were used to measure the intensity of the probe beam. That amplified voltage was then sent to a digital lock-in amplifier (SRS 830), which picked out only those components that oscillated at the reference modulation frequency, derived from a rotary mechanical chopper used to modulate the beams at up to several kHz. Thus, the recorded signal is proportional to the change in the transmitted probe power, since any DC component will be filtered by the lock-in amp.

The amplifier output was read via GPIB interface and tabulated on a personal computer using a home-written Labview (National Instruments) program that was also used to control the translation stages that were moved to set pulse delays. The experimental apparatus offers two simple ways to

perform these two-pulse measurements: using a pump pulse from either the static pump or dynamic pump arm of the Mach-Zehnder interferometer, and a probe pulse from the probe delay line. Each pulse has independent control of polarization and power. These measurements were performed at liquid Helium temperatures (typically ˜10K), with various combinations of pump and probe powers ranging from a few hundred microWatts or less to several milliWatts.

The results presented here are differential transmission $\Delta T = (T - T_0)$ data, where the change ΔT in probe transmission that is induced by the pump is *not* normalized. Frequently, the results of similar measurements are presented in the form $\Delta T/T_0 = (T - T_0)/T_o$ normalized by T_0, the probe transmission when the pump is blocked. This would simply result in changing the amplitude of the reported values by some constant; since we use arbitrary units here, such a step seems of limited value. We note that our 2dFTS data do not follow this convention, since normalization by the spectrally resolved transmitted probe has some utility that is absent in normalization of spectrally integrated measurements.

Although our experimental plan always included the use of acousto-optic modulators to perform multiple frequency lock-in detection of four-wave mixing signals from our samples, we initially did not include AOM's in the experiment for our initial measurements.

A lock-in amplifier from Stanford Research Systems was used to more accurately measure the transmitted probe power, using a mechanical chopper to modulate the pump beam.

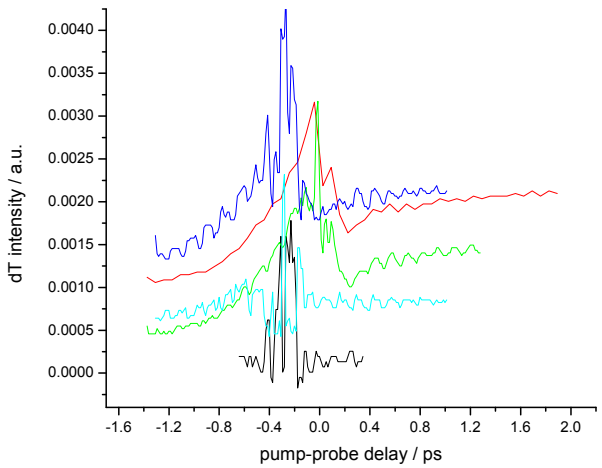

Differential transmission measurements performed on GaAs multiple quantum well sample appeared to be non-repeatable. Five dT measurements taken successively, with small adjustments to alignment to attempt to improve the pump-probe spot overlap. The fractured nature of the peak made it difficult to optimize the experiment.

Figure 5.21: Unstable differential transmission data

We were surprised to see that this simple measurement seemed highly unstable. Rather than a simple exponential decay of transmitted probe intensity as a function of the pump-probe delay, which we intended to use to extract the lifetime of exciton states, we instead saw a non-repeatable signal that had extremely high noise imposed on it. Initial guesses were a noisy and unreliable coupling into the optical fiber used to collect the transmitted probe light and couple it to the spectrometer, but this was ruled out as a likely cause by meticulously measuring the power of the probe beam as a function of the probe delay stage's translation with the pump beam blocked – the variation in power measured as the probe stage was scanned was trivial compared to the total measured power. No noise was observed in this measurement. We also attempted experiments with various different chopping frequencies, with two-frequency chopping (chopping both pump and probe beams and using the lock-in amplifier to detect the signal of interest at the difference frequency), and experiments where the probe stage was fixed and the dynamic pump stage was scanned instead. None of these experiments resolved the noise problem that broke up the differential transmission signal.

After some deliberation, a new differential transmission measurement scheme was used, where the probe stage was stepped in sufficiently small increments that any features that depend upon fast effects – up to the optical frequency of the excitation laser – should be revealed. These measurements demonstrated conclusively that the pump-probe measurement was experimentally sound, but that a strong high frequency modulation of the signal had been

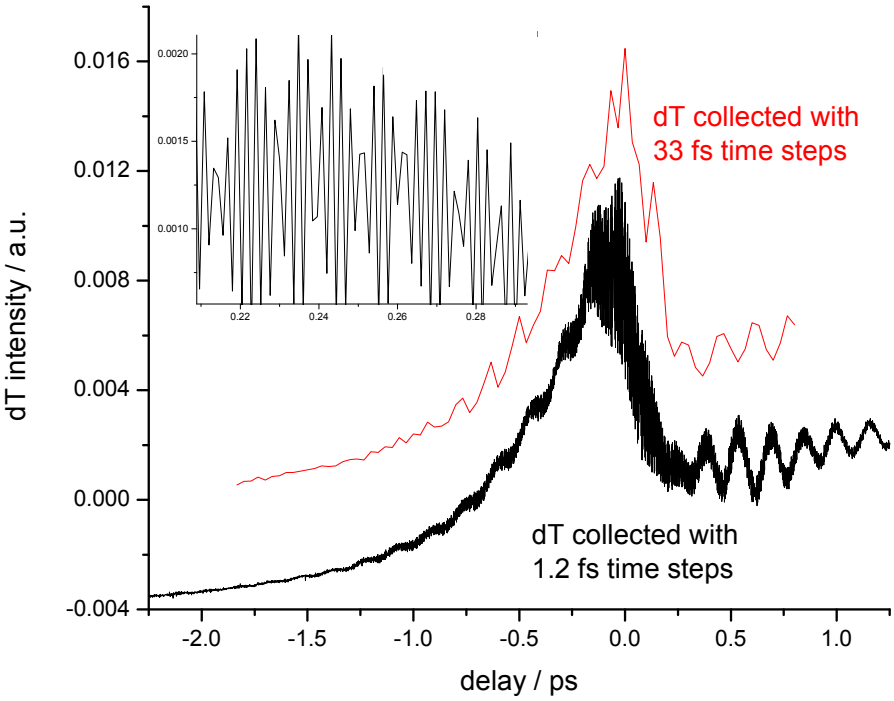

Performing measurements with higher sampling frequency suggests at least two oscillatory components present in the dT signal. Inset: expanded view of high frequency component present in the signal measured with 1.2 fs step size.

Figure 5.22: High frequency components in dT data

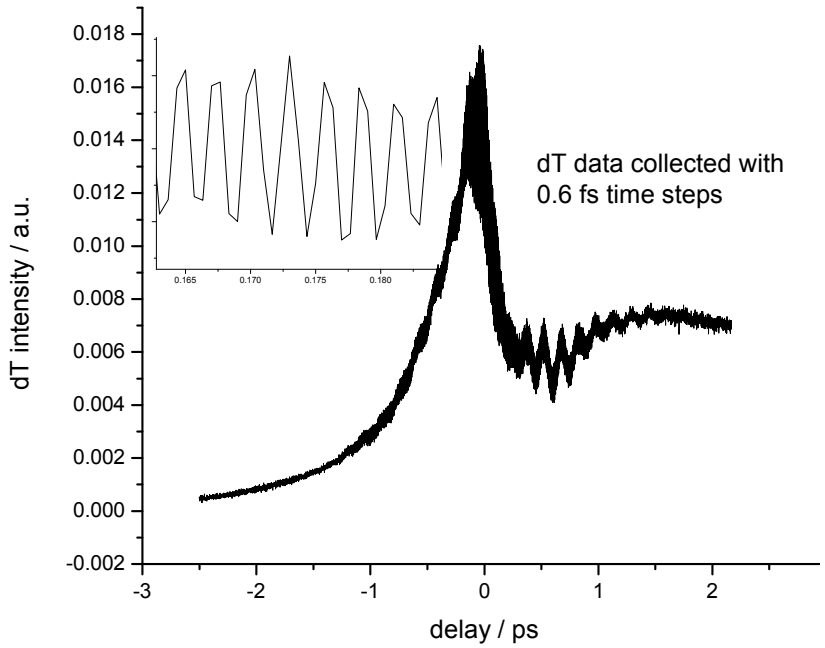

With sufficiently small step size, the differential transmission measurement is clearly resolved with no aliasing problems. These data were collected with 0.6fs step size, which allows measurement of signals with frequency components up to 833 THz. Inset: expanded view of the high frequency component.

Figure 5.23: Well resolved high frequency components in dT

aliased in the (relatively) low frequency measurements we had performed. The previous measurements that had appeared noisy most likely had perfectly reasonable signal-to-noise properties, but at each step of the probe delay scan at which we measured the differential transmission power we sampled a signal occurring at a different phase. Unaware of the fast periodic nature of this signal, we had erroneously concluded there was some source of noise overwhelming our measurement.

In order to eliminate this effect, a TeO2 AOM was placed in the combined pump beam bath (i.e., after the beam splitter that is the exit port of the Mach-Zehnder interferometer) and used to shift the pump beams by 80MHz. This AOM was driven with an RF source produced with an HP 8657A signal generator and amplified using a discrete Minicircuits amplifier. The drive frequency was not chosen for any scientific reason, but simply because it was the center of the operating band for the AOM. This immediately remedied the 'problem' of the high frequency component in the differential transmission signal, and allowed us to perform measurements with a more reasonable step size – in order to resolve the high frequency component, the delay was incremented by less than half the optical wavelength of 800nm. To perform measurements that scanned the probe delay by several centimeters – the time scale necessary to extract the sub-ns population relaxation – at this temporal resolution was impractical.

We did collect 2dFTS data sets before implementing the frequency shift on the pump beams, but did not take the time to process and analyze them

since the differential transmission measurements had (to that point) appeared to indicate some significant error in the operation of the experiment. Since the 2d data is collected in a phase-sensitive manner with sub-wavelength step size, it is likely that those data sets are in fact usable, but subsequent experiments make those sets redundant. Moreover, by this point in the development of our experiment we had not yet determined the ideal powers to use for the various beams, as that step had depended upon an analysis of a cogent set of differential transmission data.

As a result of this change to the experiment, the nonlinear optical processes we probe are not truly frequency degenerate – nonetheless, on the scale of the optical frequency (˜375THz) or on the scale of the spectral features associated with the exciton resonances (few hundred GHz) this shift is not significant.

After placing an AOM in the combined pump beam path it was found to be necessary to place an identical AOM into the probe path. While this may have the advantage of inducing identical pulse dispersion in the probe beam as that which affects the pump beams, this effect is not expected to be significant at this wavelength – a quick calculation using easily available values for the index of refraction of Tellurium Dioxide as a function of wavelength suggests that the dispersion is essentially negligible for a length of material comparable to the dimensions of the crystal used in our AOM's – we expect the pulse envelope to increase by approximately a tenth of a percent for a 150 fs duration pulse– the probe AOM was added for the more prosaic reason

that it allowed us to match the probe optical path length back to that of the pump beams. Without this second AOM it was impossible to observe an autocorrelation of the pulses, indicating that the pump AOM had extended the pump beam optical path too far to be compensated by translating the stages.

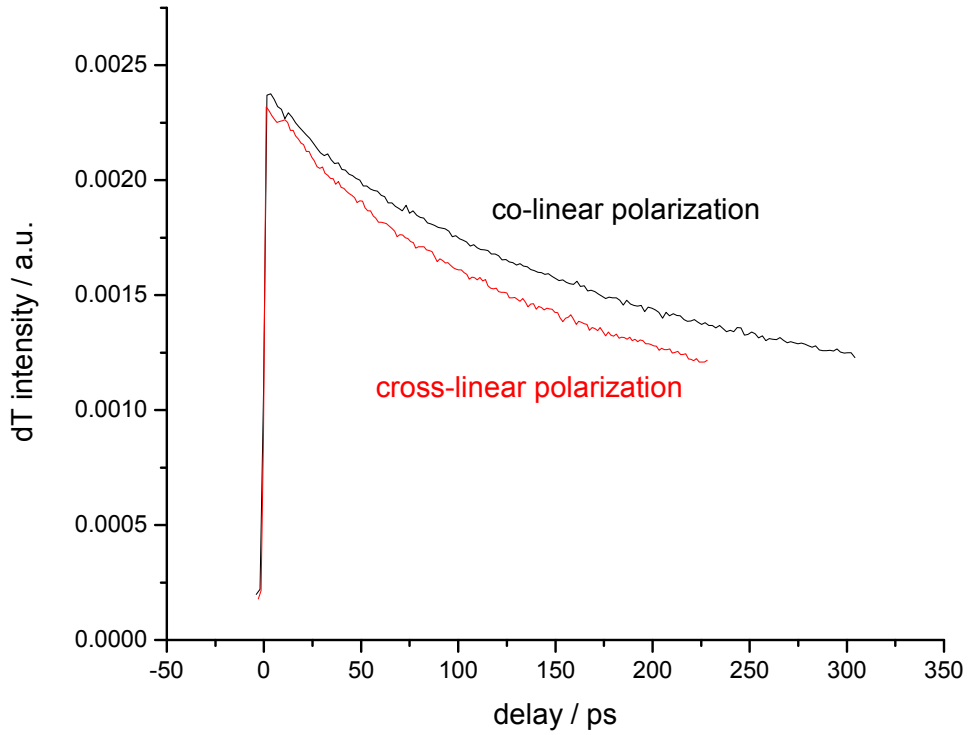

Differential transmission measurements performed on GaAs multiple quantum well samples, using parallel and perpendicular linearly polarized light. The decay of the differential transmission signal is well fit by a simple exponential function on this timescale, where the early time turn-on and signal rise is neglected.

Figure 5.24: Lifetime measurements using linear polarization

After the AOM was used to shift the pump beam power, differential

transmission measurements were taken using the lock-in amplifier. For either parallel or perpendicular linear polarizations, there is an exponential decay that can be used to extract the population relaxation time. There is additionally, however, a spike or peak that appears in the differential transmission measurements near the time when the two pulses overlap. This early time has been observed elsewhere in sub-picosecond experiments. The effect is sometimes referred to as a correlation spike, and is seen in various different media.

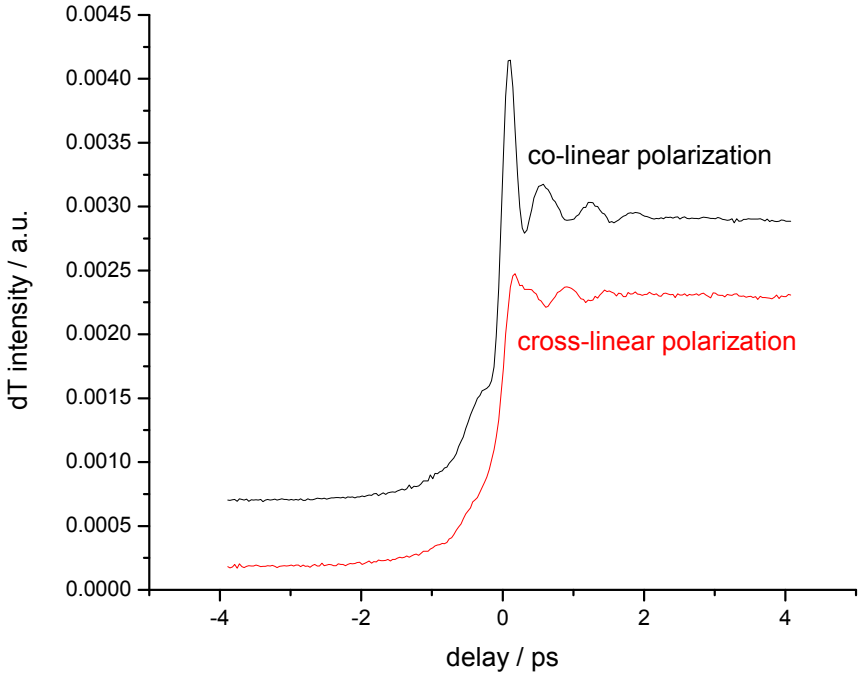

Differential transmission measurements performed on a GaAs multiple quantum well sample using cross- and co-linear polarizations. The co-linearly polarized light exhibits a strong coherence peak feature, indicating a parametric coupling of power from the intense pump beam into the transmitted probe beam.

Figure 5.25: Early time dT measurements using linear polarization

A simple explanation based on single-pulse effects is tempting, but can be shown to fail to reproduce the observed features. We outline the one-pulse argument briefly, for comparison: pulses with temporal widths shorter than the polarization decay rate $\frac{1}{T^*} = \frac{1}{T_1} + \frac{1}{T_2}$ will be spectrally broad compared to the absorption resonance. The pulse therefore has spectral components that are sufficiently far from the central frequency of the ensemble, that they do not undergo significant absorption. In this case, the pulse depletion as a function of distance traveled through the sample is substantially decreased when compared to the exponential decay predicted by the Beer's law dependence that describes most absorptive light-matter interactions [6]. This model cannot explain the coherence spike observed here, however, since this rapid transient does not appear unless the pump is present and depends upon the pump polarization state, suggesting that it is a parametric process coupling power from the strong pump beam to weak probe beam.

Shank and Ippen describe correlation spikes that occur in pump-probe measurements of organic dye molecules in solution that were studied as potential saturable absorbers for use in mode-locked lasers [337].

Those authors measured the polarization rotation of the probe pulse due to dichroism induced by a strong pump pulse to distinguish the isotropic saturation effects – due, for example, to ground state bleaching – from anisotropic saturation, which they attribute to the selective excitation of dye molecules aligned parallel to the linearly polarized pump pulse. The sharp spike that occurs in their pump-probe results is attributed to a parametric coupling be-

tween the weak probe beam and the strong pump pulse that occurs when the pulses overlap temporally. Under that condition, the interference between the two pulses produces an absorption grating that scatters a portion of the intense pump beam into the weaker probe. In liquid phase experiments it is possible to demonstrate that it is indeed an absorption grating effect and not a thermal grating by varying the solvent to one that exhibits little dependence on temperature of its index of refraction, but we cannot perform a similar test in our solid state system. Nonetheless, subsequent 2dFTS experiments strongly suggest that the formation of thermal gratings is not significant in our samples. Although one may expect that the spike shape is determined by the temporal width of the laser pulse used – the correlation spike frequently may appear comparable to autocorrelation measurements of temporal pulse width – Shank and Ippen argue that it is rather a function of the coherence of the light-matter system. The amplitude of the spike is then equal to the transmission induced by the anisotropic saturation effects of the pump – thus we should expect the correlation spike to appear roughly double to the 'next bit' of the differential transmission decay curve. This ratio is roughly correct in our experiments, although we do not expect it to be much better than an estimate or guide for the expected spike amplitude.

In a paper preceding shortly preceding that work, Shank and Auston observe a similar parametric coupling of the intense pump beam into the weak transmitted probe beam via an electron-hole plasma index grating [335]. A calculation based on the Drude model was used to provided a estimate for the

strength of the correlation spike. This result allowed the correct assignment of the population relaxation time in Germanium; previous measurements had fit the correlation spike to extract the decay time, severely under-estimating the carrier lifetime in this material. A similar correlation spike was observed in pump-probe spectroscopy of hemoglobin [339]. A much more complete theory of the correlation spike is offered by von Jena and Lessing [377] who note that the simpler models offered by Shank et al. cannot completely describe the correlation spike. They develop a much more complete model, depending upon pulse shape, the population kinetics in the excited material, dephasing and orientational relaxation. This model also obtains the result that for parallel pulse polarizations the amplitude of the correlation spike should be twice what would be observed without this effect, and notes that similar coherent features may also appear for perpendicularly polarized pulses, though their magnitude will exhibit a more sophisticated behaviour and depend on the microscopic particulars of the material. The particular shape of correlation spikes is shown to depend on the coherence length and the relaxation processes.

That work [377] also proves extremely useful from an experimental perspective, as it shows that the optimal optical alignment for a two-pulse experiment is obtained when the correlation spike is maximized – this is the metric we use in our work for fine-tuning the alignment of the pump pulses onto the spot illuminated by the probe pulse.

For further consideration of the transient coherence effects occurring in pump-probe spectroscopy, consider the density operator theoretical treatment

in [395], which considers numerous possible relaxation channels and discusses transients in both the pump-probe transmission and phase-conjugate geometry. Measurements of oscillatory coherent effects in pump-probe spectroscopy have been argued to be evidence of the influence of the Heisenberg uncertainty relationship, with the nature of the artifact determined by the relative time scales of the experimental resolution, the bleaching time, and the dephasing time [200]. Experimental observation similar to those we see here are described in the context of that theory in [348]. While the coherence spike is a problematic feature in transient absorption measurements, such as these differential transition experiments performed prior to taking 2dFT data, and is typically ignored in a density operator theoretical model, 2dFTS is able to study these early time features without difficulty [132],

Returning to our differential transmission measurements, in either the parallel or perpendicular linear polarization case, after the correlation spike has decayed there is clearly an oscillation in the transmission suggestive of coherent behaviour occurring for small probe delays. Typically, three clear periods of the oscillation can be observed before the oscillatory behaviour appears to damp out. Subsequently, the differential transmission curve appears well-fit by a single exponential function. The appearance of the oscillatory behaviour for early times suggests that this is the time period in which a 2dFTS experiment may be used to study coherent behaviour.

We also obtained differential transmission measurements for circularly polarized light. To produce circularly polarized light for the pump beams

a quarter-wave plate was placed subsequent to the beamsplitter that recombines the two arms of the Mach-Zehnder interferometer. Thus, cross-circularly polarized light for the two pump pulses may be obtained by setting the polarizers in the interferometer to produce perpendicular linearly polarized light. Co-circularly polarized light for the two pump pulses is produced by setting the polarizers in the interferometer to produce parallel linearly polarized light. There is a second quarter-wave plate used to produce circularly polarized probe light.

We show here plots for co-circularly and cross-circularly polarized differential transmission measurements. Similarly to the results for the linearly polarized experiments, there is a significant coherence spike that appears in the co-circularly polarized experimental data, a feature that again appears largely absent from the cross-circularly polarized result. Some oscillation is again observable after the coherence spike, though in the case of the cross-circulary polarized experiments it seems much weaker in amplitude. In both circular polarization cases, the amplitude of the differential transmission signal is comparable if somewhat smaller to that obtained in experiments using linear polarizations.

Some measurements were taken using a linear probe polarization to probe circular pump polarizations. In that case, the distinction between co- and cross-circular is not so significant. We note that here a coherence spike occurs, but is significantly reduced in amplitude compared to that seen for similar types of polarization. It is tempting to speculate that the peak intensity

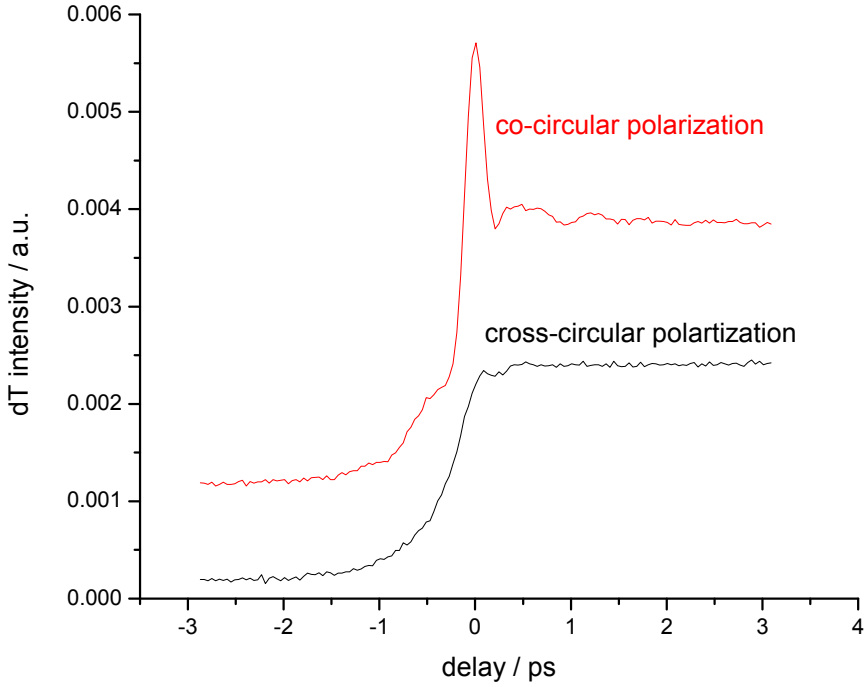

Differential transmission measurements performed on a GaAs multiple quantum well sample using either co-circularly or cross-circularly polarized light. The co-circularly polarized pump-probe measurements exhibit a substantial coherence spike during the pulse overlap.

Figure 5.26: Early time dT measurements using circular polarization

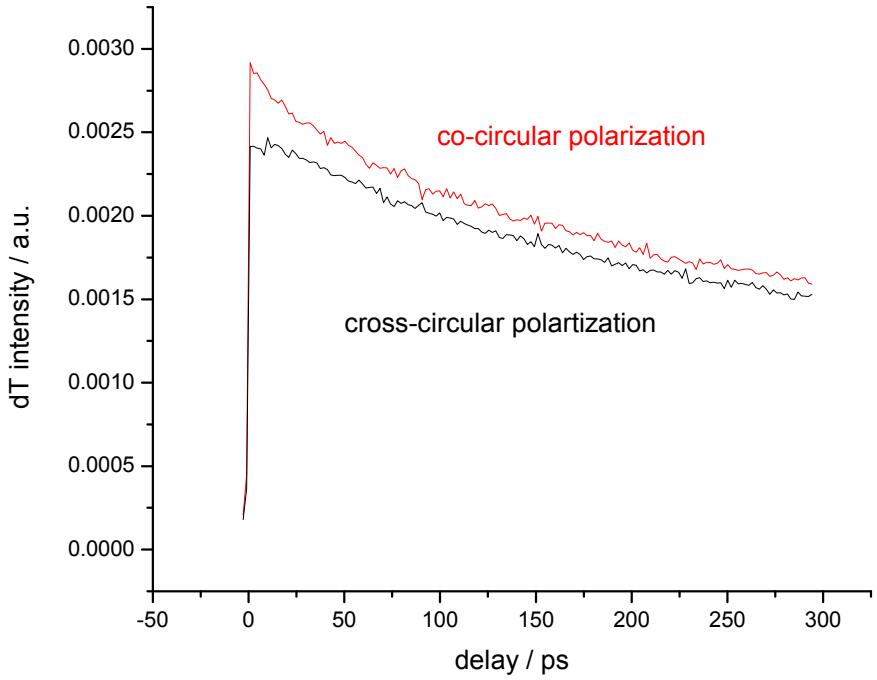

Differential transmission lifetime measurements are performed using circularly polarized pump and probe light. The polarization follows an exponential decay, governed by the population dynamics.

Figure 5.27: Lifetime dT measurements using circular polarization

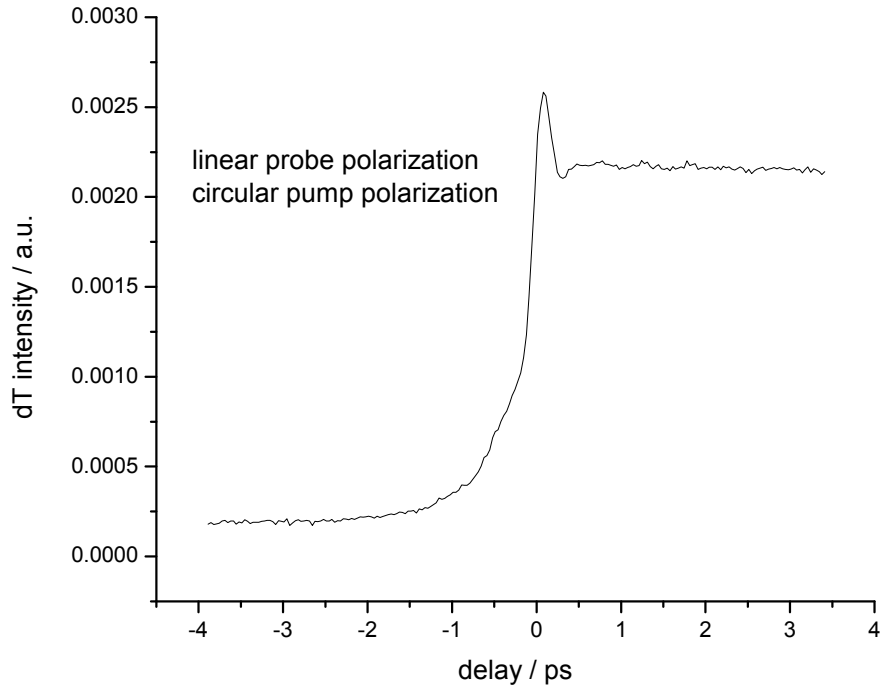

Figure 5.28: dT measurements using mixed linear and circular polarizations

is half of which is observed for the coherence spike in differential transmission experiments using only linear or only circular polarizations. That result makes intuitive sense if one considers that the linearly polarized probe light can be decomposed onto two circularly polarized beams, only one of which leads to a significant coherence spike in this system. Nonetheless, without a more rigorous analysis we do not draw any strong conclusions from these experiments.

The purpose of these experiments is not strictly scientific; instead, we use these measurements as a check that our apparatus can be controlled and the data it produces readily understood. Nonetheless, we outline a basic description of the interpretation of these differential transmission data.

The pump-probe technique relies on the third-order nonlinear polarization induced in the sample by the two pulses. Naively, it may appear surprising that this system response is a third-order effect but this can be seen readily in a density matrix treatment. In that model, the modification of the probe beam – the change in transmission along the phase-matched direction ($\mathbf{k}_s = \mathbf{k}_{pu} + \mathbf{k}_{pr} - \mathbf{k}_{pu}$) – results from two interactions with the pump pulse and one with the probe. To a first approximation the polarization in the semiconductor is proportional to $\left|AE_{pr}E_{pu}E_{pu}^* + E_{pr}^*\right|^2$, where the function A is determined by the specifics of the light-matter coupling and the second E_{pr}^* is the homodyne term due to the co-propagation of the probe beam and the electric field produced in this nonlinear interaction.

If the time scale of interest is faster than the dephasing time of the

material, it is necessary to use the semiconductor optical Bloch equations, or a more sophisticated treatment, to analyze the result of a pump-probe direction. Alternatively, if the time scale of the measurement is long compared to the dephasing time, the interpretation of experimental results may be greatly simplified by discounting the coherent effects of the light-matter interaction. This is equivalent to considering only the diagonal terms in the density matrix, which describe the occupation of the various states, and ignoring the coherences that are determined by the off-diagonal elements. In that case, assuming a two-level system, the decay of the differential transmission signal directly maps the population decay as the system relaxes to its ground state. In this limit, a pump-probe measurement reveals the population lifetime. It is tempting to look at the early time behaviour of the differential transmission behaviour as indicative of a coherent transfer of population among the various states involved, but a strict interpretation requires a more complete model. Simple models, even the simple density theoretic treatment that assumes an ensemble of non-interacting two-level systems, are typically solved analytically using Dirac delta functions to approximate the laser pulse envelope. Thus, any behaviour during or shortly after the pulse envelope cannot be strictly analyzed in that model.

5.6.9 Effects of excitation density

While performing differential transmission measurements as a diagnostic of our experimental apparatus, it was necessary to choose the excitation

density at which we wished to take data for 2dFT. As a third-order nonlinear process, the signal features should vary in amplitude as the third power of the applied electric field – or, more simply, linearly as a function of the power of each pulse that interacts only once with the sample.

We performed a one-pulse measurement to determine if we operating our experiment the appropriate conditions. Simply, a linearly polarized pulse of a certain power was focused onto the sample. The transmitted power is measured with a power meter. The reflection is not measured, but assumed to be equal to that predicted by the Fresnel equation (we expect $R \sim 0.325$) for GaAs at this wavelength. Any power not accounted for is assumed to have been absorbed by the medium and re-radiated via exciton formation and recombination. This is a crude estimate of the exciton population, but it is consistent with other measurements made in the semiconductor optics community. As such, its value is not in its predictive ability but rather its utility as a way to communicate experimental conditions to other researchers.

We performed one-pulse transmission measurements over the range 200uW to 1.5mW, and observed a linear dependence of the transmitted intensity of light over this entire range, suggesting that no significant saturation effects were occurring in our sample. The spot size was estimated using a pinhole and a translation stage, and fitting the transmitted power to a complementary error function. This provided as estimated spot size of $0.00038 cm^2$. Our multiple quantum well sample has ten periods. It is immediately obvious that depletion of the probe beam occurs in transmission, and that the exciton

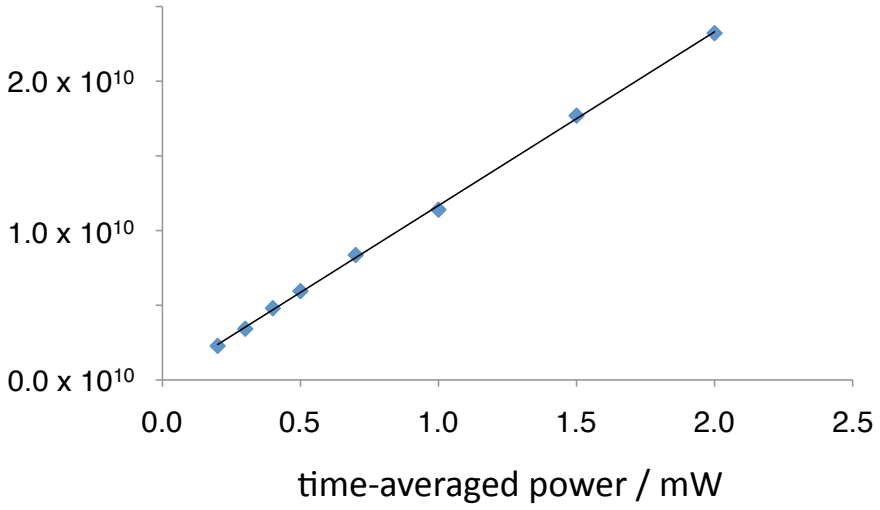

Single pulse measurements are performed to determine the absorption as a function of excitation power. The exciton population, calculated using the Fresnel equations to estimate the reflected power, appears linear as a function of power over the range used in these experiments.

Figure 5.29: Exciton density as a function of power

density in each quantum well will not be identical, thus the value we quote here is simply an approximate number.

This simple experiment would indicate that it is possible to go to even higher powers before saturation issues occurred in the material. We expect that the third-order nonlinear signal would be more intense using greater excitation power, and that the signal to noise would be improved by performing higher power experiments. Nevertheless, we actually choose a somewhat lower power for our incident pulses to make simpler the comparison to other 2dFT results (and to other nonlinear spectroscopic measurements, more generally). It would be impossible to give an exhaustive list of the parameters used in various different studies of exciton dynamics in GaAs quantum wells. We list here only a few representative works for illustrative purposes.

Other data obtained in our lab using non-collinear 2dFTS to study exciton dynamics in a multiple quantum wells used an excitation density of $\sim 10^{10}$ excitons/well/cm^2 in experiments on an 8-period GaAs quantum well sample [358]]. Other experiments in the field, such as the measurements of the heavy hole - light hole beating found in [349] and [350], used pulse fluences chosen to produce exciton densities of $2 \times 10^{10}\, cm^{-2}$. The hole-burning and four-wave mixing measurements of localization found in [176] made use of an excitation density of $10^{10}\, cm^{-2}$ per well in their demonstration of a mobility edge at the center of the exciton line in GaAs multiple quantum wells. Quantum control studies have pursued the possibility of developing experimental control of the phase of population oscillations in GaAs quantum wells at exciton densities of

$10^{10}\,cm^{-2}$.

A great number of experiments have been conducted to study the effect that excitation density has on the dynamics of excitons in quantum confined systems; the measurements described in [385] used time-resolved three-pulse four-wave mixing to separate the contributions to the optical response from homogeneous and inhomogeneous broadening of the exciton resonance. These measurements were taken at a range of excitation densities, from below $8 \times 10^7\,cm^{-2}$ per layer to above $5 \times 10^9\,cm^{-2}$ per layer. Measurements using excitation densities from $4 \times 10^6\,cm^{-2}$ to over $10^9\,cm^{-2}$ to study the threshold for onset of significant exciton-exciton interactions were reported in [23].

The measurements of Raman coherence and two-exciton correlations in quantum wells reported in [167] used an excitation density of $1.4 \times 10^{10}\,cm^{-2}$. The polarization of four-wave mixing emissions from quantum wells was completely characterized in [286] at excitation densities in the range from $1.5 \times 10^9\,cm^{-2}$ to $2 \times 10^{10}\,cm^{-2}$.

In order to make comparison to the existing body of literature relatively simple, we perform 2dFTS experiments using time-averaged pump powers of 1mW. Ideally, four-wave mixing experiments are performed with equal or roughly equal powers in each of the three excitation beams to maximize the signal-to-noise of the measurement [247]; however, we resolve a (relatively) weak four-wave mixing emission that co-propagates with the probe beam. A square-law detector that is optimized for the dynamic range we expect to observe for four-wave mixing signals would typically saturate at these powers.

Thus we reduce the probe beam intensity, using a time-averaged power of 100 uW. It is a common practice in pump-probe experiments to use a probe that is approximately an order of magnitude weaker for similar reasons. We note here that our later work, using a monochromator and amplified photodiode in conjunction with a sophisticated modulation scheme rather than the spectrometer-CCD setup used for these 2dFT measurements, we were able to adjust the probe beam from 100 uW back to 1 mW, placing it on equal footing with the pump beams. No adverse effects were observed, due to the ability to perform phase-sensitive detection in conjunction with the AOM-based modulation method.

All the differential transmission data presented thus far, and the 2dFT data that we present subsequently, was recorded with 1 mW in the static pump beam, 1 mW in the dynamic pump beam, and 100 uW in the probe beam unless otherwise explicitly noted.

The appeal of performing 2dFT on GaAs quantum wells as a function of excitation power is obvious, as it may provide some insight into the relative strength of those many-body effects that dominate the nonlinear response of the exciton resonances. This study has not been performed, to the best of our knowledge; here, instead, we rely on a theoretical model for the lineshape based on a modified mean-field theory treatment of exciton-exciton correlation to assess the contributions of the different many-body effects.

5.6.10 Demonstration of partially collinear 2dFTS with linearly polarized light

We perform partially collinear geometry 2dFTS on semiconductor samples for the first time.

A single 2dFTS two-dimensional spectrum takes approximately 40 minutes of time to collect the raw data, and an additional few minutes of computer analysis at a later date. To produce a spectrum, the zero-delay positions of the τ and T delays are found. A given T value is chosen and the probe stage moved to the appropriate position. The precise T delay of interest is generally determined by studying a simpler, non-spectrally resolved pump-probe differential transmission measurement; we generally look at points along the differential transmission curve that we expect to be of interest in understanding the coherent dynamics of the exciton system.

Once the T delay is set, the probe stage is no longer moved. The dynamic pump stage is moved to its zero delay position, and the servo electronics are engaged to actively stabilize the Mach-Zehnder interferometer. The process of collecting data as a function of τ now commences: a number of spectra are taken with the pump beams alternately open and blocked and the difference spectra are averaged together to produce a single dT/T-esque spectrum. The probe spectrum with no pump beams on is also saved. Then, the computer controlling the experiment uses TTL control of the servo to unlock the interferometer. The computer instructs the stage controller to move the τ delay stage in the dynamic pump arm of the interferometer. Another TTL signal

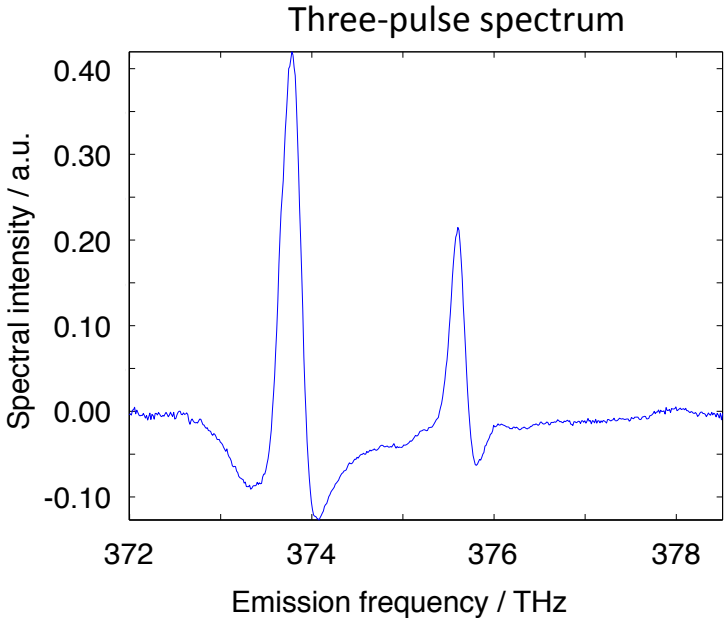

Spectra are collected at each τ delay for a set of 2dFTS raw data. Shown here is the τ=0 spectrum.

Figure 5.30: Three-pulse spectrum

re-locks the interferometer, and the data collection cycle repeats. As noted, analog voltage levels are also recorded for the output of the interferometer photodiode, the output of the loop filter used in the servo, and 1/10th the voltage used to drive the piezo. Sudden jumps in these data are taken as indicators of phase slips and invalidate the data taken after that point. In order to compensate for possible deviations in the positioning accuracy of the delay stage, the target position for each τ step is adjusted with feedback derived from the servo's loop filter.

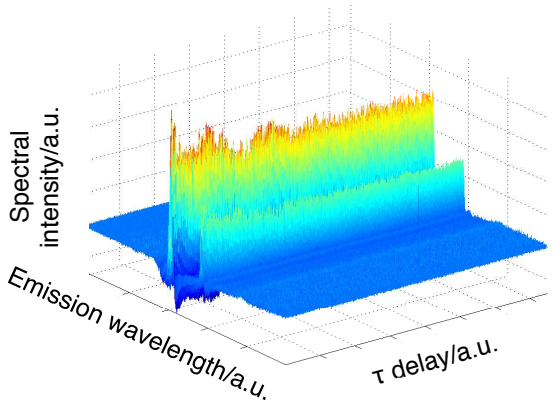

A minimally pre-processed 2dFTS data set. Shown here, the raw set of spectra have been divided by the probe transmission spectrum.

Figure 5.31: Raw 2d data

As a demonstration of our experiment, 2dFTS spectra were collected with various combinations of linear polarizations for the three pulses. Consider first the raw 2dFTS data, plotted in a mixed frequency-time space, and abruptly truncated at the end of the τ scan prior to the decay of the pump-

probe background signals to zero. As noted, it is not practical to collect densely spaced spectrally resolved data over a τ scan sufficiently long to allow the emission to decay completely to the background level. The differential transmission measurements we perform on this sample suggest a lifetime of hundreds of picoseconds; it would be impossible to repeatably scan the interferometric delay τ over that kind of time scale without experiencing phase slips due to laboratory noise. Moreover, even as $\tau \to \infty$, the signal detected in this direction would not decay to a zero, due to the presence of the pump-probe artifact arising from the static pump-probe interaction, which does not depend upon the τ delay. The long time dynamics are not of particular interest to us, however, as they are fairly accurately modeled by the single exponential dynamics that have historically been used to model population decay. More interesting are the coherent behaviour of the excitons that occurs in the first few seconds, prior to any dephasing processes substantially affecting the excitonic coherences. As such, only the first few picoseconds (as a function of τ delay) of the four-wave mixing signal are of interest to us. We typically collect only 1500 spectra in a single experiment. The resulting hard cut-off will introduce ringing artifacts into the 2dFTS spectrum if no time domain windowing procedure is performed. We discuss the processing and analysis of these data elsewhere in this thesis, but note here for specificity that the τ scans used for these data (slightly greater than 3ps in duration) would broaden a Dirac delta function spectral feature to approximately 0.316 THz along the ω_τ axis.

The processed 2dFTS data are displayed as well. These data are taken

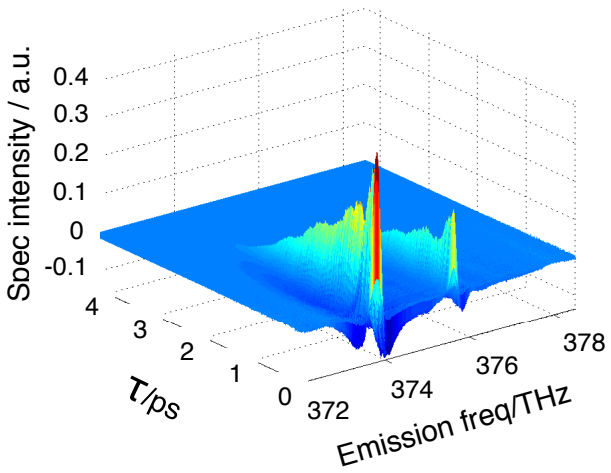

Figure 5.32: Processed 2d data

with co-parallel, linear pump polarizations and a co-parallel linear probe polarization – essentially, the simplest configuration possible. As noted elsewhere, the lineshape observed here for a GaAs quantum well sample is substantially different from that found using a non-collinear geometry 2dFTS experiment, because the results here simultaneously record the re-phasing and non-rephasing pathways. Qualitatively, we observe the diagonal features corresponding to the light hole exciton and heavy hole exciton resonance, and off-diagonal features representing coupling between those states. Unlike our non-collinear geometry experiments, these data do not provide clear evidence of the presence or absence of coupling for spectrally resolved excitons, since the sample studied was not prepared appropriately to observe the sharply split doublets resulting from monolayer fluctuation in the well thickness. Instead,

these data are useful for a qualitative modeling of the lineshape of a coupled set of resonances. Our collaborators have had some success reproducing the lineshape observed in these results, which has so far proven to be simpler to simulate than the experiments performed using circularly polarized light – perhaps counter-intuitively. In particular, simulations have managed to correctly reproduce the zero contour separating positive from negative features on the diagonal peaks. This diagonal has been studied previously as it relates to the shift of the three pulse photon echo peak shift, but we do not make a direct connection to those behaviours here – for an individual exciton resonance, a real photon echo is not even necessarily expected, although virtual echoes may still persist. All of the features in the partially collinear 2dFTS plots exhibit much more vertical, ω_τ broadening; part of this is attributable to the relatively short τ scans used here and suggest the utility of performing longer duration experiments to determine to what extent this broadening is due to systematics rather than dynamics of the exciton system. The off-diagonal feature and diagonal feature at greater ω_τ exhibit more pronounced elongation along this axis that is due to absorption from free carrier states energetically higher than the light hole exciton resonance, which relax to the lower energy light hole and heavy hole resonances. This process is rapid, but some data suggest these processes could be studied with 2dFTS. Due to the phase-twisting that occurs during pulse overlap it may be difficult to separate the real effects from the early time artifacts.

We also note here that the presence of absorption from free carrier states

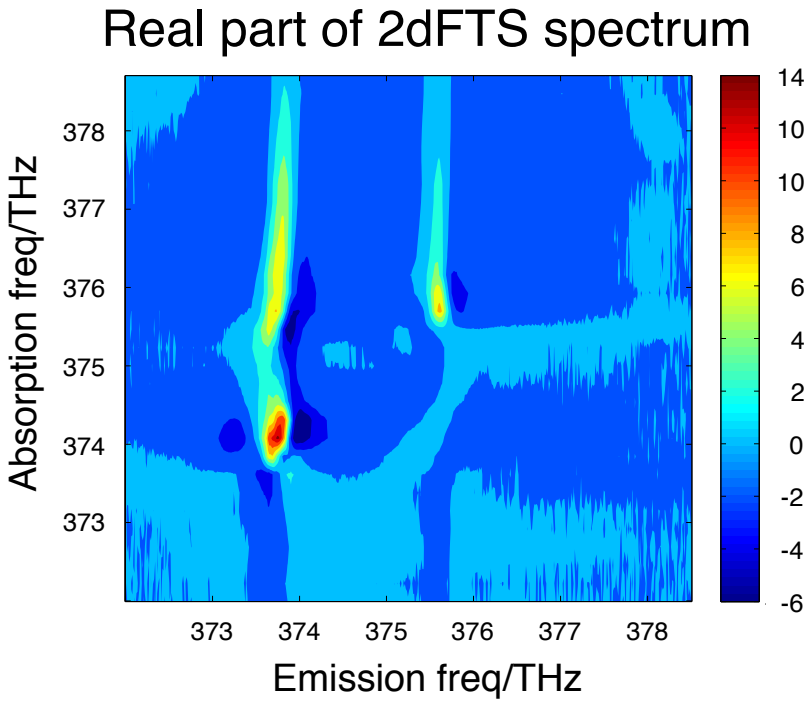

The real portion of the 2dFTS spectrum obtained for parallel, linearly polarized light. The heavy hole exciton and light hole exciton resonance are visible along the diagonal, as is a coherent coupling cross-term indicating absorption at the higher energy and emission at the lower energy. The spectrum shown here is a COSY analogue.

Figure 5.33: Real part of 2dFTS spectrum

can be significantly reduced by pulse shaping in the frequency domain. A simple 4f spectral filter device has been designed to cut out the higher frequency components of the Ti:Sapph pulse used in our 2dFTS experiments, but has not yet been constructed. While this would increase the pulse duration and thus restrict the early time behaviour that can be studied without phase-twisting the peaks (thereby mixing the imaginary and real parts of the spectrum), it would also drastically reduce the influence of free carrier states. As noted in our description of four-wave mixing experiments studying dephasing processes in semiconductors, these electron-hole pairs will have a substantial dephasing effect on the exciton system (although we emphasize that these are electron-hole pairs, not bare electrons or bare carriers, which are known to be far more destructive to exciton coherences).

We collect extensive data as a function of T for the various linear (and circular, q.v. *sub*) polarization configurations. Although the modified mean field theory our collaboration is using to study these systems cannot yet handle $T \neq 0$ relaxation, these data may prove valuable as that theory is extended. Moreover, it is possible that a relatively simple analysis may be useful to study the oscillation of the cross peaks corresponding to coupling to study the quantum beating that is also observed in the simpler differential transmission experiments. Little fundamentally new science can be gained from previous experiments that study light hole - heavy hole exciton coupling in semiconductors, and we do not pursue that avenue presently, neglecting it in favour of studying more sophisticated systems. There are also risks in looking for

oscillations in these peak heights if there isn't a well developed theory concurrently available to model their behaviour as a function of T, as artifacts may be mistakenly identified as significant physical processes. It is also possible that spectral diffusion of the exciton system might be revealed with these 2dFTS measurements, since the shape of the spectral features is expected to broaden perpendicular to the diagonal with increased mixing time T. More data would be necessary to make a significant scientific statement about these effects.

We repeat for emphasis that the linear polarization 2dFTS experiments shown here (and similarly for the circularly polarized experiments we also performed), any arbitrary polarization configuration may be used for the three pulses exciting and probing the sample. Previous 2dFTS work on semiconductors was performed using non-collinear phase matching geometries, which could not use cross-polarized pump pulses due to the need to fix an overall, global phase ambiguity using a spectrally resolved transient absorption experiment – the two-pulse experiment used to set the overall phase cannot reproduce the same possible polarization configurations available to the three plus one (local oscillator) pulse experiments used to generate the 2dFTS plots. While an all-optical method has been demonstrated recently to find the relative phases of all of the pulses used in the non-collinear 2dFTS experiment [53], that technique still requires an additional, sophisticated measurement to correctly resolve the phase ambiguity. We note here that our experiments assumed that the pulses that were correctly zeroed in τ delay were also in phase; this assumes that the optical path lengths through the dispersive ma-

terials comprising the lenses, etc, do not differ substantially between the two interferometer arms. This is an untested assumption, and could introduce phase ambiguity into the experiment and confuse the separation of real and imaginary parts of the 2dFTS spectrum. Fortunately, we have placed AOM's into each beam path, which permit independent control of the amplitudes and phases of the probe, static pump, and dynamic pump beams; in future experiments these will permit us to directly observe and control the phases of the three pulses used for these experiments. We have already demonstrated this control in two pulse differential reflectivity measurements performed on quantum well samples.

5.6.11 Demonstration of exciton selection rules using circularly polarized light

As noted, one of our motivations for constructing the partially collinear 2dFTS apparatus was to perform experiments with arbitrary polarization configurations, principally to provide data used to further develop a modified mean field theory for exciton dynamics. As a first proof of principle, the partially collinear geometry is used to consider selection rules for exciton transitions.

To perform 2dFTS with light of a particular helicity, two quarter wave plates are used to produce circularly polarized light. One is placed after the Mach-Zehnder interferometer that produces the pump pulse pair, while the other is placed in a convenient location in the probe beam path after its half wave plate and linear polarizer. To change from one circularly polarized state

to the other the wave plates are not altered, but the linear polarizers prior to the plates are rotated by $\pi/2$. After the quarter waveplates, the only optic other than steering mirrors is the focusing lens prior to the sample.

A waveplate alters the phase relationship between two perpendicular polarization components for some incident ray of light, exploiting crystal anisotropy to create a fast axis and a slow axis for orthogonal polarization states. In a typical quarter wave plate, the crystal is cut so that the optic axis is parallel to the optical surface. If incident light is linearly polarized at a 45 degree angle to that axis, it can be decomposed onto a basis of linear polarization states parallel and perpendicular to the optic axis. The indices of refraction experienced by light propagating along these directions will be different; thus, one polarization component will propagate through the medium faster than the other. As a result, a phase shift is introduced between the two components. While the incident linear light has a 0 radian phase shift between the two components, the transmitted light will exhibit a $\pi/2$ phase shift between the two linear states. As a result, the electric field co-propagating in the frame of the light is constant in magnitude, but rotates about the direction of propagation – this is a circularly polarized ray of light. To ensure that the light is circularly polarized rather than in some general helical state, careful alignment is necessary to ensure that the waveplate's optic axis is aligned at a $\pi/4$ angle to the linearly polarized light. Like most optical processes that do not exploit magnetic effects, the process is symmetric and permits circularly polarized light to be converted back into linearly polarized light.

In these measurements we did not determine if the light was left- or right-hand circularly polarized. We can determine whether it is in one or the other state, determined by which linear polarization is used to create the circularly polarized light. We label the beams used in circularly polarized experiments as A or B to distinguish between them. For brevity, 2dFTS experiments are labelled (X, Y, Z) to indicate an experiment using X polarized light for the dynamic pump, Y polarized light for the static pump, and Z polarized light for the probe beam. These data were taken with the same, standard powers used for the linearly polarized experiments, 1.00 mW in each pump beam and 100 uW in the probe beam.

2dFTS experiments have previously been performed in a non-collinear geometry to study selection rule physics in similar GaAs quantum wells [411]. There, a theoretical model was used to describe features in the real part of the observed 2dFTS spectrum (due to the $\pi/2$ phase shift between the emitted field and polarization induced by the ultrafast laser pulses, this corresponds to the imaginary part of the nonlinear susceptibility); these experiments concentrated on isolating the biexciton correlations by suppressing the single exciton features with cross-polarized excitation pulses. This measurement used an additional spectrally resolved differential transmission experiment to correctly phase the ambiguous 2dFTS spectrum produced by the non-collinear experiment.

Based solely on the spin sub-states of the valence and conduction bands, no significant coupling of light hole and heavy hole exciton resonances should

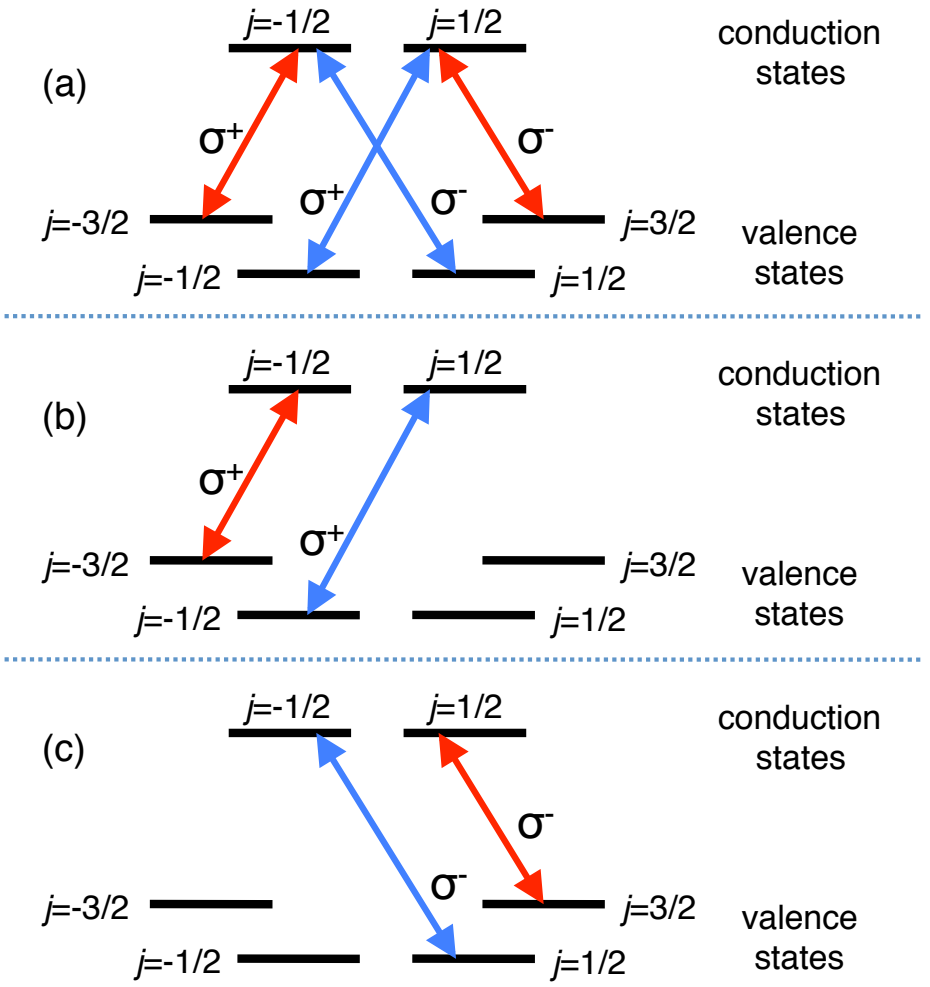

The exciton energy level diagram (a), showing the polarizations that couple the states in the conduction and valence bands. Heavy hole excitons are indicated by the red arrows, while light hole excitons are indicated by blue arrows, in reference to their higher energy. Diagrams are also shown for co-circular excitation (b), (c), where no common states are present. In either of these cases, there no coherent coupling is expected without considering many-body physics effects that are not included in this simple model.

Figure 5.34: Exciton energy diagram and coupling

be expected for co-circular excitation. Nonetheless, the coupling features are readily observed in our co-circular spectra; this suggests that the many-body interactions absent from that simplest model for exciton energy levels are responsible for the appearance of these cross-peaks. This result is comparable to previously observed coupling for co-circular 2dFTS measurements performed in a non-collinear geometry [411] and other spectroscopic techniques [122], [352], [349]. Only theories treating Coulomb correlations beyond the Hartree-Fock approximation correctly predict the strong off-diagonal features coupling the light and heavy hole exciton resonances in this system. The combination of Hartree-Fock interactions, Pauli blocking, and the Coulomb correlations among excitons is necessary to provide the correct line shape, including the free carrier absorption features that elongate along the ω_τ axis.

This previous 2dFTS work in the non-collinear geometry [411] was unable to produce properly phased 2dFTS spectra because of its reliance on an additional experiment to properly phase the measured two-dimensional spectrum. As such, only magnitude data were available. We can produce properly phased 2dFTS spectra with cross-circular polarization configurations, but lack a sophisticated model with which to analyze these results. As such, we simply consider the qualitative effects observed in the absolute magnitude spectra, in parallel to previous results.

Our experiments are capable of arbitrary polarization configurations. We note, however, that the cross-polarized pump experiments performed with $T \sim 0$, and indeed, all of the experiments performed without all three pulses co-

circularly polarized, produce 2dFTS spectra with significantly weaker features that are, in some configurations, not even apparent on the same scale as those present in the co-circular spectrum. For some combinations of the circular polarization states, the features will be suppressed by an order of magnitude compared to the spectral features present in co-circular excitation 2dFTS – although some resonances and couplings may still be observed.

To first order, then, this result is reasonably well understood in the context of the simplest model of exciton dynamics, absent any coupling of the exciton states. In that case, the 2dFTS partially collinear experiment with any of the pulses cross-circularly polarized is essentially an incomplete 2dFTS experiment – no intense, coherent, phase-matched signal is expected if one of the pulses fails to interact with the exciton population due to its cross-circular polarization. In other words, it's almost as if the experiment were missing one of its pulses, or if one of the pulses were detuned from resonance and thus returned a null spectrum.

Certain cross-circular polarization combinations do produce reasonably well-resolved features, however. Of course, both co-circularly polarized pulse configurations produce strong 2dFTS features both on the diagonal and off; we note that one all co-circular polarization configuration (type (B, B, B) in our jargon) produces stronger features than the other (type (A, A, A)).

It may be expected that experiments where the first two intense pulses are co-circular and the probe pulse is cross-circular result in stronger, more clearly resolved features than those observed with two cross-circularly polar-

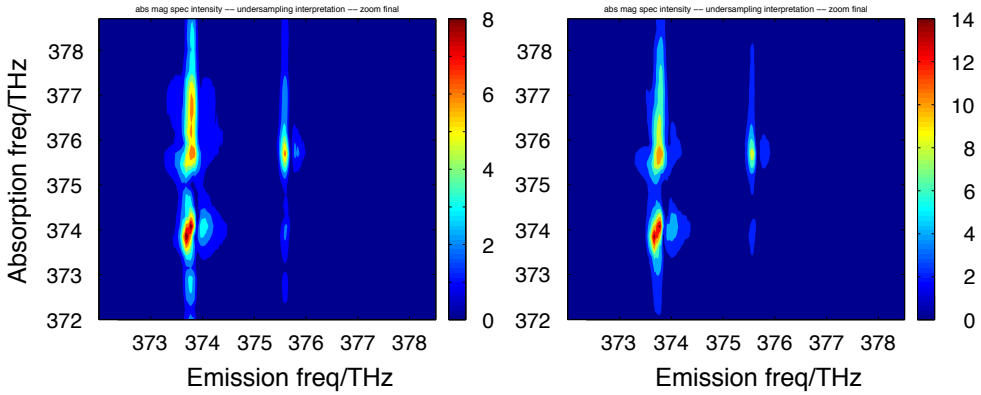

Absolute magnitude of the 2dFTS spectra for <A,A,A> (a) and <B,B,B> (b) co-circularly polarized experiments. The <A, A, A> spectrum is taken at *T*=0.060ps probe delay, while the <B,B,B> spectrum is taken at *T*=0.079ps. The co-circularly polarized experiments result in the strongest 2dFTS features, emphasizing the significant – indeed, dominant – role that the many-body physics play in this system.

Figure 5.35: Co-circular absolute magnitude 2dFTS spectra

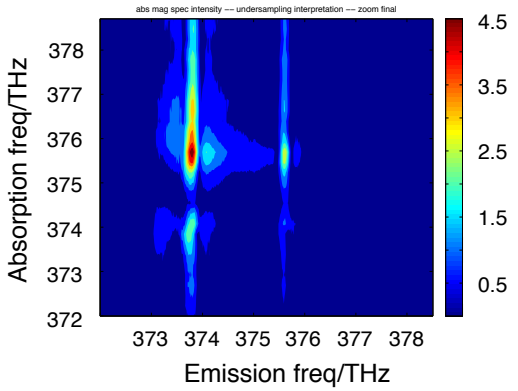

Absolute magnitude 2dFTS results for circularly polarized light, performed with <A,A,B> polarization, T=0.45 ps. The cross peak are comparable in magnitude to features seen in co-circular experiments, but the diagonal features are significantly reduces. In particular, the heavy hole exciton resonances absolute magnitude is quite small.

Figure 5.36: Mixed circular absolute magnitude 2dFTS spectrum

ized pump pulses, with a probe pulse co-circular with either pump. We note that (A, A, B) produces very strong signals, which are essentially comparable in overall strength to those found for (A, A, A), albeit with a far dominant cross-peak corresponding to light hole/free carrier absorption and subsequent heavy hole emission. In this (A, A, B) spectrum the diagonal terms are suppressed compared to the strengths seen in the (A, A, A) or (B, B, B) spectra – here, light hole diagonal feature is moderately strong but the heavy hole diagonal resonance is strongly suppressed. It is not immediately clear why this should be the case, since the (A) circularly polarized light should couple to both the exciton resonances. Further study of this weakening of the heavy hole exciton is of interest, but careful attention must be paid to replicating the

laser tuning conditions precisely, as well as collecting data at a large number of T delays to account for the effect of coherent transfer of population, and to ensure that this phenomenon (previously observed) is not responsible for the apparent polarization selection physics seen here. Indeed, this problem may be well suited to analysis using a 3dFTS experiment that could better visualize the coupling features.

(B, B, A) circularly polarized light also results in moderately strong features, though not as intense as those observed for the (A, A, B) experiment; this may seem somewhat counter-intuitive given that the (B, B, B) experiment results in stronger features than (A, A, A) co-circularly polarized pulses, but it may be that it is the final interaction of the probe light with the sample that determines the magnitude of the 2dFTS spectral features. That argument is supported by the (B, A, B) spectra possessing stronger features than the (A, B, A) spectra. It is not, however, contradicted by the (B, B, A) spectra possessing stronger features than the (A, B, B) spectra. Interestingly, the (B, B, A) experiment seems to have a turn-on effect, where the early time spectra (we show here a result for $T = 0.46$ ps) is somewhat weaker and noisier than one taken at later time ($T = 3.9$ ps here). Further data – in particular, densely spaced data as a function of T – are needed to study whether or not this is a coherent effect.

We similarly note an unusual time dependence for the (B, A, A) spectrum, where a negative T spectrum contains stronger features than those taken with $T > 0$.

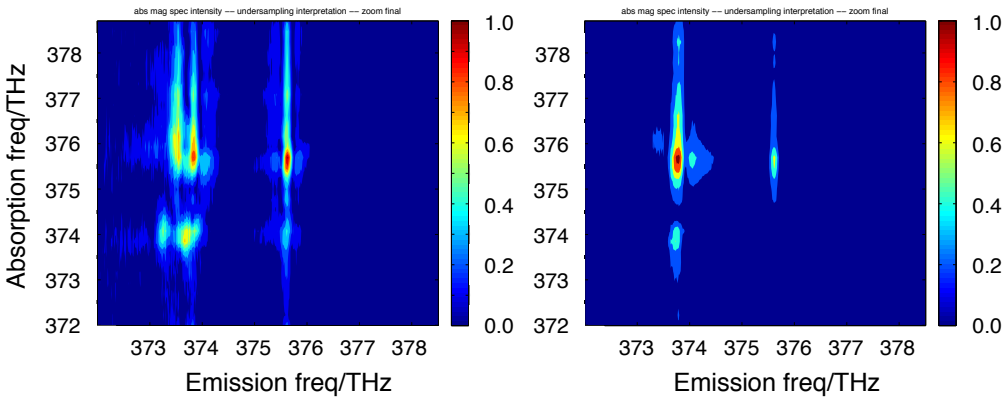

Absolute magnitude 2dFTS spectra recorded for the <B,B,A> circularly polarized combination, at *T*=0.46 ps (a) and *T*=3.9 ps (b).

Figure 5.37: Mixed circular absolute magnitude 2dFTS spectra - 2

In general, for non-cocircular experiments, the cross peak above the diagonal, indicating light hole absorption and heavy hole emission, seems to be enhanced relative to the other spectral features. This suggests a particular mechanism by which the excited populations communicate.

Further analysis is clearly necessary to understand these features. We collected data for a moderate number of T values, with the assumption that it may prove useful once the theoretical treatment used to study our other results develops the ability to properly model $T \neq 0$ relaxation dynamics. These preliminary spectra may suggest that spectra taken with cross-polarized pulses require time for the coupling between the separately excited populations to occur probabilistically, while some particular cross-polarized configurations permit $T = 0$ coherent coupling. Careful analysis of the behaviour as a function of T is needed.

5.6.12 Reflection 2dFTS experiments

Having performed experiments on GaAs quantum well samples in a partially collinear geometry, it becomes immediately obvious that reflection mode experiments are also possible. In this case, the four-wave mixing emission again simply co-propagates with the probe beam, albeit with the reflected component rather than the transmitted part. There is an obvious disadvantage to studying reflected four-wave mixing signals, as they are inherently weaker than those collected in transmission experiments; nonetheless, many complicated structures cannot be studied in a transmission geometry at all. We consider this topic at greater length in the next chapter; here, we simply present 2dFTS reflection mode data as a proof of concept.

While the multiple quantum well samples examined here are certainly amenable to spectroscopic measurements in a transmission geometry, they are used to demonstrate this technique. We perform (B, B, B) co-circularly polarized 2dFTS experiments on a GaAs/AlGaAs multiple quantum well sample, using 1.00 mW for the pump beams and 100 uW for the probe beam.

The lineshape revealed in these plots is more complicated than what we observe for 2dFTS in transmission measurements. This is not due to any systematic error in the experiment, it is simply a result of the nature of the emission from this sample. Each quantum well in the 10 period sample emits a four-wave mixing signal. Each of these emissions has a different phase, related to its depth in the sample and the distance along the optical path the incident pulses must penetrate to reach that well. Moreover, while in principal

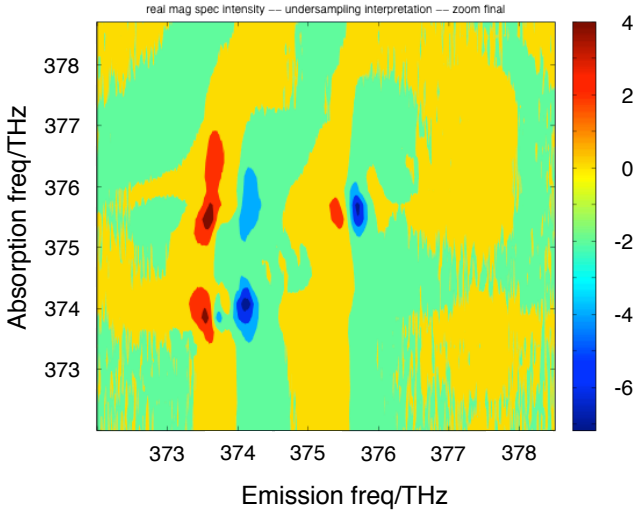

Real part of a 2dFTS spectrum of GaAs multiple quantum well obtained in reflection geometry using <B,B,B> circularly polarized light.

Figure 5.38: Reflection mode 2dFTS spectrum

a weak reflection from the interface of each quantum well could provide a heterodyne field, in reality the detected signal is proportional to the product of the individual four-wave mixing emission from each well and the strong first reflection of the probe beam off the front surface of the multiple quantum well sample. Since each four-wave mixing emission has a non-trivial phase relationship with that first reflection, the coherent sum of all of these emissions has a complicated spectral structure. Since we do not have any real control of the sample structure and can only estimate the optical path travelled by the incident and reflected beams, we do not attempt to extract substantial information from these plots. Instead, we simply note that this is the first time 2dFTS has been demonstrated in a reflection geometry. We reported this result previously this year [115].

2dFTS in a reflection geometry is a promising techniqe, as it may obviate restrictions on optical density due to signal distortion that limit the use of transmission mode experiments [409]. The non-collinear\BOXCARS geometry that has previously been used to perform 2dFTS measurements on semiconductor samples is not easily adapted to perform properly phase-sensitive measurements in a reflection geometry, but in the partially collinear geometry used here this extension is trivial due to the co-propagating probe field that acts as a local oscillator. We consider the phase effects of this homotime signal subsequently in our chapter on a novel four-wave mixing spectroscopy experiment.

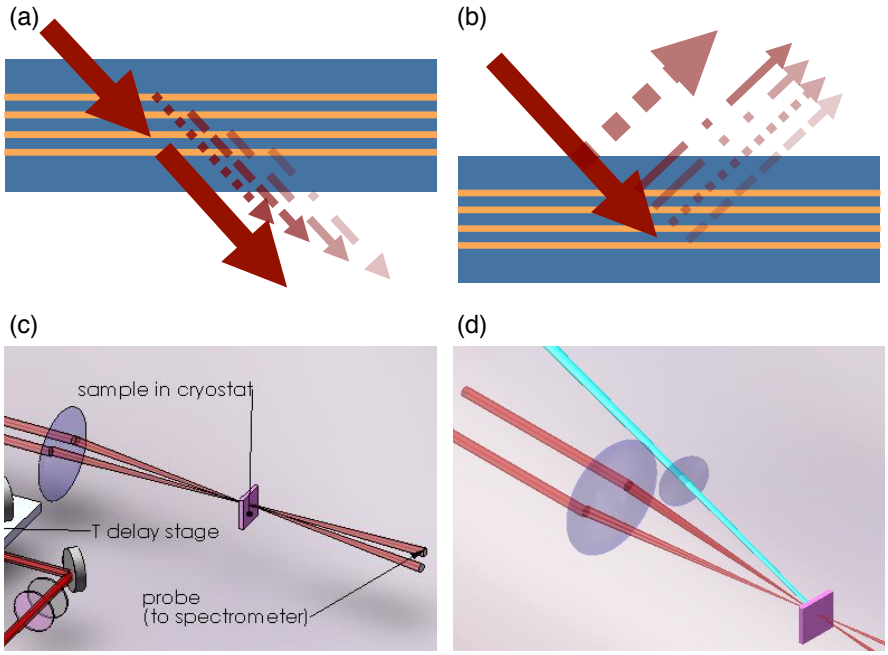

2dFTS performed in transmission (a), (c) and reflection (b), (d) geometries. In transmission mode, the four-wave mixing signal from a structured sample maintains a trivial phase relationship with the co-propagating probe beam (a) that acts as a local oscillator, whereas in the reflection experiments there is a complicated relationship among emission from various depths within the sample and the strong first reflection of the probe beam (d). This model for the reflection experiments does not consider phase mismatches between the polarization induced in the reflection geometry and the in-bound probe beam.

Figure 5.39: Phase in reflection mode 2dFTS

5.6.13 Miscellaneous extensions

Performing 2dFTS on semiconductors in this partially collinear geometry permits interesting extensions of these measurements; indeed, these reflection geometry experiments are the first such extension of conventional transmission measurements. Reflection 2dFTS allows the study of samples that cannot be probed in transmission, whether simply due to high optical density or opaque substrates – or more scientifically interesting, allowing the study of samples that cannot be probed with a completely nc2dFTS experiment due to a selection rule restricting the $\chi^{(3)}$ response of the system. Partially collinear 2dFTS permits nonlinear experiments that depend on angle-tuned momentum transfer effects, as we will describe at length in a subsequent chapter.

The partially collinear geometry is also a step toward performing 2dFTS in a single beam, completely collinear geometry that would permit the study of systems not amenable to a non-collinear experiment. For non-collinear beam geometries, if the characteristic length scale of a sample is less than the wavelength used to excite it, the translational symmetry of the system breaks down and a coherent emission will no longer be radiated along a phase-matched direction. Fully phase stabilized 2dFTS measurements of a single quantum emitter remain a significant experimental challenge.

Chapter 6

A novel coherent spectroscopy technique

6.1 Introduction to and motivation for a new experimental program

6.1.1 Coherent spectroscopy in reflection mode

We have previously demonstrated 2dFT spectroscopic measurements on a semiconductor nanostructure in a reflection geometry – albeit on what may be considered an extremely simple nanostructure: the multiple quantum well. As noted, these measurements are not technically challenging to perform in the partially collinear 2dFT geometry, since the reflected probe beam and co-propagating four-wave mixing emission is easily collected, collimated, coupled to a fiber and transmitted to a spectrometer for acquisition in a manner completely analogous to that used for the transmission mode 2dFT measurements.

We have observed, however, that performing 2dFT measurements in reflection geometry on a multiple quantum well sample is not a useful scientific pursuit, other than as a demonstration of the spectroscopic capabilities of our experiment, due to the non-trivial phase relationship between the strong first reflection of the probe beam and the four-wave mixing emission occurring from the various depths of the individual quantum well layers inside the material.

Given the moderately high index of refraction of Gallium Arsenide and Aluminum Gallium Arsenide at the relevant wavelengths, the optical path length that these beams propagate before exiting the sample and co-propagating with the strong first reflection is not insignificant, and the resulting 2dFT spectra cannot be understood by approximating the system as one with emission from only a single layer.

Results obtained from high quality single quantum well samples should, however, be able to be readily understood in the reflection geometry 2dFTS experiment. The sample we studied contained ten periods of quantum wells, but we do not anticipate that the signal intensity would drop by a factor of ten compared to the multiple quantum well sample, due to the coherent nature of the addition of the various emissions, which are not necessarily (or likely) in phase with one another, and due to the reduced excitation intensity that penetrates the sample to the various quantum well layers. Deeper in the sample, a significant fraction of the laser power will have been absorbed or scattered in overlying material, or reflected from the interfaces between wells and spacer layers, and thus less power is available to induce four-wave mixing emissions from the deeper layers. The worst case scenario should only obtain for a pathological sample with quantum wells spaced precisely an integer number of wavelengths apart as measured along the optical path of the probe beam, and even that material sample would not be expected to exhibit a tenfold decrease in four-wave mixing strength. Nonetheless, we note that a factor of ten decrease in intensity would result in a decrease in the signal-to-

noise ratio of approximately $\sqrt{10}$ – which we estimate would still allow high quality spectra to be obtained from a single quantum well sample. In certain transmission experiments performed with circular polarizations we observed a weaker spectrally resolved differential transmission signal and increased the number of spectra pairs that were captured at each τ delay to ensure a high quality 2dFT spectrum would be obtained. Doubling the number of spectra captured did not significantly affect the number of experiments that could be conducted during a given day, given the various other experimental hiccups that typically determine an experiment's duty cycle. Nor did increasing the amount of time spent at each τ step affect the ability of the apparatus to maintain interferometric stability over the course of an experiment. As such we do not anticipate that collecting 2dFT spectra from a high quality Gallium Arsenide – Aluminum Gallium Arsenide single quantum well sample.

There are, however, other samples that are of significant interest that may only be studied in a reflection mode.

6.1.2 Motivation for reflection experiments

There are several reasons why performing measurements on these samples in a reflection geometry is desirable. A brief summary of the technical arguments for studying even simple structures such as quantum wells is given in [183]. Immediately obvious are the issues related to studying samples grown on optically thick substrate materials. This is a significant problem for structures grown on direct band gap semiconductors, which are normally strong

absorbers. Excess material reduces the effective intensity of both the excitation pulses and the four-wave mixing signal (indeed, in an optically thick material the picture of a propagating electromagnetic wave is itself somewhat questionable, as the excitation may be more accurately described as a polariton due to the strong light-matter coupling – consider for example the results of [23], which used a phase and amplitude sensitive ultrafast technique to study the dynamics of excitons in GaAs heterostructures over a broad range of excitation densities and found that weakly excited systems should more accurately be described as polariton systems and require polaritonic interference and motional narrowing effects). It is true that removing the relatively opaque substrates that samples are generally grown upon is a nuisance as it adds a not trivial step to the experimental preparation, but this is may still appear more of a technical problem rather than a scientific one. Nonetheless, the interpretation of the results of measurements performed in transmission geometry may be difficult if inhomogeneous absorption of either the excitation pulses or the emission occurs while propagating through the substrate materials [327]. Additionally, the etching of samples introduces mechanical strain into the system, which can substantially affect the band structure near the band edge. To some extent, these complications could likely be avoided by heavily doping the substrate material in order to shift the onset of its absorption features to a higher photon energy, but this approach would limit the range of exciton energies that can be studied in the quantum well system – and thus dictates the minimum well thickness that is easily studied in such a

system. Chemical-mechanical etching typically results in poorer quality optical surfaces, resulting in increased scattering that deleteriously affects the signal-to-noise.

It is not advisable to perform transmission measurements on thin, unsupported GaAs platelets since the strain present in those materials is typically substantial, and results in strong inhomogeneous broadening of the exciton resonances. Without the capping layer and substrate, these transmission measurements will be affected by rapid, efficient recombination at the surface, significantly altering the dynamics of the exciton population in these materials [120], [130], [328]. Distortion effects due to the propagation through these materials near the absorption resonances have been studied, but cannot be discounted – even thin samples will introduce free-induction-decay types of distortions [215].

More significantly, however, we are interested in the ability to perform coherent ultrafast spectroscopic measurements – such as 2dFT – in a reflection geometry in order to permit the study of systems that simply cannot be studied in a transmission geometry. It is not difficult to imagine a large number of optoelectronic systems whose quantum properties and nonlinear optical response could be studied to great effect in a reflection capable apparatus – distributed Bragg reflectors with semiconductor regions where either injection of carriers or optical creation of an exciton population modulate the structure's behaviour, or a sample comprising quantum dots embedded in microcavities. We could use a reflection geometry experiment to study the exciton dynamics of quantum

dots located inside nanowires that act as waveguides for the emission of certain particular modes [33].

6.1.3 Motivation for controlling beam geometry

A significant number of these experiments would also appear to benefit greatly from the ability to control the precise geometry of the various beams interacting with the sample, in order to observe or exploit geometrical effects that alter the nature of the structure's optical response. In particular, we are interested in developing tools to coherently study nanostructured systems such as the one described in [373].

Here, a patterned gold structure is constructed on top of a 10 nm thick single AlGaAs-GaAs-AlGaAs quantum well. The quantum well is grown with standard molecular beam epitaxy techniques on top of a normal Gallium Arsenide substrate. The upper barrier layer is 20 nm of $Al_{0.3}Ga_{0.7}As$, and a relatively thin 3 nm GaAs capping layer. As a result of this structure design, the GaAs quantum well is relatively close to the surface of the semiconductor material, which nonetheless exhibits sufficiently high optical quality. On this surface, an 80 nm thick gold film is deposited, then patterned with an array of slits with a slit width of 140 nm and a translational period of 500 nm. Scanning probe electron microscopy was used to characterize the quality of the structure and confirm that it satisfied design specifications. It is expected (and indeed, demonstrated) that the presence of the grating substantially alters the nonlinear response of the exciton system; it is expected that near field effects

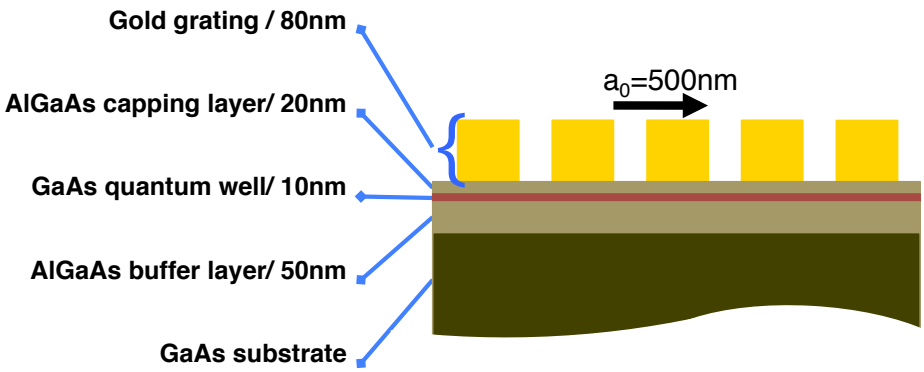

Cross-section sketch of nanostructure of interest, fabricated by our collaborators at the University of Oldenburg. The semiconductor structure is grown by molecular beam epitaxy on a GaAs substrate. A solid gold film is deposited, then patterned using electron beam lithography. 140nm slits are etched into the gold film, resulting in a one-dimensional periodic structure – a grating – with a lattice constant of 500 nm. The size of the gold structure is limited by the resolution of the lithography tool, as the grating resolution and the digital precision of the device effectively limit the total area that can be patterned.

Figure 6.1: Cross section of hybrid sample

arise due to the coupling between a surface plasmon polariton mode at the metal-semiconductor interface to the exciton mode in the GaAs quantum well. The evanescent wave for the polariton is expected to extend sufficiently into the quantum well to mediate that coupling. It is further expected that the hybrid exciton-surface plasmon polariton mode will then couple to a second surface plasmon polariton mode at the metal-air interface, resulting in emission that transmits power away from the system in a manner that can be detected in the far field.

6.2 Polaritons

We briefly consider the background of the polariton description of elementary excitations in a solid.

Polaritons were initially studied as the coupling between the long wavelength excitations of a crystal lattice and an incident optical field [118], developing a quantum mechanical model for what we would today call the longitudinal and transverse optical phonon polaritons. Prior to Fano's work, the dielectric constant had been used in classical models developed to study the response of electrons displaced from their equilibria by a driving field, but a quantum mechanical theory of dielectric effects had not previously been established using an atomic description of the medium. Subsequently, the contributions of excitons to the dielectric constant of a material was considered [186] with the conclusion that the eigenstates of the system comprising an absorptive medium and optical field are in fact a mixture of the photon and

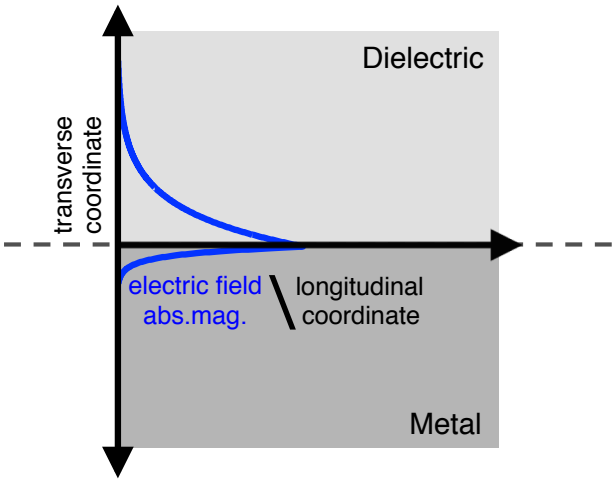

The surface plasmon polariton is a solution to Maxwell's equations that describes an excitation largely confined to propagate in the plane of the interface between a metal and a dielectric with a smaller wavelength than that of a free electromagnetic wave. By separation of variables it can be shown that the transverse surface plasmon polariton mode is an evanescent electric field that decays exponentially with increasing distance from the interface, with a characteristic length scale of less than 100nm. Typical propagation lengths are limited to a few microns before damping dissipates the excitation. Lifetimes are typically a few hundred femtoseconds.

Figure 6.2: Surface plasmon modes at an interface

exciton states – this is the exciton polariton that is of direct relevance to our own experimental program. The development of the exciton polariton model at this point is perhaps more astonishing given that early evidence had only just begun to suggest the experimental observation of exciton states [14], [16], [15], [168], [150], [13]. The approximate exciton Hamiltonian was shown at this point to be diagonalized by a hybrid eigenmode, and that interactions among the excitation eigenstates are necessary to obtain finite lifetimes (barring other perturbative effects) [186].

We are interested in a hybrid mode that describes the coupling of a surface plasmon polariton to an exciton via an optical dipole interaction. Nonetheless, because our studies have primarily focused upon exciton physics, we tend to elucidate the polariton picture in the context of the exciton polariton, due to its familiarity. The principles are largely the same, in that a material excitation that would, in a vacuum, be well described by a dispersion relation readily calculated from its Hamiltonian is coupled to an excitation of the electromagnetic field, viz. a photon, that also would be well described by eigenstates derived from a simpler Hamiltonian when in vacuum. It is the coincidence of these two particles (or excitations, or what have you) and the coupling between them that requires a more sophisticated treatment, from which the polariton quasi-particle description emerges.

In the most general statement, the coupling of an elementary excitation mode with an external field results in a new quasi-particle. A polariton is a particular example, which describes the coupling of some aspect of the

electric polarization wave and an electromagnetic wave [271]. The polariton is a general quasi-particle framework used to describe some hybrid mode that is not accurately described by a decoupled electron and material polarization excitation.

6.2.1 A general analysis of coupled oscillation modes

In this analysis we follow the useful examples and derivations of reference [271].

In a given material system it is not often physically reasonable to ignore the large number of oscillating excitations that will be present, a substantial number of which may interact with one another. Often, attempts to simplify the physics are made with an appeal to the simplifications suggested by a dilute system, but even the simplest behaviours of solids are often dependent upon these interactions; for example, electrical resistivity is due (at least in part) to the scattering of electrons by phonons.

In a first step that must be familiar to any student of mathematical physics, we simplify the analysis of the coupling between different fields representing different species of excitations by writing an interaction potential that may be linearized in the independent variable of either field. We need only consider bosonic quasi-particles, since the excitations of interest to us – excitons, photons, surface plasmons (perhaps surprisingly) – all obey Bose statistics.

The interaction between two modes can thus be expressed using the

potential

$$U(x,y) = \frac{\omega_1^2 x^2}{2} + \frac{\omega_2^2 y^2}{2} + \gamma\omega_1\omega_2 xy + (higher\ order\ terms)$$

A kinetic energy for center of mass motion for the modes of interest has the same form as always,

$$T = \frac{1}{2}\left(\dot{x}^2 + \dot{y}^2\right)$$

where the generalized coordinates (x, y) used here are chosen so as to permit us to write these terms without any explicit mass variables.

Using the kinetic and potential energy expressions above to write a Lagrangian function for the coupled modes permits the derivation of two coupled equations of motion

$$\left(\ddot{x} + \omega_1^2 x\right) + \gamma\omega_1\omega_2 y + (nonlinear\ terms) = 0$$

$$\left(\ddot{y} + \omega_2^2 y\right) + \gamma\omega_1\omega_2 x + (nonlinear\ terms) = 0$$

At which point we apply the ubiquitous trick of disregarding the nonlinear effects with the usual caveat that the amplitude of oscillation for x and y be kept sufficiently small. We note that these equations of motion are linear in each independent variable, and that even after eliminating the nonlinear

terms, the x and y degrees of freedom are still coupled with strength γ. The simultaneous solution of these equations in x and y may be found by diagonalizing the

The simultaneous solution of the two equations of motion, neglecting the nonlinear interaction, can be found by a standard technique from the study of partial differential equations, diagonalizing the matrix

$$\begin{vmatrix} \omega_1^2 - \omega^2 & \gamma\omega_1\omega_2 \\ \gamma\omega_1\omega_2 & \omega_2^2 - \omega \end{vmatrix} = 0$$

thus obtaining two eigenfrequencies, $\omega_\pm$, and the two coupled $x - y$ eigenmodes. these modes are linear combinations of the uncoupled x and y eigenmodes, with the particular dependence on each of the uncoupled eigenmodes depending on the frequencies of oscillation. The mixing of the eigenfunction solutions is greatest when the frequencies of the uncoupled modes are roughly equal, i.e. when $\omega_1 \sim \omega_2$. This solution of the equations of motion is equivalent to an orthogonal transformation of the original problem, resulting in a solution with two uncoupled harmonic oscillator solutions in the new coordinate system. These uncoupled oscillators are polariton modes for the coupled system. We note that if there are sufficiently large nonlinear terms that their effects may not be neglected then the representation of the interaction as two completely uncoupled harmonic oscillators in a new coordinate system is not valid [271].

6.2.2 The polariton as a coupled, propagating polarization-optical field

The exact solution of the full Hamiltonian, including the interaction terms that couple the two different excitation modes, results in a straightforward polariton picture of the light-matter coupling [221]. Our analysis elsewhere has been developed under the assumption that the description of the light-matter coupling does not substantially alter the eigenstates of the electromagnetic excitation modes (i.e., photons) or the material excitation modes (excitons, as we are primarily concerned with their dynamics). It is often the case that under weak excitation, useful results are thus obtained by assuming a less strongly coupled system, and treating the optical interaction as a perturbation of the semiconductor crystal system. In the perturbative approach, the material excitation and the electromagnetic field are treated as distinct entities.

If the polarization wave in some material may be given by

$$\mathbf{P}(\omega) = \varepsilon_0 (\varepsilon(\omega) - 1)\mathbf{E}$$

then a polarization wave must always be present in any material, where the index of refraction (or, alternatively stated but, excluding for the moment magnetic materials, the permittivity) are not equal to unity. At sufficiently high frequencies, the permittivity for most materials will tend to 1, and this situation no longer obtains, but for most substances that effect is insignificant until the optical frequency pushes into the x-ray portion of the spectrum. As

a result, in the materials we are interested in, the propagating electromagnetic mode in a solid substance consists of an admixture of an electromagnetic wave resembling light and a polarization wave due to the material response [221]. Mechanically, the polarization wave comprises the movement of the ionic cores comprising the crystal, collective excitations of the free electrons in the solid, and two-particle electron-hole pair excitation. In the case of the semiconductor materials we are interested in, excited below the bandgap, we have established that the polarization mode can be attributed principally to the exciton mode – unbound electron-hole pairs may be represented as continuum exciton states, and we neglect the coherent excitation of optical phonons to simplify the analysis. In metal substances, the motion of the free electrons relative to the crystal lattice is more significant than in an intrinsically doped semiconductor, and these excitations may be understood in a quantized picture as the plasmons that we discussed previously. The coupling of polarization waves due to excitons and, independently, plasmons, to the optical field is the subject of this experimental program.

As a general principle the coupling of two modes, resulting in a hybrid excitation, must be considered in the vicinity of the point the two separate dispersion relations of the isolated modes would otherwise intersect. This may be understood as a straightforward application of the familiar anti-crossing phenomenon for interacting energy levels. In particular, where the dispersion relations for the exciton and photon would intersect, a hybrid mode known as - an exciton polariton is formed. The behaviour of this particular polariton

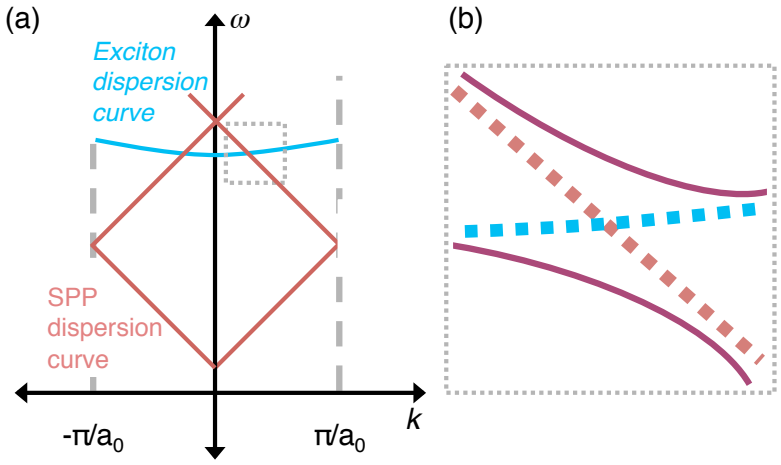

A cartoon dispersion curve for exciton modes in the semiconductor quantum well plotted with the surface plasmon-polariton dispersion curves (a). In the inset, level anti-crossing for the coupled modes results in the emergence of a hybrid, mixed excitation mode (b). Coupling only occurs for a small range of momenta, determined experimentally by the angle tuning of the excitation and probe beams.

Figure 6.3: Dispersion curve mixing

mode were studied quite early by Fano and Hopfield, obtaining a dispersion curve qualitatively similar to that derived from the Lorentz oscillator model [92].

In a vacuum, the propagating transverse modes of the electromagnetic field are light waves, which are quantized as photons. In matter the dispersion relationship for light is relatively trivial, $E_{\mathbf{k}} = \hbar\omega_{\mathbf{k}} = \frac{\hbar ck}{n_0}$, describing simply a straight line in the momentum-energy space. The dispersion relationship for the coupling material excitation is, of course, generally more complicated. As a result, the exciton polariton is more complicated than the phonon polariton, where the relatively flat longitudinal optical phonon curve simplifies emergence of the hybrid mode.

For the exciton polariton, we may write a simple toy exciton dispersion relationship based solely on the Wannier equation (see, for example [166]) as $E_{tot} = E_g + E_n + \frac{\hbar^2 K^2}{2M}$ where E_g is the bandgap energy, E_n is the exciton binding energy (which, n.b. is negative for bound states, and zero for states in the continuum) and $\frac{\hbar^2 K^2}{2M}$ is the kinetic energy of the exciton, subject to the usual provisos regarding effective masses.

The light-matter interaction is understood as a propagating electromagnetic wave that excites dipole oscillations in the material. That oscillation is, macroscopically, a polarization that then radiates an electromagnetic wave, which excites the oscillators, ad infinitum. In second quantization formalism, a Hamiltonian may be written for this system [221] as

$$H = \sum_{\mathbf{k}} \hbar\omega_{\mathbf{k}} a^{\dagger}_{\mathbf{k}} a_{\mathbf{k}} + \sum_{\mathbf{k}'} E\left(\mathbf{k}'\right) B^{\dagger}_{\mathbf{k}'} B_{\mathbf{k}'} + i\hbar \sum_{\mathbf{k}} g_{\mathbf{k}} \left(B^{\dagger}_{\mathbf{k}} a_{\mathbf{k}} + a^{\dagger}_{\mathbf{k}} B_{\mathbf{k}} \right)$$

which may be understood in a relatively straightforward manner as the photon energy (the first term), the energy of some particular excitation (the operator B is the annihilation operator for some non-specific material excitation mode; for our purposes, all the relevant excitations are Bosonic), while the third term is the coupling between the two (note that it creates a material excitation quantum for each photon it destroys, and vice versa). The g parameter merely quantifies the strength of this interaction. This Hamiltonian is then diagonalized by writing it using operators $p_{\mathbf{k}}$ that are linear combinations of the creation and annihilation operators for the optical and excitation fields. We do not describe this diagonalization process in detail here but refer the reader to the description found in [221]. The resulting Hamiltonian is simply $H = \sum_{\mathbf{k}} E_{\mathbf{k}} p^{\dagger}_{\mathbf{k}} p_{\mathbf{k}}$, where the p_k are annihilation operators for the polariton mode and $E_{\mathbf{k}}$the corresponding eigenenergies. The problem of understanding the light-matter interaction is thus reduced to finding the dispersion relationship for the polariton. Sufficiently far from the exciton resonance, the polariton dispersion curve will appear more linear and photon-like, while near the transition frequency it becomes bent due to the level repulsion.

6.2.3 Polaritons in quantum well systems

Although we may make significant progress toward understanding the systems we study without introducing the polariton concept, polariton effects

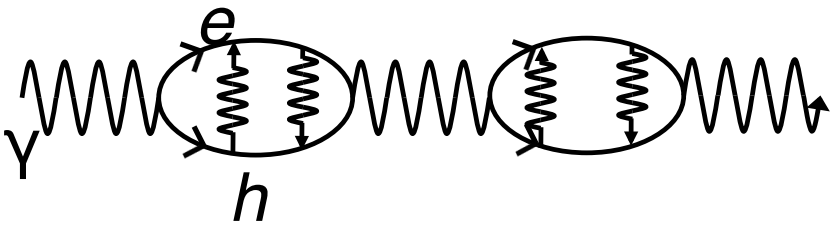

Diagrammatic representation of a polariton, where the hybrid light-material excitation mode is instead depicted as a photon that propagates (left to right) until it is annihilated during exciton emission. The electron and hole that comprise the exciton exchange virtual photons that mediate the Coulomb interaction. Upon exciton absorption, a photon is emitted that propagates until it is once again absorbed.

Figure 6.4: Polariton propagation diagram

must necessarily be considered for multiple quantum well samples, where electromagnetic modes propagate through regions that contain resonances (the wells) and regions that do not (the barriers). Since the characteristic length scales are less than the optical wavelength, it is no longer accurate to visualize the system as a propagating electromagnetic wave (light) coupling to an excitation (in this case, the exciton resonances) [221]. Instead, a polariton picture is a more accurate description of the system. While a perturbative treatment of the optical coupling is usually sufficient for dilute systems, in a strongly absorbing solid such as a direct band gap semiconductor, a polariton picture is an inherently more accurate treatment of the light-matter interaction [221]. One may develop an intuitive understanding of the polariton mode as the propagation of a coupled electromagnetic-material oscillation that results in the creation of a free photon only when it exits the material at an interface

with the vacuum [270].

6.2.4 A brief summary of plasmon physics

The field of plasmonics is rapidly growing and is of great interest from the perspective of both pure and applied physics. We do not delve in great detail into the theory of plasmon quasi-particles, despite their centrality in the samples we are presently turning our attention toward. In part this is because the exciton polariton is more approachable given the extensive descriptions of exciton optics elsewhere in this thesis, but also in part because the plasmon polariton-exciton coupling of interest to us is studied by its effects on exciton resonances, rather than its effects on the plasmon polariton.

As we have noted several times, the characteristic of a collective excitation is that it is not associated with a single particle but is instead a compound motion of the constituents of the entire material system. The excitation of an electron gas is another such elementary collective excitation. In the limit that this motion can be quantized and treated in a quasi-particle framework, it is called a plasmon. Plasmons can have a significant effect on the physical properties of the material system, as the electron plasma effectively screens the Coulomb interaction (in the highest density limit, the electron plasma may be understood intuitively as a conductor). We note that both classical treatments of plasma oscillations and quantum mechanical treatments of plasmons are useful tools to understand the behaviour of these systems [37], [292], [38].

The classical limit of the electron motion is treated directly in the

Lorentz model, which assumes a classical trajectory, harmonic response to electric fields that initially disturb the equilibrium electron distribution. The dielectric function calculated in this picture

$$\epsilon(\omega) = 1 + 4\pi\chi(\omega) = 1 - \frac{\omega_{plasma}^2}{2\omega_0'}\left(\frac{1}{\omega - \omega_0' + i\gamma} - \frac{1}{\omega + \omega_0' + i\gamma}\right)$$

(where $\omega_0' = \sqrt{\omega_0^2 - \gamma^2}$ is the renormalized resonance frequency (shifted from the natural resonance ω_0 of the dipole oscillator due to the effects of the damping term γ),) depends on the so-called plasma frequency $\omega_{plasma} = \sqrt{\frac{4\pi n_0 e^2}{m_0}}$, defined in terms of the mean electron density n_0. It can be shown that the plasma frequency is, intuitively, the frequency at which the electron density oscillates if small perturbations are made away from the mean density. The dispersion relationship found for plasma waves indicates that it is a longitudinal wave [270].

The quantized plasmon response can be understood by assuming a spatially inhomogeneous charge distribution, then calculating the temporal evolution of that density distribution. Such an analysis must approximate the four-operator terms that appear in the calculation of the two-operator term related to electron density (i.e. simply the electron number operator). The recursive nature common to field theoretic calculations leads to six-operator terms appearing in the calculation of the four-operator terms needed to calculate a two-operator observable – this iterative process runs on ad infinitum, and must be truncated at some point to perform a practical calculation. A

careful calculation performed in the second quantization formalism recovers the plasma frequency derived classically [166].

The plasma frequency, then, is the dividing line between the spectral regime of high transmission, occurring below the plasma frequency, and high reflectance, occurring for electromagnetic waves above that frequency. In analogy to the phonon picture, plasmons occupation number may be used to describe higher frequency collective excitations – thus, one speaks of N plasmons that oscillate at the electron plasma frequency ω_{plasma}, rather than an excitation occurring at $N \times \omega_{plasma}$ [270]. The dispersion relationship may become more complicated if a more sophisticated model is used for the electron behaviour in a solid; this result – a dispersionless plasmon mode that only occurs at discrete energies $\hbar\omega_{plasma}$ – is obtained in analogous limit to the classical Drude model for an electron gas.

In a three-dimensional material, light cannot excite a plasmon since the transverse electromagnetic field cannot drive the longitudinal oscillation of the electron gas. If an interface breaks the translational symmetry, however, the solid-vacuum barrier describes a plane where the oscillating electric field has a longitudinal component due to the discontinuity of the dielectric function. Plasmons, then, may be excited using light incident at an oblique angle, with the polarization of the electric field lying in the plane defined by the beam direction and the surface normal (i.e., for p-polarized light) [270]. Excitation of a plasmon is suggested by a corresponding drop in the transmission of light through a material at the plasma frequency, where the photon energy can res-

onantly excite plasma oscillations in the electron gas – of course, this assumes that the parameters upon which the plasma frequency depend are independently known. These surface plasmons were first proposed as an excitation mode that would occur at lower energies than the bulk plasmon [312], to explain effects observed in electron beam experiments on thin metal films. The surface plasmon was proposed shortly after the very first description of the plasmon.

In addition to the broken symmetry that occurs at a vacuum-material interface, the presence of an interface between two media may also lead to the formation of a propagating surface plasma wave, or surface plasmon. These surface waves are evanescent in the directions normal to the interface, *viz.* the probability distribution for the quasi-particle diminishes exponentially with increasing distance from the interface. Thus, the surface plasmon quasi-particle is largely bound to the interface and, we note, will only interact with other particles, quasi-particles, or other fields if they extend close to the interface.

Strictly speaking, excitation of a surface plasmon on a perfectly flat metal-vacuum interface should still be unlikely, as the dispersion relations for photons and surface plasmons would not normally intersect. Physically, the higher index of refraction of the material reduces the wavelength of light transmitted into the metal to less than that of surface plasmon mode, thereby suppressing surface plasmon excitation. This inhibition may be overcome by several different methods, one of which involves fabricating gratings on the surface. Light incident on the grating at an oblique angle results in a longi-

tudinal electric field in the plane of the interface with wavelength sufficient to excite plasmon modes that propagate as traveling modes in this plane [270]. Absent a grating, surface roughness or other surface features may still suffice to permit surface plasmon excitation.

6.2.5 Some relevant results for polariton hybrid modes

Previous experimental results had shown a range of different results related to the coupling of different excitations into hybrid modes. The literature is expansive; here we note only a few particular results – indeed, the study of evanescent modes began with Newton [275]; that problem held the attention of the likes of Fresnel, Young, Huygens, and others, and the papers cited here should not be considered representative of the total body of related scientific work. A quantum optics treatment of the behavior of evanescent waves [57] was shown to correctly predict the experimentally measured probability for exciting a monolayer of dye molecules [58], with the simple result that the likelihood of excitation by evanescent photon modes was the same as that by homogeneous photon modes (i.e. those that may be described in a semiclassical picture as propagating electromagnetic waves). The probability of absorption was found to be equal to the square modulus of the electric field, which corresponds to the intensity in a classical description of light. Contemporaneous work studied, for example, the excitation of surface plasmons in a gold film due to coupling with nearby excited dye molecules in solution [386].

Hecker et al. reported the observation of enhanced photoluminescence

(up to three-fold increase in intensity) from a single quantum well after deposition of a thin silver film on the upper surface of the semiconductor sample. The effect was shown to depend on the thickness of the metal coating, and was interpreted as the first evidence of coupling occurring between surface plasmons and light emission from a quantum well [269]. Depositing a nano-patterned gold grating on top of the silver film was found to increase the quantum well exciton emission even further, despite the fact that the semi-transparent metal surfaces actually reduce the optical power incident on the quantum well; this effect was attributed to the field due to surface plasmons induced in the metal structure [9], [174]. Gontijo et al. argue that this effect was likely due to increased absorption of the excitation laser, rather than due to a direct modification of the spontaneous emission rate due to the distance between the metal surface and the active region of the quantum well, which was likely too great to permit significant spatial overlap of the evanescent surface plasmon field with excitons formed in the semiconductor material [144], although the underlying physical principle of exciton-plasmon coupling is not questioned.

Motivated by the potential of InGaN/GaN quantum well based light emitting diodes as a commercial replacement technology for white light fluorescent tubes (and for certain telecomm applications), Okamoto et al. studied the effects of depositing metal surfaces onto single quantum wells of this material [264]. Surface plasmons in a metal layer will increase the density of states inside the adjacent semiconductor material. This is expected to increase the spontaneous emission rate, approximately given by Fermi's Golden rule

$$\frac{1}{\tau} = \frac{2\pi}{\hbar} \left| \langle f \left| \mathbf{d} \cdot \mathbf{E} \left(\mathbf{r}_e \right) \right| i \rangle \right|^2 \rho \left(\hbar\omega \right)$$

for a dipole oscillator at some position some position $\mathbf{r}_e$. Clearly, altering the density of states for photon emission will directly affect the spontaneous emission rate [295]. With back-side optical excitation of the sample they observe significant increases in the photoluminescence intensity for silver and aluminum coatings, while very little increase is found when gold is deposited on top of the quantum well capping layer. The effect is large enough (x 17 for Al) that it cannot be explained by reflectance of the excitation laser off the metal surface for a second pass through the quantum well active region. Moreover, insignificant increase in excitation was found with the deposition of a gold layer. The material dependence was attributed to the mismatch in the energies of the surface plasmon mode in the gold surface and that of the InGaN quantum well exciton, whereas the silver and aluminum plasmon energies were close enough to that of the exciton to observe a significant in luminescence due to the plasmon-exciton coupling. In all cases, it is necessary to use the renormalized surface plasmon energy, which is is affected by the presence of the other materials in contact or proximity to the metal layer [8]. An exponential dependence on the spacer distance was observed for the luminescence enhancement, which supports the model of coupling via the evanescent wave of the surface plasmon; excitons that are located within the near-field of the surface will couple effectively to the plasmon mode. That distance – the penetration of the surface polariton's fringing field – is determined by

the dielectric constants of the semiconductor and metal used to fabricate the structure. The authors note that emission from surface polaritons should be suppressed for a perfectly flat semiconductor-metal interface, since the non-propagating mode would not couple effectively to far field radiation. Inherent surface roughness in evaporated metal layers, verified with scanning probe microscopy, however, suffices to scatter surface plasmons in a process that results in photon emission. This suggests the fabrication of structured metal surfaces, and following the example of metal grating structures that have been shown to couple surface plasmons and photons, a metal grating structure is fabricated and demonstrated to enhance luminescence.

In time-resolved photoluminescence experiments [280] the effect of surface plasmon-quantum well exciton coupling on spontaneous emission rate may be directly observed. A 32x increase in spontaneous emission was observed due to coupling to surface plasmons. The effect on radiative decay rates was shown to exhibit a spectral dependence, with the greatest enhancement occurring for emission energies closer to the energies of the surface plasmon $\hbar\omega_{SP}$. At certain wavelengths, the internal process for transferring energy is believed to approach unit efficiency. Similar enhancement of spontaneous recombination rates were observed by another group studying the effect of capping layer thickness on Purcell enhancement factors [274]. This work demonstrated substantial coupling between excitons in InGaAn quantum wells and surface plasmons in a silver film deposited on top, measuring up to a 92-fold increase in spontaneous decay rate for certain wavelengths.

Prior to these results, modification of the photoluminescence from excitons in an InGaN single quantum well due to the deposition of a silver layer had been observed and explained using a quantum electrodynamic model. The calculated Purcell factor, which describes enhancement of surface plasmon emission, fit the photoluminescence dip, but no direct demonstration of increased light extraction from surface plasmon enhanced emitters was observed [144]. Even earlier, the emission of AlGaAs/GaAs LEDs was shown to be controllable by deposition of a surface grating that resulted in highly directional, more efficient emission with a reduced linewidth [224]. This development made possible improvements in the commercially desirable properties of LEDs without resorting to fabricating more complicated devices such as laser diodes. Here, a patterned grating on the front face of the diode increased efficiency by reducing Fresnel reflection loss of photons that would otherwise propagate out of the device, and by coupling certain photons emitted from the quantum well to surface plasmon modes on the grating that would subsequently emit into the far field. This coupling occurs when the photon momentum would otherwise satisfy the conditions of total internal reflection; as such, the plasmon-photon coupling here (note that it is not a plasmon-polariton-exciton hybrid coupling) exhibits specific momentum selection rules, the precise nature of which may be determined by the periodicity of the structured surface. Related results were shown in [140] and [252], which studied the effects of periodic patterns on a metal surface deposited on top of LEDs. [22] explores the problem of photon reflection at the interface, and notes the reduced cone of emission that

will occur for materials with higher indices of refraction – estimating that a bare semiconductor LED constructed with GaAs should couple out only 5% of the photons created by pair recombination. That work studied a description of the hybridization of the surface plasmon with emitted photon (a surface plasmon-polariton) that occurs where those excitations' dispersion relations would otherwise intersect.

Less related to the particular nanostructure system that we are interested in: other groups have studied plasmon-exciton couplings in systems of semiconductor and metal nanocrystals, or composite nanocrystals [147], [148], [412], [188], in a system of semiconductor nanowires and metal nanoparticles [239], or between dye molecules and metal nanoparticles [29], or a Langmuir-Blodgett grown thin films and metal surfaces [293].

6.3 First measurements on hybrid samples

We return out attention to the gold grating on GaAs quantum well structure. Due to broad scientific interest in the precise details of the energy transfer processes that result in the altered emission intensity from these structured samples, 2dFTS has a potential application to answer questions that would be difficult to otherwise resolve. Performing 2dFTS measurements with a range of mixing times T would permit the observation of the evolution of coupling between spectrally resolved plasmon and exciton states, and could provide a quantitative measure of the strength of that coupling. Such an experiment could perform a useful role in characterizing the coupling process

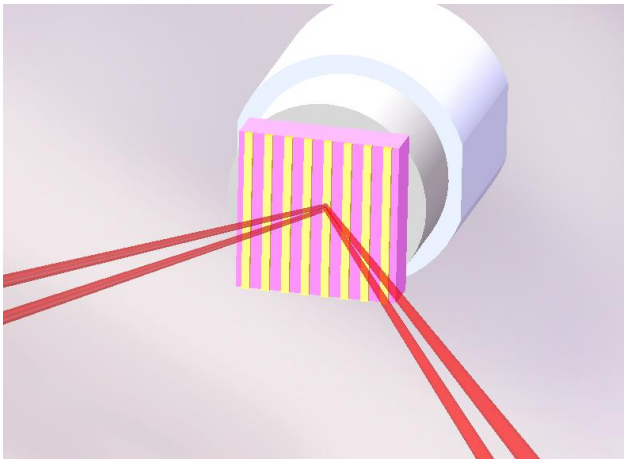

Schematic of basic experimental geometry, not to scale. The hybrid gold-semiconductor nanostructure (purple and gold) is mounted on a copper slug held in a cryostat at liquid Helium temperatures. Two beam paths are incident on the sample, propagating from the lower right hand corner in this diagram. The probe beam lies in the horizontal plane, and reflects from the sample in that same plane. The pump beampath propagates in the same vertical plane as the probe, but enters higher and exits lower. The angle between the sample normal and the plane defined by the pump and probe rays can be altered by adjusting the stages used to mount the beam steering optics prior to and after the sample.

Figure 6.5: Basic experiment sketch

and help direct fabrication of superior devices. Many of these measurements can only be performed in a reflection geometry, and due to the precise momentum transfer conditions for the exciton-surface plasmon-polariton coupling, we are particularly interested in building an apparatus that can perform angle-resolved, reflection geometry, coherent ultrafast spectroscopic experiments on these samples. For the particular sample we are considering, we specifically are interested in the nonlinear optical response to resonant excitation that occurs with the three beams all incident the same angle in the p-plane.

In collaboration with the group of Christoph Lienau at the University of Oldenburg we have performed preliminary measurements on this structure, and devised and constructed an apparatus that can perform more technically challenging four-wave mixing measurements on these samples. To that end, our 2dFTS experiment has been modified to perform a more sophisticated measurement that uses a multi-frequency modulation and lock-in detection scheme to isolate weak, phase-sensitive signals, with optical frequency temporal resolution. Fundamentally, this experiment is an extension of the three-pulse transient grating measurements first performed by Weiner et al. [392], [391] in that it allows direct measurement of a system's dephasing time without convolution with population relaxation rates. In our partially collinear geometry, however, the co-propagation of the weak four-wave mixing signal of interest with the probe beam is a perennial challenge. To develop the ability to perform 2dFTS or similar measurements, we have devised a method to generate a phase-stabilized pulse train while performing RF modulation of all three beams

for purposes of high speed lock-in detection. Angular control has been built into the experiment using a matched pair of translation and rotation stages for beam direction. Although we are currently performing measurements in what we call a periscope geometry, we expect that it should be trivial to adapt the apparatus to conduct experiments a completely collinear geometry. Although certain technical hurdles would remain, this would in principle allow us to consider performing coherent, optical phase-dependent spectroscopic measurements on single quantum emitters – e.g., to perform 2dFTS on a single quantum dot, or other isolated, individual structure.

We shall describe the development of these techniques in the subsequent sections, but we outline the time line of progress on this experiment here first. While the accidental chronology of developing a new measurement technique are not important to the final scientific conclusions resulting from such a project, relating the process of this development may be useful from the perspective of understanding the particular choices made in the design and construction of this experimental apparatus.

6.3.1 Experimental geometry control

Many of the choices regarding experimental design were made to minimize the difficulties in adapting the existing 2dFTS apparatus to perform measurements on these new samples. It was, however, necessary to alter the beam path substantially to properly observe exciton-surface plasmon polariton coupling phenomena.

Since coupling of the surface plasmon polaritons located at the semiconductor-metal interface to excitons created in the underlying GaAs quantum well occurs as a function of the momentum used to excite the plasmon mode, the optical fields used in these experiments must be able to be angle-tuned in order to control the momentum transfer. Simply put, the angle of incidence for the beams must be controllable. We construct an opto-mechanical system that permits angle tuning of the pump and probe beams used in nonlinear optical experiments. Coupling is expected when all of the optical fields used to excite or probe the system possess the same angle relative to the sample. The presence of the metal grating breaks the cylindrical symmetry that otherwise obtains, and the typical horizontal planar beam geometry common to most optical experiments and in particular to four-wave mixing measurements cannot be used.

We changed the geometry of the experimental setup, moving from a horizontal plane to a vertical plane. The pump and probe beams are aligned vertically one above the other, then focused to a point using a 20 cm lens, with the probe passing directly through the center and the pump pulses passing through the upper portion. The lens is placed a distance away from the sample equal to its focal length, so that the two spots overlap on the sample. The probe beam is reflected from the sample in the same horizontal plane, while the pump beam is reflected downward and away from the signal field, co-propagating with the probe.

The angle tuning of the incident beams is provided by rotating the stage

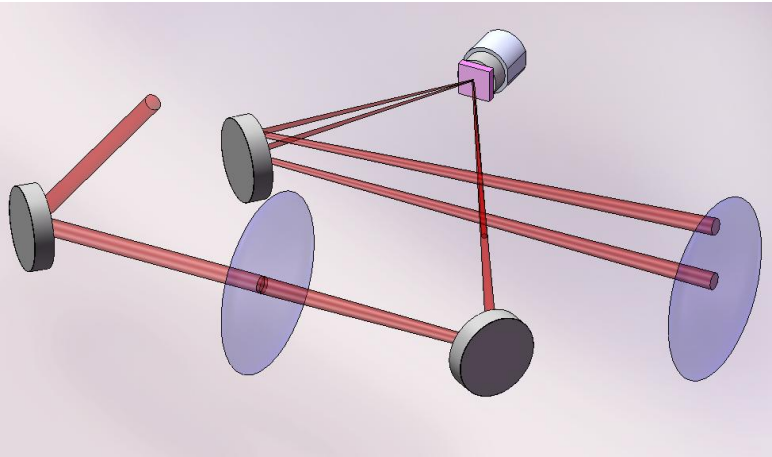

The pump and probe beams lie in the same vertical plane, entering the diagram here from the right-hand side. A single lens focuses both beams to the same spot on the sample. The reflected probe is collected and re-collimated with a second lens before being sent to the monochromator.

Figure 6.6: Experiment planar beam geometry

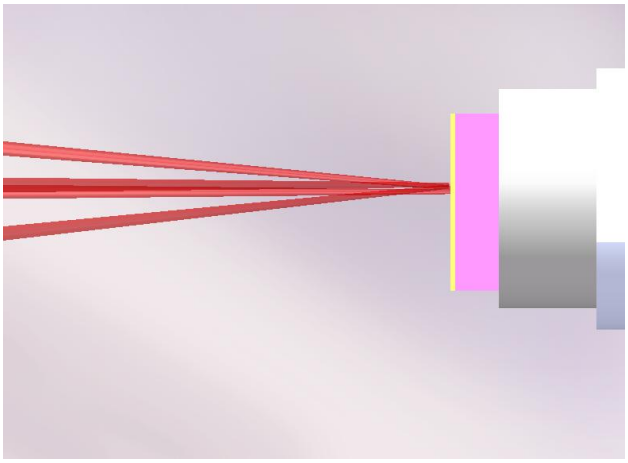

A side view of the laser geometry used in the experiment. The probe beam and the reflected probe and signal beams propagate in the same horizontal plane, and are overlapped here when viewed from this angle. The pump beam path lies in the same vertical plane as the probe, but lies above it prior to the focusing lens. Here, the pump beampath can be seen approaching the sample from an elevated position and leaving propagating downwards.

Figure 6.7: Planar beam geometry – side view

on which the final steering mirror is mounted. That mirror is used to direct the pump and probe onto the sample, but once the experiment is initially aligned at one incident angle, the mirror is not adjusted subsequently – only the various stages used to control beam geometry are moved. In order to ensure that measurements taken as a function of angle reflect physical processes directly affected by the beam angle, it is necessary to ensure that only the incident angle changes, and not the position, size, or overlaps of the spots on the sample. Thus, the final tuning mirror and its rotational stages are mounted on a translation stage that is adjusted so that the spot is always aimed at the same point on the sample for any arbitrary angle of incidence. Clearly, this also requires that the focusing lens be translated an equal distance to keep the spots of the two beams focused at the same point, with the (approximately) same size spot. Ideally, these optics should all be mounted on a single translation stage to minimize the amount of tweaking that must be done, but practical considerations prevented that refinement from being built into the current experiment.

A similar arrangement of a rotating and translating steering mirror and a translating 20 cm lens are used to collect and collimate the reflected probe beam and the co-propagating signal. We are only concerned with this beam, and ignore the pump beams. Although we do not purposefully use a beam block, the pump pulse is blocked by an anodized part of one of the stages.

Initially, we attempted to perform experiments by collecting the reflected probe, collimating that beam, and then coupling it into a fiber to sent

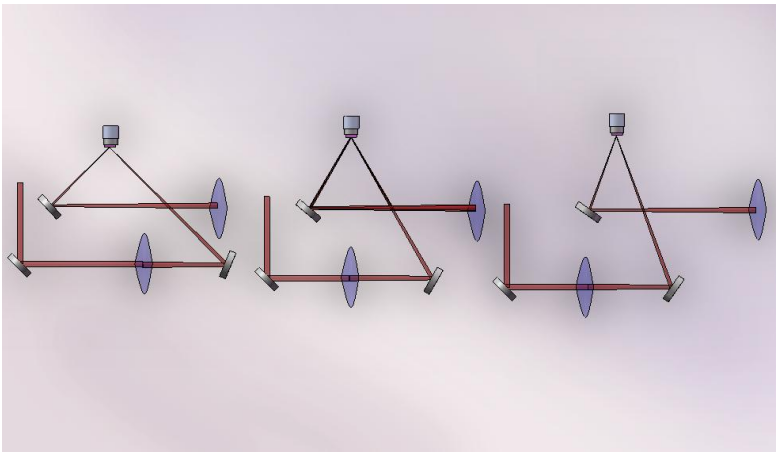

Adjustment of the position and angle of the final beam steering mirror prior to the sample and the first steering mirror after the sample, with corresponding translation of the focusing lenses, permits control of the experiment geometry. Adjusting the incident angle changes the momenta transferred to the excitation modes from the laser. Shown here are three top views, where the rotation and translation stages are omitted but their movement is indicated by changes in the position and orientation of the mirrors and the position of the lenses.

Figure 6.8: Angle tuning geometry

to a spectrometer located elsewhere on the table. It is possible to do so, and our first measurements were made in this fashion, using a CCD to observe the exciton resonances on a bare portion of the grating/plasmon sample, i.e. a region not covered by the gold grating nanostructure. This is possible but not recommended: the geometrical control is designed to permit repeatable control of the beam position and steering, and observation with a ccd suggests that the spot is easily steered onto the same portion of the sample with an accuracy of a few to a few tens of microns; nonetheless, the reflected beam does not couple into the fiber after an adjustment of the rotational and translation stages to change the angle of incidence. As such, we forgo the fiber coupler and send the collected probe beam through free space to a different spectrometer. This, a 50 cm spectrometer with a similar 1200 g/mm and similar manually controlled slits, is used as a monochromator since a second CCD is not available and, indeed, we need the sensitivity of a lock-in detection scheme to perform precise measurements on the weak signals of interest. The light is aligned into the spectrometer using a lens with a focal length of a few centimeters, placed on a three-dimensional translation stage to permit precise alignment.

Since the samples of interest for this experiment have a well-developed theory predicting exciton-surface plasmon polariton coupling for only certain well-defined angles, it is necessary to properly calibrate the angular control of the experiment. It is critical that the front surface of the final steering mirror is centered on the axis of the rotation stage so that the beam does not walk when the angle is changed.

Initial alignment is performed without the focusing lens in position. An iris is placed in the probe beam approximately a meter away from the final steering mirror. The rotation stage is set to zero degrees, so that the pump and probe beams are reflected approximately back onto themselves. The horizontal and vertical alignment of the mirrors is then adjusted until the probe beam is centered on the back side of the iris previously placed in the beam path.

The rotation stage is then rotated forty-five degrees, so that the reflected probe beam forms a right angle with the probe beam incident on the final steering mirror. The probe beam is now directed onto the sample at approximately normal incidence, and should form a spot on the sample in the cryostat. Since the beam is not focused, the spot size is fairly large, and may not be easily visible on the GaAs samples we use without the use of an IR viewer. The cryostat alignment is adjusted by shimming its mounting plate and base plate with thin metal shim stock or similar materials (pennies, paper, etc) until the probe beam is reflected back onto itself and is again centered on the back side of the iris. The geometry of the experiment is now well defined, and any angles of interest may be directly determined from the rotation of the final mirror stage.

It is necessary, now, to introduce the focusing lens into the beam path. It is important that this optic be properly aligned with the probe beam path. A small ccd camera is used to observe the position of the unfocused spot on the sample in the cryostat; on the monitor display, marks are made in erasable pen to indicate the center and shape of this spot. The focusing lens is then

inserted into the beam path and its height and horizontal alignment adjusted until the now focused spot is centered at the indicated point on the monitor. By observing the back reflection it is possible to see that the reflected probe beam is still centered on the back side of the alignment iris.

This experiment, of course, makes use of more than one beam path – the pump beams have been raised vertically by something on the order of a centimeter and are propagating parallel to the probe beam. Careful alignment of the experiment, including the use of several homemade Aluminum alignment jigs with holes drilled to pass the properly aligned beams, ensures that the two beams lie in the same vertical plane and are parallel in that plane. As a result, the pump beams passing through the upper portion of the focusing lens should be focused to the same spot at the probe beam. Since the beams used in this experiment are not perfectly collimated, the lens position that focuses the two parallel beams onto the same spot is not precisely the same as the one that produces the smallest spots. Including a telescope prior to the experiment but after the interferometrically aligned portion of the experimental apparatus is suggested to permit better beam size management; several lenses are used to bring the divergent laser from the head to the experiment over a distance of some three meters, and to correct for the increased angular divergence in the horizontal plane, but adjustment of these optics is strongly contra-indicated due to the subsequent need to realign the experiment to ensure proper parallelism of the beams with the delay stages.

We note a few other points related to the experimental alignment here.

In order to roughly align the experiment, the patterned threaded hole layout of the optical table is used as a guide, sending the beams parallel to one of the two square lattice vectors, then using a turning mirror to send it parallel to the second (and thus perpendicular to the first) in order to direct the beam onto the final steering mirror. The motion of this mirror should be made as parallel as possible to this ray; ideally, we would fix the translation stage to the optical table, then align the beam using the previous two mirrors so that there was no beam walk as the mirror (turned to normal incidence) is scanned the length of the stage. That is essentially the same procedure as is used to align the precision delay stages used to produce the τ and T delays. Such a degree of precision is not deemed necessary for this alignment, however, and instead the stage is aligned simply using the table pattern as a guide to parallelism. We have done so using a straight edge pressed against the translation stage so that deviations from parallelism can be observed over a greater distance, permitting more accurate alignment. A fairly long focal length lens is used in this experiment; in part, this is simply due to practical considerations; if a shorter length lens were used it would be difficult to find sufficient space for the rotation stage and final steering mirror. Of some note, however, is the numerical aperture of the optic. If this is too great, the difference in wave vector from one side of the focused beam to the other becomes significant, and the sharp angular features present in the coupling spectra plots may become washed out. In order to achieve high angular resolution, a reasonably long lens is preferred.

We have spent little effort in describing the stages and optics used to collect the reflected light; this is because the principle of their operation is largely identical. The alignment process is similar although somewhat less rigorously applied, because any error in the alignment of the collected beam can be corrected by adjusting the lens used to focus the light onto the slit of the spectrometer.

6.3.2 Two pulse differential reflectivity and an attempt to observe four-wave mixing

We first perform simple two-pulse measurements in a reflection geometry to observe the exciton resonances. Resonant excitation is used, and spectral data are collected over a range of angles to observe the effect that the coupling has on the exciton resonance position and width. These effects are only expected for one polarization state, as coupling of the optical field to the surface plasmon at the metal-air interface is only expected to occur over a certain range of angles. That surface plasmon polariton is expected to couple to the surface plasmon at the metal-semiconductor interface. If the extension of the evanescent electrical field associated with this plasmon couples to the excitons that are simultaneously created in the semiconductor sample by the same incident optical fields, forming a hybrid mode that is an admixture of the exciton and surface plasmon polariton, the observed emission that co-propagates with the probe beam will be shifted in frequency and width from the exciton resonances that are observed when no coupling occurs. Data are collected as a function of pump-probe delay, and as a function of wavelength. We also take

data at a number of different pump and probe power levels, to try to find the best combination to easily detect the signatures of coupling without power broadening the resonances.

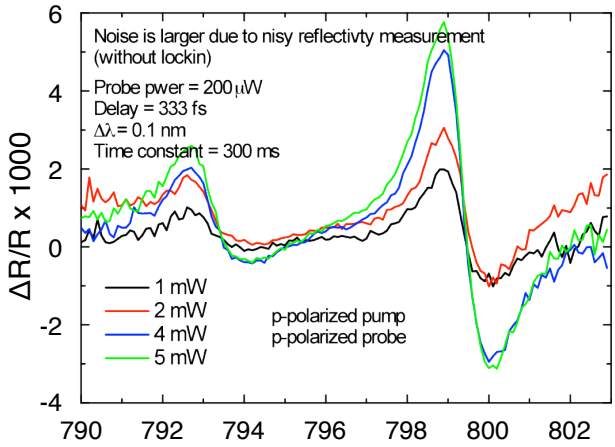

Data collected from an unpatterned, bare quantum well region of the sample using a 75cm focal length spectrometer with a CCD to record spectra. Preliminary measurements on the bare semiconductor sample were possible, while previous experimental work suggested that the weaker signal from the gold-patterned regions would require lock-in detection to isolate it from background noise.

Figure 6.9: Spectrum recorded with CCD

It is not generally effective to take data using a spectrometer and CCD to record the emission, since the signal from this sample is too weak to obtain accurate measurements above the noise floor without using some technique to narrow the bandwidth.

The high noise level in this experiment may be attributed to several factors. In part, the quantum well sample is not expected to be as high quality

as those we studied in the 2dFTS portion of this thesis. Strain and disorder in the sample increases scatter and broadens the resonances; the broader lines are, generally, less well distinguished from the background reflectivity of the sample and hence the differential reflectivity signal is not as clean. More significantly, the overlay of gold on the sample surface reduces the amount of optical power that actually penetrates into the semiconductor material underneath it; as such, the excitation density is lower. While we generally prefer to work in a low excitation limit, there is an optimal point in the pulse power space for performing a nonlinear experiment – pump probe measurements are generally performed with a ten-to-one pump-probe power ratio. While the differential effect may be larger if greater probe power were used, the presence of the stronger probe background typically makes signal detection more difficult. In addition, the increased probe intensity would complicate a theoretical description of most nonlinear experiments, which prefer to treat the population induced by the pump pulse as not strongly affected by the probe. We find here that increasing the excitation pump and probe powers from the values used in the 2dFTS experiments (typically 1 mW pump, 100 microWatt probe) to 3 mW pump and 400 microWatt probe beams provides a differential reflectivity spectral lineshape that is not substantially broadened (we do not attempt to model the recorded lineshape but simply look at the spectra to see if any distortion suggesting broadening has occurred; while this is not particularly rigorous it is a simple approach in the early stages of these experiments).

In order to detect these weak signals, we perform two-frequency modu-

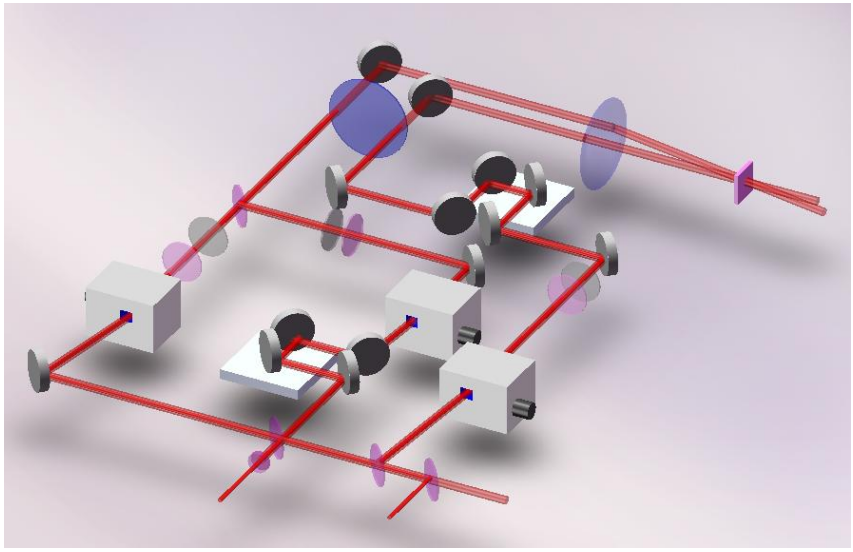

To perform lock-in detection, the experimental apparatus was changed to include an independent acousto-optic modulator in each beampath (probe, and both of the two pump beampaths). For two-pulse experiments, only one pump beam path was used. Due to space contraints, the apparatus as shown here does not include the variable geometric control stages and optics, or the reflection mode collection optics.

Figure 6.10: Experimental apparatus with 3 AOM's

lation using a commercial RF function generator built by APE (APE DFD-80, Germany). This device produces two phase-locked carrier signals at 80 MHz that are amplified to drive the acousto-optic modulators. Either carrier is modulated at an adjustable frequency, ranging from 0.10 to 10 MHz. The device outputs the two drive signals (the slow, modulated carrier waves), a reference monitor for either slow modulation frequency, and a reference for the difference frequency between the two slow modulation frequencies.

Each of the RF drive signals is used to supply an acousto-optic modulator. We describe the principles of acousto-optic modulation later in this chapter at substantial length. Here, we simply note that these devices deflect part of the input optical power into a new beam path, with the angle formed between the input beam and the diffracted beam determined by the carrier frequency supplied. The fraction of power diffracted into the new mode is determined by the power of the RF drive signal applied to the acousto-optic modulator. The acousto-optic diffracted light also undergoes a frequency shift equal to the carrier frequency applied to the modulator, but we do not exploit that effect significantly here other than to lift the exact frequency degeneracy of the beams as described in the chapter on 2dFTS.

In these two-pulse experiments, a carrier with a different modulation frequency is sent to each acousto-optic modulator. Typically we use a few hundred kHz to 1 to 2 MHz modulation frequencies, with a frequency difference of $\Delta f \sim 25$kHz. The difference frequency Δf is sent to a lock-in amplifier (q.v. *sub* for description of the principles of lock-in detection) to be used as the

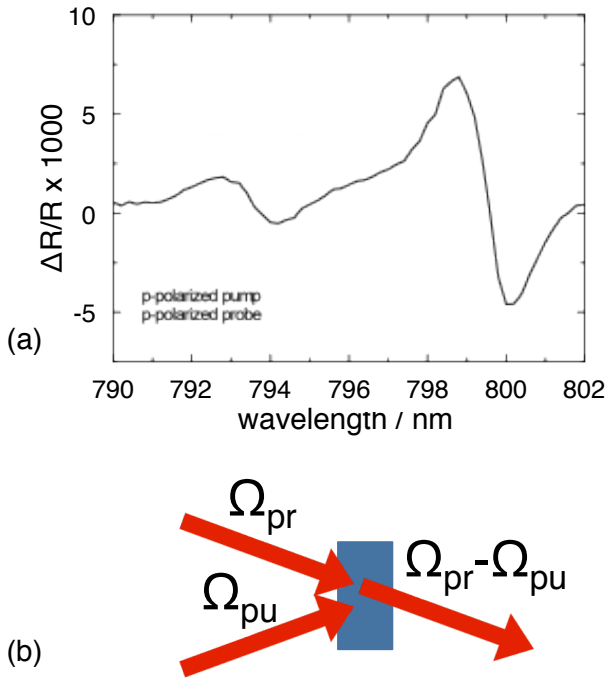

Spectrum measured in a two-pulse differential reflectivity measurement (a) using a commercial two-frequency generator to modulate the pump and probe beam intensities, and generate a signal at the difference of the two intensity modulation frequencies used as a reference for lock-in detection. This is shown schematically (b) in a diagram that indicates the intensity modulation frequencies and signal intensity frequencies used to detect the nonlinear signal. This diagram is not intended to reflect the actual experimental geometry.

Figure 6.11: 2-pulse dR with commercial drive

reference frequency in a phase-sensitive detection scheme. There is a subtle point about the difference between the modulation frequency generated by the DDS system and the actual frequency at which the intensity of the laser beam is modulated, which we will address subsequently in our discussion of the laser pulse auto-correlation measurements. For specificity, we are referring here to experiments where the *intensity* of the probe laser beam is modulated at some frequency f_1, the *intensity* of a pump laser beam is modulated at f_2, and the difference frequency $\Delta f = |f_1 - f_2|$ is sent to the lock-in amplifier as a reference frequency. Clearly, given that the laser repetition rate is 76MHz, each individual pulse is not being intensity modulated by the acousto-optic modulators; instead, a time-averaged data point is collected by the slow detector (q.v. *sub*) for a number of pulse cycles, the intensity of which changes only somewhat during the detection period. In a subsequent period, the amount of optical powers diffracted by the acousto-optic modulator will have changed slightly (evolving on the time scale of the slow modulation frequency), resulting in a data point collected with different intensity pulses. Monitoring the change in the strength of the signal field that oscillates at the difference frequency Δf, correlated to the modulated intensities of the pulses directed onto the sample, permits the extraction of a weak signal of interest from the strong background of the probe beam and, of course, the typical background noise of the laboratory environment. The reason we emphasize that the acousto-optic modulators are used to modulate the intensity of the light in the experiment is perhaps not apparent here, but will become more so when we consider the

heterodyne methods developed subsequently for three-pulse measurements.

The collected probe beam, meanwhile, is sent to a 50cm monochromator with 1200 g/mm gratings. To collect a spectrum at a given pump-probe delay time, the grating angle is tuned to change the center wavelength that is imaged onto the output slit. The intensity of the light at that particular wavelength is then sent to a biased photodiode that is terminated to provide 100 kHz of bandwidth (we experiment with various different choices of bandwidth and find this termination works the best; a slower bandwidth would result in greater photovoltage levels, but result in a signal that may saturate the other signal processing components at high gains). This photovoltage is then applied to a precision pre-amplifier with adjustable gain and programmable filters (SR560), the output of which is then sent to the digital lock-in amplifier (SR830). As noted, the frequency difference Δf is applied to this amplifier as a reference. The signal output by this lock-in amplifier is the differential reflectivity dR due to the pump-probe interaction with the sample.

We have also performed measurements where a portion of the probe beam is split off after the monochromator and detected with a homebuilt fast amplified photodiode. That voltage is sent to a second, radio-frequency lock-in amplifier (SR844). The reference signal used for this lock-in amplifier is one of the RF modulation frequencies – specifically, the one used to modulate the probe beam. Thus, the signal detected at this frequency should not depend strongly upon the pump beam, and gives us (approximately) a probe reflectivity spectrum. The measurement performed with this lock-in amplifier is

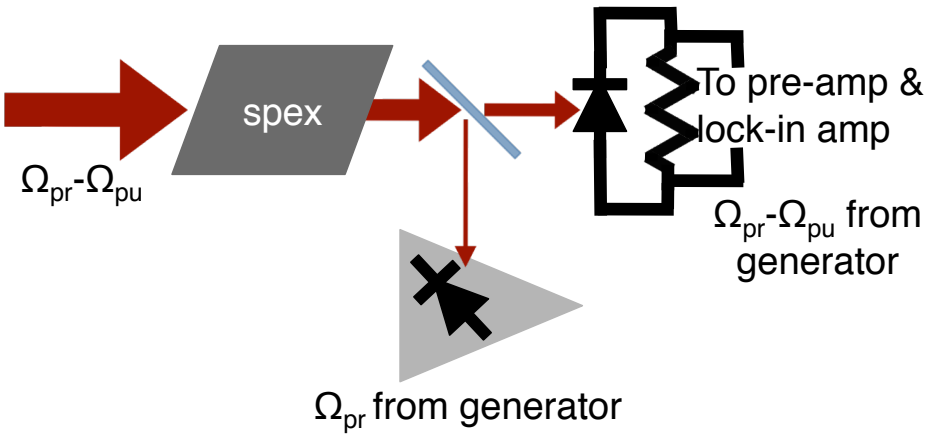

Schematic for the detection scheme used in two-pulse measurements with the commercial two-frequency generator. The signal and co-propagating probe beam are collected and collimated, then spectrally analyzed with a 50cm spectrometer, using a 1200g/mm grating. A small fraction of the analyzed light is sent to a homebuilt amplified Si PIN photodiode, then measured using a digital RF lock-in amplifier. The intensity modulation frequency used for the probe beam is used as an RF reference for the detection of the probe transmission spectrum. The greater part of the analyzed beam is sent to a biased photodiode, which is appropriately loaded, filtered, and amplified prior to lock-in detection using the difference of the two intensity modulation frequencies as a reference.

Figure 6.12: 2-pulse modulation-detection scheme

approximately equal to the probe reflectivity R; when this and dR are measured simultaneously a dR/R measurement is possible. This is not strictly necessary to observe the effects of the exciton - surface plasmon polariton coupling.

These measurements are largely a proof-of-concept project performed to develop some familiarity with the sample of interest. Scientifically, little is gained here with resonant excitation compared with the above-bandgap excitation performed previously on this sample [373]. We wish to perform more sophisticated three-pulse measurements (q.v. the chapter on 2dFTS for a general description of the principles of three-pulse four-wave mixing measurements) to study the dephasing times for this system, to see if the coupling of the hybrid mode affects the coherence compared to the uncoupled the exciton system.

To do so, the experimental configuration is changed somewhat. Three independent pulses are now needed to observe a four-wave mixing signal. We will again detect the changes in the probe beam due to the two collinear pump pulses, as in the 2dFTS experiments performed previously. Again, the optical physics are the same as in those measurements, but the method of detection and the lack of the phase controlled scan of the pump delay τ means that the resulting data cannot be used to completely characterize the amplitude and phase of the nonlinear optical response with the explicit definiteness of a 2dFTS experiment.

The two modulated RF signals previously used to drive pump-probe

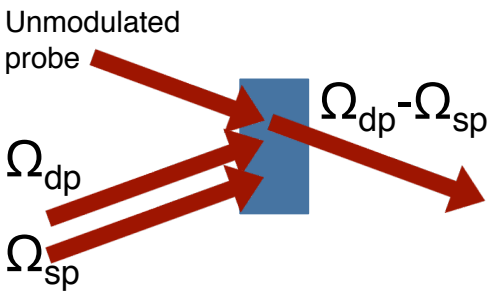

Four-wave mixing measurements were attempted using a commercial two-frequency generator to modulate the intensities of the two pump beams at different frequencies, using the difference between those frequencies (provided by the generator) as the reference signal for lock-in detection. The probe beam was not modulated; a constant RF carrier was used to deflect the beam so that no changes to the apparatus needed to be made. A four-wave mixing signal could not be found using this two-frequency scheme.

Figure 6.13: FWM two-frequency modulation-detection

acousto-optic modulators are now both used to modulate the two pump pulses independently. The probe pulse is driven with a constant cw RF carrier derived from an RF synthesizer. We detect the collected probe reflection, spectrally analyze that light as before with the monochromator, then detect it as before, using a pre-amplifier and the SR830 lock-in amplifier. The difference frequency Δf of the two pump modulations is used as the reference for this lock-in measurement.

We cannot easily pick out the probe reflectivity R as before, since the probe beam is now un-modulated. We attempt to remedy this by using an optical chopper wheel to modulate the split off portion of the probe beam at 1-2 kHz. We find this impractical, however, since the chopper wheel motor

and the controller's square reference wave produce significant RF noise that is picked up by the coaxial cables used for both measurements. Re-arranging the cables used in the experiment, wrapping various cables and connectors in tinfoil, and placing Aluminum enclosures around the chopper were unsuccessful in eliminating the parasitic noise. As such, the mechanical chopper modulation technique we have used ubiquitously is deprecated when extremely sensitive measurements are to be made.

Nonetheless, independent measurement of the probe background is not strictly necessary, and in principle a three-pulse measurement should still be able to be performed. We expect to see a four-wave mixing signal co-propagating with the probe beam, but modulated at the two RF modulation frequencies used on the pump beams. By fixing the probe delay T relative to the static pump pulse and scanning the dynamic pump pulse delay τ we expect to be able to detect a decaying four-wave mixing signal corresponding to a decay of the polarization driven strictly by dephasing processes.

Unfortunately, this proves not to be the case. We go to substantial lengths looking for this signal with a two-frequency modulation of the three pulses used in this experiment, but cannot detect any genuine four-wave mixing signals, even using extremely long integration times (3 and even 10 seconds per data point; to properly clear the low-pass filter in the lock-in amplifier it is necessary to wait 9 or 30 seconds in this case) to try to detect a weak signal. What appear at first to be four-wave mixing emissions are in fact probe artifacts – the intensity of the probe optical field is detected, rather than the

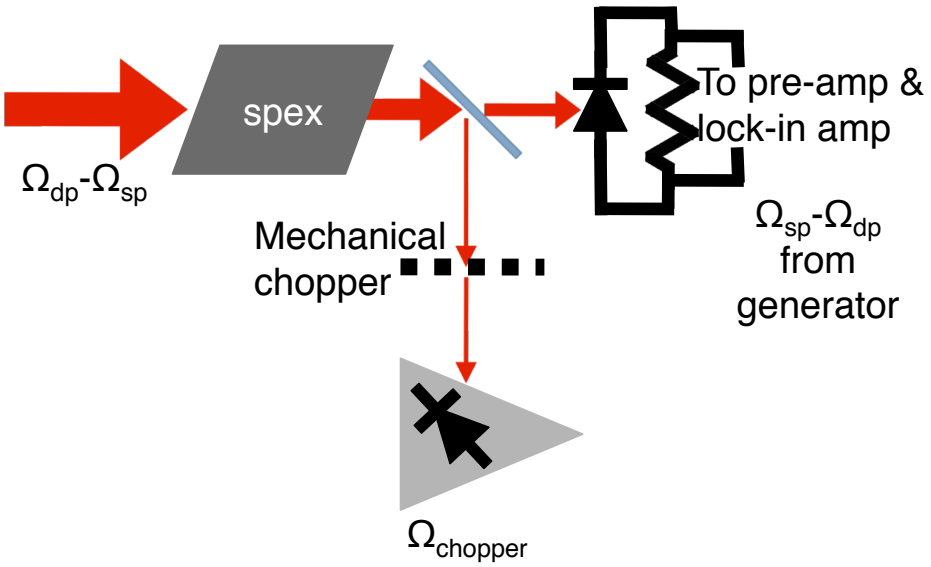

Schematic for the detection scheme used in four-wave mixing, three-pulse measurements with the commercial two-frequency generator. The signal and co-propagating probe beam are detected analogously to the scheme used for two-pulse measurements.
Since the probe beam is unmodulated, there is no immediate way to detect the probe background as before. A mechanical chopper is used but introduces too much noise into the electronics used for detecting the nonlinear signal. While ΔR/R two-pulse measurements are commonly used, the exciton-surface plasmon polariton lineshape may be studied in four-wave mixing without dividing the spectrum by the probe background.

Figure 6.14: Initial FWM modulation-detection scheme

four-wave mixing emission of interest. This can be proven by blocking one or the other of the pump beams and seeing similar spectra, indicating that the peaks observed in these experiments are not due to optical four-wave mixing processes.

The most likely cause of these spurious signals is parasitic RF coupling, perhaps among the cables used to drive the acousto-optic modulators. If the slow modulation (typically 0.5-2 MHz) RF signals used to modulate the intensity of the pump beams is inductively coupled into the signal used to power the un-modulated probe beam, a weak modulation of the probe beam will occur at that frequency. If both modulation frequencies are thus parasitically into the probe's drive signal, features will be observed in the probe spectrum at the difference between those two modulation frequencies even should both pump beams be blocked. This corresponds precisely to the observations we have of this effect. Our efforts to combat this effect were the typical ones used in every laboratory – we re-arranged our cable routes and tried to shield the cables from one another to reduce the effects of inductive coupling. When this failed, we attempted to quantify the inductive coupling effects. Using an RF spectrum analyzer, no spurious coupling was observed at the level of the noise floor of the device (i.e., no spurious frequency components corresponding to parasitic coupling were observed, with a noise floor approximately 75 dB below the peak of the applied frequency). The optical measurement is effectively a very precise check for this parasitic effect, with the subsequent filtering and amplification stages providing the ability to detect parasitic coupling even

where it cannot be seen using conventional RF measurement techniques.

We checked for this parasitic coupling at various stages throughout the experiment, including at the acousto-optic modulators themselves. Changing the connections and cables used did nothing to reduce the effect, and it was decided that a more sophisticated measurement system would be necessary to perform three-pulse measurements and record extremely weak four-wave mixing signals in order to characterize the dephasing of the hybrid exciton-surface plasmon polariton modes. We proceeded by building an RF system that allows us to produce three independent RF drive signals that are mixed with three phase-locked modulation signals. We use direct digital synthesis techniques to do so, allowing us easy experimental control of the phase, amplitude, and modulation frequency of all three pulses used in the experiment, and the generation of an agile reference frequency for lock-in detection. Having demonstrated superior performance compared to the commercial two-frequency apparatus, we turn our attention to three-pulse measurements. Although we haven't yet performed the full range of three pulse experiments we are interested in using to study the hybrid samples, our preliminary experiments with quantum well samples indicate that the agile RF system we have constructed must prompt a new reconsidered approach to performing nonlinear spectroscopy on weak four-wave mixing emitters. We outline those results subsequently. Although the final results are not of great scientific interest in the study of quantum well exciton systems, the techniques we have begun to develop promise significant advances in nonlinear optical spectroscopic techniques.

First, we must re-consider the basic principles of lock-in detection, to better understand the nature of the detection scheme we develop here. Subsequently, we present a description of acousto-optic principles and devices. The experiments we wish to perform require an acousto-optic modulator application that has not, to the best of our knowledge, been previously demonstrated, which we describe here. Finally, we consider the use of this experiment to perform basic three-pulse measurements on a quantum well system as a demonstration of the relevant principles.

6.4 Lock-in detection of weak signals for ultrafast optical measurements

6.4.1 A brief description of noise in laboratory science

In a 1918 paper titled 'ber spontane Stromschwankungen in verschiedenen Elektrizittsleitern,' Walter Schottky described shot noise and thermal noise effects observed in the electrical current flowing through vacuum tubes. The current in such a device is not a truly continuous phenomenon, but rather consists of some (generally very large) number of discrete charge carriers. The question of whether or not the electrons flowing through a vacuum tube exhibit wavelike characteristics is immaterial to an analysis concerned with charge detection as a function of time, i.e. current measurement. The carriers are emitted from a hot filament according to a probabilistic process, and at any given instant the number of carriers may be higher or lower than the mean value measured over some interval. The similarity of charge carriers to the

pellets fired from a shotgun prompted Schottky to term this 'schrotteffekt' – shot effect, or shot noise, in English. Shot noise is now used to describe the characteristic fluctuations of any similar process, where the net observable that occurs is due to the sum of some larger number of discrete processes. In the same paper Schottky also describes effects due to thermal noise, arising when thermal motion of microscopic particles gives rise to temporary fluctuations of macroscopic observables. The experiments we perform rely on measuring an optical intensity with a square law detector, and are performed above the limit where quantum mechanical effects should be significant. Nonetheless, the absorption of photons is itself a probabilistic process, and forms a fundamental noise floor that limits the precision such an experiment could ever achieve. For these nonlinear optical experiments, much more substantial noise sources will dominate these effects. We do not explore the noise processes present in these systems in great detail, but we do mention some general properties of statistical noise here. We are primarily concerned with the power spectral density as a function of frequency, as it relates to our interest in eliminating $1/f$ noise in our optical measurements.

By the time that thermal noise was investigated experimentally by Johnson [201] and theoretically by Nyquist [279], thermal noise in conductors was often already the greatest noise source in precision electronic apparatui. Nyquist argues that equipartition implies that in a frequency interval $d\upsilon$ the power transferred from a resistor to the line is $kTd\upsilon$, and thereby finds that the voltage fluctuations across a resistor can be given by $V^2(\upsilon)\, d\upsilon = 4kTRd\upsilon$.

Generally, the resistance can (and indeed certainly will) be a function of frequency, but in an ideal resistor that would indicate white noise with no frequency dependence for the power spectral density. While this result is derived in the context of (again) charges measured in conductors, the fluctuation-dissipation theorem that underlies this result is applicable to other physical processes. We note that this analysis is not properly applicable to systems where the quantum mechanical nature of particle statistics is relevant, and indeed, tends to deviate from observed noise spectral densities in the Terahertz regime. If instead of equipartition a quantum mechanical argument is used to determine the occupation of the individual modes of oscillation that constitute the total noise in a resistive element – using the Bose-Einstein distribution $h\upsilon/\left(e^{h\upsilon/kT}-1\right)$ to assign the energy per degree of freedom – the expression $V^2\left(\upsilon\right)d\upsilon = 4Rhd\upsilon/\left(e^{h\upsilon/kT}-1\right)$ is instead obtained for the noise power spectral density. By approximating the exponential function $e^{h\nu/kT} \simeq 1+h\nu/kT$ it can be seen that this noise power spectral density exhibits a characteristic $1/f$ frequency dependence. Such a power spectral distribution is near ubiquitous due to the general applicability of the fluctuation-dissipation theorem.

The observation of $1/f$ noise in a large number of fields is well known – consider [261] on the emergence of $1/f$ distributions for any processes where the successful completion of that process depends upon a large number of independent subprocesses. Such processes, which are characterized as noise only when they influence the observation of other effects but are present in any complex system, are characterized according to a simple stochastic law,

analogous to the central limit theorem.

In general, noise processes typically appear to obey $f^{-\beta}$ power laws over time scales of nearly arbitrary length, but a unified theory has not yet satisfactorily explained ubiquitous $1/f$ noise phenomena [21]. It is well known that $1/f$ noise can arise in semiconductor materials for a variety of reasons, where the underlying nature of the noise processes are usually of secondary interest to the primary goal of reducing the effect of such noise on device operation. Four fundamental noise sources give rise to these various effects: thermal noise, which is generated in almost any dissipative system; shot noise, noted above, due to the stochastic nature of randomly generated carriers, which leads to fluctuations around an average number state; recombination and generation noise, where the number of conduction carriers fluctuate due to interactions with the band and trap sites; and the more problematic $1/f$ noise processes.

One example of $1/f$ noise in semiconductor materials is the fluctuation in the conductance, proportional to $f^{-\beta}$, where $\beta = 1 \pm 0.1$. This effect is known to occur across a wide frequency range – in practice, typically from 1Hz to 10kHz, above which point thermal white noise will dominate the noise power spectral density [185]. Measurement down to at least the microsecond level has shown that the power spectral density continues to obey the $1/f$ power law on such timescales [220]. Unlike the other three sources, the basic principles underlying 1/f noise are not well understood [185]. As a result, experimentalists tend to take it as unavoidable, and look to work around it.

While this discussion is couched in language of conduction measurements, the underlying statistical noise processes are present in an enormous range of physical systems. The particular emphasis on carrier populations and electrical resistivity are due to the widespread use of electrical resistivity as a taxonomy of solids [77].

6.4.2 Principles of lock-in detection

Even if an experiment is designed to ensure that the signal of interest is of significantly greater intensity than specious signals, a reliable measurement may be difficult to perform if the desired signal is weak enough to be limited by statistical noise.

Lock-in detection is a standard laboratory technique used to increase the signal-to-noise ratio of such an experiment, providing the means to measure weak signals that are otherwise undetectable. This phase-sensitive detection method modulates an excitation source at a well-controlled frequency and interrogates the resulting signal to isolate a corresponding effect occurring at the same modulation frequency. This measurement of the isolated effect is then averaged over many modulation periods to gain a $\sqrt{N}$ type advantage. This technique effectively reduces the bandwidth of the measurement, and, as a result, reduces the integrated noise power present in the resulting signal.

A useful description of a number of different reduced bandwidth measurement techniques is available in [187]. We describe the particulars of phase sensitive detection and lock-in amplification only briefly here, depending pri-

marily upon the example of that text, reference [276], and the comprehensive manuals made available by Stanford Research Systems, such as [355].

The simplest approach to reduce the noise bandwidth of a measurement – low-pass filtering – will not be effective if the noise power spectral density is sufficiently great at the frequencies of interest for the measurement. Many experimental measurements are performed to quantify what are, at least approximately, DC signals, and are thus particularly sensitive to low frequency noise issues. Reducing the bandwidth by low pass filtering does not gain significant advantages for measuring a noisy signal if, as is generally the case, there is a prototypical $1/f$ noise power spectral density. In such a case, most of the total noise power will still present in the detected signal and no advantage has been gained, with the added detraction of slowing the data acquisition rate to substantially less than the corner frequency of the filter.

To obviate the difficulties of measuring DC (or low-frequency) signal, most of the bandwidth narrowing techniques depend on the detection of a repeating signal. It is relatively easy to force most typical laboratory detectors to generate a periodic signal by modulating the control of some independent variable in the experiment.

Fourier transform spectroscopy using a sufficiently sophisticated detection schemes provides simultaneous measurements of amplitude and spectral phase data sufficient to reconstruct the time-resolved electric field corresponding to four-wave mixing emission in the systems we study (*n.b.* we contrast a time resolved measurement from one that simply probes the time integrated

emission as a function of some particular variable, *viz.* pule delay times). The temporal lineshape of such a signal is complicated, determined by the optical coupling of conduction and valence band states, the narrow exciton resonance resulting from electron-hole pair interactions, dephasing and spontaneous decay processes, and exciton-exciton correlations. It may seem to a naive analysis that these relatively complicated measurements are categorically not DC signals, nor are they periodic save in the sense that any well-behaved time sequence data can be decomposed by Fourier analysis. Furthermore, the emission should rise and decay some 76 million times a second due to the repetition of the pulsed laser used as an excitation source.

Nonetheless, the actual detection step is in principle a DC measurement. Although these experiments can reconstruct the electric field as a function of real time during the emission, they do so by detecting a time-integrated intensity and extrapolating from its behaviour as a function of the phase stable delays between three excitation pulses. A slow photodiode (we variously used a Thorlabs DET36A, which is simply a biased photodiode, and a home-built detector using an amplified, biased Silicon PIN photodiode) produces a photovoltage proportional the light incident upon its active area, but does not respond fast enough to resolve either the envelope or the fast optical oscillation; typically, we use terminating resistors to set the cut-off frequency at approximately 40kHz, and only conduct experiments designed to produce signals oscillating at less than this cutoff. So, although the optical process of interest has a complicated temporal evolution and a 76MHz repetition rate, it

is necessary to modulate the low frequency or DC signals that are derived from that fast signal. In the case of the dT measurements described in the previous chapter, a chopper wheel was used to turn either just the pump or both the pump and probe (we discuss two-frequency detection at some length in this chapter, q.v *sub*) beams on and off by physically blocking and unblocking the optical path, typically in the 1-2kHz range. To perform 2dFTS spectroscopy we used a similar chopper with larger windows to perform modulation at 25Hz.

In general, the effect of modulation is to shift a signal of interest away from DC, where $1/f$ noise can dominate even intense signals, and to move it up to the modulation frequency. The the effect of taking a long measurement centered on the modulation frequency is to reduce the effective bandwidth to $\Delta f = 1/T$ for some duration T. Thus, it is possible to isolate a signal of interest and to perform an accurate measurement of it by modulating some independent variable in the experiment.

The lock-in detector itself is essentially an extension of a phase detector. In a simple implementation, this is a gated inverting buffer, so that the gain of the circuit can be flipped between $+1$ and -1. By applying an input signal to such a device,

$$E_s \cos(\omega t + \phi)$$

while using a square wave reference signal that has edges as the zeros of $\sin(\omega t)$ to control the gating of the inverting element ad. If the output level

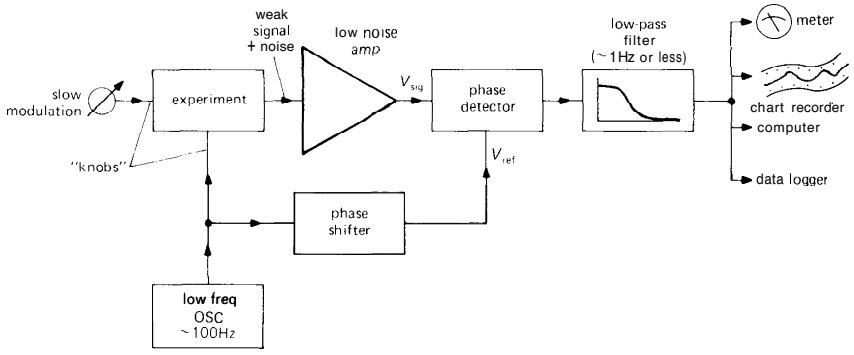

Schematic outlining the process of lock-in detection. Reproduced from Horowitz and Hill, The Art of Electronics, 2nd ed., New York: Cambridge University Press, 1989

Figure 6.15: Principles of lock-in detection

of this phase detector is then applied to a low pass filter with a time constant greater than one period of the reference signal,

$$\tau = RC \gg 2\pi/\omega$$

then the low pass filter output is given by

$$\langle E_s \cos(\omega t + \phi) \rangle \,|_0^{\pi/\omega} - \langle E_s \cos(\omega t + \phi) \rangle \,|_{\pi/\omega}^{2\pi/\omega}$$

where the two averages have different signs due to being taken with reversed gains from the analog linear phase detector. After taking the time average, the output level is given by

$$\langle V_{out} \rangle = -\left(\frac{2E_s}{\pi}\right) \sin\phi$$

where the phase ϕ is determined by the phase difference between the reference signal used as a gate on the inverting circuit and the signal of interest $E_s \cos(\omega t + \phi)$. Thus the output of the combined phase detector and low pass filter is, for any input signal synchronous with the reference signal applied to gate the inverter, proportional to the amplitude of that signal, E_s. The constant of proportionality, aside from any particulars related to the physical implementation of this device, is given by the phase difference between the reference and the signal. Adjustment of this phase permits optimized detection of the signal of interest.

If the input signal occurs at a modulation frequency that is close to, but not equal to the reference signal, the phase ϕ varies slowly in the preceding results, at a frequency equal to the difference between the reference and signal frequencies:

$$\cos(\omega + \Delta\omega)\, t = \cos(\omega t + \phi) \Longrightarrow \phi = t\Delta\omega$$

with the result that the output of the phase detector-low pass filter is a slow sinusoidal signal in time,

$$V_{out} = \frac{2E_s}{\pi} \sin(\Delta\omega)\, t$$

for small errors $\Delta\omega$ between the reference and signal frequencies. If that frequency difference is small compared to the corner frequency of the low pass filter, i.e. if $\Delta\omega < \frac{1}{\tau} = \frac{1}{RC}$, then an oscillating signal will be detected. If

the difference frequency is greater than the corner frequency, if $\Delta\omega > \frac{1}{\tau}$. the output will be heavily attenuated. The degree of suppression is a function of the size of the frequency mismatch and the slope of the low pass filter transfer function. On a digital device such as the two lock-in amplifiers used in our experiment, this may be trivially adjusted, but certain consideration must be given to the waiting time used for the low pass filter to lose the memory of its previous state after some change has been made to the experimental parameters (in our case, to the waiting times between pulses or the wavelength selected by the monochromator).

In summary, lock-in detection is used to measure a weak signal contaminated by noise. The apparatus producing the weak signal is controlled in such a way that the signal is modulated. The raw measurement from some detector is amplified, then a phase-detection stage is used to compare the signal to a reference signal derived from the modulation source. Most all experiments collect data as a function of some variable, rather than considering a single point; as such, to use lock-in techniques the experiment needs two 'knobs,' one providing a slow modulation to sweep the experiment through the interesting features present in the signal's domain space, and a fast modulation that is used for the phase sensitive detection. The choice of the low pass filter rolloff sets the bandwidth of the measurement, so that a 1 second time constant for the filter results in sensitivity to those signals and noise only occurring within 1Hz of the reference signal. The choice of bandwidth also determines maximum rate at which the slow modulation can occur. If the slow modulation

rate were comparable to the low pass time constant then any changes in the features of interest that would otherwise be observed will instead be filtered. The experiment cannot be swept across its domain faster than the filter can respond. So, in toto, the bandwidth for the measurement has been narrowed to a range determined by the low pass filter stage, centered on the modulation frequency used to make the weak signal periodic. Since this frequency can be made relatively fast, lock-in methods alleviate problems with ubiquitous laboratory $1/f$ noise.

There is a distinction that may be made between lock-in detected signals proportional to the signal of interest, obtained by effectively chopping the signal on and off, or detected signals proportional to the derivative of that signal's lineshape, which are found by using a small sinusoidal modulation on some independent variable in the experiment. We perform the former, gating the light sources used to induce four-wave mixing emission, either using a mechanical chopper or an acousto-optic modulator that is employed to provide amplitude modulation of the light it diffracts.

6.4.3 Multi-frequency modulation and lock-in detection

If a signal of interest is generated using more than one excitation source, it is possible to use a multiple frequency modulation scheme to perform extremely sensitive measurements. If a signal A is modulated sinusoidally in time at two different frequencies, the measured signal $A\cos(2\pi f_1 t)\cos(2\pi f_2 t)$ can be decomposed using trigonometric identities,

$$A\cos\left(2\pi f_1 t\right)\cos\left(2\pi f_2 t\right) = \frac{A}{2}\left\{\cos\left[2\pi\left(f_1+f_2\right)t\right]+\cos\left[2\pi\left(f_1-f_2\right)t\right]\right\}$$

Thus, this intensity A of this weak signal could be detected and measured by considering a small frequency band centered on either $(f_1 + f_2)$ or $(f_1 - f_2)$. Since this lock-in detection is a phase-sensitive technique, it is strictly necessary that the two modulation frequencies and the reference frequency used to select the lock-in pass band maintain a constant, well-defined phase relationship. Should phase drift occur, the fraction of the lock-in signal power desired to be in-phase with the reference frequency may drift into the out-of-phase component, or vice versa; in such a case, the desired signal of interest will be distorted or lost. Often, due to experimental contraints, a difference frequency modulation scheme will be used when the excitation source can only be easily modified at frequencies that are too high to permit straightforward detection; in that case the beat frequency $f_1 - f_2$ can be chosen to lie within the accessible range of slower detectors. Since laboratory environments often exhibit something like a $1/f$ law for noise power spectral density (or, at least, almost always tend to have far greater noise power spectral density at lower frequencies – see, for example [217], [21]), it is advantageous to use high modulation frequencies to shift the signal of interest away from the significant noise sources present at low frequency. In difference frequency detection, the difference frequency term will be chosen to be as fast as the available detector; in optical experiments using two excitation sources modulated using acousto-optic or other nonlinear optical processes it is not uncommon to

use modulation frequencies in the MHz or tens of MHz range with difference frequencies in the few to tens of kHz range.

The difference frequency detection scheme is straightforwardly extended to three excitation sources, such as we use in our four-wave mixing experiments. We use three-frequency modulation in order to look for a weak signal superimposed on a strong, noisy background. In our experiment, one of the beams that induces the polarization in the material sample that gives rise to the four-wave mixing signal field co-propagates with that signal field. Using the common two frequency-difference frequency detection scheme does not suffice to detect the weak four-wave mixing signal. We reserve the details of our detection scheme for a later point in this chapter, but mention the three frequency detection method here as a logical extension of two frequency modulation. The three frequency lock-in detection method we develop appears to be (to the best of our knowledge) a novel tool for detecting weak nonlinear signals.

Of course, the use of two-frequency or three-frequency or indeed, any other kind of modulation scheme detection does not alter the way that the lock-in detection process works. Lock-in detection is still used to simply isolate a pass band near some particular frequency and average the power present within that band to provide an accurate measurement of a weak, noisy signal. Modulating the signal of interest in a more complicated fashion simply provides a different way to produce a detectable signal at a desired frequency. This is at times necessary if more straightforward modulation schemes do not effectively

isolate the desired signal from the background.

6.5 Acousto-optic principles and applications to our apparatus

Our experiment makes extensive use of acousto-optic modulators to control the phase and amplitude of the laser beams that excite and probe our samples. A detailed description of the theory of the acousto-optic effect and a summary of the various devices and applications that depend upon it is out of the scope of this work. Here we present only a brief summary of light-sound coupling and a discussion of its application to the particular devices we used for our measurements. The interested reader is referred to the extensive literature on the subject, beginning with the early papers describing the effect (the first theoretical exploration of the idea in [52] and the phase-grating theory for diffraction developed in [300], [301], [302], [303], [304]). While this represents a substantial digression from the greater part of the chapter, an explanation of the underlying principles of acousto-optic interaction is required to understand the use of acousto-optic modulators in our work.

The distinction between and transition from the Raman-Nath to Bragg scattering regimes [397], [289], [218] will largely be elided, partly to avoid further extending this discussion, but also because the operation of our devices as used under optimum coupling conditions can be qualitatively explained largely using the simpler Bragg picture, as may be observed from a few moments' fiddling in the laboratory. By adjusting the incident angle of the laser,

it is possible to observe far-field patterns where only the undeflected mode and one of the $m = \pm 1$ modes are clearly visible, an accepted characteristic of Bragg mode operation. It is, however, certainly true that adjusting the device alignment around the ideal angle that maximizes the power diffracted into the first order permits scattering into a number of different, weaker spots – which is suggestive of operation in the Raman-Nath regime. The frequently repeated argument is that Bragg diffraction should only permit one diffracted mode in the far-field, since repeated scattering cannot occur in a Bragg crystal due to a mismatch in the Bragg resonance condition between the first scattered light mode and the periodic grating induced by the acoustic wave. This sharply distinguished taxonomy is somewhat misleading, since the case of the ideal Bragg device – where the acoustic wave is a periodic plane wave that is (paradoxically) nonetheless confined to propagate through a perfect cylindrical or rectangular column – is not an accurate description of a real physical device. Even minor deviations from this ideal would allow non-resonant diffraction into higher order modes, albeit at a reduced efficiency – and using intense, visible laser sources would permit the observation of multiple diffraction orders from devices for which the dominant effects (i.e. first order scattering) are still well described by the simpler Bragg model. Thus, the observation of additional spots does not necessitate delving into the gorier mathematical details of the phase grating model, as the Bragg model serves accurately for an intuitive understanding of our device. Perhaps most convincing of the applicability of the Bragg description is the precise dependence on Bragg angle alignment for

the device to function with anything approaching a useful efficiency, and the modestly high RF frequencies used in the operation of these devices – operation of Raman-Nath devices at those acoustic wavelengths would require too thin an interaction region to be practical for most materials.

A treatment for the Raman-Nath, intermediate, and Bragg scattering regimes is described in [219], which used a coupled-mode theory (see [73]) to analyze the diffraction of light by acoustic waves and established an eponymous Klein-Cook parameter Q used to categorize the nature of an acousto-optic device.

The interaction of light and acoustic waves was first predicted by Brillouin in 1922 [52] and experimentally demonstrated in 1932 [86], [255]. The propagation of an acoustic wave through a medium induces a strain field in that material. That strain results in a change in the local index of refraction via the photoelastic effect. This phenomenon is found in all phases of matter. Mathematically, the effect may be described as

$$\Delta\eta_{ij} = \Delta\left(\frac{1}{n^2}\right)_{ij} = p_{ijkl}Skl$$

where the quantity of interest, $\Delta\eta_{ij}$, is the change of the optical impermeability tensor resulting from the effects of the strain tensor S_{kl}, related to the physical deformation of the medium, via the coupling p_{ijkl}, known as the strain-optic tensor. Photoelastic coupling may also depend nonlinearly on the strain tensor, but higher order effects are typically small compared to the

linear term. Generally, the elements of the strain tensor will take on values of typically $\sim 10^{-5}$, and we may expect that the local index effects will be correspondingly small.

Due to the periodic nature of the acoustic waves, the strain field is periodic grating, resulting in a grating that can scatter light passing through the medium. This physical process has substantial utility to the optical experimentalist, discounting the fascinating scientific aspects of coupling two wave phenomena (light and sounds) that occur in such different parameter spaces.

We describe the basic principles of acousto-optic interaction following the invaluable derivation in [407]. Useful reviews of acousto-optical principles and applications may be found in [368], [226]. We first turn our attention to the general problem of the propagation of electromagnetic waves in periodic crystals, before considering the specifics of light scattering by acoustic waves.

6.5.1 Propagation of light in periodic crystals

In a periodic material, the optical properties may be related to the material parameters by periodic dielectric and permeability tensors

$$\begin{aligned} \varepsilon(\mathbf{x}) &= \varepsilon(\mathbf{x}+\mathbf{a}) \\ \mu(\mathbf{x}) &= \mu(\mathbf{x}+\mathbf{a}) \end{aligned}$$

where $\mathbf{a}$ is any lattice vector describing the symmetry of the periodic structure. The Maxwell equations used to describe light propagation in this

material,

$$\begin{aligned} \nabla \times \mathbf{H} &= i\omega\varepsilon\mathbf{E} \\ \nabla \times \mathbf{E} &= -i\omega\mu\mathbf{H} \end{aligned}$$

will be symmetric under the operation n $\mathbf{x} \rightarrow \mathbf{x} + \mathbf{a}$ in either the curl operator or the tensor dielectric and permeability. The propagation of light given the translational symmetry of the periodic medium is analogous to the Schrodinger problem of an electron in a crystal potential, and suggests the use of Bloch-like solutions for the electric and magnetic fields,

$$\begin{aligned} \mathbf{E} &= \mathbf{E}_{\mathbf{K}}(\mathbf{x})\, e^{-i\mathbf{K}\cdot\mathbf{x}} \\ \mathbf{H} &= \mathbf{H}_{\mathbf{K}}(\mathbf{x})\, e^{-i\mathbf{K}\cdot\mathbf{x}} \end{aligned}$$

where the functions $\mathbf{E}_{\mathbf{K}}$ and $\mathbf{H}_{\mathbf{K}}$ inherit the same periodicity as the underlying periodic medium and the exponential functions describe the wave-character of the propagating optical field (the time dependence is omitted here but will also enter in exponentially. Wave-like propagation is described by functions whose arguments can be written $(\mathbf{k} \cdot \mathbf{r} \pm \Omega t)$ for some wavevector $\mathbf{k}$, position $\mathbf{r}$, and frequency Ω). In discussion of the propagation of electrons in a crystal, this result is known as Bloch's theorem; more generally, it is referred to as Floquet's theorem. A dispersion relation is obtained,

$$\omega = \omega\left(\mathbf{K}\right)$$

by substituting the ansatz solutions into the Maxwell equations with a result, again, in parallel to that found in a Bloch problem. We restrict our attention here to a one-dimensional, periodic, non-magnetic material – i.e. we assume that the light-matter interaction is wholly described by the dielectric constant.

For light incident on this periodic medium at angle θ, constructive interference will occur in reflection for $m\lambda = 2\Lambda\cos\theta$, where Λ is the periodicity of the material. This is the ubiquitous Bragg condition, which occurs when the phase difference between rays reflected from different planes is equal to zero (modulo 2π), resulting in constructive interference among the rays reflected from the various planes [45], [44]. This constructive interference condition obtains if the path length difference travelled by light reflecting from successive planes is equal to an integer number of whole wavelengths. The periodicity of the medium suggests an expansion of the dielectric tensor in a Fourier series over the reciprocal lattice:

$$\varepsilon\left(\mathbf{x}\right) = \sum_{G} \varepsilon_{\mathbf{G}} e^{-i\mathbf{G}\cdot\mathbf{x}}$$

which may then be substituted into the wave equation for propagation of the electric field (again, neglecting magnetic interactions) in the periodic medium

$$\nabla \times (\nabla \times \mathbf{E}) - \omega^2 \mu \varepsilon \mathbf{E} = 0$$

Fourier analysis shows that the it is possible to decompose the propagating electric field appearing in this wave equation onto a set of normal modes (mathematical probity requires barring pathological functions not amenable to Fourier analysis, i.e. only a finite number of discontinuities, finite number of extrema in the interval considered, integrated absolute magnitude must be finite, though such fields are likely unphysical; if we are working in a charge-free region we may assert that Laplace's equation would require well-behaved fields [196]). The general solution may be represented by a superposition of these modes.

For a given optical frequency ω the wave vector describing propagation of the electric field may be found via the dispersion relationship. There will be regions in the momentum-energy space (here, frequency and energy are synonymous) where the wave vector $\mathbf{K}$ will be complex, in which case the Bloch wave describing propagation through the medium will be an evanescent wave – falling off exponentially with penetration into the material. The frequency band for which that decay occurs is termed a forbidden band, and any incident light that falls in such a band will be completely reflected; via the historical antecedent of x-ray diffraction crystallography, this was known as Bragg reflection.

As always, the actual physical processes we observe are more complicated than those presented by this simple model. This description is based on

the assumption of a one-dimensional system, but is readily extended to a full three-dimensional treatment. The result of that analysis is that strong reflection will occur for specific angles θ determined by the symmetry operations of the periodic medium. In the one-dimensional case, the relevant symmetry operation is the translationally symmetry of the periodic modulation of the material's index of refraction.

This derivation also assumes that the material under consideration is isotropic. This is not the case in many physically important media – such as the TeO2 crystals used to fabricate our acousto-optical modulators – but it is a useful conceit for developing an intuitive understanding of the relevant scattering physics. In anisotropic materials a more complicated form for the dispersion relationship will be obtained, and the subsequent analysis will be slightly more complicated. In the general case, some dependence on the optical polarization is also expected [98]. Realistic models of beam shapes predict lower efficiencies than would be expected from a basic Bragg scattering analysis [74]. The treatment of acousto-optic scattering interactions in [227] recovers the behaviour found in the Bragg and Raman-Nath regime while avoiding the use of un-physical descriptions of sound, such as the restriction of acoustic waves to a columnar region, that were used in prior derivations

6.5.2 Acousto-optic modulators

Having established a simple model for the coherent scattering of light by a periodic modulation of the local index of refraction, we turn our attention

to the specifics of acousto-optical scattering in acousto-optical modulators.

Those that we use are constructed of Tellurium Dioxide, a material chosen due to the large magnitude of the elements of its strain-optic tensor over the optical wavelength range. This permits substantial acousto-optic coupling without introducing extremely high strain in the material. Effectively, it is a material with a high efficiency figure of merit for diffracting light by sound.

6.5.3 Traveling versus standing wave devices; their use as phase modulators

It is possible to construct acousto-optic modulators where reflection of the sound wave results in the formation of a standing wave; in this case, the analysis of the acousto-optic interaction follows immediately from the description of the periodic modulated medium described above. If the acoustic wave is a traveling wave, the resulting periodic perturbation of local index of refraction will also propagate at the speed of sound in the material. This speed is typically five orders of magnitude smaller than the speed of light in the material, so the periodic perturbation will appear stationary on the time scale of the light traversing the medium, and the Bragg model still serves as a useful basis for developing physical intuition for the light scattering process.

The significant distinction that must be considered for the traveling wave device is the frequency shift that occurs when light is diffracted by a propagating periodic modulation of the index of refraction. Considered from a classical optics perspective, that shift occurs due to the propagation of phase

fronts through the crystal. The analogy offered by reference [407] is that of a Doppler shift that would occur if light were reflected from a mirror moving at velocity v through the acousto-optical material. If the Bragg condition is satisfied, the shift will simply be Ω, the acoustic wave frequency. If the direction of the diffracted light compared to the incident beam tilts more toward the direction in which the acoustic wave is propagating, the frequency will be shifted up; otherwise, it will be shifted down. Alternatively, a particle-based picture of the acousto-optical interaction may be used to more intuitively understand the frequency shift effect. In that description, the acousto-optical interaction is described by (for example) the annihilation of a photon with energy ω ($\hbar = 1$ in this brief analysis), the annihilation of a phonon with energy Ω via a stimulated process in the phonon mode populating the acoustic wave in the crystal, and the creation of another photon carrying the total energy $\omega + \Omega$. Conservation of momentum requires that the final momentum of the emitted photon equal the sum of the initial photon and phonon. This picture can be used to determine if the frequency shift should be up or down from a conservation of energy argument standpoint, depending on whether the scattering involves creation or annihilation of a phonon. This is the $m = +1$ Bragg diffracted mode; the $m = -1$ mode is described by the annihilation of a photon with energy ω, the creation of a phonon with energy Ω, and the creation of a photon with energy $\omega - \Omega$.

We also note something of a hand-wavey argument offered for the application of an acousto-optic modulator as an optical phase modulator. Following

from the expression

$$\omega_f = \omega_i \pm \Omega$$

for conservation of energy, we simply multiply both sides of this equation by time t, obtaining

$$\begin{aligned} \phi_f &= \omega_f t = (\omega_i \pm \Omega)\, t = \phi_i + \phi_{AOM} \\ \phi_f &= \phi_i + \phi_{AOM} \end{aligned}$$

thus we see that by varying the phase of the RF signal used to drive the AOM we may linearly adjust the phase of light diffracted by the device [311].

A more substantive derivation of the phase modulation process in these devices requires – against our repeated objection – that we delve briefly into Raman-Nath scattering theory. We adapt a derivation from [407] to consider the dependence of the diffracted modes on an arbitrary acoustic phase. We assume an acoustic wave propagating largely in a thin sheet nearly perpendicular to the incident light ray induces a perturbation of the local index of refraction described by

$$\Delta n\,(x,\ y,\ z,\ t) = \begin{cases} \Delta n_0 \sin\left(\Omega t - \mathbf{K}\cdot\mathbf{r} + \psi\right), & 0 < z < L, \\ 0, & \text{otherwise} \end{cases}$$

where the wave-vector for the acoustic wave is given by $\mathbf{K}$. We have included here an arbitrary phase term ψ.For simplification, an isotropic medium is assumed, and the perturbation of the local index is taken to be a scalar function. It is assumed that the interaction length L is small – placing the scattering in the Raman-Nath limit, compared to the volumetric nature of Bragg scattering. In this case, the perturbation is effectively a phase grating that effects the transmission of the optical beam, initially described by $\mathbf{E} = \mathbf{E}_0 e^{i(\omega t - \mathbf{k}\cdot\mathbf{r})}$. Assuming that the only effect of the phase grating is to modulate the phase of the incident optical plane waves, the transmitted light can be expressed as $\mathbf{E} = \mathbf{E}_0 e^{i(\omega t - \mathbf{k}\cdot\mathbf{r}) - i\phi}$. The phase shift due to propagation through the interaction medium has the straightforward form

$$\phi = \int_{z=0}^{z=L} ds \frac{\omega}{c} \Delta n$$

where the integral must be evaluated over the path for a specific pencil of optical rays. Assuming a small angle of incidence θ as well as the previously stated assumption that the thickness of the phase grating is small, the resulting phase can be found

$$\phi = \frac{\omega}{c} \Delta n_0 \frac{L}{\cos\theta} \sin\left(\Omega t - \mathbf{K}\cdot\mathbf{r} + \psi\right)$$

which is simply the product of the index modulation with the number of optical full oscillations that occur during the transmission through the phase grating. The dependence on the phase of the acoustic wave appears in

a straightforward fashion. From this expression, the transmitted light may be written $\mathbf{E}_{trans} = \mathbf{E}_0 e^{i(\omega t - \mathbf{k}\cdot\mathbf{r}) - i\delta\sin(\Omega t - \mathbf{K}\cdot\mathbf{r} + \psi)}$ where the modulation index is given by $\delta = \frac{\omega L \Delta n_0}{c\cos\theta}$. We see immediately that the transmitted light field is phase modulated due to diffraction by the acousto-optical device, as we assumed, although the expression obtained here is lamentably more complex than the hand-wavey argument borrowed from Bragg scattering theory. An identity for the Bessel functions allows the intensity to be rewritten in the form

$$\mathbf{E}_{trans} = \mathbf{E}_0 \sum_{m=-\infty}^{\infty} J_m(\delta)\, e^{i(\omega - m\Omega)t - i(\mathbf{k} - m\mathbf{K})\cdot\mathbf{r} + im\psi}$$

the physical interpretation of this result is that the transmitted light field consists of a sum of plane waves propagating in different directions $(\mathbf{k} - m\mathbf{K})$ with different frequencies $(\omega - m\Omega)$ depending on the scattering order. The diffraction efficiency for a given mode can be found here by taking the square of the appropriate order Bessel function for that mode. Here we see that the diffracted optical fields all depend on the phase of the modulated index of refraction, and thereby couple to the phase of the acoustic wave and by extension the phase of the RF signal used to drive the transducer in the modulator device. By this derivation we see that it is possible to directly control the phase of light diffracted with an AOM. The tracking relationship for the phase of diffracted beams and the phase of the RF drive used to power an AOM has been noted before [382], but a rigorous proof of acousto-optical phase modulation is often eschewed in favour of an appeal to physical intuition.

We note that again, of course, the real physical processes cannot be completely described by this model. In an isotropic medium, this analysis suffices for most purposes; in an anisotropic material, the index of refraction depends upon the direction of propagation, so it is no longer as tractable a problem, and it is necessary to consider the diffraction condition more carefully. This is the case for Tellurium Dioxide, where many of the acoustic properties of interest depend on the specific acoustic or optical mode considered; nonetheless, this description suffices for our purposes.

6.5.4 The use of AOMS as amplitude modulators

The mechanism by which these devices may be used to modulate the amplitude of diffracted light beams is relatively straightforward compared to the particular details of the phase modulation effect. Since the coupling mechanism depends upon the photoelastic effect – the distortion of the local index of refraction due to mechanical strain – it is reasonable to assume that for most materials, where an increasing strain results in an increasing distortion and thus a deeper periodic grating – it is relatively straightforward to show that in a simple model the intensity of diffracted light will increase linearly with increasing acoustic wave intensity. This effect of course exhibits saturation behaviour and nonlinearity as the power is increased past some critical point.

6.5.5 Spectral purity of diffracted modes; synchronization and refresh rates in acousto-optic devices

Some substantial consideration must be given to the problem of refresh rates in a traveling wave device, as the acoustic waveform will propagate through the medium. In some applications it may be necessary to synchronize the RF signals used to drive the AOM to the laser pulse, with suitable delay. We intend to use the acousto-optical modulators in our experiment primarily as a relatively slow modulator of optical power, where typical modulation frequencies will be on the order of 1MHz. By way of contrast, the drive frequency for the AOM will be at or around 80MHz (determined not for any scientific reason, but chosen simply as it is the center frequency for the devices we use), and the laser repetition rate of 76MHz, determined by the length of our laser oscillator cavity. A keen experimentalist may note the proximity of the AOM drive frequency and the laser repetition rate and raise a note of alarm, but this is not a significant issue, since the laser is not directly modulated by the AOM drive frequency *in the time domain*. Instead, the drive frequency simply determines the spacing of the periodic grating induced in the Tellurium Dioxide crystal. It is true that in the frequency domain, scattering off the moving wavefronts in this crystal will shift the laser pulse by the AOM drive frequency (the actual shift is slightly more complicated and will also depend on the slow ˜MHz modulation frequency, but we discount that effect for the present for the sake of simplicity). Since we work with a periodically repeating pulse train, the laser spectrum does not actually consist of a single, smooth

function, but instead is represented in frequency space by a comb of components, each spaced by the repetition rate of 76MHz. Each of those components will be shifted by the 80MHz drive frequency. If the frequency shift were exactly or close to coincident with the laser mode spacing, we may be concerned about beat effects that may arise – not in the laser field itself, since none of the 'original' modes will be left in the diffracted beam [302], [397] , but possibly in the nonlinear signals produced via light-matter interactions involving several different beams shifted variously up and down in frequency.

Relatively early in the study of acousto-optical interaction it was understood that scattering by the traveling acoustic wave should result in a frequency shift for diffracted beams [302], [397]. Raman-Nath theory predicts that the light in each diffraction order should be spectrally pure – that it should contain only one frequency component. This was tested by Yeh and coworkers who performed an early laser diffraction experiment to make optical heterodyne measurements of the beat frequency between an un-deflected beam and one deflected by a water cell driven at an ultrasonic frequency. They observed high spectral purity of the diffracted orders limited only by slow thermal perturbations in the liquid at ˜0.5 Hz. By way of contrast, a standing wave device is deprecated for spectroscopic applications where the optical frequency may be experimentally important, as Raman-Nath theory predicts those devices will have complicated spectral distributions in each of the diffracted orders. The even-order diffraction maxima spectra will contain optical frequency components shifted by all even multiples of the drive frequency, while the odd-order

diffraction maxima spectra will contain optical frequency components shifted by all odd multiples of the drive frequency. [134].

Returning to the possibility of nonlinear interaction in our sample introducing a beat frequency, we note that the 4 MHz spacing is fast enough that any oscillation in signals resulting from the nonlinear interaction of two or three such shifted laser pulses will be effectively filtered by the band-pass high gain pre-amplifier and lock-in amplifier used in later data collection and signal processing steps – we typically use at least 30 ms of integration time for the lock-in's low pass filter, which should correspond to 120,000 cycles of a 4 MHz oscillation – we expect to see no interference issues due to this effect.

Additionally, we need to consider the relative timing of the slow, MHz modulation frequency and the laser pulses. During the period of a 1 MHz sinusoidal modulation, 76 separate laser pulses should be diffracted at various powers (ranging from full scale to approximately zero) onto our sample. Given the number of cycles of the experiment that should occur during one period of the slow modulation, we expect the error introduced to our measurements by the lack of any phase-lock between modulation and laser repetition rate to be on the order of 1/76 – a few percent at best. In kiloHertz repetition rate systems, where modulation frequencies are lower, these errors may become significant – such as in reference [204], where a 500 Hz chopper wheel was synchronized to a 5 kHz laser system to ensure that a single chopping cycle would consist of 5 on pulses and 5 off pulses for pump-probe polarization anisotropy measurements.

6.5.6 Tests of amplitude modulation depth and speed with our AOM devices

Modulation speed is limited in a traveling wave device to the time it takes for the acoustic waveform to refresh across the effective aperture. This is limited by the speed of sound in the material, which cannot be easily changed (it is possible of course to use a different material, or to use the same material but to excite a propagating acoustic mode with a faster speed of sound, but those choices typically involve a tradeoff with the acousto-optic figure of merit – the photoelastic coupling will be reduced in those circumstances), and the linear dimension of the laser spot. Faster modulation rates may be achieved by focusing the laser to a smaller waist before it passes through the device.

For our purposes, we did not expect to use modulation frequencies greater than a few MHz, although the availability of an RF-capable digital lock-in does raise this possibility. To ensure that our AOM's could be used to modulate the beams as desired, a fast Si photodiode with a home-built amplifier was placed after one of the modulators. We monitored the power diffracted into the first-order mode. A series of neutral density filters was used to ensure that the power did not saturate the detector, and a low-pass RC filter was used to ensure that system time constant was insufficiently fast to respond to the laser pulse repetition rate. This was necessary, since the bandwidth of the photodiode (˜GHz) and amplifier (approximately 100 MHz) were not sufficient to resolve the 76 MHz laser repetition rate, which would require a sampling frequency of at least 152 MHz. With the added restrictions of a

certain length of RG-58 cable and a 100 MHz oscilloscope, it was impossible to follow the fast laser response without significant aliasing.

The slow modulation applied by the AOM, however, was perfectly resolved. The modulation depth for a few MHz appeared to be 100% within the limits of the signal-to-noise of this simple test. From this we concluded that our AOM scheme could be used to effectively modulate our laser intensity in the 0 Hz to several MHz range. Since this was sufficient for our application, we did not make any effort to improve the response time by reducing the laser spot size through the AOM.

6.6 Homebuilt RF acousto-optic modulation system

We built a three-frequency RF modulation system in order to perform four-wave mixing measurements on samples using the variable beam geometry apparatus. First, however, we replicate the two-pulse measurements to test the functioning of this system. In order to produce the multiple RF signals used for these experiments we make use of a pc-controled direct digital synthesis function generator. We describe the operation of such a device only briefly here.

6.6.1 Direct digital synthesis

This experimental program requires several RF signals that can be readily adjusted to permit measurement of different signal components. For this application, we use a direct digital synthesis (DDS) apparatus as a high

stability, four channel frequency source. DDS sources exhibit extremely high phase and frequency stability over long test periods, and allow us agile control over frequency, phase, and amplitude of our generated signals.

A DDS source uses a high-precision frequency reference in order to generate a set of sampled signals. A phase register determines the state of this precision clock and compares the number of counted samples to a value set by a binary tuning word. If the necessary number of clock ticks have occurred, a digitally controllable phase-to-amplitude block then writes a digital word to a digital-to-analog converter, thereby updating the analog output of the device. Analog filtering removes or reduces the artifacts related to sampled method of signal generation. Careful design of the filter stages is important to avoid aliased signals from polluting the frequency pass band. In brief, the DDS device has a programmed output waveform in a memory that is divided up into a finite number of slices, which are indexed by the time they occur after the waveform begins. After a controllable number of clock cycles, the DDS increments to the next time slice. When the waveform has completed, the DDS returns to the beginning of the waveform memory and repeats its output process [11], [10].

We explored fabricating our own DDS-based function generator to generate the modulation frequencies used in our experiment. Evaluation boards available from Analog Devices permit some interesting experimentation with the ADXXXX DDS chipset, but unfortunately they are intentionally crippled and only provide two usable output channels. Our application requires

three modulation frequencies and one reference frequency, and could almost certainly be implemented with that chipset but cannot be directly performed with the evaluation board. The evaluation board itself required construction of two stabilized precision power supplies and the supply of an external precision frequency source, but it was determined that constructing a usable laboratory device from a single un-crippled chip was not worth the significant effort it would take to ensure no RF cross-talk or other issues were introduced. The construction of RF circuits is notoriously fraught with unexpected difficulties.

As a result, we purchased a PC-controllable DDS-based synthesizer from Novatech (Novatech 409b), based on the exact same Analog Devices chip. This commercially available device, however, allows the use of all four of the chip's DDS outputs. Although we cannot find a reliable reference explaining why, it has been informally suggested that the carrier frequencies that are mixed with the modulation signals from the DDS should *not* be phase-locked. We have not explored this effect ourselves, but we assume that it is therefore not advisable to use a DDS device to produce the unmodulated RF drive signal used to power the modulators since its outputs will be inherently phase-locked. Independent frequency sources are used for the acousto-optic modulator carrier frequencies. We note that the commercial two-frequency APE driver produced phase-locked carrier signals; we have not explore this effect in either two- or three-frequency modulation schemes.

The advantages of using a DDS source are the high degree of phase-stability, the low degree of frequency, phase, or amplitude noise for analog

signals produced using digital sampling, and the agility of computer control. That agility allows us to generate a reference signal using the fourth output that can be easily changed to perform a variety of different heterodyning measurements in a three-frequency modulation scheme. By contrast, using discrete mixer and filter components to produce reference frequencies is inflexible and provides an additional channel for the introduction of cross-talk that has catastrophic consequences for the measurement of weak signals.

6.6.2 Continuous frequency RF sources for acousto-optic modulator drive

The drive frequencies used to power the AOM's are produced using stabilized quartz crystal oscillators (Crystek CPRO33-80.000 oscillators, powered with homebuilt, regulated voltage supplies based on a variable output three terminal linear regulator) designed for use as frequency standards by RF engineers. These devices produce an RF signal centered on a DC offset on the order of a volt. We AC couple the signals produced by the frequency reference sources to the subsequent RF mixing and amplifying electronics via inline capacitors on the central conductor; the common ground is not altered from one side of the isolating capacitor to the other. RG-58 cables are sufficient for the frequency bands used in these experiments, though SMA connectors are preferred to reduce VSWR problems.

Unfortunately, the frequency range available in such devices is determined by commercial demand, and the 80 MHz oscillators we selected are

uncomfortably close to the Mira laser's pulse repetition frequency. Nonetheless, we chose to use these devices since three relatively inexpensive frequency reference sources allowed us to ensure that the RF drive frequencies generated were not phase correlated, which previous experimental research suggests to be necessary [249]. We argue that the near coincidence of RF drive frequency and the Mira repetition rate (76 MHz) should not cause significant problems with generation of beat frequencies, since the beam *power* deflected by an AOM does not respond to the drive signal used, but rather the modulation of that signal power, which is determined by the modulation frequencies produced by the DDS function generator.

We note that there is a possibility of an unintended beating effect occurring due to the frequency shift of the diffracted light: depending on whether the +1 or -1 mode is selected, the light diffracted by the AOM's will undergo a frequency shift of +/-80 MHz. We originally began using AOM's in these experiments to use the frequency shifting effect to move the pump and probe pulse frequencies away from one another in a degenerate dT/T measurement where classical interference effects were confusing the signal of interest – at the time, our modulation for lock-in detection was performed using a mechanical chopper and we were not concerned with using the AOM's to gate the excitation lasers. In those simpler experiments, an 80 MHz signal derived from an RF frequency generator was used simply because that drive frequency lay in the center of the AOM bandwidth. Since the shift was not precisely coincident with the Mira repetition rate no problems were anticipated. To test whether

the coincidence of the frequency shift from the new RF oscillators and the Mira's rep rate will cause any noticeable effect on our experiments we repeated the two pulse measurements performed using the original 80 MHz generator and saw no changes; from this we presume that this unfortunate choice in RF drive frequency will likely have no effect on our results. Moreover, the 4 MHz frequency difference would, if it introduced any beating, not be visible in the signals measured using the photodiode-preamplifier-programmable filter setup we use.

6.6.3 Mixing and amplification

The RF signals generated from the crystal reference sources and the DDS function generator are split, attenuated, mixed, re-combined, and amplified using discrete RF components from Mini Circuits.

Our first implementation of a mixer-amplifier circuit derived the lock-in reference frequency from the DDS modulation frequencies (i.e. the two pump and the probe modulation frequencies for a three-frequency modulation; or a single pump modulation frequency, doubled, and the probe modulation frequency for a two-frequency modulation experiment). This was awkward, as it required the use of additional doublers and filter components, and required physically changing the RF circuit to switch between different measurements. There is, furthermore, the ambiguous factor of 2 that keeps cropping up in these projects, and which must be carefully dealt with when changing the RF circuits to perform different measurements.

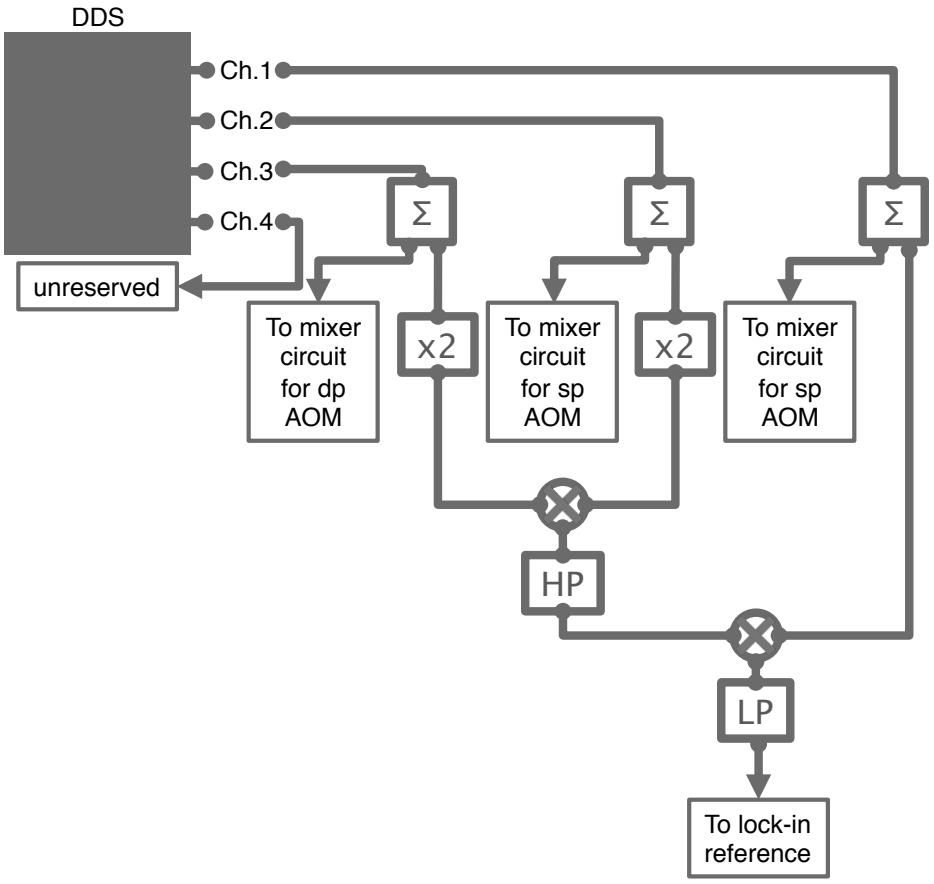

The original design for the three-frequency RF generator used discrete components to provide the reference frequency used for lock-in detection.

Figure 6.16: Generating reference with discrete RF components

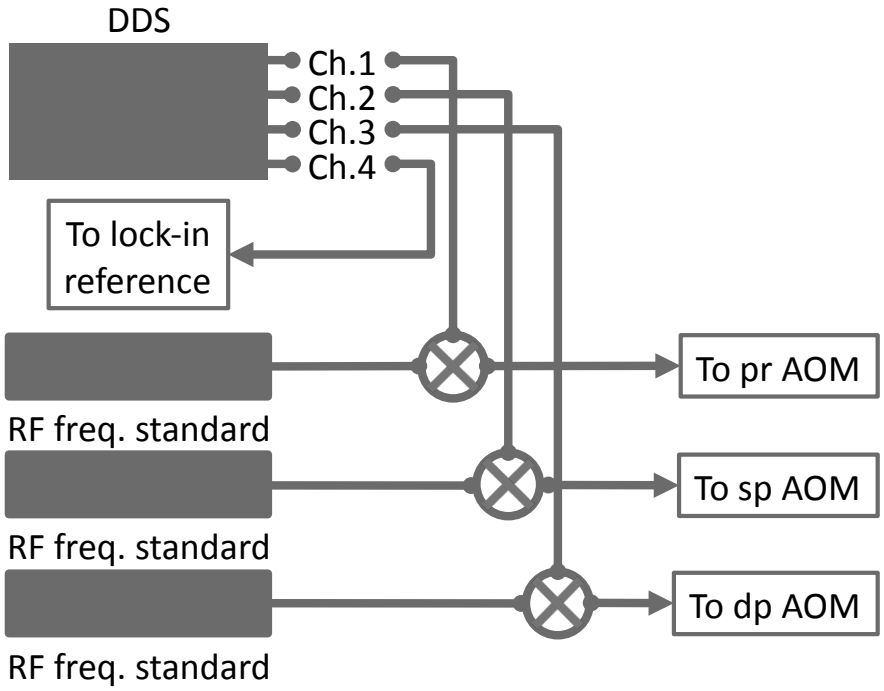

Figure 6.17: Generating reference with DDS

We had an unreserved channel on the DDS board, however, and quickly abandoned the previous method of obtaining a lock-in reference by mixing with discrete RF components in favour of using this phase-stable, high spectral purity signal.

Each RF carrier frequency is produced, as described previously, by an independently crystal reference, powered by an independent, regulated home-built supply. That RF signal is AC coupled to a mixer, where it is mixed with one channel from the DDS generator, to produce a modulated RF signal that is then amplified into the 1-2 Watt range, then sent to the acousto-optic modulator.

A slight addition to this scheme is made to perform phase-sensitive, interferometrically precise three-pulse measurements. An additional RF signal must be supplied to the acousto-optic modulators of the pump beams, in this case, as will be described elsewhere. For that purpose, an HP RF function generator is used to create a single RF carrier, which is added to both of the RF signals sent to the pump AOM's, prior to final amplifier stage. For a schematic diagram of the RF mixer constructed for these three-pulse measurements, see the final section of this chapter

To avoid saturating any of the discrete components and generating unwanted nonlinearities in the RF mixer-amplifier, we checked RF power levels at each point in the experiment. Since none of the signals used in this experiment are very high frequency, it was possible to use a fast oscilloscope with a proper 50 Ohm terminator to examine the signal at each step in the

mixer-amplifier. A number of conventional RF attenuator pads were inserted at various points throughout the experiment to ensure that no input tolerance was exceeded for any of the RF components. Since the RF crystal reference signal is a fixed amplitude, control of the final modulated RF signal amplitude was provided by adjusting the DDS function generator output levels.

6.6.4 Beam modulation method

The modulation of the laser was performed using traveling wave acousto-optical modulators, specifically three identical devices from Gooch & Housego designed for use in the visible and near-IR frequency range (Gooch & Housego/Neos Technologies AOBD model 46080-2-LTD). In these AOM's, a high frequency RF piezo transducer is used to transform RF power into a propagating acoustic wave in the crystal, in this case, TeO2, chosen for its advantageous acousto-optical properties. The bulk acoustic wave is a local pressure modulation, which results in a periodic change of the local index of refraction of the material. On the time scale characteristic of pulse propagation through the crystal, the acoustic wave essentially does not propagate, and some portion of the incident laser beam will scatter as though the light were passing through a transmission grating. We have described the function of these devices previously in this chapter, with references to the various restrictions on their use, etc.

It is possible to use either the zeroth-order mode or the first-order mode (or indeed, a higher order mode, although this is inadvisable as the acousto-

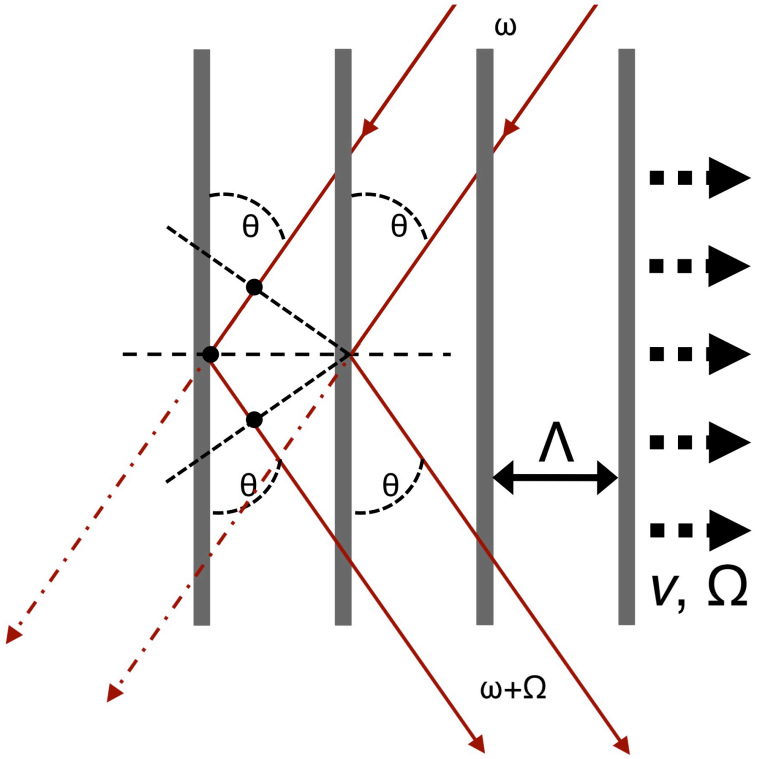

Bragg diffraction of a laser beam (at frequency ω) by a standing-wave acousto-optic modulator results in a frequency-shift for the scattered light. The first-order (m=+1) diffracted mode shown here increases its frequency by the acoustic frequency (Ω). Resonant scattering at the Bragg angle, 2θ, occurs when the incoming beam forms an angle θ with the phase fronts of the acoustic beam.

Figure 6.18: Bragg diffraction in an AOM

optic interaction in these devices approaches the Bragg limit) as the desired beam, and to block the others. The simplest choice is to use the zeroth order mode, since the beam steering of the undeflected mode does not depend upon the RF signal applied to the modulator. This is not the ideal solution, however, since the modulation depth is limited by the maximum diffraction efficiency. While manufacturers of AOM's often cite figures approaching 80% or 90% diffraction efficiency, that number depends upon an optimal alignment, and is only obtained for certain polarizations, beam size, etc. – in practice, 50% diffraction is more commonly achievable. Thus, using negative logic (in the digital circuit sense) where the high RF power state results in low optical power is deprecated. The reduced modulation depth available in this application would result in decreased lock-in sensitivity.

Instead, we use the first order diffraction modes, i.e. either the ± 1 modes. Even in these beams, however, we note that there will always be some finite amount of bleedthrough when the RF signal is in its low state, but the extinction ratio is many orders of magnitude superior to what can be obtained using the $m = 0$ mode. The disadvantage, of course, is that the beam steering depends upon the frequency used. This also has implications for the optical multiplexing method we develop (q.v. *sub*) that relies upon steering multiple wavelengths with multiple acoustic waves.

6.6.5 Replication of two-pulse measurements

To test the function of the home-built RF modulation system, we perform two pulse measurements using a pump-probe geometry. The intensities of the diffracted pump and probe beams are typically modulated at approximately 1MHz, with the difference between the two modulation frequencies used as the reference for lock-in detection.

The samples used for these trials are simple single quantum well and multiple quantum well structures studied in a reflection geometry (q.v. our remarks on the reflection geometry measurements performed in [183], n.b. that the presence of additional layers in the structure is unlikely to result in substantially stronger signals as is typical for transmission measurements; also q.v. our discussion of the complicated phase relationship that results for emission from multiple layered samples when studied in reflection geometries in the chapter on 2dFTS measurements). The samples are prepared as previously, and mounted in a liquid Helium cryostat. Two-pulse experiments that probe the population dynamics are not sensitive to dephasing, and we therefore perform these measurements at higher temperatures to conserve Helium – typically at approximately 30 K. The additional population of phonon modes is not expected to drastically alter the lineshape observed here.

Unlike our first measurements on these samples, we do not record any data using a spectrometer, as we are primarily interested in a test of the lock-in modulation system we have constructed. The reflected probe beam is collected and spectrally analyzed with a monochromator, using the same

optics and detection system previously employed. Indeed, the only difference between these measurements and those performed with the APE system are the sources of RF signals used to drive the acousto-optic modulator and sent to the lock-in amplifier for a reference.

These data are collected as a function of wavelength. Specific times for T, the pump-probe waiting time, are chosen that are sufficiently long that the coherence spike artifact and coherent population oscillations are expected to have damped out. The monochromator central wavelength is set by computer control, the experiment is directed to wait three times the lock-in time constant to allow the low-pass filter to clear, then a data point is collected and read into the home coded Labview programs used to control the experiment. The monochromator central wavelength is then incremented to a new position, and the process is repeated until an entire spectrum has been acquired.

We believe these measurements provide equal or better resolution of the lineshape seen with the commercial device. Without careful diagnostic tests it is not prudent to claim drastic improvements in performance; the observed light-hole and heavy-hole exciton resonances are clearly resolved, however, and we find that it is possible to perform two-pulse measurements using very small lock-in waiting times – indeed, we do not see any substantial changes after reducing the lock-in time constant to sufficiently small values that the rate limiting factor for collecting a spectrum is no longer the waiting period but rather the mechanical adjustment of the monochromator. Typically we collect two-pulse data with a ten millisecond time constant.

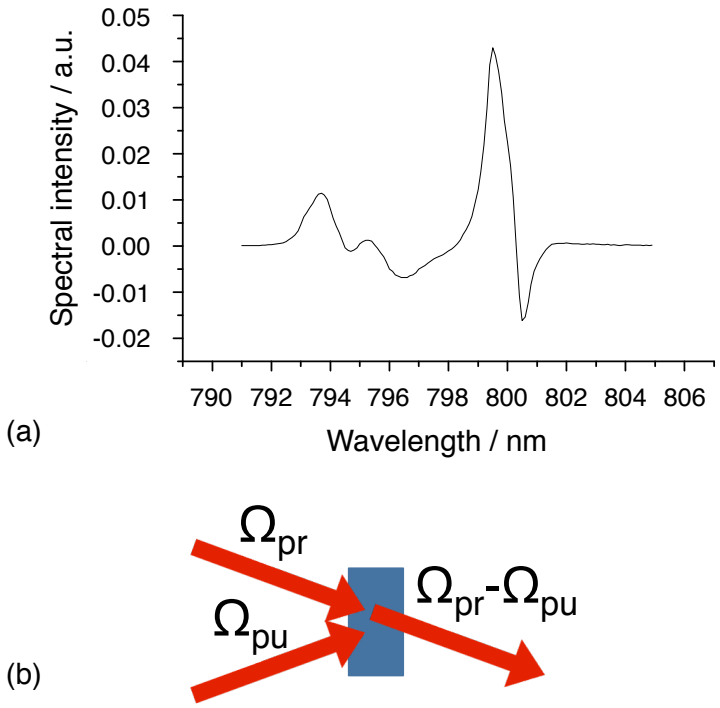

Two-pulse differential reflectivity measurements (a) taken on a GaAs quantum well sample using the homebuilt RF modulation system. Spectral data are collected by modulating the intensity of the pump and probe beams at two different frequencies using acousto-optic modulators, then using the difference of those two frequencies for lock-in detection (b). The cartoon of the modulation scheme is not intended to reflect the actual geometry of the experiment,.

Figure 6.19: 2-pulse dR with homebuilt RF system

We did not previously address the details of the phase of the spectral measurements, though we mentioned the principle of adjusting the phase of a lock-in reference to obtain the maximum signal strength. Lock-in amps can be used to determine the intensity of signal components that are in- and out-of-phase with the reference signal [355]. In some cases, there is no expected out-of-phase component, and the proper adjustment of the reference signal phase results in a null output for the out-of-phase channel; in general, however, a more complicated situation may obtain where the signal of interest has components that oscillate in and out of phase with the modulation of the excitation sources. This is the case for the exciton systems we study; specifically, for the exciton-surface plasmon polariton hybrid mode, the phase of the signal is expected to vary across the spectral line. As such, it is necessary to establish some principle to use to properly set the phase of the input signal relative to the reference.

For our first measurements, performed using the commercial two-frequency device, we followed the scheme privately communicated to us by our collaborators at the University of Oldenburg to set the phase for the lock-in amplifier. This consists of simply moving the monochromator to the peak of the heavy-hole resonance, then using the automatic phase set control on the digital lock in amplifier. The lock-in amplifier then iteratively adjusts the phase shift of an internal reference derived from the input reference frequency to maximize the in-phase signal component.

Using the computer controlled DDS function generator allows us to per-

form more sophisticated experiments with the lock-in detected signal. Since we wish to develop the toolset necessary to perform three-pulse measurements, we explore the ability of the AOM's to control the phases of the three beams that will be used. In our partially collinear 2dFTS experiments we did not concentrate on the relative phases of the three pulses used. In part, we neglected the phase between the first two pulses that interact with the sample because little effort is made to determine that relationship in typical non-collinear geometry 2dFTS measurements, where a subsequent, independent, spectrally resolved measurement is used to properly set the phase of the 2dFTS spectrum. The partially collinear detected four-wave mixing signal is purely real, unlike the phase and amplitude signal extracted from spectral interferometric heterodyne detected non-collinear 2dFTS measurements; as such, we cannot perform any adjustment of the phase of the partially collinear measurements after the fact. We assume that the phase relationship between the pump pulses in the partially collinear experiment is trivial ($\varphi = 0$) when the two pulses are temporally overlapped, but that assumption may be questioned. With the more sophisticated amplitude and phase modulation scheme we develop here, it is possible to arbitrarily control the phase of any of the pulses used in a 2dFTS measurement, which should allow us to remove this ambiguity in any subsequent experiments.

To that end, we perform a two-pulse experiment using one pulse coming from either the static pump or dynamic pump arm of the Mach-Zehnder Interferometer as the pump pulse – call that (1) –, and the probe beam. The

other arm of the Mach-Zehnder interferometer is blocked – call that (2) –, but we set the AOM in that beam to modulate the intensity of the beam at the same frequency used for the pump beam (1). Thus, the intensity modulation of both pump pulses (1) and (2) are performed at the same frequency, but only pulse (1) is incident on the sample during the first experiment. This pump-probe experiment is used to perform a spectral measurement, resolving the two exciton resonance features. We set the phase of the lock-in amplifier as before on the peak of the heavy hole exciton resonance.

We then block the original pump pulse (1), and perform a second pump-probe experiment with the other pump pulse (2). The precise phase relationship between the light diffracted into beam (1) and (2) is not known at this point, but it is constant since the two modulation signals have a well-defined phase relationship. We can thus perform another spectral measurement with pump (2) and the probe beam, and recover a lineshape that is multiplied by some factor ranging from -1 to 1. Again, with this measurement we are only resolving a real valued function – the intensity due to the probe and co-propagating signal fields – and therefore we do not distort the lineshape other than this scaling. We can easily set the phase of the (2) pump beam to be equal to the (1) pump beam by adjusting the phase of (2)'s modulation signal generated using the DDS until the spectrum observed while scanning the monochromator reproduces the correctly phased one obtained with pump (1) and the probe. It is possible to rotate the phase difference between the two spectra very simply by adjusting the phase of the modulation signal sent

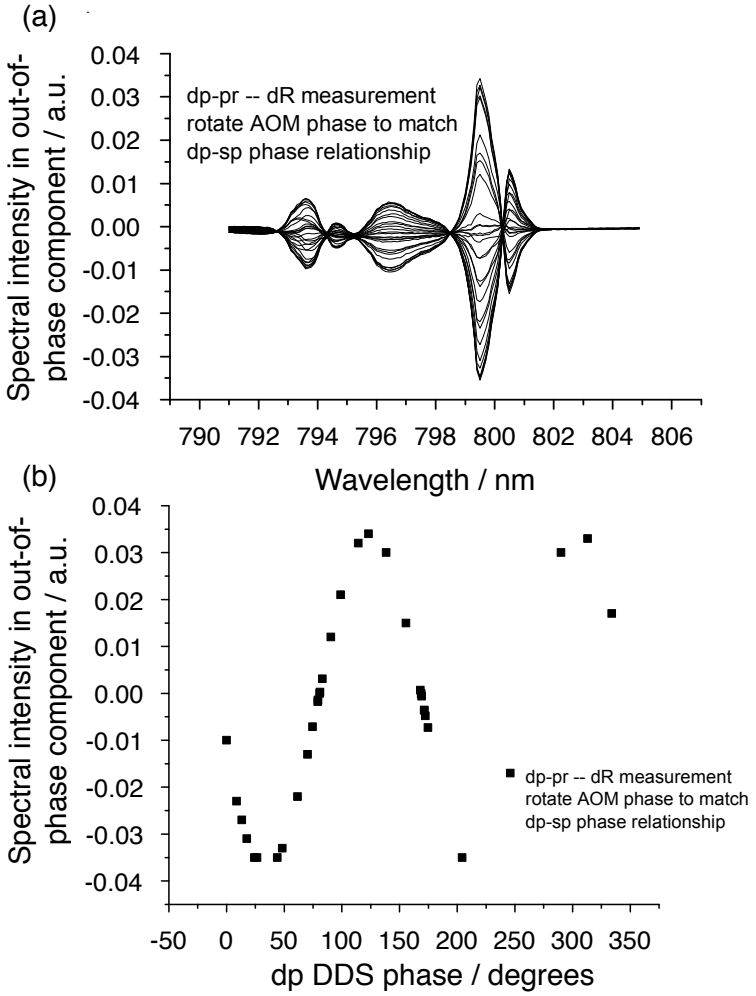

Adjusting the phase of the DDS signal used to generate the modulated RF signal driving the dynamic pump beam AOM results in a change of the signal phase relative to the lock-in reference signal (a). A two-pulse differential reflectivity spectrum using the static pump and the probe beams is used to set the lock-in phase. Keeping that phase relative to the reference signal but switching to the dynamic pump beam, a spectrum may be obtained with a different phase relationship. We measure the out-of-phase signal component as a function of the DDS RF phase sent to mixer circuit driving the dynamic pump AOM (b). Note that the phase of the acousto-optic modulator varies at twice the rate of the drive signal generated via the DDS; this factor of two is also reflected in the frequency of intensity modulation compared to the DDS frequency.

Figure 6.20: 2-pulse dR with homebuilt RF system

second AOM. We show here a plot of the out-of-phase component of the signal detected with pump (2) and the probe beam. By scanning the phase of the DDS drive signal, it is possible to move the spectral information into or out of phase with the internal lock-in reference set from using the reference signal generated on the fourth channel of the DDS device. When actually setting the phases of the two pump pulses to be equal, it is simpler to examine the out-of-phase component while sitting on top of the heavy hole exciton peak, and adjust the phase of the DDS modulation signal until the out-of phase signal component is minimized. This same pump-probe comparison procedure may be used to establish a phase relationship among the two collinear pump pulses used to perform a three-pulse experiment.

6.7 Three-pulse measurements of weak ultrafast four-wave mixing signals

The goal motivating the construction of this RF modulation system is, of course, to perform more complicated nonlinear experiments that permit the measurement of dephasing times – and, conceivably, the application of these detection schemes to performing a full 2dFTS measurement.

For the moment, this is not practical with our experimental apparatus. Although we have had success in resolving four-wave mixing signals in a reflection geometry, we need to change the detection method in order to increase the data acquisition rate. Otherwise, a full 2dFTS data set (or the similarly complicated data for some other three-pulse, spectrally resolved experiment)

will take too long to acquire, and will not be able to be fully captured before the experiment can be expected to lose interferometric stability. The rate limiting factor for performing these measurements is the serial collection of spectral data; in order to reduce the necessary experiment time, a parallel method of detection is needed. There are possible technical solutions to these issues, which we will address subsequently.

First, we consider an intermediate result – the measurement of the laser pulse autocorrelation traces using the RF lock-in detection scheme. These measurements are normally made to determine the pulse temporal overlap positions, in order to accurately determine the τ and T delays. Using the RF-AOM modulation scheme to detect these signals reveals different features from those observed using a mechanical chopper to modulate the laser beams. We did not expect to observe these different correlation traces, but realized that the unusual features present in these signals reveal some interesting aspects of the nature of heterodyne detection with this apparatus. Having observed strange effects in the two-pulse autocorrelation measurements that we normally use as a diagnostic, we then perform a two-pulse measurement on the semiconductor system we have previously studied using the commercial acousto-optic modulation system and our homebuilt RF system, now using a different modulation scheme. The unusual nature of these measurements greatly informs our subsequent approach to observing four-wave mixing emissions in three-pulse measurements.

We then turn our attention to a digression on multiple acoustic fre-

quency, multiple optical wavelength operation of acousto-optic modulators. This discussion is necessary to better understand the trick we develop to use the acousto-optic modulators in our experiment with both the modulated Ti-Sapph beams used for the experiment itself and a co-propagating, unmodulated HeNe beam that is used to interferometrically stabilize the experimental apparatus. There is extensive literature on the use of acousto-optic devices in various applications that are somewhat similar, but no other method has been demonstrated (to the best of our knowledge) that is quite as simple as the one we use. Partially, we expend so much energy cataloguing these more sophisticated acousto-optic devices because we are surprised that our more-or-less dumb solution works as well as it does.

We then consider the problems of intensity and field heterodyne detection that arise when using the three-frequency lock-in detection method. To the best of our knowledge, these issues have not been explored elsewhere, if only because three-frequency modulation has not previously been used to extract weak signals that co-propagate with an additional field that may be used as a local oscillator – generally, optical measurements of extremely weak signals are designed to result in a background-free emission that can be spatially isolated from other light sources, and then integrated for a sufficient long time to improve the signal to noise. As noted, we are interested in developing an optical experiment that works in a partially collinear geometry where the phase-matched four-wave mixing emission co-propagates with a strong, incident field. Here, we show that it is possible to observe not just the transient

time-integrated envelope of a four-wave mixing signal, but also to directly observe the optical frequency oscillation of that emission via a phase-sensitive detection technique that would permit direct, straightforward extension to a 2dFTS or similar sophisticated measurement.

6.7.1 Unusual two-pulse measurement results

Here, we describe the unexpected results of two-pulse measurements that we performed specifically as preparation for the three pulse measurements. Specifically, we report unusual autocorrelation measurements performed using two-frequency detection with acousto-optic modulators used to modulate the laser. This result suggests re-examination of the two-pulse measurement we performed previously, using an alternative reference signal. The conclusions from these measurements strongly influence the method we use to detect the weak four-wave mixing signals with which we are primarily concerned in this project.

6.7.1.1 Laser pulse correlation trace measurements

A broad range of three-pulse measurements can be performed without accurately determining the temporal pulse overlaps to zero the T and τ times. Many experiments use a two-pulse coherence spike artifact to approximately find the zero, although the exact shape of this feature is, as we have noted, not easily modeled and as a result it may not provide a high degree of accuracy. It is also possible to observe phase-matched emission in two complementary

directions, and to assume that the pulse zero time overlap occurs when the coherent artifact intensities in those two channels are equal; this method makes certain assumptions about the symmetry of the system being probed (most likely true in transmission measurements) but is also susceptible to simple errors introduced by unbalanced detection of two spatially separate signal fields. Some of the interesting early work studying four-wave mixing lineshapes from semiconductor exciton systems was performed without significant ability to characterize the temporal behaviour of the pulses at all; the work presented in reference [324], for example, relied on assumptions of the picosecond pulses used since a nonlinear measurement was not available for those experiments.

To perform a measurement like 2dFTS where a transient four-wave mixing signal is effectively time-resolved (we, like other groups performing these coherent spectroscopy techniques, observe our signal of interest in a Fourier conjugate domain but can transform those results to obtain a time-resolved signal), however requires accurate timing of the pulse delays. Auto-correlation and cross-correlation measurements provide the ability to roughly resolve the temporal behaviour of the pulses used in these ultrafast nonlinear experiments.

Electronic instruments cannot respond quickly enough to make direct measurements of femtosecond scale phenomena; it is therefore necessary to effectively sample-and-hold these phenomena, freezing some record of their effects until a relatively slow electronic device can respond and a measurement can be made. Almost any optoelectronic device will exhibit a nonlinear re-

sponse if it is sufficiently highly excited (c.f. the oft repeated remark of Arthur Schawlow, that "anything will lase if you hit it hard enough," [75] which led perhaps most famously to the demonstration of Jell-O lasers by Ted Hansch and coworkers [288]). As a result of the nonlinearity exhibited by such a device, it can be difficult to perform a linear measurement of the pulse characteristics – pulse duration, etc – as the instrument used will introduce distortion itself. As a result, careful pulse measurements should strictly be analyzed using a well characterized device such that the signal of interest may be de-convoluted from the instrument response function [96]. Most laboratory techniques indeed rely on nonlinearity to characterize laser pulses. An entire discipline of optical science is dedicated to developing new tools to better study and parameterize ultrafast pulses; we will avoid extensive discussion of FROG and all of its related technologies here, for as powerful as they may be we have not made use of any of these more sophisticated methods in our own experimental program, which depends upon the older time-domain characterization methods described here.

If a sufficiently fast phenomenon is available to use as a reference (for all intents and purposes, we are referring to a faster laser pulse), a cross-correlation measurement where an unknown optical field is characterized using that faster phenomenon would be possible. Typically this is not possible for most ultrafast experiments, where the fastest available pulse on an optical table – the one being used to perform nonlinear optical measurements – is the phenomenon in need of characterization. Thus, auto-correlation measure-

ments are performed, where the pulse is used itself to characterize the pulse characteristics.

An intensity autocorrelation measurement, where a pulse is split and one part of its power delayed relative to the other fraction before being combined on a square-law detector, would result in a signal given by the convolution integral

$$A_C(\tau) = \int_{-\infty}^{\infty} I_s(t) I_r(t-\tau) dt$$

where the function $I(t)$ represents the intensity due to the combined optical fields, and τ describes the delay between the two pulses. In this thesis, we will go back and forth between the terms 'autocorrelation' and 'cross-correlation' without any significant difference: it is true that all of the pulses used in these experiments derive from the same laser source, suggesting the use of 'autocorrelation,' but the measurements performed on the frequency shifted pulses of interest here are perhaps most accurately called 'cross-correlation' measurements, since the beams are no longer frequency degenerate. Since the distinction does not seem significant here, we use these terms essentially interchangeably.

This measurement is necessarily a symmetric function about its zero, and provides only very limited information about the laser pulse studied [96]. There are an infinite number of symmetric and anti-symmetric pulse shapes that will exhibit the same intensity autocorrelation function. Nonetheless, the

symmetry about the zero-delay position makes this relatively simple measurement useful, and it is therefore sometimes used to estimate pulse timing.

Higher order intensity autocorrelation measurements, described by

$$A_n(\tau) = \int_{-\infty}^{\infty} I(t) I^n(t-\tau) dt$$

can provide more information about the pulse characteristics. The functional form used here may be somewhat surprising at first as it *prima facie* treats the intensities at different times differently, until one considers that for high n, the n-th order autocorrelation measurement is an integral convolution of the intensity function with some increasingly high-localized function. In the limit of $n \to \infty$, the second intensity term in the integrand would become a Dirac delta function and the higher order autocorrelation would provide a direct measurement of the pulse shape [96].

In order to determine the pulse temporal overlaps, we used a two-photon detector to perform an interferometric autocorrelation measurement. This technique is well established, and functionally similar to the use of a non-linear crystal to generate a temporally gated second harmonic optical field, which depends in intensity upon the delay and phase between two pulses [97]. Those measurements observed interferometric, fringed signals for collinear pulses, similar to the signals we observe for the auto-correlation of the pump pulses. A semiconductor device with a sufficiently wide band gap can be substituted for the second-harmonic crystal; see, for example [309], where an

unbiased AlGaAs detector with a bandgap in the 660nm range is used to measure interferometric autocorrelation signals. It is not strictly shown whether the millivolt signal observed for pulsed lasers are due to a second harmonic generation effect over a single coherence length inside the diode or simply due to two-photon absorption, but the LED derived signal worked equally well as that derived from a second harmonic crystal to characterize the laser pulse. The additional advantage of using a semiconductor device rather than the purely optical second harmonic method is that no phase-matching is required, so that the measurement is largely insensitive to polarization, alignment, and wavelength. Similar autocorrelation measurements performed using two photon absorption in biased ZnSe detectors demonstrate the usefulness of these techniques [314], which may be more practical for the characterization of very short pulses where propagation through the relatively thick nonlinear crystals used for second harmonic generation results in dispersion that would limit the temporal resolution of such a measurement. Photocurrents derived from a two-photon absorption process have also been demonstrated as a tool for characterizing pulses generated from low repetition laser systems [154]. A logical extension to higher order photon absorption processes has been demonstrated; in analogy to the increased pulse information available in a second order autocorrelation measurement, these higher order measurements will provide further information unavailable using a two-photon detector. Three-photon processes can be used to study asymmetry in the pulse, such as frequency chirp [236]

More explicitly, a two-photon detector can be used to measure a photo-

voltage signal that depends upon the intensity squared of the combined optical field, yielding a signal represented by

$$G_2(\tau) = \int_{-\infty}^{\infty} \left\langle \left| (E_1(t-\tau) + E_2(t))^2 \right|^2 \right\rangle dt$$

where we have used the electric fields rather than the intensity fields, for reasons relevant to our subsequent discussion of field versus intensity heterodyne schemes. The subscript of 2 here refers to the order of the autocorrelation measurement. The signal provided by a second order autocorrelation measurement such as this contains components that depend distinctly on the delay τ that is scanned between the two pulses; there are constant background terms, a term that depends upon the product $\omega\tau$ of the optical frequency and the delay, and a term that depends upon twice that product $2 \times \omega\tau$ [96].

When we performed our previous 2dFTS (and differential transmission) experiments, we would determine the pulse timings using this kind of measurement. A flipper mirror diverted the beams away from the cryostat and onto a wide gap semiconductor photodiode. The photocurrent induced in the diode was dumped across a load resistor to produce a photovoltage, which was then amplified using a precision instrumentation pre-amplifier (SR560, Stanford Research Systems) then detected using a lock-in amplifier (SR830, Stanford Research Systems). The modulation was provided using a mechanical chopper wheel, which interrupted the beams at typically 1-2 kHz. When measuring the static pump-dynamic pump autocorrelation, the chopper would

be used to modulate both beams simultaneously, after the point where the two arms of the Mach-Zehnder interferometer recombine. In the case of the static pump-probe autocorrelation, the chopper, still in the same position, was used to modulate only the pump beam.

For the non-collinear static pump-probe autocorrelation measurements, the high frequency components were not present in the detected signal. This is presumably due to either the variation of the spatial interference fringe across the focused spot on the two-photon detector, or the frequency shift of the pump beam relative to the probe beam. That shift may have resulted in a beating between the frequency components of the two optical fields that would not be detected using the relatively low bandwidth loaded photodiode, and which would exceed the bandwidth of the precision pre-amp.

For those autocorrelation measurements that were performed for the collinear beams, an interferometric autocorrelation was observed. The finest resolution used for incrementing the delay stages in these experiments was typically 0.15 um, resulting a change in optical path length of 0.30 um for each step. In order to observe an oscillation occurring at the optical wavelength of (approximately) 800 nm, a sampling resolution of 0.40 um is required – this condition was satisfied, and the $\omega\tau$ dependent features were revealed in the autocorrelation trace. We did not look for the higher frequency components occurring at $2 \times \omega\tau$, which would have required a more precise scan of 0.20 um, but would (at times) see some modulation of the fringe pattern that may be due to the higher frequency component aliasing down into our observed

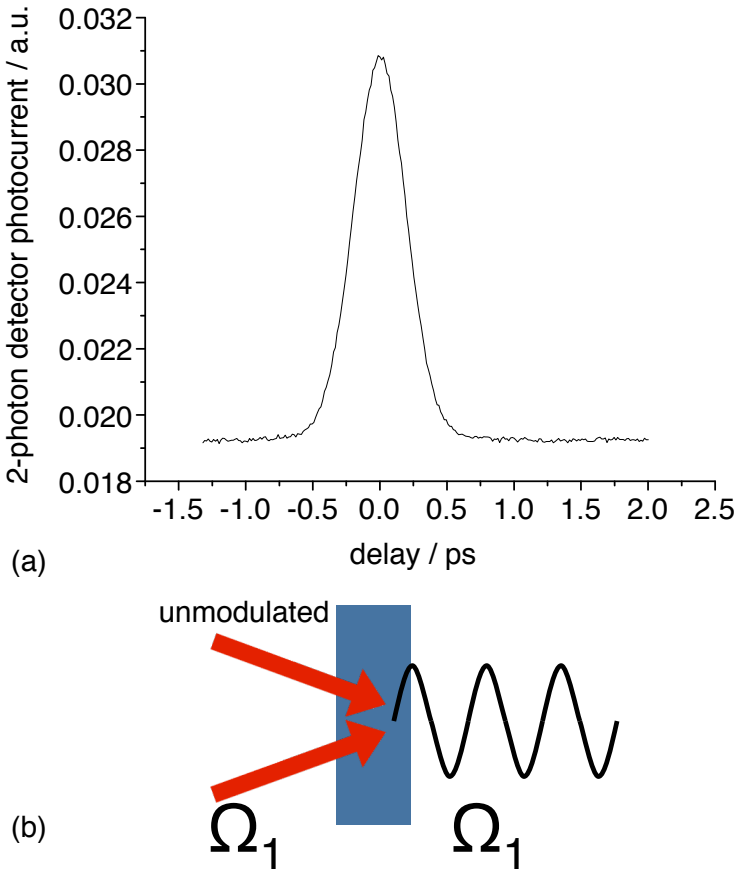

Auto-correlation trace taken for a non-collinear pulse pair, using the static pump and probe beams (a). The *T* delay is scanned by translating the probe stage. A schematic of the the modulation and detection scheme (b) indicates that the intensity of one excitation pulse is modulated using a mechanical chopper that interrupts the beampath. An electrical signal corresponding to the photocurrent induced by a nonlinear process in the wide-gap semiconductor is detected at the same modulation frequency. This diagram is not intended to reflect the actual geometry of the detector and excitation beams.

Figure 6.21: Noncollinear autocorrelation with chopper

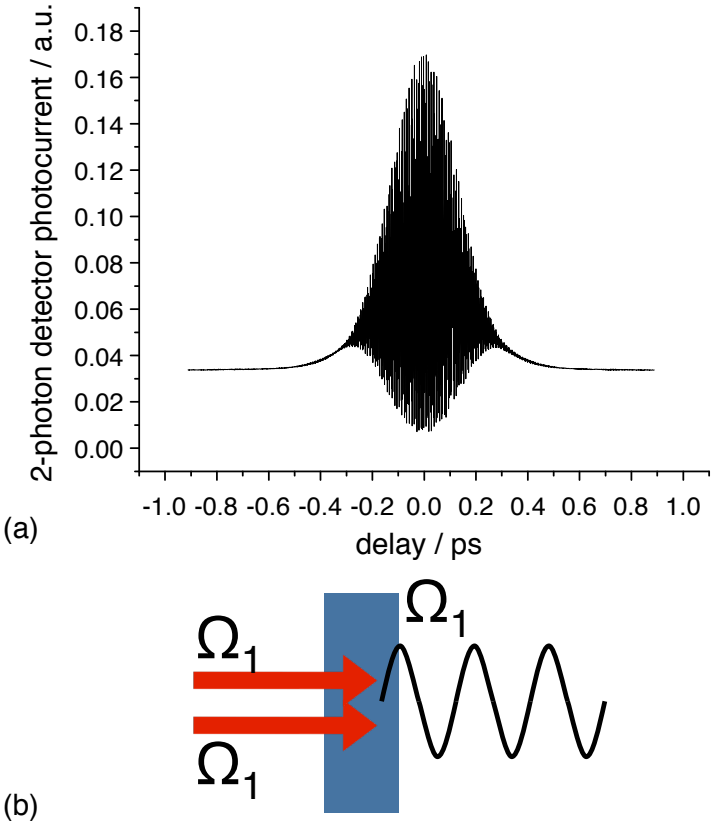

Auto-correlation trace taken for the collinear pump pulse pair (b). The τ delay is scanned by translating the dynamic pump stage. A schematic (b) of the modulation and detection scheme indicates that the intensities of both excitation pulses are modulated at the same frequency using a mechanical chopper that interrupts the beampath. An electrical signal corresponding to the photocurrent induced by a nonlinear process in the wide-gap semiconductor is detected at the same modulation frequency. This diagram is not intended to reflect the actual geometry of the detector and excitation beams.

Figure 6.22: Collinear autocorrelation with chopper

signal.

To determine the temporal overlap of these pulses, a slow envelope function was fit to the measured autocorrelation trace. In the future, given the points raised regarding maintaining a precise phase relationship between the two pump pulses, it is recommended that more careful attention is paid to accurately determining the pulse temporal overlap and relative phase. With the addition of the acousto-optic modulators to the experimental apparatus, we have the ability to control independently the phases of any of the three pulses, providing precise control of this degree of freedom. It is suggested that the autocorrelation measurement using the two-photon detector may suffice as a diagnostic for this purpose, or a two-pulse differential reflectivity measurement may be used to monitor the pump relative phase.

In order to perform three-pulse measurements on the exciton systems we study, we then attempted to measure the autocorrelations of the laser pulses using those acousto-optic modulators as the modulation source in place of the mechanical chopper. The DDS function generator is used to produce a modulation signal typically in the 0.500 MHz range; when mixed with the AC-coupled CW RF 80 MHz signals from the oscillators, this results in a high frequency signal with an envelope at twice the modulation frequency generated by the DDS board – thus, the 0.500 MHz modulation signal will actually result in a modulation of the RF power being sent to the acousto-optic modulator at 1.000 MHz, twice the generated frequency. We have not previously remarked on the difference between the synthesized frequencies and the in-

tensity modulation frequencies, but it becomes increasingly relevant to this discussion here. The intensity of the light diffracted into the $m = \pm 1$ modes is approximately linear over the range of RF powers used here; as a result, the time-averaged intensity of the light in each of the beams is modulated at twice the DDS frequency. The intensity of the diffracted light is determined by the amount of high frequency RF carrier power sent to the acousto-optic modulator – it is that high frequency signal that is transformed into a grating via the acousto-optic effect. The slow modulation frequency may simply be thought of as modulating the depth of that grating, and hence, the intensity of the diffracted light at any particular time.

We perform these correlation measurements where one beam is intensity modulated at f_1 and the other at f_2, and detect at the reference frequency $\Delta f = f_1 - f_2$. For specificity, we took most of the autocorrelation data with the probe beam intensity modulated at 1.000 MHz (using a DDS generated signal at 0.500 MHz) and the static pump beam intensity modulated at 1.050 MHz (using a DDS generated signal at 0.525 MHz). The DDS generator is used to produce a 0.050 MHz reference.

The results for the non-collinear, static pump-probe measurement appear essentially identical to the result found in the previous incarnation of our experiment, using the mechanical chopper. We see a slow envelope function related to the convolution of the instrument response function with the square of the intensity envelope of the laser pulse. The signal peak occurs at the stage position when the T delay is zeroed; we find the center by fitting a slow

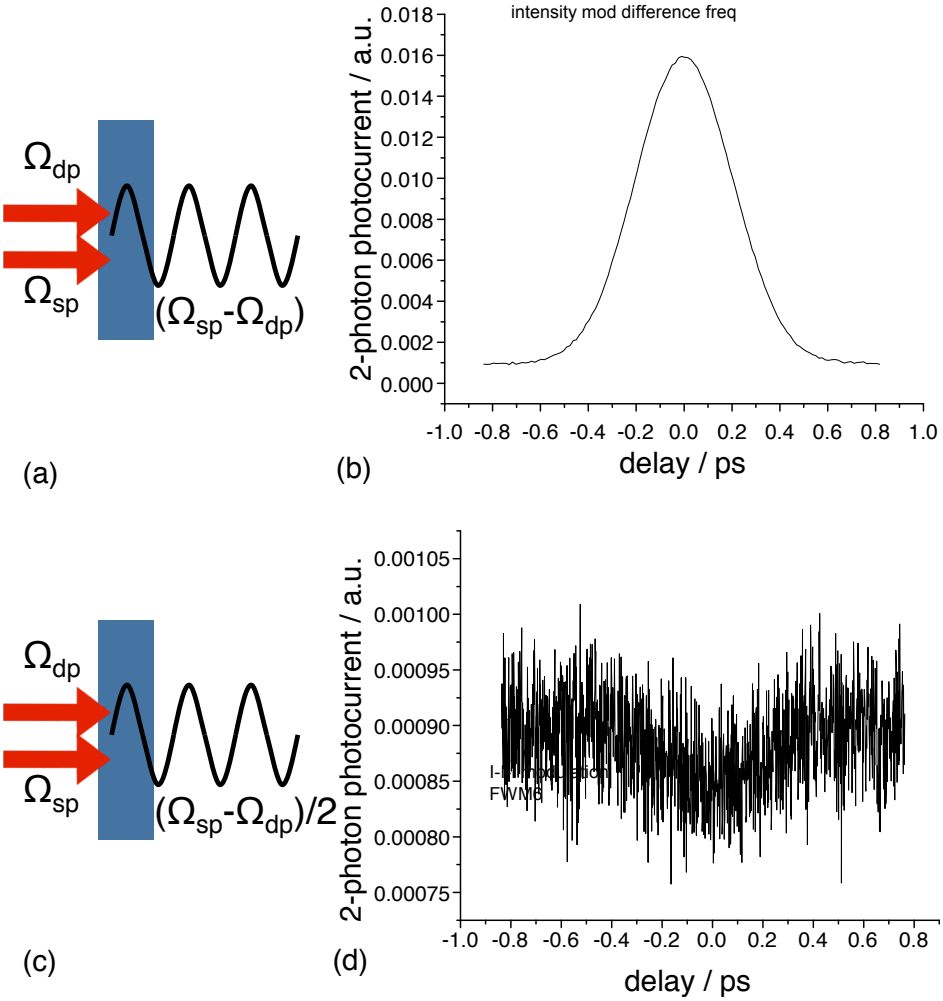

Two-photon autocorrelation measurements of the non-collinear pump pulse and probe pulse taken using AOMS to gate the intensity of the two beams. Modulation of the intensities at two different frequencies and detection at the difference of those frequencies (a) produces a simple envelope function when the *T* delay is scanned (b). Modulation of the intensities at two different frequencies and detection at half of the difference of those frequencies (c) results in no clear signal above the noise floor of the measurement (d). Both autocorrelation traces (b), (d) were collected with a time step of 1.16 fs, which is a sampling frequency sufficiently high to observe interferometric structure at the Ti-Sapph wavelength. The data were not collected with active phase-stabilization.

Figure 6.23: Noncollinear autocorrelation with AOM's

function (a Gaussian, although the pulse may be slightly more accurately represented by a sech^2 function; we have not previously closely investigated the pulse shape produced by our laser source). Since we are only concerned with finding the pulse overlaps, the exact pulse characteristics as measured by the fit are not vital.

When we tried to perform similar measurements to find the autocorrelation trace for the collinear pump pulse pair, a surprising result obtained. Using two different intensity modulation frequencies f_1 and f_2 and detecting at the difference frequency Δf only produced a slow envelope function, without any of the high frequency fringing present in the measurements obtained using the single frequency chopper modulation.

Keeping track of the factor of 2 involved in the frequency modulation scheme (i.e. the doubling of the intensity modulation frequency compared to the modulation signal generated by the DDS) had caused us to be somewhat skeptical that the difference between the observed signal found using acousto-optic modulators and that obtained using the mechanical chopper was a real, physical effect, and not an artifact of the detection scheme. We had previously shown analytically that the *electric field amplitude* of a laser beam would be modulated at a different frequency than the *intensity* of a laser beam when considering how the multiple frequency acousto-optic scheme would work. For these two reasons, we considered looking for a signal that we suspected may be related to the interference of the electric fields of the two beams. We will show this more rigorously, but if the intensities are modulated at f_1 and f_2,

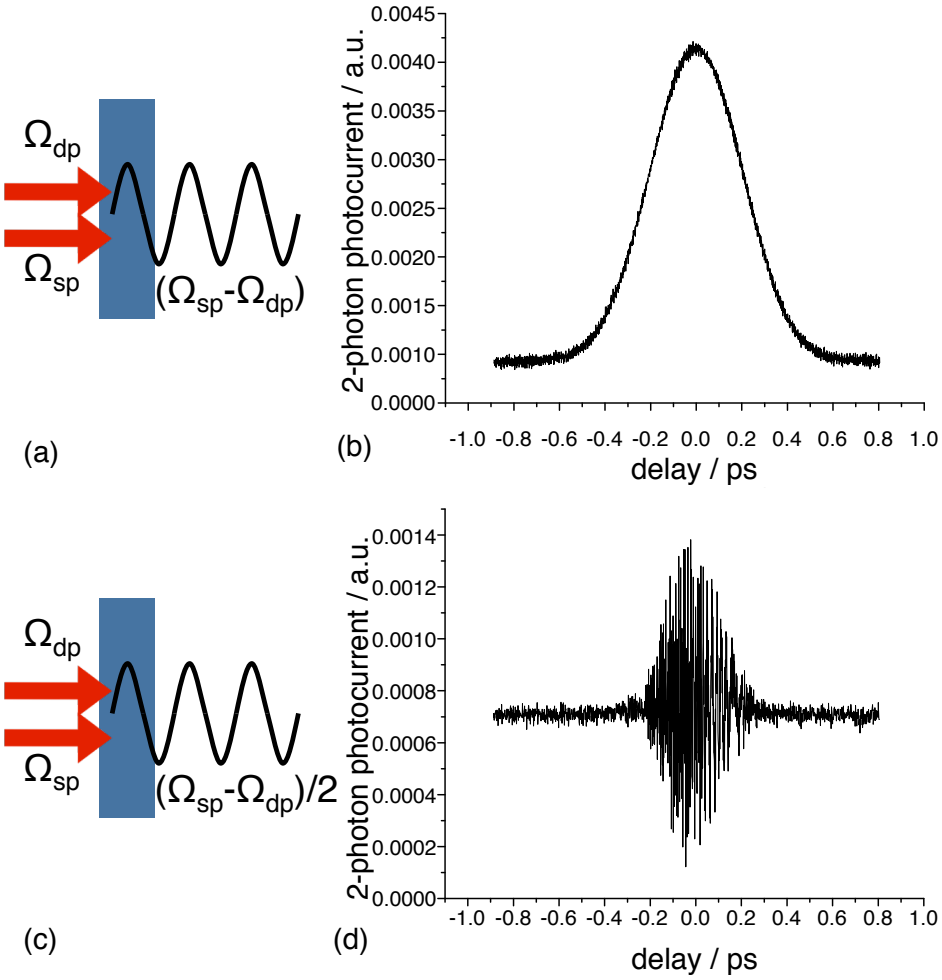

Two-photon autocorrelation measurements of the collinear pump pulse pair taken using AOMS to gate the intensity of the two beams. Modulation of the intensities at two different frequencies and detection at the difference of those frequencies (a) produces a simple envelope function when the τ delay is scanned (b). Modulation of the intensities at two different frequencies and detection at half of the difference of those frequencies (c) results in a bipolar interferometric signal that is centered on the background level (d). Both autocorrelation traces (b), (d) were collected with a time step of 1.16 fs, which is a sampling frequency sufficiently high to observe interferometric structure at the Ti-Sapph wavelength. The data were not collected with active phase-stabilization, which may explain the non-uniform fringe, but it is also possible that a signal at half the Ti-Sapph wavelength (see main text for explanation of this 2ω autocorrelation signal) is being aliased into the detected signal.

Figure 6.24: Collinear autocorrelation with AOM's

the electric fields would be modulated at $f_1/2$ and $f_2/2$. Therefore, we used the DDS function generator to produce a reference signal at $\Delta' = f_1/2 - f_2/2$, while keeping the experiment otherwise unchanged. We immediately recover a signal with high frequency components; this time, the observed correlation trace is an AC signal, rather than the positive semi-definite envelope trace. The observed fringe signal is weaker and noisier than that we had previously seen in our measurements using a mechanical chopper.

We suspected that this different signal occurs due to modulation of different cross terms in the integrand of G_2 compared to those found by looking for a signal at the intensity modulation frequency Δ. The full width-half of the signal detected using either modulation scheme appears to be the same.

We note now that we neglected to consider the possibility that the signal observed here was different from that seen with the mechanical chopper not due to different detection scheme, but because the two pump beams were no longer degenerate. When we examined auto-correlation measurements obtained using the mechanical chopper, we were looking at a signal obtained for two pulses that were deflected by the same acousto-optic modulator, and thus had the same optical frequency. The two pump beams here are deflected by two different acousto-optic modulators operating at two different frequencies, generating two optical fields with different carrier frequencies. Thus, the resulting nonlinear signal in the two-photon detector may oscillate at the sum and difference frequencies of the two optical fields, and the interferometric autocorrelation high frequency components may be washed out. Further an-

alytical study of the nonlinear process is necessary to properly consider the effect the carrier frequency shift has here.

Regardless, the observation of a high frequency signal at the electric field frequency was surprising and unexpected. This prompted us to consider the question of which terms would be detected by the square law detector used to perform three-pulse four-wave mixing measurements on the exciton systems we study. We describe that at some length subsequently.

6.7.1.2 Two-pulse measurements with electric field modulation

In order to investigate this effect further, we turn our attention again to the two-pulse measurements we have been using to characterize the behaviour of our experimental apparatus. Using the sample previously studied, we now perform an identical nonlinear optical measurement except we choose a new reference frequency. In our prior measurements, we had modulated the intensity of the optical fields at f_1 (for, say the probe beam) and f_2 (the pump), and detected at $\Delta = f_1 - f_2$. Now, using otherwise identical conditions, we instead generate a reference frequency at $\Delta' = f_1/2 - f_2$. This choice is suggested by the results found for the autocorrelation measurement. Here, we expect that the pump-probe electric field, proportional to $E_{pump}E^*_{pump}E_{probe}$ will result in a signal detected at $\Delta' = f_1/2 - f_2$ due to the dissimilar dependence on the pump and probe intensities, while the unusual autocorrelation signal, found at $f_1/2 - f_2/2$, presumably depends upon the two pump intensities to the same power.

The results are remarkably different – the same lineshape is observed, but at a greatly reduced signal strength, and much noisier than the signal observed previously. The reduction in signal strength and increase in noise are similar to the effects we observed for the two-pulse measurements using the two-photon\autocorrelation detector. The conventional data presented here were taken using the reference signal Δ with an integration time constant of 30ms, though we note that further reduction of the lock-in time constant does not deleteriously affect the signal to noise (we do not perform these measurements with a faster time constant simply because below 30ms, the rate limiting constant for data collection is the time it take to scan the grating in the monochromator), while the Δ' reference signal measurement took a full second for integration. Plotted on the same scale here, the Δ' measurement must be multiplied by a factor of 20 to show comparable magnitude features. We note here that the choice of the new reference frequency – which we refer to as a hybrid measurement – is different from the 'novel' measurement performed using the autocorrelation two-photon detector; the difference is to be expected due to the geometry involved. In a pump-probe measurement, such as these differential reflectivity measurements, the pump and probe do not interact with the material in the same way, whereas in the autocorrelation measurements the optical interactions of two pulses were treated on an equal footing.

We call the experiment performed with reference frequency Δ an intensity modulated experiment, while we call the result found using reference frequency Δ' a hybrid electric field-intensity modulated experiment. We use

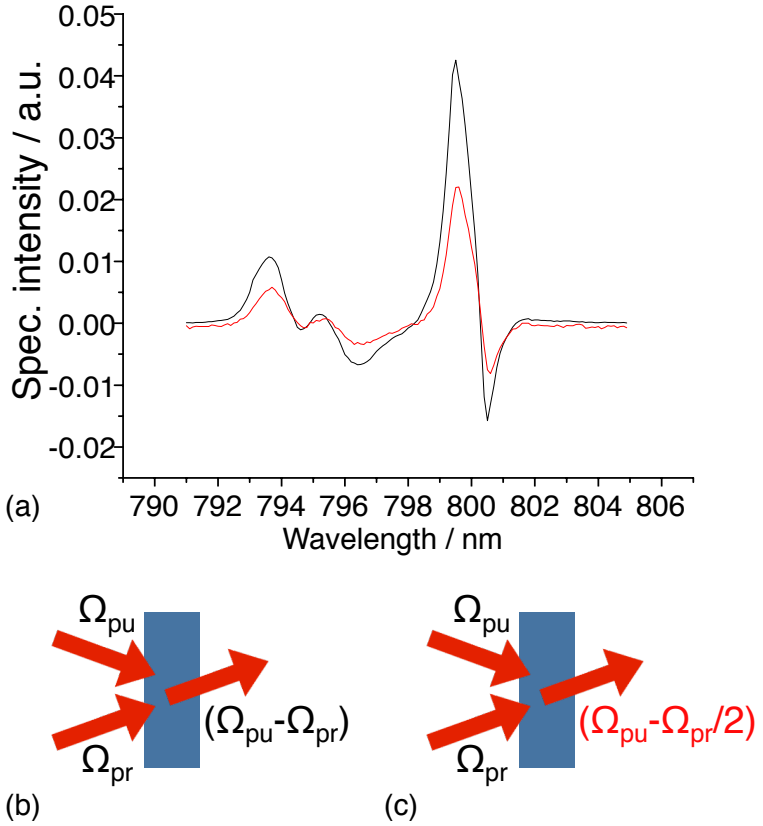

Two-pulse differential reflectivity measurements taken using our homebuilt RF electronics system to drive the AOM's used to modulate the intensities of the pump and probe beams (a). The trace in black is taken by modulating the intensities of the two beams at two different frequencies and using the difference between those frequencies as the lock-in reference (b). This measurement was taken using 30ms integration time, but faster measurements showed no noticeable decline in signal-to-noise. The trace in red, which has been multiplied by a factor of twenty, was also taken by modulating the intensities of the pump and probe at two different frequencies, but using a lock-in reference frequency equal to the difference between the pump intensity modulation frequency and half the probe intensity modulation frequency (c). This measurement, though significantly noisier than that shown in black, required an integration time of 1s.

Figure 6.25: dR with intensity and field modulations

this language since modulation of the laser intensity at some f results in a modulation of electric field at a frequency $f/2$. We suspect that the signal detected here is related to the electric field of the signal, which, for the pump-probe experiment, is linear in the electric field of the probe beam but bi-linear in the electric field of the pump beam (i.e. linear in the pump intensity). The exact details of the measurement are still somewhat unresolved, as we are not able to completely describe the nature of the photovoltage signal produced by the photodetector. Typically, we are accustomed to treating the device as a square law detector; the observation of a signal that appears to be related to an electric field rather than an intensity is thus somewhat ambiguous. In these two-pulse experiments, the argument that this alternative modulation technique represents a new detection scheme is not as clear as the corresponding argument for three-pulse measurements, q.v. *sub.*

In an appendix at the end of this thesis, we derive an expression for the intensity of the pump-probe signal detected here, which we repeat here

$$\langle I_{pr+sig} \rangle = \langle I_{pr} \rangle + \langle I_{heterodyne} \rangle + \langle I_{homodyne} \rangle$$

The heterodyne term is proportional to a time average over the product of the probe beam and the signal field that co-propagates with it, and is given by an integral function of

$$\eta \left| E_{pu}(t) \right|^2 \left(E_{pr}(t) E_{pr}^*(t+\psi') + E_{pr}^* E_{pr}(t+\psi') \right)$$

where we see the electric fields of the probe beam and the pump beam both appear bilinearly in the detected optical signal: videlicet, this signal depends upon the product of intensities of the pump and probe beam. To the best of our knowledge, other nonlinear optical experiments performed using a two-frequency modulation scheme (for example, using a mechanical chopper wheel with two sets of windows that can interrupt two spatially separate beams at different frequencies) treat the modulation of the pump and probe beam on an identical footing.

The homodyne term is, as we noted in the derivation found in the appendix, typically discounted due to the additional factor of η that appears in this term, resulting in a much weaker signal. The intensity for this homodyne signal field is given by a time average over a different field product,

$$\eta^2 \left|E_{pu}\left(t\right)\right|^4 \left|E_{pr}\left(t+\psi'\right)\right|^2$$

we note that this signal field is proportional to the square of the pump intensity, but is only linear in the probe intensity.

The exact explanation for the observed weak signal at Δ' is as yet unclear, but we believe that performing lock-in detection using a reference frequency equal to the difference between the pump intensity modulation frequency and the probe intensity modulation frequency results in detection of the heterodyne signal component, while detection using a reference frequency equal to the difference between the pump intensity modulation and the probe

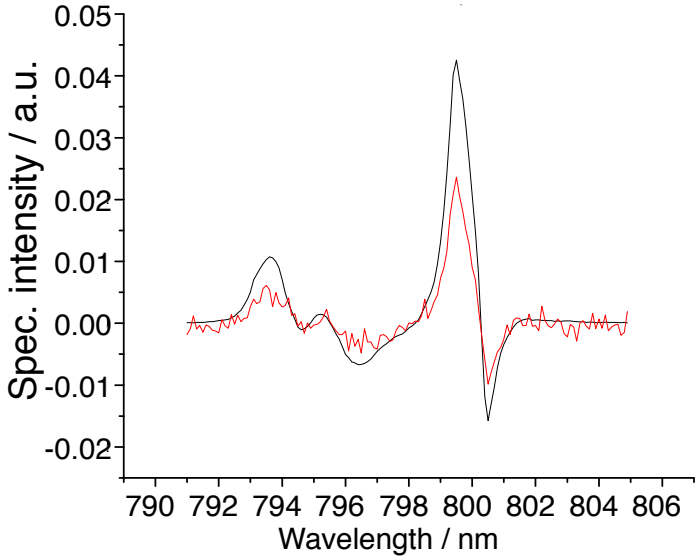

Differential reflectivity measurements taken with the same integration time constant for lock-in amplification – 30 ms in both experiments. The black trace is obtained using the conventional difference frequency detection scheme, while the noisier red trace, which has been scaled up by a factor of twenty, is obtained using the hybrid reference frequency detection scheme. The conventional scheme, which we associate with the heterodyne term, results in a substantially greater signal-to-noise for these two-pulse experiments.

Figure 6.26: Signal to noise in dR with various modulations

electric field modulation frequency results in detection of the homodyne signal component. Presumably, the distinction depends upon observing processes that depend upon the product of the electric fields compared to the square absolute magnitude of the electric field. As noted, the distinction is made more conceptually clear in three pulse measurements, since the additional optical field provides another modulation 'knob' and thus more clearly reveals the nature of the signal that is detected.

In order to ensure that the hybrid electric field - intensity modulation signal we observed is a genuine nonlinear optical signal and not an artifact of our apparatus, we made a number of measurements to test the origin of this signal. Obviously, blocking either beam eliminates the signal. We also performed differential reflectivity measurements with different frequency choices. The observed spectra do not appear to be a function of the frequency choice, suggesting that this is a real signal and not an artifact. We calculate all the possible simple linear combinations of modulation frequencies and half-modulation frequencies to ensure that our chosen reference frequency does not coincide with another possible modulation scheme; in the two-pulse measurements reported here, this is a relatively short list of combinations, but with three pulses and three modulation frequencies, it is necessary to consider a larger number of frequency combinations to ensure that a pump-probe signal is not mistaken for a four-wave mixing signal, for example.

We also tried walking our reference signal slightly off the calculated $\Delta' = f_1/2 - f_2$ hybrid detection frequency. The limiting factor here proved to

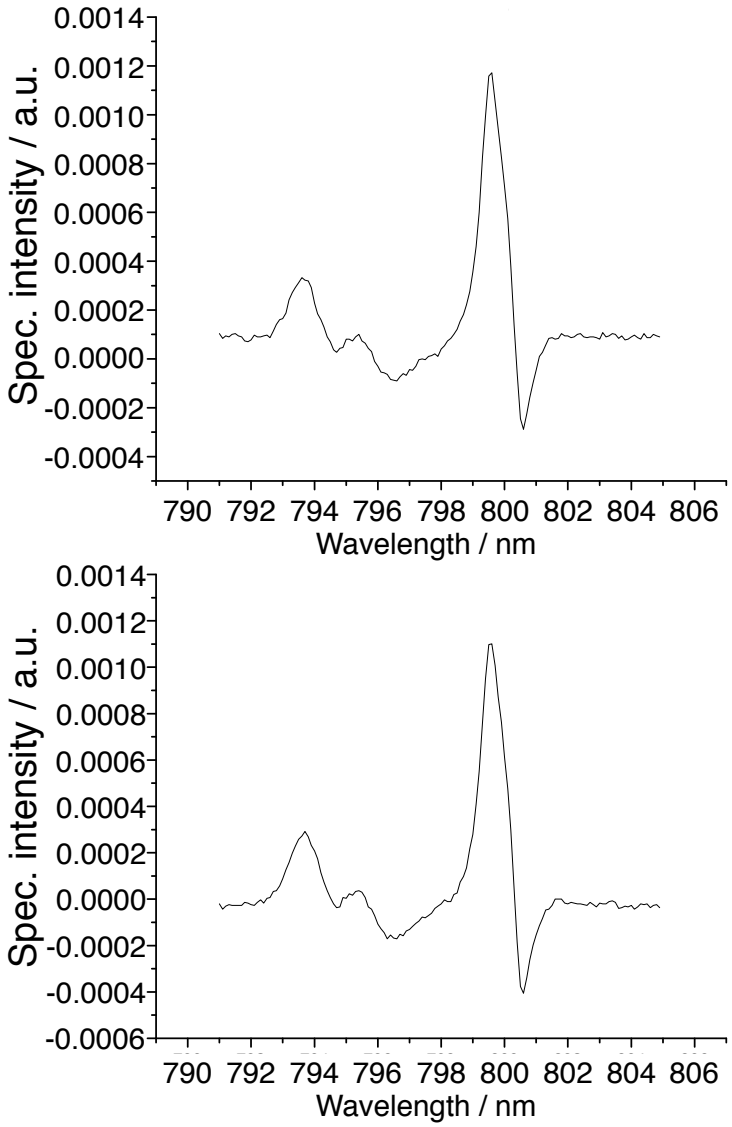

Differential reflectivity measurements recorded in the hybrid modulation-detection scheme, using two different sets of modulation frequencies. The invariance of the spectrum suggests that this signal is not an artifact due to some other signal component that inadvertently occurs at the same frequency.

Figure 6.27: Hybrid modulation dR with different frequencies

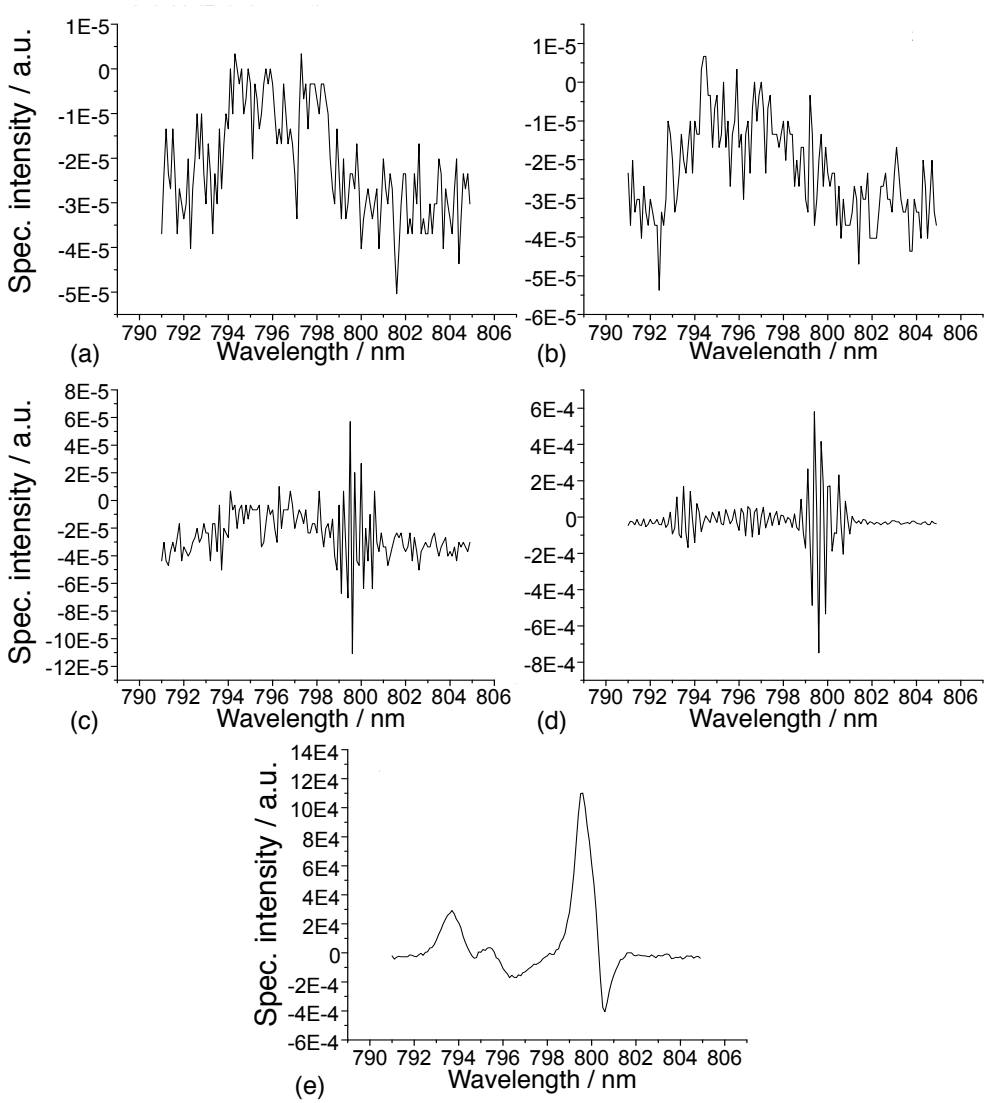

Differential reflectivity spectra taken with the hybrid modulation scheme. Detuning the reference frequency demonstrates the selectivity of this detection scheme. Changing the probe modulation frequency by 50 Hz (a) or 5 Hz (b) obscures any trace of the exciton signal. Changing the probe frequency by 0.5 Hz (c) results in an artifact with poor signal-to-noise. A detuning of 0.1 Hz (d) reveals the normal exciton line multiplied by an oscillatory term. A spectrum recorded with resonant reference frequency is shown (e) for comparison.

Figure 6.28: Hybrid modulation dR with reference detuning

be the time constant used for integration in the lock-in amplifier. In practice, we did this by shifting the probe modulation frequency f_1. To ensure the accuracy of these measurements, a 1s lock-in time constant was used to provide very high signal-to-noise. The on-frequency measurement is performed using a DDS frequency of 1.050 MHz, corresponding to a probe intensity modulation frequency of 2.100 MHz and a probe electric field modulation frequency of 1.050 MHz. At any frequency error of greater than 5 Hz, no signal was observed whatsoever. Decreasing the modulation frequency to 0.5 Hz resulted in the observation of some sort of distorted signal – this was to be expected, since the lock-in amplifier can not accurately discriminate between signals with components oscillating at 1.050 MHz and those oscillating at 1.0500005 MHz during a 1 second interval. Reducing the frequency error further, using $f_1 = 1.0500001$ MHz, corresponding to a frequency error of 0.1 Hz, revealed a lineshape that looked like the normal exciton features multiplied by some oscillatory signal. Again, this is expected due to the inability of the lock-in scheme to discriminate between such closely spaced signal components over that timescale. These measurements lend credibility to the argument that this is a real nonlinear optical signal rather than an artifact, and also provides a remarkable demonstration of the performance of a digital synthesis based RF system – the RF linewidths generated by this device are clearly extremely narrow.

We also note that we made some effort to observe a signal at a third reference frequency, this time determined by the difference between the probe

intensity modulation frequency and the pump electric field modulation frequency ($\Delta'' = f_1 - f_2/2$). No clear signal was observed above the noise floor of the measurement, although with a very long integration time – 1 second per point (corresponding to 4 second per point of experiment time, given the need to allow the lock-in's low pass filter to clear) revealed some extremely weak features. These were too small and noisy to assert that they are or are not related to the exciton lineshape we observed otherwise very easily using either the intensity-intensity (conventional, Δ) or probe electric field - pump intensity (hybrid, Δ') modulation schemes. A fourth detection scheme was also tested, looking for a signal at a reference frequency $\Delta''' = f_1/2 - f_2/2$. Again, no clear signal was observed even using very long integration time constants.

A surprising detail that lends further credibility to the argument that the probe electric field - pump intensity modulation (hybrid) detection scheme is related somehow to an electric field more directly than the pump-probe intensity is that when changing between the normal intensity-intensity modulation and detection scheme and the hybrid electric field-intensity modulation and detection scheme is that the phase of the signal detected with the lock-in amplifier was found to differ by almost exactly 180 degrees (when we thought to check for this effect, we found a phase difference of 181.8 degrees between the two signals). It's possible this is just a numerical quirk, but it also could be related to the phase shift between polarizations in the material and the corresponding emitted electric field. Further analysis is certainly needed to better understand these results.

6.7.1.3 Distinction between electric field modulation and intensity modulation

For completeness, we show here the connection between the electric field modulation and intensity modulation frequencies.

Consider a real electric field described by the sum of two complex fields,

$$E_0(t) = A\left(e^{i(k\cdot r-\omega t)} + c.c.\right)$$

then the corresponding intensity, proportional to the square of this field, is given by

$$\begin{aligned} I_0 \propto E_0^*(t) E_0(t) &= AA^*\left(e^{2i(kr-\omega t)} + e^{-2i(kr-\omega t)} + 2\right) \\ &= AA^*\left(2\cos\left(2\left(kr-\omega t\right)\right) + 2\right) \\ &= 4AA^*\cos^2\left(kr-\omega t\right) \end{aligned}$$

where we see that the instantaneous intensity corresponding to the simplest harmonic electric field is a positive semidefinite quantity – intensities, determined by photon counting, must of course be positive numbers, regardless of whether the electric field is instantaneously negative or positive valued. Consider then that a modulated intensity cannot be represented by a simple sinusoidal function, but must also be positive semidefinite. We model the intensity modulation as $\cos\left(\Omega_m t\right) + 1$ for some angular frequency $\Omega_m = \frac{2\pi}{T_m}$, where T_m is the period of modulation. This assumes that the sinusoidal RF

signals generated in our experiment result in a purely sinusoidal acoustic traveling wave in the acousto-optic material, and that the effective perturbation of the index of refraction due to that overpressure wave is also linear. This is usually considered a well founded assumption as long as the RF power is sufficiently low to avoid saturating the diffracted light. Using a fast homebuilt photodiode we can observe both the individual pulses generated by the laser (albeit poorly resolved, since our device has an estimated bandwidth barely sufficient to resolve the 76 MHz repetition rate) and the slower modulation envelope. The results suggest this model for the intensity modulation is at least suitable for a first approximate description of the modulation scheme.

With this model for the acousto-optic modulation, we expect a modulated intensity given by

$$\begin{aligned} I &= I_0 \times \{1 + \cos(\Omega_m t)\} \\ &= 4AA^* \cos^2(kr - \omega t)\{1 + \cos(\Omega_m t)\} \end{aligned}$$

we can show that such an instantaneous intensity is given for light where the electric field is modulated at half that frequency. Consider, therefore,

$$E = E_0 \left\{ \sqrt{2} \cos(\Omega_m t/2) \right\} = \left\{ \sqrt{2} \cos(\Omega_m t/2) \right\} A \left(e^{i(k \cdot r - \omega t)} + c.c. \right)$$

then, obviously,

$$
\begin{aligned}
I &= 2\cos^2(\Omega_m t/2)\, AA^* 4\cos^2(kr-\omega t) \\
I &= \{1+\cos\Omega_m t\}\, AA^* 4\cos^2(kr-\omega t)
\end{aligned}
$$

Thus, the strength of the electric field is modulated at half the frequency at which the intensity is modulated. We believe that a number of the nonlinear signals we observe can be attributed to detecting optical intensities that are a product of different complex electrical fields which, in some cases, do not depend upon an intensity directly.

6.7.2 Optical multiplexing with acousto-optic modulators – manipulating beam geometries with AOM's

Turning our attention to more sophisticated three-pulse measurements, we realized that our experiment was at an impasse, with a seemingly unresolvable problem related to the use of acousto-optic modulators inside the Mach-Zehnder interferometer.

As we have noted, Bragg diffraction only occurs at appreciable efficiency near the resonant condition where the incident and diffracted beams form equal angles relative to the wave vector of the sound wave in the material. In an acousto-optic modulator, that Bragg angle, specifically, is

$$
\theta_B = \arcsin\left(\frac{\lambda}{2n\Lambda}\right) = \arcsin\left(\frac{\lambda f}{2nv}\right)
$$

where n is the index of refraction of the interaction medium λ is the optical wavelength, Λ is the acoustic wavelength, f is the ultrasonic acoustic frequency, v is the phase velocity of sound in the material [407]. Thus, for a given incident beam angle there is a particular acoustic frequency that will result in efficient coupling of the incident power into a diffracted mode. Conversely formulated, for a given incident beam angle, there are two angles (one resulting in Bragg diffraction into the $m = +1$ mode, the other to the $m = -1$ mode) into which a beam may be diffracted with any appreciable efficiency. In both of these cases, we have assumed that the incident optical beam is monochromatic.

The problem we did not anticipate when we began our experiments using acousto-optic modulation of the Ti-Sapph excitation and probe beams was how to perform actively stabilized experiments using a second beam – a HeNe tracer – that would co-propagate with the first. For the purposes of stabilizing and locking the interferometer, we do not wish that second beam to be modulated by the acousto-optical modulator. Ideally, we wish to see the HeNe co-propagate with the Ti-Sapph, but not be affected by any modulation or phase shift we perform on the Ti-Sapph with the AOM's. With the RF drive system we have described thus far, the HeNe will effectively not propagate past the acousto-optic modulators in the interferometer, and we cannot actively stabilize our experiment.

For 2dFTS (and other phase-sensitive) experiments, we have always used a Mach-Zehnder interferometer with two co-propagating beams, one of

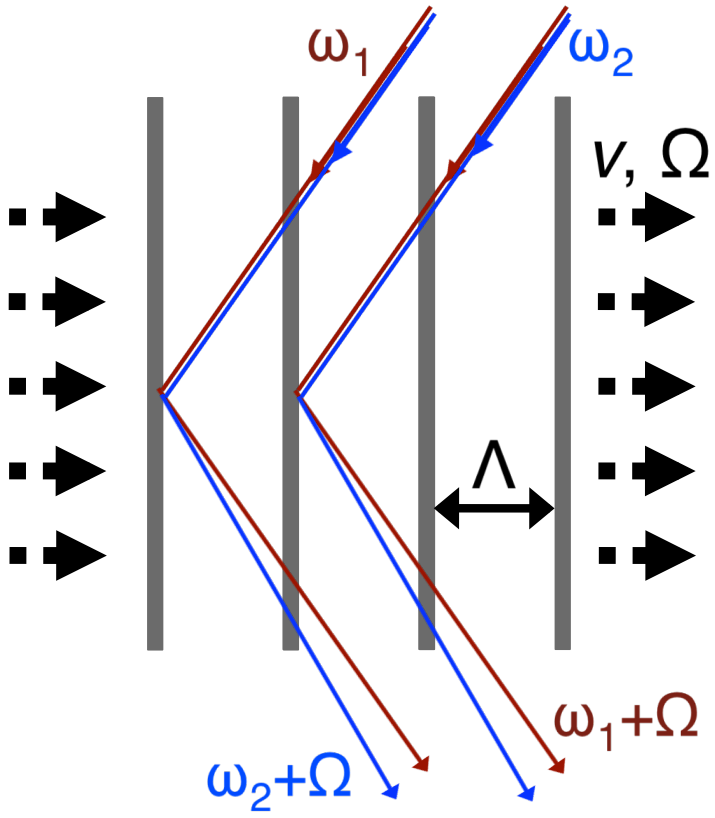

Bragg diffraction of a single beam composed of two different optical wavelengths (ω_1 and ω_2) by a single acoustic wave (frequency Ω, wavelength Λ) in an acousto-optic modulator results in two outgoing beams at different angles that are determined (to first order) by the wavelengths of the incident beams. Only one of the two beams can be resonantly diffracted, as the other will not form the Bragg angle relative to the acoustic column.

Figure 6.29: Bragg diffraction of two beams

which (the Ti-Sapph) is used to coherently excite the sample. The second (the HeNe beam) is retroreflected by a dichroic mirror that separates the two beams, and causes the HeNe to retrace its path through the interferometer; a portion of this beam is collected at the input port of the interferometer, where it is detected using an amplified photodiode. To maintain the well-defined phase relationship between the two pulses derived from that beam, the interference signal derived from the second beam is used to monitor the path length change caused by translating the high performance stage that has a corner cube mounted on it, and as the interferometric source of an error signal that may be used to stabilize the Mach-Zehnder interferometer during the periods between translation steps, when the experiment is locked and collecting data. It is insufficiently accurate to rely on the positioning system of the stage – although claims of a few to tens of nm precision have been made by the companies that build high performance stages, recording high quality spectra without active stabilization of the stages has proven impossible. This may be due largely to the noisy lab environment, rather than any inherent instability of the translation stages.

Methods of generating a pulse train other than the use of translation stages have been employed with success, but for our particular experimental program we decided the delay stage approach was preferred – we discuss this at more substantial length elsewhere in this work. For present purposes, it is enough to note that having built an experiment that used two AOMs to modulate the Ti-Sapph propagating through both arms of a Mach-Zehnder

interferometer, we now realized that we did not have a mechanism to actively stabilize this interferometer. It is not simply that the HeNe laser would be modulated at the same frequency as the Ti-Sapph laser; it would be possible to treat that problem by simply low-pass filtering the interference measurement made at the HeNe photodiode. Rather, the more substantial problem is that Bragg scattering would result in diffraction of the HeNe at a different angle, so that the beams no longer co-propagate after interacting with the acoustic wave in the AOM. Furthermore, the HeNe beam, now directed into the wrong angle, would be diffracted with essentially zero efficiency, as the angle of incidence for a laser going into the AOM needs to be very nearly equal to the Bragg angle in order to obtain diffraction at any appreciable efficiency. Thus, we have a more-or-less zero intensity HeNe beam, no longer co-propagating with the Ti-Sapph, and with an intensity modulation applied to it. This is highly undesirable.

This problem is, at its heart, geometrical, as the coupling of the various optical and acoustic modes is simply a matter of vector arithmetic. As such, we perhaps would be forgiven for considering the example of Plato, whose academy bore the inscription 'Let no one ignorant of geometry enter.' In *The Republic* Plato recounts Socrates development of a hypothetical system of government; Socrates abjures responsibility for the Gedankenexperiment, however, saying 'yet the true creator is necessity, who is the mother of our invention.' This is certainly why we built an optical multiplexer using acousto-optic modulation.

But perhaps a more useful maxim to describe our idea and experiment is *Ecclesiastes* 1:9, which states 'The thing that hath been, it is that which shall be; and that which is done is that which shall be done: and there is no new thing under the sun,' – because after we built an apparatus that let us resolve our experimental difficulties we spent a sufficiently long time looking that we eventually found evidence that others thought of this idea previously, though certainly with substantial differences.

Perhaps even more useful to keep in mind is Aristotle's remark that 'It is unbecoming for young men to utter maxims,' – or indeed, even better, that we should conscientiously strive to remind any person who choses to repeat it, present company included, of the obvious and immediate rejoinder that may be offered. *Res ipsa loquitor.*

6.7.2.1 Optical multiplexing with acousto-optical modulators

Consider an acousto-optic modulator in the interferometer. The co-propagating Ti-Sapph and HeNe lasers are incident upon the modulator at the same angle. The Ti-Sapph wavelength, in conjunction with the angle of incidence, index of refraction at that wavelength (approximately 797 nm at the central wavelength of our pulse spectrum), the acoustic frequency driving the AOM, and the phase velocity for the acoustic waveform used to drive the AOM all satisfy the condition for Bragg diffraction. For the purpose of these experiments, the Bragg angle is determined by the carrier frequency at 80 MHz, produced by a crystal reference oscillator. In order to perform lock-in

amplification of weak signals derived from this beam, we modulate the carrier at some slow frequency derived from a Direct Digital Synthesis source – typically less than a few MHz. Alternatively, one can use a frequency space description of the operation of these modulators, where the modulated signal is represented as the carrier plus the sidebands introduced by the modulation frequency; since the modulation frequency is small relative to the carrier frequency, the diffraction process still occurs with high efficiency.

Since it operates at a different wavelength (632.8 nm), the HeNe laser does not satisfy the condition for Bragg diffraction. For the purpose of completeness, we note that the index of refraction for this wavelength of light is also different, which would also result in the violation of the Bragg condition for this second laser, but this effect is relatively small (the change in the index of TeO2 is not very great between these two colours). Driving the acousto-optic modulators as we have described previously, the HeNe beam does undergo far off-resonant diffraction, producing an extremely weak beam propagating along a different direction, but this is not useful for our purposes of stabilizing the optical path of the Ti-Sapph with the HeNe. Indeed, this beam cannot even reasonably be observed in the lab. Moreover, even if the HeNe were usefully co-propagating with the Ti-Sapph, we would need to consider the best electronic filter to use to eliminate the effects of the MHz modulation in order to use the HeNe interferometer signal to monitor and servo fluctuations in the path length.

This seems problematic at first, as the inability to produce phase-

stabilized ultrafast pulses eliminates our ability to perform optical phase-sensitive measurements. In the lab, a simple solution using multiple-acoustic frequency diffraction was developed without first considering the theoretical basis for such a technique – something of a happy accident, since the existing literature would suggest that this method would not work. We now briefly turn our attention to the use of acousto-optical devices in the multiple acoustic frequency operation mode and multiple optical wavelength diffraction. Typically, most applications demonstrate either multiple acoustic frequency diffraction of a single wavelength, or diffraction of multiple wavelengths by a single acoustic wave, although there is some cross-over. We are principally concerned with the undesirable nonlinear properties and the stringent restrictions on polarization and geometry that the operation of these devices require, as one may reasonably expect to see similar complications in the apparatus we build.

6.7.2.2 Multi-frequency operation

Early applications of multi-frequency acoustic processes in acousto-optic modulators made use of the diffraction of a single laser beam into a number of different, spatially resolvable spots by an arbitrary sound wave propagating through the modulator. Imaging those spots onto a screen permitted the use of this device as a spectrum analyzer, as each spot on the display would correspond to a specific acoustic mode excited in the acousto-optic material, and thus, corresponds to a particular RF component in the signal applied to the transducer. The first such device [233] used a Raman-Nath

device, where the stringent condition of Bragg scattering is relaxed, allowing the device, in conjunction with an appropriate lens, to image multiple spots in the far field. The use of acousto-optic modulators as imaging devices or spectrum analyzers was developed further [1], suggesting the intentional chirping of modulated electrical signals to temporally separate various RF components. This permits the development of time-sequential displays, allowing acousto-optic modulation to be used for a rastered 2d display. Multiple frequency diffraction was also used in two-dimensional imaging devices. An acousto-optical pattern display diffracted a single HeNe laser into multiple spots to form a display pattern, where the intensity of each image element could be modulated in intensity. The demonstrated technique could essentially be run in reverse, allowing image pattern detection by heterodyning such a pattern with an unmodulated beam, using a photomultiplier tube to detect the interference signals at the various beat frequencies, using the resulting RF signal to power a second AOM, thereby recreating the original image [370]. A somewhat similar experiment [189] demonstrates a laser dot matrix image display technology using multiple RF signals to diffract light from a Bragg modulator, describing the trade-off between image resolution (determined by the number of resolvable spots, a function of the device's bandwidth and laser spot size) and image refresh rate (determined by the acousto-optic access time, i.e. the time it takes for an acoustic wave feature to propagate across the spot size). A smaller spot size improves image resolution but reduces the device's refresh rate. For RF powers sufficiently low as to avoid the introduction of acoustic

nonlinearities, the Bragg cells used in these experiments can be powered with multiple frequencies, resulting in multiple spots diffracted at the appropriate angle. We note that no comment is made on the decrease in efficiency of these processes due to the non-optimal alignment of the beam entering the acousto-optic device, although the issue has been addressed elsewhere [1], introducing the possibility of using multiple acoustic transducers. Each transducer may be dedicated to some range of frequencies, and its geometry chosen to ensure high efficiency diffraction at the expense of a far more complicated acousto-optic device.

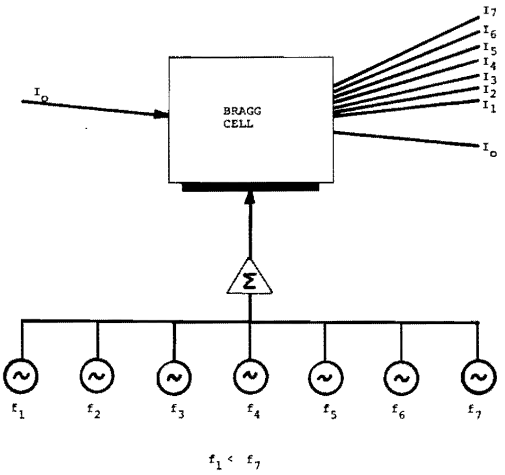

Multiple spots formed using a single laser in a Bragg cell to form an alphanumeric display as an early demonstration of multiple acoustic frequency operation. Reproduced from Hrbek and Watson, Proc. Electro-Optical Systems Design Conf., pg. 271 (1971).

Figure 6.30: Multi-frequency acousto-optic device

Beam steering may also be accomplished using a phased array of trans-

ducers that act upon the light in a step-wise process [369]. More significantly, this work describes the diffraction of a modulated beam in terms of a multiple frequency operation, depending on the diffraction of light at the carrier and sideband frequencies. This establishes a rule of thumb that a diffraction pattern containing multiple spots it is necessary to keep each spot separated by a frequency spacing more than twice the modulation bandwidth used in the device in order to avoid interference between diffracted beams. While in principle significant for our devices, this interference do not occur in our experiment, where we are not intentionally trying to create a large number of spots. The optical path length from out acousto-optic modulators to the experiment is sufficiently great that an iris may be used to remove any spurious intermodulation spots. It is shown that the modulation results in a broadening of the diffracted mode exiting the AOM [369]. In our experiments we do not observe a substantial beam divergence effect, since the modulation frequency used is small compared to the carrier frequency. The operation of acousto-optic devices across the broad frequency range necessary for many applications (here, for example, the use in display technology that requires a large number of resolvable spots) is be limited by degeneracies between the acoustic modes in the crystal. Careful design that considers the crystal geometry may shift the mode degeneracy so as to obtain a broader acoustic bandwidth [129] and may be necessary to construct the kind of sophisticated acousto-optic device one would speculate would be necessary to perform optical multiplexing.

The Klein-Cook formalism used to describe realistic acousto-optic in-

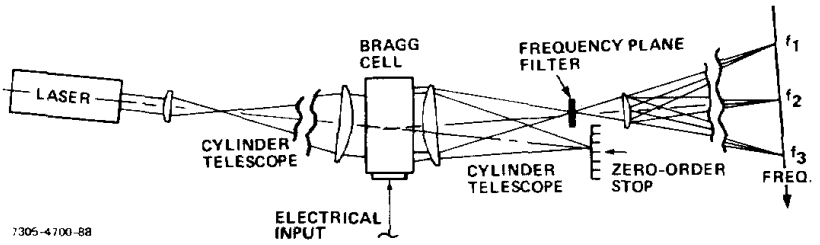

Schematic of an RF spectrum analyzer using a Bragg-diffraction cell, an optical device demonstrating multiple acoustic frequency operation of an acousto-optic device. Reproduced from Hecht et al., Bulletin of the 1973 Ultrasonics Symposium, pg. 98 (1973), which develops a theory of intermodulation products arising in the operation of acousto-optic devices with multiple frequencies.

Figure 6.31: Early multi-frequency acousto-optic device

teractions may be extended to consider the presence of multiple, independent sound waves in the interaction material [173]. Significant results concerning the acoustic bandwidth, spot resolution, the onset of intermodulation and cross-modulation effects, the sensitivity to weak RF signals and dynamic range, the diffraction efficiency, the impulse response of the acousto-optic device, and the spectrum of the intermodulation modes may be found in this framework. Significantly, multi-frequency Klein-Cook analysis indicates that intermodulation diffraction modes may appear even in the absence of any acoustic nonlinearities, i.e. even at low RF power where nonlinear acoustic wave mixing is not expected.

Fortunately, these effects are less problematic in the Bragg regime,

where our devices (approximately) operate, than they appear to be in the Raman-Nath limit of acoustic diffraction. This suppression of nonlinearities occurs due to the elimination of those multiple diffraction acousto-optic interaction pathways that are coupled via optical diffraction modes other than the zero and first order modes, which are the only two allowed in the Bragg limit. The behaviour of experimental acousto-optic spectrum analyzers operated in the Bragg regime largely agrees with these theoretical predictions.

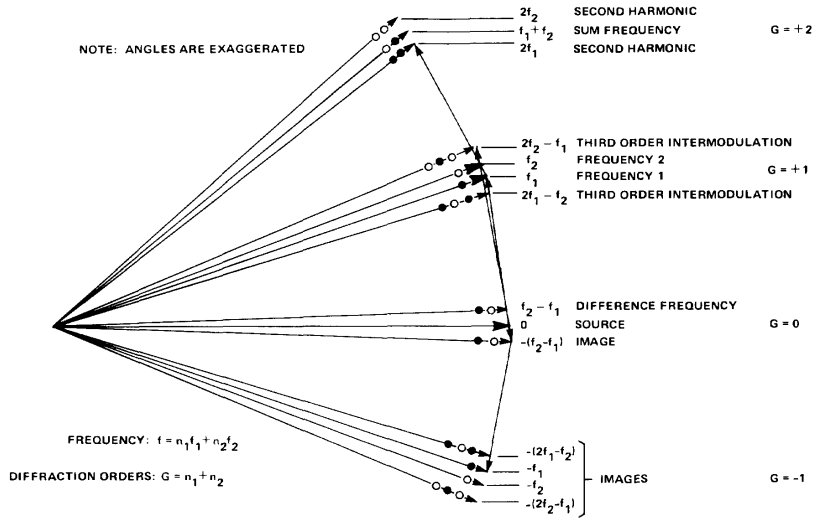

Schematic of the additional spots present in an acousto-optic device driven with two acoustic frequencies with a single applied optical wavelength. In our experiment, we use the ±1 modes, and are therefore primarily concerned with those adjacent intermodulation spots. Reproduced from Hecht, IEEE Trans. on Sonics and Ultrasonics, SU-24 (1977).

Figure 6.32: Intermodulation in multi-frequency acousto-optic devices

At first glance, it may seem that the multiple-spot pattern would not

occur at all for Bragg devices, where higher-order diffraction modes are forbidden. Simultaneous application of multiple acoustic frequencies, however, results in the emergence of additional diffracted beams in both the Raman-Nath and Bragg regimes. In general, the use of two acoustic waves actually generates an infinite number of spots at $n_1 f_1 + n_2 f_2$ where n_1 and n_2 are integers. For Bragg devices, diffraction is only observed for those spots where $n_1 + n_2 = 0, \pm 1$, i.e. the extra spots appear centered around the zeroth and first diffraction orders; nonetheless, an infinite number of spots is still technically possible under that constraint [170]. A modified Klein-Cook analysis, relying on an infinite set of coupled mode equations, would indicated that the appearance of these features does not depend upon acoustic or photo-elastic nonlinearity (those effects may be discounted theoretically simply by requiring that all the modulations of the index of refraction are sinusoidal when the driving acoustic wave is also sinusoidal [171], [172]); instead, they are a result of multiple linear diffraction processes occurring in the acousto-optic medium. Each mode is shown to be coupled to a mode in the adjacent two orders. While these spots cannot be eliminated, their effects may be minimized [170], [171], [172], [137]. It can be shown that the difference frequency diffraction modes (i.e. those arising due to acoustic waves at $f_1 - f_2$) appear in the zeroth order, and are therefore comparable in intensity to the intended diffraction modes (at the separate angles determined by f_1 and f_2). Intermodulation modes (e.g. $2f_2 - f_1$) appear in the first order, and may also exhibit significant intensity. The lowest order intermodulation terms viz. $(2f_2 - f_1)$ and $(2f_1 - f_2)$ will

have the greatest power of the intermodulation terms [110]. Harmonic ($n \times f_i$) and sum ($f_2 + f_1$) frequency beams are shown to appear only in the second order correction to the scattering process [172]. Difference and sum frequencies, as well as some intermodulation terms and harmonics, may often be ignored if they fall outside the bandwidth of the device, where propagating acoustic waves are not supported [110].

The underlying argument in this analysis is that the multifrequency nonlinearities in acousto-optic devices were predominantly due to multiple diffraction processes. The Klein-Cook formalism applied to multi-frequency operation permits the calculation of the intensities of the dominant intermodulation products, which agree with the results obtained in Bragg devices operated up to a few hundred MHz. This result may not be universal, however, as intermodulation products are observed that exhibit intensities greater than would be predicted by that theory for certain higher acoustic frequency devices (using a longitudinal mode in TeO2 in the ˜1GHz range). In such devices, extremely high acoustic power density is expected – up to a kiloWatt per square centimeter – and nonlinear acoustic effects appear to dominate the diffraction of intermodulation products at these power levels [68]. The nonlinear acoustic effects leading to the diffraction of intermodulation products places an upper limit on the dynamic range that may be achieved in a multiple frequency acousto-optic Bragg device. Of course, nonlinear acoustic effects are known to already place limits on the dynamic range of devices operated with a single acoustic frequency. In those more pedestrian applications, diffraction due

to the nonlinear acoustic interaction depletes RF power from the fundamental acoustic mode, resulting in a power-dependent acoustic attenuation effect. In multiple frequency operation, nonlinear acoustic interactions result in the coupling of harmonics both to the fundamentals and to each other. These are purely acoustic effects [111], in contrast to the acousto-optic phase grating nonlinearities previously considered [171]. It is also possible to see intermodulation and mixing terms appear due to nonlinearity in the RF amplifiers used to power the acousto-optic device [187]. Piezoelectric nonlinear effects may also be significant in some media, although only those that possess higher piezoelectric figure of merit. A general treatment of nonlinear acoustic effects provides a description of the intensity of intermodulation effects to the fourth order correction [110].

The field of multple frequency acousto-optic device design continues to be an active area of research today [208].

6.7.2.3 Multi-wavelength operation

Multiple frequencies of light should not be expected to directly couple due to the parametric processes of acousto-optic interaction. Rather, the complexity of operating an acoustic-optic device with multiple frequencies arises due to the chromaticity of the scattering process, determined by energy and momentum conservation.

Acousto-optical filters represent a large fraction of the development of techniques to manipulate multiple colours of light using a single acoustic fre-

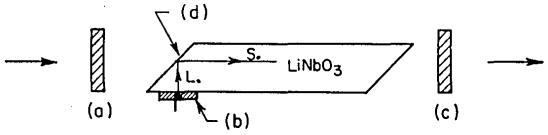

A collinear geometry acousto-optic tunable filter. The acoustic wave is launched from the side of the interaction medium, reflected from an appropriately cut crystal facet, and co-propagates with the laser beam. The two additional components (marked (a) and (c) here) are crossed polarizers used to measure the efficiency with which the filter diffracts light between the ordinary and extra-ordinary polarizations. Reproduced from Harris and Wallace, Journal of the Optical Society of America 59:744 (1969).

Figure 6.33: Collinear AOTF

quency. These are tunable devices that will allow certain optical wavelengths to propagate while blocking others. Typically, they tend to employ diffraction occurring at a large angle between the acoustic wave and the propagation direction of the light, where only one particular wavelength in the light beam satisfies the condition for resonant Bragg scattering. The first acousto-optical filter, however, was demonstrated using a collinear interaction geometry [161], [160] where anisotropy in an acousto-optical material caused the acoustic scattering of light from one polarization state, corresponding to propagation in the ordinary mode of the crystal, into another polarization, corresponding to the extraordinary mode. The effect clearly depends strongly upon the precise geometry used as it relies on optical birefringence. Nonetheless, while the process depends on a near resonant diffraction between an acoustic wave and the two optical waves, with all three relevant vectors parallel the phase-matching is

greatly simplified. This permits the use of nearly arbitrary acoustic frequencies to diffract incident polarized light of various colours into the orthogonal polarization. Selection of a different frequency resulted in the polarization diffraction of different wavelengths of light – thus, the device may be operated as an optical filter with a pass band determined by the choice of RF frequencies used. A long interaction length permits nearly unit efficiency diffraction in the passband. Both coherence and white light may be spectrally analyzed with the acousto-optical tunable filter. Strong coupling between co-propagating acoustic and light waves had been previously shown to occur when the vector sum of the momenta for the incident light and the acoustic wave were equal to the momentum for the diffracted wave [99]. Thus as such, for this effect to do anything, the initial and final light fields have to carry different momenta. This is directly accomplished using an anisotropic crystal. While the use of this device with simultaneous multiple frequency operation is not explored, it serves as a demonstration of the diffraction of light a broad range of wavelengths into the same optical path; conceptually, this is the same process we wish to perform, albeit in dramatically different fashion.

Subsequent efforts improved the performance of collinear geometry acousto-optical filter devices by constructing devices where the walk-off effect of the acoustic wave was minimized. In general, the phase velocity and group velocity for sound in these acousto-optic materials are not parallel, and a sound wave launched into such a material can co-propagate with the optical wave for only a limited distance. Launching an acoustic wave with a group

velocity parallel to the light permits a longer interaction length; the acoustic phase fronts of the sound are no longer perpendicular to the light but efficient diffraction is still obtained [230]. Further exploitation of the anisotropic properties of the acousto-optic material permit the construction of devices that perform a similar filtering process by polarization diffraction, but without the drawbacks associated with the non-co-propagating phase velocity. These devices balanced the broadening of the spectral passband by exploiting acoustic anisotropy [82] , [193]. Alternative methods to compensate for acoustic walk-off employed the use of a phased array of acoustic transducers [64].

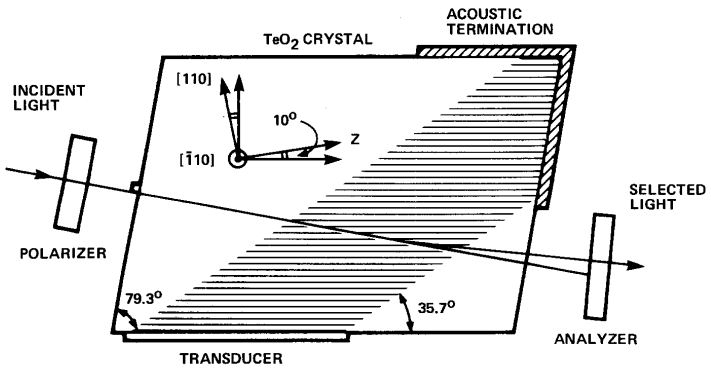

371 Appl. Phys. Lett., Vol. 25, No. 7, 1 October 1974

Substantial effort was applied to the development of acousto-optic filters, devices that use multiple RF frequencies to diffract specific wavelengths out of the transmitted beam. This device couples non-collinear acoustic and optical modes; careful choice of crystal geometry permits a wide effective aperture. Reproduced from Chang, Applied Physics Letters 25: 370 (1974).

Figure 6.34: Noncollinear AOTF

Non-collinear acousto-optic filters allow the modulation of multiple

colours of light without altering the polarization, relying on spatial separation of the diffracted and transmitted modes [62], [65]. The optical aperture of such a device is necessarily limited due to phase matching requirements. The geometry of the device is again highly restricted, and the operation employs the optical birefringence of the crystal to compensate for momentum mismatch due to deviation from the ideal phase matching condition [63]. Large angle non-collinear acousto-optic interaction provides superior filters properties by exploiting anisotropic Bragg diffraction. In a certain geometry, optically anisotropic media exhibit Bragg resonance for a given wavelength at two different angles if the angle between the light and the acoustic wave is sufficiently large. The effect is only limited to wavelengths where the medium is birefringent [384]. Other non-collinear devices also spatially separate the diffracted and transmitted colours, but achieve their high performance figures of merit at the expense of rotating the polarization of the diffracted light [66]. Other non-collinear geometries were also explored [67].

6.7.2.4 Multi-wavelength, multi-frequency operation

Multi-frequency, multiple wavelength acousto-optic modulators have been demonstrated using non-copropagating input optical beams [136]. A specific crystal cut [405] is required to obtain the desired phase-matching conditions. A single acoustic frequency component can Bragg diffract the two different wavelengths since they enter the crystal in their respective phase-matched directions. Both beams are diffracted into the same spatial mode.

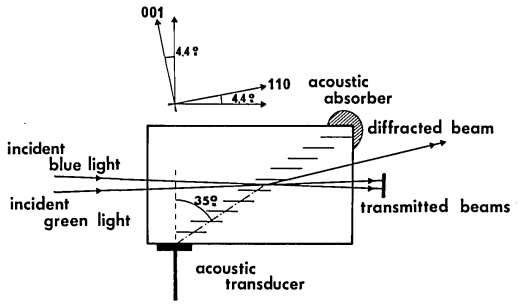

An acousto-optic device used to independently modulate the intensities of light of two different wavelengths. While the diffracted beams co-propagate, the input beams are not. Reproduced from Gazalet et al., Applied Optics 23:674 (1984).

Figure 6.35: Multi-frequency, multi-beam, non-collinear AOTF

A similar technique had been presented previously, using two non-collinear beams more closely spaced in frequency but with orthogonal polarizations [138], with significant emphasis placed on the acoustic bandwidth requirements for the device to permit independent modulation of the two colours in the diffracted beam without introducing cross-talk. In principle, the separation between the two acoustic frequencies used must be several times the bandwidth needed for the modulation. If the optical wavelengths used are relatively close, a wide bandwidth, high operating frequency device will be needed. Exploiting anisotropic effects in the crystal allows the device to use lower acoustic frequencies, simplifying the design. Further refinement of this design corrects for the chromaticity of the dispersion of the acousto-optic material, permitting the use of widely spaced colours of light. Unfortunately, since these techniques depend upon an anisotropy that breaks symmetry in

two dimensions, only two colours may be used in such a device. Extension to a larger number of wavelengths is not possible [135].

These are useful results as they provide us with suggestions for the bandwidth restrictions that need be applied to our modulation scheme, but the device itself does not fit our application, which requires collinear input and output beams.

An acousto-optic device has been shown that can diffract light of multiple wavelengths in a single beam into a different single beam [332]. The modulator uses a single transducer, rather than a phased array, driven by multiple frequency components. The intensity of the RF signals can be modulated by an electronic control system, since the apparatus was developed for use in image projection devices. In brief, an input polychromatic beam can be colour modulated into an output polychromatic beam with colour modulation.

Most red-green-blue colour projection systems based on acousto-optic modulators use an indepdendent modulator for each light source, then recombine the beams using dichroics prior to projection onto some kind of screen. This redundancy is necessary not only because of the different Bragg resonance conditions for the different colours, but because most AOM devices are not wavelength selective, and modulation of the intensity of one wavelength will result in simultaneous, unwanted modulation of the other, co-propagating wavelengths. This device can use a large number of different wavelengths to produce full spectrum projected images. Other techniques have been shown using a single AOM with three different transducers, but this may result in

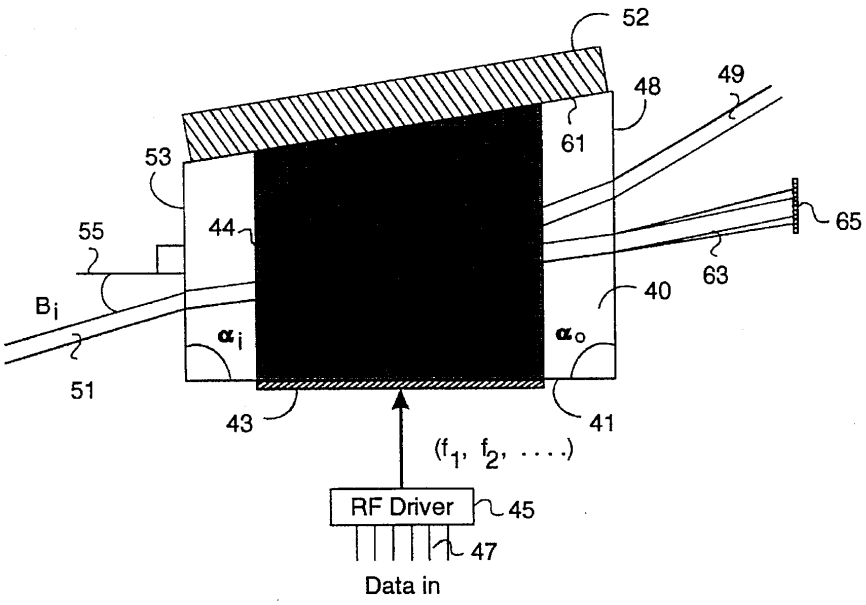

An acousto-optic device that permits modulation of multiple optical wavelengths using multiple acoustic frequencies, reproduced from Shah, United States Patent no. 5,463,493 (1995). This device largely resembles the acousto-optic modulation technique we use to independently diffract the HeNe and Ti-Sapph beams.

Figure 6.36: Multi-frequency, multi-beam, collinear AOTF

significant cross-talk, and results in a large, expensive device that is limited to modulation of only a few colours. This device uses a specific crystal geometry determined by the specific acousto-optical interaction, refraction due to dispersion of the index of refraction, and Snell's law.

In short, this technique would work for our experiment *if* we had the resources and expertise to fabricate a custom acousto-optic device. Even then, it may be necessary to restrict the polarizations used, and the layout of our experiment on the optical table would likely need to be substantially altered to use a similar device. Nonetheless, this device at least shows that the diffraction of a polychromatic beam into another polychromatic beam is possible – an encouraging result.

6.7.3 Our solution for optical multiplexing with acousto-optic modulators

Prior to researching the literature on the subject, we simply turned out attention to trying to solve this problem in our own lab with our existing experimental apparatus. Fortunately, a relatively simple solution presented itself.

We use a second frequency source to cause resonant Bragg scattering of the HeNe at the same angle as the Ti-Sapph. While this second acoustic frequency source should result in weak, non-Bragg resonant scattering of the Ti-Sapph (just as the first acoustic frequency results in weak, non-Bragg resonant scattering of the HeNe beam), physical intuition suggests that oper-

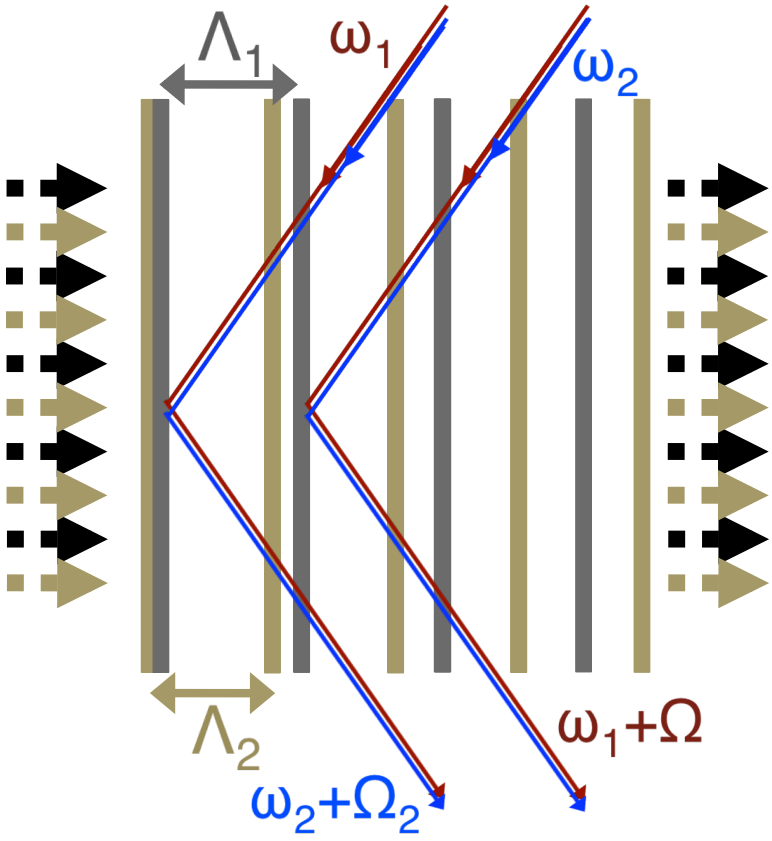

We provide a second acoustic frequency to the conventional acousto-optic modulators used in this experiment. Each acoustic frequency separately satisfies the resonant Bragg diffraction condition for one of the two optical wavelengths. This cartoon neglects the chromaticity of the index of refraction, which is expected to be a secondary effect.

Figure 6.37: Optical multiplex solution

ating the AOM well within its linear regime should result in that second mode diffracting at a different angle, thereby averting any unintended modulation or distortion of the desired Ti-Sapph beam properties. We expect that depletion of the incident Ti-Sapph power by the second set of diffracted spots arising from diffraction by the new frequency component will require greater RF power in the first frequency in order to obtain the desired Ti-Sapph power at the sample.

The second RF signal is generated by the HP 8657A function generator previously used to power the AOM on the combined pump beams for differential transmission and 2dFT experiments. A discrete RF splitter/combiner is used to linearly add the two RF drive signals prior to amplification and transmission to the modulator. The frequency for this second RF signal may be estimated by a simple calculation, assuming the Bragg angles of the two beams to be identical:

$$\begin{aligned} \theta_{TiSapph} &= \arcsin\left(\frac{(800\times10^{-9}\mathrm{m})\,(80\times10^{6}s^{-1})}{2nv}\right) \\ &= \arcsin\left(\frac{(633\times10^{-9}\mathrm{m})\,(f_2)}{2nv}\right) \\ &= \theta_{HeNe} \end{aligned}$$

A brief search of the literature indicates that the index of refraction and sound phase velocity varied little over the range of interest; as a result, the same value was used for both the Ti-Sapph and HeNe Bragg conditions. An

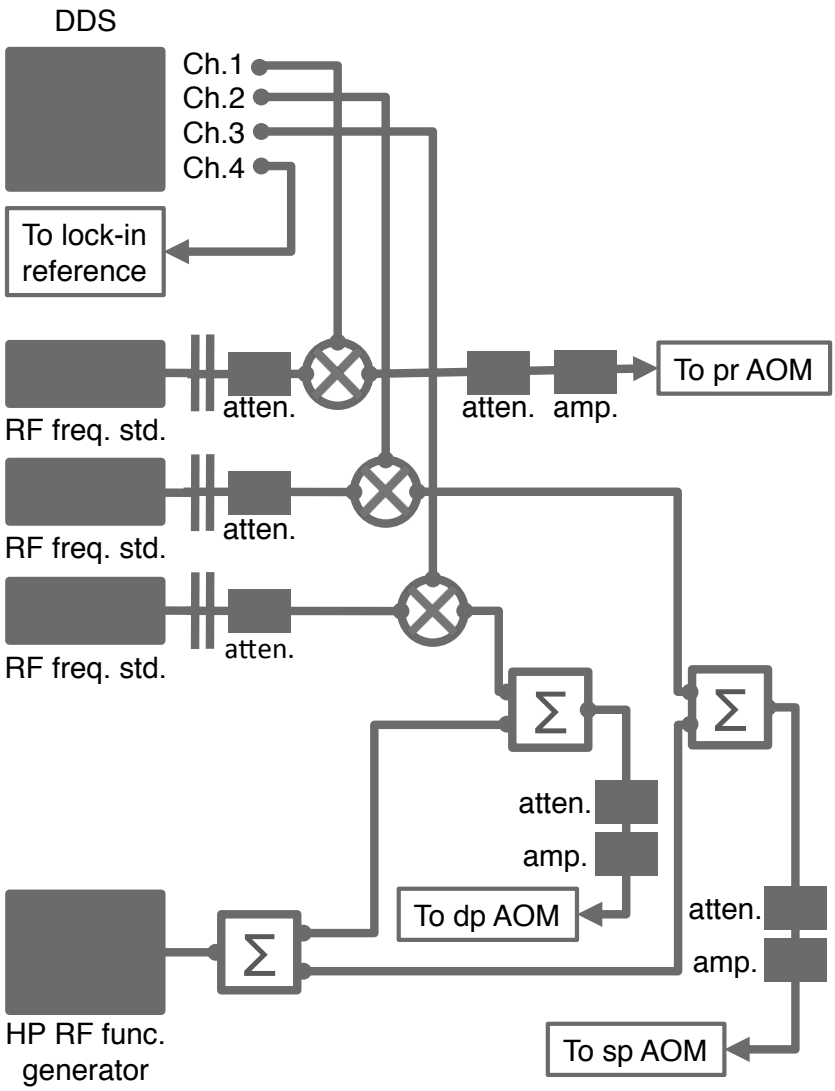

Schematic for the three-channel RF mixer circuit. The DDS function generator produces three modulation frequencies with variable amplitudes and phases, which are mixed with three independently sourced RF carriers to deflect and modulate the Ti-Sapph beams. A cw, unmodulated RF signal is added to the modulated signal driving the static pump and dynamic pump acousto-optic modulators to deflect the HeNe laser through the same angle at the Ti-Sapph beam.

Figure 6.38: Full RF schematic for dual AOM drive

estimated value of was found for the necessary drive frequency for the second frequency source. Using the RF function generator to insert this acoustic carrier into the acousto-optic modulators in the pump beams resulted in the diffraction of the HeNe beam at a much more intense power than was seen without the second frequency, and the diffracted spots were relatively close to that of the Ti-Sapph beam – however, some additional spots could be seen in the far-field pattern of both lasers. Adjusting the frequency of the second source allowed us to effectively collimate the central spot in the HeNe diffraction pattern with the central spot in the Ti-Sapph pattern. Selecting the central spot in each pattern with an iris, we used nearly parallel mirrors to lengthen the optical path and fine tune the precise RF frequency needed to collimate the two laser beams. No deviation between the two beams was visible over a length of approximately 8 meters.

Removing the aperture and examining the diffraction pattern, we noted that the far field patterns of both lasers had similar structure: a stronger central spot with two spots to either side. We used the aperture to select the center spot for use in our experiment.

The second RF/acoustic frequency is supplied to the two pump acousto-optic modulators using two more discrete splitter/combiners. The signal from the RF function generator is split using a 50-50 power splitter from Minicircuits; then each half is combined with the drive RF signal previously used to power one of the acousto-optic modulators, using another splitter/combiner prior to the final amplifier stages. The combined signal is then used to drive

the acousto-optic modulator.

Several frequency components thus comprise the RF drive signals sent to the pump acousto-optic modulators: the modulated drive frequency chosen to satisfy the Bragg condition for the Ti-Sapph, which itself can be represented as the sum of two frequency components spaced by the modulation frequency and centered on the carrier frequency, and the constant RF signal derived from the function generator. We note explicitly that the modulated drive signal used to control the Ti-Sapph at each acousto-optic modulator is independent of that used for that purpose in the first acousto-optic modulator: each was generated using an independent reference oscillator crystal, which was mixed with a slow reference signal derived from the computer controlled DDS generator. The slow modulations for the two acousto-optic modulators exhibit a well-defined phase relationship, since they were generated by a single digital counting process. This phase stability is necessary for the use of these modulation signals in multiple-frequency lock-in detection scheme. The 80 MHz drive signals derived from the independent crystal references should not possess a well-defined phase relationship, since these devices should be operating independently; based on anecdotal suggestion, we made the conscious decision to use separate frequency sources for the acousto-optic modulator drive frequency rather than deriving the carrier for all three acousto-optic modulators from a single source. It is possible that coupling could occur through some cross-talk mechanism and lead to a Huygens Odd Sympathy effect (see, for example, [258], but we saw no particular evidence to suggest this. As our ex-

periment operated satisfactorily with the independent drive frequency sources, we did not study the effects of substituting a single RF source for the three (two pump + one probe) independent frequency reference sources used here.

After reading the literature on multiple frequency operation of acousto-optic modulators, we note that the problems of nonlinearities in this apparatus need to be considered. First, we note that for a given optical wavelength there is an inherent coupling between the frequency shift applied to a beam and its angular deflection. Since a modulation signal can be represented as the sum $\sin\left(\left(\Omega_0+\delta\right)t\right)+\sin\left(\left(\Omega_0-\delta\right)t\right)$ of two frequency components rather than the product of two sinusoidal signals, i.e. $\cos\left(\Omega_0 t\right)\cos\left(\delta t\right)$, the question of cross-modulation of the two different laser sources can similarly be reduced to a geometric argument. We know that applying a second constant frequency from the HP RF signal generator will deplete the intensity of the Ti-Sapph beam somewhat due to the deflection of that laser via non-resonant Bragg scattering. That effect is trivial, however, since the intensity of the non-resonant diffracted beam is vanishingly small. Similarly, the application of the modulated RF carrier signal intended to drive the Ti-Sapph will cause non-resonant diffraction of the HeNe; again, that effect is small enough to be neglected.

Of more significant concern is the effect of the modulated signal on the intensity of the HeNe diffracted beam. Barring any non-linearities in the device due to e.g. higher order acoustic or photo-acoustic effects, we do not expect these to be a significant problem. Examining the photodiode output

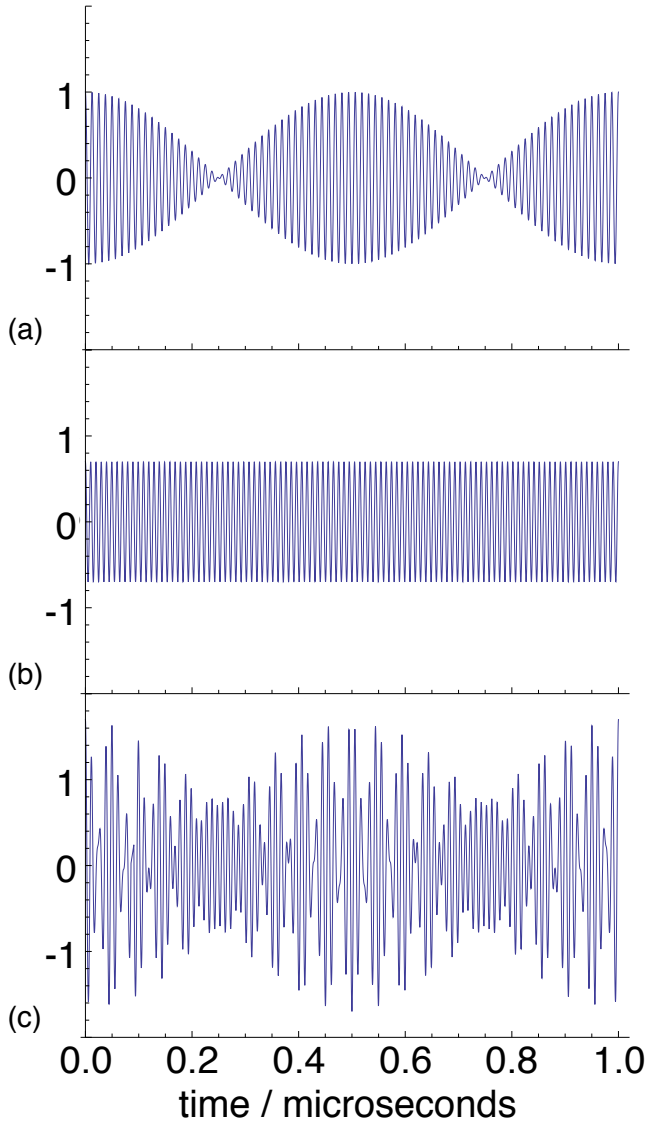

A modulated RF signal, generated by nonlinear mixing of an 80 MHz carrier and a modulation signal produced by the DDS function generator (1 MHz is used in the signal shown here) (a) is used to deflect and modulate the Ti-Sapph beam. An unmodulated carrier generated by an RF function generator (b) is used to deflect the HeNe beam that co-propagates with the Ti-Sapph. The two are combined (c) prior to the acousto-optic modulator.

Figure 6.39: Modulation and cw dual AOM drive

while scanning the PZT-mounted mirror reveals a normal interferometer fringe at the HeNe wavelength, with no sign of modulation due to the other RF signal. This does not mean that these effects have been completely eliminated, since the typical frequencies involved in the acousto-optic processes are too fast for the homebuilt interferometer fringe to resolve a direct signature, but it does indicate that no such processes are occurring that would prevent normal operation of our interferometric, lock-and-step system. Indeed, we find that the interferometer locks with the same stability observed when using only the cw drive frequency that deflects the HeNe beam (i.e. with the Ti-Sapph beams effectively blocked at the acousto-optic modulators). If there are cross-modulation effects occurring, they do not result in any effect on the interferometer, which locks normally and allows us to step our τ delay stage with interferometric precision. This is the sine qua non for phase-sensitive experiments like 2dFTS.

We do not expect intermodulation products – those terms that occur due to frequency mixing – to be a problem because they are spatially separated. The interference terms at the difference frequencies and the intermodulation frequencies at $2\Omega_i - \Omega j$ will result in a diffraction of some fraction of the otherwise usable optical power through different angles, but as long as they can be spatially filtered from our beam of interest and do not excessively reduce the efficiency of the experiment, we are not concerned with their effects. They are readily visible as secondary spots that surround the mode we wish to use, but can easily be blocked using the apertures that are already placed in the exper-

iment for alignment purposes. The efficiency of the experiment is somewhat troublesome at this point, as it now throws away a significant fraction of the Ti-Sapph power that we use to excite and probe the sample. Since the probe beam is split first from the input Ti-Sapph, the efficiency issue only really is a concern for the dynamic and static pump beams, which are subsequently split to share the remaining power using a 50%-50% ultrafast beam splitter. When the laser source is operating optimally, power is not an issue, and some Ti-Sapph efficiency can be gained by sacrificing some of the HeNe power by reducing its cw RF drive intensity at the HP function generator. Unfortunately, because the HeNe beams are retroreflected to operate the interferometer, they must double pass the multi-frequency acousto-optic modulator, and hence require greater RF power than might otherwise be expected. This effect can be somewhat accounted for by using a sufficiently high gain on the photodiode used to detect the HeNe interference fringe.

Some questions can be raised regarding the intensity of the Ti-Sapph beams directed toward the experiment, videlicet: does introducing the additional RF signal result in some time-dependent intensity modulation of those beams. The demonstration of the interferometer locking and stability suggest that the HeNe beams are not disturbed in any way that would impede their function does *not* prove that no such modulation or other effect occurs – merely that it is not observed when monitored with a relatively slow photodiode.

Such an effect might be somewhat problematic to observe in the Ti-Sapph pump beams, because it would require a relatively high bandwidth

measurement recorded over a relatively long duration. The necessary bullet-proof demonstration would require sufficient bandwidth to properly resolve the individual laser pulses rather than the modulation envelope. The laser repetition rate is 76 MHz, but to ensure that the amplitude of each pulse is properly resolved suggests using a sampling frequency faster than twice that. Data would need to be collected over a sufficiently long period to observe effects corresponding to the slowest time scale; the immediate choice for that is the slow modulation frequency, typically in the range of half a MHz to a few MHz. This should probably suffice to provide direct proof of the spectral purity of the modulated Ti-Sapph beam. We do not provide such a direct measurement. Instead, we simply note that two-pulse differential reflectivity measurements performed using the static (or dynamic) pump and probe beam, with the dynamic (or static, as appropriate) pump blocked reproduced the previous set of two-pulse data. Barring any unexpected results, we take this as suggestive that the device operates as we hypothesize it to.

Thus, we assert that this experimental apparatus in all likelihood allows us to diffract a Ti-Sapph and HeNe beam through very nearly the exact same beam paths, with the Ti-Sapph beams modulated at independently selectable frequencies, and with the HeNe beam retroreflected through the interferometer to provide an error signal that can be used to actively stabilize this experiment.

6.7.4 Three-pulse four-wave mixing measurements in reflection mode with variable beam geometries: a new technique for studying structured samples

In this section we describe some experiments we made as a proof of concept, to demonstrate the potential of our apparatus.

The experimental program outlined in this chapter describes a work in progress. We wish to develop the ability to perform four-wave mixing measurements on samples that require specific control of three independent beams in order to observe momentum coupling effects. The nature of these samples requires us to work in a reflection geometry, which is a useful spectroscopic tool to develop due to the broad range of samples that it permits us to study that are intractable to transmission mode experiments. The signals of interest to us are extremely weak, requiring the use of a sophisticated three-frequency lock-in detection scheme. In order to perform phase-sensitive measurements we require the ability to interferometrically stabilize two optical path lengths to less than one part in a hundred of the relevant wavelength; to do this while simultaneously using acousto-optic modulators to modulate the Ti-Sapph beam we demonstrated that introducing a second acoustic frequency permits resonant Bragg diffraction of a HeNe beam along the same beam path. Two-pulse measurements alone reveal coherent oscillations at early times, but cannot provide a direct measurement of the dephasing rate (at least, when not performed using a self-diffracted geometry that would allow spatial separation of the four-wave mixing emission).

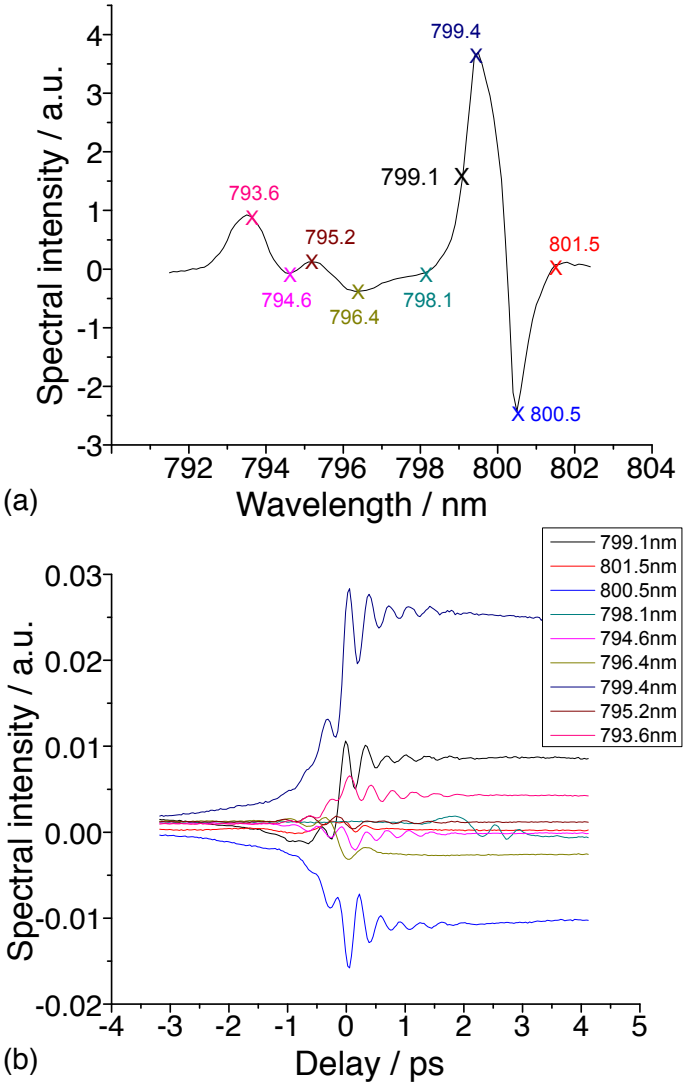

Two-pulse dR/R spectrum of a GaAs quantum well sample taken at T=2.5 ps delay with selected points along the exciton lineshape indicated (a) and subsequently plotted as a function of probe delay T (b). The early time behaviour reveals clear evidence of coherent oscillations, but does not provide a simple, direct measurement of the dephasing time without a complete model of the temporal lineshape.

Figure 6.40: 2-pulse early time coherent behaviour

During the development of this apparatus we have also performed experiments that suggest that the conventional intensity modulation schemes used for two-pulse experiments only sample a subset of the terms present in a heterodyned measurement. We develop that idea further here. In an appendix to this thesis, we show that the intensity detected along the probe beam after it reflects from a sample is given by

$$\begin{aligned} |E_{pr} + E_{sig}|^2 &= |E_{pr}|^2 \\ &\quad + \zeta \, |E_{dp}| \, |E_{sp}| \, E_{pr}(t) \, E_{pr}(t + \pi/2) \\ &\quad + \left(\zeta \, |E_{dp}| \, |E_{sp}| \, E_{pr}(t + \pi/2)\right)^2 \end{aligned}$$

The first term, $|E_{pr}|^2$, is simply the probe background and will be rejected by the lock-in detection method. This signal component is analogous to the probe background spectrum that is detected with the pump beams blocked, and then subtracted from the signal spectrum in our 2dFTS experiments.

The third term is a homodyne term, and is proportional to the intensity of each of the three beams used to induce four-wave mixing emission, and to the square of the proportionality constant determined by the light-matter interaction. This, we note, is the term that would be detected by a conventional extension of normal two-frequency modulation schemes; it will be detected

if the intensities of the three beams are modulated at (Ω_{sp}, Ω_{dp}, Ω_{pr}), where the Ω_i refer to the angular frequency of intensity modulation of a given beam by its acousto-optic modulator. For this conventional scheme, the reference frequency for lock-in detection is given by $\Omega_{sp} \pm \Omega_{dp} \pm \Omega_{pr}$. We refer to that as an intensity modulation scheme, and present its results below.

The second term is a heterodyne term. Interestingly, the intensity of this component is proportional to the intensity of the probe beam, but to the electric field strength of the static pump and dynamic pump fields; the emission described by this term is linear in the pump electric fields but bilinear in the probe field. The result quoted here, which may be found in a simplified derivation in the appendix, contains an apparent contradiction, in that the time-averged intensity of this term would appear to be zero due to the $\pi/2$ phase difference between the probe and emitted four-wave mixing field; that term only appears because this toy model did not consider the real, physical geometry of the sample. In fact, there will be a phase difference between the probe field reflected from the sample front surface and the four-wave mixing emission that actually occurs within the material system itself. Modelling that phase difference itself is not trivial, and will depend upon the precise geometry used, the index of refraction of the medium, and the distance between the front surface and the active region. Only for a pathological geometry would the phase difference here actually work out to $\pi/2$, and in general we should expect some observable signal here. We suggest that this term may be isolated from the background and homodyne terms by proper choice of the lock-in reference

frequency. We use a frequency given by $\Omega_{pr} + \Omega_{sp}/2 - \Omega_{dp}/2$ to isolate this term from the other two in our experiments.

We emphasize that *the extension of intensity modulation from conventional two-frequency optical measurements to a three-frequency intensity modulation scheme would pick out only the homodyne term*, which depends upon the square of the proportionality constant that describes the nonlinear optical processes. The intensity modulation measurement will thus only provide a positive semi-definite measurement, and will lose the ability to discriminate the sign of the constant of proportionality.

The hybrid intensity-electric field modulation scheme described here that treats the three pulses on an unequal footing that is appropriate due to the dissimilar way the pulses interact with the sample. While we used a simple dipole coupling approximation to describe the light-matter interaction, the geometry of the probe beam is different from that of the two collinear pump beams. This point must be re-visited in any attempt to move toward a fully collinear geometry where all three beams co-propagate along the same beam path; in such an experiment, the only distinction would be the phase-stability between two of the three pulses, but cross terms between the four-wave mixing signal field and all three of the incident optical fields would be present in the detected intensity. Choosing the appropriate reference frequency in such an experiment may provide a way to remove the degeneracy between these fields and choose a specific heterodyne term. These considerations are not academic, as our experimental apparatus was specifically constructed to permit both par-

tially collinear and fully collinear experiments: a periscope placed in the beam path of the combined pump beams lifts those beams slightly above the horizontal plane in which all other beams in the experiment lie. Removing that periscope will immediately provide a fully collinear experiment. The immediate question, whether a weak four-wave mixing signal can be detected against this background, seems likely to be answered in the affirmative, as we have already moved from performing three-pulse experiments with two strong (1.00 mW) pump beams and one weak (100 uW) probe beam to performing our experiments with three equally strong beams (static pump, dynamic pump, and probe all equal to 1.75 mW in these data). We realized shortly after moving from CCD detection to lock-in detection that the ability to discriminate between the signal modulated at the reference frequency and the strong background of the probe beam permitted us to increase the strength of the probe beam. This allows us to perform these experiments with equal intensities in the three incident beams, which should provide us with the strongest four-wave mixing signal. There are no apparent deleterious issues associated with using the higher probe power. Moving from 100 uW to 1.75 mW is a factor of 17.5 increase in the power present in the probe beam, but it does not seem to cause any problems detecting the weak four-wave mixing field. This suggests that the increase by a factor of three that would occur when working in a completely collinear geometry should not cause any significant problems.

We show here data collected with both the conventional intensity modulation scheme and the hybrid intensity-electric field modulation scheme. Since

we were interested in observing a four-wave mixing that decays on a time scale determined by the system dephasing time, we reduce the temperature to typically 5K in order to reduce the acoustic phonon population. These data are taken with 1.75 mW in each of the three beams. The reflected probe beam is collected as described previously, spectrally resolved using a 0.5m monochromator, and detected using a biased Silicon photodiode. The photocurrent is converted to a photovoltage across a resistor; the bandwidth of the loaded detector is estimated to be greater than 100 kHz. We use the same precision pre-amplifier (SR 560) to filter the signal, using a frequency bandpass that should eliminate a significant fraction of the noise on the photodetector. The conditioned signal is then sent to a lock-in amplifier for detection and averaging. The lock-in amplifier is controlled via GPIB interface by the experiment control computer. Home coded Labview software on that pc controls the unlocking of the interferometer, the movement of the dynamic pump translation stage to increment the τ delay, the re-locking of the interferometer, and the polling of the lock-in amplifier to readout the detected signal.

Data recorded using the intensity modulation scheme are presented for only one wavelength, corresponding to the heavy hole exciton resonance peak, while hybrid scheme data are shown at two different wavelengths, corresponding to the heavy hole exciton resonance peak and the light hole exciton resonance peak. For both experiments, the conditions are identical other than the reference frequency sent to the lock-in amplifier and the lock-in time constant used. The probe pulse is delayed by $T = 5.00$ ps compared to the arrival

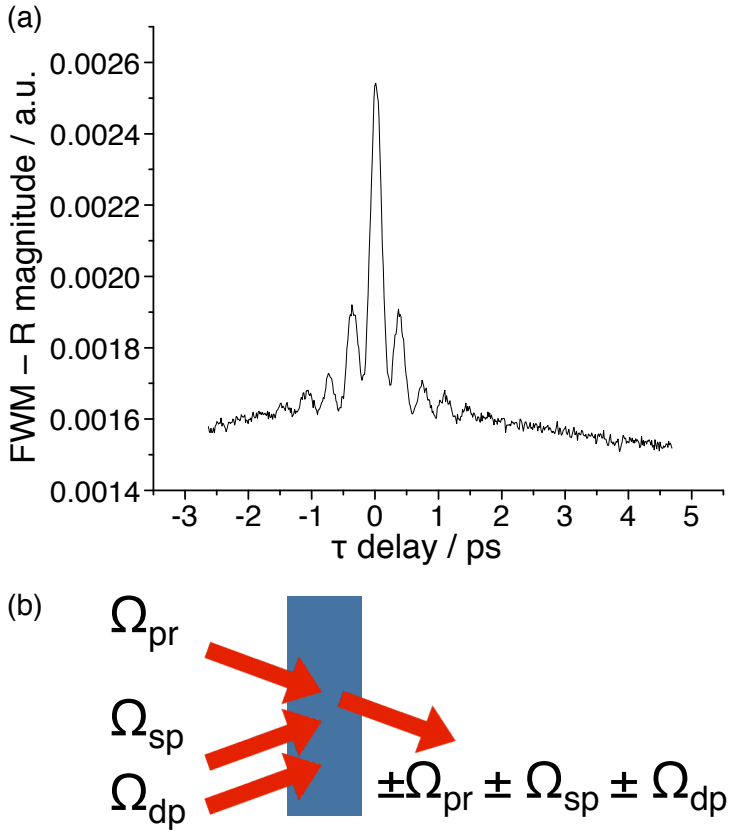

A four-wave mixing signal (a) detected using the three-frequency modulation and detection scheme that is a conventional extension of the difference frequency detection (b) more commonly used with two modulated excitation sources. The intensity of each of the three beams used in this experiment is modulated at particular frequency; lock-in detection is performed using a reference signal generated as a linear combination of the three frequencies, i.e. ($\pm\Omega_{pr}$ $\pm\Omega_{sp}$ $\pm\Omega_{dp}$). The data shown here are collected with the probe pulse delayed 2.5ps from its coincidence with the static pump pulse. A monochromator is used to spectrally analyze the four-wave mixing signal and co-propagating probe beam prior to detection; these data were taken at 799.5nm, corresponding to the peak of the heavy hole exciton resonance. The sketch of the detection scheme is not intended to represent the actual geometry of the reflection measurement.

Figure 6.41: FWM using intensity modulation

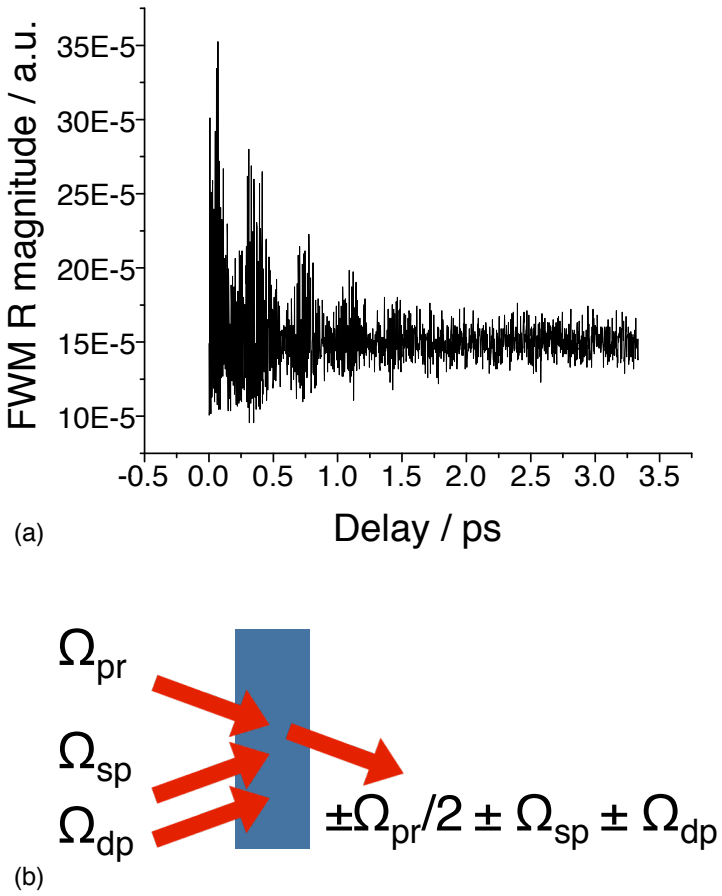

Four-wave mixing data (a) collected with the hybrid detection scheme (b) with phase-locked pump pulses generated from the Mach-Zehnder interferometer using the multi-frequency acousto-optic modulator drive system. These data were taken at 799.5nm with a probe delay time T=2.5ps; we plot R magnitude data rather than the in-phase X-component of the lock-in signal because we wished to observe the largest magnitude signal possible when demonstrating the technique. The slow oscillation superimposed on the decay is determined by the splitting between the light hole and heavy hole exciton resonance, while the presence of the high frequency component will permit the extraction of the optical phase.

Figure 6.42: FWM using intensity modulation

of the static pump pulse. The dynamic pump starts coincident in time with the static pump and is stepped backwards in time, arriving earlier by 0.002109 picoseconds with each step. We run the experiment with 1404 steps, corresponding to a τ delay scan of approximately 3 picoseconds. This appears to suffice to see a decay of the observed four-wave mixing signal to the level of the noise-floor in the hybrid detection experiment. We note (and discuss *sub*) that the signal detected using conventional intensity modulation does not decay to a zero background level during this scan.

For the hybrid detection scheme, 300 ms integration time was used, while the intensity detection scheme signal could be well-resolved with 30ms. As a result, the time needed for a single τ scan of the hybrid experiment, approximately 25 minutes, was a factor of ten greater than that needed for the intensity modulation scheme. It is not entirely clear why the hybrid scheme signal requires greater time to accurately resolve, but we note that it may be related to the high frequency fringe that appears in the hybrid signal but not in the intensity modulated signal.

We cannot say definitively why the homodyne term lacks these fringes, but suggest that it may be due to the manner in which the intensity terms appear in the expression for this component of the $|E_{signal} + E_{probe}|^2$ expression. It is suggested that a more careful analysis that keeps track of how the field amplitudes enter into the expression for the heterodyne and homodyne terms will better explain this effect – but we note that it is significant for our purposes. If we wish to perform a 2dFTS measurement, we rely on resolving

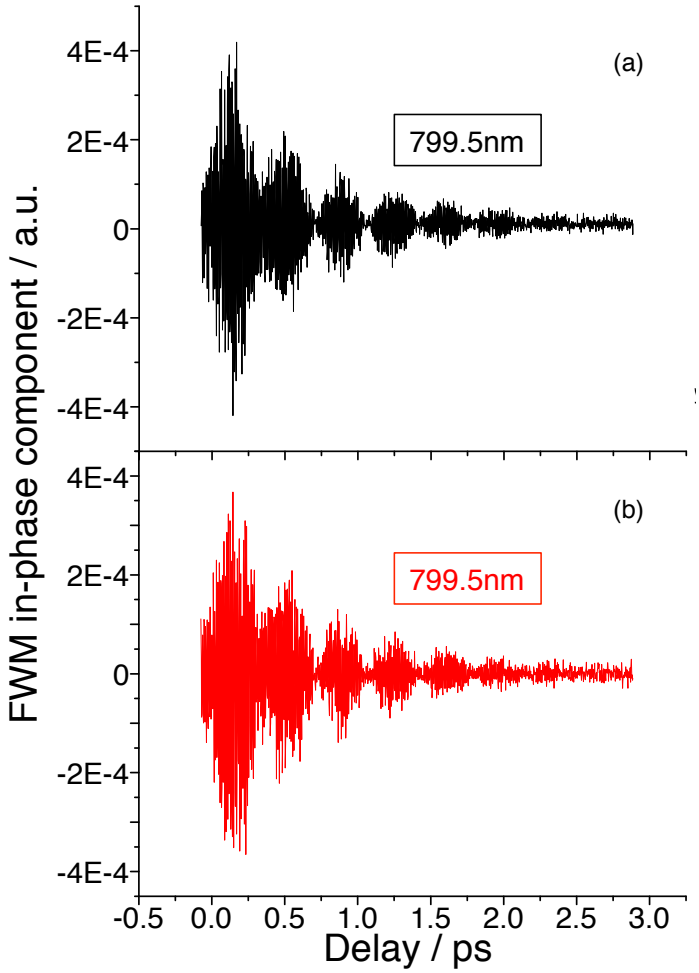

Four-wave mixing signal detected in the partially collinear geometry using the hybrid electric field-intensity modulation scheme with interferometrically phase-locked pump pulses. These data were collected at 799.5nm (a), the heavy hole exciton peak, and at 793.6nm (b), the light hole exciton peak. Note the high frequency component in the signal, demonstrating the ability to resolve the optical phase of the four-wave mixing emission – a prerequisite to perform 2dFTS experiments. Note the absence of background to the signal, since the detection scheme eliminates the pump-probe background

Figure 6.43: Phase-sensitive FWM using hybrid modulation

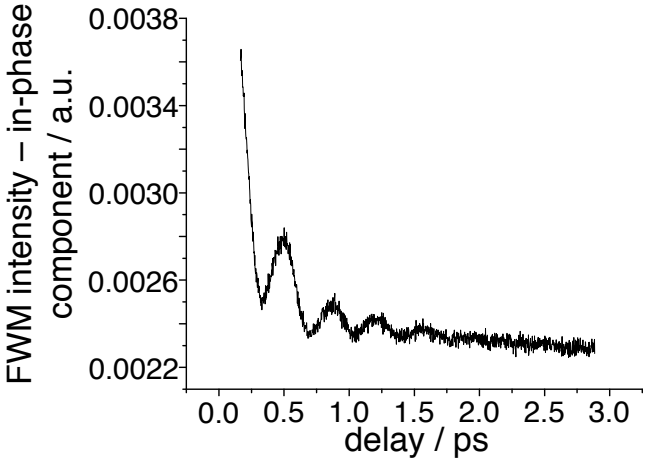

Four-wave mixing signal collected in the partially collinear geometry using the conventional modulation and detection scheme, performed using phase-locked pump pulse pairs generated using the locked Mach-Zehnder interferometer. The slow oscillation of the four-wave mixing signal occurs due to the interaction between the heavy hole and light hole exciton resonances, but note the absence of any optical frequency component in the decay. This lack of optical frequency information prevents the use of this modulation-detection method to perform 2dFTS, which requires the ability to measure the optical phase of the emission occurring after the arrival of the third (probe) pulse. Note the presence of the background due to the pump-probe artifacts.

Figure 6.44: Phase-sensitive FWM with conventional intensity modulation

the optical frequency signal in the t period. The intensity modulation scheme, which only reveals the envelope of the four-wave mixing signal, cannot be used to perform this kind of experiment.

To re-iterate and emphasize this point: *it is not clear that it is possible to perform 2dFTS using the conventional detection scheme.* A straightforward implementation of 2dFTS requires that the experiment can resolve the phase of the nonlinear signal at the beginning of the detection period in order to correlate those events that occur in the first time period with those that occur during the third. That capability is demonstrated here for the hybrid modulation and detection scheme. For comparison purposes, the fast, optical frequency component may be seen directly in the mixed frequency-time (ω_t, τ) domain measurements we performed during our 2dFTS measurements. We note the similarity of that signal to the time domain data presented here (for only two wavelengths, of course) collected using the hybrid modulation scheme.

It is absolutely necessary to use phase-stabilized pump pulses to perform these measurements. The high-frequency component cannot accurately be recorded without active stabilization, using the optical multiplex acousto-optic system to modulate the Ti-Sapph beams while simultaneously permitting the use of a HeNe beam to lock the Mach-Zehnder interferometer. Consider the counter-example of hybrid modulation and detection scheme measurements performed without phase stabilization.

The hybrid detected signal has certain other advantages compared to

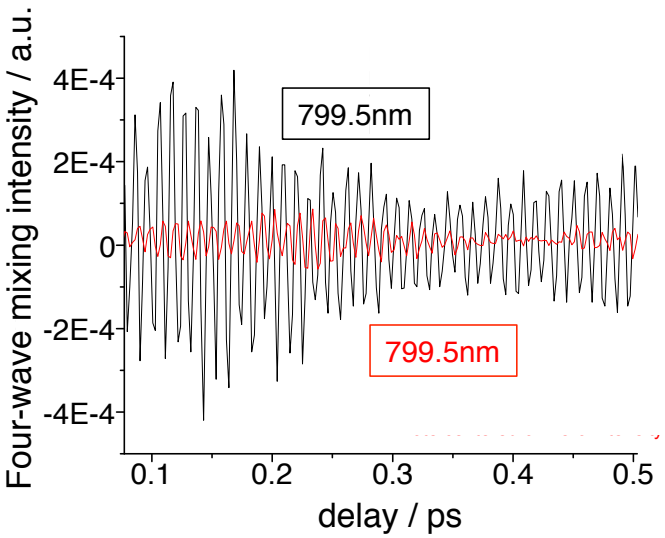

High resolution segments of four-wave mixing signals collected using the hybrid modulation and detection scheme, revealing the optical frequency component present in the decaying, oscillating signal emitted at the heavy hole exciton (black trace) and light hole exciton (red trace) wavelengths. The ability to resolve the optical frequency and thus, the optical phase of the emission, permits 2dFTS measurements using this detection scheme.

Figure 6.45: High-res hybrid phase-sensitive FWM

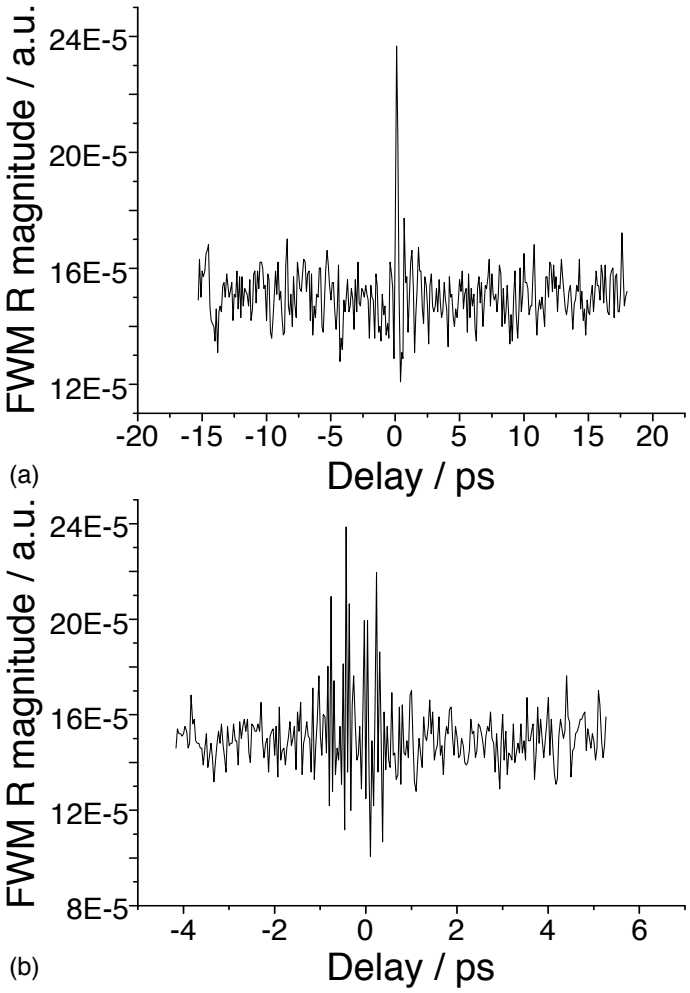

Four-wave mixing signals recorded with the hybrid modulation-detection scheme without active phase stabilization. These data were collected at a probe delay of *T*=2.5ps, at a wavelength of 799.5nm. Without locking the interferometer used to generate the pump pulse pair, acoustic noise in the apparatus largely washes out the signal, as small perturbations in the path length walk the signal across the fringe pattern (q.v. *sub*). Increased integration times may actually decrease the signal-to-noise, as they provide greater time for random walks to wash out the fringe. These data demonstrate the necessity of active stabilization.

Figure 6.46: Hybrid FWM without phase stabilization

the intensity modulated, conventional signal.

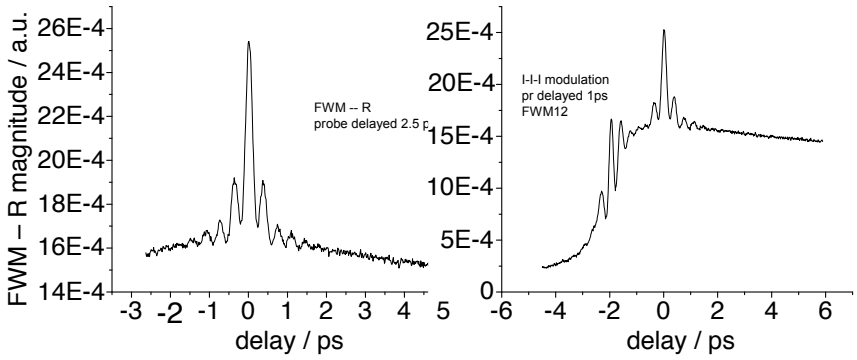

Four-wave mixing signals detected using the conventional, intensity three-frequency modulation and detection scheme. The features centered on τ=0 are composed of an exponential decay determined by dephasing dynamics, multiplied by an oscillatory, interference signal (a). These features reveal an asymmetry due to the superposition of the four-wave mixing signal on top of a pump-probe artifact that can be revealed by expanding the range of the τ scan (b). The data shown here were collected with probe delays *T*=2.5ps (a) and *T*=1ps (b).

Figure 6.47: Conventional FWM superimposed on pump-probe

The conventional signal is actually superimposed on a background, appearing superimposed on something like the pump-probe artifacts with which we are familiar from our 2dFTS measurements detected using the CCD and mechanical chopper. Those measurements also decayed slowly to a non-zero baseline, with a characteristic time scale determined by the population relaxation rate. Using the hybrid detection scheme avoids this problem, since the signal component it resolves is governed entirely by the dephasing time. It also decays to a zero background level, reducing the number of experimental

parameters that must be fit in an analysis. In any analysis, we note that it is possible to extract the dephasing rate from the intensity modulation scheme data, but not with the same precision that can be achieved analyzing the hybrid scheme data. Indeed, if the slow decay that the intensity modulation four-wave mixing signal sits on top of were to decay faster – i.e., if there were less separation between the population relaxation and dephasing rates – it would not be possible to accurately extract the dephasing rate from the recorded data. The hybrid intensity-electric field modulation scheme permits direct extraction of the dephasing rate regardless of the population relaxation time.

The elimination of the background from this signal is not completely dissimilar to the application of various phase-cycling schemes to manipulate a 2dFTS spectrum. We have not concentrated on these techniques in our description of 2dFTS because we did not (at the time we constructed it) have the ability to readily control the phases of the three different pulses used for that experiment. With the introduction of the three independently controlled acousto-optic modulators, we now have the ability to perform phase modulation experiments using the DDS function generator. At present, the DDS parameters are set prior to running a three-pulse experiment, but the device can be controlled readily simply by writing to the serial port with which it communicates with the experiment pc. Serial control of this device to perform phase shifts at each step during a multi-step experiment could be implemented in a straightforward fashion using the home-coded Labview control software

for our apparatus.

We are, of course, most interested in the potential to perform 2dFTS or similar sophisticated measurements using this scheme. At the moment, 2dFTS is not practical, since we can only detect a single wavelength at a time. To record a mixed time-frequency data set for 2dFTS analysis would, at the current rate, take something like 500 minutes for only 50 different wavelengths. The spectra recorded in the two-pulse experiments shown in this thesis use 0.1 nm resolution – thus, to properly map our 5 nanometers spectral bandwidth with a 3 picosecond time scan would require nearly eight and a half hours. When we take 2dFTS data, our experiments typically took approximately 30 to 40 minutes to collect sufficient data to record a high quality spectrum. Occasionally, the lab environment would be too noisy to maintain the interferometer lock on even that relatively short time scale. Data collected in experiments performed overnight, during holiday weekends, was far less susceptible to losing the interferometer lock, but that requirement does not make for a practical experiment. To study the coupling of the surface plasmon polariton to the quantum well exciton as a function of momentum in the sample we're currently interested in would require perhaps ten spectra collected at different angles. In order to follow the transfer of energy between the coupled states in this system may require several 2dFTS spectra be collected as a function of the T delay. Further refinement of the experimental technique is clearly called for before it is practical to study these systems, but the fundamental proof of concept of this method has been demonstrated.

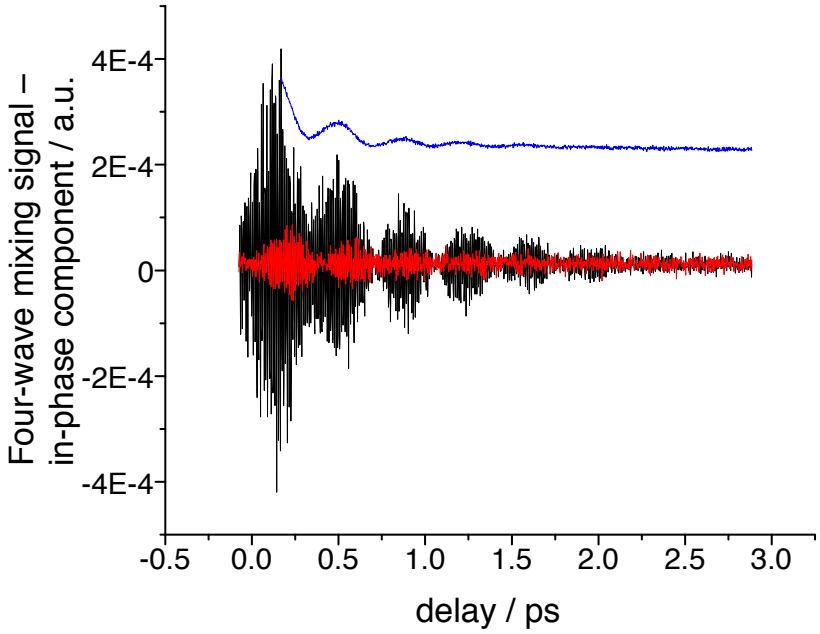

Comparison of four-wave mixing signals detected using the hybrid modulation and detection scheme (black trace, 799.5nm; red trace, 793.6nm) and a conventional intensity modulation and detection scheme (blue trace, 799.5nm). The hybrid detection scheme traces are centered on zero, whereas the intensity modulation scheme trace is offset by a pump-probe background that is itself a function of the τ scan. The hybrid scheme permits direct, straightforward extraction of the dephasing time, regardless of the population relaxation rate, while the conventional scheme would require fitting the background artifact using the population relaxation rate. The hybrid traces also permit extension to more sophisticated measurements, such as 2dFTS. The disadvantage of using the hybrid scheme is the much longer time necessary – the hybrid traces shown here require approximately 25 minutes each to collect, compared to approximately 2.5 minutes for the conventional intensity modulation scheme.

Figure 6.48: Comparison of hybrid and conventional FWM signals

Some parallelization is necessary; we suggest that a fast detector array could be used, and that the reference signal could be simultaneously recorded. A post-experiment data processing step functionally equivalent to lock-in detection could subsequently be performed to extract the signal of interest. Developing an ability to perform parallel measurement of some number of wavelengths would radically decrease the time necessary to collect sufficient data for a 2dFTS or similar experiment.

It is also possible that the signal-to-noise may be increased simply by improving the optical alignment. The exact cancellation of the $\mathbf{k}_{dp}$ and $\mathbf{k}_{sp}$ wavevectors requires that those beams be perfectly overlapped. Any mismatch in those beams' wavevectors would result in a four-wave mixing signal that is not perfectly mode-matched into the probe beam. As the probe beam propagates further away from the sample, the difference between it and the (ostensibly) co-propagating four-wave mixing signal's wavevectors would decrease the intensity of the four-wave mixing signal that will be detected by collecting the probe beam.

Some success may also be had by moving to a different choice of modulation frequencies. The values used in these experiments (the probe intensity is modulated at 0.643 MHz, the static pump intensity is modulated at 0.748 MHz, and the dynamic pump intensity is modulated at 0.967 MHz) were chosen in order that the linear combination of interest, *viz.* the hybrid intensity-electric field detection frequency at $0.643 + 0.748 - 0.967$ MHz did not coincide with any other linear combinations of electric field and intensity modulation fre-

quencies. This frequency choice is therefore largely determined by the need to avoid inadvertently detecting another signal and mistaking that artifact (for example, any of the two-pulse signal components) for a genuine four-wave mixing signal. Significant attention was not paid to finding the ideal combination of the modulation frequencies that would optimize the signal-to-noise given the photo detector and signal processing.

In summary, the tools described in this chapter provide a promising foundation for developing a sophisticated spectroscopic toolbox that may be used to perform 2dFTS and other similarly complicated measurements on samples that could not otherwise not studied.

Appendix

Appendix 1

Density operator calculations in the partially collinear geometry

Multi-dimensional spectroscopy depends upon the measurement of a nonlinear polarization induced by a tailored sequence of pulses. Some measurements have detected the signal of interest by observing the effects that phase-cycling the excitation pulses has upon incoherent fluorescence [363] in a technique analogous to the detection schemes commonly used in nuclear resonance experiments, but most rely upon the observation of a coherent emission along a particular phase-matched direction. A simple density operator calculation may be used to understand the direction and time-evolution of the four-wave mixing signal. Although a more sophisticated microscopic model is necessary to understand the rich dynamics of many complicated condensed matter systems, a simple Taira/optical Bloch calculation is a useful approximation for these purposes.

For experiments where the polarization is induced by a time-sequenced pulse train, the quantum mechanical equations of motion for a single pulse may be used iteratively, with the result for one pulse – characterized by populations and coherences – used as the initial state for the calculation of the next

pulse. In practice, this is effected by calculating a first-order perturbation correction due to the first pulse to arrive, a second-order perturbation correction due to the second pulse to arrive, and a third-order perturbation correction due to the third pulse that interacts with the sample. After all three pulses are considered, the resulting perturbation calculation of the dipole operator expectation value contains terms that are linear in each of the applied fields; the emission arising from the macroscopic polarization depending on a phased array of dipoles is the four-wave mixing signal of interest. Analysis of this field as a function of the pulse delays permits the extraction of the relaxation parameters characterizing the system in a Taira/optical Bloch model. Calculation in the density matrix theoretical framework does not require the addition of a directional filter function because the interaction geometry is explicitly considered in the integral functional form for the nonlinear polarization. This treatment neglects the possibility of bound-free transitions driven by intense electric fields [42], although certain features in the 2dFTS plots produced in our experiment suggest the presence of absorption from free carrier states.

We have shown elsewhere in this thesis that the optical physics with which we are concerned can be described using the interaction of several possible different excitonic states – bound and free – which relate the interactions between electrons in at least three different energy bands. We outlined the use of the Optical Bloch equations, developed first in the context of NMR experiments relying on spin flips, and their utility as a tool for studying approximate two- or few-level systems. We have also briefly described the semiconductor

optical Bloch equations, a more sophisticated field theoretical method for more completely approaching the problems of many-body physics in materials characterized by band structures. This last model is a strong theoretical tool for understanding the behaviour of optical excitations in semiconductor nanostructures, but will nonetheless fail to reproduce all the features in the complicated spectra that often arise in multiple pulse experiments such as those with which we are interested. Clearly, sophisticated theoretical models are necessary to understand the complexities of these systems.

Nonetheless, a toy picture of a two level system is often useful for calculating the basic behaviour of these systems, as the simpler model results in predictions that have clear physical interpretations, such as dephasing and decay rates arising from microscopically unspecified processes. A slightly more sophisticated model that approximates the excitonic physics using four possible energy levels (the ground, no exciton state; two states where either an hh or lh exciton is created; and a fourth state with both an lh and hh exciton (the interaction between which substantively alters the behaviour of this system, and prevents us from using a model consisting of two independent, non-interacting two level systems) provides a more complete physical understanding [178], but the fundamental effects are easily understood in the elementary two-level model we describe here. We may use the results of this calculation as a means to establish a useful language for describing the general behaviour of more complicated models, which shall similarly rely on the ideas of coherence, population, dephasing, and population decay.

We start with the initial conditions for the perturbation calculation

$$\rho_{21}^{(0)} = \rho_{12}^{(0)} = 0, \quad \rho_{11}^{(0)} = 1, \quad \rho_{22}^{(0)} = 0$$

for the Hamiltonian

$$\hat{H} = \hat{H}_0 + \hat{H}'$$

where the perturbation term

$$\hat{H}' = -\hat{\mu} \cdot \hat{\mathbf{E}}(t)$$

is defined with the dipole matrix operator given by

$$\mu_{12} = \mu_{21} = \mu, \quad \mu_{11} = \mu_{22} = 0$$

We will assume that the dipole matrix element μ_{12} is real. For a purely two-level system that is not a problematic assumption, but in a multi-level system the product of dipole matrix elements appearing in a wave-mixing expression for the nonlinear polarization may not necessarily be real [133]. The expectation for the dipole operator can be found by tracing out its product with the appropriate reduced density operator for the system,

$$\langle \mu \rangle = Tr\left\{\hat{\rho}\hat{\mu}\right\} = Tr\left\{\begin{pmatrix} \rho_{11} & \rho_{12} \\ \rho_{21} & \rho_{22} \end{pmatrix}\begin{pmatrix} 0 & \mu \\ \mu & 0 \end{pmatrix}\right\} = \mu\left\{\rho_{12} + \rho_{21}\right\}$$

From the quantum equivalent of the Liouville equation, we know that the time evolution of the density operator is given by

$$d_t\rho = -\frac{i}{\hbar}\left[\hat{H},\,\hat{\rho}\right] + \partial_t\hat{\rho}$$

where here (as in many cases) there is no explicit dependence of the density operator on time, and the partial derivative with respect to time vanishes. The time evolution of the density operator is more easily considered on an element-by-element basis for the purposes of this perturbation calculation

$$\begin{aligned}
d_t\rho_{21} &= \frac{i}{\hbar}\left[\hat{H}_0 + \hat{H}',\,\hat{\rho}\right]_{21} \\
&= -\frac{i}{\hbar}\left[\begin{pmatrix} E_1 & 0 \\ 0 & E_2 \end{pmatrix}\begin{pmatrix} \rho_{11} & \rho_{12} \\ \rho_{21} & \rho_{22} \end{pmatrix} + \begin{pmatrix} 0 & V_{12} \\ V_{21} & 0 \end{pmatrix}\begin{pmatrix} \rho_{11} & \rho_{12} \\ \rho_{21} & \rho_{22} \end{pmatrix}\right]_{21} \\
&\quad -\frac{i}{\hbar}\left[-\begin{pmatrix} \rho_{11} & \rho_{12} \\ \rho_{21} & \rho_{22} \end{pmatrix}\begin{pmatrix} E_1 & 0 \\ 0 & E_2 \end{pmatrix} - \begin{pmatrix} \rho_{11} & \rho_{12} \\ \rho_{21} & \rho_{22} \end{pmatrix}\begin{pmatrix} 0 & V_{12} \\ V_{21} & 0 \end{pmatrix}\right]_{21} \\
&= -\frac{i}{\hbar}\left[\begin{pmatrix} V_{12}\rho_{21} - \rho_{12}V_{21} & V_{12}\rho_{22} + E_1\rho_{12} - \rho_{12}E_2 - \rho_{11}V_{12} \\ E_2\rho_{21} + V_{21}\rho_{11} - \rho_{21}E_1 - \rho_{22}V_{21} & V_{21}\rho_{12} - \rho_{21}V_{12} \end{pmatrix}\right]_{21} \\
&= -\frac{i}{\hbar}\left[\begin{pmatrix} V_{12}\rho_{21} - \rho_{12}V_{21} & +\rho_{12}\left(E_1 - E_2\right) + V_{12}\left(\rho_{22} - \rho_{11}\right) \\ \rho_{21}\left(E_2 - E_1\right) + V_{21}\left(\rho_{11} - \rho_{22}\right) & V_{21}\rho_{12} - \rho_{21}V_{12} \end{pmatrix}\right]_{21} \\
&= -\frac{i}{\hbar}\left\{\rho_{21}\left(E_2 - E_1\right) + V_{21}\left(\rho_{11} - \rho_{22}\right)\right\}
\end{aligned}$$

If we define the resonance frequency for a transition between two states by $\hbar\omega_0 = E_2 - E_1$ we may write

$$d_t\rho_{21} = -i\omega_0\rho_{21} - \frac{iV_{21}}{\hbar}\left(\rho_{11} - \rho_{22}\right)$$

for the interaction matrix we are interested in, $V_{21} = -\mu\cdot\mathbf{E}\left(t\right)$ which we will write as simply $V_{21} = -\mu E\left(t\right)$, neglecting for simplicity of notation the vector nature of the dipole and the electric field. We then write an expression for the time derivative of the density matrix element of interest as

$$d_t\rho_{21} = -i\omega_0\rho_{21} + \frac{i\mu E\left(t\right)}{\hbar}\left(\rho_{11} - \rho_{22}\right)$$

We may similarly calculate the other matrix element's time derivatives, obtaining the complete set

$$\begin{aligned}
d_t\rho_{21} &= -i\omega_0\rho_{21} + \frac{iV_{21}}{\hbar}\left(\rho_{22} - \rho_{11}\right) \\
d_t\rho_{12} &= +i\omega_0\rho_{12} - \frac{iV_{12}}{\hbar}\left(\rho_{22} - \rho_{11}\right) \\
d_t\rho_{11} &= -\frac{i}{\hbar}\left(V_{12}\rho_{21} - V_{21}\rho_{12}\right) \\
d_t\rho_{22} &= +\frac{i}{\hbar}\left(V_{12}\rho_{21} - V_{21}\rho_{12}\right)
\end{aligned}$$

Where we reverted to the V_{ij} form for the interaction terms simply for brevity.

We now add in phenomenological decay effects as described above. We consider the dephasing effects, which we describe with the dephasing rate T_2, used to keep track of the loss of phase coherence among the ensemble of dipoles.

The term transverse relaxation time is sometimes used, as the Bloch equation formalism developed here was first used in the context of NMR experiments where dephasing principally occurred due to spin-spin interactions. Population relaxation is accounted for with the T_1 time, called the longitudinal or lattice relaxation time constant, again due to historical precedent from NMR theory. In this calculation we express both of these relaxation times by their inverse, using the dephasing rate $\gamma = 1/T_2$, and the population decay rate $\Gamma = 1/T_1$. With the phenomenological relaxation terms, we obtain

$$\begin{aligned}
d_t\rho_{21} &= -i\omega_0\rho_{21} + \frac{iV_{21}}{\hbar}\left(\rho_{22} - \rho_{11}\right) - \gamma\rho_{21} \\
d_t\rho_{12} &= +i\omega_0\rho_{12} - \frac{iV_{12}}{\hbar}\left(\rho_{22} - \rho_{11}\right) - \gamma\rho_{12} \\
d_t\rho_{11} &= -\frac{i}{\hbar}\left(V_{12}\rho_{21} - V_{21}\rho_{12}\right) + \Gamma\rho_{22} \\
d_t\rho_{22} &= +\frac{i}{\hbar}\left(V_{12}\rho_{21} - V_{21}\rho_{12}\right) - \Gamma\rho_{22}
\end{aligned}$$

We consider electrical fields of the form $E\left(t\right) = \widetilde{E}_i\left(t\right) + \widetilde{E}_i^*\left(t\right)$, where

$$\widetilde{E}_i = E_i\left(t\right)e^{i(\mathbf{k}_i\cdot\mathbf{r} - \Omega_i t)}$$

$$\widetilde{E}_i^* = E_i^*\left(t\right)e^{-i(\mathbf{k}_i\cdot\mathbf{r} - \Omega_i t)}$$

which couple to the material system via the dipole interaction,

$$\begin{aligned} V_{12} &= (-\mu \cdot \mathbf{E})_{12} = -\mu_{12} E \\ &= -\frac{\mu_{12}}{2} \sum_i \widetilde{E}_i^* + \widetilde{E}_i \end{aligned}$$

As noted above, we will drop the subscript and refer to the dipole matrix element as μ, since the coupling strength should be the same for μ_{12} as μ_{21}. We proceed by assuming that the interaction is a weak perturbation that does not drastically shift the structure of the energy manifolds of this system. Then, to zeroth order,

$$\rho_{22}^{(0)} = 0, \quad \rho_{11}^{(0)} = 1 = g(\omega_0) = \frac{1}{(\Delta\omega_0)\sqrt{\pi}} e^{-(\omega_0-\omega)^2/(\Delta\omega_0)^2}$$

where we have written the lower state as a distribution function to explicitly permit some inherent spectral width to the transition between the two states in the material samples. Considering the coherence terms:

$$d_t \rho_{12} = i\omega_0 \rho_{12} - \frac{iV_{12}}{\hbar}(\rho_{22} - \rho_{11}) - \gamma \rho_{21}$$

and the population terms

$$d_t \rho_{11} = -\frac{i}{\hbar}(V_{12}\rho_{21} - V_{21}\rho_{12}) + \Gamma \rho_{22}$$

we can see that, under the assumption that the coherence terms are initially zero ($\rho_{21}^{(0)} = \rho_{12}^{(0)} = 0$) in the zeroth order of the perturbation calculation,

and assuming that the initial population of the upper state is zero ($\rho_{22}^{(0)} = 0$), then the time derivative of the lower state population will also be identically zero. That analysis does not obtain for the coherence terms, however, due to the presence of the ρ_{11} term, which is non-zero in the zeroth order (indeed, integrated over ω_0 it equals unity). To find more accurate perturbation solutions we apply a step-by-step iterative method to find the density operator elements to the n-th order.

We proceed by solving the differential equations describing the time evolution of the coherence terms.

$$\begin{aligned}\dot{\rho}_{21} &= -i\omega_0\rho_{21} + \frac{iV_{21}}{\hbar}\left(\rho_{22} - \rho_{11}\right) - \gamma\rho_{21} \\ &= -\left(i\omega_0 + \gamma\right)\rho_{21} + \frac{iV_{21}}{\hbar}\left(\rho_{22} - \rho_{11}\right)\end{aligned}$$

Multiply the time derivative of the coherence by the integrating factor $e^{(i\omega_0+\gamma)t}$

$$\begin{aligned}e^{(i\omega_0+\gamma)t}\dot{\rho}_{21} &= -\left(i\omega_0 + \gamma\right)\rho_{21}e^{(i\omega_0+\gamma)t} + \frac{iV_{21}}{\hbar}\left(\rho_{22} - \rho_{11}\right)e^{(i\omega_0+\gamma)t} \\ e^{(i\omega_0+\gamma)t}\left\{\dot{\rho}_{21} + \left(i\omega_0 + \gamma\right)\rho_{21}\right\} &= \frac{iV_{21}}{\hbar}\left(\rho_{22} - \rho_{11}\right)e^{(i\omega_0+\gamma)t} \\ d_t\left\{e^{(i\omega_0+\gamma)t}\rho_{21}\right\} &= \frac{iV_{21}}{\hbar}\left(\rho_{22} - \rho_{11}\right)e^{(i\omega_0+\gamma)t} \\ e^{(i\omega_0+\gamma)t}\rho_{21} &= \int_{-\infty}^{t} dt' \frac{iV_{21}\left(t'\right)}{\hbar}\left(\rho_{22}\left(t'\right) - \rho_{11}\left(t'\right)\right)e^{(i\omega_0+\gamma)t'} + C\end{aligned}$$

from which we obtain

$$\rho_{21}(t) = \int_{-\infty}^{t} dt' \frac{iV_{21}(t')}{\hbar} (\rho_{22}(t') - \rho_{11}(t')) e^{-(i\omega_0+\gamma)(t-t')} + Ce^{-(i\omega_0+\gamma)t}$$

The second term on the right hand side, arising from the constant of integration, can be eliminated by setting $C = 0$ using the boundary conditions of the initial value problem, from the requirement $\rho_{21}(t) = 0$. We have moved the exponential term $e^{-(i\omega_0+\gamma)t}$ inside the integral even though it does not depend on the dummy variable t' because the functional form written in this manner clearly shows that the coherence at a given time t arises from the effect of the product of the interaction element with the population inversion (the term $\rho_{22} - \rho_{11}$) at some previous point in time t', with the strength of that effect decreasing as a function of the increasing time interval that has elapsed since the interaction (viz. the exponential decay of the weighting term $e^{-\gamma(t-t')}$) while simultaneously exhibiting the optical oscillation (arising from the complex term $e^{-i\omega_0(t-t')}$). This functional form thus provides more physical insight into the processes occurring at the microscopic level.

Using the zeroth order terms for the level populations we can determine the first order coherences,

$$
\begin{aligned}
\rho_{21}(t) &= \int_{-\infty}^{t} dt' \frac{iV_{21}(t')}{\hbar} \left(\rho_{22}(t') - \rho_{11}(t')\right) e^{-(i\omega_0+\gamma)(t-t')} \\
\rho_{21}^{(1)}(t) &= \int_{-\infty}^{t} dt' \frac{iV_{21}(t')}{\hbar} \left(\rho_{22}^{(0)}(t') - \rho_{11}^{(0)}(t')\right) e^{-(i\omega_0+\gamma)(t-t')} \\
\rho_{21}^{(1)}(t) &= \frac{i}{\hbar} \int_{-\infty}^{t} dt' \left(-\frac{\mu}{2} \sum E_i(t')\right) (0 - g(\omega_0)) e^{-(i\omega_0+\gamma)(t-t')} \\
\rho_{21}^{(1)}(t) &= \frac{i\mu g(\omega_0)}{2\hbar} \int_{-\infty}^{t} dt' e^{-(i\omega_0+\gamma)(t-t')} \sum_i E_i(t')
\end{aligned}
$$

The two coherence terms, to first order, are thus

$$
\begin{aligned}
\rho_{21}^{(1)}(t) &= \frac{ig(\omega_0)}{2\hbar} \mu \sum_i \int_{-\infty}^{t} dt' e^{-(i\omega_0+\gamma)(t-t')} E_i(t') \\
\rho_{12}^{(1)}(t) &= -\frac{ig(\omega_0)}{2\hbar} \mu \sum_i \int_{-\infty}^{t} dt' e^{-(-i\omega_0+\gamma)(t-t')} E_i(t')
\end{aligned}
$$

where for brevity we have written the electric field terms $\sum_i \widetilde{E}_i^* + \widetilde{E}_i = \sum_i E_i$. We are neglecting to consider the conjugate electric fields, as the field must necessarily be a real quantity. We note that this may result in a different convention for labeling the fields that contribute to a particular quantum mechanical pathway compared to other calculations.

For the population terms we again solve the differential equation describing the population time evolution using an integrating factor,

$$
\begin{aligned}
d_t\rho_{22} &= \frac{i}{\hbar}\left(V_{12}\rho_{21} - V_{21}\rho_{12}\right) - \Gamma\rho_{22} \\
e^{\Gamma t}\left\{d_t\rho_{22} + \Gamma\rho_{22}\right\} &= \frac{i}{\hbar}\left(V_{12}\rho_{21} - V_{21}\rho_{12}\right)e^{\Gamma t} \\
d_t\left(e^{\Gamma t}\rho_{22}\right) &= \frac{i}{\hbar}\left(V_{12}\rho_{21} - V_{21}\rho_{12}\right)e^{\Gamma t} \\
e^{\Gamma t}\rho_{22} &= \frac{i}{\hbar}\int_{-\infty}^{t} dt'\left(V_{12}\left(t'\right)\rho_{21}\left(t'\right) - V_{21}\left(t'\right)\rho_{12}\left(t'\right)\right)e^{\Gamma t'} + C \\
\rho_{22}\left(t\right) &= \frac{i}{\hbar}\int_{-\infty}^{t} dt'\left(V_{12}\left(t'\right)\rho_{21}\left(t'\right) - V_{21}\left(t'\right)\rho_{12}\left(t'\right)\right)e^{-\Gamma(t-t')} + Ce^{-\Gamma t}
\end{aligned}
$$

And again, we can fix the constant of integration to zero by applying the initial value conditions, requiring the population of the excited state to be zero at $t = 0$. We have again moved the exponential term related to relaxation processes, here $e^{-\Gamma t}$, inside the integrand. As with the decoherence effect found in the integral equation for the coherence terms, the purpose of this is to emphasize that the population at some time t depends upon a light-matter interaction occurring at some earlier time – here, the commutative terms coupling the interaction element to the coherences, both evaluated at some earlier time t', with the strength of that effect having decayed during the intervening period, per the integral's kernel $e^{-\Gamma(t-t')}$.

To second order, then,

$$
\rho_{22}^{(2)}\left(t\right) = \frac{i}{\hbar}\int_{-\infty}^{t} dt'\left(V_{12}\left(t'\right)\rho_{21}^{(1)}\left(t'\right) - V_{21}\left(t'\right)\rho_{12}^{(1)}\left(t'\right)\right)e^{-\Gamma(t-t')}
$$

As an intermediate step, we calculate the portion of the integrand that is not part of the kernel,

$$\begin{aligned} V_{12}\left(t'\right)\rho_{21}\left(t'\right) &= \left(-\frac{\mu}{2}\sum_{j}E_{j}\left(t'\right)\right)\frac{ig\left(\omega_{0}\right)\mu}{2\hbar}\int_{-\infty}^{t'}dt''e^{-(i\omega_{0}+\gamma)(t'-t'')}\sum_{i}E_{i}\left(t''\right) \\ &= \left(-\frac{ig\left(\omega_{0}\right)\mu^{2}}{4\hbar}\right)\int_{-\infty}^{t'}dt''e^{-(i\omega_{0}+\gamma)(t'-t'')}\sum_{i,\,j}E_{i}\left(t''\right)E_{j}\left(t'\right) \end{aligned}$$

and

$$\begin{aligned} V_{21}\left(t'\right)\rho_{12}\left(t'\right) &= \left(-\frac{\mu}{2}\sum_{j}E_{j}\left(t'\right)\right)\frac{-ig\left(\omega_{0}\right)\mu}{2\hbar}\int_{-\infty}^{t'}dt''e^{-(-i\omega_{0}+\gamma)(t'-t'')}\sum_{i}E_{i}\left(t''\right) \\ &= \left(\frac{ig\left(\omega_{0}\right)\mu^{2}}{4\hbar}\right)\int_{-\infty}^{t'}dt''e^{-(-i\omega_{0}+\gamma)(t'-t'')}\sum_{i,\,j}E_{j}\left(t'\right)E_{i}\left(t''\right) \\ &= \left(\frac{ig\left(\omega_{0}\right)\mu^{2}}{4\hbar}\right)\int_{-\infty}^{t'}dt''e^{-(-i\omega_{0}+\gamma)(t'-t'')}\sum_{i,\,j}E_{j}\left(t'\right)E_{i}\left(t''\right) \end{aligned}$$

Taking the difference, we obtain

$$
\begin{aligned}
\left\{V_{12}\left(t'\right)\rho_{21}\left(t'\right)-V_{21}\left(t'\right)\rho_{12}\left(t'\right)\right\} &= \left(\frac{ig\left(\omega_0\right)\mu^2}{4\hbar}\right)\times \\
&\quad \left[-\int_{-\infty}^{t'}dt''e^{-(i\omega_0+\gamma)(t'-t'')}\sum_{i,\,j}E_j\left(t'\right)E_i\left(t''\right)\right] \\
&\quad +\left[-\int_{-\infty}^{t'}dt''e^{-(-i\omega_0+\gamma)(t'-t'')}\sum_{i,\,j}E_j\left(t'\right)E_i\left(t''\right)\right] \\
&= -\left(\frac{ig\left(\omega_0\right)\mu^2}{4\hbar}\right)\times \\
&\quad -\int_{-\infty}^{t'}dt''\left(e^{-(i\omega_0+\gamma)(t'-t'')}+e^{-(-i\omega_0+\gamma)(t'-t'')}\right) \\
&\quad \times\sum_{i,\,j}E_j\left(t'\right)E_i\left(t''\right) \\
&= -\left(\frac{ig\left(\omega_0\right)\mu^2}{4\hbar}\right)\int_{-\infty}^{t'}dt''e^{-\gamma(t'-t'')} \\
&\quad \times 2\cos\left(\omega_0\left(t'-t''\right)\right)\sum_{i,\,j}E_j\left(t'\right)E_i\left(t''\right)
\end{aligned}
$$

Substituting that expression into the population integral, we find

$$
\rho_{22}^{(2)}\left(t\right)=\frac{i}{\hbar}\int_{-\infty}^{t}dt'\left(V_{12}\left(t'\right)\rho_{21}^{(1)}\left(t'\right)-V_{21}\left(t'\right)\rho_{12}^{(1)}\left(t'\right)\right)e^{-\Gamma(t-t')}
$$

$$\begin{aligned}
\rho_{22}^{(2)}(t) &= \frac{i}{\hbar}\left(-\frac{i\mu^2 g(\omega_0)}{4\hbar}\right)\int_{-\infty}^{t} dt' e^{-\Gamma(t-t')} \times \\
&\quad \left\{\int_{-\infty}^{t'} dt'' e^{-\gamma(t'-t'')} 2\cos(\omega_0(t'-t''))\sum_{i,j} E_j(t') E_i(t'')\right\} \\
\rho_{22}^{(2)}(t) &= \left(\frac{\mu^2 g(\omega_0)}{4\hbar^2}\right) \times \\
&\quad \int_{-\infty}^{t} dt' \int_{-\infty}^{t'} dt'' e^{-\Gamma(t-t')} e^{-\gamma(t'-t'')} 2\cos(\omega_0(t'-t''))\sum_{i,j} E_j(t') E_i(t'')
\end{aligned}$$

The conservation of probability requires that $\rho_{22}+\rho_{11}=1$, from which $\rho_{22}-\rho_{11}=\rho_{22}-(1-\rho_{22})=2\rho_{22}-1$. Using this we may calculate the third order coherence without explicitly solving for the second order population of the lower level. We find

$$\begin{aligned}
\rho_{21} &= \int_{-\infty}^{t} dt' \frac{iV_{21}(t')}{\hbar}\left(\rho_{22}(t')-\rho_{11}(t')\right) e^{-(i\omega_0+\gamma)(t-t')} \quad \rightarrow \\
\rho_{21}^{(3)} &= \frac{i}{\hbar}\int_{-\infty}^{t} dt' V_{21}(t')\left(2\rho_{22}^{(2)}(t')-1\right) e^{-(i\omega_0+\gamma)(t-t')}, \\
\rho_{12}^{(3)} &= -\frac{i}{\hbar}\int_{-\infty}^{t'} dt' V_{12}(t')\left(2\rho_{22}^{*(2)}(t')-1\right) e^{-(-i\omega_0+\gamma)(t-t')}
\end{aligned}$$

and explicitly substituting for the second order density operator matrix element and the same interaction potential,

$$
\begin{aligned}
\rho_{21}^{(3)}(t) &= \frac{i}{\hbar}\int_{-\infty}^{t} dt' V_{21}(t')\left(2\rho_{22}^{(2)}(t')-1\right)e^{-(i\omega_0+\gamma)(t-t')} \\
&= \frac{i}{\hbar}\int_{-\infty}^{t} dt'\left(-\frac{\mu}{2}\sum_k E_k(t')\right)2\left(\frac{\mu^2 g(\omega_0)}{4\hbar^2}\right)e^{-(i\omega_0+\gamma)(t-t')}\times \\
&\quad\left(\left[\int_{-\infty}^{t'} dt''\int_{-\infty}^{t''} dt''' e^{-\Gamma(t'-t'')}e^{-\gamma(t''-t''')}2\cos(\omega_0(t''-t'''))\sum_{i,j}E_j(t'')E_i(t''')\right]-1\right) \\
&= \left(-\frac{i\mu^3 g(\omega_0)}{4\hbar^3}\right)\int_{-\infty}^{t} dt'\int_{-\infty}^{t'} dt''\int_{-\infty}^{t''} dt''' e^{-\Gamma(t'-t'')}e^{-(i\omega_0+\gamma)(t-t')}e^{-\gamma(t''-t''')} \\
&\quad\times 2\cos(\omega_0(t''-t'''))\sum_{i,j,k}E_k(t')E_j(t'')E_i(t''') \\
&\quad+\frac{i}{\hbar}\int_{-\infty}^{t} dt'\left(-\frac{\mu}{2}\sum_k E_k(t')\right)(-1)e^{-(i\omega_0+\gamma)(t-t')} \\
&= \left(-\frac{i\mu^3 g(\omega_0)}{2\hbar^3}\right)\int_{-\infty}^{t} dt'\int_{-\infty}^{t'} dt''\int_{-\infty}^{t''} dt'''\sum_{i,j,k}E_k(t')E_j(t'')E_i(t''')\times \\
&\quad e^{-\Gamma(t'-t'')}e^{-(i\omega_0+\gamma)(t-t')}e^{-\gamma(t''-t''')}\cos(\omega_0(t''-t''')) + \\
&\quad\frac{i\mu}{2\hbar}\int_{-\infty}^{t} dt'\sum_k E_k(t')e^{-(i\omega_0+\gamma)(t-t')}
\end{aligned}
$$

The first term contains the behaviour we are particularly interested in. We will selectively detect this particular term out of the total signal propagating in the pump direction by modulating each field independently. The second term results in a linear response that does not provide us much ability to study the underlying microscopic physics of the system – the only time interval appearing in the integrand is the difference between the experiment clock's real time t and the time t' at which the last pulse interacted with the material sample. As such, it will not be simple to separate the decay of

this linear polarization field into relaxation due to dephasing and relaxation due to population decay. Without synchronizing the detection to the moment of excitation t' – i.e., without performing a time-resolved rather than time-integrated experiment – we cannot extract much meaningful information from this term; by contrast, the first term depends upon several time intervals that we may scan in order to extract the relaxation parameters that characterize the dynamics of the system in this toy model. We note that (after the π phase shift that arises from inserting the polarization into Maxwell's equations as a source term) the linear term will result in an electric field with the opposite sign of the particular E_k field that gives rise to its emission; for this reason we interpret this effect as linear absorption of the incident laser pulses; naturally, the phase-matching condition for this term is coincident with the direction of propagation of each original pulse. The nonlinear polarization hand, alternatively, will possess the same sign as the product of the three electric fields, after the π phase shift; as such, we associate this term with a four-wave mixing emission.

This expression for the coherence term is already fairly complicated in appearance, but the full, expanded form where the electric field products are completely expanded, is even more intractable. The combination of wave vectors results in a number of different polarizations that must be considered in the context of what any given experiment will actually measure. We can go ahead and expand those terms and then try to pick out the terms of interest, but we can simplify that problem by applying certain choices that select out

only a few combinations of the electric fields.

We first choose a pulse sequence. We will make certain choices regarding pulse ordering based upon the parameters of interest we wish to extract and the experimental geometry available to us.

1.1 Pump-probe measurements

We first consider the simpler case where only two pulses interact with the sample, and consider a pump-probe experiment. We label the pump pulse (it can originate in either arm of the interferometer, q.v. *sub*) as E_2, and arrives at $t = 0$. We label the probe pulse E_1, and assume that it arrives at $t = T$. Physically, the pump pulse complex field interacts twice with the material sample (this is an unfortunate way to describe the actual optical physics, but it is nonetheless the commonly used jargon), creating a population that depends upon the pump intensity, $E_2^* E_2$. The probe pulse arrives subsequently, and scatters from the population created by the first pulse; physically, we expect the absorption of the probe pulse to be increased or decreased depending upon the interaction of the first pulse with the sample. Specifying this concrete pulse sequence simplifies our expression for the third order coherence, giving us

$$\sum_{i,\,j,\,k} E_k\left(t'\right) E_j\left(t''\right) E_i\left(t'''\right) \rightarrow E_1\left(t'\right) E_2\left(t''\right) E_2\left(t'''\right)$$

The obvious problem with this analysis is that when we perform a differential transmission (or differential reflectivity) pump-probe measurement,

we scan the probe pulse from a time preceding the pump pulse to some time long after the pump pulse has arrived – where long refers to the time scale of the relaxation processes in the system. Clearly, this simple analysis cannot replicate the complete temporal lineshape. In particular, the finite duration pulses will overlap significantly for some range of probe times T, during which window this analysis (which will assume Dirac delta function pulse envelope for analytical simplicity) will fail. Nonetheless, it will help us to understand the quantum mechanical pathways giving rise to the signals detected during the decay of the pump-probe signal, and will be useful when we consider the effect various modulation schemes (described in the chapter on our variable geometry, two- and three-frequency modulation schemes) have on selecting particular components from the probe beam.

We thus need to consider third order coherences that depend on the product

$$\left(\widetilde{E}_1(t') + \widetilde{E}_1^*(t')\right)\left(\widetilde{E}_2(t'') + \widetilde{E}_2^*(t'')\right)\left(\widetilde{E}_2(t''') + \widetilde{E}_2^*(t''')\right)$$

in the expression for $\rho_{21}^{(3)}(t)$. Expanded, this yields

$$\begin{aligned}\widetilde{E}_1(t')\,\widetilde{E}_2(t'')\,\widetilde{E}_2(t''') + \widetilde{E}_1(t')\,\widetilde{E}_2(t'')\,\widetilde{E}_2^*(t''') + \widetilde{E}_1(t')\,\widetilde{E}_2^*(t'')\,\widetilde{E}_2(t''') + \\ \widetilde{E}_1(t')\,\widetilde{E}_2^*(t'')\,\widetilde{E}_2^*(t''') + \widetilde{E}_1^*(t')\,\widetilde{E}_2(t'')\,\widetilde{E}_2(t''') + \widetilde{E}_1^*(t')\,\widetilde{E}_2(t'')\,\widetilde{E}_2^*(t''') + \\ \widetilde{E}_1^*(t')\,\widetilde{E}_2^*(t'')\,\widetilde{E}_2(t''') + \widetilde{E}_1^*(t')\,\widetilde{E}_2^*(t'')\,\widetilde{E}_2^*(t''')\end{aligned}$$

We collect emission in the direction that the probe beam propagates, i.e. we only look for terms that obey a wave equation where the solution's argument is given in the form $(\mathbf{k_1} \cdot \mathbf{r} - \omega t)$. Thus, we look for terms that exhibit an functional dependence of $e^{i(\mathbf{k_1} \cdot \mathbf{r} - \omega t)}$ or $e^{-i(\mathbf{k_1} \cdot \mathbf{r} - \omega t)}$.

If we approximate the pulses used in the experiment as delta functions, the integrals for the density matrix elements are analytically solvable. We use

$$\begin{aligned} E_1(t') &= A_1 \delta(t' - T)\left(e^{i(\mathbf{k}_1 \cdot \mathbf{r} - \Omega_1 t')} + e^{-i(\mathbf{k}_1 \cdot \mathbf{r} - \Omega_1 t')}\right) \\ E_2(t'') &= A_2 \delta(t'')\left(e^{i(\mathbf{k}_2 \cdot \mathbf{r} - \Omega_2 t'')} + e^{-i(\mathbf{k}_2 \cdot \mathbf{r} - \Omega_2 t'')}\right) \\ E_2(t''') &= A_2 \delta(t''')\left(e^{i(\mathbf{k}_2 \cdot \mathbf{r} - \Omega_2 t''')} + e^{-i(\mathbf{k}_2 \cdot \mathbf{r} - \Omega_2 t''')}\right) \end{aligned}$$

where, if we use our notation for complex fields, where $E = \widetilde{E} + \widetilde{E}^*$, we may write the field terms and their conjugates as, for example,

$$\begin{aligned} \widetilde{E}_1(t') &= A_1 \delta(t' - T) e^{i(\mathbf{k}_1 \cdot \mathbf{r} - \Omega_1 t')} \\ \widetilde{E}_1^*(t') &= A_1 \delta(t' - T) e^{-i(\mathbf{k}_1 \cdot \mathbf{r} - \Omega_1 t')} \end{aligned}$$

We consider the coherence term depending on the $\widetilde{E}_1(t')\,\widetilde{E}_2(t'')\,\widetilde{E}_2(t''')$ field combination first as an illustration of the phase-matching geometry. We omit the linear absorption term identified previously, and concentrate on the nonlinear response, obtaining

$$\begin{aligned}\rho_{21}^{(3)} \propto & \int dt'dt''dt'''A_1A_2A_2\delta\left(t'-T\right)\delta\left(t''\right)\delta\left(t'''\right)e^{i(\mathbf{k}_1\cdot\mathbf{r}-\Omega_1 t')}e^{i(\mathbf{k}_2\cdot\mathbf{r}-\Omega_2 t'')}e^{i(\mathbf{k}_2\cdot\mathbf{r}-\Omega_2 t''')} \\ & \times e^{-\Gamma(t'-t'')}e^{-(i\omega_0+\gamma)(t-t')}\left(e^{-(i\omega_0+\gamma)(t''-t''')}+e^{-(-i\omega_0+\gamma)(t''-t''')}\right)\end{aligned}$$

Using the Dirac delta functions to spike the integrals, we find

$$\begin{aligned}\rho_{21}^{(3)}\left(t\right) &\propto A_1A_2A_2e^{i(\mathbf{k}_1\cdot\mathbf{r}-\Omega_1 T)}e^{i(\mathbf{k}_2\cdot\mathbf{r})}e^{i(\mathbf{k}_2\cdot\mathbf{r})}e^{-\Gamma(T)}e^{-(i\omega_0+\gamma)(t-T)} \\ &\quad\times\left(e^{-(i\omega_0+\gamma)(0)}+e^{-(-i\omega_0+\gamma)(0)}\right) \\ \rho_{21}^{(3)}\left(t\right) &\propto A_1A_2A_3\left\{e^{i[(\mathbf{k}_1+\mathbf{k}_2+\mathbf{k}_2)\cdot\mathbf{r}-\Omega_1 T]}\right\}e^{-\Gamma T}e^{-(i\omega_0+\gamma)(t-T)} \quad (2) \\ \rho_{21}^{(3)}\left(t\right) &\propto e^{i[(\mathbf{k}_1+\mathbf{2k}_2)\cdot\mathbf{r}-\omega_0 t]}\end{aligned}$$

from which we see that this combination of complex field components ($\widetilde{E}_1\left(t'\right)\widetilde{E}_2\left(t''\right)\widetilde{E}_2\left(t'''\right)$) would result in emission that propagates in a different direction than that along which we collect the probe beam. Hence, the $\widetilde{E}_1\left(t'\right)\widetilde{E}_2\left(t''\right)\widetilde{E}_2\left(t'''\right)$ coherence does not lead to any contribution to a detectable signal. By contrast, the $\widetilde{E}_1\left(t'\right)\widetilde{E}_2\left(t''\right)\widetilde{E}_2^*\left(t'''\right)$ complex field combination will result in a coherence that maybe similarly calculated, yielding

$$\begin{aligned}\rho_{21}^{(3)}\left(t\right) &\propto A_1A_2A_2^*e^{i(\mathbf{k}_1\cdot\mathbf{r}-\Omega_1 T)}e^{i(\mathbf{k}_2\cdot\mathbf{r})}e^{-i(\mathbf{k}_2\cdot\mathbf{r})}e^{-\Gamma(T)}e^{-(i\omega_0+\gamma)(t-T)} \\ &\quad\times\left(e^{-(i\omega_0+\gamma)(0)}+e^{-(-i\omega_0+\gamma)(0)}\right) \\ \rho_{21}^{(3)}\left(t\right) &\propto A_1A_2A_2\left\{e^{i[(\mathbf{k}_1)\cdot\mathbf{r}-\Omega_1 T]}\right\}e^{-\Gamma T}e^{-(i\omega_0+\gamma)(t-T)} \quad (2) \\ \rho_{21}^{(3)}\left(t\right) &\propto e^{i[\mathbf{k}_1\cdot\mathbf{r}-\omega_0 t]}\end{aligned}$$

which does satisfy the appropriate wave equation, and thus results in a signal that is directed along the probe propagation direction. We can see that the terms that will contribute to this signal require opposite signs for the arguments of the exponential functions depending on $\mathbf{k}_2$. Thus, we expect to see a contribution from the $\widetilde{E}_1(t')\,\widetilde{E}_2^*(t'')\,\widetilde{E}_2(t''')$ field combination, *viz.*

$$\begin{aligned}
\rho_{21}^{(3)}(t) &\propto A_1 A_2^* A_2 e^{i(\mathbf{k}_1\cdot\mathbf{r}-\Omega_1 T)} e^{-i(\mathbf{k}_2\cdot\mathbf{r})} e^{i(\mathbf{k}_2\cdot\mathbf{r})} e^{-\Gamma(T)} e^{-(i\omega_0+\gamma)(t-T)} \\
&\quad \times \left(e^{-(i\omega_0+\gamma)(0)} + e^{-(-i\omega_0+\gamma)(0)}\right) \\
\rho_{21}^{(3)}(t) &\propto A_1 A_2 A_2 \left\{e^{i[(\mathbf{k}_1)\cdot\mathbf{r}-\Omega_1 T]}\right\} e^{-\Gamma T} e^{-(i\omega_0+\gamma)(t-T)} \quad (2) \\
\rho_{21}^{(3)}(t) &\propto e^{i[\mathbf{k}_1\cdot\mathbf{r}-\omega_0 t]}
\end{aligned}$$

but not for the $\widetilde{E}_1(t')\,\widetilde{E}_2^*(t'')\,\widetilde{E}_2^*(t''')$ field combination, which yields

$$\begin{aligned}
\rho_{21}^{(3)}(t) &\propto A_1 A_2^* A_2^* e^{i(\mathbf{k}_1\cdot\mathbf{r}-\Omega_1 T)} e^{-i(\mathbf{k}_2\cdot\mathbf{r})} e^{-i(\mathbf{k}_2\cdot\mathbf{r})} e^{-\Gamma(T)} e^{-(i\omega_0+\gamma)(t-T)} \\
&\quad \times \left(e^{-(i\omega_0+\gamma)(0)} + e^{-(-i\omega_0+\gamma)(0)}\right) \\
\rho_{21}^{(3)}(t) &\propto A_1 A_2 A_3 \left\{e^{i[(\mathbf{k}_1-2\mathbf{k}_2)\cdot\mathbf{r}-\Omega_1 T]}\right\} e^{-\Gamma T} e^{-(i\omega_0+\gamma)(t-T)} \quad (2) \\
\rho_{21}^{(3)}(t) &\propto e^{i[(\mathbf{k}_1-2\mathbf{k}_2)\cdot\mathbf{r}-\omega_0 t]}
\end{aligned}$$

and again, cannot lead to emission along the phase-matched direction we are using. We also consider the contributions from field combinations where the probe pulse appears as the conjugate complex field term. For $\widetilde{E}_1^*(t')\,\widetilde{E}_2(t'')\,\widetilde{E}_2(t''')$ we find

$$\begin{aligned}
\rho_{21}^{(3)} &\propto \int dt' \int dt'' \int dt''' A_1^* A_2 A_2 \delta\left(t'-T\right)\delta\left(t''\right)\delta\left(t'''\right) e^{-i(\mathbf{k}_1\cdot\mathbf{r}-\Omega_1 t')} e^{i(\mathbf{k}_2\cdot\mathbf{r}-\Omega_2 t'')} e^{i(\mathbf{k}_2\cdot\mathbf{r}-\Omega_2 t''')} \\
&\quad \times e^{-\Gamma(t'-t'')} e^{-(i\omega_0+\gamma)(t-t')}\left(e^{-(i\omega_0+\gamma)(t''-t''')}+e^{-(-i\omega_0+\gamma)(t''-t''')}\right) \\
&\propto A_1^* A_2 A_2 e^{-i(\mathbf{k}_1\cdot\mathbf{r}-\Omega_1 T)} e^{i(\mathbf{k}_2\cdot\mathbf{r})} e^{(\mathbf{k}_2\cdot\mathbf{r})} e^{-\Gamma(T)} e^{-(i\omega_0+\gamma)(t-T)}\left(e^{-(i\omega_0+\gamma)(0)}+e^{-(-i\omega_0+\gamma)(0)}\right) \\
&\propto A_1^* A_2 A_3 \left\{e^{i[(-\mathbf{k}_1+2\mathbf{k}_2)\cdot\mathbf{r}+\Omega_1 T]}\right\} e^{-\Gamma T} e^{-(i\omega_0+\gamma)(t-T)}\,(2) \\
&\propto e^{-i[(\mathbf{k}_1-2\mathbf{k}_2)\cdot\mathbf{r}+\omega t]}
\end{aligned}$$

similarly, we again find that we do not see emission in the right direction when the two E_2 terms have the same sign exponent. Accounting for this, we consider the coherence term depending n the field product $\widetilde{E}_1^*\left(t'\right)\widetilde{E}_2\left(t''\right)\widetilde{E}_2^*\left(t'''\right)$ and find

$$\begin{aligned}
\rho_{21}^{(3)} &\propto A_1^* A_2 A_2 e^{-i(\mathbf{k}_1\cdot\mathbf{r}-\Omega_1 T)} e^{i(\mathbf{k}_2\cdot\mathbf{r})} e^{-(\mathbf{k}_2\cdot\mathbf{r})} e^{-\Gamma(T)} e^{-(i\omega_0+\gamma)(t-T)}\left(e^{-(i\omega_0+\gamma)(0)}+e^{-(-i\omega_0+\gamma)(0)}\right) \\
&\propto A_1^* A_2 A_3 \left\{e^{i[(-\mathbf{k}_1)\cdot\mathbf{r}+\Omega_1 T]}\right\} e^{-\Gamma T} e^{-(i\omega_0+\gamma)(t-T)}\,(2) \\
&\propto e^{-i[\mathbf{k}_1\cdot\mathbf{r}+\omega t]}
\end{aligned}$$

which is a solution of the wave-equation, but one that represents backwards propagation along the direction of the probe beam. As such, it does not contribute to the polarization that results in phase-matched emission along our selected vector.

Thus, the coherences that need to be considered are, for this two pulse experiment with specified pulse temporal ordering, given by

$$\rho_{21}^{(3)} \propto \propto \widetilde{E}_1(t')\,\widetilde{E}_2(t'')\,\widetilde{E}_2^*(t''') \propto e^{i[\mathbf{k}_1\cdot\mathbf{r}-\omega_0 t]}$$
$$\rho_{21}^{(3)} \propto \propto \widetilde{E}_1(t')\,\widetilde{E}_2^*(t'')\,\widetilde{E}_2(t''') \propto e^{i[\mathbf{k}_1\cdot\mathbf{r}-\omega_0 t]}$$

and, the Hermitian conjugate terms

$$\rho_{12}^{(3)} \propto \propto \widetilde{E}_1^*(t')\,\widetilde{E}_2^*(t'')\,\widetilde{E}_2(t''') \propto e^{-i[\mathbf{k}_1\cdot\mathbf{r}-\omega_0 t]}$$
$$\rho_{12}^{(3)} \propto \propto \widetilde{E}_1^*(t')\,\widetilde{E}_2(t'')\,\widetilde{E}_2^*(t''') \propto e^{-i[\mathbf{k}_1\cdot\mathbf{r}-\omega_0 t]}$$

As we have noted previously, the expectation value for the dipole operator $\hat{\mu}$ (related to the macroscopic polarization $\mathbf{P}$ via $\mathbf{P} = N\langle\hat{\mu}\rangle$) may be found by taking the trace of the product of the density operator and the dipole operator

$$\langle\mu\rangle = Tr\{\hat{\rho}\hat{\mu}\} = Tr\left\{\begin{pmatrix}\rho_{11} & \rho_{12}\\ \rho_{21} & \rho_{22}\end{pmatrix}\begin{pmatrix}0 & \mu\\ \mu & 0\end{pmatrix}\right\} = \mu\{\rho_{12}+\rho_{21}\}$$

For the pump-probe measurements here, under the stated assumptions, and omitting those terms that are linear in the applied optical fields or which do not contribute to a signal that may be detected along the probe direction, we find

$$
\begin{aligned}
\rho_{21}^{(3)} &= \left(-\frac{i\mu^3 g\left(\omega_0\right)}{2\hbar^3}\right)\int_{-\infty}^{t} dt' \int_{-\infty}^{t'} dt'' \int_{-\infty}^{t''} dt''' \widetilde{E}_1\left(t'\right)\widetilde{E}_2\left(t''\right)\widetilde{E}_2^*\left(t'''\right) \\
&\quad \times e^{-\Gamma(t'-t'')} e^{-(i\omega_0+\gamma)(t-t')} e^{-\gamma(t''-t''')} \cos\left(\omega_0\left(t''-t'''\right)\right) \\
&+ \left(-\frac{i\mu^3 g\left(\omega_0\right)}{2\hbar^3}\right)\int_{-\infty}^{t} dt' \int_{-\infty}^{t'} dt'' \int_{-\infty}^{t''} dt''' \widetilde{E}_1\left(t'\right)\widetilde{E}_2^*\left(t''\right)\widetilde{E}_2\left(t'''\right) \\
&\quad \times e^{-\Gamma(t'-t'')} e^{-(i\omega_0+\gamma)(t-t')} e^{-\gamma(t''-t''')} \cos\left(\omega_0\left(t''-t'''\right)\right) \\
&= \left(-\frac{i\mu^3 g\left(\omega_0\right)}{2\hbar^3}\right) A_1 A_2 A_2^* e^{i(\mathbf{k}_1\cdot\mathbf{r}-\Omega_1 T)} e^{i(\mathbf{k}_2\cdot\mathbf{r})} e^{-i(\mathbf{k}_2\cdot\mathbf{r})} \\
&\quad \times e^{-\Gamma(T)} e^{-(i\omega_0+\gamma)(t-T)} e^{-\gamma(0)} \cos\left(\omega_0\left(0\right)\right) + \\
&+ \left(-\frac{i\mu^3 g\left(\omega_0\right)}{2\hbar^3}\right) A_1 A_2^* A_2 e^{i(\mathbf{k}_1\cdot\mathbf{r}-\Omega_1 T)} e^{-i(\mathbf{k}_2\cdot\mathbf{r})} e^{i(\mathbf{k}_2\cdot\mathbf{r})} \\
&\quad \times e^{-\Gamma(T)} e^{-(i\omega_0+\gamma)(t-T)} e^{-\gamma(0)} \cos\left(\omega_0\left(0\right)\right) \\
&= \left(-\frac{i\mu^3 g\left(\omega_0\right)}{\hbar^3}\right) A_1 A_2 A_2^* e^{i(\mathbf{k}_1\cdot\mathbf{r}-\Omega_1 T)} e^{-\Gamma T} e^{-(i\omega_0+\gamma)(t-T)} \\
&= \left(-\frac{i\mu^3 g\left(\omega_0\right)}{\hbar^3}\right) A_1 A_2 A_2^* e^{i(\mathbf{k}_1\cdot\mathbf{r}-\omega_0 t)} e^{-\Gamma T} e^{-\gamma(t-T)} e^{-i(\Omega_1 T-\omega_0 T)}
\end{aligned}
$$

and, correspondingly,

$$
\rho_{12}^{(3)} = \left(\frac{i\mu^3 g\left(\omega_0\right)}{\hbar^3}\right) A_1^* A_2^* A_2 e^{-i(\mathbf{k}_1\cdot\mathbf{r}-\omega_0 t)} e^{-\Gamma T} e^{-\gamma(t-T)} e^{i(\Omega_1 T-\omega_0 T)}
$$

If we take the electric field strength to be real, we can set $A_i^* = A_i$ and simplify the sum of these coherence terms,

$$
\left\{\rho_{12}+\rho_{21}\right\} = \left(\frac{i\mu^3 g\left(\omega_0\right)}{\hbar^3}\right) A_1 A_2 A_2 e^{-\Gamma T} e^{-\gamma(t-T)} \left\{e^{-i(\mathbf{k}_1\cdot\mathbf{r}-\omega_0 t-\psi)} - e^{i(\mathbf{k}_1\cdot\mathbf{r}-\omega_0 t-\psi)}\right\}
$$

where the phase $\psi = (\Omega_1 T - \omega_0 T)$. Thus,

$$\begin{aligned}\mathbf{P} &= N\langle\hat{\mu}\rangle \\ &= N\left(\frac{i\mu^4 g(\omega_0)}{\hbar^3}\right) A_1 A_2 A_2 e^{-\Gamma T} e^{-\gamma(t-T)} \left\{e^{-i(\mathbf{k}_1\cdot\mathbf{r}-\omega_0 t-\psi)} - e^{i(\mathbf{k}_1\cdot\mathbf{r}-\omega_0 t-\psi)}\right\}\end{aligned}$$

and the emission along the probe direction due to the nonlinear polarization is given by

$$E_{sig} = -N\left(\frac{\mu^4 g(\omega_0)}{\hbar^3}\right) A_1 A_2 A_2 e^{-\Gamma T} e^{-\gamma(t-T)} \left\{e^{-i(\mathbf{k}_1\cdot\mathbf{r}-\omega_0 t-\psi)} - e^{i(\mathbf{k}_1\cdot\mathbf{r}-\omega_0 t-\psi)}\right\}$$

Although we have played somewhat fast and loose with the field conjugation values, we recognize that the product $A_2 A_2$ here corresponds to the pump intensity, while the interaction with the probe field A_1 is linear, rather than quadratic in the electric field. If we are more careful with the conjugation terms, we can write a somewhat longer expression for the electric field that will allow us to split the dependence of the signal field up with respect to the two different complex electric fields. Within a few factors of two, that should take a functional form given by

$$\begin{aligned}E_{sig} &= -N\left(\frac{\mu^4 g(\omega_0)}{\hbar^3}\right) A_2^* A_2 e^{-\Gamma T} e^{-\gamma(t-T)} \left\{A_1^* e^{-i(\mathbf{k}_1\cdot\mathbf{r}-\omega_0 t-\psi)} - A_1 e^{i(\mathbf{k}_1\cdot\mathbf{r}-\omega_0 t-\psi)}\right\} \\ &= \eta\,|A_2|^2 \left\{A_1^* e^{-i(\mathbf{k}_1\cdot\mathbf{r}-\omega_0 t-\psi)} - A_1 e^{i(\mathbf{k}_1\cdot\mathbf{r}-\omega_0 t-\psi)}\right\}\end{aligned}$$

$$\begin{aligned} E_{sig}(t) &= \eta' |E_{pu}(t)|^2 E_{pr}(t + \psi/\omega_0 + \pi/2\omega_0) \\ &= \eta' |E_{pu}(t)|^2 E_{pr}(t + \psi') \end{aligned}$$

We note that the electric field due to the nonlinear interaction in this system is therefore proportional to the intensity of the pump beam, but only to the electric field of the probe, i.e., it is bilinear in the electric field for one of the optical interactions but not the other.

We can write a simple expression for the total field that propagates along the probe direction if we assume that the probe intensity is not substantially affected by the nonlinear optical process; this is sometimes referred to as an un-depleted probe assumption. In that case, we may write the intensity of this beam as

$$\begin{aligned} |E_{pr} + E_{sig}|^2 &= \left(E_{pr} + \eta' |E_{pu}(t)|^2 E_{pr}(t + \psi')\right)\left(E_{pr}^* + \eta' |E_{pu}(t)|^2 E_{pr}^*(t + \psi')\right) \\ &= |E_{pr}|^2 + \eta' |E_{pu}(t)|^2 E_{pr} E_{pr}^*(t + \psi') + \eta' |E_{pu}(t)|^2 E_{pr}^* E_{pr}(t + \psi') \\ &\quad + \eta' |E_{pu}(t)|^2 E_{pr}(t + \psi') \eta' |E_{pu}(t)|^2 E_{pr}^*(t + \psi') \\ &= |E_{pr}|^2 + \eta' |E_{pu}(t)|^2 \left(E_{pr}(t) E_{pr}^*(t + \psi') + E_{pr}^*(t) E_{pr}(t + \psi')\right) \\ &\quad + \eta'^2 |E_{pu}(t)|^4 |E_{pr}(t + \psi')|^2 \end{aligned}$$

Of course, electronic detectors are not available to measure the instantaneous electric field at optical frequencies. Instead, a slow square law detector

is used that will integrate over many pulses. Only a mean intensity is extracted in such a measurement. We may directly associate the three different terms in this expression – proportional to the instantaneous intensity – with average intensity components:

$$\langle I_{pr+sig} \rangle = \langle I_{pr} \rangle + \langle I_{heterodyne} \rangle + \langle I_{homodyne} \rangle$$

Typically, the homodyne term is preferred, since it will be much stronger than the weak homodyne signal due to the additional factor of η' present in the homodyne term. We spend some time in these experiments considering the effect of different modulation schemes on the detection of different signal components present in a field such as this, so we turn some attention to that in our chapter on the novel experimental techniques we developed using multi-frequency acousto-optic modulation and detection.

1.2 Four-wave mixing measurements

Once again, we consider the third-order coherences in order to understand the four-wave mixing processes in these systems. We previously found

$$\begin{aligned} \rho_{21}^{(3)} &= \left(-\frac{i\mu^3 g(\omega_0)}{2\hbar^3} \right) \int_{-\infty}^{t} dt' \int_{-\infty}^{t'} dt'' \int_{-\infty}^{t''} dt''' \sum_{i,j,k} E_k(t') E_j(t'') E_i(t''') \\ &\quad \times e^{-\Gamma(t'-t'')} e^{-(i\omega_0+\gamma)(t-t')} e^{-\gamma(t''-t''')} \cos(\omega_0 (t''-t''')) \\ &\quad + \frac{i\mu}{2\hbar} \int_{-\infty}^{t} dt' \sum_{k} E_k(t') e^{-(i\omega_0+\gamma)(t-t')} \end{aligned}$$

using an interactive perturbative technique. Using only two pulses, as in the pump-probe measurement outlined above, restricts the amount of information that can be extracted from this system, but with a third pulse the observed nonlinear response can be used to determine far more information about the microscopic processes involved in the system dynamics.

We are interested in the dephasing rate in particular, for a coherent emission along the phase matched direction determined in the partially collinear geometry. Our experimental apparatus provides two collinear pump pulses, one of which may be scanned in time, which we label the dynamic pump pulse. The fixed pump is labeled the static pump. The non-collinear pulse is labeled the probe pulse, since in 2dFTS experiments where we spectrally resolve one of the pulses we use lower power in the probe beam to avoid saturating the CCD detector. The pulse sequence we intend to use may be illustrated thus:

{pulse seq figure}

The dp pulse arrives first, at time $t = -\tau$. We label the dynamic pump pulse as E_3. The fixed static pump pulse, labeled E_2, arrives at $t = 0$. The probe pulse arrives at $t = T$ and is labeled E_1. Physically, the electric field E_3 couples to the material system and creates a coherence. Subsequently, E_2 arrives before significant dephasing occurs and creates a population grating. The last pulse, E_1 results in a coherence that we analyze in connection with the emission arising from its associated polarization. This allows us to simplify the pulse ordering, in that we only need to consider one time-sequence of pulses

$$\sum_{i,\,j,\,k} E_k\left(t'\right) E_j\left(t''\right) E_i\left(t'''\right) \rightarrow E_1\left(t'\right) E_2\left(t''\right) E_3\left(t'''\right)$$

We note here the obvious problems that arise when the pulses overlap in time. The analysis used here to study the effects of the pulse interactions clearly breaks down at least to some extent during those periods when the pulses are not temporally separated. Regardless, the behaviour of the polarization that occurs when the pulses are separated can be suitably modeled using this framework.

What possible terms need to be considered? The electric field term in the first term in our expression for $\rho_{21}^{(3)}\left(t\right)$ depends on the expansion of

$$\left(\widetilde{E}_1\left(t'\right)+\widetilde{E}_1^*\left(t'\right)\right)\left(\widetilde{E}_2\left(t''\right)+\widetilde{E}_2^*\left(t''\right)\right)\left(\widetilde{E}_3\left(t'''\right)+\widetilde{E}_3^*\left(t'''\right)\right)$$

which yields

$$\widetilde{E}_1\widetilde{E}_2\widetilde{E}_3+\widetilde{E}_1\widetilde{E}_2\widetilde{E}_3^*+\widetilde{E}_1\widetilde{E}_2^*\widetilde{E}_3+\widetilde{E}_1\widetilde{E}_2^*\widetilde{E}_3^*+\widetilde{E}_1^*\widetilde{E}_2\widetilde{E}_3+\widetilde{E}_1^*\widetilde{E}_2\widetilde{E}_3^*+\widetilde{E}_1^*\widetilde{E}_2^*\widetilde{E}_3+\widetilde{E}_1^*\widetilde{E}_2^*\widetilde{E}_3^*$$

where for brevity we have omitted the time arguments of the electric field terms, since these field terms have already been determined to always depend on only one particular time variable – $\widetilde{E}_1$ on t', $\widetilde{E}_2$ on t'', and $\widetilde{E}_3$ on t''', and similarly for the conjugate field terms. We consider the coherence term that gives rise to a macroscopic polarization that leads to emission in a

specific direction. In the partially collinear geometry, we collect the= probe beam and the four-wave mixing signal emitted collinearly with it; thus we consider coherences that describe solutions to the wave equation that have an argument given by $(\mathbf{k_1} \cdot \mathbf{r} - \omega t)$. Given the assumption of harmonic electrical fields, we thus expect to find solutions with the functional form $e^{i(\mathbf{k}\cdot\mathbf{r}-\Omega t)}$ or $e^{-i(\mathbf{k}\cdot\mathbf{r}-\Omega t)}$, describing motion along some wave vector $\mathbf{k}$, where $\mathbf{k}$ is parallel to the probe wave vector $\mathbf{k}_1$. To obtain solutions that propagate in the 'forward' direction, i.e. moving in the same direction as the probe pulse instead of in the opposite direction, we need to ensure that the sign relationship between the dot-product and the frequency-time product is negative. This selects forward-propagating four-wave mixing signals.

If we approximate the pulses used in the experiment as delta functions, the integrals for the density matrix elements are analytically solvable. We write the electric fields for the three pulses as

$$\begin{aligned} E_1(t') &= A_1\delta(t'-T)\left(e^{i(\mathbf{k}_1\cdot\mathbf{r}-\Omega_1 t')}+e^{-i(\mathbf{k}_1\cdot\mathbf{r}-\Omega_1 t')}\right) \\ E_2(t'') &= A_2\delta(t'')\left(e^{i(\mathbf{k}_2\cdot\mathbf{r}-\Omega_2 t'')}+e^{-i(\mathbf{k}_2\cdot\mathbf{r}-\Omega_2 t'')}\right) \\ E_3(t''') &= A_1\delta(t'''+\tau)\left(e^{i(\mathbf{k}_3\cdot\mathbf{r}-\Omega_3 t''')}+e^{-i(\mathbf{k}_3\cdot\mathbf{r}-\Omega_3 t''')}\right) \end{aligned}$$

Again making use of our notation for complex fields, where $E = \widetilde{E}+\widetilde{E}^*$, we can write the field terms and their conjugates as, for example,

$$\begin{aligned}
\widetilde{E}_1(t') &= A_1\delta(t'-T)\,e^{i(\mathbf{k}_1\cdot\mathbf{r}-\Omega_1 t')} \\
\widetilde{E}_1^*(t') &= A_1\delta(t'-T)\,e^{-i(\mathbf{k}_1\cdot\mathbf{r}-\Omega_1 t')}
\end{aligned}$$

Consider, then, the $\rho_{21}^{(3)}$ terms. First, we solve for the $\widetilde{E}_1\widetilde{E}_2\widetilde{E}_3$ coherence,

$$\begin{aligned}
\rho_{21}^{(3)} \propto & \int dt'dt''dt'''A_1A_2A_3\delta(t'-T)\,\delta(t'')\,\delta(t'''+\tau)\,e^{i(\mathbf{k}_1\cdot\mathbf{r}-\Omega_1 t')}e^{i(\mathbf{k}_2\cdot\mathbf{r}-\Omega_2 t'')}e^{i(\mathbf{k}_3\cdot\mathbf{r}-\Omega_3 t''')} \\
& \times e^{-\Gamma(t'-t'')}e^{-(i\omega_0+\gamma)(t-t')}\left(e^{-(i\omega_0+\gamma)(t''-t''')}+e^{-(-i\omega_0+\gamma)(t''-t''')}\right)
\end{aligned}$$

where we have dropped the second term in the coherence, since it depends only on one electric field, and will be rejected by our modulation-detection scheme. Using the Dirac delta functions to spike the integrals, we find

$$\begin{aligned}
\rho_{21}^{(3)}(t) &\propto A_1A_2A_3e^{i(\mathbf{k}_1\cdot\mathbf{r}-\Omega_1 T)}e^{i(\mathbf{k}_2\cdot\mathbf{r})}e^{i(\mathbf{k}_3\cdot\mathbf{r}-\Omega_3(-\tau))}e^{-\Gamma(T)}e^{-(i\omega_0+\gamma)(t-T)} \\
&\quad\times\left(e^{-(i\omega_0+\gamma)(-(-\tau))}+e^{-(-i\omega_0+\gamma)(-(-\tau))}\right) \\
\rho_{21}^{(3)}(t) &\propto A_1A_2A_3\left\{e^{i[(\mathbf{k}_1+\mathbf{k}_2+\mathbf{k}_3)\cdot\mathbf{r}-\Omega_1 T+\Omega_3\tau]}\right\}e^{-\Gamma T}e^{-(i\omega_0+\gamma)(t-T)} \\
&\quad\times\left(e^{-(i\omega_0+\gamma)\tau}+e^{-(-i\omega_0+\gamma)\tau}\right) \\
\rho_{21}^{(3)}(t) &\propto e^{i[(\mathbf{k}_1+\mathbf{k}_2+\mathbf{k}_3)\cdot\mathbf{r}-\omega_0 t]}
\end{aligned}$$

This would lead to terms that propagate in the wrong direction to be detected along the direction of the probe beam. Thus, the $\widetilde{E}_1\widetilde{E}_2\widetilde{E}_3$ coherence does not lead to a detectable signal. We next consider the $\widetilde{E}_1\widetilde{E}_2\widetilde{E}_3^*$ coherence:

$$\begin{aligned}\rho_{21}^{(3)} \propto & \int dt'dt''dt'''A_1A_2A_3\delta\left(t'-T\right)\delta\left(t''\right)\delta\left(t'''+\tau\right)e^{i(\mathbf{k}_1\cdot\mathbf{r}-\Omega_1t')}e^{i(\mathbf{k}_2\cdot\mathbf{r}-\Omega_2t'')}e^{-i(\mathbf{k}_3\cdot\mathbf{r}-\Omega_3t''')} \\ & \times e^{-\Gamma(t'-t'')}e^{-(i\omega_0+\gamma)(t-t')}\left(e^{-(i\omega_0+\gamma)(t''-t''')}+e^{-(-i\omega_0+\gamma)(t''-t''')}\right)\end{aligned}$$

which simplifies to

$$\begin{aligned}\rho_{21}^{(3)} \propto & A_1A_2A_3e^{i(\mathbf{k}_1\cdot\mathbf{r}-\Omega_1T)}e^{i(\mathbf{k}_2\cdot\mathbf{r})}e^{-i(\mathbf{k}_3\cdot\mathbf{r}-\Omega_3(-\tau))} \\ & \times e^{-\Gamma(T)}e^{-(i\omega_0+\gamma)(t-T)}\left(e^{-(i\omega_0+\gamma)(-(-\tau))}+e^{-(-i\omega_0+\gamma)(-(-\tau))}\right) \\ \rho_{21}^{(3)} \propto & A_1A_2A_3\left\{e^{i[(\mathbf{k}_1+\mathbf{k}_2-\mathbf{k}_3)\cdot\mathbf{r}-\Omega_1T-\Omega_3\tau]}\right\} \\ & \times e^{-\Gamma T}e^{-(i\omega_0+\gamma)(t-T)}\left(e^{-(i\omega_0+\gamma)\tau}+e^{-(-i\omega_0+\gamma)\tau}\right) \\ \rho_{21}^{(3)} \propto & e^{i[(\mathbf{k}_1+\mathbf{k}_2-\mathbf{k}_3)\cdot\mathbf{r}-\omega_0T]}\end{aligned}$$

In our experiment the dynamic pump and static pump pulses are collinear and (nearly) degenerate, and thus have identical wavevectors. As a result, the $\mathbf{k}_2$ and $\mathbf{k}_3$ dependence of the exponential function drop out, and the coherence for the $\widetilde{E}_1\widetilde{E}_2\widetilde{E}_3^*$ field product will propagate parallel to the probe wave vector; explicitly,

$$\rho_{21}^{(3)} \propto e^{i[\mathbf{k}_1\cdot\mathbf{r}-\omega_0T]}$$

We must therefore keep track of this coherence term in our model for the polarization emission detected along with the probe pulse.

We turn our attention now to the $\widetilde{E}_1\widetilde{E}_2^*\widetilde{E}_3$ coherence. Other than breaking time symmetry between the dynamic pump and static pump pulses, this coherence is expected to lead to a similar result as the previous $\widetilde{E}_1\widetilde{E}_2\widetilde{E}_3^*$ coherence we calculated due to the otherwise interchangeable nature of the electric fields corresponding to dp and sp (of course in actual experiments where we may control, for example, the polarizations of these two fields – we have neglected the vectorial nature of the electric field for the time, which means the picture developed here cannot really accurately describe the optical physics we're studying, which would properly require us to introduce different effective dipole matrix elements. We reiterate that this calculation is only intended to provide an intuitive tool for understanding the typical behaviour of this system, rather than be used as a rigorous model for analyzing our results). We therefore intuitively expect that the $\widetilde{E}_1\widetilde{E}_2^*\widetilde{E}_3$ coherence will exhibit a similar behaviour:

$$\begin{aligned}\rho_{21}^{(3)} \quad \propto \quad & \int dt'dt''dt'''A_1A_2A_3\delta\left(t'-T\right)\delta\left(t''\right)\delta\left(t'''+\tau\right)e^{i(\mathbf{k}_1\cdot\mathbf{r}-\Omega_1t')}e^{-i(\mathbf{k}_2\cdot\mathbf{r}-\Omega_2t'')}e^{i(\mathbf{k}_3\cdot\mathbf{r}-\Omega_3t''')} \\ & \times e^{-\Gamma(t'-t'')}e^{-(i\omega_0+\gamma)(t-t')}\left(e^{-(i\omega_0+\gamma)(t''-t''')}+e^{-(-i\omega_0+\gamma)(t''-t''')}\right)\end{aligned}$$

from which we obtain

$$
\begin{aligned}
\rho_{21}^{(3)} &\propto A_1 A_2 A_3 e^{i(\mathbf{k}_1\cdot\mathbf{r}-\Omega_1 T)} e^{-i(\mathbf{k}_2\cdot\mathbf{r})} e^{i(\mathbf{k}_3\cdot\mathbf{r}-\Omega_3(-\tau))} \\
&\quad \times e^{-\Gamma(T)} e^{-(i\omega_0+\gamma)(t-T)} \left(e^{-(i\omega_0+\gamma)(-(-\tau))} + e^{-(-i\omega_0+\gamma)(-(-\tau))}\right) \\
\rho_{21}^{(3)} &\propto A_1 A_2 A_3 \left\{e^{i[(\mathbf{k}_1-\mathbf{k}_2+\mathbf{k}_3)\cdot\mathbf{r}-\Omega_1 T+\Omega_3\tau]}\right\} e^{-\Gamma T} e^{-(i\omega_0+\gamma)(t-T)} \\
&\quad \times \left(e^{-(i\omega_0+\gamma)\tau} + e^{-(-i\omega_0+\gamma)\tau}\right) \\
\rho_{21}^{(3)} &\propto e^{i[(\mathbf{k}_1-\mathbf{k}_2+\mathbf{k}_3)\cdot\mathbf{r}-\omega_0 t]} \\
\rho_{21}^{(3)} &\propto e^{i[\mathbf{k}_1\cdot\mathbf{r}-\omega_0 t]}
\end{aligned}
$$

which is, again, parallel to the probe wave vector since the $\mathbf{k}_2$ and $\mathbf{k}_3$ terms cancel in the exponential. We have now shown that the $\widetilde{E}_1\widetilde{E}_2\widetilde{E}_3^*$ and $\widetilde{E}_1\widetilde{E}_2^*\widetilde{E}_3$ field products yielding coherences that will result in radiation in the direction that we detect.

We write the coherences for the remaining five field products in an abbreviated form, since the calculation of each of these results proceeds in much the same manner as those shown. We find the following relations between

field products and eigenfunctions for the wave equation:

$$\begin{aligned}
\widetilde{E}_1\widetilde{E}_2\widetilde{E}_3 &\rightarrow e^{i[(\mathbf{k}_1+\mathbf{k}_2+\mathbf{k}_3)\cdot\mathbf{r}-\omega_0 t]} \\
\widetilde{E}_1\widetilde{E}_2\widetilde{E}_3^* &\rightarrow e^{i[(\mathbf{k}_1+\mathbf{k}_2-\mathbf{k}_3)\cdot\mathbf{r}-\omega_0 t]} \\
\widetilde{E}_1\widetilde{E}_2^*\widetilde{E}_3 &\rightarrow e^{i[(\mathbf{k}_1-\mathbf{k}_2+\mathbf{k}_3)\cdot\mathbf{r}-\omega_0 t]} \\
\widetilde{E}_1\widetilde{E}_2^*\widetilde{E}_3^* &\rightarrow e^{i[(\mathbf{k}_1-\mathbf{k}_2-\mathbf{k}_3)\cdot\mathbf{r}-\omega_0 t]} \\
\widetilde{E}_1^*\widetilde{E}_2\widetilde{E}_3 &\rightarrow e^{i[(-\mathbf{k}_1+\mathbf{k}_2+\mathbf{k}_3)\cdot\mathbf{r}-\omega_0 t]} \\
\widetilde{E}_1^*\widetilde{E}_2\widetilde{E}_3^* &\rightarrow e^{i[(-\mathbf{k}_1+\mathbf{k}_2-\mathbf{k}_3)\cdot\mathbf{r}-\omega_0 t]} \\
\widetilde{E}_1^*\widetilde{E}_2^*\widetilde{E}_3 &\rightarrow e^{i[(-\mathbf{k}_1-\mathbf{k}_2+\mathbf{k}_3)\cdot\mathbf{r}-\omega_0 t]} \\
\widetilde{E}_1^*\widetilde{E}_2^*\widetilde{E}_3^* &\rightarrow e^{i[(-\mathbf{k}_1-\mathbf{k}_2-\mathbf{k}_3)\cdot\mathbf{r}-\omega_0 t]}
\end{aligned}$$

Thus, we see that $\widetilde{E}_1\widetilde{E}_2\widetilde{E}_3^*$ and $\widetilde{E}_1\widetilde{E}_2^*\widetilde{E}_3$ lead to terms in the expansion of $\rho_{21}^{(3)}$ that result in a polarization that will result in emission in the direction of interest, viz. along the $\mathbf{k}_1$ wave vector. We must now consider the terms that arise in the expansion of $\rho_{12}^{(3)}$ as well. By the Hermiticity of the density operator, we know that $\rho_{21}^{(3)} = \rho_{12}^{(3)*}$; thus, the terms corresponding to the phase matched $\rho_{21}^{(3)}$ terms

$$\begin{aligned}
\rho_{21}^{(3)} &\propto \widetilde{E}_1(t')\,\widetilde{E}_2(t'')\,\widetilde{E}_3^*(t''') \propto e^{i(\mathbf{k}_1\cdot\mathbf{r}-\omega_0 t)} \\
\rho_{21}^{(3)} &\propto \widetilde{E}_1(t')\,\widetilde{E}_2^*(t'')\,\widetilde{E}_3(t''') \propto e^{i(\mathbf{k}_1\cdot\mathbf{r}-\omega_0 t)}
\end{aligned}$$

are found to be the conjugate terms

$$\rho_{12}^{(3)} \propto \widetilde{E}_1^* (t') \widetilde{E}_2^* (t'') \widetilde{E}_3 (t''') \propto e^{-i(\mathbf{k}_1 \cdot \mathbf{r} - \omega_0 t)}$$
$$\rho_{12}^{(3)} \propto \widetilde{E}_1^* (t') \widetilde{E}_2 (t'') \widetilde{E}_3^* (t''') \propto e^{-i(\mathbf{k}_1 \cdot \mathbf{r} - \omega_0 t)}$$

We note for completeness that if the probe were incident on the sample at normal incidence and thus retroreflected along $-\mathbf{k}_1$, it would be necessary to consider additional contributions to the coherence to include backward-propagating polarization waves; however, we do not perform any experiments in this particular geometry and can therefore neglect these additional terms.

In summary, the choice of a pulse sequence and a detection geometry has allowed us to select out only four coherence terms that need to be considered. Further, we discount those terms arising in the coherence that depend upon only one electric field term, as these will not be selected by our modulation scheme (in the case of the RF amplitude modulation setup) or will not appear in the appropriate spectral region of interest in the 2dFTS plots.

The $\rho_{21}^{(3)}$ and $\rho_{12}^{(3)}$ coherence terms are, explicitly,

$$\left(\rho_{21}^{(3)}(t)\right)_{\widetilde{E}_1 \widetilde{E}_2 \widetilde{E}_3^*} = \left(-\frac{i\mu^3 g(\omega_0)}{2\hbar^3}\right) A_1 A_2 A_3 e^{-\Gamma T} e^{i\omega_0 T} e^{-\gamma(t+\tau-T)} \cos(\omega_0 \tau)\, e^{-i(\Omega_1 T + \Omega_3 \tau)} \times e^{i((\mathbf{k}_1 + \mathbf{k}_2 - \mathbf{k}_3)\cdot \mathbf{r} - \omega_0 t)}$$

$$\left(\rho_{21}^{(3)}(t)\right)_{\widetilde{E}_1 \widetilde{E}_2^* \widetilde{E}_3} = \left(-\frac{i\mu^3 g(\omega_0)}{2\hbar^3}\right) A_1 A_2 A_3 e^{-\Gamma T} e^{i\omega_0 T} e^{-\gamma(t+\tau-T)} \cos(\omega_0 \tau)\, e^{-i(\Omega_1 T - \Omega_3 \tau)} \times e^{i((\mathbf{k}_1 - \mathbf{k}_2 + \mathbf{k}_3)\cdot \mathbf{r} - \omega_0 t)}$$

$$\left(\rho_{12}^{(3)}(t)\right)_{\widetilde{E}_1^*\widetilde{E}_2^*\widetilde{E}_3} = \left(\frac{i\mu^3 g(\omega_0)}{2\hbar^3}\right) A_1 A_2 A_3 e^{-\Gamma T} e^{-i\omega_0 T} e^{-\gamma(t+\tau-T)} \cos(\omega_0\tau)\, e^{i(\Omega_1 T+\Omega_3\tau)} \times e^{-i((\mathbf{k}_1+\mathbf{k}_2-\mathbf{k}_3)\cdot\mathbf{r}-\omega_0 t)}$$

$$\left(\rho_{12}^{(3)}(t)\right)_{\widetilde{E}_1^*\widetilde{E}_2^*\widetilde{E}_3} = \left(\frac{i\mu^3 g(\omega_0)}{2\hbar^3}\right) A_1 A_2 A_3 e^{-\Gamma T} e^{-i\omega_0 T} e^{-\gamma(t+\tau-T)} \cos(\omega_0\tau)\, e^{i(\Omega_1 T-\Omega_3\tau)} \times e^{-i((\mathbf{k}_1-\mathbf{k}_2+\mathbf{k}_3)\cdot\mathbf{r}-\omega_0 t)}$$

As noted above, the expectation value for the dipole operator $\hat{\mu}$ (related to the macroscopic polarization $\mathbf{P}$ via $\mathbf{P} = N\langle\hat{\mu}\rangle$) is given by the trace of the product of the density operator and the dipole operator

$$\langle\mu\rangle = Tr\{\hat{\rho}\hat{\mu}\} = Tr\left\{\begin{pmatrix}\rho_{11} & \rho_{12}\\ \rho_{21} & \rho_{22}\end{pmatrix}\begin{pmatrix}0 & \mu\\ \mu & 0\end{pmatrix}\right\} = \mu\{\rho_{12}+\rho_{21}\}$$

With our third-order perturbation calculations for the density operator matrix elements, we find

$$
\begin{aligned}
\mu\left\{\rho_{12}+\rho_{21}\right\} &= \mu\left\{\left(\rho_{21}^{(3)}\left(t\right)\right)_{\widetilde{E}_1\widetilde{E}_2\widetilde{E}_3^*}+\left(\rho_{21}^{(3)}\left(t\right)\right)_{\widetilde{E}_1\widetilde{E}_2^*\widetilde{E}_3}+\left(\rho_{12}^{(3)}\left(t\right)\right)_{\widetilde{E}_1\widetilde{E}_2\widetilde{E}_3^*}+\left(\rho_{12}^{(3)}\left(t\right)\right)_{\widetilde{E}_1\widetilde{E}_2^*\widetilde{E}_3}\right\} \\
&= \mu\left(\frac{i\mu^3 g\left(\omega_0\right)}{2\hbar^3}\right)A_1A_2A_3e^{-\Gamma T}e^{-\gamma(t+\tau-T)}\cos\left(\omega_0\tau\right) \\
&\quad\times\left[-e^{i(\mathbf{k}_1\cdot\mathbf{r}-\omega_0 t+\omega_0 T-\Omega_1 T-\Omega_3\tau)}-e^{i(\mathbf{k}_1\cdot\mathbf{r}-\omega_0 t+\omega_0 T-\Omega_1 T+\Omega_3\tau)}\right] \\
&\quad+\mu\left(\frac{i\mu^3 g\left(\omega_0\right)}{2\hbar^3}\right)A_1A_2A_3e^{-\Gamma T}e^{-\gamma(t+\tau-T)}\cos\left(\omega_0\tau\right) \\
&\quad\times\left[+e^{-i(\mathbf{k}_1\cdot\mathbf{r}-\omega_0 t+\omega_0 T-\Omega_1 T-\Omega_3\tau)}+e^{-i(\mathbf{k}_1\cdot\mathbf{r}-\omega_0 t+\omega_0 T-\Omega_1 T+\Omega_3\tau)}\right] \\
&\propto \left(e^{-i(\mathbf{k}_1\cdot\mathbf{r}-\omega_0 t+\omega_0 T-\Omega_1 T-\Omega_3\tau)}-e^{i(\mathbf{k}_1\cdot\mathbf{r}-\omega_0 t+\omega_0 T-\Omega_1 T-\Omega_3\tau)}\right) \\
&\quad+\left(e^{-i(\mathbf{k}_1\cdot\mathbf{r}-\omega_0 t+\omega_0 T-\Omega_1 T+\Omega_3\tau)}-e^{i(\mathbf{k}_1\cdot\mathbf{r}-\omega_0 t+\omega_0 T-\Omega_1 T+\Omega_3\tau)}\right) \\
&\propto 2i\sin\left(\mathbf{k}_1\cdot\mathbf{r}-\omega_0 t+\omega_0 T-\Omega_1 T-\Omega_3\tau\right)+ \\
&\quad 2i\sin\left(\mathbf{k}_1\cdot\mathbf{r}-\omega_0 t+\omega_0 T-\Omega_1 T+\Omega_3\tau\right) \\
&= \left(\frac{-\mu^4 g\left(\omega_0\right)}{\hbar^3}\right)A_1A_2A_3e^{-\Gamma T}e^{-\gamma(t+\tau-T)}\cos\left(\omega_0\tau\right)\times \\
&\quad\left[\sin\left(\mathbf{k}_1\cdot\mathbf{r}-\omega_0 t+\omega_0 T-\Omega_1 T-\Omega_3\tau\right)+\right. \\
&\quad\left.\sin\left(\mathbf{k}_1\cdot\mathbf{r}-\omega_0 t+\omega_0 T-\Omega_1 T+\Omega_3\tau\right)\right] \\
&= \left(\frac{-\mu^4 g\left(\omega_0\right)}{\hbar^3}\right)A_1A_2A_3e^{-\Gamma T}e^{-\gamma(t+\tau-T)}\cos\left(\omega_0\tau\right) \\
&\quad\times\left[\sin\left(\mathbf{k}_1\cdot\mathbf{r}-\omega_0 t+\phi_1\right)+\sin\left(\mathbf{k}_1\cdot\mathbf{r}-\omega_0 t+\phi_2\right)\right]
\end{aligned}
$$

where we have implicitly defined the two phases $\phi_1 \equiv -\Omega_1 T-\Omega_3\tau+\omega_0 T$ and $\phi_2 \equiv -\Omega_1 T+\Omega_3\tau+\omega_0 T$. We note that it can be more illustrative to express the exponential dependence upon the dephasing rate γ and the population decay rate Γ with the product $e^{-\Gamma T}e^{-\gamma(t+\tau-T)}=e^{-\Gamma T}e^{-\gamma(t-T)}e^{-\gamma\tau}$, which presents a more straightforward physical interpretation of the dynamics of the expectation value of the dipole operator:

1. The dynamic pump pulse interacts with the material first, at time $-\tau$. This will induce an ensemble dipole oscillation or coherence between the two levels; that coherence will decay in the time interval between the arrival of the dynamic pump pulse at $-\tau$ and the arrival of the static pump pulse at the time origin (0). That dephasing is accounted for by the exponential term $e^{-\gamma\tau}$.

2. Upon the arrival of the static pump pulse at the time origin (0), the coherence created by the first pulse is converted into a population, which will relax with the slower population decay rate, accounted for by the term $e^{-\Gamma T}$. That decay continues until the population interacts with the probe pulse, arriving at time T.

3. When the probe pulse arrives that population is then converted back into a coherence, after which the dipole shall decay in proportion to the interval between the probe pulse and the moment at which the dipole is measured (more explicitly, the time interval between the probe pulse interacting with the material and a particular time t when emission form the nonlinear polarization occurs), accounted for by the $t-T$ dependence of the exponential term $e^{-\gamma(t-T)}$.

This completes the interpretation of the decay behaviour of the dipole expectation value as a function of time during the various steps of the three pulse experiments.

In addition to the decay terms present in this expression, we also note the presence of the trigonometric functions. The cosine function results in a fast (optical frequency) oscillation in the strength of the dipole operator as a function of the delay between two pump pulses. This makes sense in light of the cartoon model of the interaction of a coherence with an impulse – the idea that the second excitation source must arrive in phase with the oscillation induced by the first source to result in the maximum excited population is immediately intuitive. Since the frequency of the oscillation of the coherence in the period between the two pump pulses is determined by the energy difference between the two levels, the dependence upon the optical frequency is expected.

Finally, there are two sine functions that describe the propagation of a polarization wave of dipoles. The phase terms that appear are related to the relative phases of the three pulses interacting with the material system at the various moments when they arrive at the sample.

The overall co-efficient for this expression is simply related to the coupling strength of the optical field to the electronic structure of the system; we note that it depends upon the fourth power of the dipole matrix element. As noted, the use of a distribution function for the central frequency ω_0 allows us to back out the behaviour of an inhomogeneous system, although we note that we have not been rigorous here in applying that distribution, as we did not use an integrated frequency distribution to describe the flopping behaviour captured in the Bloch equations, but simply used a single frequency value ω_0.

Significantly, we note the linear dependence of the dipole (and, by ex-

tension, the polarization) upon the electric field amplitudes. This is relevant to the modulation method we use to pick out weak signals in the presence of background noise.

It is possible to further simplify this expression. Using trigonometric identities, it is possible to show that the sum of the two sine functions can be rewritten as $2\sin\left(\mathbf{k}_1\cdot\mathbf{r}-\omega_0 t-\Omega_1 T+\omega_0 T\right)\cos\left(\Omega_3\tau\right)$. Then, if we assume that the carrier frequencies of the optical fields are all equal and are on resonance, $\Omega_1=\Omega_2=\Omega_3\sim\omega_0$, we may further reduce the complexity of this expression to

$$\begin{aligned}\mu\left\{\rho_{12}+\rho_{21}\right\} &= \left(\frac{-\mu^4 g\left(\omega_0\right)}{\hbar^3}\right)A_1A_2A_3e^{-\Gamma T}e^{-\gamma(t+\tau-T)}\cos\left(\omega_0\tau\right)\\ &\quad\times\left[2\sin\left(\mathbf{k}_1\cdot\mathbf{r}-\omega_0 t-\Omega_1 T+\omega_0 T\right)\cos\left(\Omega_3\tau\right)\right]\\ &= \left(\frac{-\mu^4 g\left(\omega_0\right)}{\hbar^3}\right)A_1A_2A_3e^{-\Gamma T}e^{-\gamma(t+\tau-T)}\cos^2\left(\omega_0\tau\right)\\ &\quad\times 2\sin\left(\mathbf{k}_1\cdot\mathbf{r}-\omega_0 t\right)\end{aligned}$$

which is sensitive to the phase relationship between the pump pulses (due to the square cosine term that depends upon their relative timing) but not upon the relationship to the phase of the third, probe pulse. It should come as no surprise that this is readily physically interpreted in the context of many similar four-wave mixing experiments, where the coherent interaction of the second pulse to couple with the coherence (corresponding to the dipole oscillation, physically) established by the first pulse 'freezes' the information on the dephasing processes into a population, which will then decay slowly

during the T time period until the probe arrives. This can be visualized with the following cartoon.

We note that making the assumption of resonant excitation helps to simplify the expression for the polarization, but does prevent us from properly keeping track of inhomogeneity using the distribution function $g(\omega_0)$. We drop that frequency distribution here, letting $g(\omega_0) \to 1$. It is possible to keep the more general expression for the polarization, rather than assuming the fields are on resonance, but that problem then becomes more suited to a numerical simulation due to the resulting complex analytical expression.

We did not build the pulse ordering into this expression analytically – hence, there are no Heaviside unit step functions that appear in this expression for the polarization. We can add their effect in after the fact by noting that causality should imply no four-wave mixing emission will occur along the phase-matched direction (co-propagating with the pump) if the pulses have not arrived in order. Hence, there is a product $\Theta(t+\tau)\,\Theta(t)\,\Theta(t-T)$ that should appear here, which prevents any emission at the 'wrong' time in this toy model.

The important features of this result are that it separates the dependence on dephasing from the dependence on population decay. We see by inspection that scanning the position of the probe pulse will reveal a complicated functional form, determined by the exponential decay term $e^{-\Gamma T}$ and the oscillatory dependence on the phase that the probe pulse has when it arrives at the sample, $\varphi_{probe} = \omega_0 T$, which appears in both of the trigonometric

functions. The dephasing rate, however, will be directly revealed by a scan of the position of the dynamic pump pulse, modulated by an oscillatory dependence on the phase the dynamic pump has when it interacts with the sample – $\cos^2(\omega_0\tau)\, e^{-\gamma\tau} = \frac{1}{2}(1+\cos(2\omega_0\tau))\, e^{-\gamma\tau}$. We may easily test the validity of this assumption by looking for an oscillating decay with half the optical wavelength. Any deviation from that is likely to arise due to the questionable assumption that we could set all frequency components in the various pulses – which effectively rolls back the analysis somewhat to a more complicated functional form, which should nonetheless still contain the physics of interest, since the previous expression

$$e^{-\Gamma T} e^{-\gamma(t+\tau-T)} \cos(\omega_0\tau) \left[\sin(\mathbf{k}_1\cdot\mathbf{r}-\omega_0 t+\phi_1)+\sin(\mathbf{k}_1\cdot\mathbf{r}-\omega_0 t+\phi_2)\right]$$

still allows the extraction of the dephasing rate by fitting the envelope of an oscillatory decay curve.

As we did for the pump-probe experiment, we write an expression for the nonlinear polarization here, which is simply proportional to the expectation value for the dipole operator

$$\begin{aligned}
\mathbf{P} &= N\langle\hat{\mu}\rangle \\
&= N\left(\frac{-2\mu^4}{\hbar^3}\right) A_1A_2A_3 e^{-\Gamma T}\cos^2(\omega_0\tau)\, e^{-\gamma(t+\tau-T)}\sin(\mathbf{k}_1\cdot\mathbf{r}-\omega_0 t) \\
&= \left(\frac{i\mu^4}{\hbar^3}\right) A_1A_2A_3 e^{-\Gamma T}\cos^2(\omega_0\tau)\, e^{-\gamma(t+\tau-T)}\left(e^{i(\mathbf{k}_1\cdot\mathbf{r}-\omega_0 t)}-e^{-i(\mathbf{k}_1\cdot\mathbf{r}-\omega_0 t)}\right)
\end{aligned}$$

and the electric field, which we assume is proportional to the polarization with a phase shift of i,

$$\begin{aligned} E_{sig} &= NiP \\ &= \left(-\frac{N\mu^4}{\hbar^3}\right) A_1 A_2 A_3 e^{-\Gamma T} \cos^2(\omega_0 \tau)\, e^{-\gamma(t+\tau-T)} \left(e^{i(\mathbf{k}_1\cdot\mathbf{r}-\omega_0 t)} - e^{-i(\mathbf{k}_1\cdot\mathbf{r}-\omega_0 t)}\right) \\ &\propto \zeta |E_{dp}| |E_{sp}| A_1 \left(e^{i(\mathbf{k}_1\cdot\mathbf{r}-\omega_0 t)} - e^{-i(\mathbf{k}_1\cdot\mathbf{r}-\omega_0 t)}\right) \\ &\propto \zeta E_{dp} E_{sp} E_{pr}(t+\pi/2) \end{aligned}$$

from which we find, calculating the interference term for the signal detected with the co-propagating probe beam,

$$\begin{aligned} |E_{pr}+E_{sig}|^2 &= |E_{pr}|^2 \\ &\quad +\zeta |E_{dp}| |E_{sp}| E_{pr}(t) E_{pr}(t+\pi/2) \\ &\quad +\left(\zeta |E_{dp}| |E_{sp}| E_{pr}(t+\pi/2)\right)^2 \end{aligned}$$

where we identify the term $\zeta |E_{dp}| |E_{sp}| E_{pr}(t) E_{pr}(t+\pi/2)$ as a heterodyne term, which is bilinear in the probe electric field (albeit with a phase shift) and linear in the other electrical fields. Thus, we note and emphasize that the electric fields appear here on a different footing from one another. The homodyne term, which is expected to be weaker, is given by $\left(\zeta |E_{dp}| |E_{sp}| E_{pr}(t+\pi/2)\right)^2$, where all three electrical fields appear as a bilinear form. Thus, the homodyne term is proportional to the intensity of all

of the experimental controllable electrical fields, while the heterodyne term is proportional to the intensity of only the probe field, but is proportional to electric field strength of the other fields driving the nonlinear system response.

The conscientious reader may point out that the heterodyne term should vanish due to the $pi/2$ phase shift between the two instances of the probe electric field. We excuse this inconsistency as a result of an overly simple analysis: we have neglected to properly consider the phase of the electric field of the co-propagating probe beam. A simple explanation is not available. Accounting only for reflection from the front surface of the sample should result in a simple π phase shift, resulting in, again, a $\pi/2$ phase difference between the two fields. In addition, however, this expression should properly be evaluated by considering the total optical phase accumulated by the portion of the probe beam that penetrates into the sample to induce four-wave mixing emission as well as the total phase accumulated by the light subsequently escaping the sample. This complete analysis will remove the apparent contradiction, but is beyond the scope of this thesis. A careful analysis, considering the phase mismatch between polarization and electromagnetic waves, is suggested.

Bibliography

[1] R. L. Whitman A. Korpel, S. N. Lotsoff. The interchange of time and frequency in television displays. *Proc. IEEE*, 57:160–170, Feb 1969.

[2] I. D. Abella, N. A. Kurnit, and S. R. Hartmann. Photon echoes. *Phys. Rev.*, 141(1):391–406, Jan 1966.

[3] I. Abram. Theory of optical coherence for wannier excitons: Application to photon echoes. *Phys. Rev. B*, 40(8):5460–5472, Sep 1989.

[4] Allison W. Albrecht, John D. Hybl, Sarah M. Gallagher Faeder, and David M. Jonas. Experimental distinction between phase shifts and time delays: Implications for femtosecond spectroscopy and coherent control of chemical reactions. *J. Chem. Phys.*, 111(24):10934–10956, 1999.

[5] L. Allen and J. H. Eberly. *Optical Resonance and Two-Level Atoms*. Dover, New York, 1987.

[6] L. Allen and J. H. Eberly. *Optical Resonance and Two-Level Atoms*. Dover, New York, 1987.

[7] Luis W. Alvarez and F. Bloch. A quantitative determination of the neutron moment in absolute nuclear magnetons. *Phys. Rev.*, 57(2):111–122, Jan 1940.

[8] D. Brunner; H. Angerer; E. Bustarret; F. Freudenberg; R. Höpler; R. Dimitrov; O. Ambacher; and M. Stutzmann. Optical constants of epitaxial algan films and their temperature dependence. *J. Appl. Phys.*, 82(10):5090–5096, 1997.

[9] N. E. Hecker; R. A. Hopfel; N. Sawaki; amd T. Maier. Large luminescence enhancements from a quantum well located near gold gratings. In *Quantum Electronics Conference, 1998. IQEC 98. Technical Digest. Summaries of papers presented at the International Quantum Electronics Conference*, pages 213–214, May 1998.

[10] Inc. Analog Devices. A technical tutorial on digital signal synthesis. Technical report, Analog Devices, Inc., 1999.

[11] Inc. Analog Devices. Fundamentals of direct digital synthesis (dds) mt-085 tutorial rev.0. Technical report, Analog Devices, Inc., 10 2008.

[12] D.A. Andrews, J.G. Baker, B.G. Blundell, and G.C. Petty. Spectroscopic applications of three-level microwave double resonance. *Journal of Molecular Structure*, 97:271 – 283, 1983. Determination of Molecular Structure by Microwave Spectroscopy and Electron Diffraction.

[13] J. H. Apfel and L. N. Hadley. Exciton absorption in cuprous oxide. *Physical Review*, 100(6):1689–1691, 1955.

[14] L. Apker and E. Taft. Photoelectric emission from f-centers in ki. *Phys. Rev.*, 79(6):964–966, Sep 1950.

[15] L. Apker and E. Taft. Energy distribution of external photoelectrons from f-centers in rbi. *Phys. Rev.*, 82(6):814–819, Jun 1951.

[16] L. Apker and E. Taft. Exciton-enhanced photoelectric emission from f-centers in rbi near 85°k. *Phys. Rev.*, 81(5):698–701, Mar 1951.

[17] N. David Ashcroft, Neil W.; Mermin. *Solid State Physics*. Holt, Rinehart and Winston, New York, 1976.

[18] W. P. Aue, E. Bartholdi, and R. R. Ernst. Two-dimensional spectroscopy. application to nuclear magnetic resonance. *J. Chem. Phys.*, 64:2229—2246, 1976.

[19] D. H. Auston and C. V. Shank. Picosecond ellipsometry of transient electron-hole plasmas in germanium. *Phys. Rev. Lett.*, 32(20):1120–1123, May 1974.

[20] Carlos R. Baiz, Porscha L. McRobbie, Jessica M. Anna, Eitan Geva, and Kevin J. Kubarych. Two-dimensional infrared spectroscopy of metal carbonyls. *Accounts of Chemical Research*, 42(9):1395–1404, 2009. PMID: 19453102.

[21] Per Bak, Chao Tang, and Kurt Wiesenfeld. Self-organized criticality: An explanation of the 1/f noise. *Phys. Rev. Lett.*, 59(4):381–384, Jul 1987.

[22] W. L. Barnes. Electromagnetic crystals for surface plasmon polaritons and the extraction of light from emissive devices. *J. Lightwave Technol.*, 17(11):2170, Nov 1999.

[23] J. J. Baumberg, A. P. Heberle, A. V. Kavokin, M. R. Vladimirova, and K. Köhler. Polariton motional narrowing in semiconductor multiple quantum wells. *Phys. Rev. Lett.*, 80(16):3567–3570, Apr 1998.

[24] N.C. Beaulieu. Introduction to 'certain topics in telegraph transmission theory'. *Proceedings of the IEEE*, 90(2):276 –279, feb 2002.

[25] P. C. Becker, H. L. Fragnito, J. Y. Bigot, C. H. Brito Cruz, R. L. Fork, and C. V. Shank. Femtosecond photon echoes from molecules in solution. *Phys. Rev. Lett.*, 63(5):505–507, Jul 1989.

[26] P. C. Becker, H. L. Fragnito, C. H. Brito Cruz, R. L. Fork, J. E. Cunningham, J. E. Henry, and C. V. Shank. Femtosecond photon echoes from band-to-band transitions in gaas. *Phys. Rev. Lett.*, 61(14):1647–1649, Oct 1988.

[27] R. F. Begley, A. B. Harvey, and R. L. Byer. Coherent anti-stokes raman spectroscopy. *Applied Physics Letters*, 25(7):387 –390, oct 1974.

[28] Paul R. Berman, J. M. Levy, and Richard G. Brewer. Coherent optical transient study of molecular collisions: Theory and observations. *Phys. Rev. A*, 11(5):1668–1688, May 1975.

[29] Somnath Bhowmick, Sangeeta Saini, Vijay B. Shenoy, and Biman Bagchi. Resonance energy transfer from a fluorescent dye to a metal nanoparticle. *J. Chem. Phys*, 125(18):181102, 2006.

[30] D. Bimberg, J. Christen, T. Fukunaga, H. Nakashima, D. E. Mars, and J. N. Miller. Cathodoluminescence atomic scale images of monolayer islands at gaas/gaalas interfaces. *Journal of Vacuum Science Technology B: Microelectronics and Nanometer Structures*, 5(4):1191 –1197, jul 1987.

[31] D. Birkedal, J. Shah, and L. N. Pfeiffer. Coherent secondary emission from resonantly excited two-exciton states: An intrinsic phenomenon. *Phys. Rev. B*, 60(23):15585–15588, Dec 1999.

[32] David A. Blank, Laura J. Kaufman, and Graham R. Fleming. Fifth-order two-dimensional raman spectra of cs2 are dominated by third-order cascades. *J. Chem. Phys.*, 111(7):3105–3114, 1999.

[33] Joël Bleuse, Julien Claudon, Megan Creasey, Nitin. S. Malik, Jean-Michel Gérard, Ivan Maksymov, Jean-Paul Hugonin, and Philippe Lalanne. Inhibition, enhancement, and control of spontaneous emission in photonic nanowires. *Phys. Rev. Lett.*, 106(10):103601, Mar 2011.

[34] F. Bloch. Nuclear induction. *Phys. Rev.*, 70(7-8):460–474, Oct 1946.

[35] F. Bloch, W. W. Hansen, and M. Packard. The nuclear induction experiment. *Phys. Rev.*, 70(7-8):474–485, Oct 1946.

[36] N. Bloembergen, E. M. Purcell, and R. V. Pound. Relaxation effects in nuclear magnetic resonance absorption. *Phys. Rev.*, 73(7):679–712, Apr 1948.

[37] David Bohm and David Pines. A collective description of electron interactions. i. magnetic interactions. *Phys. Rev.*, 82(5):625–634, Jun 1951.

[38] David Bohm and David Pines. A collective description of electron interactions: Iii. coulomb interactions in a degenerate electron gas. *Phys. Rev.*, 92(3):609–625, Nov 1953.

[39] Camelia N. Borca, Tianhao Zhang, Xiaoqin Li, and Steven T. Cundiff. Optical two-dimensional fourier transform spectroscopy of semiconductors. *Chemical Physics Letters*, 416(4-6):311 – 315, 2005.

[40] R. W. Boyd. *Nonlinear Optics*. Academic Press, San Diego, 2nd edition, 2003.

[41] R. W. Boyd. *Nonlinear Optics*. Academic Press, San Diego, 2nd edition, 2003.

[42] Thomas Brabec and Ferenc Krausz. Intense few-cycle laser fields: Frontiers of nonlinear optics. *Rev. Mod. Phys.*, 72(2):545–591, Apr 2000.

[43] R. N. Bracewell. *The Fourier transform and its applications*. McGraw-Hill, New York, 2nd edition, 1978.

[44] W. H. Bragg and W. L. Bragg. The reflection of x-rays by crystals. *Proc. R. Soc. Lond. A*, 88:428–438, 1913.

[45] W.L. Bragg. The diffraction of short electromagnetic waves by a crystal. *Proceedings of the Cambridge Philosophical Society*, 17:43–57, 1913.

[46] B. H. Bransden and C. J. Joachain. *Physics of Atoms and Molecules*. Pearson Education, London, 2003.

[47] J. W. Brault and O. R. White. The analysis and restoration of astronomical data via the fast fourier transform. *Astron. and Astrophys.*, 13:169, July 1971.

[48] Richard G. Brewer and Azriel Z. Genack. Optical coherent transients by laser frequency switching. *Phys. Rev. Lett.*, 36(16):959–962, Apr 1976.

[49] Richard G. Brewer and Klaus E. Rieckhoff. Stimulated brillouin scattering in liquids. *Phys. Rev. Lett.*, 13(11):334–336, Sep 1964.

[50] Richard G. Brewer and R. L. Shoemaker. Photo echo and optical nutation in molecules. *Phys. Rev. Lett.*, 27(10):631–634, Sep 1971.

[51] Richard G. Brewer and R. L. Shoemaker. Optical free induction decay. *Phys. Rev. A*, 6(6):2001–2007, Dec 1972.

[52] L. Brillouin. Diffusion de la lumière et des rayons x par un corps transparent homogène, influence de l'agitation thermique. *Annales de physique*, 17:88, 1922.

[53] A. D. Bristow, D. Karaiskaj, X. Dai, and S. T. Cundiff. All-optical retrieval of the global phase for two- dimensional fourier-transform spectroscopy. *Opt. Express*, 16(22):18017, 2008.

[54] A. D. Bristow, D. Karaiskaj, X. Dai, T. Zhang, C. Carlsson, K. R. Hagen, R. Jimenez, and S. T. Cundiff. A versatile ultrastable platform for optical multidimensional fourier-transform spectroscopy. *Rev. Sci. Instrum.*, 80:073108, 2009.

[55] G. K. Campbell. *87Rubidium Bose-Einstein Condensates in Optical Lattices*. Doctor of phil., Massachusetts Institute of Technology, September 2006.

[56] R. L. Carman, R. Y. Chiao, and P. L. Kelley. Observation of degenerate stimulated four-photon interaction and four-wave parametric amplification. *Phys. Rev. Lett.*, 17(26):1281–1283, Dec 1966.

[57] C. K. Carniglia and L. Mandel. Quantization of evanescent electromagnetic waves. *Phys. Rev. D*, 3(2):280–296, Jan 1971.

[58] C. K. CARNIGLIA, L. MANDEL, and K. H. DREXHAGE. Absorption and emission of evanescent photons. *J. Opt. Soc. Am.*, 62(4):479–486, Apr 1972.

[59] H. Y. Carr and E. M. Purcell. Effects of diffusion on free precession in nuclear magnetic resonance experiments. *Phys. Rev.*, 94(3):630–638, May 1954.

[60] T.P. Carter, B.L. Fearey, J.M. Hayes, and G.J. Small. Optical dephasing of cresyl violet in a polyvinyl alcohol polymer by non-photochemical hole burning. *Chemical Physics Letters*, 102(2-3):272 – 276, 1983.

[61] Hervé Castella and John W. Wilkins. Splitting of the excitonic peak in quantum wells with interfacial roughness. *Phys. Rev. B*, 58(24):16186–16193, Dec 1998.

[62] I. Chang. Noncollinear acoustooptic filters. *IEEE Journal of Quantum Electronics*, 9(6):660–661, June 1973.

[63] I. C. Chang. Noncollinear acousto-optic filter with large angular aperture. *Applied Physics Letters*, 25:370, 1974.

[64] I. C. Chang. Tunable acousto-optic filter utilizing acoustic beam walkoff in crystal quartz. *Applied Physics Letters*, 25:323, 1974.

[65] I. C. Chang. Analysis of the noncollinear acousto-optic filter. *Electronics Letters*, 11(25):617–618, Dec. 1975.

[66] I.-C. Chang. Noncollinear tunable acousto-optic filter. U.S. Patent 4,052,121, 1977.

[67] I.-C. Chang. Transverse tunable acousto-optic filter,. U.S. Patent 4,342,502, 1982.

[68] I.C. Chang and R.T. Weverka. Multifrequency acousto-optic diffraction in wideband bragg cells. *1983 Ultrasonics Symposium*, pages 445–448, 1983.

[69] L. L. Chase. Microwave-modulated fluorescence in caf_2:eu^{2+}. *Phys. Rev. Lett.*, 21(13):888–891, Sep 1968.

[70] A. L. Smirl; X. Chen; and O. Buccafusca. Heavy-hole and light-hole quantum beats in the polarization state of coherent emission from quantum wells. *IEEE Journal of Quantum Electronics*, 35(4):523, Apr. 1999.

[71] W. M. Zhang; V. Chernyak; and S. Mukamel. Multidimensional femtosecond correlation spectroscopies of electronic and vibrational excitons. *J. Chem. Phys.*, 110:5011, 1999.

[72] R. Y. Chiao, C. H. Townes, and B. P. Stoicheff. Stimulated brillouin scattering and coherent generation of intense hypersonic waves. *Phys. Rev. Lett.*, 12(21):592–595, May 1964.

[73] R.-S. Chu and T. Tamir. Guided-wave theory of light diffraction by acoustic microwaves. *IEEE Transactions on Microwave Theory and Techniques*, MIT-17(11):1002–1020, November 1969.

[74] Ruey-Shi Chu and Theodor Tamir. Bragg diffraction of gaussian beams by periodically modulated media. *J. Opt. Soc. Am.*, 66(3):220–226, Mar 1976.

[75] S. Chu and C. H. Townes. *Arthur Schawlow, 1921-1999, A Biographical Memoir*, volume 83. National Academy of Sciences, Washington D.C., 2003.

[76] T. D. W. Claridge. *High-Resolution NMR Techniques in Organic Chemistry*. Elsevier B. V., Amsterdam, 1999.

[77] M. L. Cohen and J. R. Chelikowsky. *Electronic structure and optical properties of semiconductors*, volume 75 of *Springer Series in Solid-State Sciences*. Springer-Verlag, Berlin, 1988.

[78] F. D. Colegrove, P. A. Franken, R. R. Lewis, and R. H. Sands. Novel method of spectroscopy with applications to precision fine structure measurements. *Phys. Rev. Lett.*, 3(9):420–422, Nov 1959.

[79] S. T. Cundiff. Effects of correlation between inhomogeneously broadened transitions on quantum beats in transient four-wave mixing. *Phys. Rev. A*, 49(4):3114–3118, Apr 1994.

[80] Steven T. Cundiff. Coherent spectroscopy of semiconductors. *Opt. Express*, 16(7):4639–4664, Mar 2008.

[81] D. P. DeMille D. Budker, D. F. Kimball. *Atomic Physics: an exploration through problems and solutions*. Oxford University Press, New York, 2004.

[82] D. A. Wilson D. L. Hammond, J. A Kusters. Electronically tunable acousto-optic filter having selected crystal orientation. U.S. Patent 3,756,689, 1973.

[83] Wim P. de Boeij, Maxim S. Pshenichnikov, and Douwe A. Wiersma. On the relation between the echo-peak shift and brownian-oscillator correlation function. *Chemical Physics Letters*, 253(1-2):53 – 60, 1996.

[84] Wim P. de Boeij, Maxim S. Pshenichnikov, and Douwe A. Wiersma. Heterodyne-detected stimulated photon echo: applications to optical dynamics in solution. *Chemical Physics*, 233(2-3):287 – 309, 1998.

[85] D. R. Dean and R. J. Collins. Transient phase gratings in zno induced by two-photon absorption. *Journal of Applied Physics*, 44(12):5455 –5457, dec 1973.

[86] P. Debye and F. W. Sears. On the scattering of light by supersonic waves. *Proc Natl Acad Sci U S A*, 18(6):409–414, June 1932.

[87] Lauren P. DeFlores, Rebecca A. Nicodemus, and Andrei Tokmakoff. Two-dimensional fourier transform spectroscopy in the pump-probe geometry. *Opt. Lett.*, 32(20):2966–2968, Oct 2007.

[88] B. Deveaud, J. Y. Emery, A. Chomette, B. Lambert, and M. Baudet. Observation of one-monolayer size fluctuations in a gaas/gaalas superlattice. *Applied Physics Letters*, 45(10):1078 –1080, nov 1984.

[89] R. G. DeVoe, A. Szabo, S. C. Rand, and R. G. Brewer. Ultraslow optical dephasing of laf_3: pr^{3+}. *Phys. Rev. Lett.*, 42(23):1560–1563, Jun 1979.

[90] Ralph G. DeVoe and Richard G. Brewer. Experimental test of the optical bloch equations for solids. *Phys. Rev. Lett.*, 50(17):1269–1272, Apr 1983.

[91] D. L. Dexter. Exciton models in the alkali halides. *Phys. Rev.*, 108(3):707–712, Nov 1957.

[92] R. S. Dexter, D. L; Knox. *Excitons*. Number 25 in Interscience Tracts on Physics and Astronomy. Interscience Publications (John Wiley and Sons), New York, 1965.

[93] R. S. Dexter, D. L; Knox. *Excitons*. Number 25 in Interscience Tracts on Physics and Astronomy. Interscience Publications (John Wiley and Sons), New York, 1965.

[94] R. H. Dicke. Coherence in spontaneous radiation processes. *Phys. Rev.*, 93(1):99, Jan 1954.

[95] Jean-Claude Diels and Wolfgang Rudolph. *Ultrashort Laser Pulse Phenomena: Fundamentals, Techniques, and Applications on a Femtosecond Time Scale*. Academic Press, Burlington, MA, 2nd edition, 2006.

[96] Jean-Claude Diels and Wolfgang Rudolph. *Ultrashort Laser Pulse Phenomena: Fundamentals, Techniques, and Applications on a Femtosecond Time Scale*. Academic Press, Burlington, MA, 2nd edition, 2006.

[97] Jean-Claude M. Diels, Joel J. Fontaine, Ian C. McMichael, and Francesco Simoni. Control and measurement of ultrashort pulse shapes (in ampli-

tude and phase) with femtosecond accuracy. *Appl. Opt.*, 24(9):1270–1282, May 1985.

[98] R. W. Dixon. Acoustic diffraction of light in anisotropic media. *IEEE Journal of Quantum Electronics*, QE-3(2):85, February 1967.

[99] R. W. Dixon. "photoelastic properties of selected materials and their relevance for applications to acoustic light modulators and scanners. *Journal of Applied Physics*, 38(13):5149, Dec. 1967.

[100] Christophe Dorrer, Nadia Belabas, Jean-Pierre Likforman, and Manuel Joffre. Spectral resolution and sampling issues in fourier-transform spectral interferometry. *J. Opt. Soc. Am. B*, 17(10):1795–1802, Oct 2000.

[101] M. A. Dugan, J. X. Tull, and W. S. Warren. High-resolution acousto-optic shaping of unamplified and amplified femtosecond laser pulses. *J. Opt. Soc. Am. B*, 14(9):2348–2358, Sep 1997.

[102] Koos Duppen and Douwe A. Wiersma. Picosecond multiple-pulse experiments involving spatial and frequency gratings: a unifying nonperturbational approach. *J. Opt. Soc. Am. B*, 3(4):614–621, Apr 1986.

[103] Alan C. Eckbreth. Boxcars: Crossed-beam phase-matched cars generation in gases. *Applied Physics Letters*, 32(7):421 –423, apr 1978.

[104] H. Eichler, U. Klein, and D. Langhans. Coherence time measurement of picosecond pulses by a light-induced grating method. *Ap-*

plied Physics A: Materials Science and Processing, 21:215–219, 1980. 10.1007/BF00886171.

[105] H. Eichler, U. Klein, and D. Langhans. Coherence time measurement of picosecond pulses by a light-induced grating method. *Applied Physics A: Materials Science and Processing*, 21:215–219, 1980. 10.1007/BF00886171.

[106] H. Eichler, G. Salje, and H. Stahl. Thermal diffusion measurements using spatially periodic temperature distributions induced by laser light. *Journal of Applied Physics*, 44(12):5383 –5388, dec 1973.

[107] C. Ell, J. F. Müller, K. E. Sayed, L. Banyai, and H. Haug. Evaluation of the hartree-fock theory of the excitonic optical stark effect. *physica status solidi (b)*, 150(2):393–399, 1988.

[108] C. Ell, J. F. Müller, K. El Sayed, and H. Haug. Influence of many-body interactions on the excitonic optical stark effect. *Phys. Rev. Lett.*, 62(3):304–307, Jan 1989.

[109] R. J. Elliott. Intensity of optical absorption by excitons. *Phys. Rev.*, 108(6):1384–1389, Dec 1957.

[110] G. Elston. Intermodulation products in acousto-optic signal processing systems. In *IEEE 1985 Ultrasonics Symposium*, pages 391 – 397, 1985.

[111] G. Elston and P. Kellman. The effects of acoustic nonlinearities in acousto-optic signal processing systems. *1983 Ultrasonics Symposium*, pages 449 – 453, 1983.

[112] Michel F. Emde, Wim P. de Boeij, Maxim S. Pshenichnikov, and Douwe A. Wiersma. Spectral interferometry as an alternative to time-domain heterodyning. *Opt. Lett.*, 22(17):1338–1340, Sep 1997.

[113] Mikhail Erementchouk, Michael N. Leuenberger, and L. J. Sham. Many-body interaction in semiconductors probed with two-dimensional fourier spectroscopy. *Phys. Rev. B*, 76(11):115307, Sep 2007.

[114] Mikhail Erementchouk, Michael N. Leuenberger, and L. J. Sham. Many-body interaction in semiconductors probed with two-dimensional fourier spectroscopy. *Phys. Rev. B*, 76(11):115307, Sep 2007.

[115] T. W. Jarvis; Z. Sun; X. Li; M. Erementchouk; and M. N. Leuenberger. Reflection geometry electronic two-dimensional fourier transform spectroscopy. In *Bulletin of the American Physical Society APS March Meeting 2011*, volume 56, 2011.

[116] Z. Sun; T. Jarvis; X. Li; M. Erementchouk; and M. Leuenberger. Quantifying excitonic coupling in disordered semiconductor quantum wells. In *Bulletin of the American Physical Society APS March Meeting 2010*, volume 55, 2010.

[117] A. Euteneuer, E. Finger, M. Hofmann, W. Stolz, T. Meier, P. Thomas, S. W. Koch, W. W. Rühle, R. Hey, and K. Ploog. Coherent excitation spectroscopy on inhomogeneous exciton ensembles. *Phys. Rev. Lett.*, 83(10):2073–2076, Sep 1999.

[118] U. Fano. Atomic theory of electromagnetic interactions in dense materials. *Phys. Rev.*, 103(5):1202–1218, Sep 1956.

[119] B. L. Fearey, T. P. Carter, and G. J. Small. Efficient nonphotochemical hole burning of dye molecules in polymers. *The Journal of Physical Chemistry*, 87(19):3590–3592, 1983.

[120] G. W. Fehrenbach, W. Schäfer, J. Treusch, and R. G. Ulbrich. Transient optical spectra of a dense exciton gas in a direct-gap semiconductor. *Phys. Rev. Lett.*, 49(17):1281–1284, Oct 1982.

[121] Richard P. Feynman, Frank L. Vernon, and Robert W. Hellwarth. Geometrical representation of the schrödinger equation for solving maser problems. *Journal of Applied Physics*, 28(1):49 –52, jan 1957.

[122] E. Finger, S. Kraft, M. Hofmann, T. Meier, S.W. Koch, W. Stolz, W.W. Rühle, and A. Wieck. Coulomb correlations and biexciton signatures in coherent excitation spectroscopy of semiconductor quantum wells. *physica status solidi (b)*, 234(1):424–434, 2002.

[123] A. Flusberg, T. Mossberg, R. Kachru, and S. R. Hartmann. Observation and relaxation of the two-photon echo in na vapor. *Phys. Rev. Lett.*,

41(5):305–308, Jul 1978.

[124] R. L. Fork, B. I. Greene, and C. V. Shank. Generation of optical pulses shorter than 0.1 psec by colliding pulse mode locking. *Applied Physics Letters*, 38(9):671–672, 1981.

[125] H.L. Fragnito, J.-Y. Bigot, P.C. Becker, and C.V. Shank. Evolution of the vibronic absorption spectrum in a molecule following impulsive excitation with a 6 fs optical pulse. *Chemical Physics Letters*, 160(2):101 – 104, 1989.

[126] H.L. Fragnito, J.-Y. Bigot, P.C. Becker, and C.V. Shank. Evolution of the vibronic absorption spectrum in a molecule following impulsive excitation with a 6 fs optical pulse. *Chemical Physics Letters*, 160(2):101 – 104, 1989.

[127] J. Frenkel. On the transformation of light into heat in solids. *Physical Review*, 37:17, 1931.

[128] J. Friedrich, H. Wolfrum, and D. Haarer. Photochemical holes: A spectral probe of the amorphous state in the optical domain. *J. Chem. Phys.*, 77(5):2309–2316, 1982.

[129] T. Yano; M. Kawabuchi; A. Fukumoto; and A. Watanabe. Teo2 anisotropic bragg light deflector without midband degeneracy. *Applied Physics Letters*, 26:689, 1975.

[130] W. Schäfer G. W. Fehrenbach and R. G. Ulbrich. Excitonic versus plasma screening in highly excited gallium arsenide. *Journal of Luminescence*, 30(1-4):154 – 161, 1985.

[131] Sarah M. Gallagher, Allison W. Albrecht, John D. Hybl, Brett L. Landin, Bhavani Rajaram, and David M. Jonas. Heterodyne detection of the complete electric field of femtosecond four-wave mixing signals. *J. Opt. Soc. Am. B*, 15(8):2338–2345, Aug 1998.

[132] Sarah M. Gallagher Faeder and David M. Jonas. Two-dimensional electronic correlation and relaxation spectra:äâ theory and model calculations. *The Journal of Physical Chemistry A*, 103(49):10489–10505, 1999.

[133] Sarah M. Gallagher Faeder and David M. Jonas. Phase-resolved time-domain nonlinear optical signals. *Phys. Rev. A*, 62(3):033820, Aug 2000.

[134] H. Cummins; N. Knable; L. Gampel; and Y. Yeh. Frequency shifts in light diffracted by ultrasonic waves in liquid media. *Appl. Phys. Lett.*, 2:62–64, 1963.

[135] M. G. Gazalet, C. Bruneel, G. Waxin, J. M. Rouvaen, and E. Bridoux. Tunable bichromatic acoustooptic deflector. *Appl. Opt.*, 24(2):243–246, Jan 1985.

[136] M. G. Gazalet, S. Carlier, J. P. Picault, G. Waxin, and C. Bruneel. Multifrequency paratellurite acoustooptic modulators. *Appl. Opt.*, 24(24):4435–4438, Dec 1985.

[137] M. G. Gazalet, J. C. Kastelik, C. Bruneel, O. Bazzi, and E. Bridoux. Acousto-optic multifrequency modulators: reduction of the phase-grating, intermodulation products. *Appl. Opt.*, 32(13):2455–2460, May 1993.

[138] M. G. Gazalet, G. Waxin, J. M. Rouvaen, R. Torguet, and E. Bridoux. Independent acoustooptic modulation of the two wavelengths of a bichromatic light beam. *Appl. Opt.*, 23(5):674–681, Mar 1984.

[139] E. Gerdau, R. Rüffer, R. Hollatz, and J. P. Hannon. Quantum beats from nuclei excited by synchrotron radiation. *Phys. Rev. Lett.*, 57(9):1141–1144, Sep 1986.

[140] S. Gianordoli, R. Hainberger, A. Köck, N. Finger, E. Gornik, C. Hanke, and L. Korte. Optimization of the emission characteristics of light emitting diodes by surface plasmons and surface waveguide modes. *Appl. Phys. Lett.*, 77(15):2295–2297, 2000.

[141] E. O. Göbel, K. Leo, T. C. Damen, J. Shah, S. Schmitt-Rink, W. Schäfer, J. F. Müller, and K. Köhler. Quantum beats of excitons in quantum wells. *Phys. Rev. Lett.*, 64(15):1801–1804, Apr 1990.

[142] H. Goldstein, C. Poole, and J. Safko. *Classical Mechanic.* Addison–Wesley, New York, 3rd edition, 2002.

[143] Leon Goldstein, Yoshiji Horikoshi, Seigo Tarucha, and Hiroshi Okamoto. Effect of well size fluctuation on photoluminescence spectrum of alas–gaas superlattices. *Japanese Journal of Applied Physics*, 22(Part 1, No. 10):1489–1492, 1983.

[144] I. Gontijo, M. Boroditsky, E. Yablonovitch, S. Keller, U. K. Mishra, and S. P. DenBaars. Coupling of ingan quantum-well photoluminescence to silver surface plasmons. *Phys. Rev. B*, 60(16):11564–11567, Oct 1999.

[145] J. P. GORDON, C. H. WANG, C. K. N. PATEL, R. E. SLUSHER, and W. J. TOMLINSON. Photon echoes in gases. *Phys. Rev.*, 179(2):294–309, Mar 1969.

[146] W. Gornik, D. Kaiser, W. Lange, J. Luther, and H. H. Schulz. Quantum beats under pulsed dye laser excitation. *Optics Communications*, 6(4):327 – 328, 1972.

[147] Alexander O. Govorov, Garnett W. Bryant, Wei Zhang, Timur Skeini, Jaebeom Lee, Nicholas A. Kotov, Joseph M. Slocik, and Rajesh R. Naik. Excitonàíplasmon interaction and hybrid excitons in semiconductoràímetal nanoparticle assemblies. *Nano Letters*, 6(5):984–994, 2006.

[148] Alexander O. Govorov, Jaebeom Lee, and Nicholas A. Kotov. Theory of plasmon-enhanced förster energy transfer in optically excited semiconductor and metal nanoparticles. *Phys. Rev. B*, 76(12):125308, Sep 2007.

[149] D. J. Griffiths. *Introduction to quantum mechanics*. Prentice Hall, Englewood Cliffs, N.J., 1995.

[150] Ye. F. Gross, B. P. Zakharchenya, and N. M. Reinov. Excitons in cuprous oxide crystals at the temperature of liquid helium (4.2k). *Doklady Akad. Nauk S.S.S.R.*, 97(57):221, 1954.

[151] Stephen B. Grossman, A. Schenzle, and Richard G. Brewer. Pulse fourier-transform optical spectroscopy. *Phys. Rev. Lett.*, 38(6):275–278, Feb 1977.

[152] E. M. Grumstrup, S.-Hee Shim, M. A. Montgomery, N. H. Damrauer, and M. T. Zanni. Facile collection of two-dimensional electronic spectra using femtosecond pulse-shaping technology. *Opt. Express*, 15:16681–16689, 2007.

[153] J. B. Grun, A. Mysyrowicz, F. Raga, A. Bivas, R. Levy, and S. Nikitine. Phonon-assisted emission in cdse. *physica status solidi (b)*, 22(2):K155–K156, 1967.

[154] A. Gutierrez, P. Dorn, J. Zeller, D. King, L. F. Lester, W. Rudolph, and M. Sheik-Bahae. Autocorrelation measurement of femtosecond laser pulses by use of a znse two-photon detector array. *Opt. Lett.*, 24(16):1175–1177, Aug 1999.

[155] R. Van Den Berg H. P. H. Thijssen and S. Völker. Thermal broadening of optical homogeneous linewidths in organic glasses and polymers stud-

ied via photochemical hole-burning. *Chemical Physics Letters*, 97(3):295 – 302, 1983.

[156] E. L. Hahn. Spin echoes. *Phys. Rev.*, 80(4):580–594, Nov 1950.

[157] E. L. Hahn and D. E. Maxwell. Chemical shift and field independent frequency modulation of the spin echo envelope. *Phys. Rev.*, 84(6):1246–1247, Dec 1951.

[158] Peter Hamm, Manho Lim, William F. DeGrado, and Robin M. Hochstrasser. The two-dimensional ir nonlinear spectroscopy of a cyclic penta-peptide in relation to its three-dimensional structure. *Proceedings of the National Academy of Sciences*, 96(5):2036–2041, 1999.

[159] E. G. Harris. *A Pedestrian Approach to Quantum Field Theory*. John Wiley and Sons, Inc., New York, 1972.

[160] S. E. Harris. Tunable acousto-optic method and apparatus. U.S. Patent 3,679,288, 1972.

[161] S. E. HARRIS and R. W. WALLACE. Acousto-optic tunable filter. *J. Opt. Soc. Am.*, 59(6):744–747, Jun 1969.

[162] R. G. Harrison, P. Key, V. I. Little, G. Magyar, and J. Katzenstein. Bragg reflection of laser light from a phase grating in a q-switching liquid. *Applied Physics Letters*, 13(8):253 –255, oct 1968.

[163] S. Hartmann. Photon, spin, and raman echoes. *Quantum Electronics, IEEE Journal of*, 4(11):802 – 807, nov 1968.

[164] H. Hatanaka and T. Hashi. Transient nutations and spin echoes associated with two-quantum transition in multi-level nmr system. *J. Phys. Soc. Jpn.*, 39:1139–1140, 1975.

[165] H. Haug and S. W. Koch. *Quantum Theory of the Optical and Electronic Properties of Semiconductors*. World Scientific Publishing Co., Singapore, 4th edition, 2004.

[166] H. Haug and S. W. Koch. *Quantum Theory of the Optical and Electronic Properties of Semiconductors*. World Scientific Publishing Co., Singapore, 4th edition, 2004.

[167] Scot A. Hawkins, Eric J. Gansen, Martin J. Stevens, Arthur L. Smirl, I. Rumyantsev, R. Takayama, N. H. Kwong, R. Binder, and D. G. Steel. Differential measurements of raman coherence and two-exciton correlations in quantum wells. *Phys. Rev. B*, 68(3):035313, Jul 2003.

[168] Malcolm H. Hebb. Mechanism of exciton-enhanced photoelectric emission in alkali halides. *Phys. Rev.*, 81(5):702–705, Mar 1951.

[169] A. P. Heberle, J. J. Baumberg, and K. Köhler. Ultrafast coherent control and destruction of excitons in quantum wells. *Phys. Rev. Lett.*, 75(13):2598–2601, Sep 1995.

[170] D. L. Hecht. Acousto-optic nonlinearities in multi- frequency acousto-optic diffraction. *IEEE Journal of Quantum Electronics*, 10(9):759 – 760, Sept. 1974.

[171] D. L. Hecht. Multifrequency acousto-optic diffraction. *IEEE Trans. on Sonics and Ultrasonics*, Vol. SU-24(1), 1977.

[172] D. L. Hecht, G. Petrie, and S. Wofford. Multifrequency acousto-optic diffraction in optically birefringent media. In *1979 Ultrasonics Symposium*, pages 46– 50, 1979.

[173] D.L. Hecht. Broadband acousto-optic spectrum analysis. In *1973 Ultrasonics Symposium*, pages 98– 100, 1973.

[174] N. E. Hecker, R. A. Höpfel, N. Sawaki, T. Maier, and G. Strasser. Surface plasmon-enhanced photoluminescence from a single quantum well. *Appl. Phys. Lett.*, 75(11):1577–1579, 1999.

[175] C. V. Heer and N. C. Griffen. Generation of a phase-conjugate wave in the forward direction with thin na-vapor cells. *Opt. Lett.*, 4(8):239–241, Aug 1979.

[176] J. Hegarty and M. D. Sturge. Studies of exciton localization in quantum-well structures by nonlinear-optical techniques. *J. Opt. Soc. Am. B*, 2(7):1143–1154, Jul 1985.

[177] T. F. Heinz. Second-order nonlinear optical effects at surfaces and interfaces. In H.-E. Ponath and G. I. Stegeman, editors, *Nonlinear Surface*

Electromagnetic Phenomena, chapter 5, page 354. Elsevier Science Publishers B. V., Amsterdam, 1991.

[178] J. Kuhl; E. J. Mayer; G. Smith; R. Eccleston; D. Bennhardt; P. Thomas; K. Bott; O. Heller. Optical dephasing of excitons in iii-v semiconductors. In R. T. Phillips, editor, *Coherent Optical Interactions in Semiconductors*, volume 330 of *NATO ASI Series, Series B: Physics*, New York, 1994. Plenum Press.

[179] W. R. Heller and A. Marcus. A note on the propagation of excitation in an idealized crystal. *Physical Review*, 84:809, 1951.

[180] K. Hess. *Advanced Theory of Semiconductor Devices*. Solid state physical electronics series. Prentice-Hall, Englewood Cliffs, N.J., 1988.

[181] G. B. Hocker and C. L. Tang. Observation of the optical transient nutation effect. *Phys. Rev. Lett.*, 21(9):591–594, Aug 1968.

[182] C. A. Hoffman, K. Jarasiunas, H. J. Gerritsen, and A. V. Nurmikko. Measurement of surface recombination velocity in semiconductors by diffraction from picosecond transient free-carrier gratings. *Applied Physics Letters*, 33(6):536 –539, sep 1978.

[183] A. Honold, L. Schultheis, J. Kuhl, and C. W. Tu. Reflected degenerate four-wave mixing on gaas single quantum wells. *Applied Physics Letters*, 52(25):2105 –2107, jun 1988.

[184] A. Honold, L. Schultheis, J. Kuhl, and C. W. Tu. Collision broadening of two-dimensional excitons in a gaas single quantum well. *Phys. Rev. B*, 40(9):6442–6445, Sep 1989.

[185] F N Hooge, T G M Kleinpenning, and L K J Vandamme. Experimental studies on 1/f noise. *Reports on Progress in Physics*, 44(5):479, 1981.

[186] J. J. Hopfield. heory of the contribution of excitons to the complex dielectric constant of crystals. *Physical Review*, 112:1, 1958.

[187] P. Horowitz and W. Hill. *The Art of Electronics*. Cambridge University Press, New York, 2nd edition, 1989.

[188] Koshin Hosoki, Takeshi Tayagaki, Shinpei Yamamoto, Kazunari Matsuda, and Yoshihiko Kanemitsu. Direct and stepwise energy transfer from excitons to plasmons in close-packed metal and semiconductor nanoparticle monolayer films. *Phys. Rev. Lett.*, 100(20):207404, May 2008.

[189] G. Hrbek and W. Watson. A high speed laser alphanumeric generator. In *Proc. Electro-Optical Systems Design Conf.*, pages 271–275, New York, Sept. 1971.

[190] K. Huang. *Statistical Mechanics*. John Wiley and Sons, Inc., New York, 1987.

[191] J. M. Hvam, V. G. Lyssenko, and D. Birkedal. Ultrafast exciton dynamics in semiconductors: Effects of disorder and confinement. *Pure Appl. Chem.*, 67:401, 1995.

[192] John D. Hybl, Allison W. Albrecht, Sarah M. Gallagher Faeder, and David M. Jonas. Two-dimensional electronic spectroscopy. *Chemical Physics Letters*, 297(3-4):307 – 313, 1998.

[193] D. L. Hammond J. A. Kusters, D. A. Wilson. Optimum crystal orientation for acoustically tuned optical filters. *Journal of the Optical Society of America*, 64(4):434, Apr. 1974.

[194] A. Mysyrowicz J. B. Grun, R. Lévy and S. Nikitine. Luminescence of cucl at low temperatures excited by very high intensity light (laser). *Physics Letters A*, 24(1):50 – 52, 1967.

[195] J. D. Jackson. *Classical Electrodynamics*. John Wiley and Sons, Inc., New York, 3rd edition, 1999.

[196] J. D. Jackson. *Classical Electrodynamics*. John Wiley and Sons, Inc., New York, 3rd edition, 1999.

[197] K. Jarasiunas and H. J. Gerritsen. Ambipolar diffusion measurements in semiconductors using nonlinear transient gratings. *Applied Physics Letters*, 33(2):190 –193, jul 1978.

[198] Thomas W. Jarvis, Zheng Sun, and Xiaoqin (Elaine) Li. A simple implementation of optical two-dimensional fourier transform spectroscopy. In

Conference on Lasers and Electro-Optics/International Quantum Electronics Conference, page IThF2. Optical Society of America, 2009.

[199] J. Jeener. Ampère international summer school, basko polje, yugoslavia. 1971.

[200] M. Joffre, D. Hulin, A. Migus, A. Antonetti, C. Benoit à la Guillaume, N. Peyghambarian, M. Lindberg, and S. W. Koch. Coherent effects in pump-probe spectroscopy of excitons. *Opt. Lett.*, 13(4):276–278, Apr 1988.

[201] J. B. Johnson. Thermal agitation of electricity in conductors. *Phys. Rev.*, 32(1):97, Jul 1928.

[202] David M. Jonas. Two-dimensional femtosecond spectroscopy. *Annual Review of Physical Chemistry*, 54(1):425–463, 2003.

[203] David M. Jonas, Stephen E. Bradforth, Sean A. Passino, and Graham R. Fleming. Femtosecond wavepacket spectroscopy: Influence of temperature, wavelength, and pulse duration. *The Journal of Physical Chemistry*, 99(9):2594–2608, 1995.

[204] David M. Jonas, Matthew J. Lang, Yutaka Nagasawa, Taiha Joo, and Graham R. Fleming. Pump-probe polarization anisotropy study of femtosecond energy transfer within the photosynthetic reaction center of rhodobacter sphaeroides r26. *The Journal of Physical Chemistry*, 100(30):12660–12673, 1996.

[205] T. Joo, Y. Jia, J.ÄêY. Yu, M. J. Lang, and G. R. Fleming. Thirdäêorder nonlinear time domain probes of solvation dynamics. *J. Chem. Phys.*, 104(6089), 1996.

[206] J. V. José and E. J. Saletan. *Classical Dynamics: A Contemporary Approach*. Cambridge University Press, Cambridge, U.K, 1988.

[207] Denis Karaiskaj, Alan D. Bristow, Lijun Yang, Xingcan Dai, Richard P. Mirin, Shaul Mukamel, and Steven T. Cundiff. Two-quantum many-body coherences in two-dimensional fourier-transform spectra of exciton resonances in semiconductor quantum wells. *Phys. Rev. Lett.*, 104(11):117401, Mar 2010.

[208] J. C. Kastelik, S. Dupont, H. Benaissa, and M. Pommeray. Bifrequency acousto-optic beam splitter. *Rev. Sci. Instrum.*, 77(7):075103, 2006.

[209] H Kawashima, M M Wefers, and K A Nelson. Femtosecond pulse shaping, multiple-pulse spectroscopy, and optical control. *Annual Review of Physical Chemistry*, 46(1):627–656, 1995.

[210] F. Keilmann. Infrared saturation spectroscopy in p-type germanium. *Quantum Electronics, IEEE Journal of*, 12(10):592 – 597, oct 1976.

[211] Chandler J. Kennedy, John C. Matter, Arthur L. Smirl, Hugo Weiche, Frederic A. Hopf, Sastry V. Pappus, and Marlan O. Scully. Nonlinear absorption and ultrashort carrier relaxation times in germanium under

irradiation by picosecond pulses. *Phys. Rev. Lett.*, 32(8):419–421, Feb 1974.

[212] Dorine Keusters, Howe-Siang Tan, and Warren. Role of pulse phase and direction in two-dimensional optical spectroscopy. *The Journal of Physical Chemistry A*, 103(49):10369–10380, 1999.

[213] P. Key, R. Harrison, V. Little, and J. Katzenstein. Bragg reflection from a phase grating induced by nonlinear optical effects in liquids. *Quantum Electronics, IEEE Journal of*, 6(10):641 – 646, oct 1970.

[214] M. Khalil, N. Demirdöven, and A. Tokmakoff. Obtaining absorptive line shapes in two-dimensional infrared vibrational correlation spectra. *Phys. Rev. Lett.*, 90(4):047401, Jan 2003.

[215] D. S. Kim, J. Shah, D. A. B. Miller, T. C. Damen, A. Vinattieri, Wilfred Schäfer, and L. N. Pfeiffer. Femtosecond pulse distortion in gaas quantum wells and its effect on pump-probe or four-wave-mixing experiments. *Phys. Rev. B*, 50(24):18240–18249, Dec 1994.

[216] Dai-Sik Kim, Jagdeep Shah, T. C. Damen, W. Schäfer, F. Jahnke, S. Schmitt-Rink, and K. Köhler. Unusually slow temporal evolution of femtosecond four-wave-mixing signals in intrinsic gaas quantum wells: Direct evidence for the dominance of interaction effects. *Phys. Rev. Lett.*, 69(18):2725–2728, Nov 1992.

[217] C. Kittel. *Thermal Physics*. John Wiley and Sons, Inc., 1969.

[218] W. R. Klein. Theoretical efficiencyof bragg devices. *Proc. IEEE (Lett.)*, 54:803–804, May 1966.

[219] W. R. Klein and B. D. Cook. Unified approach to ultrasonic light diffraction. *IEEE Transactions on Sonics and Ultrasonics*, SU-14(3):123, 1967.

[220] A. H. Kleinpenning, T. G. M.; de Kuijper. Relation between variance and sample duration of 1/f noise signals. *Journal of Applied Physics*, 63(1):43–45, 2009.

[221] C. F. Klingshirn. *Semiconductor Optics*. Springer-Verlag, Berlin, 1997.

[222] M. Koch, J. Feldmann, G. von Plessen, S. T. Cundiff, E. O. Göbel, P. Thomas, and K. Köhler. Koch et al. reply. *Phys. Rev. Lett.*, 73(1):210, Jul 1994.

[223] M. Koch, J. Feldmann, G. von Plessen, E. O. Göbel, P. Thomas, and K. Köhler. Quantum beats versus polarization interference: An experimental distinction. *Phys. Rev. Lett.*, 69(25):3631–3634, Dec 1992.

[224] A. Kock, E. Gornik, M. Hauser, and W. Beinstingl. Strongly directional emission from algaas/gaas light-emitting diodes. *Applied Physics Letters*, 57(22):2327 –2329, nov 1990.

[225] W. Kohn and J. M. Luttinger. Quantum theory of cyclotron resonance in semiconductors. *Phys. Rev.*, 96(2):529–530, Oct 1954.

[226] A. Korpel. Acousto-optics-a review of fundamentals. In *Proceedings of the IEEE*, volume 69, page 48, January 1981.

[227] Adrianus Korpel. Two-dimensional plane wave theory of strong acousto-optic interaction in isotropic media. *J. Opt. Soc. Am.*, 69(5):678–683, May 1979.

[228] R. Kubo. *A Stochastic Theory of Line Shape*, pages 101–127. John Wiley and Sons, Inc., 2007.

[229] N. A. Kurnit, I. D. Abella, and S. R. Hartmann. Observation of a photon echo. *Phys. Rev. Lett.*, 13(19):567–568, Nov 1964.

[230] J. A. Kusters. Electronically tunable acousto-optic filter having improved light and acoustic wave interaction. U.S. Patent 3,687,521, 1972.

[231] I. Kuznetsova, T. Meier, S. T. Cundiff, and P. Thomas. Determination of homogeneous and inhomogeneous broadening in semiconductor nanostructures by two-dimensional fourier-transform optical spectroscopy. *Phys. Rev. B*, 76(15):153301, Oct 2007.

[232] I. Kuznetsova, P. Thomas, T. Meier, T. Zhang, X. Li, R.P. Mirin, and S.T. Cundiff. Signatures of many-particle correlations in two-dimensional fourier-transform spectra of semiconductor nanostructures. *Solid State Communications*, 142(3):154 – 158, 2007.

[233] L. B. Lambert. Wide-band, instantaneous spectrum analyzers employing delay-line light modulators. In *IRE Int. Convention Rec., Pt. 6*, volume 10, pages 69–78, 1962.

[234] Wolfgang Langbein and Brian Patton. Heterodyne spectral interferometry for multidimensional nonlinear spectroscopy of individual quantum systems. *Opt. Lett.*, 31(8):1151–1153, Apr 2006.

[235] F. Langhojer. *New techniques in liquid-phase ultrafast spectroscopy.* PhD thesis, Julius-Maximilians-Universität Würzburg, Würzburg, Germany, Oct. 2009.

[236] Patrick Langlois and Erich P. Ippen. Measurement of pulse asymmetry by three-photon-absorption autocorrelation in a gaasp photodiode. *Opt. Lett.*, 24(24):1868–1870, Dec 1999.

[237] A. Laubereau, G. Wochner, and W. Kaiser. Collective beating of molecular vibrations in liquids on the picosecond time scale. *Optics Communications*, 17(1):91 – 94, 1976.

[238] Kees Lazonder, Maxim S. Pshenichnikov, and Douwe A. Wiersma. Easy interpretation of optical two-dimensional correlation spectra. *Opt. Lett.*, 31(22):3354–3356, Nov 2006.

[239] Jaebeom Lee, Alexander O. Govorov, John Dulka, and Nicholas A. Kotov. Bioconjugates of cdte nanowires and au nanoparticles:äâ plas-

monàíexciton interactions, luminescence enhancement, and collective effects. *Nano Letters*, 4(12):2323–2330, 2004.

[240] K. Leo, T. C. Damen, J. Shah, and K. Köhler. Quantum beats of free and bound excitons in gaas/alxga1-xas quantum wells. *Phys. Rev. B*, 42:11359—11361, 1990.

[241] K. Leo, E. O. Göbel, T. C. Damen, J. Shah, S. Schmitt-Rink, W. Schäfer, J. F. Müller, K. Köhler, and P. Ganser. Subpicosecond four-wave mixing in gaas/al_xga_{1-x}as quantum wells. *Phys. Rev. B*, 44(11):5726–5737, Sep 1991.

[242] K. Leo, M. Wegener, J. Shah, D. S. Chemla, E. O. Göbel, T. C. Damen, S. Schmitt-Rink, and W. Schäfer. Effects of coherent polarization interactions on time-resolved degenerate four-wave mixing. *Phys. Rev. Lett.*, 65(11):1340–1343, Sep 1990.

[243] Karl Leo, Theo C. Damen, Jagdeep Shah, Ernst O. Gobel, and Klaus Kohler. Quantum beats of light hole and heavy hole excitons in quantum wells. *Applied Physics Letters*, 57(1):19 –21, jul 1990.

[244] Karl Leo, Jagdeep Shah, Ernst O. Göbel, Theodore C. Damen, Stefan Schmitt-Rink, Wilfried Schäfer, and Klaus Köhler. Coherent oscillations of a wave packet in a semiconductor double-quantum-well structure. *Phys. Rev. Lett.*, 66(2):201–204, Jan 1991.

[245] L. Lepetit, G. Chériaux, and M. Joffre. Linear techniques of phase measurement by femtosecond spectral interferometry for applications in spectroscopy. *J. Opt. Soc. Am. B*, 12(12):2467–2474, Dec 1995.

[246] L. Lepetit and M. Joffre. Two-dimensional nonlinear optics using fourier-transform spectral interferometry. *Opt. Lett.*, 21(8):564–566, Apr 1996.

[247] M. Levenson and G. Eesley. Polarization selective optical heterodyne detection for dramatically improved sensitivity in laser spectroscopy. *Applied Physics A: Materials Science and Processing*, 19:1–17, 1979. 10.1007/BF00900531.

[248] Xiaoqin Li, Tianhao Zhang, Camelia N. Borca, and Steven T. Cundiff. Many-body interactions in semiconductors probed by optical two-dimensional fourier transform spectroscopy. *Phys. Rev. Lett.*, 96(5):057406, Feb 2006.

[249] Xiaoqin Li Li. *Coherent Transient Nonlinear Spectroscopy Studies of Single Semiconductor Quantum Dots*. PhD thesis, University of Michigan at Ann Arbor, Ann Arbor, August 2003.

[250] M. Lindberg, R. Binder, and S. W. Koch. Theory of the semiconductor photon echo. *Phys. Rev. A*, 45(3):1865–1875, Feb 1992.

[251] M. Lindberg and S. W. Koch. Effective bloch equations for semiconductors. *Phys. Rev. B*, 38(5):3342–3350, Aug 1988.

[252] J. Vučković; M. Lončar; and A. Scherer. Surface plasmon enhanced light-emitting diode. *IEEE Journal of Quantum Electronics*, 36(10):1131, October 2000.

[253] H. A. Lorentz. *Theory of Electrons*. Dover, New York, 2nd edition, 1952.

[254] Michael Lorke, Jan Seebeck, Torben R. Nielsen, Paul Gartner, and Frank Jahnke. Many-body effects in semiconductor quantum dots. In M. Kremer G. Münster, D. Wolf, editor, *NIC Symposium 2006*, volume 32 of *NIC Series*, pages 167–172, Jülich, 2006. John von Neumann Institute for Computing.

[255] R. Lucas and P. Biquard. Propriétés optiques des milieux solides et liquides soumis aux vibrations élastiques ultra sonores. *J. Phys. Radium*, 3(10):464–477, 1932.

[256] Marie S. C. Luo, Shun Lien Chuang, Paul C. M. Planken, Igal Brener, and Martin C. Nuss. Coherent double-pulse control of quantum beats in a coupled quantum well. *Phys. Rev. B*, 48(15):11043–11050, Oct 1993.

[257] V. G. Lyssenko, J. Erland, I. Balslev, K.-H. Pantke, B. S. Razbirin, and J. M. Hvam. Nature of nonlinear four-wave-mixing beats in semiconductors. *Phys. Rev. B*, 48(8):5720–5723, Aug 1993.

[258] H. Rockwood M. Bennett, M. F. Schatz and K. Wiesenfeld. Huygens's clocks. *Proc. R. Soc. Lond. A*, 458:563–579, 2002.

[259] T. H. Maiman. Stimulated optical radiation in ruby. *Nature*, 187(4736):493–494, 08 1960.

[260] G. E. Martin and A. S. Zektzer. *Two-Dimensional NMR Methods for Establishing Molecular Connectivity.* John Wiley and Sons, New York, 1988.

[261] Elliott W. Montroll and Michael F. Shlesinger. On 1/f noise and other distributions with long tails. *Proceedings of the National Academy of Sciences*, 79(10):3380–3383, 1982.

[262] T. Mossberg, A. Flusberg, R. Kachru, and S. R. Hartmann. Total scattering cross section for na on he measured by stimulated photon echoes. *Phys. Rev. Lett.*, 42(25):1665–1669, Jun 1979.

[263] G. Mourou. Spectral hole burning in dye solutions. *Quantum Electronics, IEEE Journal of*, 11(1):1 – 8, jan 1975.

[264] K. Okamoto; I. Niki; A. Shvartser; Y. Narukawa; T. Mukai; and A. Schere. Surface-plasmon-enhanced light emitters based on ingan quantum wells. *Nature Materials*, 3:601 – 605, 2004.

[265] S. Mukamel. *Principles of Nonlinear Optical Spectroscopy.* Oxford University Press, New York, 1995.

[266] Jeffrey A. Myers, Kristin L. Lewis, Patrick F. Tekavec, and Jennifer P. Ogilvie. Two-color two-dimensional fourier transform electronic spectroscopy with a pulse-shaper. *Opt. Express*, 16(22):17420–17428, Oct 2008.

[267] A. Mysyrowicz, J. B. Grun, F. Raga, and S. Nikitine. Luminescence of cds at low temperature excited by very high intensity light (laser). *Physics Letters A*, 24(6):335 – 336, 1967.

[268] A. Mysyrowicz, J.B. Grun, A. Bivas, R. Levy, and S. Nikitine. Intensity dependence of emission lines in cds upon excitation intensity (laser) at very low temperature. *Physics Letters A*, 25(3):286 – 287, 1967.

[269] N. Sawaki N. E. Hecker, R. A. Hopfel. Enhanced light emission from a single quantum well located near a metal coated surface. *Physica E: Low-dimensional Systems and Nanostructures*, 2(1-4):98 – 101, 1998.

[270] A. Mysyrowicz N. Peychambarian, S. W. Koch. *I. Introduction to Semiconductor Optics*. Prentice Hall, Englewood Cliffs, N.J., 1993.

[271] S. Nakajima, Y. Toyozawa, and R. Abe. *The Physics of Elementary Excitation*, volume 12 of *Springer Series in Solid-State Sciences*. Springer-Verlag, Berlin, Heidelburg, 1980.

[272] David A. Naylor, Brad G. Gom, Trevor R. Fulton, Margaret K. Tahic, and Gary R. Davis. Increased efficiency through undersampling in fourier transform spectroscopy. In *Fourier Transform Spectroscopy/*

Hyperspectral Imaging and Sounding of the Environment, page FTuD14. Optical Society of America, 2005.

[273] Keith A. Nelson, Roger Casalegno, R. J. Dwayne Miller, and M. D. Fayer. Laser-induced excited state and ultrasonic wave gratings: Amplitude and phase grating contributions to diffraction. *J. Chem. Phys.*, 77(3):1144–1152, 1982.

[274] Arup Neogi, Chang-Won Lee, Henry O. Everitt, Takamasa Kuroda, Atsushi Tackeuchi, and Eli Yablonovitch. Enhancement of spontaneous recombination rate in a quantum well by resonant surface plasmon coupling. *Phys. Rev. B*, 66(15):153305, Oct 2002.

[275] I. Newton. *Philosophiae naturalis principia mathematica*, volume I. 1687.

[276] R. B. Northrop. *Introduction to Instrumentation and Measurements*. Taylor and Francis Group, Boca Raton, FL, 2nd edition, 2005.

[277] H. M. Nussenzveig. *Causality and Dispersion Relations*. Academic Press, Inc, New York, 1972.

[278] H. Nyquist. Certain topics in telegraph transmission theory. *Transactions of the A. I. E. E.*, 47(2):617–644, February 1928.

[279] H. Nyquist. Thermal agitation of electric charge in conductors. *Physical Review*, 32:110, July 1928.

[280] Koichi Okamoto, Isamu Niki, Axel Scherer, Yukio Narukawa, Takashi Mukai, and Yoichi Kawakami. Surface plasmon enhanced spontaneous emission rate of ingan/gan quantum wells probed by time-resolved photoluminescence spectroscopy. *Appl. Phys. Lett.*, 87(7):071102, 2005.

[281] Ko Okumura, Andrei Tokmakoff, and Yoshitaka Tanimura. Two-dimensional line-shape analysis of photon-echo signal. *Chemical Physics Letters*, 314(5-6):488 – 495, 1999.

[282] A. Ourmazd, D. W. Taylor, J. Cunningham, and C. W. Tu. Chemical mapping of semiconductor interfaces at near-atomic resolution. *Phys. Rev. Lett.*, 62(8):933–936, Feb 1989.

[283] H. Wang; Z. Zheng; D. E. Leaird; A. M. Weiner; T. A. Dorschner; J. J. Fijol; L. J. Friedman; H. Q. Nguyen; L. A. Palmaccio. 20-fs pulse shaping with a 512-element phase-only liquid crystal modulator. *IEEE Journal of Selected Topics in Quantum Electronics*, 7(4):718–727, 2001.

[284] M. Cho; J.-Y. Yu; T. Joo; Y. Nagasawa; S. A. Passino; and G. R. Fleming. The integrated photon echo and solvation dynamics. *J. Phys. Chem.*, 100:11944–11953, 1996.

[285] C. K. N. Patel and R. E. Slusher. Photon echoes in gases. *Phys. Rev. Lett.*, 20(20):1087–1089, May 1968.

[286] Shekhar Patkar, A. E. Paul, W. Sha, J. A. Bolger, and Arthur L. Smirl. Degree and state of polarization of the time-integrated coherent four-

wave mixing signal from semiconductor multiple quantum wells. *Phys. Rev. B*, 51(16):10789–10794, Apr 1995.

[287] B. Patton, W. Langbein, U. Woggon, L. Maingault, and H. Mariette. Time- and spectrally-resolved four-wave mixing in single *cdte*?*znte* quantum dots. *Phys. Rev. B*, 73(23):235354, Jun 2006.

[288] T. Hansch; M. Pernier; and A. Schawlow. Laser action of dyes in gelatin. *IEEE Journal of Quantum Electronics*, 7(1):45–46, 1971.

[289] P. Phariseau. On the diffraction of light by progressive supersonic waves. *Proc. Indian Acad. Sci.*, 44A:165–170, October 1956.

[290] Donald W. Phillion, Dirk J. Kuizenga, and A. E. Siegman. Subnanosecond relaxation time measurements using a transient induced grating method. *Applied Physics Letters*, 27(2):85 –87, jul 1975.

[291] Mark Phillips and Hailin Wang. Coherent oscillation in four-wave mixing of interacting excitons. *Solid State Communications*, 111(6):317 – 321, 1999.

[292] David Pines and David Bohm. A collective description of electron interactions: Ii. collective *vs* individual particle aspects of the interactions. *Phys. Rev.*, 85(2):338–353, Jan 1952.

[293] I. Pockrand, A. Brillante, and D. Möbius. Exciton–surface plasmon coupling: An experimental investigation. *J. Chem. Phys.*, 77:6289, 1982.

[294] W. Thomas Pollard, Susan L. Dexheimer, Qing Wang, Linda A. Peteanu, Charles V. Shank, and Richard A. Mathies. Theory of dynamic absorption spectroscopy of nonstationary states. 4. application to 12-fs resonant impulsive raman spectroscopy of bacteriorhodopsin. *The Journal of Physical Chemistry*, 96(15):6147–6158, 1992.

[295] E. M. Purcell. Spontaneous emission probabilities at radio frequencies. *Phys. Rev.*, 69:681, 1946.

[296] A. Wokaun R. R. Ernst, G. Bodenhausen. *Principles of Nuclear Magnetic Resonance in One and Two Dimensions*. Clarendon Press, Oxford, 1987.

[297] I. I. Rabi. Space quantization in a gyrating magnetic field. *Phys. Rev.*, 51(8):652–654, Apr 1937.

[298] I. I. Rabi, S. Millman, P. Kusch, and J. R. Zacharias. The magnetic moments of ${}_3li^6$, ${}_3li^7$ and ${}_9f^{19}$. *Phys. Rev.*, 53(6):495, Mar 1938.

[299] I. I. Rabi, S. Millman, P. Kusch, and J. R. Zacharias. The molecular beam resonance method for measuring nuclear magnetic moments. the magnetic moments of ${}_3li^6$, ${}_3li^7$ and ${}_9f^{19}$. *Phys. Rev.*, 55(6):526–535, Mar 1939.

[300] C. V. Raman and N. S. Nagendra Nath. The diffraction of light by high frequency sound waves: Part i. *Proceedings Mathematical Sciences*, 2:406–412, 1935.

[301] C. V. Raman and N. S. Nagendra Nath. The diffraction of light by sound waves of high frequency: Part ii. *Proceedings Mathematical Sciences*, 2:413–420, 1935.

[302] C. V. Raman and N. S. Nagendra Nath. The diffraction of light by high frequency sound waves: Part iii doppler effect and coherence phenomena. *Proceedings Mathematical Sciences*, 3(1):75–84, 1936.

[303] C. V. Raman and N. S. Nagendra Nath. The diffraction of light by high frequency sound waves: Part iv generalised theory. *Proceedings Mathematical Sciences*, 3(2):119–125, 1936.

[304] C. V. Raman and N. S. Nagendra Nath. The diffraction of light by high frequency sound waves: Part v general considerations—oblique incidence and amplitude changes. *Proceedings Mathematical Sciences*, 3(5):459–465, 1936.

[305] N. F. Ramsey and E. M. Purcell. Interactions between nuclear spins in molecules. *Phys. Rev.*, 85(1):143–144, Jan 1952.

[306] Alfred G. Redfield. Nuclear magnetic resonance saturation and rotary saturation in solids. *Phys. Rev.*, 98(6):1787–1809, Jun 1955.

[307] L. Frank Register. Unpublished course notes on semiconductor physics. 2009.

[308] L. E. Reichl. *A modern course in statistical physics.* Wiley-Interscience, New York, 1998.

[309] D. T. Reid, M. Padgett, C. McGowan, W. E. Sleat, and W. Sibbett. Light-emitting diodes as measurement devices for femtosecond laser pulses. *Opt. Lett.*, 22(4):233–235, Feb 1997.

[310] D. C. Reynolds, K. K. Bajaj, C. W. Litton, P. W. Yu, Jasprit Singh, W. T. Masselink, R. Fischer, and H. Morkoc. Determination of interfacial quality of gaas-gaalas multi-quantum well structures using photoluminescence spectroscopy. *Applied Physics Letters*, 46(1):51 –53, jan 1985.

[311] F. Riehle. *Frequency Standards: Basics and Applications*. Wiley-VCH Verlag GmbH and Co. KGaA, Weinheim, Germany, 2004.

[312] R. H. Ritchie. Plasma losses by fast electrons in thin films. *Phys. Rev.*, 106(5):874–881, Jun 1957.

[313] M. J. Rosker, F. W. Wise, and C. L. Tang. Femtosecond relaxation dynamics of large molecules. *Phys. Rev. Lett.*, 57(3):321–324, Jul 1986.

[314] W. Rudolph, M. Sheik-Bahae, A. Bernstein, and L. F. Lester. Femtosecond autocorrelation measurements based on two-photon photoconductivity in znse. *Opt. Lett.*, 22(5):313–315, Mar 1997.

[315] J. J. Sakurai. *Modern quantum mechanics*. Addison-Wesley Pub. Co., Reading, Mass., 1994.

[316] V. Saptari. *Fourier-Transform Spectroscopy Instrumentation Engineering*. SPIE – The International Society for Optical Engineering, Bellingham, Washington, 2004.

[317] R. I. Scarlet. Diffractive scattering of picosecond light pulses in absorbing liquids. *Phys. Rev. A*, 6(6):2281–2291, Dec 1972.

[318] K.-H.; Schäfer, W.; Schuldt and R. Binder. Theory of the optical stark effect in semiconductors. *physica status solidi (b)*, 150(2):407–412, 1988.

[319] Wilfried Schäfer. Recent developments in the theory of highly excited semiconductors. In U. Rössler, editor, *Festkörperprobleme 28*, volume 28 of *Advances in Solid State Physics*, pages 63–85. Springer Berlin / Heidelberg, 1988. 10.1007/BFb0107848.

[320] S. Schmitt-Rink and D. S. Chemla. Collective excitations and the dynamical stark effect in a coherently driven exciton system. *Phys. Rev. Lett.*, 57(21):2752–2755, Nov 1986.

[321] S. Schmitt-Rink, D. S. Chemla, and H. Haug. Nonequilibrium theory of the optical stark effect and spectral hole burning in semiconductors. *Phys. Rev. B*, 37(2):941–955, Jan 1988.

[322] S. Schmitt-Rink, D. S. Chemla, and D. A. B. Miller. Theory of transient excitonic optical nonlinearities in semiconductor quantum-well structures. *Phys. Rev. B*, 32(10):6601–6609, Nov 1985.

[323] S. Schmitt-Rink, D.S. Chemla, and D.A.B. Miller. Linear and nonlinear optical properties of semiconductor quantum wells. *Advances in Physics*, 38(2):89–188, 1989.

[324] L. Schultheis and J. Hegarty. Phase coherence of 2d excitons in gaas-algaas quantum wells. *Journal de Physique Colloques*, 46(C7):C7–167–C7–171, 1985.

[325] L. Schultheis, A. Honold, J. Kuhl, K. Köhler, and C. W. Tu. Optical dephasing of homogeneously broadened two-dimensional exciton transitions in gaas quantum wells. *Phys. Rev. B*, 34(12):9027–9030, Dec 1986.

[326] L. Schultheis, J. Kuhl, A. Honold, and C. W. Tu. Picosecond phase coherence and orientational relaxation of excitons in gaas. *Phys. Rev. Lett.*, 57(14):1797–1800, Oct 1986.

[327] L. Schultheis, J. Kuhl, A. Honold, and C. W. Tu. Picosecond phase coherence and orientational relaxation of excitons in gaas. *Phys. Rev. Lett.*, 57(14):1797–1800, Oct 1986.

[328] L. Schultheis, J. Kuhl, A. Honold, and C. W. Tu. Ultrafast phase relaxation of excitons via exciton-exciton and exciton-electron collisions. *Phys. Rev. Lett.*, 57(13):1635–1638, Sep 1986.

[329] L. Schultheis, M. D. Sturge, and J. Hegarty. Photon echoes from two-dimensional excitons in gaas-algaas quantum wells. *Applied Physics*

Letters, 47(9):995 –997, nov 1985.

[330] M. O. Scully and M. S. Zubairy. *Quantum optics*. Cambridge University Press, Cambridge, U.K, 1997.

[331] J. Shah. *Ultrafast Spectroscopy of Semiconductors and Semiconductor Nanostructures*, volume 115 of *Springer Series in Solid-State Science*. Springer-Verlag, Berlin, 1996.

[332] M. L. Shah. Acousto-optic polychromatic light modulator. U.S. Patent 5,463,493, 1995.

[333] C. Shank and D. Auston. Picosecond diffusion dynamics of optically excited electron-hole plasmas in semi-conductors. *Quantum Electronics, IEEE Journal of*, 10(9):745, sep 1974.

[334] C. H. Brito Cruz; J. P. Gordon; P. C. Becker; R. L. Fork; C. V. Shank. Dynamics of spectral hole burning. *IEEE Journal of Quantum Electronics*, 24(2):261–269, 1988.

[335] C. V. Shank and D. H. Auston. Parametric coupling in an optically excited plasma in ge. *Phys. Rev. Lett.*, 34(8):479–481, Feb 1975.

[336] C. V. Shank and E. P. Ippen. Anisotropic absorption saturation with picosecond pulses. *Applied Physics Letters*, 26(2):62 –63, jan 1975.

[337] C. V. Shank and E. P. Ippen. Anisotropic absorption saturation with picosecond pulses. *Applied Physics Letters*, 26(2):62 –63, jan 1975.

[338] CV Shank, EP Ippen, and R Bersohn. Time-resolved spectroscopy of hemoglobin and its complexes with subpicosecond optical pulses. *Science*, 193(4247):50–51, 1976.

[339] CV Shank, EP Ippen, and R Bersohn. Time-resolved spectroscopy of hemoglobin and its complexes with subpicosecond optical pulses. *Science*, 193(4247):50–51, 1976.

[340] R. Shankar. *Principles of Quantum Mechanics*. Kluwer Academic/Plenum Publishers, New York, 2nd edition, 1994.

[341] C.E. Shannon. Communication in the presence of noise. *Proceedings of the IRE*, 37(1):10–21, Jan. 1949.

[342] S.-H. Shim and M. T. Zanni. How to turn your pump probe instrument into a multidimensional spectrometer: 2d ir and vis spectroscopies via pulse shaping. *Physical Chemistry Chemical Physics*, 11:737–884, 2009.

[343] John A. Shirley, Robert J. Hall, and Alan C. Eckbreth. Folded boxcars for rotational raman studies. *Opt. Lett.*, 5(9):380–382, Sep 1980.

[344] R. L. Shoemaker and Richard G. Brewer. Two-photon superradiance. *Phys. Rev. Lett.*, 28(22):1430–1433, May 1972.

[345] R. L. Shoemaker and Frederic A. Hopf. Observation of quantum beats in photon echoes and optical nutation. *Phys. Rev. Lett.*, 33(26):1527–1530, Dec 1974.

[346] M S Skolnick, P R Tapster, S J Bass, A D Pitt, N Apsley, and S P Aldred. Investigation of ingaas-inp quantum wells by optical spectroscopy. *Semiconductor Science and Technology*, 1(1):29, 1986.

[347] A. Smirl, T. Boggess, B. Wherrett, G. Perryman, and A. Miller. Picosecond transient orientational and concentration gratings in germanium. *Quantum Electronics, IEEE Journal of*, 19(4):690 – 700, apr 1983.

[348] A. Smirl, T. Boggess, B. Wherrett, G. Perryman, and A. Miller. Picosecond transient orientational and concentration gratings in germanium. *Quantum Electronics, IEEE Journal of*, 19(4):690 – 700, apr 1983.

[349] A. L. Smirl, X. Chen, and O. Buccafusca. Heavy-hole and light-hole quantum beats in the polarization state of coherent emission from quantum wells. *IEEE Journal of Quantum Electronics*, 35(4):523, April 1999.

[350] A. L. Smirl, W. J. Walecki, Xiayuan Chen, and O. Buccafusca. Dynamics of the amplitude, phase and polarization state of coherent emission from quantum wells. *physica status solidi (b)*, 204(1):16–19, 1997.

[351] Arthur L. Smirl, Thomas F. Boggess, and F. A. Hopf. Generation of a forward-traveling phase-conjugate wave in germanium. *Optics Communications*, 34(3):463 – 468, 1980.

[352] Arthur L. Smirl, Martin J. Stevens, X. Chen, and O. Buccafusca. Heavy-hole and light-hole oscillations in the coherent emission from quantum wells: Evidence for exciton-exciton correlations. *Phys. Rev. B*, 60(11):8267–8275, Sep 1999.

[353] J. J. Song, J. H. Lee, and M. D. Levenson. Picosecond relaxation measurements by polarization spectroscopy in condensed phases. *Phys. Rev. A*, 17(4):1439–1447, Apr 1978.

[354] Charles Stafford, Stefan Schmitt-Rink, and Wilfried Schaefer. Nonlinear optical response of two-dimensional magnetoexcitons. *Phys. Rev. B*, 41(14):10000–10011, May 1990.

[355] Stanford Research Systems, Sunnyvale, CA. *MODEL SR830 DSP Lock-In Amplifier*, 2.3 edition, 12 2006.

[356] Katherine W. Stone, Kenan Gundogdu, Daniel B. Turner, Xiaoqin Li, Steven T. Cundiff, and Keith A. Nelson. Two-quantum 2d ft electronic spectroscopy of biexcitons in gaas quantum wells. *Science*, 324(5931):1169–1173, 2009.

[357] T. Stroucken, A. Knorr, C. Anthony, A. Schulze, P. Thomas, S. W. Koch, M. Koch, S. T. Cundiff, J. Feldmann, and E. O. Göbel. Light propagation and disorder effects in semiconductor multiple quantum wells. *Phys. Rev. Lett.*, 74(12):2391–2394, Mar 1995.

[358] Zheng Sun, Thomas Jarvis, and Xiaoqin Li. Interplay between disorder and coulomb correlations in semiconductors. In *Conference on Lasers and Electro-Optics/International Quantum Electronics Conference*, page IThF1. Optical Society of America, 2009.

[359] Zheng Sun, Thomas W. Jarvis, Xiaoqin Li, Mikhail Erementchouk, and Michael N. Leuenberger. Probing many-body interactions in a disordered semiconductor quantum well with electronic two-dimensional fourier transform spectroscopy. In *Proc. SPIE*, volume 7600, page 76000U. SPIE, 2010.

[360] Dieter Suter, Harald Klepel, and Jürgen Mlynek. Time-resolved two-dimensional spectroscopy of optically driven atomic sublevel coherences. *Phys. Rev. Lett.*, 67(15):2001–2004, Oct 1991.

[361] Patrick F. Tekavec, Jeffrey A. Myers, Kristin L. M. Lewis, and Jennifer P. Ogilvie. Two-dimensional electronic spectroscopy with a continuum probe. *Opt. Lett.*, 34(9):1390–1392, May 2009.

[362] A. ten Wolde, L. D. Noordam, A. Lagendijk, and H. B. van Linden van den Heuvell. Observation of radially localized atomic electron wave packets. *Phys. Rev. Lett.*, 61(18):2099–2101, Oct 1988.

[363] Peifang Tian, Dorine Keusters, Yoshifumi Suzaki, and Warren S. Warren. Femtosecond phase-coherent two-dimensional spectroscopy. *Science*, 300(5625):1553–1555, 2003.

[364] H. C. Torrey. Transient nutations in nuclear magnetic resonance. *Phys. Rev.*, 76(8):1059–1068, Oct 1949.

[365] C. W. Tu, R. C. Miller, B. A. Wilson, P. M. Petroff, T. D. Harris, R. F. Kopf, S. K. Sputz, and M. G. Lamont. Properties of (al,ga)as/gaas heterostructures grown by molecular beam epitaxy with growth interruption. *Journal of Crystal Growth*, 81(1-4):159 – 163, 1987.

[366] D. B. Turner and K. A. Nelson. Coherent measurements of high-order electronic correlations in quantum wells. *Nature*, 466:1089–1092, 2010.

[367] Daniel B. Turner, Katherine W. Stone, Kenan Gundogdu, and Keith A. Nelson. Three-dimensional electronic spectroscopy of excitons in gaas quantum wells. *J. Chem. Phys.*, 131(14):144510, 2009.

[368] N. Uchida and N. Niizeki. Acoustooptic deflection materials and techniques. In *Proceedings of the IEEE*, volume 61, page 1073, August 1973.

[369] N. Uchida and N. Niizeki. Acoustooptic deflection materials and techniques. *Proc. IEEE*, 61(8):1073, August 1973.

[370] Naoya Uchida. Acousto-optical pattern display using pulse-modulated ultrasound. *Optical and Quantum Electronics*, 2:43–45, 1970. 10.1007/BF01436154.

[371] D. J. Ulness, J. C. Kirkwood, and A. C. Albrecht. *Encyclopedia of Chemical Physics and Physical Chemistry*, volume II, chapter Raman spectrscopy, pages 1017–1062. Inst. Phys., Philadelphia, 2001.

[372] H. Umezawa. *Quantum Field Theory.* North-Holland Publishing Company, Amsterdam, 1956.

[373] P. Vasa, R. Pomraenke, S. Schwieger, Yu. I. Mazur, Vas. Kunets, P. Srinivasan, E. Johnson, J. E. Kihm, D. S. Kim, E. Runge, G. Salamo, and C. Lienau. Coherent exciton–surface-plasmon-polariton interaction in hybrid metal-semiconductor nanostructures. *Phys. Rev. Lett.*, 101(11):116801, Sep 2008.

[374] S. Velsko, J. Trout, and R. M. Hochstrasser. Quantum beating of vibrational factor group components in molecular solids. *J. Chem. Phys.*, 79(5):2114–2120, 1983.

[375] B. Vogelsanger, M. Andrist, and A. Bauder. Two-dimensional correlation experiments in microwave fourier transform spectroscopy. *Chemical Physics Letters*, 144(2):180 – 186, 1988.

[376] B. Vogelsanger and A. Bauder. Two-dimensional microwave fourier transform spectroscopy. *J. Chem. Phys.*, 92(7):4101–4114, 1990.

[377] A. von Jena and H. Lessing. Coherent coupling effects in picosecond absorption experiments. *Applied Physics A: Materials Science and Processing*, 19:131–144, 1979. 10.1007/BF00932387.

[378] G. Wäckerle, St. Appelt, and M. Mehring. Two-dimensional optical spectroscopy by periodic excitation of sublevel coherence with subdoppler resolution. *Phys. Rev. A*, 43(1):242–250, Jan 1991.

[379] Wolfgang Wagner, Chunqiang Li, John Semmlow, and Warren Warren. Rapid phase-cycled two-dimensional optical spectroscopy in fluorescence and transmission mode. *Opt. Express*, 13(10):3697–3706, May 2005.

[380] D. W. Wang and S. Das Sarma. Many-body effects on excitonic optical properties of photoexcited semiconductor quantum wire structures. *Phys. Rev. B*, 64(19):195313, Oct 2001.

[381] G. H. Wannier. The structure of electronic excitation levels in insulating crystals. *Physical Review*, 52:191, 1937.

[382] W. S. Warren and Ahmed H. Zewail. Multiple phase-coherent laser pulses in optical spectroscopy. i. the technique and experimental applications. *J. Chem. Phys.*, 78(5):2279–2297, 1983.

[383] C. A. Warwick, W. Y. Jan, A. Ourmazd, and T. D. Harris. Does luminescence show semiconductor interfaces to be atomically smooth? *Applied Physics Letters*, 56(26):2666 –2668, jun 1990.

[384] T. Yano; Y. Nabeta; K. Saito; A. Watanabe. Acousto-optic filter. U.S. Patent 3,953,107, 1976.

[385] M. D. Webb, S. T. Cundiff, and D. G. Steel. Observation of time-resolved picosecond stimulated photon echoes and free polarization decay in gaas/algaas multiple quantum wells. *Phys. Rev. Lett.*, 66(7):934–937, Feb 1991.

[386] W. H. Weber and C. F. Eagen. Energy transfer from an excited dye molecule to the surface plasmons of an adjacent metal. *Opt. Lett.*, 4(8):236–238, Aug 1979.

[387] M. Wegener, D. S. Chemla, S. Schmitt-Rink, and W. Schäfer. Line shape of time-resolved four-wave mixing. *Phys. Rev. A*, 42(9):5675–5683, Nov 1990.

[388] A. Weiner. *Ultrafast optics*. John Wiley and Sons, Inc., Hoboken, NJ, 2009.

[389] A. M. Weiner. Femtosecond optics pulse shaping and processing. *Prog. Quant. Electr.*, 19:161–237, 1995.

[390] A. M. Weiner. Femtosecond pulse shaping using spatial light modulators. *Rev. Sci. Instrum.*, 71(5):1929–1960, 2000.

[391] A. M. Weiner, S. De Silvestri, and E. P. Ippen. Three-pulse scattering for femtosecond dephasing studies: theory and experiment. *J. Opt. Soc. Am. B*, 2(4):654–662, Apr 1985.

[392] Andrew M. Weiner and Erich P. Ippen. Novel transient scattering technique for femtosecond dephasing measurements. *Opt. Lett.*, 9(2):53–55, Feb 1984.

[393] Andrew M. Weiner and Erich P. Ippen. Novel transient scattering technique for femtosecond dephasing measurements. *Opt. Lett.*, 9(2):53–55, Feb 1984.

[394] D. E. Leaird; A. M. Weiner. Femtosecond direct space-to-time pulse shaping. *IEEE Journal of Quantum Electronics*, 37(4):494–504, 2001.

[395] B. Wherrett, A. Smirl, and T. Boggess. Theory of degenerate four-wave mixing in picosecond excitation-probe experiments. *Quantum Electronics, IEEE Journal of*, 19(4):680 – 690, apr 1983.

[396] T. A. Wiggins and Alfred Salik. Temporary gratings on germanium. *Applied Physics Letters*, 25(8):438 –440, oct 1974.

[397] G. W. Willard. Criteria for normal and abnormal ultrasonic light diffraction effects. *J. Acoust. Soc. Am.*, 21(2):101–108, 1949.

[398] J.P. Woerdman and B. Bölger. Diffraction of light by a laser induced grating in si. *Physics Letters A*, 30(3):164 – 165, 1969.

[399] S. Wolf and R. N. Tauber. *Silicon processing for the VLSI era*. Lattice Press, Sunset Beach, Calif., 2nd edition, 2000.

[400] Tatsuo Yajima and Hirotoshi Souma. Study of ultra-fast relaxation processes by resonant rayleigh-type optical mixing. i. theory. *Phys. Rev. A*, 17(1):309–323, Jan 1978.

[401] Tatsuo Yajima, Hirotoshi Souma, and Yuzo Ishida. Study of ultra-fast relaxation processes by resonant rayleigh-type optical mixing. ii. experiment on dye solutions. *Phys. Rev. A*, 17(1):324–334, Jan 1978.

[402] Tatsuo Yajima and Yoichi Taira. Spatial optical parametric coupling of picosecond light pulses and transverse relaxation effect in resonant media. *Journal of the Physical Society of Japan*, 47(5):1620–1626, 1979.

[403] Suxia Yan and Howe-Siang Tan. Phase cycling schemes for two-dimensional optical spectroscopy with a pump-probe beam geometry. *Chemical Physics*, 360(1-3):110 – 115, 2009.

[404] Y. J. Yan and S. Mukamel. "electronic dephasing, vibrational relaxation, and solvent friction in molecular nonlinear optical line shapes. *J. Chem. Phys.*, 89:5160, 1988.

[405] T. Yano, M. Kawabuchi, A. Fukumoto, and A. Watanabe. Teo2 anisotropic light deflector without midband degeneracy. *Appl. Phys. Lett.*, 26:689, 1975.

[406] A. Yariv. *Quantum Electronics*. John Wiley and Sons, Inc., New York, 3rd edition, 1989.

[407] A. Yariv and P. Yeh. *Optical Waves in Crystals*. John Wiley and Sons, Inc., Hoboken, NJ, 2003.

[408] John A. Yeazell and C. R. Stroud Jr. Observation of spatially localized atomic electron wave packets. *Phys. Rev. Lett.*, 60(15):1494–1497, Apr 1988.

[409] Michael K. Yetzbacher, Nadia Belabas, Katherine A. Kitney, and David M. Jonas. Propagation, beam geometry, and detection distortions of peak

shapes in two-dimensional fourier transform spectra. *J. Chem. Phys.*, 126(4):044511, 2007.

[410] Tianhao Zhang, Camelia Borca, Xiaoqin Li, and Steven Cundiff. Optical two-dimensional fourier transform spectroscopy with active interferometric stabilization. *Opt. Express*, 13(19):7432–7441, Sep 2005.

[411] Tianhao Zhang, Irina Kuznetsova, Torsten Meier, Xiaoqin Li, Richard P. Mirin, Peter Thomas, and Steven T. Cundiff. Polarization-dependent optical 2d fourier transform spectroscopy of semiconductors. *Proceedings of the National Academy of Sciences*, 104(36):14227–14232, 2007.

[412] Wei Zhang, Alexander O. Govorov, and Garnett W. Bryant. Semiconductor-metal nanoparticle molecules: Hybrid excitons and the nonlinear fano effect. *Phys. Rev. Lett.*, 97(14):146804, Oct 2006.

[413] Xuejun Zhu, Mark S. Hybertsen, and P. B. Littlewood. Quantum beats in photon echo from four-waving mixing. *Phys. Rev. Lett.*, 73(1):209, Jul 1994.

[414] R. Zimmermann. On the dynamical stark effect of excitons. the low-field limit. *physica status solidi (b)*, 146(2):545–554, 1988.

Vita

Thomas William Jarvis was born in London, England, on Halloween 1980, the son of William J. Jarvis and Susan R. H. Jarvis. He graduated as valedictorian of John Handley High School in 1999 before receiving a Bachelor of Science with high honors in Physics from the University of North Carolina in 2003. He worked at the Microelectronic Center of North Carolina prior to enrolling in the University of Texas at Austin as a graduate student in physics. He loves dogs and Indian food.

Permanent address: 116 Latane St.
Winchester, VA 22601

This dissertation was typeset with LaTeX[†] by the author.

[†]LaTeX is a document preparation system developed by Leslie Lamport as a special version of Donald Knuth's TeX Program.